

THÈSE DE DOCTORAT

Soutenue à Aix-Marseille Université
le 4 avril 2024 par

Rémy TORRO

High throughput analysis of dynamic single cell interactions imaged by multimodal optical microscopy

Discipline

Physique et Sciences de la Matière

Spécialité

Biophysique

École doctorale

ED 352 Physique et Sciences de la Matière

Laboratoire/Partenaires de recherche

Laboratoire Adhésion & Inflammation
Centre Interdisciplinaire de Nanosciences
de Marseille
CENTURI

Composition du jury

Alice NICOLAS
Directrice de Recherche
Université de Grenoble, LTMLab
Rapporteuse

David ROUSSEAU
Professeur
Université d'Angers, ImHorPhen
Rapporteur

Daniel SAGE
Ingénieur
EPFL, STI IMT LIB
Examineur

Loïc DUPRÉ
Directeur de Recherche
Université de Toulouse, INFINITY
Président du jury

Laurent LIMOZIN
Directeur de Recherche
Aix-Marseille Université, LAI
Directeur de thèse

Khaya SENGUPTA
Directeur de Recherche
Aix-Marseille Université, CINaM
Co-directrice de thèse

Affidavit

I, undersigned, Rémy Torro, hereby declare that the work presented in this manuscript is my own work, carried out under the scientific supervision of Laurent Limozin and Kheya Sengupta, in accordance with the principles of honesty, integrity and responsibility inherent to the research mission. The research work and the writing of this manuscript have been carried out in compliance with both the french national charter for Research Integrity and the Aix-Marseille University charter on the fight against plagiarism.

This work has not been submitted previously either in this country or in another country in the same or in a similar version to any other examination body.

Marseille 5 February 2024



This work is licensed under [Creative Commons Attribution-NonCommercial-NoDerivatives 4.0 International Public License](https://creativecommons.org/licenses/by-nc-nd/4.0/)

À mes grands-mères

Liste de publications et participation aux conférences

Liste des publications et/ou brevets réalisées dans le cadre du projet de thèse :

1. Rémy TORRO, Beatriz DÌAZ-BELLO, Dalia El ARAWI, Lorna AMMER, Patrick CHAMES, Kheya SENGUPTA et Laurent LIMOZIN. *Celldetective : An AI-enhanced Image Analysis Tool for Unraveling Dynamic Cell Interactions*. 17 mar. 2024. DOI : 10.1101/2024.03.15.585250. URL : <https://www.biorxiv.org/content/10.1101/2024.03.15.585250v1> (visité le 08/04/2024). preprint. Submitted to *Communications Biology*.
2. Beatriz BELLO, Rémy TORRO, Adrien AIMARD, Florian DUPUY, Lorna AMMER, FRANCESCO PIAZZA, Brigitte KERFELEC, Patrick CHAMES et Laurent LIMOZIN. *AI-enhanced Real-Time Immune Killing Imaging : From Single Cell to Ensemble Assay*. preprint. In preparation.
3. Merlin SANICAS, Remy TORRO, Laurent LIMOZIN et Patrick CHAMES. *Antigen Density and Applied Force Control Enrichment of Nanobody-Expressing Yeast Cells in Microfluidics*. 3 jan. 2024. DOI : 10.1101/2024.01.03.574015. URL : <https://www.biorxiv.org/content/10.1101/2024.01.03.574015v1> (visité le 04/01/2024). preprint. Submitted to Lab-on-a-chip.
4. Farah MUSTAPHA, Martine PELICOT-BIARNES, Remy TORRO, Kheya SENGUPTA et Pierre-henri PUECH. *Cellular Forces during Early Spreading of T Lymphocytes on Ultra-Soft Substrates*. 11 fév. 2022. DOI : 10.1101/2022.02.11.480084. URL : <https://www.biorxiv.org/content/10.1101/2022.02.11.480084v1> (visité le 10/11/2022). preprint

Participation aux conférences et écoles d'été au cours de la période de thèse :

1. EMBO workshop : “ImmunoBiophysics : From fundamental physics to understanding the immune response”, contributed talk and poster, 09 – 14 April 2023, École des Houches, Les Houches, France
2. GDR AQV, IMABIO workshop : “New microscopies for cell biology”, contributed co-talk with Beatriz Bello, 13 December 2022, Institut Jacques Monod, Paris, France

3. Physics of Living Matter Symposium 2022 - PLM16, poster, 27–28 September 2022, Palais du Pharo, Marseille, France

Résumé

Un défi actuel dans l'analyse d'images biologiques est la quantification de cellules uniques au sein de populations de cellules à partir de vidéos multimodales en microscopie. Bien que de nombreux outils soient disponibles pour segmenter, traquer et mesurer des cellules, l'assemblage d'un pipeline d'analyse d'images pour un nouveau système biologique nécessite des compétences de codage avancées et, très souvent aujourd'hui, des connaissances approfondies dans les techniques de supervision de modèles de *Deep learning*, avec la nécessité d'annoter pour entraîner les modèles. Certains logiciels tout-en-un ont été développés pour effectuer l'analyse d'images de cellules uniques, mais aucun d'entre eux n'est particulièrement adapté au traitement et à la visualisation de données dynamiques, manquant d'une description en signaux des cellules uniques. De plus, les fonctions d'annotation et d'entraînement des données de *Deep learning* sont systématiquement absentes de ces logiciels, limitant la transférabilité à de nouveaux systèmes biologiques. Nous avons développé Celldetective, un logiciel open-source qui intègre à la fois des techniques de segmentation basées sur l'IA et des techniques traditionnelles, un algorithme de *tracking* personnalisable et l'analyse automatisée des signaux dans une interface graphique conviviale, offrant des capacités complètes de visualisation interactive, d'annotation et d'entraînement. Celldetective prend nativement en charge une description en cellule unique pour une ou deux populations de cellules en coculture, en présence potentielle d'autres populations cellulaires, complétée par un mécanisme de voisinage. Nous démontrons son applicabilité à un nouvel essai de cytotoxicité cellulaire dépendante des anticorps (ADCC) basé sur de la microscopie optique, afin d'évaluer l'efficacité de nouveaux anticorps à double spécificités et de déchiffrer les interactions individuelles entre les cellules cibles et les cellules effectrices immunitaires. Par ailleurs, nous appliquons Celldetective à un système de cellules effectrices immunitaires s'étalant sur des substrats fonctionnalisés imagés à l'aide de la microscopie à contraste interférentiel par réflexion (RICM), pour laquelle nous décrivons des événements de cellules uniques consécutifs et effectuons une exploration approfondie des signaux. Nous étudions la possibilité d'accélérer le processus de reconstruction de topographie cellulaire avec du *Deep learning*. Au-delà de la démonstration de l'applicabilité, pour les deux applications, nous nous appuyons sur la description en cellule unique pour mieux caractériser et comprendre les systèmes biologiques étudiés.

Mots clés : analyse d'images biologiques, cellules uniques, RICM, vidéomicroscopie, Deep learning, ADCC

Abstract

A current challenge in bioimage analysis is the quantification of single cells among cell populations from multimodal time-lapse microscopy images. While a plethora of tools are available to perform cell segmentation, tracking and measurements, assembling an image analysis pipeline for a new biological system requires advanced coding skills and, very often nowadays, extensive knowledge in Deep-learning supervision techniques, with the need to perform annotations to train models. While some all-in-one softwares emerged to perform single-cell image analysis, none of them are particularly adapted to process and visualize time-lapse data, lacking a single-cell signal description. In addition, Deep-learning data annotation and training features are systematically absent from these softwares, limiting transferability to new biological systems. We developed Celldetective, an open-source software that integrates Deep-learning and traditional segmentation techniques, a customizable tracking algorithm, and automated signal analysis into a user-friendly graphical user interface, offering complete interactive visualization, annotation, and training capabilities. Celldetective natively supports a single-cell description for up to two cell populations in co-culture, potentially in the presence of other cell populations, complete with a neighborhood scheme. We demonstrate its applicability to a novel optical microscopy based antibody-dependent cellular cytotoxicity (ADCC) assay, to assess the efficiency of new bispecific antibodies as well as decipher one-to-one interactions between target and immune effector cells. In addition, we apply Celldetective to a system of immune effector cells spreading on functionalized substrates imaged using reflection interference contrast microscopy (RICM), for which we describe consecutive single-cell events and perform in-depth signal and feature exploration. We study the possibility of accelerating the cell topography reconstruction process with *Deep learning*. Going beyond a demonstration of applicability, for both applications we build on the single-cell description to characterize and better understand the biological systems under scrutiny.

Keywords: bioimage analysis, single-cells, RICM, time-lapse microscopy, Deep learning, ADCC

1 Résumé étendu en français

1.1 Introduction

Le problème de détection est au cœur de l'analyse d'image. Une bonne détection permet des mesures précises. Pendant longtemps, la détection de cellules sur les images biologiques était le facteur limitant à la quantification des systèmes biologiques. Pour obtenir des améliorations, il fallait attendre l'introduction de nouvelles techniques en microscopie ou de nouvelles façons de préparer les échantillons biologiques. L'introduction des premiers modèles de convolution à la fin des années 1990 a changé le paradigme [101]. Pour la première fois, des modèles pouvaient apprendre à détecter directement à partir d'images, en propageant les erreurs de détection dans leur poids pour mieux s'optimiser. Cette innovation a pris de l'élan au début des années 2010, révolutionnant les problèmes de classification d'images [95], de régression et de segmentation avec U-net en 2016 [144].

L'imagerie cellulaire doit faire un compromis sur les résolutions spatiales et temporelles ainsi que sur le débit. En effet, bien qu'il soit techniquement possible d'acquérir de nombreuses images par seconde avec une résolution spatiale inférieure au micron, les capacités de stockage sont limitées et le champ de vue peut être trop restreint. La microscopie optique permet d'observer de nombreuses cellules en même temps, à une résolution temporelle comprise entre moins d'une seconde et plusieurs heures, avec un grossissement permettant d'imager des populations de cellules tout en pouvant discerner clairement les cellules uniques, ainsi que des molécules biologiques. Pour beaucoup d'applications, les techniques sans label comme l'observation en fond clair suffisent. Si des structures cellulaires spécifiques doivent être imagées tout en conservant un haut débit, la technique d'épifluorescence est appropriée. Pour des phénomènes proches de la surface des cellules ou dans le contexte de l'adhésion cellulaire, les techniques de microscopie optique de surface comme la microscopie de fluorescence par réflexion totale interne (TIRF) [55] ou la microscopie à contraste interférentiel de réflexion (RICM) [104] sont les meilleurs choix.

De nombreuses méthodes s'appuient sur des mesures moyennes sur une population de cellules, masquant les hétérogénéités entre cellules [112]. Des cellules identiques génétiquement peuvent quand même se comporter différemment [58]. Ces différences peuvent provenir d'un contexte cellulaire inégal, des différences dans les cellules de voisinage, des asymétries dans la distribution de nutriments ou même des phénomènes moléculaires aléatoires dans l'expression de leur gènes affectant

le phénotype [81, 109, 164]. Imager des cellules uniques avec ou sans marqueurs fluorescents donne des informations précieuses sur la localisation de protéines, la distribution des organelles, les morphologies et bien plus. Les nouvelles techniques d'analyse d'images en Deep learning permettent de détecter les cellules presque aussi bien que l'œil humain, à très haut débit, remplaçant petit à petit les méthodes traditionnelles dans les pipelines d'analyses d'images. Néanmoins, les connaissances en programmation et en Deep learning requises pour implémenter de telles techniques restent un frein pour de nombreux laboratoires.

Dans cette thèse, nous allons introduire dans un premier temps un nouveau logiciel, *Celldetective*, pour analyser des cellules uniques au sein de populations cellulaires en interactions, à partir de vidéos de microscopie à plusieurs canaux. La première partie décrit en détail les fonctionnalités du logiciel et les difficultés rencontrées. Puis, nous explorons deux applications pour des systèmes biologiques dans le contexte du système immunitaire. Dans la première application, nous appliquons l'analyse de cellules uniques à deux populations directement en interactions : des cellules modèles du cancer du sein MCF-7 et des cellules effectrices immunitaires, les *natural killer* (NK), imagée en épifluorescence et fond-clair au microscope. Pour la deuxième application, nous appliquons l'analyse de cellules uniques pour étudier des cellules NK s'étalant sur des surfaces recouvertes d'anticorps, imagés en RICM.

1.2 Celldetective

1.2.1 Rationnel court

Malgré des efforts notables dans le développement de logiciels conviviaux qui intègrent des méthodes de pointe pour faire de l'analyse de cellules uniques, très peu sont conçus pour des vidéos en microscopie, et encore moins pour des problèmes multimodaux où des populations de cellules sont mélangées et ne peuvent être séparées qu'en exploitant cette information multimodale. Nous avons décidé de créer un logiciel qui intègre les fonctionnalités suivantes :

- Une analyse de cellules uniques complète : segmenter, suivre et mesurer les propriétés des cellules à chaque pas de temps, détecter les événements à partir de signaux de cellules uniques pour chaque population d'intérêt.
- Une intégration de solutions de pointe : nous exploitons des outils de segmentation de référence (StarDist [155] et Cellpose [169]) ainsi qu'un algorithme de suivi personnalisable bTrack [176], et le visualiseur napari [1] quand c'est possible. Nous interfaçons ces algorithmes pour les intégrer convenablement et les rendre conviviaux pour le public visé, dans le contexte d'applications difficiles.
- L'annotation d'événements et l'interprétation associée : nous développons un cadre généraliste pour annoter et automatiser la détection d'événement à partir

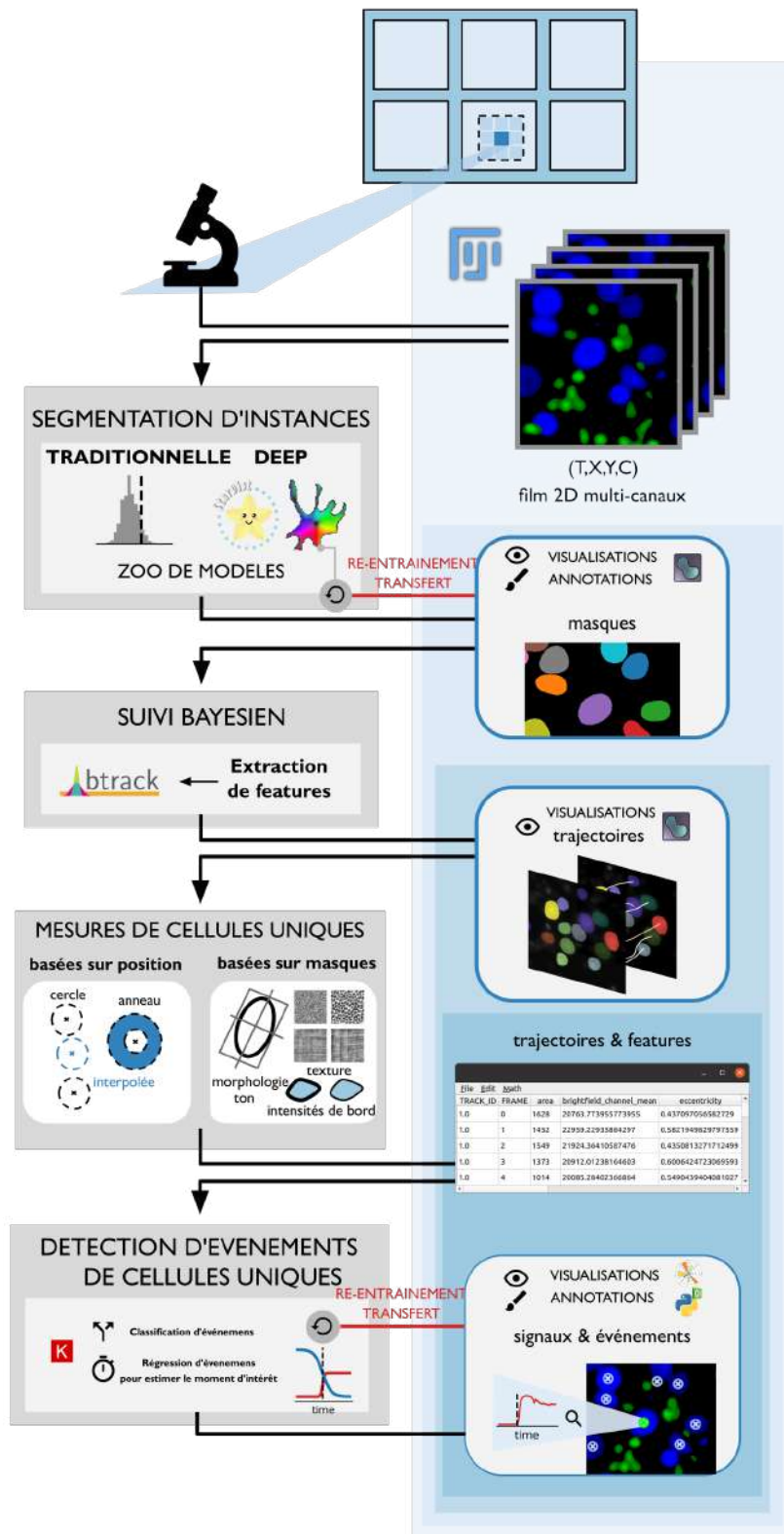


FIGURE 1.1 – Description fonctionnelle de CellDetective. Des vidéos de microscopie multimodales sont données en entrée au logiciel, dans une structure de fichiers mimant les échantillons multi-puits. Les modules d'analyse sont montrés du côté gauche. La sortie et les modules de visualisation sont montrés à droite. La population cellulaire d'intérêt peut être segmentée en utilisant soit un pipeline de segmentation traditionnel ou un modèle de Deep learning. Les masques de sortie peuvent être visualisés dans napari, corrigés et exportés en annotations d'entraînement pour un nouveau modèle de DL, plus spécialisé. Les masques sont fournis à bTrack avec l'option d'ajouter des mesures de cellules uniques pour améliorer le suivi des cellules. Les trajectoires de sortie peuvent être visualisées dans napari. Des mesures morphologiques, d'intensités ou de texture peuvent être faites à partir des masques ou des positions. Les signaux de cellules uniques peuvent être classifiés par les modèles de DL et explorés dans une interface désignée pour l'annotation d'événements de cellules uniques, facilitant l'export de signaux annotés pour entraîner des modèles de DL.

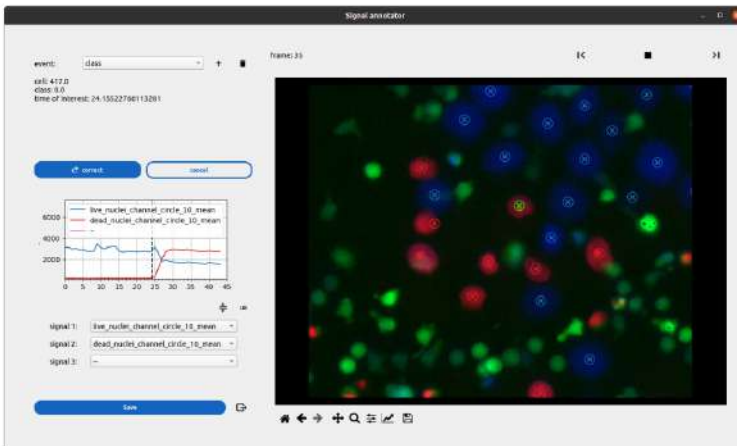
de signaux de cellules uniques, en classifiant et en régressant les signaux avec des modèles de Deep learning. Nous définissons les réponses de survie de populations à partir des événements de cellules uniques.

- Interactions entre cellules : nous proposons un mécanisme de voisinage pour connecter des mesures de deux populations indépendantes en co-culture.
- Personnalisation des modèles de Deep learning : nous proposons aux utilisateurs de spécialiser des modèles de Deep learning sur leurs données avec un minimum d'efforts en facilitant la création d'une base de données d'annotations et l'entraînement ou le réentraînement de ces modèles avec une interface graphique.
- Analyse dans le logiciel : nous introduisons des modules pour faire des figures représentant les données de cellules uniques et comparer des conditions biologiques.
- Logiciel accessible aux biologistes sans expérience en codage. Le logiciel, les bases de données et modèles associés sont présentés en *open-source* pour encourager la transparence et la reproductibilité.

Nous espérons que ce logiciel complètement *open-source* peut simplifier et démocratiser l'accès à une analyse de cellules unique précise pour des chercheurs qui n'ont pas le temps ou l'envie d'apprendre tous les détails des modules qui composent le logiciel. Dans les semaines et mois à venir, nous continuerons de mettre à jour les différents modules pour fournir plus de fonctionnalités, guidés par les besoins des utilisateurs, afin de converger vers une solution complète pour l'analyse de cellules uniques.

1.2.2 Focus sur l'analyse de signaux

Parmi tous les défis relevés dans la conception de Celldetective, nous mettons la lumière sur le formalisme d'annotation et d'interprétation de signaux de cellules uniques permettant de caractériser des événements cellulaires. La figure 1.2 synthétise les éléments-clés de ce nouveau cadre d'analyse. Premièrement, nous introduisons une classification d'événements cellulaires en trois classes : 1) l'événement d'intérêt se produit pendant l'observation, 2) l'événement ne se produit pas pendant l'observation, 3) l'événement s'est déjà produit ou autre. Avec cette description minimale, nous pouvons facilement construire des courbes de survie décrivant la probabilité qu'un événement ne se soit pas produit au cours du temps, pour tout événement d'intérêt. Pour rendre conviviale et pratique cette caractérisation, nous avons conçu un outil de visualisation des cellules uniques dynamique (figure 1.2a). Un film interactif est diffusé en boucle. Les positions de toutes les cellules suivies sont représentées et évoluent avec le film. En cliquant sur une cellule, l'utilisateur peut visualiser les signaux associés, qu'ils soient morphologiques, texturaux ou des intensités. L'utilisateur peut définir un événement d'intérêt et attribuer chaque cellule à une classe parmi les trois évoquées ci-dessus vis-à-vis de l'événement d'intérêt.



MODEL 1: CLASSIFICATEUR
Les signaux contiennent un événement ou pas

MODEL 2: REGRESSEUR
s'il y a un événement, quand ?

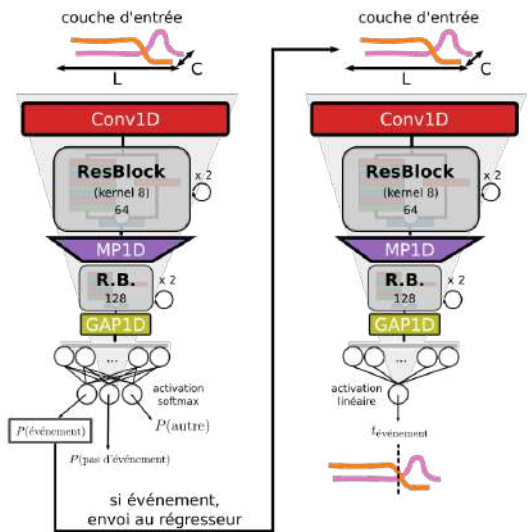


FIGURE 1.2 – Formalisme de caractérisation de signaux dans Celldetective. a) Outil d'annotations de signaux de cellules uniques dans Celldetective, illustré pour des mesures de mort cellulaire avec une composition RGB d'un film de cellules cancéreuses tuées par des cellules immunitaires. Une cellule cancéreuse tuée voit son noyau devenir rouge. b) Détection d'événements par des modèles de Deep learning. La détection d'un changement synchronisé dans deux signaux de fluorescence (intensité *versus* temps) est faite en série par un modèle classificateur et un modèle de régression. Dans cet exemple, le classificateur indique la probabilité qu'une mort cellulaire soit survenue pendant l'observation à partir des signaux. La régression indique le moment de mort, si celle-ci a eu lieu.

Les annotations peuvent être exportées pour entraîner des modèles de Deep learning qui vont classifier et faire une régression sur les signaux d'intérêt pour détecter le moment de l'événement s'il a lieu (figure 1.2b).

1.3 Test d'interactions entre cellules

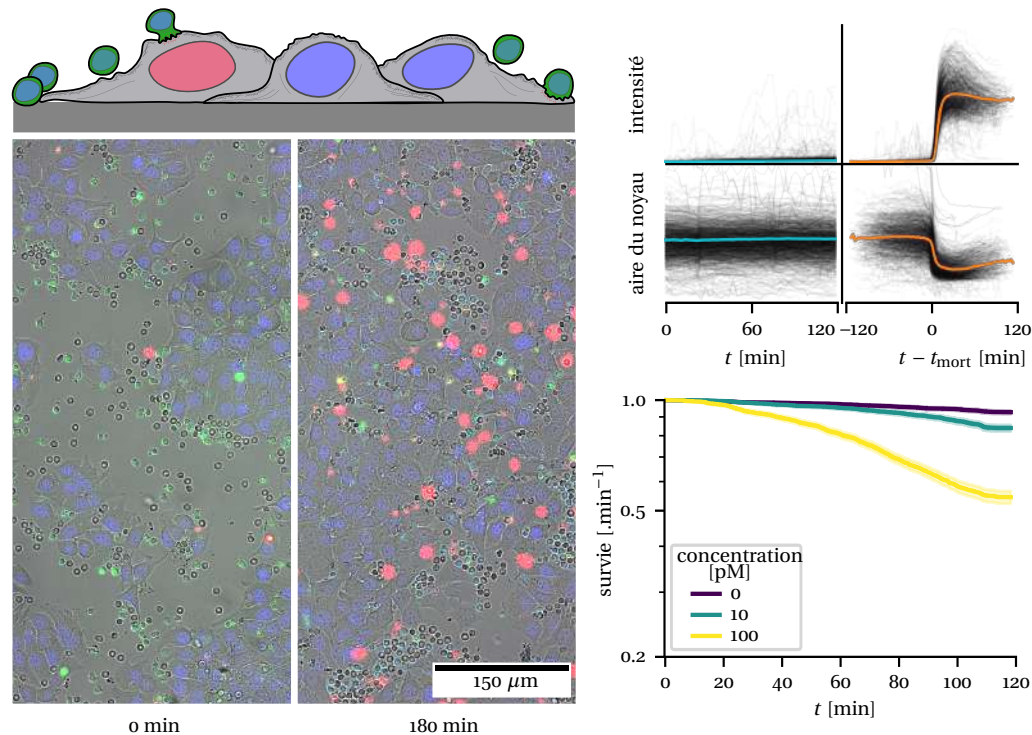


FIGURE 1.3 – Panel sur l'ADCC. a) Vue schématique d'une co-culture de cibles MCF-7 et NKs testant l'ADCC, avec un anticorps bispécifique. Image composite multimodale représentative, avec les noyaux des cibles labellisés en bleu, les noyaux des cellules mortes en rouge et les NKs en vert, à deux pas de temps (initialement et après trois heures). b) Signaux d'intensité de PI et de l'aire apparente du noyau des MCF-7 pour les cellules qui ne meurent pas (gauche) et les cellules qui meurent (droite). Courbes de survie des MCF-7 à différentes concentrations de l'anticorps bispécifique.

Dans le cadre de la cytotoxicité à médiation cellulaire dépendante des anticorps (ADCC), des cellules immunitaires du système immunitaire inné, les cellules tueuses naturelles (NK) reconnaissent et détruisent des cellules cibles, comme des cellules cancéreuses, qui ont été recouvertes d'anticorps [126]. Nous nous intéressons plus particulièrement à une co-culture de cellules NK humaines en interactions avec des cellules modèles du cancer du sein MCF-7, en présence d'un anticorps bispécifique avec une affinité pour un récepteur des NKs d'un côté et pour un récepteur sur-exprimé à la surface des MCF-7 de l'autre. L'anticorps bispécifique forme un pont moléculaire entre la cellule immunitaire et la cellule cancéreuse, encourageant la formation de synapse. La synapse peut conduire au relâchement de granzymes et perforines de la NK, déclenchant la mort de la cellule cancéreuse [163].

Nous appliquons l'analyse de cellules uniques à un test de l'ADCC à haute densité cellulaire permettant d'équilibrer le débit et la résolution temporelle. Le système est imagé avec des techniques peu onéreuses et disponibles dans la plupart des

laboratoires : la microscopie en épifluorescence et en fond-clair, avec des marqueurs fluorescents introduits au moment de l'observation, sans préparation préalable des cellules (une image multimodale représentative est illustrée dans la figure 1.3a). Des échantillons multi-puits sont utilisés pour imager simultanément différentes conditions biologiques comme des concentrations différentes d'anticorps bispécifiques ou des anticorps bispécifiques différents. Les expériences ont été menées par Beatriz Diaz-Bello, Lorna Ammer et Florian Dupuy au laboratoire Adhésion & Inflammation (LAI).

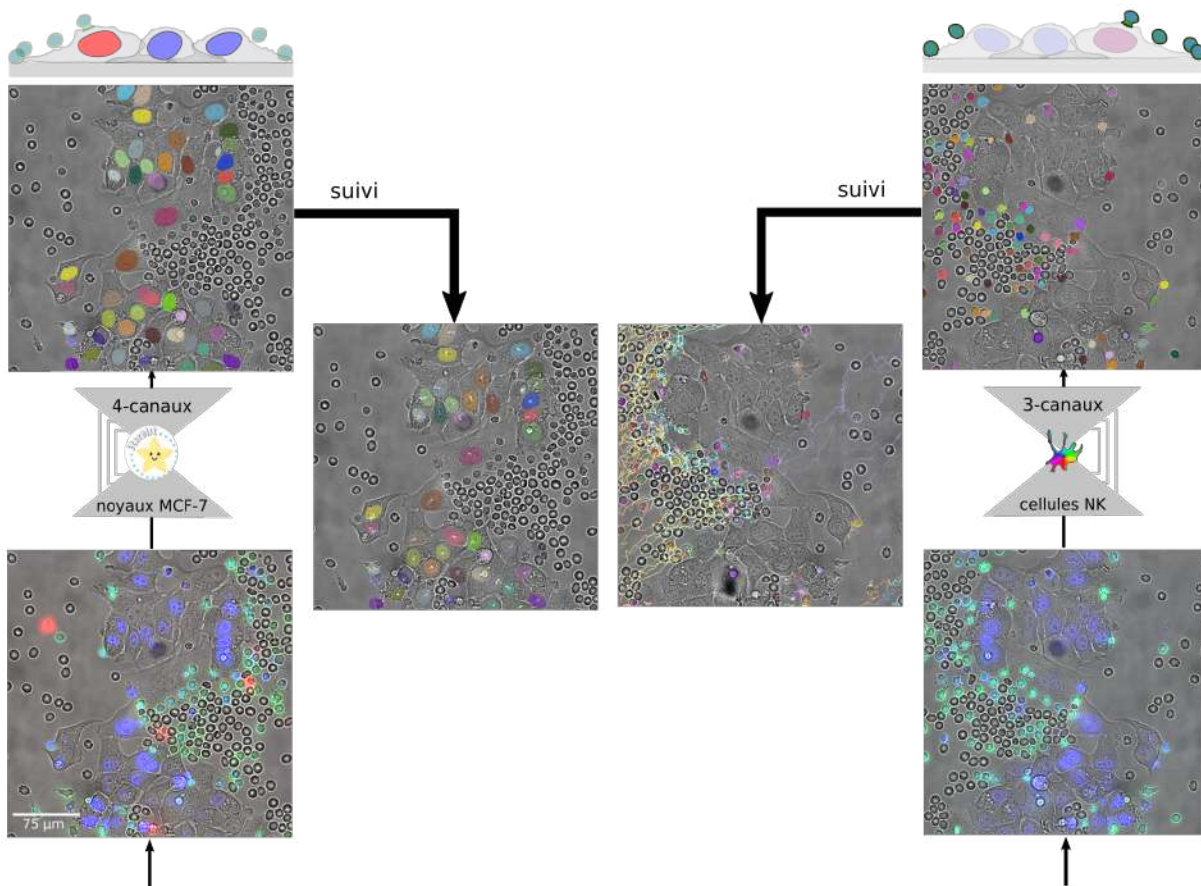


FIGURE 1.4 – Pipeline de détection des cellules uniques dans le test d'ADCC. a) un modèle StarDist multimodal segmente spécifiquement les noyaux des MCF-7 en interprétant quatre canaux simultanément (fond-clair, PI, Hoechst et CFSE). Les masques sont envoyés à bTrack pour suivre les noyaux avant de mesurer toutes les features. b) Un modèle Cellpose multimodal segmente spécifiquement les cellules NKs en interprétant trois canaux (fond-clair, CFSE et Hoechst). Les masques sont envoyés à bTrack pour suivre les cellules avant de les mesurer.

Le système est imagé avec jusqu'à cinq canaux. Les principales modalités sont le fond-clair (permettant d'imager simultanément toutes les populations cellulaires), le marqueur nucléaire Hoechst (initialement donné aux MCF-7 seulement), le marqueur nucléaire propidium iodide (marquant toutes les noyaux de cellules mortes)

et le CFSE (un marqueur du cytoplasme des cellules NK). En pratique, les cellules NKs incorporent le marqueur Hoechst au cours du temps. Nous avons exploité Celldetective pour faire décrire avec une analyse de cellules uniques la population de cibles (MCF-7) et de cellules immunitaires (NKs) en développant des modèles spécifiques de segmentation comme illustré dans la figure 1.4. Les informations de co-présence spatiales entre les cellules des deux populations ainsi qu’au sein de la population ont été déterminées avec un calcul de voisinage dans Celldetective.

Nous avons exploité les signaux d’intensité PI ainsi que l’aire apparente des noyaux de chaque cellule cible unique pour détecter les événements de morts comme décrit dans la section 1.2.2. Les signaux de cellules uniques sont représentés dans la figure 1.3b. À partir de ces temps de morts nous avons pu établir des courbes de survie pour chaque condition biologique comme illustré dans la figure 1.3c. Nous avons ainsi mesuré la variabilité de la survie en fonction des donneurs de NKs, l’effet de différents anticorps et de leur concentration.

Poussant l’analyse plus loin, nous avons étudié l’effet du nombre de NKs dans le voisinage des cellules cibles sur leur chance de survie au cours du temps, ainsi que l’effet de la densité en cellules cibles sur les chances de survie des cibles. Nous avons caractérisé les changements de la dynamique des NKs en contact avec les cellules cibles, proposant des descripteurs pour déterminer automatiquement les couples tueurs / victimes.

1.4 Test d’interactions entre cellules et surfaces

Nous remplaçons les cellules cibles par un substrat couvert d’anticorps ou d’anti-corps bispécifiques. L’interface entre les cellules immunitaires et ces surfaces fonctionnalisées peut être imagée en grand détail en utilisant une technique de microscopie de surface comme la RICM [104]. La technique permet d’imager la lumière réfléchiée à chaque interface dans l’échantillon et les cellules. Cette lumière interfère, faisant apparaître des franges d’interférence sur les images RICM, reliées directement à la topographie du système (épaisseur de chaque couche, indices de réfraction).

Nous appliquons les méthodes d’analyse de cellules uniques à un test d’étalement cellulaire où des cellules NKs peuvent s’étaler sur des surfaces recouvertes d’anticorps bispécifiques. L’expérience illustrée ici a été conduite par Dalia El Arawi, au LAI. Comme illustré dans la figure 1.5a, les cellules étalées laissent des empreintes plus sombres que l’arrière-plan sur les images RICM, alors que les cellules proches de la surface ne s’étalant pas ressemblent à des blobs brillants. Nous caractérisons précisément les temps d’arrivée t_{contact} , où les cellules commencent à être visibles sur les images en RICM et les temps d’étalement t_{spread} où les cellules décident de s’étaler irréversiblement après une durée de survol $\Delta t = t_{\text{spread}} - t_{\text{contact}}$. Les signaux d’aire d’étalement et d’intensité des cellules uniques sont représentés dans la figure 1.5b. La survie en survol, représentant la probabilité de n’être toujours pas étalée après une durée t est représentée pour différentes concentrations d’anticorps

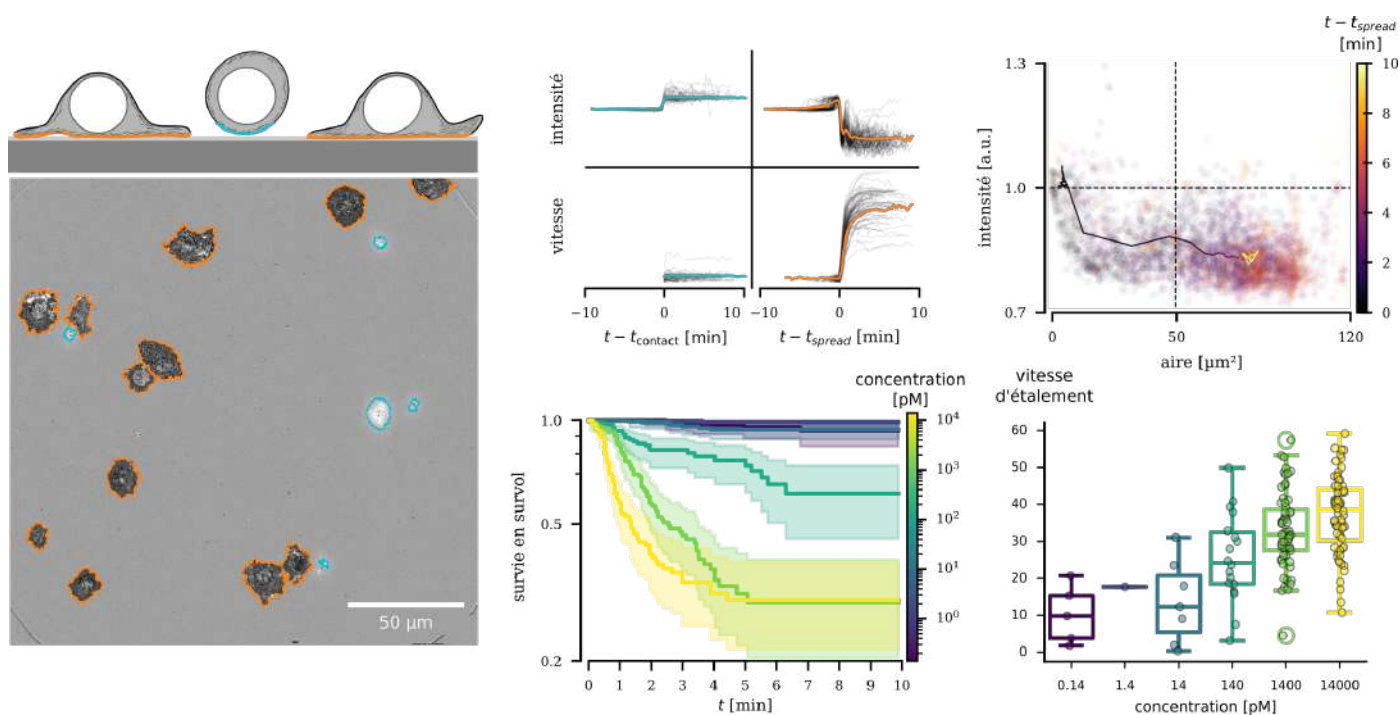


FIGURE 1.5 – Résumé graphique de l'étude de test d'étalement cellulaire. a) Schéma de l'étalement de cellules NK sur une surface recouverte d'antigènes, médié par un anticorps bispécifique. Des-sous : une image RICM normalisée représentative, montrant des cellules dans des états différents d'étalement. Les masques de segmentation sont montrés comme des contours colorés (orange pour les cellules étalées, cyan pour les cellules non étalées). b) L'intensité et l'aire de contact en fonction du temps, pour un groupe de cellules non étalées (gauche) et de cellules étalées (droite). Le temps de référence est le temps de première détection sur l'image RICM t_{contact} pour les cellules non étalées, et le moment du début d'étalement t_{spread} pour les cellules qui s'étalent. Les courbes colorées représentent les courbes moyennes sur toutes les cellules du groupe concerné. c) Représentation de l'intensité *versus* l'aire d'étalement pour les cellules étalées à tous les pas de temps, avec un code couleur représentant le temps qui s'est écoulé depuis le début de l'étalement. La ligne continue représente la trajectoire moyenne des cellules qui s'étalent dans cet espace. d) La survie de survol est définie comme $t_{\text{spread}} - t_{\text{contact}}$. e) La vitesse d'étalement initiale (en $\mu\text{m}^2 \cdot \text{min}^{-1}$) est représentée en fonction de la concentration en anticorps bispécifique.

bispécifique, montrant que les cellules s'étalent après un temps plus court quand il y a plus d'anticorps. Une fraction de cellules ne s'étale jamais comme on peut le voir à temps long (~ 10 min). Cette fraction décroît avec la concentration en anticorps. Nous caractérisons également la vitesse d'étalement des cellules uniques (figure 1.5e) qui s'étalent d'autant plus vite que la concentration d'anticorps est élevée. Nous comparons les signaux d'intensité et d'aire d'étalement synchronisés au temps d'étalement pour différentes conditions biologiques. Nous proposons une représentation dans l'espace (intensité *versus* aire) de cet étalement, faisant émerger des différences entre les anticorps.

Nous exploitons des mesures de texture faites à partir de la modalité en fond-

clair dans un test d'étalement de ce type pour explorer la possibilité de classifier des phénotypes courants de ce type d'expériences. Nous étudions également la possibilité de contourner les mesures et de classifier directement des images de cellules uniques en utilisant un classificateur DL.

Dans une dernière partie, nous nous intéressons à un problème intrinsèque à l'utilisation de la RICM qui est la reconstruction de la topographie d'une partie de cellules (comme le lamellipodium). Le processus est actuellement possible en simulant de nombreuses topographies possibles et en calculant l'intensité RICM qui doit en résulter. En comparant les intensités mesurées expérimentalement aux intensités simulées, nous pouvons remonter à la topographie la plus probable. Nous évaluons la possibilité d'utiliser des outils de DL supervisés pour accélérer ce processus. Nous remarquons que malgré un important effort d'acquisition multicolore pour enlever les plus de dégénérescences liées aux interférences possibles, celles-ci ne sont pas toutes résolues. Les formulations de DL classiques mélangent les solutions dégénérées rendant difficile l'interprétation de résultats produits par un modèle DL.

Remerciements

Avant toute chose, je tiens à remercier mes directeurs de thèse Laurent Limozin et Kheya Sengupta de m'avoir accompagné pendant ces trois belles années pleines de projets, de m'avoir laissé suivre et fructifier mes passions scientifiques, de m'avoir encouragé à travailler avec les personnes de mon entourage et de m'avoir apporté un soutien moral, scientifique et administratif en périodes de doutes. Le suivi régulier et la rigueur scientifique de Laurent m'a permis d'explorer des terrains sur lesquels je n'aurais jamais mis les pieds sans m'égarer. L'esprit de compromis de Kheya m'ont permis de sortir la tête haute d'impasses dans les eaux troubles de la biophysique. Elle m'a accordé sa confiance sur les bancs de la fac, et je ne la remercierai jamais assez pour cela.

Je remercie mes rapporteurs Alice Nicolas et David Rousseau d'avoir accepté de se plonger dans mes travaux de recherche. Je remercie également les membres du jury de me donner de leur temps pour cette ultime épreuve académique.

Je remercie chaleureusement mon organisme financeur Centuri et l'équipe de management, passée et présente, Melina, Jasmina, Marlène, Simon pour ne citer qu'eux, de m'avoir accordé leur confiance et d'avoir organisé de mémorables excursions ponctuant chaque année de thèse.

Je remercie les membres de mon comité de suivi individuel, Pierre Recouvreux, Stéphane Ayache et Pierre Müller de m'avoir apporté un regard scientifique et stratégique sur mes travaux de recherche. Je remercie tout particulièrement Pierre R. de m'avoir introduit à la biophysique en tant que professeur ainsi qu'en tant que superviseur de stage, m'apportant un suivi régulier malgré la singularité du COVID-19.

Je tiens à remercier tous mes collaborateurs, passés, présents, et futurs, Patrick Chames, Brigitte Kerfelec, Francesco Piazza, Beatriz Díaz-Bello, Lorna Ammer, Florian Dupuy de participer aux réflexions sur les problématiques de l'ADCC, Marie Dessard et Yannick Hamon sur les problématiques de l'étalement cellulaire, et Pierre-Henri Puech, qui a trouvé moyen de m'impliquer dans tous ses projets au LAI (thèses de Farah, Marie, Jana). En plus d'assumer son rôle de modérateur de l'humeur des étudiants à plein temps, Pierre-Henri est au centre de certaines de mes plus belles discussions pendant ces trois années de recherche, qu'elles soient scientifiques, culturelles, politiques, sociétales ou œnologiques. Je remercie également tous les stagiaires qui ont travaillé sur les projets associés à ma thèse (ou pas), Yannis, Lorna, Mohammad, Corentin, Ksenija.

Je tiens tout particulièrement à remercier mon binôme scientifique, Beatriz. Sa patience et sa gentillesse m'ont motivé à plonger tête baissée dans l'ADCC, repoussant toujours un peu plus les limites de ce que je pensais réalisable. Grâce à elle,

je n'ai jamais ressenti qu'aller au travail était une corvée, je savais que de belles discussions et de nouveaux problèmes stimulants m'attendaient chaque jour.

Je remercie les anciens du LAI, qui m'ont parfois formé, Julien, dont la réplique en carton qui l'a remplacé pendant son absence COVID trône toujours au-dessus de mon bureau, Dalia, Jim. En particulier, je remercie Dalia de m'avoir sorti de mes nombreuses crises existentielles face au microscope. Je remercie Marie-Pierre Valignat et Arnaud Sergé d'avoir pris le temps de m'expliquer en détail, crayon à papier en main, une partie de leurs travaux de recherche. Au même titre, je remercie Thierry Galliano d'avoir comblé mon manque de confiance dans la manipulation d'interfaces graphiques, à un moment critique dans ma thèse.

Je remercie les collègues du Cinam de m'avoir accueilli lors de mes brefs passages, en particulier Ahmed, Mariem et Zakaria ainsi que toute l'équipe PIV. Je remercie Olivier, Martine, qui peut sortir un paquet de café aux moments les plus critiques, Florian, Thi-Thien, Stéphanie, le pôle administratif Sophie et Christine, Dylan, les nouveaux Aurélien et Magali, pour toutes ces interactions dans la cuisine et les couloirs. Je m'excuse des bouchons que j'ai pu provoquer en salle de culture cellulaire, je n'étais pas dans mon élément. Je remercie chaleureusement Dominique pour tout ce sucre apporté lors de ses passages très appréciés. Je remercie infiniment Philippe pour sa générosité sans limite et sa bonne humeur, ses grands apéros, sa confiance. Je remercie également tout le LAI de m'avoir accueilli.

En particulier, je remercie les collègues devenus amis, Dalia, Beatriz, Julien, Loriane, Luc, Jim, Sarah, Merlin, Emma, Lisa, Ying, Marc, Jana, Marie pour toutes les discussions scientifiques et carrément pas scientifiques, ces apéros, ces raclettes – pour certains seulement comme les absents aiment tant me le faire remarquer – ces excursions parfois extrêmes : je vous ai fait regarder un lever de soleil à 3000 mètres par -10 °C pour certains, je vous ai fait perdre votre sang-froid sur des randonnées techniques pour d'autres. Merci de m'avoir accompagné pendant ces années.

Je remercie mes compatriotes de semelles et de bières Dorian, Victor, Hugo, Nicolas, Hélène, d'être passés me voir de temps en temps ou d'avoir pris de mes nouvelles pendant ces trois années. Et puis, disons-le franchement, je ne vais pas avoir beaucoup d'autres occasions dans ma vie d'écrire des remerciements.

Je remercie ma petite chienne de 17 ans de m'avoir apporté un amour inconditionnel pendant toutes ces années et dont la garde occasionnelle m'a rappelé qu'il y a d'autres choses importantes que le travail. Et je croise les doigts de pouvoir la prendre dans mes bras en tant que jeune docteur.

Je remercie ma famille, tantes et oncles, cousins et cousines, pépé et en particulier mes grand-mères de m'avoir accompagné pendant cette thèse, en prenant très souvent de mes nouvelles, en soutenant tous mes choix. En particulier, je pense à mamie qui ne verra pas l'aboutissement de cette période de ma vie, mais qui n'a jamais douté que j'allais y arriver.

Je remercie mes parents et leur coloc, ma sœur, pour leur soutien sans faille, tous ces repas, tous ces fous rires, tous ces bons moments ainsi que d'avoir accommodé tous mes besoins pendant toutes ces années. Je sais qu'ils ne m'appelleront jamais

docteur tant que je n'aurai pas la fiche de paie d'un docteur, mais bon... on verra bien!

Enfin, je remercie ma compagne Lama qui est la grande découverte de ma thèse. Tu es douce, patiente et très intelligente et tu m'as soutenu dans tous les passages à vide et autres moments difficiles, sans condition. Nous sommes tellement en phase que je suis certain que si je cite un grand maître Jedi, tu pourras en compléter les mots dans ton manuscrit :

“Do or do not...”

Table of contents

Affidavit	2
Liste de publications et participation aux conférences	4
Résumé	5
Abstract	6
1 Résumé étendu en français	7
1.1 Introduction	7
1.2 Celldetective	8
1.2.1 Rationnel court	8
1.2.2 Focus sur l'analyse de signaux	10
1.3 Test d'interactions entre cellules	12
1.4 Test d'interactions entre cellules et surfaces	14
Remerciements	17
Table of contents	20
List of figures	23
List of tables	27
List of acronyms	28
Behind the scenes : the cast	31
2 Introduction	32
2.1 The image analysis revolution	32
2.2 Cell imaging	34
2.3 Why do we need single-cell image analysis?	35
2.4 Single cells of the immune system	36
2.5 Contents of this thesis	37

3	Celldetective	38
3.1	Introduction	38
3.1.1	Building blocks of single cell analysis	38
3.1.2	Existing softwares for cell analysis	42
3.1.3	Rationale for Celldetective	44
3.2	Materials and methods	48
3.2.1	Environment, packages and libraries	48
3.2.2	Deep learning for signal quantification	50
3.2.3	Mathematical descriptors	55
3.3	Results	56
3.3.1	Experiment manager	56
3.3.2	Segmentation	60
3.3.3	Bayesian tracking	72
3.3.4	Single cell measurements	75
3.3.5	Single cell signal analysis	80
3.3.6	Generalizing survival analysis	88
3.3.7	Collapsed signal representations	91
3.3.8	Neighborhoods and cell-cell interactions	92
4	Cell-cell interaction assay	97
4.1	Introduction	97
4.1.1	ADCC and NK-engagers	97
4.1.2	Measuring ADCC without imaging	98
4.1.3	Imaging ADCC	98
4.1.4	Rationale	99
4.2	Materials and methods	99
4.2.1	Cells	99
4.2.2	Molecules : proteins and dyes	100
4.2.3	Microscopy and experimental protocol	102
4.2.4	Mathematical descriptors	103
4.2.5	Analysis	105
4.3	Results	109
4.3.1	Single-cell decription with Celldetective	109
4.3.2	Detection of cell death	118

4.3.3	Cell morphologies : MCF-7	123
4.3.4	Cell morphologies : primary NK	131
4.3.5	neighborhood	132
4.3.6	Target-centric survival analysis	137
4.3.7	Target-effector interactions	143
5	Cell-surface interaction assay	167
5.1	Introduction	167
5.1.1	RICM historical development	167
5.1.2	Cellular foot-print	168
5.1.3	Cell to surface distance	168
5.1.4	Rationale	169
5.2	Materials and methods	170
5.2.1	Substrate preparation	170
5.2.2	Cells	170
5.2.3	Microscopy techniques	170
5.3	Results	172
5.3.1	Anatomy of a RICM image	172
5.3.2	An improved RICM normalization technique	172
5.3.3	Alignment on surface defects	175
5.3.4	Single-cell analysis with Celldetective	175
5.3.5	Hovering survival of cells	179
5.3.6	Spreading dynamics	182
5.3.7	Texture for cell classification	187
5.3.8	Deep-learning classification of cross-modality phenotypes . . .	193
5.3.9	Cell topography reconstruction	196
	Conclusion and perspectives	202
	Bibliography	205
	Articles	223

List of figures

1.1	Description fonctionnelle de Celldetective.	9
1.2	Formalisme de caractérisation de signaux dans Celldetective.	11
1.3	Panel sur l'ADCC.	12
1.4	Pipeline de détection des cellules uniques dans le test d'ADCC.	13
1.5	Résumé graphique de l'étude de test d'étalement cellulaire.	15
2.1	U-net	33
2.2	Single-cell heterogeneity	36
3.1	The StarDist method.	39
3.2	The Cellpose method.	40
3.3	Functional description of Celldetective.	47
3.4	Celldetective's logo.	48
3.5	Main dependencies of Celldetective.	49
3.6	Min-max normalization	51
3.7	Principle of the resblock	53
3.8	Anatomy of a Deep Learning model	55
3.9	Main GUI.	58
3.10	Labeling the wells.	59
3.11	The threshold configuration wizard in action.	61
3.12	Applicability of generalist models.	66
3.13	Overview of segmentation options in Celldetective.	68
3.14	Using napari to visualize and correct segmentation output.	69
3.15	Training segmentation models.	71
3.16	GUI to configure the tracking parameters.	72
3.17	Post-processing on trajectories.	74
3.18	Napari to view trajectories and optimize bTrack	75
3.19	GUI to pilot single cell measurements.	76
3.20	GUI to pilot texture measurements.	77
3.21	GUI to pilot isotropic measurements.	78
3.22	The signal annotator	81
3.23	Signal model backbones.	85
3.24	Training signal models.	87
3.25	Left and right censorship of single cell events.	88
3.26	An interface to represent survival functions at multiple scales.	90
3.27	An interface to collapse signals to events.	91

3.28	Proposed neighborhood counting methods.	92
3.29	Refinements for immune-target interactions.	94
3.30	GUI for neighborhood configuration.	94
3.31	Isotropic neighborhood of a population with itself.	96
4.1	Principle of ADCC.	97
4.2	PI spectra	101
4.3	Hoechst 33342 spectra.	101
4.4	CFSE spectra.	102
4.5	Workflow for the correction of bulk fluorescence.	106
4.6	Step by step normalization of the Cell Index signal.	107
4.7	The ADCC assay under the microscope.	110
4.8	Multimodal models to detect MCF-7 nuclei.	111
4.9	Visualizing MCF-7 tracks with napari.	113
4.10	QC on lysis detection with Celldetective.	115
4.11	Visualizing NK tracks with napari.	117
4.12	PI as a marker of cell death.	118
4.13	Strong PI intake correlates well with apparent nucleus shrinking.	119
4.14	Chronology of PI intake and apparent nucleus shrinking.	121
4.15	PI-Hoechst co-interactions.	122
4.16	MCF-7 cells in the livecell dataset.	123
4.17	MCF-7 cells showcase a variety of morphologies.	124
4.18	Optimization scheme for Cellpose.	126
4.19	The optimized Cellpose segmentation is a good estimator of MCF-7 cell morphology.	127
4.20	MCF-7 nuclei are often off-center.	128
4.21	Nuclei are moderate estimators of MCF-7 cell morphology.	129
4.22	Voronoi partitions are poor estimators of MCF-7 cell morphology.	130
4.23	Comparison of MCF-7 cell shape estimators.	131
4.24	Morphologies of primary NK cells in the ADCC assay.	132
4.25	Neighborhood from manual annotations for MCF-7 cells	133
4.26	MCF-7 density and neighborhood.	134
4.27	Isotropic neighborhood optimization	135
4.28	CE4-28 bsAb concentration dependence within a single ADCC assay.	138
4.29	CE4-28 bsAb-concentration dependence within a single ADCC assay.	139
4.30	CE4-28 bsAb-concentration assessments show high variability across donors.	139
4.31	Lysis is measured stronger on HER2+ cells.	140
4.32	RTCA measurements correlate well with MCF-7 survival from microscopy images.	141
4.33	Spatial sub-sampling of the survival response shows high heterogeneities that cannot be explained by statistics alone.	142
4.34	Survival vs E:T.	143

4.35	E : T ratio decorrelates with NK neighbors.	144
4.36	Survival decrease with the number of NK neighbors.	145
4.37	Survival increases with target density.	146
4.38	Joint distribution of neighbors.	147
4.39	Lysis rate decomposition.	148
4.40	Lysis rate variation for each variable.	148
4.41	Antibody efficiency assessment at fixed neighbors.	149
4.42	Normalization : target survival in each condition.	150
4.43	Normalization : dynamic mean number of NK neighbor per cell.	151
4.44	Normalization : derivative of the survival.	151
4.45	Normalization : total lysis function.	152
4.46	Extraction of a constant lysis rate per NK neighbor.	153
4.47	Assessment of per-NK lysis rates and α functions for several donors.	154
4.48	NK cells move differently in and off-contact with the target cells.	155
4.49	NKs seem to slow down upon contact with targets.	157
4.50	Synapse annotation with Celldetective.	158
4.51	NKs in synapse exhibit different features.	159
4.52	More synapses than targets killed.	160
4.53	Empirical probability functions for determining NK killers.	162
4.54	Probability of a victim/killer pair.	162
4.55	Optimization of victim/killer detection parameters.	164
4.56	Optimized probability of a victim/killer pair.	166
5.1	The RICM microscopy technique.	171
5.2	Anatomy of a RICM image.	173
5.3	Improved pipeline for RICM normalization.	174
5.4	RICM normalization : histograms.	175
5.5	Alignment on surface defects.	176
5.6	Traditional segmentation pipeline for RICM.	177
5.7	Spreading event identification from signals	178
5.8	Characterizing a hovering survival in RICM.	179
5.9	Hovering duration distribution depends on bsAb concentration.	181
5.10	Spreading survival.	181
5.11	Decision rates and spread fractions.	182
5.12	Spreading area response.	182
5.13	Spreading area of single-cells.	183
5.14	Spreading survival.	183
5.15	Spreading quantification.	184
5.16	Instantaneous spreading rate.	185
5.17	RICM intensities during spreading.	186
5.18	Mean signal response during spreading.	186
5.19	Spreading phase portrait.	187
5.20	Spreading phase portrait varies with the antibody.	188

5.21	Texture quantification in a spreading assay.	189
5.22	Select texture features separate well the cell phenotypes.	190
5.23	Perturbation of image shifts texture values.	190
5.24	PCA representations of texture features.	191
5.25	Decision tree.	192
5.26	CNN classifier activations : NK cell.	194
5.27	CNN classifier activations : RBC.	195
5.28	Principle of topography reconstruction from RICM images.	197
5.29	Deep learning reconstruction of topography parameters.	200

List of tables

3.1	Segmentation features.	45
3.2	Last-layer activation functions and loss.	52
3.3	Image preprocessing functions.	62
3.4	Generalist models.	65
3.5	Benchmark of signal detection DL models.	86
4.1	MCF-7 nuclei segmentation models	112
4.2	Event detection models.	114
4.3	Primary NK segmentation models	116
4.4	Features of target/effector pairs	161
4.5	Top optimization results on victim/killer detection parameters without the synapse annotation.	165

List of acronyms

ADCC

antibody-dependent cell-mediated cytotoxicity. 37, 38, 45, 98–100, 104, 108, 110–116, 124, 125, 131, 137–139, 141, 143–145, 155, 158, 203, 204

AI

artificial intelligence. 33, 100, 200

APC

allophycocyanin. 102

BN

batch normalization. 52

bsAb

bispecific antibody. 98–101, 104, 119, 138, 139, 141, 144, 146, 148–151, 153–155, 160, 168, 171, 180–188

CD16

cluster of differentiation 16. 98, 101

CFSE

carboxyfluorescein succinimidyl ester. 102–104, 106, 107, 110–113, 115–118, 133, 163

CI

cell index. 107, 108

CINaM

Centre Interdisciplinaire de Nanoscience de Marseille. 45

CNN

convolutional neural network. 33, 35, 41, 43, 194–196

CPU

central processing unit. 49

CRCM

Centre de Recherche en Cancérologie de Marseille. 45

DL

Deep learning. 36, 39, 42, 44–48, 50, 55, 58, 61, 65, 69, 70, 84, 86, 87, 90, 114, 171, 194, 199, 200

GAN
generative adversarial network. 201, 202

GAP
global average pooling. 52

GPU
graphics processing unit. 33, 49

GUI
graphical user interface. 43, 45, 49, 50, 59, 60, 116

HER2
human epidermal growth factor receptor 2. 98–101, 139–143, 147, 150, 151, 154–161, 171

HR
hazard ratio. 106

INA
illumination numerical aperture. 170, 172, 173, 197–200

IoU
intersection over union. 55, 126–128, 136, 137, 164, 165

IRM
interference reflection microscopy. 168

LAI
Laboratoire Adhésion & Inflammation. 32, 45, 100

LAMP1
lysosomal-associated membrane protein 1. 101, 102, 104, 106, 107, 118, 160, 163, 166, 203

LSTM
long short-term memory. 43, 86

MAE
mean absolute error. 55, 87

MCF-7
Michigan Cancer Foundation-7. 38, 67, 77, 82, 97, 98, 100, 102, 103, 106, 108, 110–116, 118–120, 124–126, 128–148, 150, 151, 154, 155, 158, 161, 163

MSD
mean squared displacement. 80, 81, 104, 105, 157

MSE
mean squared error. 54, 55, 175, 201

NA

numerical aperture. 35

NCI

normalized cell index. 108, 141

NK

natural killer. 37, 38, 67, 70, 98–101, 104, 108, 110–113, 115–119, 125, 128, 131–139, 143–156, 158–164, 166–168, 171–173, 176, 177, 180–183, 188–190, 193–197, 199, 203, 204

NLP

natural language processing. 34, 35

PCA

principal component analysis. 192, 197

PI

propidium iodide. 102, 103, 106, 110, 111, 115, 116, 118–123, 138

RBC

red blood cell. 170, 173, 174, 189, 190, 193, 194, 196, 197

ResNet

residual network. 33, 53, 86, 199, 201

RICM

reflection interference contrast microscopy. 36, 46, 65, 67, 70, 168, 169, 171–173, 175–180, 183, 186, 187, 194–198, 200, 203, 204

ROI

region of interest. 41, 43, 70, 76, 78, 79, 176, 189

RTCA

real-time cell analysis. 99, 107, 141, 142

TCW

threshold configuration wizard. 61, 62

TIRF

total internal reflection fluorescence microscopy. 36

VGG

visual geometry group. 33

ViT

vision transformer. 35

Behind the scenes : the cast

As someone who analyzed a lot of data produced by others, I cannot proceed without giving proper credit to all of the experimentalists who created the sandbox in which I played for three years. Beatriz Díaz-Bello, currently a contractual researcher at Universidad Nacional Autónoma de México (UNAM), designed the antibody-dependent cell-mediated cytotoxicity (ADCC) assay under the microscope with Laurent Limozin during her post-doc at Laboratoire Adhésion & Inflammation (LAI) between January 2021 and January 2023. She conducted all of the ADCC experiments until her departure. Beatriz has been extensively involved in the conceptualization of Celldetective in its original form, applied to ADCC experiments only, by giving me daily feedback and by challenging me constantly as data poured in.

Lorna Ammer, currently a Ph.D. student at Laboratoire Adhésion & Inflammation (LAI), took over the ADCC experiments during her Master's internship in 2023, under L. Limozin's supervision. Her great work allowed us to push the ADCC assay in new directions by varying the experimental conditions considerably, bringing physical understanding and pushing spatio-temporal resolution to its limits.

Florian Dupuy, assistant engineer at LAI, is the last experimentalist to perform ADCC experiments and the first of the three experimentalists to benefit from the revamped Celldetective. His recent work allowed us to characterize the propidium iodide dye and his efforts to image directly the bispecific antibodies opened up many perspectives on where to take the ADCC assay next.

On the spreading assay side, I will present some results extracted from Dalia El Arawi's experimental work. Dalia is currently a post-doc at Institut de Biologie du Développement de Marseille (IBDM). Dalia conducted a large amount of spreading experiments during her post-doc in 2020 under L. Limozin's supervision. Her perfectionism led to hours of hard-to-achieve reflection interference contrast microscopy (RICM) images; perfect raw material for Celldetective.

I imaged some spreading assays in RICM, in collaboration with Marie Dessard, Ph.D. student under PH. Puech and Y. Hammon's supervision, shared between LAI and Centre d'Immunologie de Marseille-Luminy (Ciml), who prepared integrally the samples from the cells to the surface chemistry and assisted the image acquisition. I also sparsely performed multi-color-multi-aperture RICM imaging throughout the Ph.D.

2 Introduction

2.1 The image analysis revolution

At the heart of image analysis is the problem of detection, which can range from a rough point detection, a bounding box, or a precise outline of the objects of interest. Extracting the contours, that is to say, segment, provides a canvas for measurements, allowing for quantitative analyses. For decades, cell segmentation from microscopy images was a bottleneck. The main emphasis for improvement was on better imaging hardware. Paradigm shifts happened upon the introduction of new image modalities, new hardware, or the invention of new modes of sample preparation. Typically, images had to be of high enough quality and the cell system simple and sparse enough to be segmented with a traditional segmentation technique such as thresholding. A different kind of paradigm shift happened with the advent of machine learning approaches.

Convolutional neural networks (CNNs) were first developed decades ago, in 1989 [101]. Models could *learn* directly from images, back-propagating errors to update their weights, with a direct application to read the numbers of handwritten checks. The process remained computationally expensive. Moreover, the artificial intelligence (AI) field was suffering from a lack of interest at the time.

CNNs came back to the spotlight in 2012 when the number of parameters and the size of their training data was increased considerably [95]. AlexNet made about 10 % less error than the runner-up in the ImageNet classification contest, in a field where improvements rarely exceeded 1-2 % each year. AlexNet consists of an encoding architecture with 60 million parameters and 650,000 neurons, with alternating convolution and max pooling layers bringing down an image into a thousand neurons (one per class). A model with more parameters is much more computationally expensive, which would not have been practical, were it not for the use of graphics processing units (GPUs). The conclusive lines of the AlexNet paper anticipated what was yet to come at the time : “our results have improved as we have made our network larger and trained it longer but we still have many orders of magnitude to go in order to match the infero-temporal pathway of the human visual system”. Deeper models, with a larger number of parameters, have been developed since AlexNet, with visual geometry groups (VGGs) [161] introducing smaller convolution kernels, which are now standard. As the models became deeper and deeper, their performance started to saturate and even deteriorate, which seemed counterintuitive and was qualified as a “degradation” problem. It is to face this issue that residual networks

(ResNets) [70] introduced identity connections to ease the training of deeper models by constraining the layers to only learn the residual with respect to their input. These models excelled at classification and regression tasks, encoding images down to one or more values or classes.

Segmentation could be achieved by extracting small patches and classifying the central pixel one pixel at a time, with overlaps, until a whole image was scanned by a classifier model [34]. This process was quite slow and computationally expensive, limiting the context around each pixel, that the classifiers exploit. U-net [144] was introduced to face these pitfalls, proposing an encoder-decoder architecture, u-shaped, with direct skip pathways to feed the feature maps of the encoder directly to the symmetric decoder block, as illustrated in figure 2.1. This model could take an image as its input and have an output as wide as the image, without loss of resolution. The segmentation task was formulated like a classification problem for each pixel of the output map, with a foreground class (cell) and a background class. The authors introduced extra weight at the contacts between cells to force the model to learn the separation lines that are under-represented in the data. Some architectural variations have been introduced since, such as U-net++ [196], which modifies the skip pathway to transform encoder features by convolution layers before they read the decoder. U-net and its variations solved once and for all the problem of segmentation, with it being the backbone of numerous algorithms.

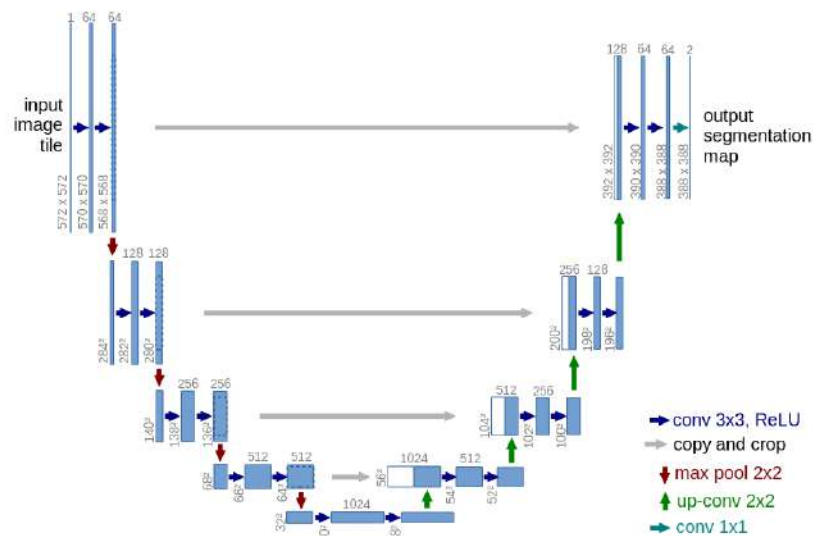


FIGURE 2.1 – From [144]. U-net model architecture. In this figure from the original U-net paper, the lowest dimension of the image is $(32 \times 32 \text{ px})$. The number of filters/channels is written on top of each blue box, with the latent image size written on the left side.

However, a recent development came from the field of natural language processing (NLP). Transformer models [181] proposed a token framework to interpret and communicate in natural language, usually functioning as a sequence-to-sequence

model. Vision transformers (ViTs) [48] started to be used as a replacement for the CNN backbones, converting image patches as tokens, as a word would be in an NLP application. ViTs outperformed CNN models on classification tasks when the dataset is large. Large multimodal language models such as GPT-4 [128] and Gemini [170], use transformers as building blocks to process images, text, and more all at once, letting the text prompt define the task that has to be performed. New levels of interactivity and accessibility are expected to be achieved with such models [74], which can once again revolutionize the image analysis field.

2.2 Cell imaging

Cell imaging has to balance spatiotemporal considerations, as well as throughput. Indeed, the time and spatial resolutions can be technically increased to the order of subseconds or submicrons but at the cost of a smaller field of view and generating a volume of data that might be difficult to store. Optical microscopy provides the best compromise, allowing us to observe many cells at a time, at a resolution ranging from sub-seconds to many hours, with a typical magnification perfectly adequate to image cell populations while being able to discern single cells and even single bio-molecules. However, the inherent transparency of biological objects creates a need for contrast enhancement.

Label-free techniques such as brightfield, were quite limited due to the lack of contrast, specificity, and the introduction of many artifacts. The late 19th century saw the introduction of fluorescent substances [71, 168] for improved contrast. Researchers later experimented with exciting these substances in living organisms using light and filters to observe the red-shifted emission light [52]. The 1940s marked the development of immunolabeling [35], exploiting antibodies to deliver dyes to specific sites. More recently, genetic encoding [171] enables labeling specific proteins. New fluorophores offer strong photobleaching resistance, allowing for detailed spatiotemporal visualization of subcellular structures, protein distribution, and precise quantification. Additionally, label-free techniques are seeing a resurgence, particularly in medical diagnosis where genetic modification is not always possible.

The maximum lateral resolution of microscopy images is imposed by the numerical aperture (NA) of the objective and the wavelength of light, following Abbe's law of diffraction. The super-resolution technique introduced a paradigm shift combining the discovery of photoactivatable fluorescent proteins with novel image reconstruction methods to overcome the resolution barrier. Objectives with higher numerical apertures improved the sensitivity and resolution of microscopy images [189].

The simplest technique to use is widefield microscopy, in which the whole sample is exposed to the light source. Confocal and light sheet microscopy techniques address the limitations of widefield microscopy, such as out-of-focus light, but are fairly slow to acquire images and involve sample labeling. For many applications, simple brightfield is still preferred. If specific cell structures have to be imaged

while maintaining a high throughput, the epifluorescence technique can replace or complement brightfield. For phenomena happening close to the cell surface or in the context of cell adhesion, optical surface microscopy techniques such as total internal reflection fluorescence microscopy (TIRF) [55] and reflection interference contrast microscopy (RICM) [104], are the best choice.

Deep learning (DL) methods are pushing boundaries further, offering techniques for resolution improvement [4, 138], noise and defect correction [61, 97], and even visualizing structures in label-free images as if they were stained [94, 143].

2.3 Why do we need single-cell image analysis?

In the previous section, we talked about the tradeoff between widefield imaging and high-resolution imaging. It is often important to be able to study cells in the context of population. Many methods rely on bulk measurements to describe how a cell population reacts to stimulation or stress, completely averaging cell heterogeneities [112]. Single cells that are genetically identical and grown in the same environment can still display different behavior, response, and phenotype [58]. Bulk analysis, like in the popular example of averaging personal incomes in France, misses individual variations and important disparities. Such differences can emerge from uneven cellular context, *i.e.* different neighboring cells [164], asymmetries in the distribution of nutrients [81], or even stochastic differences in gene expression affecting the exhibited phenotype [109, 141].

Single-cell techniques like RNA sequencing (scRNA-Seq) analyze individual transcriptomes, correlating gene expression with cell states [103]. Alongside, single-cell imaging assays using fluorescent reporters offer insights into protein localization, cell fates, organelle distributions, morphologies, and more. A key challenge lies not only in quantifying single-cell variability but also in understanding the micro-environment's influence on individual cell behavior within the limits of molecular stochasticity. Recent advancements in high-throughput microscopy and image analysis enable gathering and analyzing spatiotemporally resolved images to address these challenges illustrated in figure 2.2.

Some high-throughput methods analyze millions of cells, striking a balance between spatial/temporal resolution and statistical power. Developing both the image analysis pipeline and the biological assay concurrently ensures that the analysis captures the desired single-cell phenomena. Traditionally, images were simplified by reducing cell density, increasing time resolution, and rigorously cleaning surfaces. Recent DL advancements allow image analysis to match human eye performance, enabling single-cell studies in more realistic conditions. DL methods are replacing traditional segmentation, tracking, and classification modules in single-cell pipelines [22, 49, 107]. However, the required computational skills remain a barrier for some labs.

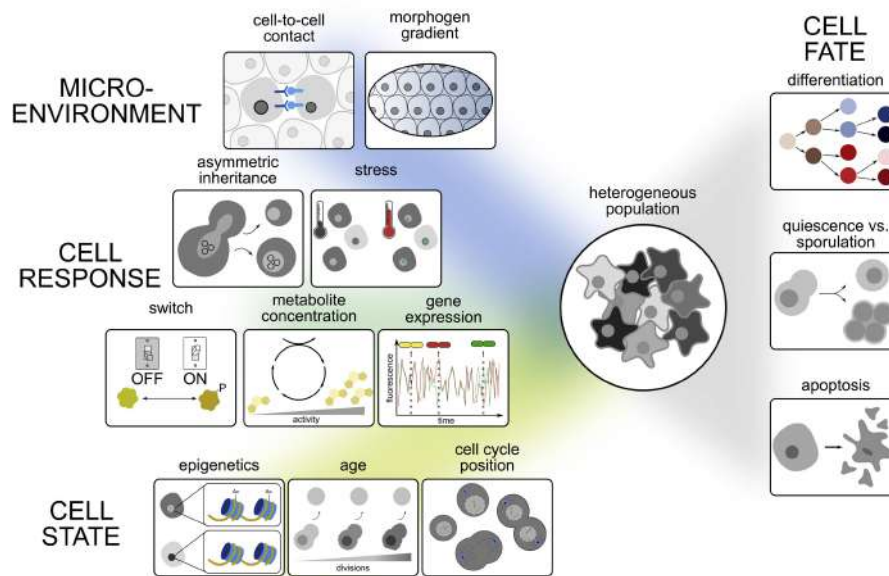


FIGURE 2.2 – From [112]. Sources of phenotypic heterogeneity.

2.4 Single cells of the immune system

The immune system is a complex and refined network of organs, cells, and molecules. Collectively, they orchestrate the immune responses needed to protect the body from the vast array of pathogens to which we are constantly exposed. These immune responses are divided into innate and adaptive responses [133].

The innate immune response is a generalized immediate response mediated by pre-existing mechanisms such as physical barriers, non-specific cells, and certain chemicals. In contrast, adaptive immunity is a more specific response that has evolved to recognize pathogens capable of evading the innate line of defense. The adaptive immune cells (T and B cells) are at the heart of this response, they not only provide targeted protection against known pathogens but also form the basis for immunological memory, conferring long-lasting protection upon re-exposure to familiar threats [119]. These activated cells that respond to pathogens or cancer cells are the effectors. While playing distinctive roles, the collaborative efforts of innate and adaptive immune responses are crucial for the overall effectiveness of the immune system.

One prime example of this collaboration is the antibody-dependent cell-mediated cytotoxicity (ADCC). ADCC is a mechanism through which certain effector cells of the innate immune system, the natural killer (NK) cells, recognize and destroy target cells such as cancer cells that have been tagged by antibodies [126]. Antibodies are soluble molecules that recognize with high affinity and specificity one target or antigen. This recognition marks the foreign invaders for destruction by various components of the immune system [119]. They are produced by B cells as part of

the adaptive immune response.

Studying these interacting populations poses imaging challenges. A standard approach involves replacing target cells with antibody-coated surfaces. This allows utilizing the optical surface microscopy techniques mentioned earlier. An advantage of such an approach is that the biochemical and physical properties of the surface are well-defined whereas target cells are largely of unknown properties and difficult to manipulate.

2.5 Contents of this thesis

In this thesis, we will first introduce a new software, Celldetective, for the analysis of single-cells among one or two interacting populations, from 2D multichannel time-lapse microscopy data. This chapter will remain descriptive about the functionalities of the software and the challenges addressed. The next two chapters will dive into applications to two different biological systems in the context of immune cells. For the first application, we will apply single-cell analysis to two cell populations, respectively Michigan Cancer Foundation-7 (MCF-7) breast cancer cells and primary NK cells, co-cultured in an ADCC assay imaged under the microscope using fluorescent labeling. In the second application, we will apply single-cell analysis to study primary NK cells, spreading on antibody-coated surfaces, imaged using surface microscopy.

3 Celldetective

3.1 Introduction

First, we will discuss briefly the state-of-the-art in segmentation, tracking, and single-cell measurements, before conducting a non-exhaustive review of software that integrates these building blocks for single-cell analysis. We will give a rationale for Celldetective, a new software addressing open challenges in single-cell analysis from microscopy images. We provide a brief material & methods on supervised DL using convolutional methods before describing quite extensively the features of the software step-by-step, justifying all conceptual and technical choices and highlighting the range of applications. Detailed applications form the basis for the next two chapters.

3.1.1 Building blocks of single cell analysis

3.1.1.1 Segmentation

Cell detection is a primary step in single-cell analysis. Counting and segmentation algorithms are traditionally used to perform this task. Here we focus on segmentation algorithms as counting does not provide the single-cell scale description we are after.

On a homogeneous image, automatic threshold techniques such as OTSU [130] classify the pixels into foreground and background pixels, by minimizing intra-class intensity variance. Unfortunately, this kind of technique fails on less homogeneous images, with distortion at the edge, or background fluorescence. Adaptive thresholding methods [123, 153] face the inhomogeneity problem by computing a different threshold for each pixel based on the distribution of intensities in the local neighborhood. These methods only focus on intensity levels and are independent of the shape of the objects. In addition, they are quite unstable to noise.

The watershed method [15, 159], on the other hand, considers an image as a topological map, converting intensities into altitudes. Under this point of view, intensity minima form local basins. Flooding the basins, or increasing the intensity threshold, up to the watershed mark, allows to segment objects nearby. Watershed performs well in separating objects in contact but is still as sensitive to noise and image preprocessing as the threshold technique.

Machine-learning-based pixel classifiers for segmentation, implemented in Ilastik [14] and QuPath [7], extract local texture and tone to classify pixels one by one. The

classifiers can be trained from sparse user annotations, making these algorithms particularly interactive. A drawback of this approach is that the small field of view around each pixel does not always provide enough context to properly classify the pixel.

Deep-learning models avoid this pitfall by interpreting images at higher scales but are usually more computationally expensive. A few state-of-the-art segmentation algorithms share the same U-net backbone [37, 111, 155, 169], with different formulations for the input and output of the model.

StarDist [155] is one such segmentation method that applies well to convex objects. As illustrated in figure 3.1, instead of directly predicting masks, the StarDist U-net outputs an Euclidean distance transform image (also called the probability map) accompanied by n_{rays} distance maps. Each distance map represents the distance of each pixel to the object boundary along a different axis (among n_{rays}). The probability and distance maps are fused back together with a non-maximum suppression operation to form convex polygons, defining the actual cell masks, presented as an instance segmentation. This method outperformed the classical U-net formulation on nucleus segmentation tasks. The StarDist team trained generalists models, by feeding large datasets to StarDist models. The obvious limitation of this algorithm is that the masks have to be deconstructed and reconstructed as convex polygons, which does not apply to all cell shapes.

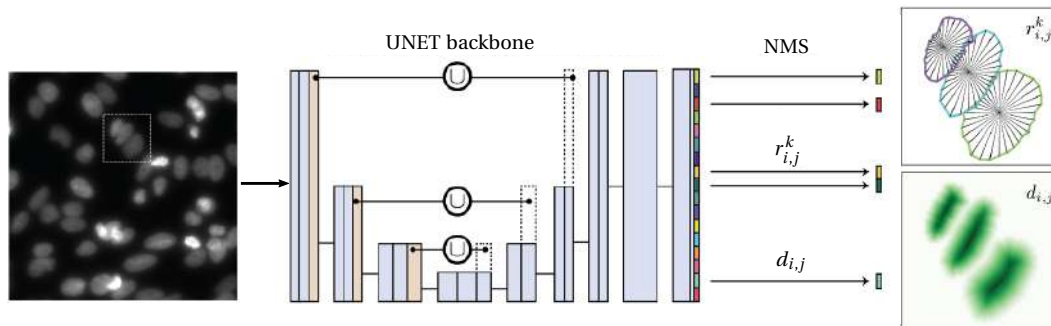


FIGURE 3.1 – The StarDist method. Adapted from [155]. Euclidean distance transform (probability map) and distance to mask edge oriented along n_{rays} axes (distance maps) is output by the U-net from a 2D microscopy image.

The Cellpose [131, 169] method introduces an alternative output formulation to face this problem, as illustrated in figure 3.2. Instead of distance maps, a diffusion process is simulated from the center of each cell mask to the border. The horizontal and vertical gradients of such representation are computed for each mask and called the flow maps (figure 3.2a). The U-net backbone now has to predict 1) a binary cell probability (foreground, background), similar to the traditional U-net formulation and, 2) the two flow maps (figure 3.2c). A post-processing function assembles the three outputs into a flow field. The pixel values of the probability map are activated with a sigmoid function. Before activation, the pixels with a value higher than the `cellprob_threshold`, ranging from -6 to 6, are selected to

estimate the regions of interest (ROIs). Pixels converging to the same fixed point are associated with the same mask, yielding an instance segmentation, like StarDist (figure 3.2e and f). As a quality check, the gradients are recomputed for each ROI and compared to the flow output of the model. If the difference is higher than the `flow_threshold` parameter, the ROI is rejected. Cellpose models were trained on wide datasets containing several modalities, with one (cytoplasm) or two channels (cytoplasm plus a nuclear marker). To facilitate robustness all images were rescaled in such a way that cells always averaged 30 pixels in size. The diameter parameter pilots this rescaling when segmenting a new image.

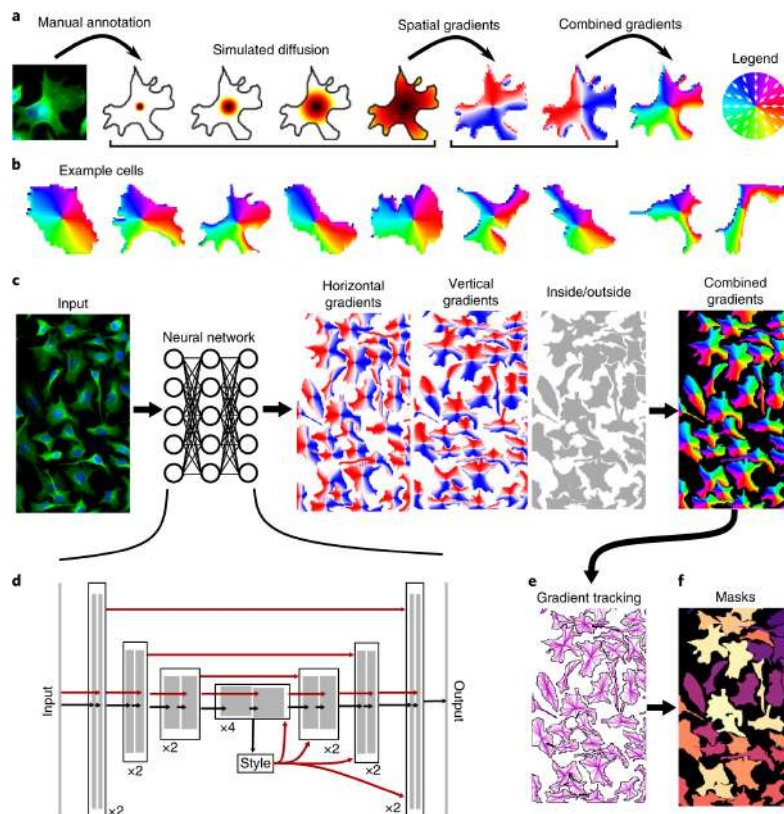


FIGURE 3.2 – The Cellpose method. Directly from [169].

StarDist, Cellpose, and their variations are currently the most popular cell segmentation algorithms, with their pre-trained models acting as foundational models for respectively cell nuclei and cell shapes. Another foundational approach emerged from the field of computer vision in recent months, the Segment Anything Model [91] (SAM), that embeds text prompt, object bounding boxes, point locations and images to *segment anything*. The architecture is modified compared to StarDist and Cellpose, exploiting transformers instead of a CNN U-net. SAM outputs up to three masks to address the most common cases of nested masks. SAM is the first truly generalist segmentation model, impressive in its capacity to detect objects of any kind. A pitfall of this approach is that it is extremely expensive to run locally, making

it currently quite unfit for high throughput detection.

3.1.1.2 Tracking

In the context of microscopy time-series, tracking is a necessary step to achieve a temporal description of the single cells. Many methods have been proposed to solve the problems of single-cell tracking and single-particle tracking, using state-of-the-art algorithms and DL frameworks. TrackMate [54, 172], a user-friendly Fiji plugin, embeds the Linear Assignment Problem (LAP) tracker based on reference [82] and able to accurately track splitting and merging particles. TrackMate also packs a Kalman tracker, exploiting the position history to guess about a particle or cell's next position. TrackMate has arguably the best track visualization modules, making it easy to correct tracking errors. Since version 7 [54], TrackMate can take labeled images as its input, making it compatible with state-of-the-art segmentation methods.

The Bayesian tracker [176] (bTrack) also uses Kalman filters to predict the future position of a cell from its previous observations.

Initially, each cell from the next frame is considered a likely candidate, with a uniform probability, to be the next position in a tracklet. Each tracklet forms its own motion model, cell state, and feature sequence that are used to reduce or increase the probability of the cell's candidates to be the next position in the tracklet. On top of this, a second optimization is performed to connect truncated tracklets based on linking, mitosis, apoptosis, and false positive hypotheses. bTrack is a Python package, making it a prime candidate for integration into Python-based single-cell software.

Other notable frameworks include DeLTA [108] and Caliban [157] that combine segmentation and tracking using DL. DeLTA uses two consecutive U-Net-based models to first segment the cells, and then to perform tracking and lineage reconstruction. To perform tracking, the input is composed of the microscopy images for the current and previous frame, with a binary mask outlining the “seed” to be tracked from the previous frame and the complete segmentation mask for the current frame. The expected output is a binary mask of the “seed” cell on the current frame and potentially of a daughter cell in that current frame. Caliban first segments all cells for each frame. Then features are computed for each cell and passed through a neighborhood encoder model to generate a vector embedding of each cell. The vectors and cell positions are passed into a tracking inference model that predicts the probability of a cell of the current frame to be the same in the next frame or to have divided in the next frame. A linear assignment framework uses these weights to construct cell lineages frame by frame. These methods are promising but much harder to implement and optimize than conventional trackers.

3.1.1.3 Measurements & signals

Many different measurements can be performed at the single-cell scale. Some of them describe the cell itself using the mask (morphology, intensity). Other measurements relate to the context and neighborhood. The authors of reference [84] extracted 484 single-cell measurements to train a classifier model to segregate cell types. Recurring single-cell descriptors include Haralick texture features [68], Zernike polynomials [125]. To describe the local cellular organization and provide a context, Delaunay triangulation [80] and Gabriel graphs [113] can be used.

Single-cell measurements can also be studied as signals if they emerge from tracked data. Chollet [32] noted that signals could be processed using both recurrent neural networks, such as long short-term memory (LSTM) [73] or gated recurrent unit [31] (GRU) networks, and CNNs [95] for classification and regression tasks.

3.1.2 Existing softwares for cell analysis

3.1.2.1 ImageJ/Fiji

Purpose ImageJ [147, 156] is a Java-based software to visualize and quantify microscopy data. Fiji [154] is a variation of ImageJ that packs hundreds of plugins for bioimage analysis.

Description Hundreds of java-based plugins developed by laboratories across the world to solve specific tasks are centralized together in a simple graphical user interface (GUI) and can be called and combined using a complete macro language. The plugin collection is quite exhaustive, covering most algorithms commonly used in image analysis pipelines (image filtering, image registration, noise removal, thresholding, segmentation, ROI management, and tracking). Deep-learning models for segmentation and super-resolution can be called using the DeepImageJ plugin [60].

Lack Most of these plugins operate on single images, or single stacks, leaving to the user the task of programming loops, the collection of measurements, the saving of files, and in general the automation of an image analysis pipeline. Direct quantification through the macro language is possible but ImageJ lacks the functionalities of common Python packages such as the table manipulation functions of pandas or the tensor calculus of numpy, making sophisticated analysis difficult, despite recent efforts to bridge the gap between Python and ImageJ [146].

Popularity ImageJ/Fiji is a reference in the bioimage analysis community, widely adopted across the world, with over 37000 citations for reference [156], and over 33000 citations for reference [154].

3.1.2.2 CellProfiler

Purpose CellProfiler [27, 86, 115, 167] is one of the most popular integrated image-analysis software for high-throughput measurement of size, shape, intensity, and texture across diverse cell types.

Description Originally optimized for the analysis of 2D images, the software encompasses illumination correction, and cell segmentation using variations of the watershed algorithm [110, 117, 129, 184, 185], refined strategies to separate touching cells and propagate cell masks from the nuclei [83], and a comprehensive measurement and data analysis toolkit, complete with viewing and plotting modules. Subsequent versions and companion software introduced machine-learning methods for segmentation, plugins to call state-of-the-art DL models, and tracking. CellProfiler has been applied to many cell types [28].

Lack Despite all of these functionalities, CellProfiler was not designed to accommodate natively Deep-Learning models, lacks annotation and retraining capabilities, and is not very convenient to visualize and annotate trajectories.

Popularity As one of the most popular integrated software to quantify single cells, the original 2006 article [27] was cited over 5000 times, with the subsequent paper adding over 3000 citations.

3.1.2.3 CellACDC

Purpose CellACDC [132] (**Cell-Analysis of the Cell Division Cycle**) is a Python-based software designed to annotate cell cycles from movies of budding yeasts.

Description CellACDC was applied to a system of budding yeast cells and the cell-cycle annotations were carried out manually. To our knowledge, this is the closest solution to the one we propose with a focus on time-lapse microscopy images and the measurement of single-cell signals (fluorescence, cell cycle states). At the time of publishing, CellACDC has embedded two state-of-the-art DL segmentation solutions Cellpose and YeaZ, with the possibility to manually correct segmentation results. Additionally, CellACDC integrates natively trackers.

Lack Importing extra segmentation and tracking solutions is possible but requires some basic coding skills. Since the time of publication, the authors exploited the modular scripting approach to add more published models from Segment Anything Model (SAM) [91], StarDist [155], YeastMate [21], omnipose [37], DeLTA [108], DeepSea [192]... CellACDC does not propose any retraining or transfer learning feature from these models, limiting its applicability to images on which generalist models were trained.

Popularity CellACDC is quite new to the field, with 14 citations since 2022.

3.1.3 Rationale for Celldetective

Despite notable efforts in the development of user-friendly software that integrate state-of-the-art solutions to perform single cell analysis [27, 132], very few are designed for time-lapse data [132] and even less for multimodal problems where cells populations are mixed and can only be separated through the use of multimodal information. Furthermore, none of the software solutions provide, to our knowledge, the extraction of response functions from single-cell events such as the dynamic survival of a population directly in the GUI, requiring coding skills to do so (see comparative table 3.1).

We want to study complex data which is often multimodal time-lapse microscopy images of interacting cell populations, without loss of generality. This can be exemplified by ADCC assays in development at the LAI, assessing the efficiency of molecules developed by the Centre de Recherche en Cancérologie de Marseille (CRCM) [175], or spreading assays studied in both LAI and the Centre Interdisciplinaire de Nanoscience de Marseille (CINaM) [18, 46, 62, 135, 136, 183]. In the context of ADCC, where effector cells kill target cells, separation of each species is not obvious and requires multiple modalities and physical interpretation of the cell morphologies relative to the other population. On a large scale, we need to be able to assess the efficiency of a bridging antibody between the two populations. At the local scale, we want to be able to study the one-to-one interactions between these populations, the existing heterogeneities, dynamics, and time scales. In the context of the spreading assays, we want to investigate a system of effector cells spreading on functionalized surfaces serving as a proxy for antigen-presenting cells, in optical surface microscopy modalities very rare in the datasets that were originally used to train generalist DL segmentation models.

With a high need for an easy-to-use, no-coding-skill-required software adapted to images that can be as complex as the above-mentioned examples and intended for biologists, we decided to create an open-source Python-based software to face the following challenges.

Challenges

- Multimodal Complexity : the integration and interpretation of multimodal information are critical in mixed-population scenarios, as exemplified in the ADCC assays. No software currently facilitates the training of DL models on profoundly multimodal data, which is required in the case of ADCC for accurate analysis and separation of the distinct cell populations.
- Dynamic survival : in the context of immunotherapies, cells exhibit events (death, spreading) after characteristic durations, the extraction of which is not adequately addressed by current software.

Table 3.1 – Comparative table of select analysis features. By convention a ✓ can only be attributed if the task can be carried without having to code. The use of an integrated solution or plugin is indicated in parentheses.

Software feature	ImageJ/Fiji	CellProfiler	CellACDC	Celldetective
Traditional segmentation	✓	✓	✓	✓
DL segmentation	✓	✓	✓	✓
Corrections annotations	✓ (Labkit)	✓ (GIMP)	✓	✓ (napari)
Training	✗	✗	✗	✓
Transfer	✗	✗	✗	✓
Tracking	✓ (TrackMate)	✓ (TrackObjects)	✓	✓ (bTrack)
Visualization	✓ (TrackMate)	✗	✓	✓ (napari)
Position-based measurements	✗	✗	✗	✓
Measurement classification	✗	✓	✗	✓
Signal annotations	✗	✗	(✓) cell-cycle	✓
Interaction analysis	✗	✓	✗	✓
Experiment manager	✗	✗	✓	✓
Multi-condition data exploration	✗	✓ (CP Analyst)	✗	✓
Survival analysis	✗	✗	✗	✓

- Interpretation of cell population behavior : single-cell analysis sheds light on the local determinants of cell survival. Relating local factors to global survival is beyond the scope of currently available software.
- Underrepresented imaging modalities : some imaging modalities such as RICM are

insufficiently represented in the datasets used to train generalist DL segmentation models, limiting the applicability of existing tools in scenarios involving such microscopy techniques.

Focus and goals

- Comprehensive single-cell analysis : perform segmentation and tracking, measure features at each time point, detect events from single-cell signals as detailed in figure 3.3, for each population of interest.
- Integration of state-of-the-art solutions : harness state-of-the-art segmentation techniques (StarDist [155], Cellpose [131, 169]) and tracking algorithm (bTrack [176]), as well as the napari viewer [1] where applicable. Interface these algorithms to make them well-integrated and user-friendly for the target audience, in the context of difficult applications.
- Event annotation and interpretation : develop a broad and intuitive framework to annotate and automate the detection of events from single-cell signals through DL signal classification and regression. Use event formulation to define global survival responses.
- Cell-cell interaction : implement a neighborhood scheme to relate the measurements of two cell populations, allowing the study of how cell-cell interactions affect global responses.
- DL customization : allow users to specialize DL models or create new ones adapted to their data, by facilitating the curation of training sets and the training of such models.
- In-software analysis : build visualization tools to extract population responses from trajectory tables and compare biological conditions.
- Software design features : ensure accessibility for biologists with no coding skills. Make the software, its datasets, and models fully open source to encourage transparency and reproducibility.

In conclusion, the proposed software aims to address current challenges in single-cell analysis from microscopy data. By developing user-friendly interfaces for segmentation and tracking algorithms, the automation of event detection, the exploration of cell-cell interactions, and the customization of DL models, we hope to provide a comprehensive solution for the biologist audience, who may lack the coding skills to analyze their data autonomously.

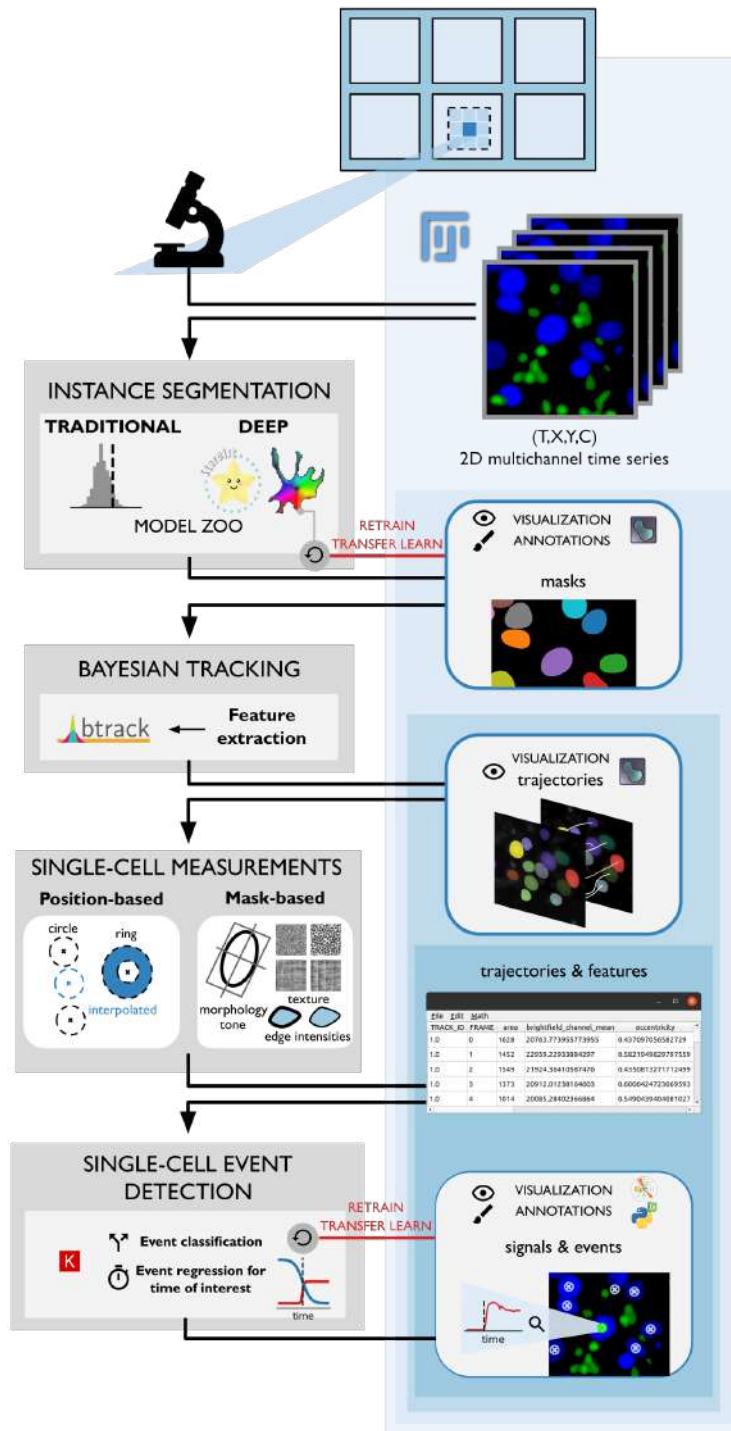


FIGURE 3.3 – Functional description of Celldetective. Multichannel time-series microscopy data is fed into Celldetective, in a file structure mimicking that of multi-well plates. The processing modules are shown on the left side, whereas the output and visualization modules are displayed on the right. The cell population of interest in a movie can be segmented using either a traditional segmentation pipeline or a DL model. The output can be viewed in napari, corrected, and exported back into annotations which can be used to train a new DL model. The masks are fed to bTrack with the option to add morpho-tonal measurements in the tracking. The output trajectories can be viewed in napari. Morphological, tonal, and textural measurements can be performed either from the cell masks or from the positions. Cell signals can be classified by DL models and explored in an interface designed for the annotation of single-cell events, allowing for the export of annotated signals to train a new DL model.

3.2 Materials and methods

3.2.1 Environment, packages and libraries

Software development and analysis were carried out on an Intel-core i9 central processing unit (CPU), NVIDIA RTX 3070 GPU, 16 Go of RAM, Ubuntu 20.04 desktop. The software was extensively tested on an Intel-core i9 CPU desktop running on Windows 11, an Intel-core i7-8565U laptop running on Windows 11, and an older Intel(R) Core(TM) i5 CPU 750 @ 2.67 GHz desktop running on Ubuntu 20.04.

The GUI was developed in PyQt5 and integrates Matplotlib canvases for plots and animations. Double-handle sliders were imported from the package `superqt`. An early version of the signal annotation UI was developed in Tkinter in 2021 but full migration to PyQt5 has been completed since then. The GUI styling is inspired by Material Design, introduced by Google in 2014, using monochromatic roundish buttons and the MDI6 icon set which is free to use. On startup, a splash screen displays Celldetective's logo while the initial libraries load. With the logo shown in figure 3.4, we tried to follow untold conventions of Python packages, *i.e.* a sketch illustrating the purpose on the left side (here, correlated single cell fluorescence signals) and on the right side, the name with not more than three colors overall. The Python packages imported by Celldetective are summarized in figure 3.5.



FIGURE 3.4 – Celldetective's logo. The single cell signals were artificially produced in Python by defining sigmoid functions and plotting them in matplotlib. The overall logo was assembled on Inkscape.

Each of the processing modules (segmentation, tracking, measurement, signal analysis) triggers a subprocess that applies to a single movie at a time. Upon completion of the subprocess, CPU, and GPU memories are fully released, allowing us to reiterate the process on the next movie or to unfreeze the GUI. Multi-threading was implemented where it is applicable and can be configured in the software.

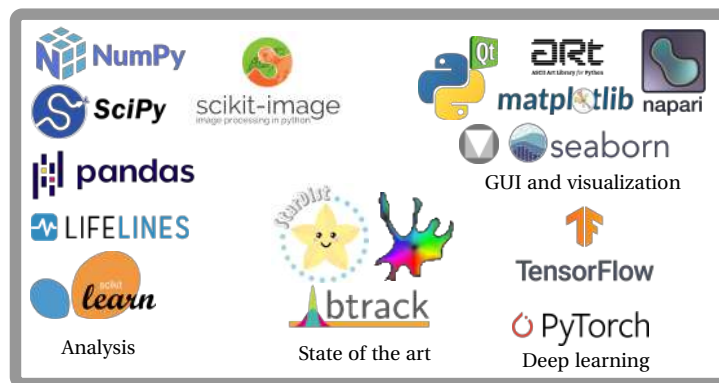


FIGURE 3.5 – Main dependencies of Celldetective. Celldetective makes extensive use of many Python libraries which can be grouped in four families : 1) the analysis packages, which allowed us to perform all computations, tensor, table and image analysis tasks, 2) the state-of-the-art methods which we implemented under the same roof in Celldetective, 3) the DL packages and 4) the GUI, plotting and visualization related packages.

3.2.2 Deep learning for signal quantification

Introduction To detect and estimate the time of occurrence of events in single cell signals, we implemented a convolutional neural network using Keras [32, 33], a Python API built on top of Tensorflow, where neural network components can be intuitively manipulated as layers that process input data and yield an output, not unlike filters. Everything mentioned here is also applicable to data of higher dimensions (images, movies, etc.) by simply increasing the dimension of the layers.

Data The input data is a series of M multichannel signals, for which we want to detect events. The event detection can be decomposed into two tasks : 1) classification, the assessment of whether or not an event of interest is contained in the signal, and 2) regression, *i.e.* if the event occurs, at which time. To homogenize the input tensor shape, we can set the maximum length of a signal to an arbitrary value T in such a way that the input is a tensor of shape $(M \times T \times n_{\text{channels}})$, respectively the *sample*, *time* and *channel* axes. Signals shorter than T are padded with zeros. It is common practice to normalize the input data to facilitate the convergence of the models and give similar value ranges to the different modalities expressed across the channels. For a sample $x(t) \in \mathbf{x}$, we define the min-max normalization as :

$$x_{\text{normed}}(t) = \frac{x - p(\mathbf{x}, \%_{\text{low}})}{p(\mathbf{x}, \%_{\text{high}}) - p(\mathbf{x}, \%_{\text{low}})} \quad (3.1)$$

where p is the percentile function, $\%_{\text{low/high}}$ the lower and upper percentage values to determine the “min” and “max” over \mathbf{x} . The transform is illustrated in figure 3.6. We avoid using direct minima and maxima values due to the regular presence of outliers that can make these estimates unstable (see section 3.3.5 for more details about our strategy). If convenient, we can replace the percentile estimates of the upper and lower bounds with absolute values (*e.g.* a morphological feature such as eccentricity is always between 0 and 1). On top of that, one may wish to clip values outside of $[0, 1]$, it is common practice in computer vision, but at the cost of a slight information loss. The data is split into three sets : 1) a train set, *i.e.* the data that will enter the model, 2) a validation set : the data that is used to measure the model’s performance outside of its training data and that may guide the selection of the “best” model and 3) the test set : a set that has no effect on the training and that is used after the training to assess the model’s robustness. It is recommended to perform data augmentation on the train set only, to introduce noise and variations that could occur in practice and help the model to be more robust. Details about our signal augmentation can be found in section 3.3.5.3.

Layers Several layers are adapted to process 1D data : tensors of shape $(M \times T \times n_{\text{channels}})$. Stacked together, and activated with non-linear functions, they form the model. Here is a non-exhaustive and brief description of the layers we used :

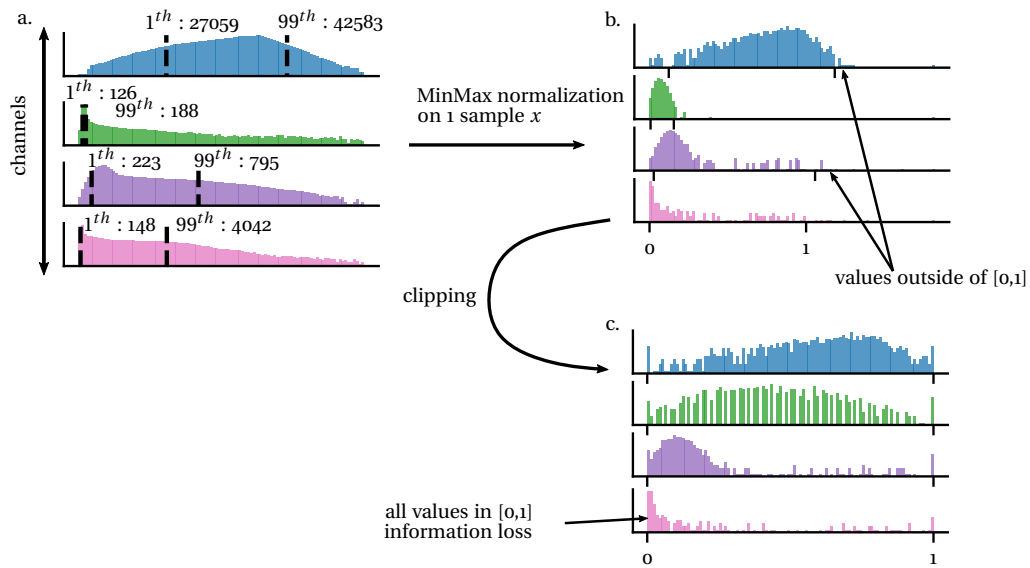


FIGURE 3.6 – Min-max normalization with multichannel data. a) The histogram of each feature-channel across all samples is represented. The values associated respectively to the 1st and 99th percentiles are shown on top of each histogram and serve as lower and upper bounds for the min-max normalization. b) the result of applying this normalization to a single sample is shown for each channel. Since we do not strictly perform a “min-max” normalization, some values remain outside the $[0,1]$ bound. c) if clipping is applied, then we flatten extra values to $[0,1]$, losing some information in the process.

- Dense (also called *fully connected*) : a layer of neurons that are densely connected to the previous layer, *i.e.* all neurons receive input from all the neurons of the upper layer.
- Convolution : n_{filters} convolution kernels of controlled size are convolved with the input layer over the *time* axis.
- Max pooling : a window of controlled size is scanned along the *time* axis, taking the maximum value in each window. With a pool size of 2 and a stride of 2, the length of the *time* axis is divided by two.
- Global average pooling (GAP) : average the tensor values along the *time* axis, removing this axis in the process.
- Batch normalization (BN) [78] : this regularization layer stabilizes the distribution shifts that can occur as the previous layers’ parameters are updated by the learning process.
- Dropout [72] : this regularization layer randomly sets to zero a fraction of the total number of output features of the layer it is applied on during training. This perturbation has been shown to decrease the learning of irrelevant patterns in the data.

Table 3.2 – Last-layer activation functions and loss. Reproduced from [32]. To each problem, an appropriate last-layer activation and loss function.

Problem type	Last-layer activation	Loss function
Binary classification	sigmoid	binary cross-entropy
Multiclass, single-label classification	softmax	categorical cross-entropy
Multiclass, multilabel classification	sigmoid	binary cross-entropy
Regression to arbitrary values	None	mean squared error (MSE)
Regression to values between 0 and 1	sigmoid	MSE or binary cross-entropy

Layer activation Activation functions play an important role in introducing non-linearities, usually critical to be able to fit complex phenomena. The most common non-linearity is the rectified linear unit activation function ReLU that essentially switches negative values in the tensors to zero. Other non-linearities include the sigmoid function which saturates small and large values respectively to 0 and 1. The choice of activation function is critical in the last layer as it determines the range and nature of the model output. Table 3.2 summarizes the last-layer activation to choose for different applications.

Architecture *Input.* The input to the model is a tensor of shape $(M \times T \times n_{\text{channels}})$. In practice, not all signals are passed to the model at once, instead, they are broken down into small batches (the size of which is the batch size). By convention, the channel axis is put last, and the convolution layers scan the time axis T .

Residual block. Instead of simply alternating convolution and pooling layers, we use 1D residual blocks, the 1D equivalent to the main constituent of ResNet [70]. The main characteristic of the residual block, as illustrated in figure 3.7, is that the input to the block is fed to a layer down the line, creating an “identity connection”. With this identity connection, the only thing left for the block to learn is the residual between the input and output of the block. The identity connection has been shown to compensate for the degradation problem in deep models, where adding layers leads to a worse performance than what would be expected for a shallower network. The technique is now widely spread as variations of the residual block can be found in transformers (used notably for large language models [19, 43]).

Backbone. The backbone is a stack of layers that brings the input layer down to the task-specific head of the neural network. The architecture of the backbone can be quite complex, with parallel branches, links between layers, and blocks stacked on top of each other. A chain rule must be respected between the input layer and the last layer.

Head. The backbone is concluded with either a “flatten” operation or a global-average pooling layer, that averages out the time dimension, leaving only the channel axis. To this, we can add optionally a dense layer of $n_{\text{collection}}$ neurons, which serves as a “collector” of the information brought by the convolution backbone. A dropout layer can add some regularization at this stage and prevent overfitting. Finally, for

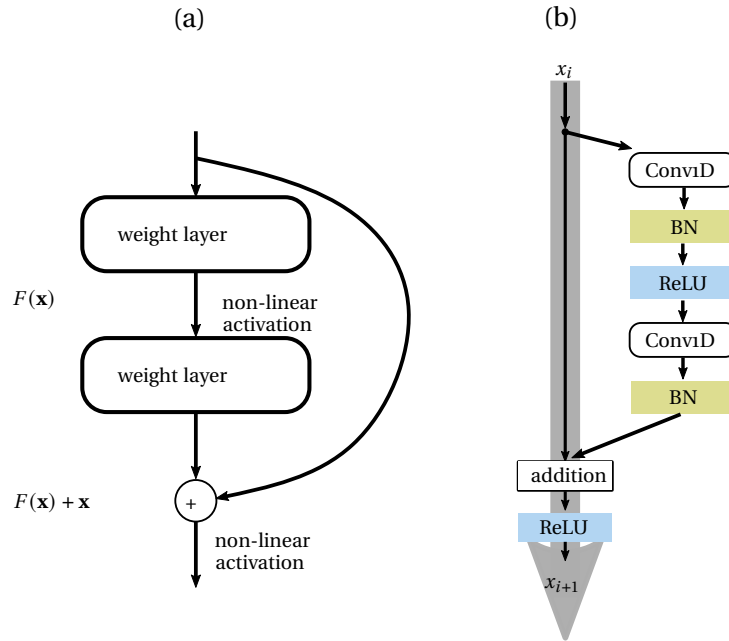


FIGURE 3.7 – Principle of the residual block. a) schematic of the residual block, from [70]. The input to the block is added directly to a layer deeper in the block. The non-linearity is then applied to addition of both branches. b) In more details, the processing branch for our residual block alternates 1D convolutions, batch normalization and a ReLU activation.

a classification task, we define a dense layer with n_{class} neurons and a softmax activation function, whereas for a regression task, we define the dense layer with a single neuron and a linear activation function.

Optimization *Loss.* Following table 3.2, we use the categorical cross-entropy loss function for a classification task and the MSE loss for a regression task. The categorical cross-entropy for a M -class, single-label classification problem can be written for n samples as :

$$L = \frac{1}{n} \sum_{j=0}^n \left(\sum_{i=0}^M p_i \log \hat{p}_i \right) \quad (3.2)$$

where \hat{p}_i is the probability predicted by the model for class i and p_i the true probability (0 or 1). The MSE over n points on a time prediction \hat{y}_i can be expressed as :

$$\text{MSE} = \frac{1}{n} \sum_{i=0}^n (y_i - \hat{y}_i)^2 \quad (3.3)$$

Optimizer. We use the Adam optimizer [90], a stochastic gradient descent algorithm based on adaptive estimation of first-order and second-order moments, widely

used in DL, with a controlled learning rate.

Metrics. One can use metrics to control the model’s performance during training as, for example, an improvement in the mean categorical cross-entropy does not imply an improvement in the model’s precision, which relates directly to its classification performance. Here we define the main metrics that are used repeatedly in the following sections to measure model performances. Classification metrics are built around the notion of true positives, false positives, and false negatives. The precision can be expressed as :

$$\text{Precision} = \frac{\text{TP}}{\text{TP} + \text{FP}} \quad (3.4)$$

and evaluates the specificity of the classification in each class. On a multiclass system, it is possible to decompose the precision “per class”, giving as many precision scores as there are classes. For a sample, if the true class is “event” and the model predicts “no event”, then the prediction is false negative concerning the “event” class, and false positive in the “no event” class. A complementary metric, the recall, is defined as :

$$\text{Recall} = \frac{\text{TP}}{\text{TP} + \text{FN}} \quad (3.5)$$

which evaluates the fraction of correctly classified signals for each class. A third metric that is not commonly used in classification problems but that is extremely relevant in segmentation and object detection problems is the intersection over union (IoU) :

$$\text{IoU} = \frac{\text{TP}}{\text{TP} + \text{FN} + \text{FP}} \quad (3.6)$$

This score penalizes both false positive and false negative detections. For a regression task, the MSE loss is also a good metric and can be accompanied by a mean absolute error (MAE) metric, written as :

$$\text{MAE} = \frac{1}{n} \sum_{i=0}^n |y_i - \hat{y}_i| \quad (3.7)$$

To summarize, for classification we measure the precision and recall metrics, either overall or decomposed per class, whereas for regression we measure the MSE and MAE.

Training The models train for a controlled number of epochs. The epoch is a complete pass of the training data in the model. Since the data is split in batches, it takes a certain number of iterations to complete an epoch. The typical number of epochs that we set is 300 for a classification task and double for a regression task. The batch size is set to 64. At each iteration, the loss is computed and the optimizer performs

backpropagation, modifying very slightly the weights of all the trainable parameters to go against the loss gradient. Figure 3.8 illustrates how all the components come together to train a model. We introduce several callbacks to monitor model training : 1) we save automatically the model with the highest validation precision (classification) or validation MSE (regression), 2) we introduce a scheduler on the learning rate to divide it by a magnitude if no progress was observed for 200 epochs, 3) we force the model to stop if no improvement was observed for 1000 epochs, 4) we collect the performance at each epoch in a csv file.

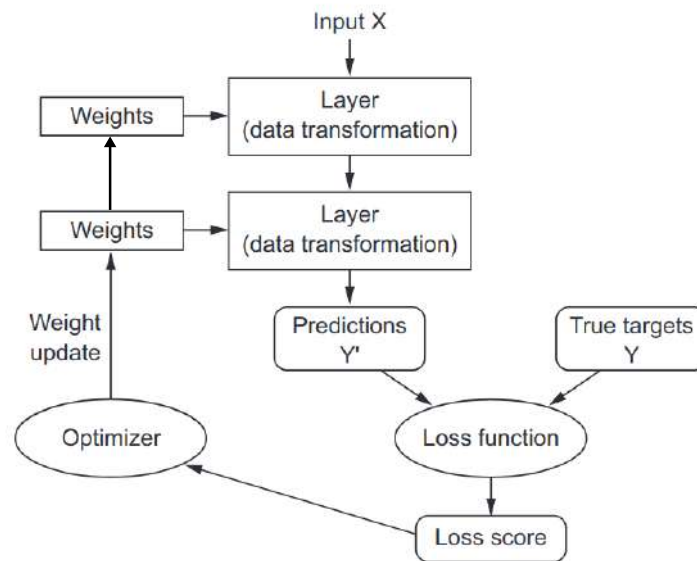


FIGURE 3.8 – Anatomy of a Deep Learning model. slightly adapted from reference [70]. The input data is transformed by successive layers, yielding a prediction. The prediction is compared with the ground truth by computing the loss function. The optimizer computes the loss gradient and updates all the weights accordingly. The process is reiterated for n_{epochs} .

3.2.3 Mathematical descriptors

3.2.3.1 Kaplan Meier estimator

We applied extensively the Kaplan-Meier estimator to compute survival functions from the event detection data. Let $\tau_1, \tau_2, \dots, \tau_k$ be a series of observed durations between a reference event (say the beginning of the observation) and either the event of interest happening (say death for simplicity) or the end of observation. Let n_i be the number of individuals at risk at time t_i : individuals that were observed alive at t_i plus the individuals that died exactly at t_i . Let's define d_i as the number of individuals who died precisely at $t = t_i$. Then the Kaplan-Meier estimator is defined as :

$$\hat{S}(t) = \prod_{t_i \leq t} \left(1 - \frac{d_i}{n_i}\right) \quad (3.8)$$

Greenwood [64] proposed the following confidence interval, building on an estimate of the variance of the survival function :

$$\begin{aligned} \hat{S}(t) \pm z_{\alpha/2} \sqrt{\widehat{\text{Var}} [\hat{S}(t)]} \\ \widehat{\text{Var}} [\hat{S}(t)] = \hat{S}(t)^2 \sum_{t_i \leq t} \frac{d_i}{n_i(n_i - d_i)} \end{aligned} \quad (3.9)$$

where z_α is the α -th quantile of the normal distribution. Here, $z_{\alpha/2} = -1.96$ for a 95% confidence interval. In practice, an alternate expression for the confidence interval is used with survival functions as equation 3.9 can lead to upper and lower bounds outside the [0,1] range. This second confidence interval, nicknamed the “exponential” Greenwood formula was introduced in a textbook by KALBFLEISCH et PRENTICE [85] and proposes asymmetric confidence intervals that strictly respect the [0,1] bounds.

$$\exp(-\exp\{c_+(t)\}) < S(t) < \exp(-\exp(c_-(t))) \quad (3.10)$$

where

$$\begin{aligned} c_\pm(t) &= \log(-\log \hat{S}(t)) \pm z_{\alpha/2} \sqrt{\widehat{V}} \\ \widehat{V} &= \frac{1}{(\log \hat{S}(t))^2} \sum_{t_i \leq t} \frac{d_i}{n_i(n_i - d_i)} \end{aligned} \quad (3.11)$$

Throughout the report, all confidence intervals associated with survival functions are computed using equation 3.10. Whenever a survival function was fitted in this report, we weighted the survival points with the standard deviation $\sigma = \sqrt{\widehat{\text{Var}} [\hat{S}(t)]}$ estimated from equation 3.9 and let this error propagate to the fit parameters. To simplify, the event durations were rounded to the nearest frame timepoint when performing complex modeling of the survival.

3.3 Results

3.3.1 Experiment manager

General considerations We designed a software that structures experimental data into nested well and position folders, mimicking the spatial segregation in a multi-well plate. The per-well partitioning allows experimentalists to test in parallel multiple biological conditions, such as different cell types, drugs or antibodies at different concentrations, pre-treatments on the cells or surfaces, and so on. Since cells

are microscopic objects, observed at high magnification, it is rarely possible to image all the cells at once. At best, experimentalists pick multiple positions within the well, in the hope that the sampling is representative enough of the whole well.

In Celldetective, single-cell detection is always performed at the single position level, with the possibility of looping over many positions or wells. Higher representations, such as population responses, can pool the single-cell information from a whole well (*i.e.* multiple positions).

Practicality *Get started.* To start Celldetective, the user must open a terminal and type `python -m celldetective`. The command executes a `__main__.py` script in the package that in turn starts the PyQt graphical interface. First, a splash panel displays Celldetective’s logo while the Python libraries load in the background. Then the startup window illustrated in figure 3.9a opens. The user can either create a new experiment (button New or shortcut `Ctrl+N`) or load one. The menu bar adds some extra functionalities. Under `File/Open Recent`, the user can locate recently loaded experiments. `File/Open Models location` is a shortcut to open in the file navigator the folder containing all of the software’s DL models.

Creating a new experiment. Upon clicking on the New button, a file dialog window opens to locate where, on the disk, the experiment is to be located. The “new experiment utility”, shown in figure 3.9b opens automatically once the path is set. The user can give a name to the experiment. The name should not contain any space and special characters should be avoided. The movie settings section of the UI defines the structure of the experiment as well as basic metadata for the movies. Two sliders control respectively the number of wells and the number of positions per wells. The spatial and temporal calibration of the movies can be set in the respective fields. The user can set a prefix for the filenames of the movies, in such a way that it is possible to have more than one movie in each position and still “pilot” which one should be processed. The next section sets the modality content of the movies, *i.e.* the name and order of the movie channels. The user can pick channels from the list that follow our naming conventions or define as many new channels as needed. The channel index must also be set consistently, leaving no gaps and matching with the actual number of channels in the movies. Once everything is filled, the user can submit which opens a final window, shown in figure 3.10. This window exploits the provided number of wells to allow the user to describe specifically the biological conditions associated with each well. As an attempt towards a general-purpose solution, we propose to specify the cell populations on the images, the antibody(ies) used, their respective concentration, and whether extra pharmaceutical agents have been used. Upon submission, the path to the new experiment is automatically set in the startup window and the control panel (figure 3.9c) can be opened.

Experiment folder. At this stage, nothing can be processed since the experimental data has not been provided yet. A Celldetective experiment is only a folder plus a configuration file (written in the `ini` format). The experiment folder contains well folders (as many as there are wells). Naturally, each well folder contains as many

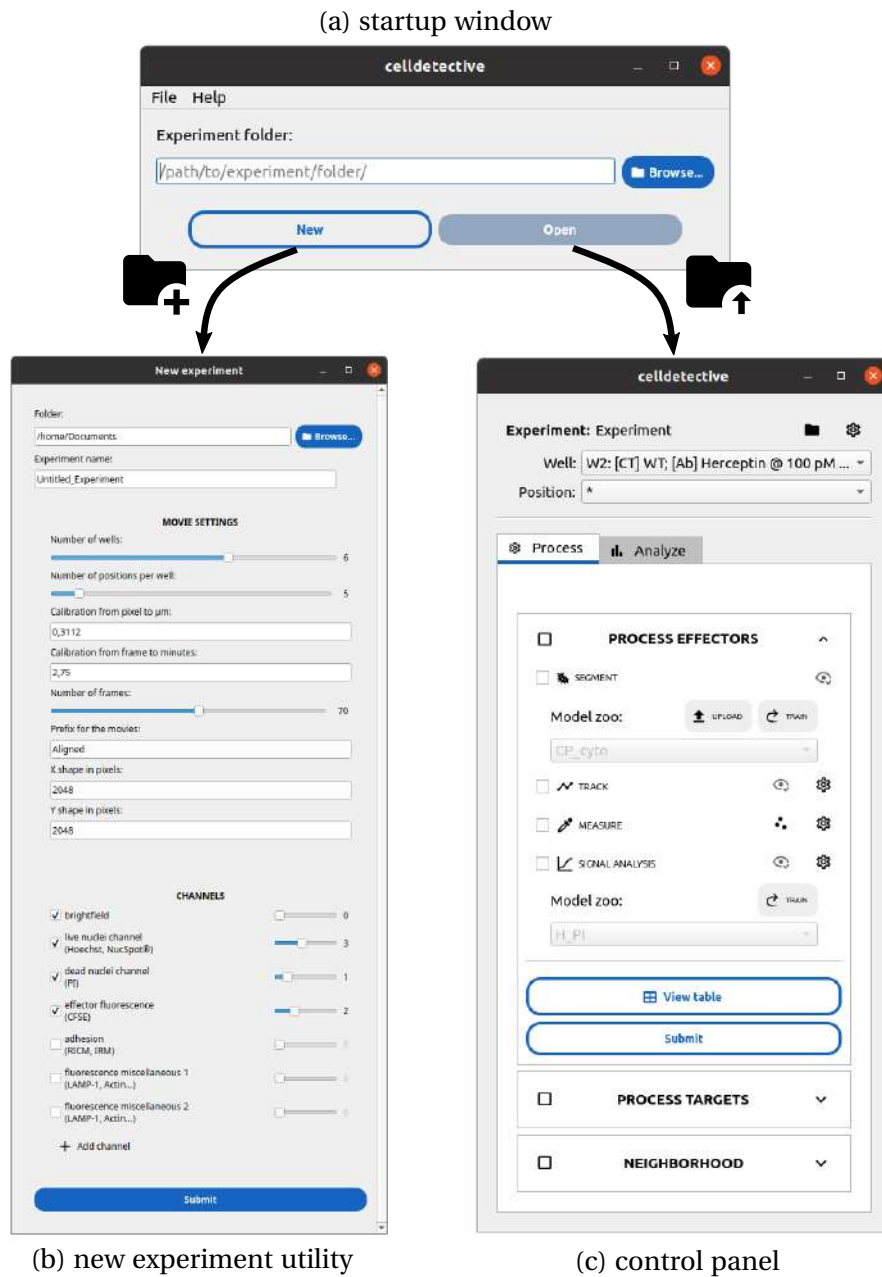


FIGURE 3.9 – CellDetective's main GUI. a) the startup window can be used to either (b) create a new experiment or (c) load an experiment. b) The new experiment utility guides the user in the making of an experiment configuration, providing all the necessary information to manipulate the experimental data. c) A control panel interfaces all the processing functions.

position folders as there are positions per well. A position folder only contains a movie/ subfolder, where the user must drop the data associated with that position. By force of habit, processing a movie implies processing a position and *vice versa*.

Compatible data. CellDetective only supports multichannel time-lapse microscopy data which translates into 3D (TXY) or 4D hyperstacks (TCXY). We recommend

The screenshot shows a window titled "Well conditions" with a standard macOS-style title bar. Inside, there are six rows labeled "well 1" through "well 6". Each row contains four text input fields with placeholder text: "cell type: e.g. T-cell, NK", "antibody: e.g. anti-CD4", "concentration: e.g. 100 pM", and "pharmaceutical agents: e.g. dextran". At the bottom of the window, there are two buttons: a light blue "Skip" button and a dark blue "Submit" button.

FIGURE 3.10 – Labeling the wells in the new experiment utility. Celldetective collects information about the biological conditions tested in each well. This information is propagated down to the single-cell description.

opening the experimental stacks on ImageJ first to ensure that the dimensions of the stack are properly set. With microscopy data acquired through μ Manager, it is quite common to have the channel dimension interlaced with the time dimension. On a large stack (above 5 Gb), we found it useful to save the stacks using the *Bioformat Exporter* plugin of ImageJ. If the data is not a time series but the user still wants to use Celldetective for segmentation and measurements then a trick to make it work is to replace the missing time dimension with a position dimension. In this case, each stack “frame” is in an image sampled at a different position within a well, and there is only one position folder and movie for this well.

Control panel. Once the stacks are in their proper place, within position folders, the user can start interacting with the control panel. The top part of the window provides shortcuts to the experiment folder and the configuration file. The well and position lists right below control which data is to be processed when the user triggers processing and analysis modules (one position, one well, everything). The Process tab provides modules to achieve a single-cell description for two different populations, complete with a neighborhood module. The Analyze tab groups visualization modules to explore the single-cell data. In the next sections, we will explore step by step the behavior and reasoning behind all of the modules presented in this control panel. Note that the design of figure 3.3 follows closely that of the control panel.

Multiple experiments. The user can seamlessly hop from one experiment to another using the startup window. There is currently no support for meta-analysis through the GUI, but the structure and configurations of the experiments are so standardized that we routinely write scripts to collect information from multiple experiments.

3.3.2 Segmentation

3.3.2.1 Traditional segmentation

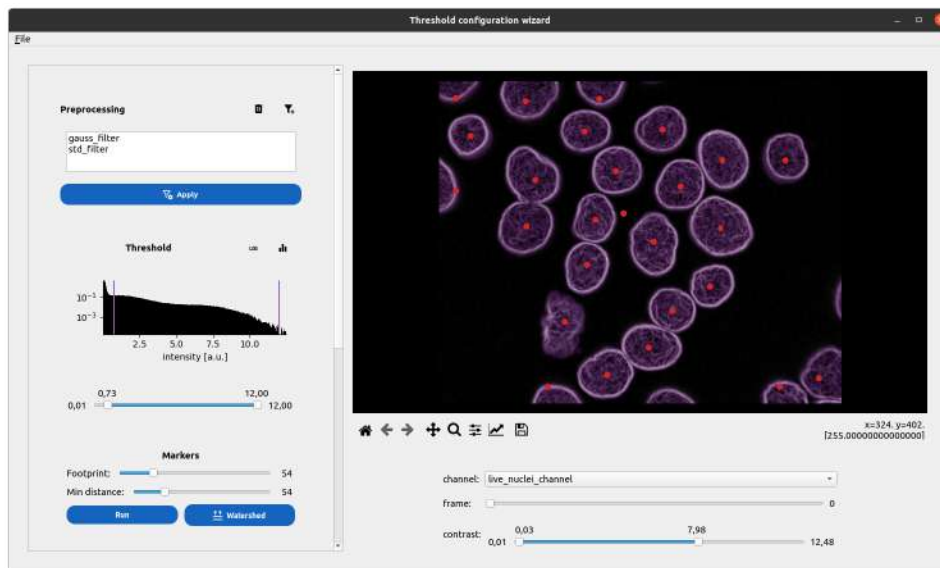
General considerations In many applications, cell or nucleus segmentation can be achieved through the use of filters and thresholds, without having to resort to a DL model. Adapting such a model to a new system can be time-consuming and computationally expensive, as it usually requires numerous annotations. To ensure a user-friendly experience with Celldetective, we developed a robust framework for traditional segmentation as a potent alternative to calling a DL model. The framework, called the threshold configuration wizard (TCW) is shown in figure 3.11. In broad terms, this interface allows the user to define a segmentation pipeline which can be broken into the following steps : 1) applying filters to activate the relevant regions in the images, 2) setting a threshold on the processed image to generate a binary segmentation, 3) using the watershed method to transform the latter into an instance segmentation and 4) eliminating objects based on morpho-tonal features and spatial location.

Practicality *Get started.* To launch the TCW, the user begins by setting a specific position within an experiment. Then for the population of interest, the user must click on the UPLOAD button of the segmentation section. Eventually, the user can toggle the threshold option, revealing a button to either access the TCW or import a threshold configuration generated with the TCW.

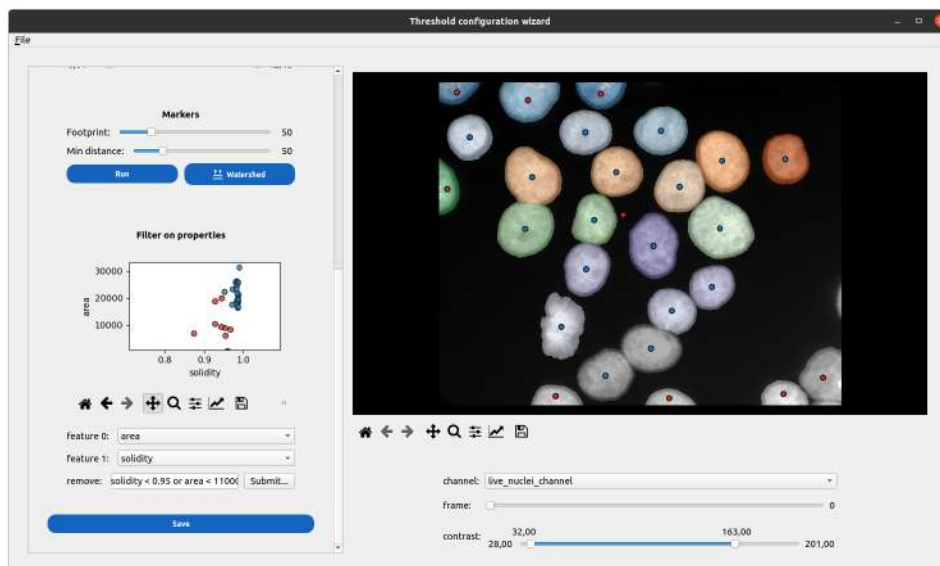
Startup. Upon startup, the TCW loads the initial frame of the movie associated with the selected position, operating in virtual-stack mode where only one frame is in memory at a time. An automatic threshold binarization of the image is overlaid to the image, in semi-transparent magenta, as shown in figure 3.11a. Users can choose a different channel, navigate to another time-point, and re-adjust the image contrast. Once satisfied with the image selection, modifications should be avoided until the configuration process is complete.

Filtering. The building blocks of the segmentation are centralized on the left panel and are designed to be run sequentially. First, the user can compile a set of preprocessing filters, mathematical operations, and local-threshold techniques from the list in table 3.3. For example, the white tophat filter was applied to brightfield images to detect yeast cells. The filter successfully activated the bright center of contrasted cells, making them easy to count. This work is illustrated in article [150]. As another example, variance and standard deviation filters can successfully activate the heterogeneous regions of the images, such as cell edges. Upon addition, the user must set the parameters of the preprocessing function. The user can add or delete as many of these functions as needed. Once applied, these functions are executed sequentially resulting in the update of the image on the right side panel and of the histogram on the left panel.

Thresholding. A double slider located below the histogram allows to fine-tune the



(a) Prefiltering the image for an easier thresholding.



(b) Using morpho-tonal features to filter out false positives.

FIGURE 3.11 – The threshold configuration wizard in action. Application of the TCW to an image of HaCaT cell nuclei stained with DAPI from the dataset S-BSST265 [96] is loaded into the TCW of Celldetective. a) the raw image undergoes a series of preprocessing filters, namely a Gauss filter with kernel (2×2) and a standard deviation filter with a kernel (2×2) . The upper and lower thresholds on the transformed intensities are set and the image is binarized. Peak detection parameters are optimized to the size of the nuclei. b) Post-watershed application, the original image, and its instance segmentation are shown on the right-side panel. Single object measurements are automatically performed to facilitate the identification and removal of false-positive detections. In this application, a filter based both on area and solidity effectively eliminates nuclei truncated at the edges and smaller objects.

Table 3.3 – Image preprocessing functions. This table summarizes respectively the different filters, mathematical operations and local thresholding techniques implemented in Celldetective that can be called in any combination when defining a traditional segmentation pipeline in the TCW.

name	parameters	qualitative effect
gauss_filter	σ	blur, smoothing
median_filter	size	Edge-preserving smoothing
max_filter	size	dilation
min_filter	size	erosion
percentile_filter	size percentile value	intermediate
variance_filter std_filter	size	variance standard deviation
laplace_filter	None	edge enhancement
dog_filter	σ_{low} σ_{high}	Difference of Gaussian edge enhancement
log_filter	σ	Laplacian of Gaussian edge enhancement
tophat_filter	size connectivity	isolate small bright objects
abs_filter subtract_filter ln_filter	/	pixelwise mathematical operations
otsu_filter local_filter niblack_filter	/	local thresholding

upper and lower bounds for the binarization. The semi-transparent binarization overlay is updated in real-time on the right panel as the slider handles are adjusted. Visualizing the histogram values in the y-log-scale has proven to be particularly advantageous and can be triggered by simply clicking on the LOG button. Users have the option to activate a histogram matching function that will be implemented at scale during the segmentation of entire movies.

Watershed. After achieving satisfactory binarization, the user must tune peak detection from the Euclidean distance transform of the binary image. A first slider tunes the footprint size for searching peaks at each point in the image, a square of dimension (footprint size \times footprint size). The second slider sets the minimum separation allowed between peaks. Upon clicking on the run button, the detected peaks are presented as a scatter of red dots on the filtered image. Executing the watershed function merges information from the Euclidean distance transform and

the coordinates of the peaks, resulting in an instance segmentation around each peak. The instance segmentation replaces the binary image on the right side, and the original image takes the place of the filtered one to assess whether or not the segmentation is representative of the real objects.

Feature filtering. Right after the watershed, features are computed for all objects and shown in an interactive scatter plot on the left panel. The features can be spatial (absolute position, radial distance to the center), morphological (area, eccentricity), or tonal (mean intensity in each channel). The user has the option to establish conditions based on these measurements to filter out false-positive detections. The syntax for the conditions is that of pandas query expressions, enabling the user to effortlessly formulate and or or conditions involving two or more measurements. Objects that are rejected as a result of these conditions have their centers highlighted in red.

Configuration management. Upon clicking on the Save button, all choices are written down in a json configuration file, saved automatically in a configs/ sub-folder of the experiment folder, and the TCW closes automatically. The path to this configuration file is automatically loaded in the Upload model window, and it is up to the user to click on Upload to effectively load it in Celldetective. In other words, the configuration file is attached to an experiment and has to be imported every time an experiment is loaded. To apply this pipeline to the whole movie or many movies from the experiment, the user can choose the Threshold option in the model zoo for segmentation and launch the analysis.

3.3.2.2 Deep learning segmentation

General considerations The DL formulation for segmentation has made possible accurate cell segmentation in instances where traditional algorithms almost always fail such as high cell density or when the background is far from smooth.

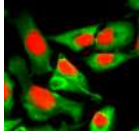
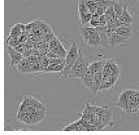

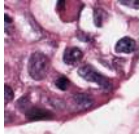
We propose segmentation models trained with the StarDist [155] or Cellpose [169] algorithm. They are split into two families : the generalist models on one hand, and models specific to a cell population in particular modalities on the other hand. The generalist models published in the literature (see table 3.4) have been trained on thousands of images with one or two channels, on general tasks such as segmenting all nuclei visible on the images. In some cases, more than one modality was passed in the channel slots during training to force the model to generalize and be less sensitive to the modality. The second are models that we trained from scratch on brand new multimodal data to achieve more specific tasks such as detecting the nuclei of a population in the presence of another. In this configuration, accurate segmentation often requires looking at multiple channels at once, *i.e.* performing a multimodal integration. These models will be discussed in the next two chapters, in the context of their application.

In practice, generalist models are quite robust to changes in cell types but lack specificity when cell populations are mixed, as exemplified in figure 3.12a. On a fluorescence image showing the nuclei of immune and cancer cells, the StarDist *versatile fluo* generalist model detects all cell nuclei, sometimes at the cost of accuracy when effector nuclei overlap with target nuclei. Most of these models have been trained on cytoplasm, membrane or nucleus fluorescence images and brightfield images, which covers a lot of potential modalities but not all of them (*e.g.* RICM, illustrated in figure 3.12b). Applying Cellpose models on RICM images mostly fail, with only *cyto2* achieving a correct segmentation of the spread cells. We can speculate that some RICM images were part of the undisclosed user-submitted dataset that was used to train this model or that the model is generalist enough to understand cell shape on such images, a zero-shot learning situation. Whenever possible, it is best to keep track of the training data for each of these published models to know what is likely to work best on user data or to assess this through trial and error.

Models can be fitted to new data, either to optimize performance or to perform what is known as a transfer, modifying slightly the model’s task to make it, for example, more precise. For example, a model that segments round nuclei can be repurposed to segment a cell type that is almost round and observed in a similar modality. Transfer can be extremely convenient if the annotated dataset is very small as the learning does not have to start from random. A drawback is that some task modifications are subtle and imply much more than a fine-tuning of the model weights.

Practicality *Calling a DL segmentation model.* The segmentation section contains a model zoo, *i.e.* a list of segmentation models stored in Celldetective. Each cell popu-

Table 3.4 – Generalist models. This table lists the different generalist models (Cellpose or StarDist) which can be called natively in Celldetective. The images have been sampled from their respective datasets, cropped to (200×200) px and rescaled homogeneously to fit in the table.

name	modalities	# channels	dataset	sample image
CP	cytoplasm nucleus	2	Cellpose	
CP_cyto	cytoplasm nucleus	2	Cellpose	/
CP_cyto2	cytoplasm nucleus	2	Cellpose & user-submitted images	/
CP_livecell	cytoplasm (BF) blank	2	LiveCell [51]	
CP_tissuenet	cytoplasm nucleus	2	TissueNet [9]	/
CP_nuclei	nucleus blank	2	?	/
SD_paper_dsb2018	nucleus	1	subset of DSB 2018 [63]	
SD_versatile_fluo	nucleus	1	subset of DSB 2018	/
SD_versatile_he	H&E RGB	1	MonoNuSeg 2018 [98] TNBC 2018 [79]	

lation has its model zoo, split into two parts : 1) the models specific to the population and 2) the generalist models that are shared. The user can tick the segmentation option, pick a model from the list, and launch the analysis to apply the model to the data set by the control panel header. In the background, a subprocess reads the input configuration file associated with the model, defining the input channels and how they should be normalized as well as the expected spatial calibration Δx_{model} of the images. The actual spatial calibration of the images Δx is read from the experiment configuration. The rescaling factor is computed as : $f = \Delta x / \Delta x_{\text{model}}$. Each

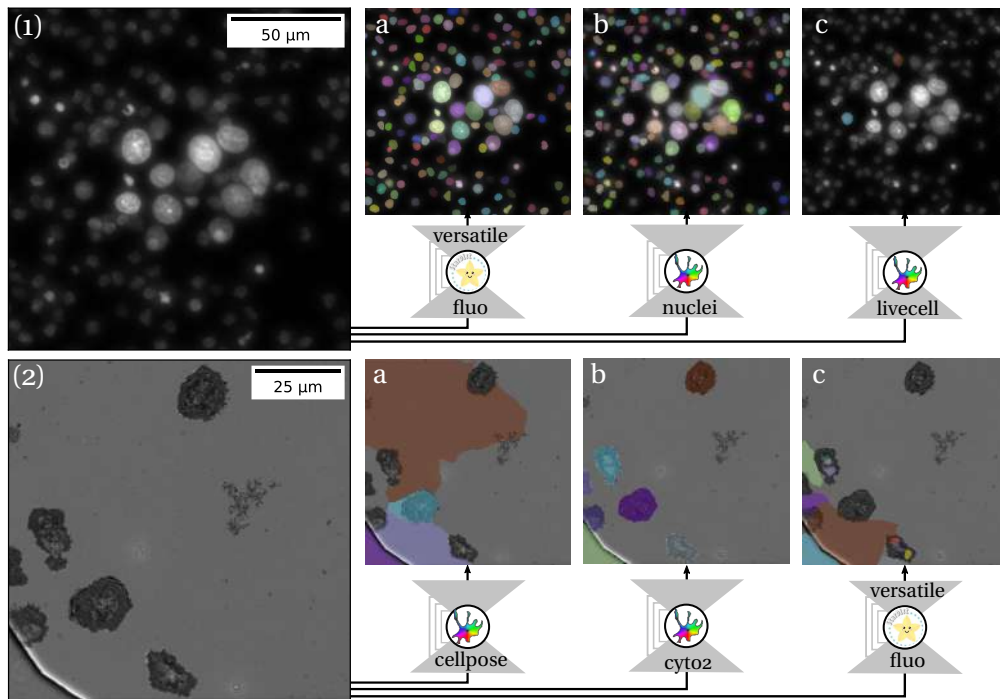


FIGURE 3.12 – Applicability of generalist models. Published generalist models can be applied to the user’s microscopy data provided the images are not too different from the training set of these models. In general, these models will be nonspecific. a) an image of fluorescent nuclei of a mixed population of effector (human primary NK cells) and target cells (MCF-7 breast cancer cells) is segmented using different published models. The StarDist *versatile fluo* model yields an excellent segmentation of both cell populations simultaneously but separating the cells in post can be a difficult process as a blurry NK nucleus is close in size to a small MCF-7 nucleus. 1b) The Cellpose *nuclei* model also achieves a high segmentation precision but the edges are pretty rough, as the images have to be considerably shrunk down before passing into the model (17-pixel nuclei). 1c) the Cellpose *livecell* model, trained mostly on brightfield images, does not understand the nuclei data and misses most of the cells. b) an RICM image of human primary NK cells spreading on a surface. 2a) the Cellpose model misunderstands completely what a cell is in this kind of image. 2b) the Cellpose *cyto2* model yields a very sharp segmentation of the spread cells but ignores non-spread cells. It also mistakenly segments the diaphragm at the bottom left corner of the image. 2c) the StarDist *versatile fluo* model is the wrong model for this kind of data as the convex hypothesis is broken. The *cyto2* model is the best candidate for a transfer learning process.

multichannel frame is loaded, rescaled, normalized, and segmented one by one, writing the output labels in the position folder. If the image had to be rescaled to be segmented, then the labels are rescaled by a factor $1/f$ before being saved.

On the fly configuration for generalist models. Generalist models add an extra step between the launching of the analysis and the segmentation, as their input configuration is often ill-defined. Typically, model architectures impose the number of channels, but the actual channel selection is very context-dependent. Some models have been trained on different image modalities (e.g. the “cyto” channel of Cellpose can be a brightfield image or a cytoplasm fluorescence modality), therefore the

user must be free to pass any channels in the slots defined by the architecture. The channel selection is written on the fly in the generalist model’s input configuration. In addition, generalist Cellpose models need an estimate of the cells’ diameter and some extra threshold parameters (flow and cell probability). The original training data for the Cellpose models was always rescaled in such a way that the diameter of the cells on the images averaged 30 px^{*}. In other words, these models are only used to seeing 30-px-sized cells and are therefore insensitive to the physical size of the cells, which we found problematic, particularly when handling a mixture of cell populations where cell size is a critical determinant in the identification of a cell type. In practice, we convert the cell diameter estimate provided by the user into an equivalent spatial calibration Δx^{eq} for this Cellpose model, on this cell population. If the cells have an average diameter $d = 60$ pixels in an image with a spatial calibration $\Delta x = 0.1 \mu\text{m}$, then :

$$\Delta x^{\text{eq}} = \frac{\Delta x \times d}{d_{\text{cellpose}}} = \frac{0.1 \times 60}{30} = 0.2 \mu\text{m} \quad (3.12)$$

To segment one of our $0.1 \mu\text{m}$ per pixel image, we have to shrink it by a factor $f = \Delta x / \Delta x_{\text{model}} = 0.1 / 0.2 = 0.5$. The Cellpose model is told to look for 30-px-sized cells, which is true after rescaling. If we perform a transfer learning from such a model, to specialize it on a cell population, the concept of diameter becomes obsolete and all images are standardized to this equivalent spatial calibration which becomes effectively Δx_{model} .

3.3.2.3 Design overview

General considerations The process of instance segmentation takes an image (2D or 3D if multichannel) as its input and yields a label image (2D), where each segmented object is attributed a single label. As a consequence, we ensured that both the traditional and Deep-learning segmentation modules yielded an identical output. This output is visualized and annotated in the napari viewer, which we completed with simple plugins to manage corrections and export annotations. Figure 3.13 illustrates the many entry points possible to perform segmentation in Celldetective. The goal is to achieve a single-cell description for up to two cell populations independently.

As mentioned before, generalist models lack specificity when tasked with segmenting mixed-cell populations. Nevertheless, if the population of interest can be isolated on a single modality and the modality is not too remote from the training set of the model, then a generalist model is often the best starting point. It can be applied to the user’s data, lack and non-specificities can be corrected in napari for a few images, and the generalist model can be retrained on the new data, making it more *fit* to the user’s data. This technically new model shifts from generalist to

*. 17 pixels for the *Cellpose nuclei* model

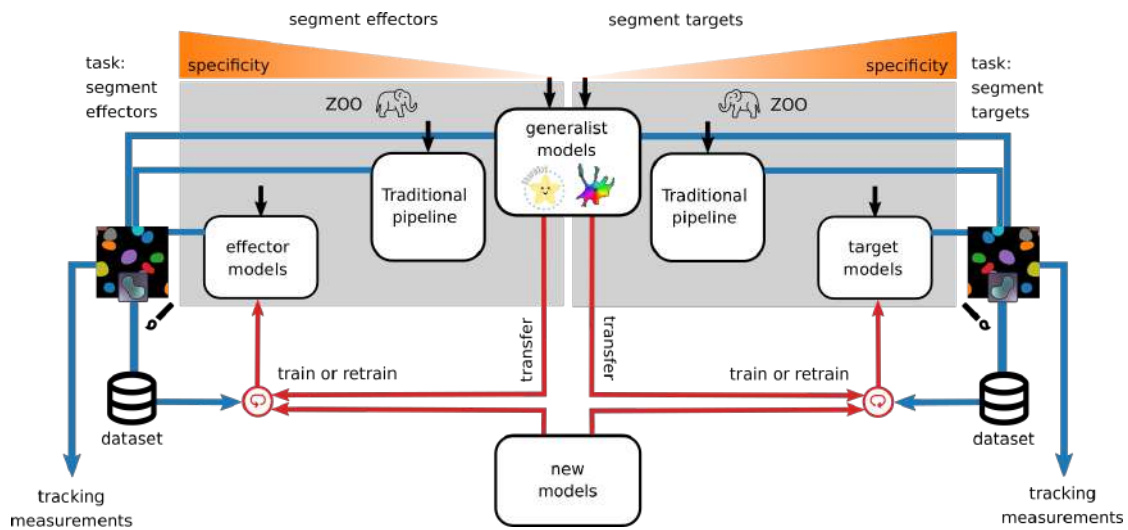


FIGURE 3.13 – Overview of segmentation options in Celldetective. Celldetective provides several entry points (black arrows) to perform segmentation, with the intent of segmenting specifically a cell population (left : effectors, right : targets). The mask output from each segmentation technique can be visualized and manually corrected in napari. Exporting these corrections into a paired image and mask dataset can be used either to fit a generalist model (transfer learning) or train one from scratch. Once the segmentation is satisfactory enough, the user can decide to proceed with the tracking and measurement modules.

specific to the new task it is trained on, *e.g.* segmenting effectors or targets.

When the experimental data is too different from the original training set of the generalist models, an alternative entry point is to define a traditional segmentation pipeline, as described in section 3.3.2.1. If the cells are sparsely distributed and isolated in a single channel, then a traditional pipeline can outperform DL methods. It is likely to fail if image quality fluctuates and, despite the watershed improvement, not be very accurate when cells are in contact with each other. Traditional segmentation pipelines are much faster to design and run than DL segmentation models but leave little room for improvement. As before, the label images can be corrected in napari to serve as a dataset for a specialized and accurate DL model created from scratch, that can take over from a traditional segmentation pipeline.

Practicality *Visualization & annotation in napari.* To open the napari viewer, the user must click on the eye button in the segmentation section for the cell population of interest. If no segmentation was performed before opening the viewer, the software suggests creating an empty segmentation (all zero-valued label images) on the spot, which allows to annotate images from scratch. Each movie channel is loaded as a separate layer in napari, with a bottom slider to explore the time axis. Channels can be colored and viewed together with opacity tuning. The label images are assembled as a segmentation layer, with different options, including its image manipulation toolbox. A brush allows one to paint any desired mask value on the

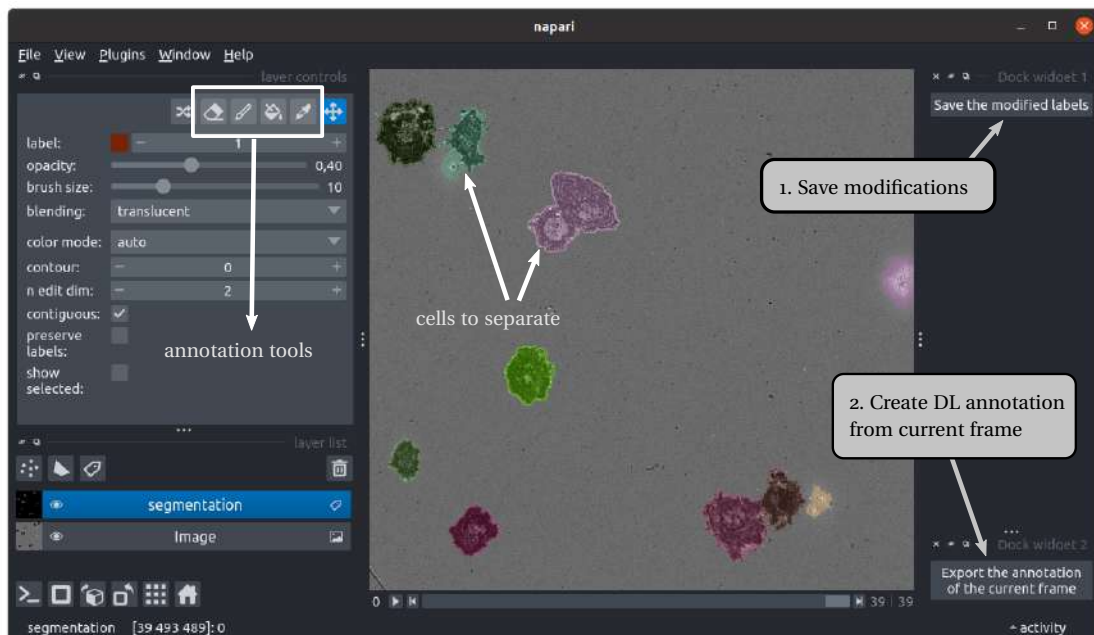


FIGURE 3.14 – Using napari to visualize and correct segmentation output. napari provides the basic requirements of image manipulation software, namely a brush, rubber, bucket, and pipette, to work on the segmentation layer. In this RICM image of spreading NK cells, two couples of cells have been mistakenly segmented as one object and must be separated. On the right panel, two plugins specific to Celldetective allow 1) the export of the modified masks directly in the position folder, and 2) to create automatically an annotation consisting of the current multichannel frame, the modified mask, and a configuration file specifying the modality content of the image and its spatial calibration.

images. If a cell is under-segmented, the user could use the pipette to pick up its value and apply the brush over the missed pixels. On the other hand, if a cell is over-segmented or if cells that should be separated are segmented as one, the rubber can help. Typical segmentation errors include incomplete segmentation of a cell, nonspecific segmentation of a surface or image defect, nonspecific segmentation of the wrong cell type, a fusion of two or more cells, or a completely missed cell.

Annotation rules. Since we only deal with instance segmentation in the context of Celldetective, extra care must be taken not to label different cells with the same value. This can be achieved comfortably in napari by pressing the key M to set the brush value to a value that has not been used on the current frame. We found it convenient to have a bounding box representation of the annotated cells to quickly detect anomalies of this kind in the training data of the DL segmentation models. This representation is not currently implemented in Celldetective. By convention, we annotated cells cut at the edges of the movies. Currently, the whole field of view must be corrected for the annotation to be valid, as there is no support yet for ROIs. If it is too cumbersome because there are too many cells to correct, we recommend cropping the original movie before segmentation. Annotations of a smaller field of

view are perfectly fine to train a model that can be applied to the whole image later on.

Export annotated data. We implemented a simple napari button plugin to organize and export the annotations, ready to serve as inputs to Deep-learning segmentation models. The plugin reassembles the current multichannel frame as a `tif` file and collects the current label image (also as a `tif`). In addition, it generates a small `json` configuration file listing the channel names and the spatial calibration (extracted automatically from the experiment configuration). If initially napari was opened from the effector processing block, an `annotations_effectors/` folder containing the annotation would have been generated at the root of the experiment folder. As the process is reiterated, either within the same movie or, ideally, across different movies from the experiment, the user can efficiently constitute a small dataset.

Training from annotations. The user can use her annotations to train a specialized model. The TRAIN button above the segmentation model zoo opens a utility to configure the training or retraining of a segmentation model, illustrated in figure 3.15. If the user decides to load a pre-trained model, the number of channels is set, the input channels of that model are suggested in the proper slots and the model spatial calibration is set. If more channels are needed then the user should remove the pre-trained model and train from scratch. The normalization settings for each channel can be finely tuned, choosing between a percentile and an absolute min-max normalization (see 3.1), with or without clipping. If the channel has been normalized before analysis, or if the absolute intensity value is relevant to the segmentation, then an absolute normalization is appropriate. If the channel intensities fluctuate wildly across experiments then a percentile normalization should be preferred. The clipping can help the model converge faster during training, at the cost of information loss around the clipping values. The spatial calibration of the model Δx_{model} must be set to constrain the model to learn the physical size of the cells it segments. The volume of augmented data relative to the size of the train set can be defined. The data augmentation includes image translations, flipping, the addition of noise, and blur. The validation split defines the fraction of validation data in the dataset, images that are not augmented and that do not pass through the model, but over which metrics are computed at each epoch, guiding the model selection process. The model trains for n_{epochs} in the backend of Celldetective. Upon completion, the model is added at the source of Celldetective with its input configuration file, in the population-specific segmentation model folder and shows up in the model zoo, ready to be applied.

Details on the data augmentation. Our image augmentation starts with random flipping (vertical or horizontal). Then we perform Gaussian blur, with a σ sampled from a uniform distribution in the interval $[0, \sigma_{\text{max}}]$. Zero-valued regions in the original image (such as an image edge) are reset to zero after the blur. We add physical noise to the image with a certain probability and in random order, which includes Gaussian, speckle, Poisson and local-variance noise. Finally, the image is randomly shifted along the -x and -y axes. The empty regions are filled with zeros. It

is not currently possible to select a specific combination of augmentation functions in the software but can be achieved through the Python API.

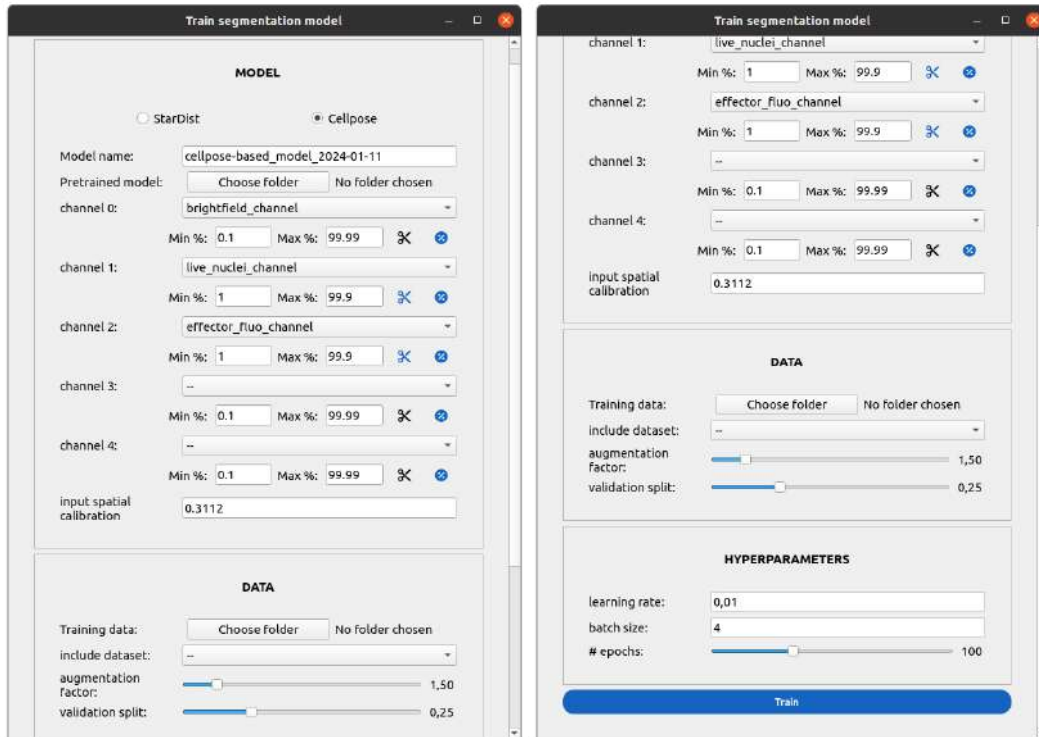


FIGURE 3.15 – Training segmentation models. a) From top to bottom : the user chooses between a StarDist and Cellpose model, and names the model. A pretrained model (generalist, specific) can be loaded to perform transfer learning. The channels and their normalization settings are defined. The desired spatial calibration for the input data is defined. In the DATA section, the user can point towards a folder containing annotations generated with napari (e.g. the annotations_effectors/ folder). The user can include a dataset, a folder of annotations integrated directly in Celldetective. The augmentation factor slider controls the volume of augmented data in the train set. The validation split slider sets the volume of the validation set. In the HYPERPARAMETERS section, the user must set the number of training epochs, the learning rate and the batch size.

3.3.3 Bayesian tracking

3.3.3.1 Adapting the tracker

General considerations After segmentation, tracking the cells is a necessary step to attribute a unique label, an identity, to each cell in a movie. Since cells exhibit complex motion that often goes well beyond the scope of Brownian motion, we decided to interface the state-of-the-art tracking method bTrack, exploiting both the motion history and the appearance of the cells to make the best tracking hypotheses. bTrack requires a configuration file to set all of its motion and tracklet hypotheses. This configuration can be produced interactively using the bTrack-napari plugin highlighted in figure 3.18. Each cell passed to the tracker can be attached to some features, which can be used to help with the tracking.

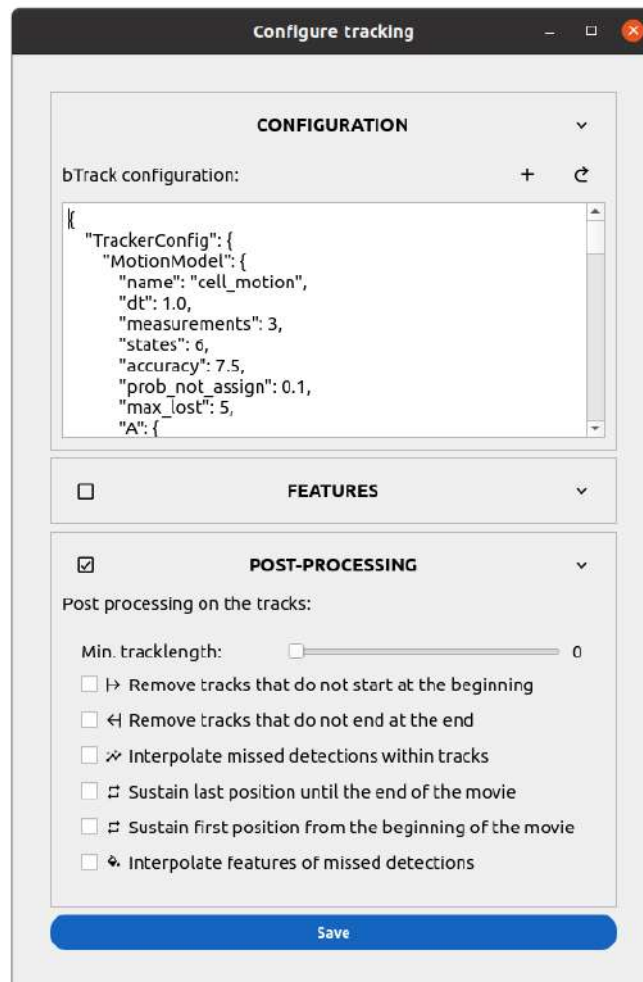


FIGURE 3.16 – GUI to configure the tracking parameters. A bTrack configuration can be modified in place, or other configurations can be loaded. Features can be passed to the tracker. Post-processing modules clean up the raw trajectories for subsequent analysis.

Practicality *Managing bTrack configurations.* The bTrack configuration should be optimized for each cell system. Therefore, we added to the tracking configuration window (figure 3.16) a text box to edit directly the current json bTrack configuration. In addition, users can import configurations that were produced with the napari-bTrack plugin, accessible directly in Celldetective, which is the recommended way to optimize a tracking configuration.

Adding features. The user can decide to pass features to the tracking (choosing among morphological, tonal, and textural features). If an intensity feature is chosen, the user can select which channels should be passed to bTrack.

Execution. Upon submission, a subprocess loads the multichannel images and the masks one frame at a time, to extract all cell locations. If features are enabled, they are measured along the way. Then the tracking configuration is loaded, as well as all the cells from all time points. The potential features are all normalized independently, using a standard scaler. The tracking mode switches from `motion` to `motion + visual` depending on the presence of features. The tracking is performed and a csv table containing at minima `TRACK_ID`, `FRAME`, `POSITION_X`, `POSITION_Y` columns is generated to store the tracks.

3.3.3.2 Post-processing on tracks

General considerations To correct obvious tracking mistakes, and measure beyond existing positions, we defined a track post-processing toolbox. Some highlights of the toolbox are illustrated in figure 3.17. To eliminate spurious tracks, we introduce a filter on the minimum track duration. In addition, we introduce endpoint filters to either remove tracks that do not start at the beginning of the movie (*e.g.* a cell entering the field of view midway through the movie) or tracks that do not last until the end of the movie (*e.g.* an incomplete track that truncated). A more exotic function is track sustaining, *i.e.* prolonging the first or last position in a trajectory respectively to the beginning and the end of the movie. We exploit this feature to perform background measurement in systems where cell sediment in the field of view only sometime after the movie starts. The last family of functions is the interpolation of position gaps and the associated features if some are being measured in the tracking process.

Practicality The last section of the tracking parameter UI (figure 3.16) pilots which post-processing functions are to be applied to the raw bTrack trajectories. The functions are applied automatically right after tracking.

3.3.3.3 Visualization

General considerations Due to some redundancy with the signal annotator described later and the obvious difficulty it entails, we do not provide direct and interactive track correction functions. Instead, we rely on the post-processing functions described in the previous section to remove false-positive tracks and minimize errors.

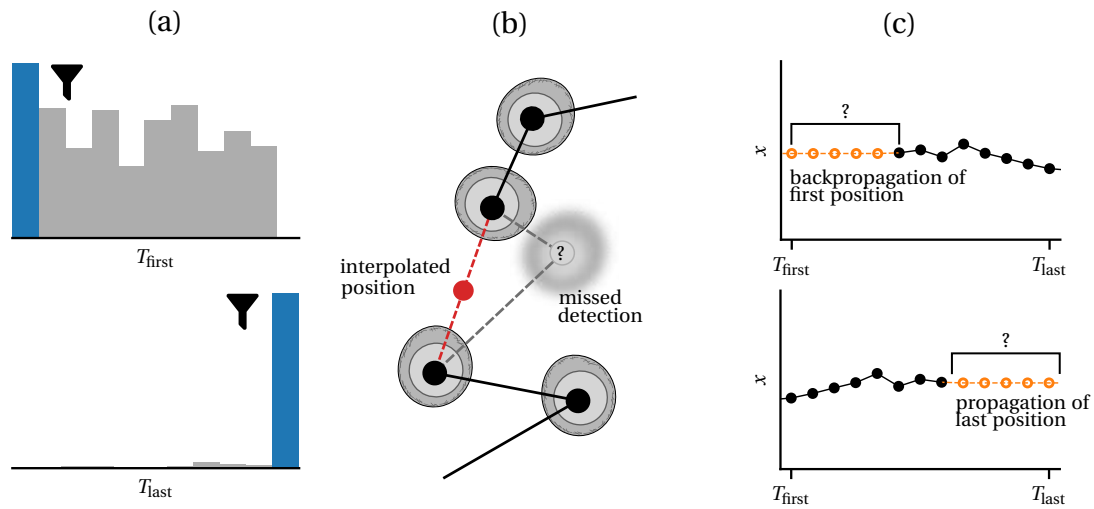


FIGURE 3.17 – Post-processing operations on trajectories. a) Endpoint filtering to remove tracks that do not start or end at the beginning and end of the movie. b) Interpolation of tracking gaps. c) Sustain on trajectories to extend the time range of the tracks.

We provide a visualization of the direct bTrack output (before the post-processing step) in napari. Track correction functionalities are likely to come shortly as a napari plugin, from the napari team, or as an independent effort. For viewing convenience, we relabel on the fly the cell masks to propagate the track identity directly in the mask value and therefore keep the same color across frames for a given cell.

Practicality To view the raw bTrack trajectories, the segmentation masks, and the movie in napari, the user must first set a single position in the control panel header, then click on the eye button in tracking section for the cell population of interest. The bTrack plugin can be called in the Plugins tab of napari and applied to the segmentation layer, to test new tracking parameters.

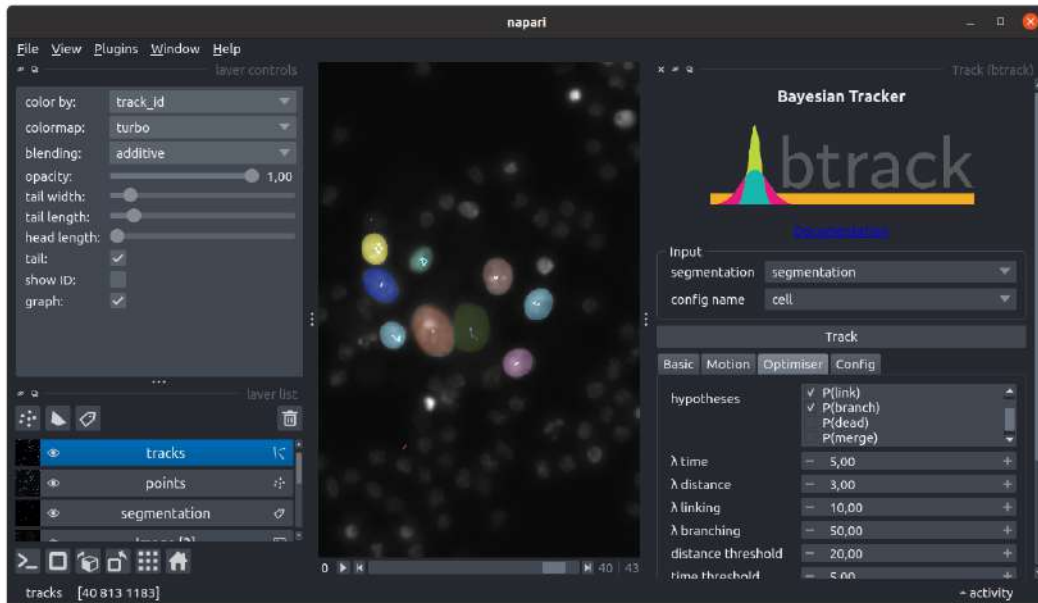


FIGURE 3.18 – Napari to view trajectories and optimize bTrack. Calling the bTrack plugin in napari to test bTrack tracking parameters interactively on the loaded movie and masks. In the Config tab of the plugin, the tracking configuration can be exported as a json file and be directly uploaded in the tracking parameter UI of Celldetective (3.16).

3.3.4 Single cell measurements

3.3.4.1 Mask-based measurements

General considerations The segmentation mask is an obvious starting point for performing single-cell measurements that are tonal, textural, and morphological. The mask provides an ROI over which a series of measurements can be performed at each time point. The mask can also be used to define sub-sections. One practical subsection that can be extracted from the Euclidean transform of the mask is to perform a threshold on the distance to the mask boundary, leaving a contour that reflects that of the mask but is smaller. With two threshold distances, it is possible to define a slice as shown in figure 3.19. This decomposition of the mask could be used to assess the peripherality of a fluorescence signal. For morphological and tonal measurements, we rely on the scikit-image library [178] and more specifically regionprops that provides a fast computation of features from masks.

Texture measurements, as defined by [68] can be computationally expensive. Indeed, a key step in this computation is building a Gray-level-co-occurrence matrix, which is as big as the square of all occurring intensity values on the image. For a 16-bit gray-scale microscopy image, the number of values can reach up to 2^{16} , and therefore the matrix can contain up to 2^{32} combinations. The sizes get impractically large for 32-bit images, *i.e.* images on which we performed some preprocessing (normalization, background subtraction). As a result, it is necessary to reduce the

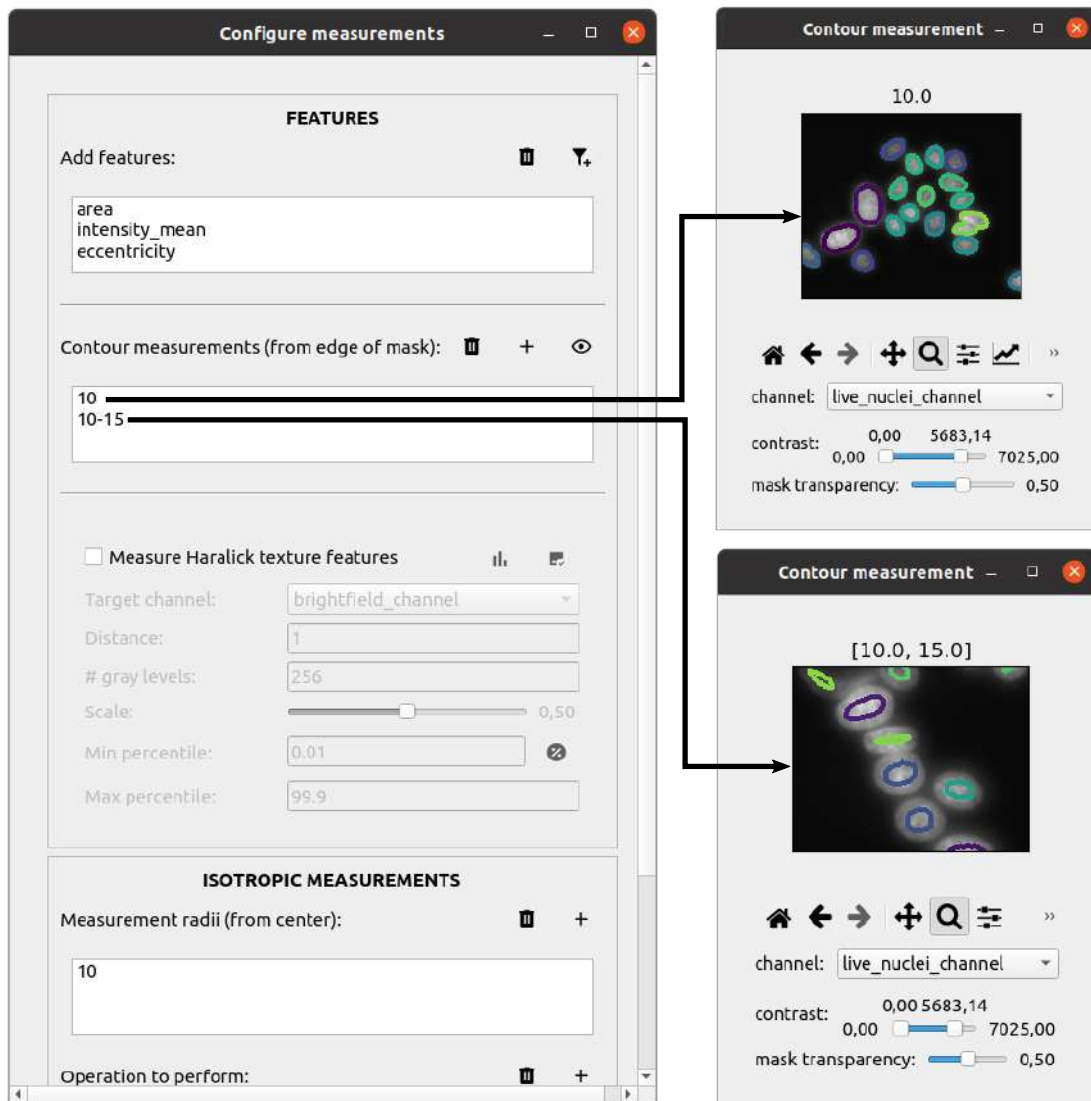


FIGURE 3.19 – GUI to pilot single cell measurements, with a highlight on contour intensity measurements. Mask-based measurements are picked from the list of region properties defined by [178]. The user can define and visualize contour bands, over which to compute tonal features. Here, the bands are shown for an image of MCF-7 cell-stained nuclei. The user can enable the computation of Haralick texture features and pilot isotropic measurements.

number of occurring values before performing a texture measurement. For a given channel, we propose to do it in two subsequent steps : first, the image must be rescaled with clipping using a min-max transform. The user can decide to use percentiles to define the min/max bounds or absolute values of intensity when applicable (e.g. pre-normalized images). The image is rescaled to the desired number of intensity values (a third parameter n_{GL}). Second, the image must be digitized. To do this, we make a n_{GL} -bins histogram of the rescaled image. For integer-valued images

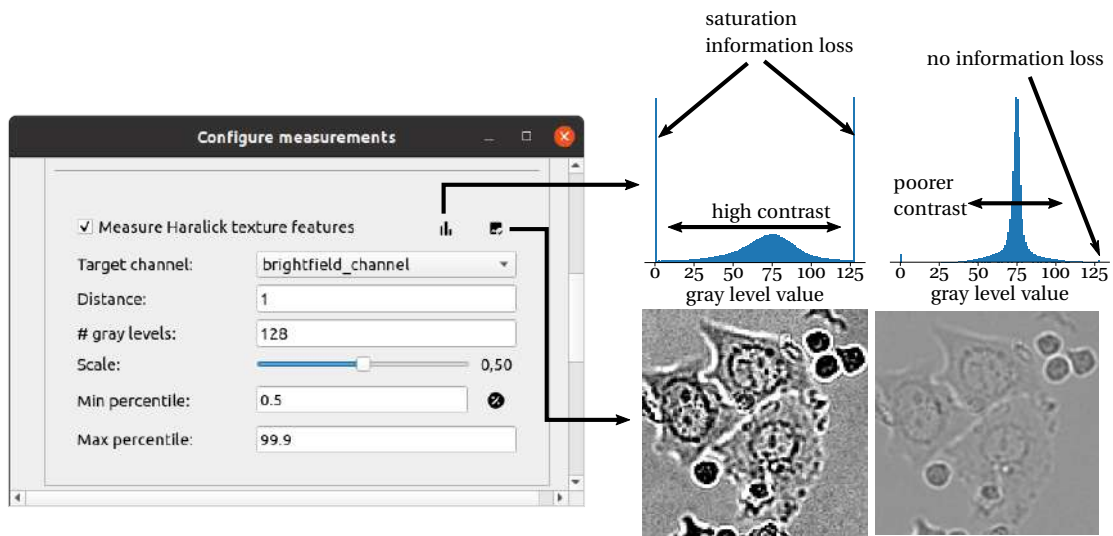


FIGURE 3.20 – GUI to pilot texture measurements. A section of the measurement configuration window is dedicated to the measurement of the Haralick texture features. As it is computationally expansive, measuring the texture is optional. The user selects the channel of interest within all of the channels available in the loaded experiment. A slider sets the scale parameter to scale down the image before textural computations. The # gray levels field sets the n_{GL} parameter. A switch button allows you to turn the min/max percentile fields into min/max value fields. A distance field sets the distance over which to compute intensity co-occurrences. On the top right corner, two visualization tools allow us to control respectively the histogram of the digitized image and the digitized image itself.

this step is not necessary, for float-valued images we replace each intensity value by the mean value of the bin to which it belongs, drastically reducing the number of values and achieving a total of n_{GL} intensity values. Both steps are critical to textural measurements, so we implement visual controls on 1) the histogram of the digitized image can be displayed, to assess that there is no saturation at the clipping values (which would indicate a loss of information for low and high intensities, as illustrated in figure 3.20); 2) the digitized image itself can be viewed, before texture measurements, to ensure that the texture we aim to measure has not been annihilated by our preprocessing.

The ROI and the co-occurring distance are two other critical parameters in texture measurements. Currently, in the GUI, the users can only use the segmentation mask of each cell as an ROI. In other words, we compute one GLCM and one set of texture features per cell and per time point. To still drive down computation time, we allow the users to downsize the image before preprocessing, which reduces the absolute number of pixels to compute.

Practicality As illustrated in figure 3.19, adding measurements is quite simple. The user can simply add and manage them from the list of available regionprops properties. The definition of contours takes one (distance from the edge) or distance values (slice), in pixel units. As many contours as needed can be configured and

viewed with a utility that loads the first frame of the movie of the position set in the control panel and displays, the mask slices on top of the original image. Texture measurements have to be explicitly enabled as they are slower to compute than the other measurements. Figure 3.20 shows in detail how texture measurements can be configured, complete with a histogram and digitized image visualization utility.

3.3.4.2 Position-based measurements

General considerations The post-processing operations performed on the trajectories can introduce spatial locations for which there is no associated mask. Indeed, interpolating missing points in trajectories leaves open the question of how and what to measure in these new locations. An even more extreme case is track sustaining, which creates a completely new set of locations where the cell may not even exist. In the absence of orientational information, the best course of action was to go for an isotropic (circle or ring) measurement of intensities, centered on the positions, irrespective of whether they were interpolated or not. Therefore, for a complete track, we could always expect a complete intensity measurement. Tuning the radius of this circle (or radii for the ring) is an important choice.

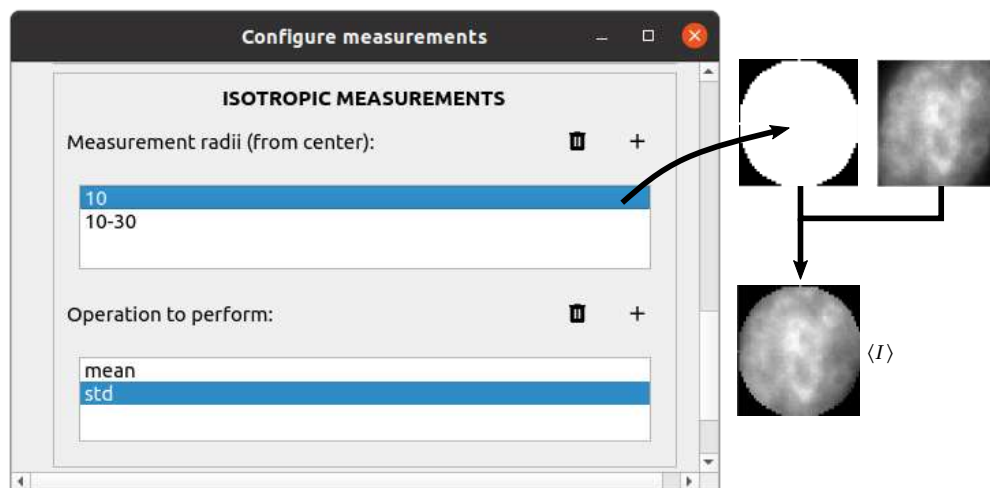


FIGURE 3.21 – GUI to pilot isotropic measurements. The last section of the measurement configuration window is dedicated to setting up isotropic tonal measurements. The user can define and manage as many circles and rings as desired. Then the operations to be performed on the intensities within the circle or ring are defined right below. By default, all measurements are applied to all available channels in the experiment.

Practicality The isotropic measurements are interfaced in almost the same way as the contour measurements, with the exception that the operation to perform over the circle (or ring) ROI has to be defined below (among mean, standard deviation, and others). Upon submission a subprocess is launched to take each multichannel

frame one by one and perform first the mask measurements and second the isotropic measurements with the kernel defined here. Figure 3.21 describes how we interfaced the configuration of position-based measurements in Celldetective. If this example is for three-channel microscopy data then $3 \times 2 \times 2 = 12$ signals will be generated for each tracked single cell.

3.3.4.3 Cell dynamics

General considerations Cell motion is quantified directly from the trajectories. Various techniques have been used to assess cell migration, diffusion, and velocity, all revolving around the same fundamental problem of timescale over which to compute these quantities. Velocity estimators are usually instantaneous, and defined over small time windows, whereas diffusion coefficients often pertain to the trajectory as a whole. This timescale numerically takes the form of a sliding window. Say that we look at the velocity in a 1D trajectory, in such a way that the estimator for the velocity is simply an estimator for the derivative. Let's take a sliding window of 3. If the velocity is estimated from the points “forward”, in a one-sided manner, then the velocity v_0 can be expressed as $(x_2 - x_0)/(t(x_2) - t(x_0))$ [134]. The velocity could also be expressed using both points forward and backward, with a “bidirectional” estimator, using what is called mathematically the central difference. In this case v_0^{bi} is not defined because we cannot define x_{-1} but $v_1^{\text{bi}} = (x_2 - x_0)/(t(x_2) - t(x_0))$ is strictly equal to v_0^f . Finally, the third extreme is to measure the “backward” velocity, also in a one-sided manner, in which case neither v_0^b or v_1^b are defined but $v_2^b = (x_2 - x_0)/(t(x_2) - t(x_0))$ is equal to v_0^f and v_1^{bi} . Changing the derivative convention simply shifts in time the velocity values. Still, we made sure to let the user choose the convention, as it can be convenient to associate a certain velocity to a time-point to characterize, for example, an abrupt transition. A larger sliding window averages the velocity at a larger time scale, smoothing out noise in the velocity estimate as well as actual motion noise which could be due to diffusion and might be critical to the description. Notice that we used $t(x_2) - t(x_0)$ as a denominator instead of $2\Delta t$ as trajectories can be incomplete. We observed that interpolating gaps can generate inconsistent velocity values and is particularly detrimental to diffusion estimators, therefore it should be avoided.

Diffusion is traditionally defined over a whole trajectory, often for single particles that are arguably more regular in their motion than cells. Cells interact with their environment, exhibit directed motion, and change direction, therefore a diffusion estimate averaged over the whole trajectory seems unfair. As a result, we re-implemented a sliding-mean squared displacement (MSD) method to estimate local diffusion from [89, 127], providing a diffusion signal, comparable to the velocity signal. Establishing the MSD involves extracting all observed displacements in an increasing time window (or time lag in the jargon). If the trajectory contains gaps and no interpolation is performed, then extra care must be taken not to mix displacements coming from different time windows when looping over frames. This

is achieved by first performing a loop to extract all observed physical time gaps in the system, then collecting the displacements in each proper time gap bin, before averaging in each bin to create an accurate MSD that is a function of physical time lag and not frame lag.

Practicality Motion estimators are not currently implemented in the Celldetective GUI but can be found in the `celldetective.signals` submodule of the Python package. We lack a good application to decide how to interface these measurements while maintaining a user-friendly experience. These motion estimators have been applied occasionally, through the API, on results presented in the next chapters.

3.3.5 Single cell signal analysis

3.3.5.1 Introduction

The single cell measurements described in the previous section are performed instantaneously, one image at a time, implying that there is not yet any integration of time or any description of dynamic phenomena[†]. The time dependence emerges naturally when these measurements are represented as single cell signals, *i.e.* 1D time-series, over which we can hope to detect transitions characterizing the dynamic biological phenomena of interest. Our formulation for this problem is that cells can be classified into three categories concerning an event : 1) cells that exhibit an event of interest during the observation window (“event”), 2) cells that do not exhibit it (“no event”) and 3) cells that either exhibited the event before the observation started or else (“else”). Cells belonging to the first class can be associated with a time t_{event} . First, we describe how we designed a visualization and annotation interface adapted to single-cell signal analysis. Second, we detail how we implemented a Deep-learning framework to automatize event detection from single-cell signals, complete with training and transfer capabilities.

3.3.5.2 Visualization & annotation

General considerations *Design.* To be able to comfortably explore and annotate single-cell signals, we had to make an interface that 1) shows the original microscopy images in motion (a looped animation) and 2) allows us to click on single cells, explore every measured signal, and characterize the event. We insist on showing the original images as some phenomena may not be completely contained in the measured signals and require a look at the images. Since the phenomenon of interest might be a crossing of modalities (*i.e.* a cell disappearing from a channel and appearing in another), we enable multi-modal viewing of the movie using an RGB trick described below. Representing the original images also makes it possible to annotate phenomena that go completely beyond the scope of single-cell signals, but

†. Apart from dynamical measurements based on the trajectories.

that can be described visually from the images. A screenshot of the actual interface is shown in figure 3.22.

Multi-events. More than one dynamic event can emerge from a cell population, therefore we introduced a simple manager to navigate from one event description to another within the signal annotator, described below.

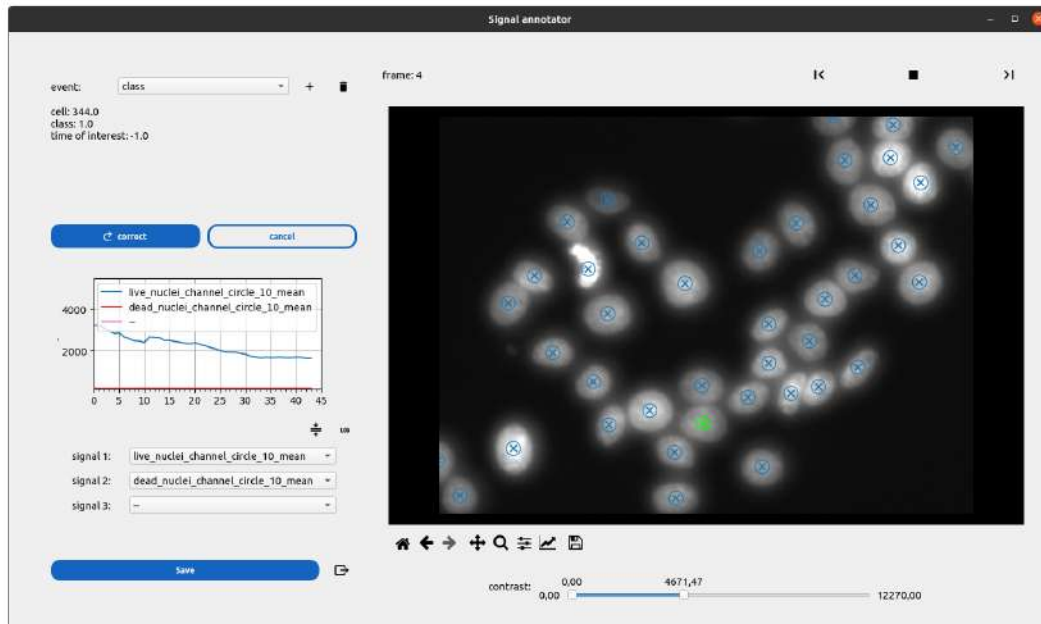


FIGURE 3.22 – The signal annotator interface. The right panel shows an interactive animation of a movie of MCF-7 cell nuclei stained with the Hoechst dye. An interactive scatter facilitates the selection of a cell, simply by clicking. Upon selection, the marker is colored in lime and the signals on the left panel are updated. The correct button activates to modify the cell class and time of interest.

Practicality *Get started.* If a single position is set and tracking has been performed[‡] for a cell population, the eye icon in the signal analysis section becomes active. The configuration button next to the eye can be accessed to configure the image displayed and animation parameters in the signal annotator. The available options are either to show a single channel in grayscale or an RGB composite, in which case each channel's normalization must be set independently, using either percentile or absolute values. The fraction slider below controls the rescaling applied to the images as they are loaded in memory. The interval slider sets the gap in milliseconds between each frame in the animation. Upon saving, a small configuration file is saved in the experiment folder in such a way that the settings can be reloaded in later sessions.

[‡]. Ideally, measurements should also be performed to have actual signals, other than $x(t)$ and $y(t)$ to look at.

First event class. Upon clicking on the eye button, the animation is mounted together and starts automatically. The trajectory table for the cell population of interest is loaded and provides the center of mass of all cells as a scatter plot. If no event was defined previously, the trivial “first detection” event (a cell appears on the image) sets the colors of the scatter plot. Each marker is composed of a cross and a circumscribed circle. The circle encodes the class and takes the color red for class “event”, blue for class “no event” and yellow for class “else”. The cross encodes the status, *i.e.* whether or not the event happened by time t , going from blue to red when an event occurs. To select a cell, the user can simply click on one such marker. The signals on the left panel will update automatically and the correct button will activate.

Exploring a cell's signals. Once a cell is selected, its signals are displayed in the plot box of the left panel. The three lists below control which signals are being displayed. A normalization button applies a min-max transform independently to all signals, allowing one to view very different quantities on the same plot. A LOG button triggers a y-log scale.

Changing a cell's attributes. Triggering correct button shows the three class options, namely “event”, “no event” and “else”. Additionally, there is an option to mark the cell for suppression (shortcut : Del), which means that it will be erased from the trajectories the moment global modifications are saved. The marker of one such cell is colored in black until it is erased. Below the class options, a field to modify the time of reference is disabled unless the “event” option is toggled. Upon submitting the modifications to the selected cell, its marker recolors accordingly.

Managing events. The first element of the side panel is a small manager to create, remove, and navigate from one event description to another. By convention, the creation of an event, named “event” gives rise to three columns in the trajectory table : `class_event`, `t_event` and `status_event`, that determine the colors of the scatter plot and store all information about the event. The event class can be initialized directly to one of the three classes. If the initialization class is “event”, the times of interest have to be set manually.

Annotation set. When all cells have been annotated for a given event description, the user can export an annotation set. The set is a reshaping of the trajectory table into a list of dictionaries, where each dictionary summarizes information about a single cell, namely its class and time of interest for the currently displayed event and all of its signals. The set is bundled in a numpy file.

Minor details that can make your life much easier. The keyboard shortcuts L and F can be used to show respectively the last and first frame of the movie, which is very helpful to perform quality checks on event classification.

Reversible events. If the event of interest is reversible or cyclic, then the chain rule should apply. The user must decompose each transition as a different event. An immune cell forming a synapse is a first event. If the cell detaches it is another event, that could be qualified as “the synapse is ruptured”. The absence of an event would be “the synapse is not observed to rupture” and all cells that did not form a synapse

in the first place are irrelevant to that event and could be classified as “else”, for this event.

3.3.5.3 Deep-learning automation

General considerations *Introduction.* To automatize the detection of events from single-cell signals, we decompose the problem into 1) signal classification and 2) signal regression. As a result, we combine two DL models with the proper head following section 3.2.2 of the material & methods. The two models are trained independently but subsequently. Only the signals classified as “event” are passed to the regression model, as we observed bad performance when trying to train a model that must predict a negative (or arbitrary) time in the absence of an event. We implemented a `SignalDetectionModel` object in the Celldetective API to facilitate the training of the sub-models, handle the signal preprocessing, and apply the models to new data. In the following, we provide some details about our implementation, explaining the choices we made and how this framework was interfaced in Celldetective to be as user-friendly as possible.

Geometric constraints. As mentioned in the material & methods, the input signals can be cast in a tensor of shape $(M \times T \times n_{\text{channels}})$. Each signal’s value is cast in the proper frame slot, on the T axis, leaving not-a-number-valued gaps for missing time points. A linear interpolation is performed to fill these not-a-number gaps. If a signal does not start at $T = 0$ (the first frame slot) then it is valued 0 in the tensor until it starts. Symmetrically, All signals are padded with zeros after they stop.

Signal normalization. The biophysical meaning of these signals can be very different (some might be intensities, others morphological descriptors, etc.), so particular care must be taken when normalizing them, before serving as input to a neural network. We follow the procedure described in figure 3.6, with the subtlety that the signal set \mathbf{x} over which we determine the lower and upper bound for normalization is the set of all cell signals coming from one movie. With this strategy, we can correct the discrepancy in intensity values across different experiments (due to different fluorophore concentrations or simply different exposures). The drawback is that if the event of interest does not occur in the movie we are looking at, the bounds for normalization may be poorly estimated and the data distorted as it enters the model. A solution that can be accomplished through the Python package but not currently the GUI is to perform the normalization at the experiment scale instead of the movie scale, as the intensities are usually stable within an experiment, and the event of interest must occur more than once. This solution is valid at the prediction step. For the training stage, the input data is always bundled “per-movie” as this is how it is annotated. Therefore, we must be careful to only annotate movies where both events and absence of events occur. We implemented a routine to check for this condition as a signal dataset is loaded for training. A much simpler scenario is when the bounds for a feature-channel are well-known and defined in the absolute sense (areas may always be in the same $[0, \mathcal{A}_{\text{max}}]$ range, an intensity relative to background

is always centered around 1.0). In this case, the percentile normalization should be avoided, and the upper and lower values should be passed directly.

Signal augmentation. As mentioned in 3.2.2, the augmentation of a training set is usually beneficial to the model’s performance and robustness. We decide to augment the signals dataset by a user-determined factor (say $\times 2$). For each signal in the train set, we have an 80% probability of applying an augmentation. For cells belonging to the class event and no event (excluding else), the signal can be time-shifted (which is the equivalent of an image translation). Special care is ensured to never shift the signal to the extent that we have to change the class from event to no event. The purpose of this augmentation is to kill the bias in the distribution of event times. We transform the real distribution of event times into a uniform distribution of times. This has the nice property of teaching the model to never learn the probability of a time happening in a dataset and thus to be able to predict times far beyond the range of what it has encountered, which could happen experimentally simply by recording longer movies.

Backbone optimization. The model’s backbone provides a canvas to connect the thousands or millions of training parameters needed to approximate the event detection tasks. We have tested many architectures over the years, at first through trial and error. We wanted to embed in Celldetective a model that can fit accurately every event detection task from signals. To our knowledge, no such model exists, but some architectures are worse and less robust than others. To support this observation, we prepared three signal datasets, using the signal annotator. The first dataset is associated with a lysis detection task, from a fluorescence and an area signal. Both signals respond as step functions when the lysis event occurs, which makes the event quite straightforward to detect. The second dataset annotates nucleus condensation events from a nucleus area signal. These signals are noisier and the condensation can be quite subtle, making this event detection intermediate in difficulty. The third dataset also annotates lysis events but in this case, the fluorescence intake can be very slow and gradual, but always irreversible. A very subtle change in the fluorescence is the be expected around the lysis time, and this is the only signal considered. Each backbone presented in figure 3.23 is assembled into a model using strictly the same input layer and classification or regression head. The model is tested 10 times on each of the three event detection tasks. 70 % of the data goes into the training set, 20 % in the validation set and the remaining 10 % of cell signals are used to measure the model’s performance after training. We use precision and recall metrics to quantify classification performance. Both metrics are expressed “per-class” and we perform an average over the three scores, therefore compensating for class imbalance in the scoring. The regression performance is assessed using a mean absolute error metric. Since the event time is normalized to the length of the time axis T during training, the score can be multiplied by $T = 128$ to have an idea about the average error in frame units. The models are trained for 300 epochs for the classification sub-task and 600 epochs for the validation sub-task, with a learning rate of 0.001 and a batch size of 64. Table 3.5 summarizes the test results

for all tasks and models. The first observation is that the ResNet-derived models (“Resblock + MP”, “Multi-scale ResNet” and “ResNet”) perform better on average at the event detection tasks than Dense, LSTM-derived, and convolutional encoders. As expected, the average performances degrade as the task becomes harder. We find the “Resblock + MP” backbone to be on average the best at the task six times out of nine, while also achieving the best-observed score on seven tasks. Therefore, we decided to embed this specific model in Celldetective for both classification and regression.

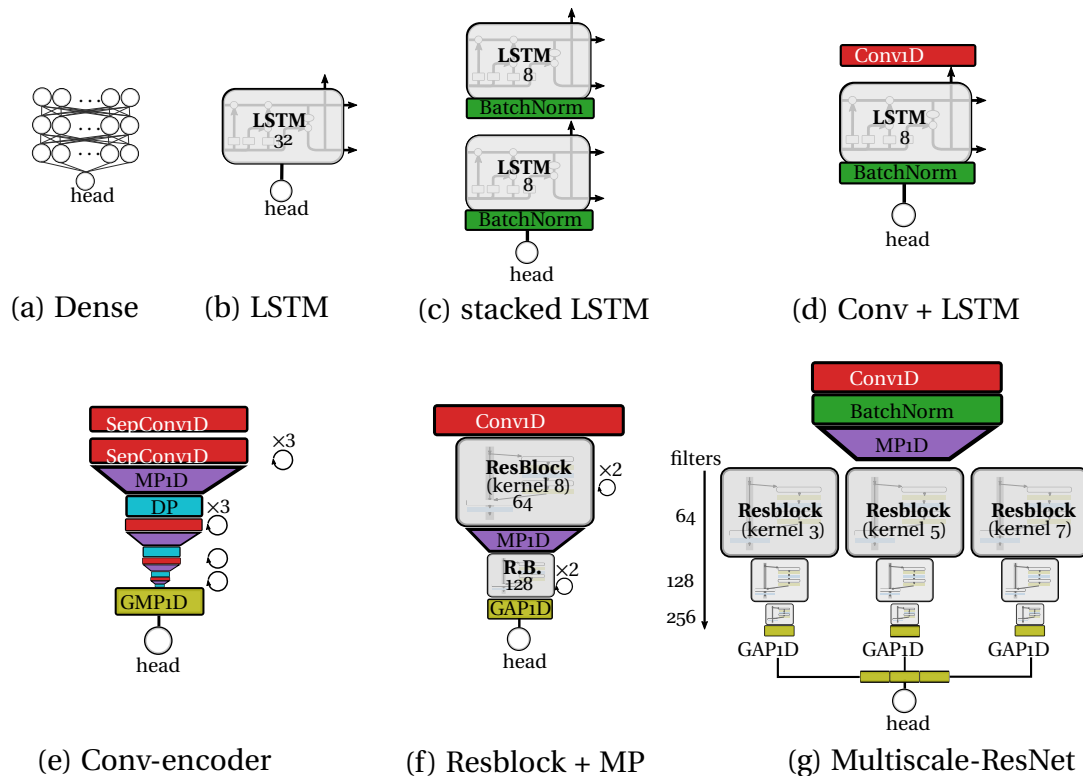


FIGURE 3.23 – Signal model backbones. DL backbones tested to perform regression and classification tasks. All models share a common input and output layer. a) a multi-layer perceptron, composed of fully connected dense layers, b) an LSTM model, consisting of a single LSTM unit, c) stacked LSTM units, d) a convolution layer + a LSTM unit, e) a convolutional encoder, f) a ResNet-like model that replaces the strides 2 convolution with a max pooling operation, g) a multiscale ResNet model, with parallel branches that process the signal at increasing kernel sizes.

Practicality *Calling a DL signal model.* The signal analysis section contains a model zoo, exactly as for the segmentation models. The models are stored in the `models/signal_detection/` folder of Celldetective and are the same for both cell populations. The user can pick a model from the list and launch the analysis to apply it to her data. In practice, the models are bundled with an input configuration file that states which channels should be passed as the input, how they should be

Table 3.5 – Benchmark of select DL models, associated to different backbones, on signal event detection tasks. For each task, among 1) a strong lysis event 2) nucleus condensation 3) a subtle lysis event, we report three scores established on a test set : the average of the “per-class” precision and recall for the classification task, the MAE for the regression task. Each backbone was tested 10 times on each task, with a random splitting of the data into train, validation, and test sets. The average performance is represented in this table \pm the standard deviation. The best average performance is shown in bold, whereas a star marks the model for which the best performance was observed.

model	strong lysis			nucleus condensation			weak lysis		
	precision	recall	MAE	precision	recall	MAE	precision	recall	MAE
Dense	0.90 \pm 0.04	0.95 \pm 0.03	0.011 \pm 0.002	0.73 \pm 0.08	0.77 \pm 0.09	0.026 \pm 0.003	0.57 \pm 0.19	0.65 \pm 0.16*	0.07 \pm 0.04
LSTM	0.65 \pm 0.17	0.79 \pm 0.14	0.009 \pm 0.003	0.55 \pm 0.13	0.61 \pm 0.11	0.05 \pm 0.03	0.52 \pm 0.21	0.57 \pm 0.19	0.06 \pm 0.01
Conv + LSTM	0.59 \pm 0.18	0.66 \pm 0.12	0.012 \pm 0.006	0.69 \pm 0.05	0.69 \pm 0.08	0.078 \pm 0.007	0.47 \pm 0.17	0.50 \pm 0.11	0.06 \pm 0.009
Conv-encoder	0.87 \pm 0.07	0.92 \pm 0.10*	0.013 \pm 0.004	0.71 \pm 0.10	0.75 \pm 0.08	0.035 \pm 0.008	0.59 \pm 0.09	0.59 \pm 0.1	0.06 \pm 0.008
Resblock + MP	0.89 \pm 0.05*	0.95 \pm 0.04	0.007 \pm 0.003*	0.77 \pm 0.07*	0.78 \pm 0.09*	0.019 \pm 0.004*	0.69 \pm 0.16*	0.69 \pm 0.17	0.05 \pm 0.02*
Multi-scale ResNet	0.92 \pm 0.04	0.95 \pm 0.05	0.010 \pm 0.003	0.78 \pm 0.02	0.80 \pm 0.03	0.021 \pm 0.003	0.64 \pm 0.2	0.68 \pm 0.18	0.06 \pm 0.02
ResNet	0.88 \pm 0.05	0.93 \pm 0.05	0.014 \pm 0.004	0.77 \pm 0.05	0.76 \pm 0.05	0.023 \pm 0.004	0.62 \pm 0.16	0.62 \pm 0.15	0.06 \pm 0.01

normalized, what the size of the time axis T of the input tensor should be, and how the class and time results should be called (a one-word description of the event).

Training from annotations. Following the template of the segmentation section, the user can click on a TRAIN button to pilot the training or retraining of a signal model on new data. The interface and the associated settings are detailed in figure 3.24. If the user decides to load a pre-trained model, the original input channels of that model are suggested in the proper channel slot, and the input tensor length T is set. The user is not allowed to add another channel (as this would mean changing the architecture) but can modify the input channels if it makes sense (*e.g.* a sigmoid signal still looks similar whether it is a fluorescence signal or a morphological signal). The training data must be presented as a folder containing npy annotations, generated with the signal annotator. In practice, the training is performed as a subprocess. The data is loaded, normalized, and split into train and validation sets. The train data is augmented. The classifier is trained first. The training process is shown in the Celldetective backend but can be monitored in detail by opening TensorBoard in the models/ folder of Celldetective (tensorboard -logdir path/to/models). Upon completion, a plot of the history of the training and validation losses is temporarily displayed and a set of metrics are shown in the backend. The training of the regression model concludes in the same way with an additional representation that shows the ground truth times vs the predicted times, a quick and efficient diagnostic of what the model learned (see figure 3.24b). Eventually, the model is bundled with an input configuration file and added in the models/signal_detection/ folder of Celldetective and, as a consequence, in the model zoo.

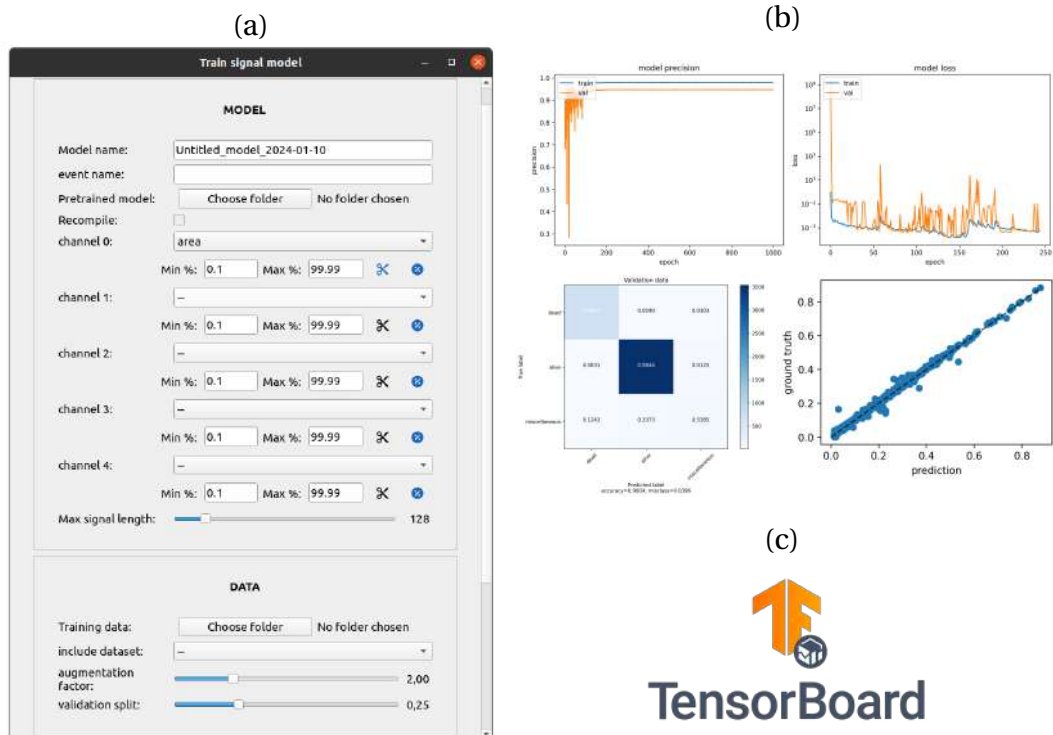


FIGURE 3.24 – Training signal models. a) From top to bottom : the user names the model and the event (one word). A pre-trained model can be loaded to perform transfer learning or gather a specific architecture. The pre-trained model can be recompiled. All input channels and their normalization are defined. The length T of the input tensor is set with a slider (max signal length). The folder containing the annotations is set, with the option to load extra data stored as in Celldetective as datasets. The augmentation factor slider controls how many signals are to be augmented in the train set. The validation split slider sets the volume of the validation set. Extra options (not shown) include setting the number of training epochs, the learning rate, and the batch size. b) visualizations are produced at the end of the training process to control the quality of the best models. c) the training process can be monitored in detail in TensorBoard.

3.3.6 Generalizing survival analysis

General considerations The survival function, more precisely the Kaplan-Meier estimator described in section 3.2.3.1, is a practical way to visualize a distribution of event durations Δt_{event} for a cell population. It takes two events to define one such duration, the first event acting as a synchronization time for all the cells. A typical reference event could be the appearance of a cell on the image after sedimentation. Say that we are interested in a subsequent event, *e.g.* the cell divides after some time, then in the signal annotator we annotate the absolute time t_{division} at which each cell divides, and use the time of first appearance $t_{1\text{st}}$ to synchronize the cells in the survival, defining $\Delta t_{\text{event}} = t_{\text{division}} - t_{1\text{st}}$ for each cell. The rules of left and right censorship still apply, therefore a cell that is already on the image at the start of the observation (left-censored) should be discarded using this definition of Δt_{event} whereas a cell that does not exhibit a division event is right censored and can be fed into the Kaplan-Meier estimator with a duration $T_{\text{max}}^{\text{obs}} - t_{1\text{st}}$ and labeled as “no event”, with $T_{\text{max}}^{\text{obs}}$ the maximum observation time (the movie duration). Figure 3.25 illustrates most occurring patterns in single-cell assays, with the general rule that left censored durations are excluded from the Kaplan-Meier estimator, unlike the right censored durations which still provide relevant information, *i.e.* the event has not happened *yet* in the observed duration.

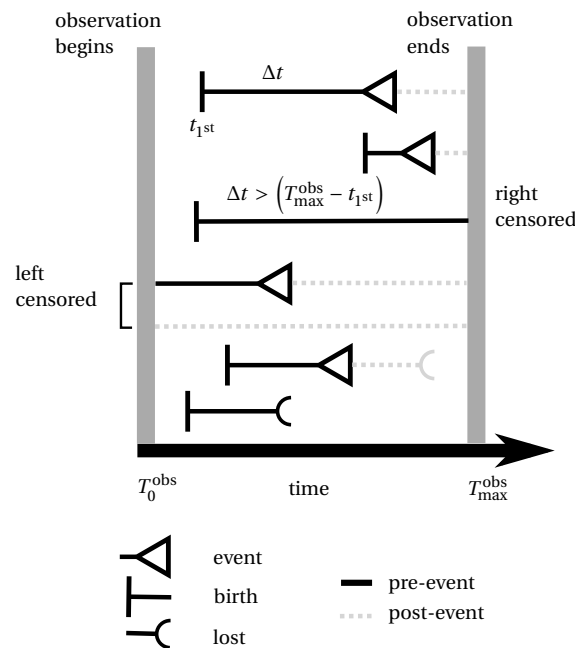


FIGURE 3.25 – Left and right censorship of single cell events.

One exception to the rule that we encountered is when the population of interest has been seeded before the experiment, in which case the cells are all technically here, on the image, at the beginning of the acquisition. The purpose of the first event is to synchronize the cells. Therefore, if we are interested in the cells’ response

to stimulation (a drug is introduced, a population of effectors is introduced), the true first event is the time of introduction of the stimulant, which is shared for all cells. If the acquisition starts later, then it is equivalent to adding a time offset to the reference time of all cells ($T_0^{\text{obs}} = t_{\text{stimulant}} + \Delta t_{\text{offset}}$). We can safely take T_0^{obs} as the new reference time for the cells, provided Δt_{offset} is smaller than the timescale of the event of interest, otherwise most cells end up being left censored. Similarly, one should be careful to exclude cells born after T_0^{obs} , through mitosis, as they were subject to the stimulation for a shorter amount of time that is not comparable to that of the other cells.

Practicality *Visualizing a survival function.* Celldetective embeds an analysis module to build survival functions, illustrated in figure 3.26. Once events have been annotated for a population using either a DL signal model or the signal annotator, the user can go to the Analyze tab of the control panel and click on the plot survival module. The user sets the population of interest, the time of the event of interest (among all annotated times), and the time of reference. The time of reference can be either one of the annotated times or 0, *i.e.* T_0^{obs} described above. The color palette for the survival lines can be set, and the experiment’s temporal calibration can be modified if appropriate. Upon submission, Kaplan-Meier estimators are fit to the data set by the control panel header and a visualization window opens. Pooled survival functions always pool all the cells in a well. In multi-position mode, the survival is shown with a 95 % confidence interval for each position, as well as the pool survival. Positions can be filtered by name or by spatial location provided the μ Manager metadata of the movie stack was put in the movie folder. This feature is convenient to control acquisition errors, *i.e.* attributing a position to the wrong well, which can happen. In multi-well mode, pooled survivals can be easily compared across the wells, and it is still possible to monitor per-position survivals, to assess the amount of sampling fluctuations.



FIGURE 3.26 – An interface to represent survival functions at multiple scales. a) An analysis module pilots the making of survival functions. A cell population of interest is set, and a reference time and an event time are picked from the list of events available for that population. The control panel header informs about the data selection, between a single position, multiple positions, and multiple wells. b) In multiple-positions mode, each position’s survival function is plotted with its 95 % confidence interval, as well as the pooled survival function for the well. Positions can be added or removed from the plot. c) In multiple-wells mode, individual positions are still shown but without the 95 % confidence interval. Emphasis is put on the pooled survival functions that can be compared across wells. As before, wells can be added or removed from the plot.

3.3.7 Collapsed signal representations

General considerations The signal analysis module allows to extract a characteristic time t_{event} associated to an event, for each cell. This time is often annotated by looking for a transition in one or several signals. To ensure that this annotation is consistent across all cells, a practical solution is to select one signal and plot it for all the cells as a function of $t - t_{\text{event}}$. If the traces collapse well at $t - t_{\text{event}} = 0$, then the annotation is consistent. This method can also be used in a more exploratory approach, to see what single-cell measurements are affected by an event, annotated through other means.

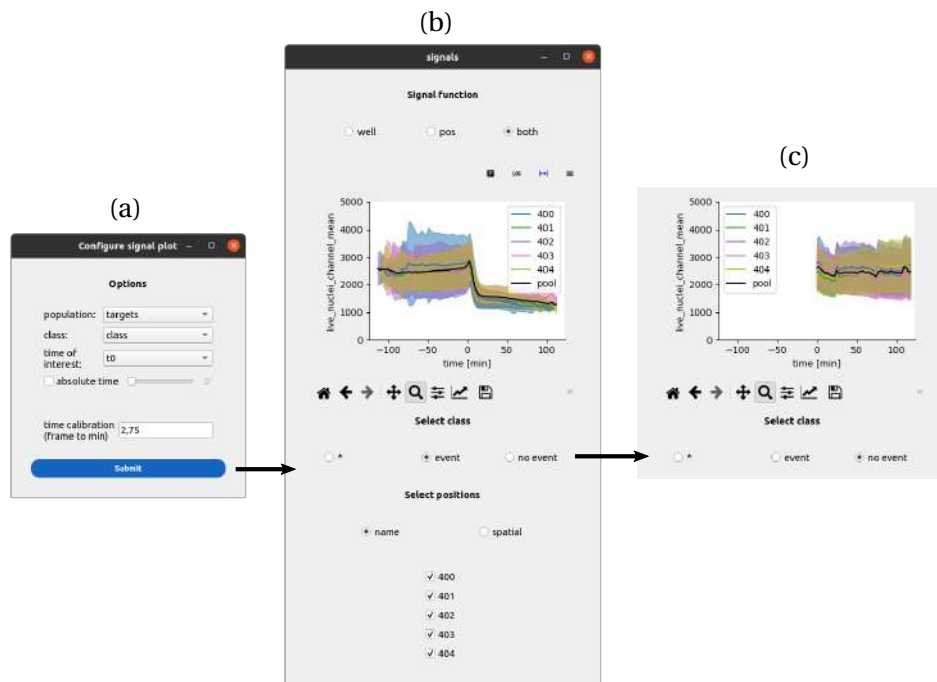


FIGURE 3.27 – An interface to collapse signals to events. a) The cell population, class to segregate the cells, and time of the event is set. Upon submission, a second window asks to select a single signal among the signals measured for that cell population. The control panel header informs about the data selection, between a single position, multiple positions, and multiple wells. b) In multiple position mode, the mean signal trace (plus or minus the standard deviation) is generated for each position, as well as a pool trace pooling cells from all positions. The cells can be filtered between the ones that experienced the event (b) and the ones that did not (c), affecting the mean traces.

Practicality This analysis module is implemented in the same way as the general survival analysis module, with some details provided in figure 3.27. Instead of fitting a Kaplan-Meier estimator, all the single-cell signals are synchronized and averaged for each spatial (position, well) and class (event, no event) decomposition. The mean signal \pm the standard deviation is represented, time-centered around t_{event} . When no event occurred, by default $t_{\text{event}} = -1$.

3.3.8 Neighborhoods and cell-cell interactions

General considerations *Isotropic neighborhood.* Celldetective allows a complete and independent characterization of two cell populations that evolve simultaneously on microscopy images. To study the effect of one population on the other, we developed a simple neighborhood scheme. In the most general case, it is always possible to define an isotropic neighborhood around the center of mass of each object in the system. The only control parameter is the radius of the circle R^{neigh} , which determines the largest distance over which two cells can be matched as neighbors. This kind of neighborhood can be defined between one population and another but also within a population, e.g. to describe local cell density. In the next chapter, we will show that the isotropic neighborhood is the only practical solution for systems of interacting cells when the cell shape of the reference population is not easily accessible.

Counting considerations. Most of the difficulties are displaced to the quantification step, as the isotropic neighborhood rarely reflects the true geometry of the system and is therefore subject to over or underestimation of the real number of neighboring cells. To face these difficulties, we introduced three different counting methods.

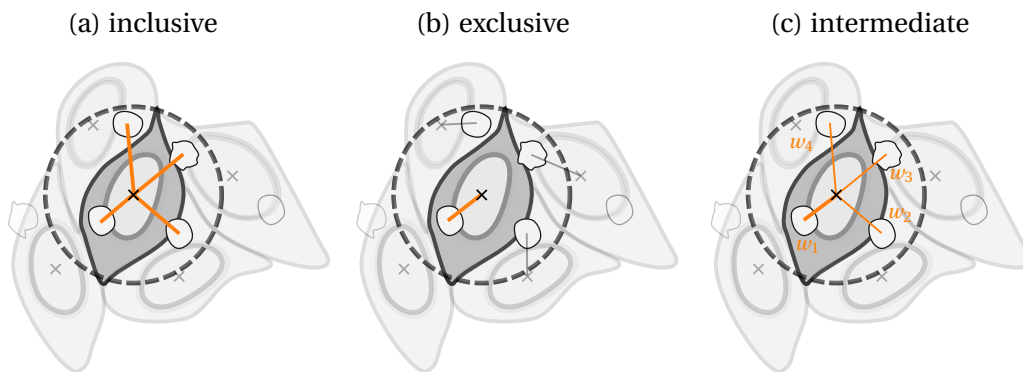


FIGURE 3.28 – Proposed neighborhood counting methods. Notice the weights attributed in (c).

Inclusive. The first is a method that we named “inclusive”, in which all cells inside the circle are counted as neighbors to the reference cell (figure 3.28a). This kind of counting method can be very redundant in crowded environments, where neighborhoods can overlap considerably implying that the same neighbor is attributed to more than one neighborhood. It overestimates the total number of neighbors around a reference cell population. On the other hand, it is a good estimate of local cell density, in the frame of reference of the reference cell population. Therefore, we propose to use the “inclusive” counting method to estimate cell density and/or concentration.

Exclusive. The second method we propose is named “exclusive”. As its name implies, it attributes each neighbor to one cell of the reference set only : the closest (figure 3.28b). Therefore, at the scale of a population, the sum of neighbors for each reference cell matches the actual number of neighboring cells for the population.

There is no longer an overestimation, unlike the “inclusive” method. A considerable pitfall though, is that we have noticed that if the neighbors tend to accumulate at the edges of the reference cells, then the counting around each cell is wrong most of the time, despite averaging out at the population scale.

Intermediate. As a result, we developed a method that falls in between the two methods described above, named “intermediate”. This method differs from the “inclusive” method in one critical point, which is that it attributes weights to all neighbors in such a way that the sum of the weights is always equal to the total number of neighbors in the system (figure 3.28c). From the point of view of the neighbors, we describe this as an attention weight, illustrated in figure 3.29a : the neighboring cell has attention divided across M neighborhoods and is therefore attributed a weight of $1/M$. At the local scale, the weights smooth out counting errors and reflect better the true neighborhood than the “exclusive” method.

Equivalence. For the whole population of reference cells, the “exclusive” and the “intermediate” methods predict the same total of neighbor cells. At the local scale, the “inclusive” and the “intermediate” methods predict the same neighboring cells, but the count is different. If a binning over the number of neighbors is performed, then the equivalence at the population scale between the “exclusive” and “intermediate” methods breaks, as the cell selection for each bin varies across the two methods due to the different local counts.

Refinements. Neighboring cells evolve dynamically and could die, in which case one may wish to exclude them from the neighborhoods as they are not expected to contribute anymore. Similarly, a reference cell that dies may not mobilize a neighbor cell as much as before. In other words, the neighbor cell shifts its attention to the still-alive reference cells in its neighborhood. This concept is explained in figure 3.29b.

Practicality *Get started.* If the user wants to compute the neighborhood of a cell population with itself, then this can be done as soon as the trajectories (or measurements) are available for that cell population. For a two-population neighborhood, a single-cell description for both populations must be achieved first. Once the condition is satisfied, the user can go the NEIGHBORHOOD section of the control panel and open the setting window associated to the Distance cut option, shown in figure 3.30.

Defining the populations. The user must define the reference and neighbor populations. The neighbor population is associated a status, in order to decompose the neighborhood into sub-populations (*e.g.* dead and alive neighbor cells). A NOT gate on the side can be used to switch the 0 and 1 in the status column. An option can be ticked to compute the cumulated presence of a neighbor in a neighborhood. The second option is to symmetrize the neighborhood written in the table of the reference cells to that of the neighbor cells. The event time option defines a pre-event window for the reference cells over which to compute the average number of neighboring cells, using the three methods described above. The idea is to have an estimator of

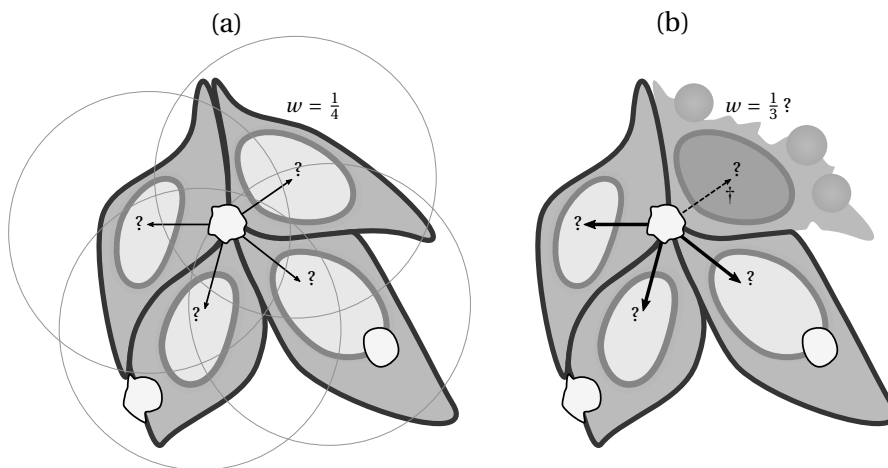


FIGURE 3.29 – Refinements for immune-target interactions. a) the attention weights emerge in the frame of reference of the effector population. An effector may stand at the intersection of many target-centric neighborhoods. The attention weight tries to account both for uncertainty in neighbor attribution and a potential dilution of the effector activity across the many targets. This weight is attached to the effector in each target neighborhood. Only the intermediate counting method is sensitive to the attention weights. b) In addition, a target that has known an event such as apoptosis may not mobilize an effector cell as much. Therefore we propose to optionally exclude eventful cells from the attention mechanism.

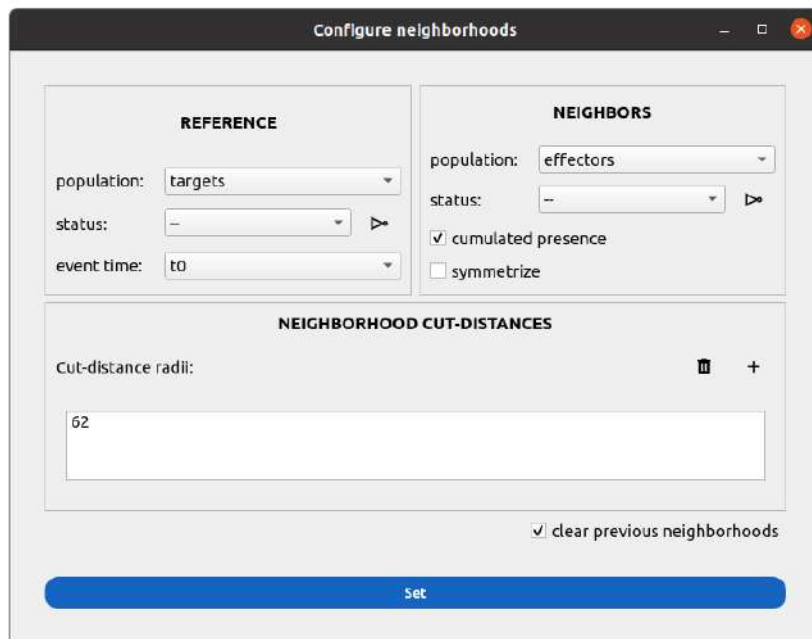


FIGURE 3.30 – GUI for neighborhood configuration. After setting the reference and neighbor populations, which can be identical, the user defines as many radii as there are neighborhood distances of interest.

the average neighbor presence before an event occurred to the reference cell.

Distances. The user can define as many neighborhood distances as needed, simply by adding radii one by one.

Execution. Upon submitting, the tables for both populations are loaded, and for each time point, the distance for all cell pairs across the populations is computed. This distance matrix is exemplified in figure 3.31b. The matrix is thresholded to the neighborhood radius. Then it is scanned column-wise to determine the attention weights of the neighbors. Finally it is run row-wise, to attribute to each reference cell its neighbors, as a dictionary containing basic information about each neighbor (identity, attention weight, status) at this neighborhood size. This process is repeated for each time step and for each neighborhood radius, yield as many “neighborhood” columns as radii were set. Then for each neighborhood size, reference cells that are too close to the image edge and for which the neighborhood is incomplete are masked from the neighborhood analysis. The problem of cell proximity to the edge of the image is illustrated in figure 3.31a. Finally, the neighborhood counts are performed, using each of the three techniques described before, and decomposing by the status of the neighbor cells, yielding 9 counting metrics. In addition, the event time of the reference cell information is exploited to measure the mean neighborhood before the event. Therefore, 12 counting metrics are obtained for each neighborhood. The complete tables that include a neighborhood column with dictionaries in each cell are saved as pickle files. The counting metrics are equivalent to the single cell signals measured before and are written in the csv tables, in such a way that they can be exploited by the signal annotator. Examples of “counting signals” for one of the 12 metrics is shown in figure 3.31c.

Survival of interacting populations. In the previous software iteration of Celldetective, we developed a module to bin survival function by any single-cell measurement, which included the mean number of neighbors until the event. The principle was to group the cells of interest by this quantity and extract the survival function of each group, showing the effect of the quantity on the distribution of t_{event} . Going beyond, we introduced the possibility to perform a binning over two variables, *e.g.* neighbors from the same population and neighbors from the other population, in which case we were no longer plotting the survival response but only a slope estimate of the function in a matrix format. These analysis modules need more time to be ready and broadened to the scope of Celldetective.

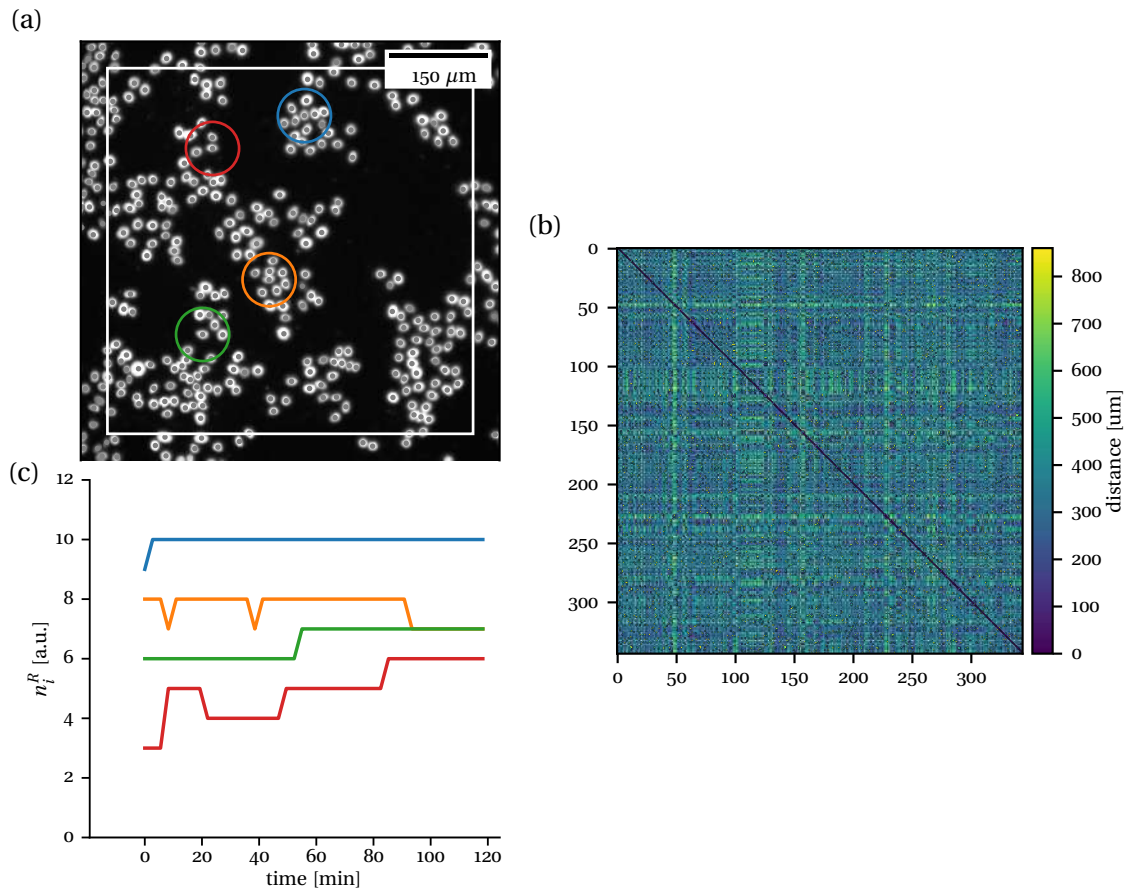


FIGURE 3.31 – Isotropic neighborhood of a population with itself. a) first frame of a movie of a MCF-7 cell population stained with the Hoechst nucleus marker. The centers of mass of the nuclei are shown as a gray scatter. The $40\text{-}\mu\text{m}$ neighborhood is shown directly for four cells of interest. The continuous white line shows the edge censorship to apply with such a neighborhood. b) the distance matrix between every pair of cell in the system (including the cell with itself). A threshold is applied on these distances to obtain in c) single cell traces of neighborhood occupancy. The counting method shown here is the inclusive method, showing the absolute number of cells in the $40\text{-}\mu\text{m}$ neighborhood of the cell of interest over time (same color code as in a.).

4 Cell-cell interaction assay

4.1 Introduction

We can harness the functionalities of CellDetective to study cell-cell interactions that are central to immunological and fundamental research, such as co-cultures of cell populations imaged in time-lapse microscopy using fluorescent labeling and label-free techniques. Here we focus on a specific co-culture of human primary natural killer (NK) effector cells with MCF-7 breast cancer target cells, in the presence of a bispecific antibody (bsAb), mediating the antibody-dependent cell-mediated cytotoxicity (ADCC).

4.1.1 ADCC and NK-engagers

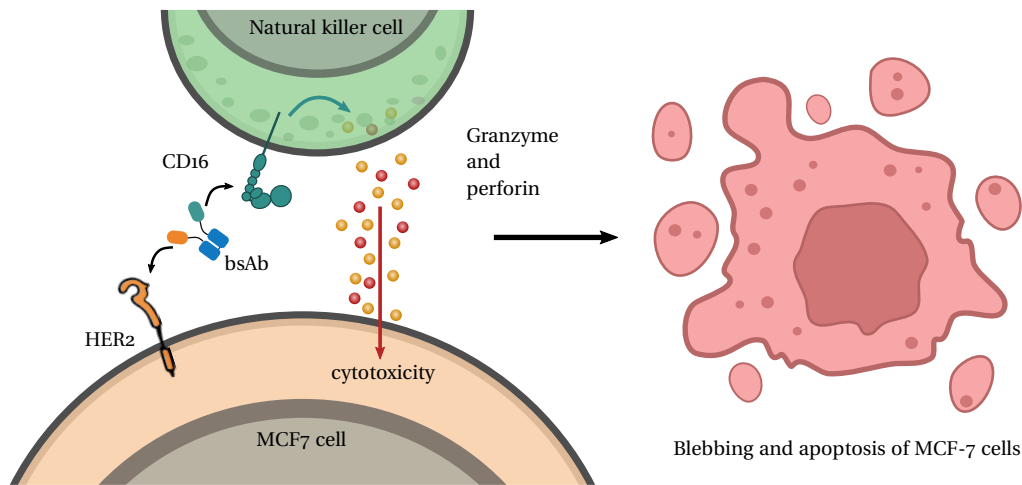


FIGURE 4.1 – Principle of ADCC. The human epidermal growth factor receptor 2 (HER2) surface receptors of the MCF-7 target cells are tagged by the bispecific antibody (bsAb). The cluster of differentiation 16 (CD16) receptor of the NK effector cell binds to the specific part of the bsAb, forming molecular bridges, and encouraging synapse formation. The synapse can lead to granzyme and perforin release by the NK cell, triggering the target cell death.

As illustrated in figure 4.1, in the context of ADCC, and after recognizing the antigen, the antibody interacts with specific receptors on the surface of NK cells [124, 158, 162]. This interaction triggers a signaling cascade leading up to the NK cell activation followed by the secretion of cytotoxic granules and cytokines which mediate the killing of the pathogen cell [163]. With several studies demonstrating

ADCC as a predominant effector mechanism of action against cancer cells, and thanks to their exquisite specificity while taking part in ADCC, antibodies reign as a major therapeutic target in the fight against cancer [76].

A powerful alternative to antibodies has emerged, namely single domain antibodies (sdAbs or nanobodies) [29, 39, 67], obtained from heavy chain antibodies of Camelids. These very small fragments represent unique building blocks for the design of more complex constructs [39, 148, 166]. For example, they can be used to make cell engagers, which are aimed at redirecting immune cells to recognize and kill cancer cells. One such construct is the bispecific antibody (bsAb). This approach combines two specificities in a single molecule. These molecules are bivalent with one valency for each antigen [17]. Some nanobodies are used to create bsAb aiming at recruiting and activating human NK cells to the tumor microenvironment through well-characterized tumor markers, such as EGFR/HER1, Erb-B2/HER2 and HER3 [175].

4.1.2 Measuring ADCC without imaging

Ensemble For decades, the main technique to assess the ADCC was the measurement of ^{51}Cr release upon lysis of ^{51}Cr labeled target cells [20, 121]. This costly and dangerous technique only provides a single time point readout and involves extensive sample preparation [20, 87, 121]. Alternative *in-vitro* methods emerged, such as colorimetric, luminescent and enzymatic assays [57, 93]. A pitfall of these techniques is that they yield a single endpoint readout.

The xCelligence® real-time cell analysis (RTCA) addresses this limitation by providing a continuous reading of the net adhesion of cells on high-density gold electrode arrays printed on culture plates over hours [88]. Under the assumption that cells detach upon death, RTCA provides a proxy for cell death counts that can be sensitive to cell shape and size, surface chemistry, and adhesion conditions, making the interpretation of the readout ambiguous. We will use the RTCA technique as a validation technique for our ADCC assay under the microscope.

Single-cell Flow cytometry combined with fluorescence-activated cell sorting (FACS) analysis exploit combinations of fluorescent dyes to sort single cells as target or effector, alive or dead, yielding an endpoint readout of the fraction of dead targets. To achieve this result, the cells must be detached, at the risk of denaturing them [5, 118, 149, 179, 188, 190].

4.1.3 Imaging ADCC

To this day, microchip or organ-on-a-chip assays present the best option to assess ADCC under the microscope, allowing high throughput [65, 122, 151]. However, the reductionist approach of these assays does not take into account the complexity of

ADCC in a physiological context. In addition, these techniques can be laborious and time-consuming, requiring trained people to make the chips [65, 122].

A recent imaging effort was developed to study T cell and cancer organoids interactions in 3D, at high throughput, with multispectral imaging [41]. The effector-to-target ratio remained quite low (ratio of 1 :30 or 1 :25), and tumor cell death was estimated every 30 minutes only at the highest number of simultaneous conditions, yielding a low time resolution on killing dynamics.

4.1.4 Rationale

We want to dynamically and accurately estimate target cell killing in the context of ADCC with minimum disturbance of the co-culture, as directly as possible. Latest developments in high-throughput assays and progress in image analysis, with the development of AI detection tools [116, 195] have made it possible to consider microscopy assays working at cell densities that would have been considered impossible to analyze not so long ago. As a result, we developed an assay that exploits higher target and effector cell densities to balance high throughput with high time resolution. Imaging is performed using cheap, readily available, epifluorescence microscopy and brightfield, with dyes introduced at the time of observation, without prior preparation of the cells. The goal of this assay is to assess the efficiency of new bsAbs in increasing NK cell-mediated ADCC. The experiments were conducted at LAI by Beatriz Díaz-Bello, Lorna Ammer, and Florian Dupuy.

In this chapter, we will apply Celldetective to images of this biological system to extract cell death events. Using morphological and context considerations, we will justify our neighborhood estimates to relate the target and effector populations. We will study extensively the effects of the biological condition on target cell survival before focusing on interactions with the effector cells, by relating local measurements to population survival as well as exploiting these measurements to identify one-to-one victim/killer pairs.

4.2 Materials and methods

4.2.1 Cells

MCF-7. Michigan Cancer Foundation-7 (MCF-7) is a human breast cancer cell line, derived from the pleural effusion of Frances Mallon, a 69-year-old Caucasian with metastatic breast cancer (adenocarcinoma) [165]. MCF-7 is the most commonly used cell line worldwide to study breast cancer. MCF-7 cells can grow in monolayers on surfaces or form domes.

MCF-7-HER2+. Cells were transfected from MCF-7 cell line to overexpress HER2 receptors. These cells were obtained by Martine Biarnes at the LAI laboratory. Determination of HER2 levels on the cells was performed by flow cytometry with a

Herceptin antibody that recognized the HER2 protein. A secondary fluorescent anti-human antibody was used at 1 :1000 dilution. Fluorescence intensity was determined and correlated with HER2 levels. Cells were maintained in RPMI 1640 media (Gibco, Life Technologies), supplemented with 10 % of Fetal Bovine Serum, FBS (Gibco, Life Technologies), and 50 mg/mL of hygromycin as an antibiotic resistance selection. Cells were amplified three times per week and kept in the incubator at 37°C under 5 % CO₂ atmosphere.

Primary human NK cells. NK cells were isolated as described in [62]. Briefly, blood samples were obtained from the Etablissement Français du Sang (Marseille, France), using the MACSxpress whole-blood human NK cell isolation kit (Miltenyi Biotec, Bergisch Gladbach, Germany) a negative selection was performed. The characterization of the sorted cells was determined by flow cytometry with anti-CD16, anti-CD3, and anti-CD56 antibodies. Cells were maintained in RPMI 1640 medium and 10% FBS at 37°C, 5% CO₂, and used in the following 24 hours.

4.2.2 Molecules : proteins and dyes

4.2.2.1 Cell receptors

HER2. The human epidermal growth factor receptor 2 (HER2) protein is a transmembrane receptor that controls cell growth and division. HER2 is over-expressed in 20 % of breast cancer [66] and is associated with tumor formation by letting cells multiply uncontrollably.

CD16. The CD16 is a transmembrane receptor expressed at the surface of NK cells, macrophages, monocytes, and neutrophils. It is a major activating receptor of NK cells.

CD107a. CD107a or lysosomal-associated membrane protein 1 (LAMP1) is a transmembrane receptor residing primarily across lysosomal membranes. Lysosomal fusion with the plasma membrane can result in LAMP1 expression at the cell surface. LAMP1 expression has been shown to correlate with both cytokine secretion and NK cell-mediated lysis of target cells [2]. It is often used as a degranulation marker for cytotoxic T cells and NK cells [145].

4.2.2.2 Bispecific antibodies

The bispecific antibodies (bsAbs) are a fusion of two nanobodies coming from llamas, one against CD16 (anti-CD16) and the other against HER2 (anti-HER2), to create a bsAb against HER2 positive breast cancer. The resultant bsAb is the HER2-bsAb-CD16. The production was previously reported by [175]. Both CE4-21 and CE4-28 share the same anti-HER2 nanobody. They are differentiated by their respective anti-CD16 nanobody, C21 and C28 [10].

4.2.2.3 Dyes

Propidium iodide. Propidium iodide (PI) is a charged fluorescent probe that is generally excluded from live cells [193]. When the plasma membrane integrity is disrupted, *e.g.* at cell death, the probe penetrates inside the cell and binds to DNA by intercalation. The fluorescence increases 30-fold upon intercalation. At low concentrations, many cell lines, including MCF-7 cells are unaffected by the presence of PI. As shown in figure 4.2, PI emits in red and can be excited at a green wavelength.

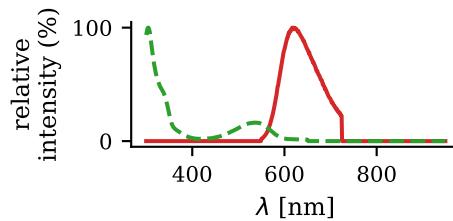


FIGURE 4.2 – PI spectra. The excitation spectrum (green) and emission spectrum (red).

Hoechst 33342. Hoechst 33342 is a cell-permeable DNA stain, excited by ultraviolet light and emitting blue fluorescence, as shown in figure 4.3. Hoechst 33342 is used to stain specifically the nuclei of living or fixed cells and tissues. Hoechst 33342 and PI are frequently used together for simultaneous flow cytometric and fluorescence imaging analysis of the stages of apoptosis and cell-cycle distribution [12, 53].

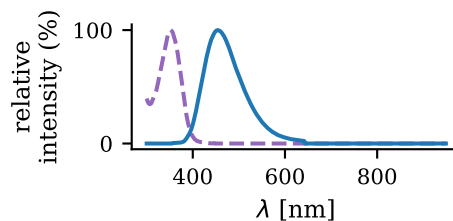


FIGURE 4.3 – Hoechst 33342 spectra. The excitation spectrum (purple) and emission spectrum (blue).

CFSE. Carboxyfluorescein succinimidyl ester (CFSE) is a cell-permeable fluorescent marker that binds covalently to all free amines on the surface and inside of cells. Thanks to its strong and stable fluorescence, CFSE has been used to follow lymphocyte migration and proliferation. As shown in figure 4.4, CFSE can be excited in blue and emits in green.

LAMP1. Anti-human CD107a (LAMP1) antibody conjugated with allophycocyanin (APC) was used to label specifically CD107a [3]. It is excited in orange and emits in far red.

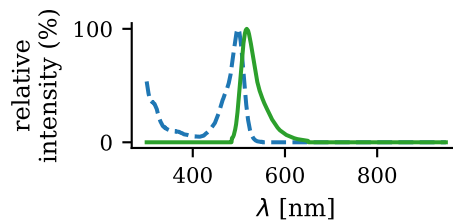


FIGURE 4.4 – CFSE spectra. The excitation spectrum (blue) and emission spectrum (green).

4.2.3 Microscopy and experimental protocol

4.2.3.1 Microscopy techniques

Microscope. Images were acquired on a Zeiss AxioObserver inverted microscope with temperature control at 37°C, with a motorized xy stage, definite focus, and motorized cube turret. The acquisition was controlled using Micromanager [50], defining multiple positions per well (tiling), selected either manually or defining a grid centered about a reference position, with no overlap. For each position, all channels are taken sequentially, with the minimum time interval between the images, before moving on to the next position, and eventually the next well. The cycle repeats for two to three hours until the end of the acquisition.

Epifluorescence. The dyes introduced in the system are imaged using epifluorescence. Briefly, the excitation light coming from a metal-halide light source passes through an appropriate cube where it is filtered by an excitation filter, and sent to the objective with a dichroic mirror before reaching the sample. The dyes in the sample emit light in response to the excitation light that is collected through the objective, crosses the dichroic mirror, and is filtered by the emission filter of the cube, before reaching the camera. The cubes used were the Zeiss filter set # 38 [25] (CFSE), Zeiss filter set # 49 [26] (Hoechst) and Zeiss filter set # 25 [24] (PI).

Brightfield. Brightfield is one of the most simple imaging techniques, in which the sample is illuminated from above, and light is transmitted through the sample and the objective below on an inverted microscope, before reaching the camera.

4.2.3.2 Protocol

100,000 MCF-7 cells were seeded in each well of the 8-well chamber μ Slide, polymer bottom, TC treated from Ibidi®. Cells were cultured overnight in RPMI complemented media and allowed to reach exponential growth (at least 18 h) under 37 °C and 5 % CO₂. On the next day, the medium was aspirated and cells moved to a solution of Hoechst (Invitrogen : Hoechst 33342 Cat. H1399) diluted 1 :2000 in PBS (Sigma(R)). The cells were incubated at 37°C for 10 minutes. After that time, the Hoechst solution was removed and the cells were rinsed 5 times with warm colorless RPMI media (300 μ L/well). Then 3 more rinses were performed with warm colorless RPMI media complemented with 10 % of FBS. Cells were sent back to the incubator.

NK primary cells were optionally stained with CFSE dye (kit de prolifération cellulaire CFSE CellTrace™) according to the manufacturer instructions [92]. About 2.5 million cells were centrifuged at 1500 rpm for 5 min. The supernatant was discarded and the cells were incubated with 2.5 mL of CFSE diluted in PBS for 20 min at 37°C. Then, 12.5 mL of colorless RPMI + 10 % FBS were added to the medium and the cells were left to incubate for five additional minutes. Then the cells were centrifuged at 1500 rpm for 5 min. Cells were resuspended in complemented media and put back in the incubator.

In some experiments, the LAMP1 (aka CD107a) marker (reference Biolegend CD107 APC Clone. H4A3 Cat. 328619) was introduced at a concentration of 5 μL per 1 M of NK cells.

ADCC assay. Dilutions of the bsAb CE4-21 or CE4-28 were prepared to obtain a final concentration of 1, 10, and 100 pM (or 1 nM). The proper bsAb solution was added to each well where the target cells were previously marked with Hoechst and incubated at 37°C for 30 min. After that time, Propidium Iodide (Sigma) was added in dilution 1 :500 on each well condition, then the cells were taken from the incubator and 250,000 NK cells were added to each well to have an E : T ratio of 2.5.

Then the multiwell plate was put inside the epifluorescence microscope Nikon with temperature control at 37°C, and imaged at 20X magnification using the objective LD Plan-Neofluar 20x/0.4 Corr M27. For LAMP1 experiments, the system was imaged at 40X magnification using the oil objective Zeiss Plan-APOCHROMAT 40x / 1.3 Oil Dic (UV) VIS-IR 420762-9800. The acquisition strategy was to image 3 to 9 non-overlapping positions per well, for 2 to 4 hours, in all fluorescent modalities as well as brightfield. The time resolution varied from around a minute per frame to 5 min per frame depending on the number of positions acquired. The acquisition was configured using MicroManager 1.4 [50].

4.2.4 Mathematical descriptors

4.2.4.1 Anomalous diffusion

The dynamics of the center of mass of a cell can be used as an estimator for the cell's motion [6, 99, 127]. With such a proxy, the problem of estimating cell diffusion, migration, and velocities is mathematically equivalent to a single particle tracking formulation. Single particle tracking (SPT) on a movie yields a set of two-dimensional trajectories $\vec{r} = (x(t), y(t))$. Each associated particle undergoes either free diffusion or anomalous diffusion, *i.e.* confinement, superdiffusion. For cells, it is usually the latter that occurs, with occasionally an active velocity component to motion. All such quantifications require first building an MSD profile, the average displacement of the particle over different time scales. Assuming stationarity, the MSD can be defined within a single trajectory as the average square displacement in a time window or time lag $\tau = n\Delta t$, with Δt the time interval between two frames and $n = 1, 2, \dots$. At each time lag τ , there are $N - n$ displacements, where N is the duration of the

trajectory in frames. The MSD can be expressed as :

$$\text{MSD}(\tau = n\Delta t) = \frac{1}{N-n} \sum_{i=1}^{N-n} (\vec{r}_{i+n} - \vec{r}_i)^2 \quad (4.1)$$

To capture different motility regimes that cells may exhibit, instead of computing the MSD over a whole trajectory, some authors proposed to partition trajectories and compute the MSD in each section [127]. The standard procedure to extract diffusion coefficients and active velocity terms is to fit the MSD with a model. The most famous model is the 2D Brownian motion that can be related to the diffusion coefficient D as [100] :

$$\text{MSD}(\tau) = 4D\tau \quad (4.2)$$

As a one-size-fits-all approach, a model for anomalous diffusion added a power exponent α to the Brownian model [8, 23, 173] :

$$\text{MSD}(\tau) = 4D\tau^\alpha \quad (4.3)$$

with D becoming a generalized diffusion coefficient of inconsistent units if α varies. An exponent $\alpha > 1$ suggests superdiffusion and active displacements, whereas a coefficient $\alpha < 1$ suggests sub-diffusion and constrained motion.

In this manuscript, we exploit a model for free diffusion that adds a constant velocity component V which can be conceived as a drift velocity [30] :

$$\text{MSD}(\tau) = 4D\tau + V^2\tau^2 \quad (4.4)$$

The advantage of this model is that the diffusion coefficient extracted has consistent units, and still accounts for a constant velocity term, which could reflect the characteristic velocity of a migrating cell or that of a cell under flow.

4.2.4.2 Cox model

The proportional-hazards model (or Cox model) evaluates the simultaneous effect of several variables (covariates) on survival [42]. The model works under the proportional-hazards assumption that states that the covariates must be multiplicatively related to the hazard. The hazard function is decomposed into two parts with a baseline hazard which describes the global time variation of the risk of event per time unit, when all covariates are equal to zero, and a part that captures the effect of the variables on the risk of event. The hazard could be expressed as :

$$h(t) = h_0(t) \exp(b_1x_1 + b_2x_2 + \dots b_px_p) = h_0(t) \exp\left(\sum_{i=0}^p b_ix_i\right) \quad (4.5)$$

where $X = (x_1, x_2, \dots x_p)$ are the covariates, $h_0(t)$ the baseline hazard and $b =$

(b_1, b_2, \dots, b_p) coefficients measuring the effect of the covariates. By convention, the quantities $\exp(b_i)$ are called hazard ratio (HR). A positive HR indicates that an increase of the associated co-variate by one unit increases the chance of an event occurring, symmetrically decreasing survival. A HR close to one implies a small to null effect of the covariate on survival whereas a negative HR suggests a protective effect, increasing survival chances as the covariate is increased.

We used the `CoxPHFitter` from the `lifelines` python package to fit the HR for each covariate using the Cox model on our MCF-7 survival data.

4.2.5 Analysis

4.2.5.1 Bulk fluorescence correction

We did not perform any fluorescence correction on Hoechst, PI and CFSE as we did not intend to measure the fluorescence levels, and were instead looking at time variations and transitions in these intensity levels. The only exception was for the LAMP1 fluorescence channel for which we observed a strong bulk fluorescence, whose lateral variations often exceeded the faint LAMP1 signal. In addition, this bulk fluorescence was changing and moving slightly from one frame to the next preventing an average or median background estimate. We modeled the background fluorescence at each time point using a paraboloid surface described in figure 4.5.

Before fitting, we masked obvious cells on the images using another channel, CFSE, to roughly detect cell presence and mask the associated pixels in the input to the fit. If CFSE is not available then the filtering and cell masking step can be performed directly on the LAMP1 image. Once the background was estimated for a given time point we could either subtract or divide it from the raw microscopy image. We observed some cells that could block the bulk fluorescence and end up slightly darker than the background. A problem we faced with the subtraction approach was that because of these cells, some intensities could become negative. One usual fix is to perform clipping, destroying information in the process, and losing precious quality control over the background correction process, which did not seem right. Furthermore, the LAMP1 signal was often only a few percent higher than the background, therefore we found it practical to exploit LAMP1 intensity signals relative to the background instead, without sacrificing any information.

This normalization procedure was implemented in a Jupyter Notebook to process a whole CellDetective experiment almost automatically, requiring only a user-check on the threshold parameters for the cell detection before background fitting.

4.2.5.2 Image registration

Each multichannel movie was registered before analysis using the multichannel linear SIFT alignment plugin on Fiji [106, 154]. The Hoechst channel was always chosen as the reference channel, over which transformation is estimated before

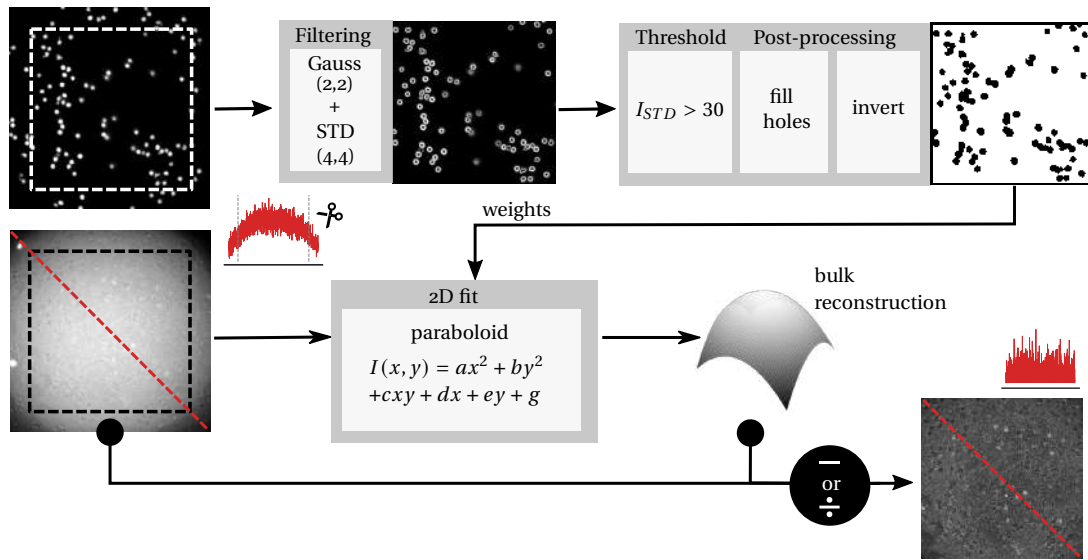


FIGURE 4.5 – Workflow for the correction of bulk fluorescence. The fluorescence image is cropped symmetrically along the $-x$ and $-y$ axes to avoid a diaphragm contribution to the intensity distribution. The cells are roughly segmented from the CFSE channel using successively an STD filter (kernel (4, 4)), a threshold on the STD transform to binarize the image, a fill holes operation to fill the inside of the detected cell edges and an inversion to set value 0 where the cells are, 1 otherwise. This binary image is used as a weight map to fit the background of the LAMP1 fluorescence image with a 6-parameter paraboloid model. The fitted background is then either subtracted or divided from the raw microscopy image. The process is then reiterated for the next frame.

being applied to all the other channels. To achieve good results, the Hoechst channel was auto-contrasted first, the initial Gaussian blur lowered to 0.8-1.2, and the number of steps per scale octave, *i.e.* the number of consecutive blurring operations applied at a fixed magnification, increased to 7 (sometimes 9 when the registration was inaccurate, at the cost of a longer computation time). The expected transformation was set to rigid. We wrote a macro to be able to perform this alignment directly within Celldetective experiment folders, adding automatically `Aligned_` prefix to the registered movie.

4.2.5.3 RTCA

To perform cytotoxicity measurements using RTCA, the authors introduced a unitless quantity called the cell index (CI) :

$$CI(t) = Z(t) - Z_0 \quad (4.6)$$

where $Z(t)$ is the impedance at time t and Z_0 the impedance in the absence of cells. The CI ranges from zero when no cell is on the E-plates® to a saturation value when the cells are fully confluent. The saturation value depends on the cell type, the surface, and potentially other factors. The CI can be normalized by collapsing

all condition signals to one at a desired time point (*e.g.* right after the introduction of the NK). This quantity has been reported as the normalized cell index (NCI) :

$$\text{NCI}(t) = \frac{\text{CI}(t)}{\text{CI}(t_{\text{critical}} + \Delta t)} \quad (4.7)$$

The CI is expressed relative to that of the selected time point. Since introducing immune cells and antibodies in the system can technically affect impedance values at least at the timescale of sedimentation, it is reasonable to take a timepoint slightly ulterior to the change in the system. By having a control containing only target cells, we can estimate the proliferation contribution to the NCI. We then express the other NCIs relative to the proliferation NCI, NCI^P :

$$\text{NCI}^P(t) = \frac{\text{NCI}(t)}{\text{NCI}^P(t)} \quad (4.8)$$

This does not yield a survival function but gives an idea of the relative effect of drug concentrations on ADCC.

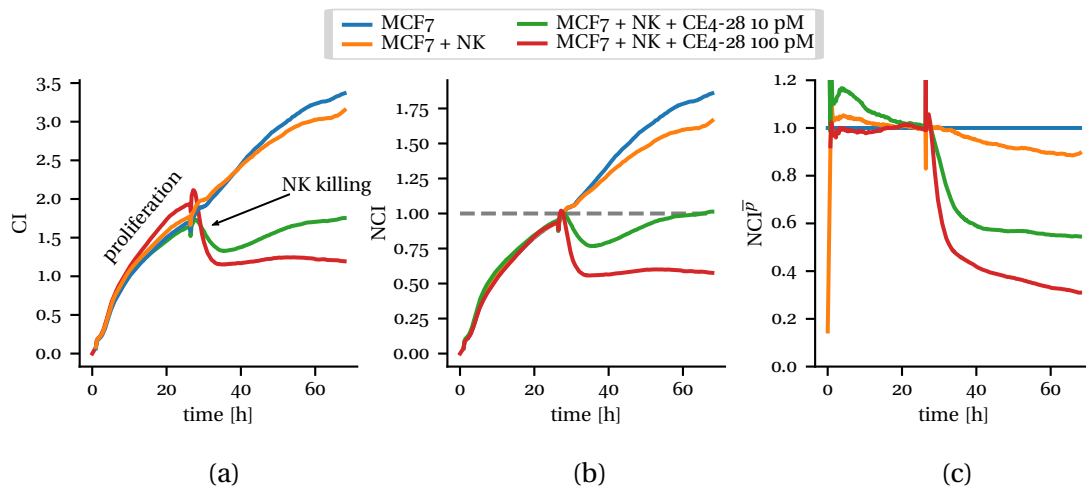


FIGURE 4.6 – Step by step normalization of the CI signal. a) The CI shows differences in the proliferation phase, as the cell seeding is not perfect. At time 26h30min, the NK and antibodies are introduced in the respective wells, which leads to a quick increase of the CI. As the NK do their work, the impedance in the high antibody concentrations decreases faster than the proliferation rate. b) The CI is normalized with respect to the value at the NK introduction time + 30 min. The initial proliferation rate does not show differences anymore. The MCF-7+NK condition is lower than the MCF-7 condition due to spontaneous killing from the NK cells. c) The NCI signals are expressed relative to the NCI of NK-less condition, *i.e.* the proliferation signal, following equation 4.8. Assuming that the NK do not interfere with the proliferation of the MCF-7 cells, NCI^P is a quantity akin to survival with the subtlety that it may not scale linearly with the number of death events.

4.2.5.4 Packages and libraries

Some of the analyses presented in this chapter made use of Celldetective, particularly for the cell detection, tracking, and measurement pipelines. The remaining analyses were performed in Python, using custom scripts written specifically to answer the questions at hand. All plots were generated in Python using Matplotlib [75], Seaborn [186] and Plotly [77] unless mentioned otherwise. Inkscape was used to assemble composite figures and perform some minor relabeling.

4.2.5.5 Statistical tests

T-test (independent). Compare the mean of two independent samples of score to reject the null hypothesis that the two samples have identical average. Unless mentioned otherwise, the alternative hypothesis is that the first sample has an average lower than that of the second sample. From the `scipy.stats` package, as `ttest_ind`.

T-test (relative). Compare the mean of two related samples to test for the null hypothesis that the two samples have identical averages. The alternative hypothesis is that the first sample has an average lower than the second. From the `scipy.stats` package, as `ttest_rel`.

Kolmogorov-smirnov test. Compares the underlying continuous distributions $F(x)$ and $G(x)$ of two independent samples. We apply this test to non-Gaussian data as a test for difference. From the `scipy.stats` package, as `ks_2samp`.

Log-rank test. Compare the distribution of time until the event of interest occurs in independent groups. We apply this test to compare survival functions, from the event data. Pairwise log-rank test using package `lifelines`.

For all tests, we adopt the following convention : ns (p-value > 0.05), * (p-value ≤ 0.05), ** (p-value ≤ 0.01), *** (p-value ≤ 0.001), **** (p-value ≤ 0.0001).

4.3 Results

4.3.1 Single-cell description with Celldetective

ADCC images are rich and complex in content as illustrated in figure 4.7. The $637 \mu\text{m} \times 637 \mu\text{m}$ field of view allows a throughput of between 400 to 1200 MCF-7 cells per position that are interacting with a few thousand primary NK cells. Additionally, some erythrocytes remain from the donor's blood, that do not seem to play any major role, although studies have suggested that they might reduce the search time of NK cells [194]. As the NK cells interact and kill MCF-7 cells, membrane permeabilities become compromised and nuclei take in the Propidium Iodide dye, turning red. The system is imaged with up to five modalities, the most recurrent being brightfield (showing all cell populations), the Hoechst nuclear stain (initially given to the MCF-7 cells only), the Propidium Iodide nuclear stain (nuclei of all dead cells) and CFSE (a marker for the cytoplasm of the primary NK cells). In practice, as can be seen in figure 4.7b, primary NK cells incorporate the Hoechst dye over time, making the Hoechst channel non-specific to the MCF-7. Primary NK nuclei are nevertheless much smaller than MCF-7 nuclei which could help if it was not for the fact that the nuclei of dead MCF-7 cells are hard to discriminate from out-of-focus NK nuclei, based on the Hoechst channel. Primary NK cells can also hover above MCF-7 nuclei, effectively screening them. The CFSE marking is also quite heterogeneous, and NK cells can be quite polarized, making it almost impossible to discriminate between two NK and a polarized one without inspecting the brightfield image. These are the complications intrinsic to the cell system under study. One must add to that experimental complications that happen regularly such as temporary loss of focus and incomplete fluorescence markings.

We exploited Celldetective to perform a complete and independent description of both the target (MCF-7 cells) and effector (primary NK cells) populations, despite the cell detection challenges mentioned above. Both population descriptions were then combined using a neighborhood scheme in the software.

4.3.1.1 MCF-7 cells

Segmentation From the experimental design, with the use of nuclei markers Hoechst and PI, our first challenge was to segment accurately and specifically the nuclei of the MCF-7 cells. At first, we attempted to use a generalist model on the Hoechst channel and then filter out NK nuclei using morphological criteria. Figure 4.8a illustrates the output of the StarDist *versatile fluo* on the Hoechst channel of a perfectly in-focus image. This approach was quite unstable, as it was very sensitive to the image quality. Hovering NK cells could be picked up by the StarDist model, to the detriment of the MCF-7 nucleus segmentation, below. Unfiltered NK cells interfered with the tracking of the MCF-7 nuclei. Therefore, we decided to provide more information to the segmentation model and train it from scratch on a new dataset that

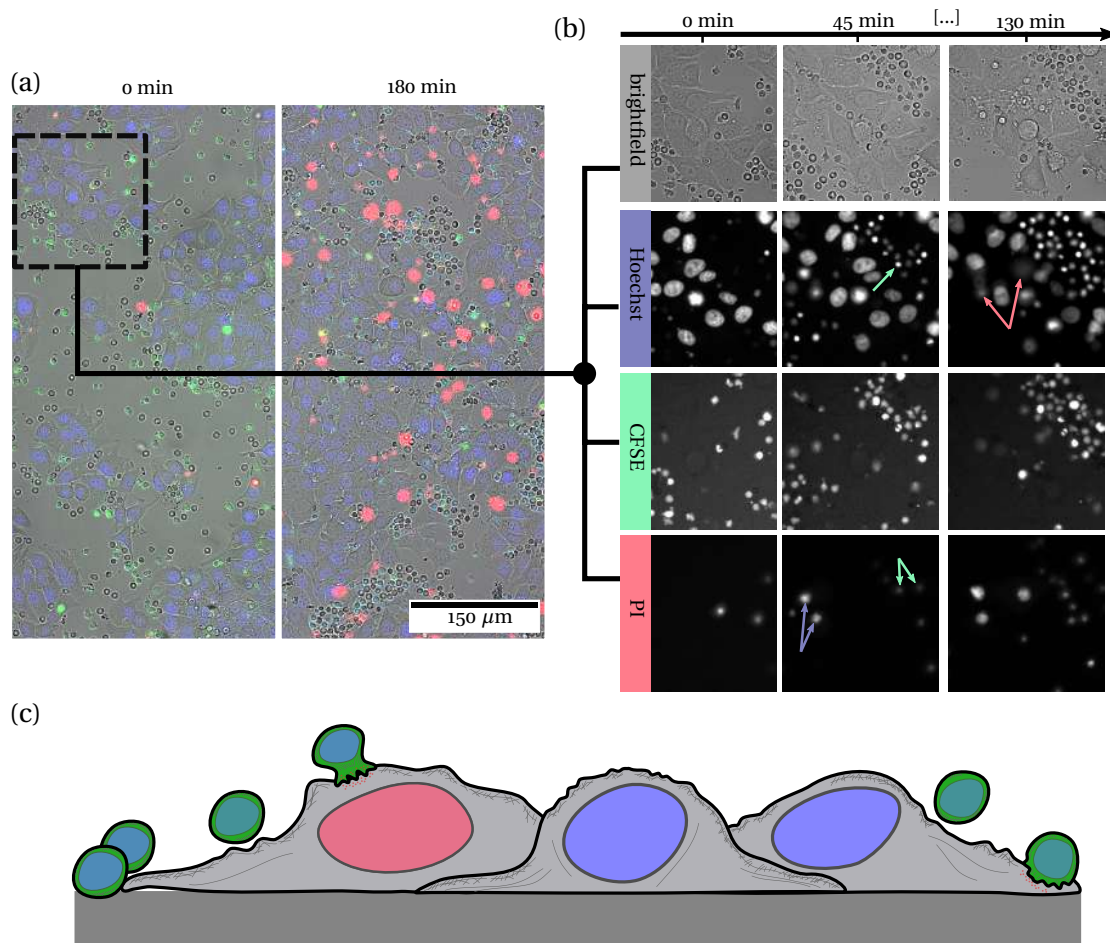


FIGURE 4.7 – The ADCC assay under the microscope. (a) full field of view of a position, with an RGB+gray composite of all channels at $T = 0$ min and $T = 180$ min. The brightfield channel is in gray, the nuclear stains Hoechst and PI respectively in blue and red, and the CFSE marker in green, reflecting the emission spectra of these fluorophores. b) a crop of the full field of view is decomposed by channels for four-time points. The green arrow in the Hoechst row shows NK that intake the Hoechst dye over time. The red arrows highlight the nuclei of dead MCF-7 that moved out of focus but can be seen clearly in the PI channel (blue arrows in the PI row). The green arrows in the PI row show the nuclei of dead NK. c) Schematic lateral with effector NK cells interacting with the MCF-7 cells, sometimes hovering above them (not to scale).

we annotated. The dataset consists of 95 manually annotated multimodal ADCC microscopy images with a total of 3889 cell nuclei of MCF-7 cells in the presence of primary NK cells. Initially, the images to annotate were picked randomly from the ADCC data, as quarter-size crops of the position field of view. A proto-model was trained and additional samples were picked in places where the proto-model failed to segment. The mean number of MCF-7 nuclei per image was 40.9 cells with a standard deviation of 32 cells, covering a large spectrum of densities.

From this dataset, several StarDist instances could be trained, with a slight mo-

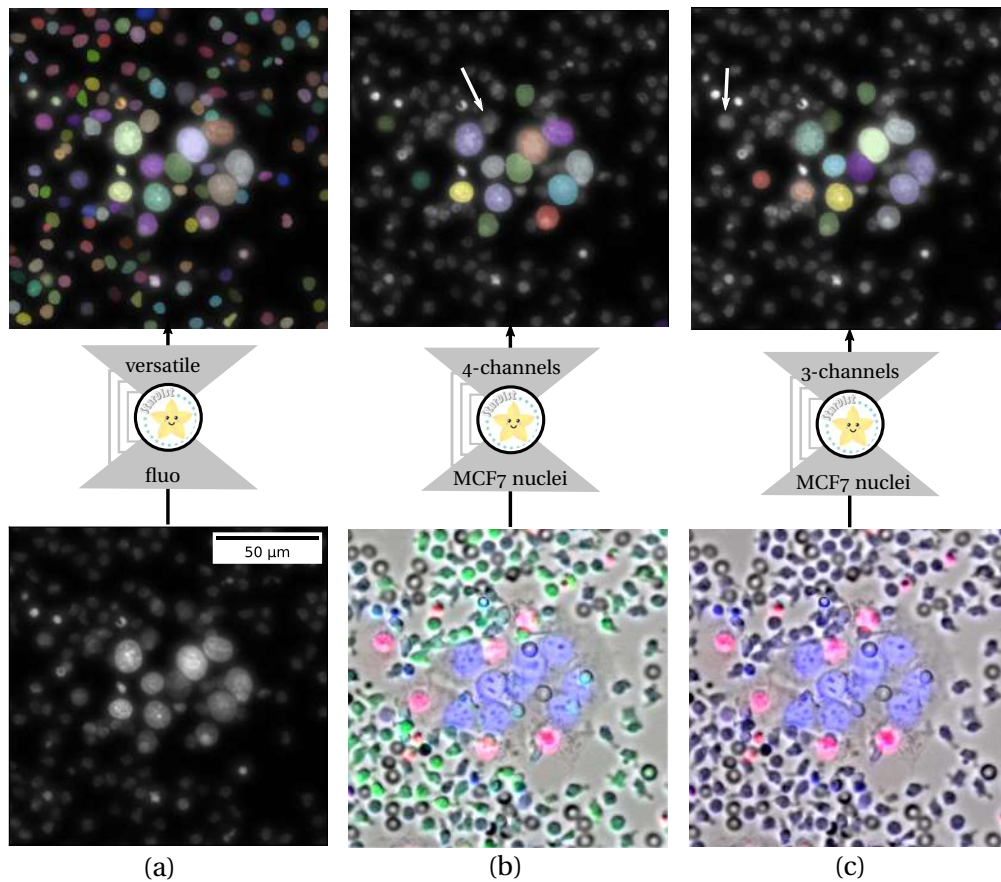


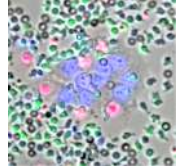
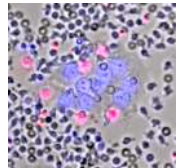
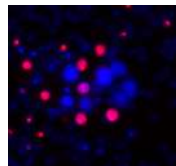
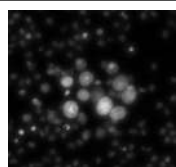
FIGURE 4.8 – Multimodal models to detect MCF-7 nuclei. (a) the generalist StarDist model *versatile fluo* is applied to the Hoechst channel to detect cell nuclei. As expected, all cell nuclei are detected, with no specificity to the MCF-7 nuclei. b-c) new StarDist trained from scratch on multimodal data (3 or 4 channels) can accurately and specifically segment the nuclei of MCF-7 cells from the multimodal images, despite occasionally missing a nucleus (white arrow). Such nuclei are usually segmented properly in the next frame.

dification in the input architecture to accommodate more channels. The different models associated with different channel combinations occurring in the ADCC data (e.g. the use of CFSE was not systematic) are listed in table 4.1. In addition to the new multimodal models, we fitted the StarDist *versatile fluo* model to our task, by pursuing the training on our new data (with only the Hoechst channel as input), adjusting the pre-trained weights instead of starting from scratch.

We also tried to mask randomly channels during training to make some channel input optional, but this approach requires more testing. Figure 4.8 illustrates two of these models applied to respectively the BF+PI+H+CFSE and the BF+PI+H modalities to segment specifically the MCF-7 cell nuclei.

These models have applied to all the frames of all ADCC movies to reliably and selectively detect MCF-7 nuclei in the presence but also the absence of primary NK cells, making the tracking of MCF-7 nuclei much easier.

Table 4.1 – MCF-7 nuclei segmentation models in the presence of primary NK cells. Each model was trained on the same dataset of ADCC images, *MCF7_nuclei_w_primary_NK*, picking only the relevant channels. Details on the training parameters and data augmentation performed can be found in chapter 3.3.2.2.

Name	Channels	Type	Pretrained	Pixel size (μm)	sample image
<i>MCF-7_bf_pi_cfse_h</i>	brightfield PI CFSE Hoechst	StarDist	None	0.3112	
<i>MCF-7_bf_h_pi</i>	brightfield Hoechst PI	StarDist	None	0.3112	
<i>MCF-7_h_pi</i>	Hoechst PI	StarDist	None	0.3112	
<i>MCF-7_h_versatile</i>	Hoechst	StarDist	<i>versatile_fluo</i>	0.3112	

Tracking We exploited the napari-bTrack plugin through Celldetective to optimize a tracking configuration for the MCF-7 cell nuclei. We removed the “apoptosis” tracklet connection hypothesis, as it does not fit with our description (cells did undergo apoptosis but they remained visible and we wanted to track them). We kept the “branch” hypothesis but reduced its probability by decreasing its scaling factor λ_{branch} from the default value of 50.0 to 1.0, as MCF-7 cells were observed to occasionally undergo mitosis during the acquisition. The time threshold was considerably increased (from 2 to 20) to allow tracklet linking after long time gaps : MCF-7 nuclei do not travel great distances. Figure 4.9 shows typical MCF-7 trajectories viewed in napari. We applied systematically the same track post-processing pipeline to MCF-7 trajectories : we discarded all cell tracks that did not start at the beginning of the movie, to limit to a minimum the number of false-positive NK tracks, that could still be occasionally detected despite the model’s specificity. We interpolated tracking gaps. We sustained the last position of a track until the end of the movie, to be able to measure local intensities even when a trajectory was truncated. When needed, we introduced a minimum track duration of about a quarter of that of the

movie, to limit the number of transient false-positive tracks. Under the best image conditions, we could segment up to 100% of the MCF-7 nuclei all the way through. Segmentation and tracking were challenging in conditions that broke away from the 2D assumption, *i.e.* when the MCF-7 cells started overlapping or when a MCF-7 detached from the monolayer.

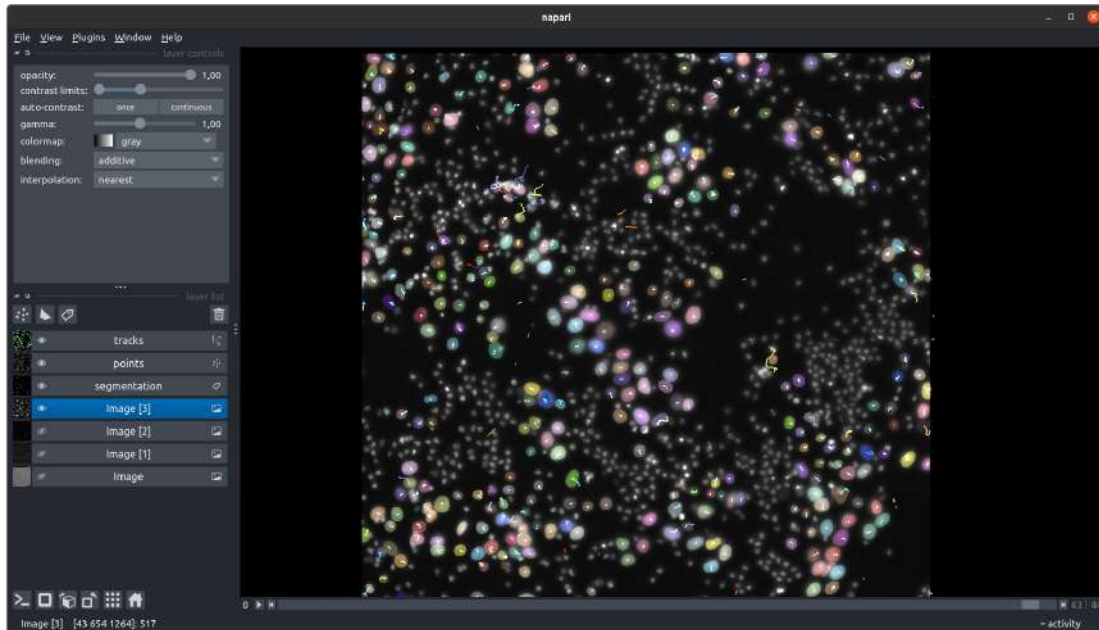
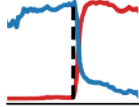
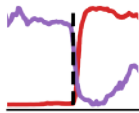
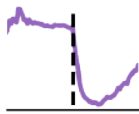
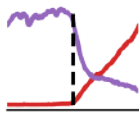


FIGURE 4.9 – Visualizing MCF-7 tracks with napari. Full (637×637) μm field of view, only the Hoechst channel is shown. The full trajectories are shown (over two hours), before track post-processing.

Measurements & signal analysis By experimental design, the lysis information was expected to be contained in the Propidium Iodide fluorescence signal. Considering that our MCF-7 nuclei segmentation quality started much worse than it is now, we relied a lot on track interpolation to measure intensities despite the lack of a nucleus mask at many time points. By convention, we systematically measured the intensities in a circle of radius 10 px ($3.1 \mu\text{m}$ in a typical ADCC image) to have an alternate reading of the nucleus fluorescence, very redundant with the intensity average over the nucleus mask. This process, combined with track filtering and sustaining described above, gave us continuous intensity signals for each MCF-7 cell. In addition, we measured morphological descriptors of the nuclei (area, eccentricity, major and minor axes). We exploited these single-cell signals to train and automatize event detection with DL models listed in table 4.2. The initial annotations were performed from scratch using Celldetective’s signal annotator shown in figure 4.10. This interface is routinely used to assess event detection quality and correct errors from the DL models. Initially, we were only interested in lysis events characterized

by a PI intake in the nuclei, in which case cells could be classified as dead with a death time t_{\dagger} , not observed to die or already dead. We revisited the cell signals later on to annotate other phenomena of interest such as nucleus shrinking, blebbing, apparent death in brightfield, etc.

Table 4.2 – Event detection models. The following event detection models were trained to automatize event annotation from signals. The associated datasets are made available directly in Celldetective.

37 Name	Signals	Task	Pattern	Dataset
<i>lysis_H_PI</i>	Hoechst PI	Strong PI intake		NucPI
<i>lysis_PI_area</i>	PI area	Strong PI intake		NucPI
<i>NucCond</i>	area	Nucleus shrinking		NucCondensation
<i>lysis_lowPI</i>	PI area	low PI intake		LowPI

4.3.1.2 NK cells

Segmentation In some ADCC experiments, the cytoplasm of the NK cells has been labelled with the CFSE dye. This channel is a good candidate to apply a published Cellpose model as no MCF-7 cell is visible in the CFSE channel. Since the NK are pretty small on the image we could also get away with applying a low-resolution StarDist model on the NK, that would not capture the NK cell shape well but would be very accurate at counting. At high NK cell density, we observed that it could be difficult to discriminate between a polarized NK or more than one circular NK side by side. Furthermore, we notice that the CFSE marking is very weak for NK forming synapses, and those are the ones we are most interested in. Therefore we had to create segmentation models that could also use the brightfield channel and Hoechst. Since the MCF-7 cells show up in those channels, we had to create a dataset for the primary NK cells in the presence of MCF-7 cells and define a more multimodal task. The cells were primarily annotated from brightfield or CFSE. Let's call this dataset the *primary_NKs_w_MCF-7* dataset. The models trained on this dataset are

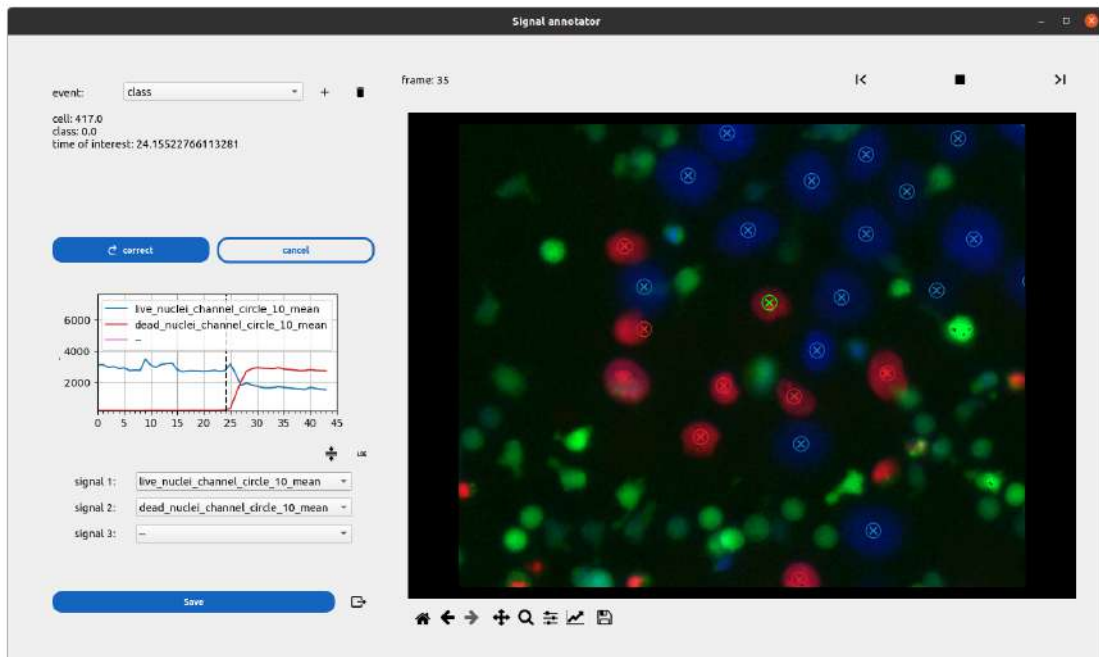
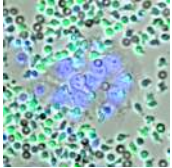
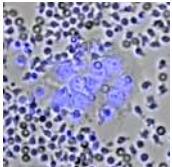
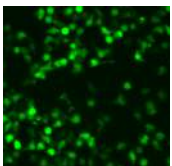


FIGURE 4.10 – QC on lysis detection with Celldetective. After applying the *lysis_H_PI* lysis detection model, a visual QC is performed using Celldetective’s signal annotation GUI. The global quality is assessed and depending on the need, detection errors are manually corrected. The image is an RGB composite of respectively the PI, CFSE and Hoechst channels (crop of a $(637 \times 637) \mu\text{m}$ field of view). The position-based intensity signal of PI (red), and Hoechst (blue) is represented for the selected cell. The black vertical dotted line shows the t_{\dagger} estimated by the model.

summarized in table 4.3 (that is not completely true as at least one model was only trained on a subset of the dataset).

Tracking NK cells move much faster than the MCF-7 cells and can have very different motility regimes [127]. In most ADCC experiments, we did not achieve a time resolution high enough to track the NK. Under such conditions, NK tracking was skipped and we proceeded directly to measurements. Some experiments were designed to accommodate NK tracking by decreasing the number of positions and the NK cell density. As for the MCF-7 nuclei, we used the *napari-btrack* plugin to optimize the tracking on the NK cells. The “branch” and “apoptosis” hypotheses were removed, respectively as the primary NK cells did not undergo mitosis during the ADCC experiments and did not escape the field of view through the -Z dimension. The tracklet linking probability was increased by increasing the scaling factor λ_{link} from 10.0 to 30.0. The distance threshold was considerably increased, from 40 to 99 to link tracklets at larger distances. We took extra effort to make the segmentation as perfect as possible, correcting manually missed NK cell detections on *napari* through the segmentation visualizer tool of Celldetective. Indeed, the best time

Table 4.3 – Primary NK segmentation models. The models have been trained on the *primary_NKs_w_-MCF-7* dataset. Channels in parentheses are optional (a black frame can be passed instead). Details on the training parameters and data augmentation performed can be found in chapter 3.3.2.2.

Name	Channels	Type	Pretrained	Spatial calib. (μm)	sample image
primNK_multimodal	brightfield CFSE Hoechst	Cellpose	None	0.2178	
primNK_SD	brightfield Hoechst	StarDist	None	0.3112	
primNK_cfse	CFSE None	Cellpose	CP-cyto2	0.2178	

resolution achieved, while maintaining a reasonable throughput, was around 1 min 10 seconds per frame, which was still arguably low compared to NK dynamics. Raw bTrack trajectories were monitored in napari through Celldetective as illustrated in figure 4.11. We applied a filter on track duration to remove transient tracks and interpolated gaps in the trajectories.

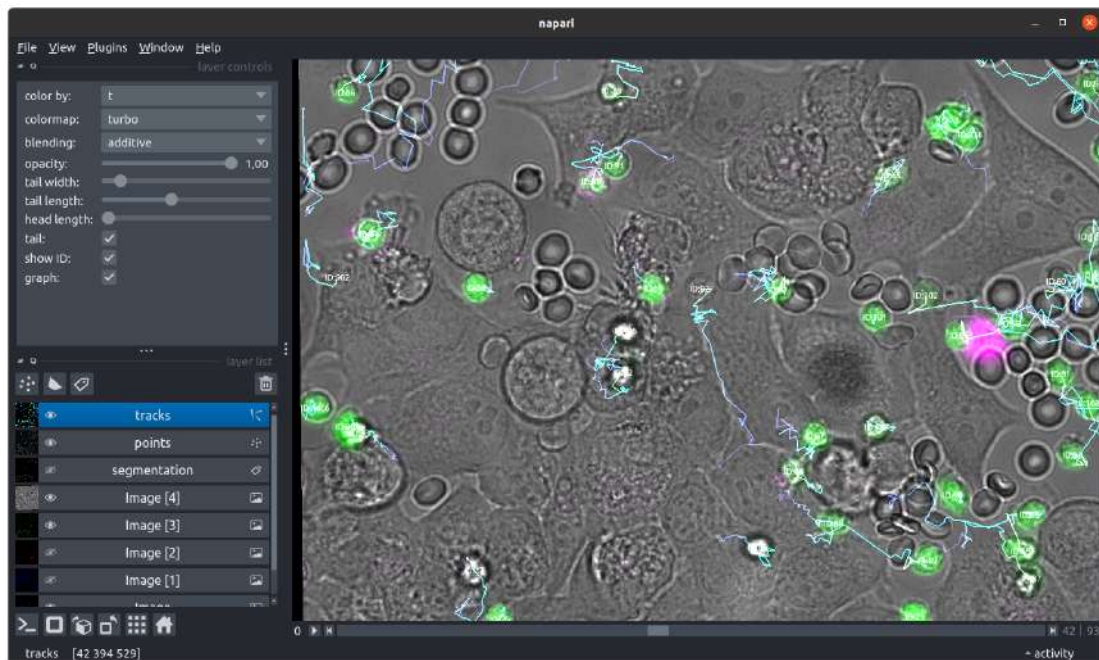


FIGURE 4.11 – Visualizing NK tracks with napari. The brightfield (gray), CFSE (green) and LAMP1 (purple) channels are composited behind the NK tracks. The trajectories are represented over the previous 70 minutes.

Measurements We measured the morphological descriptors and mean intensities across all available channels of the NK cells. Since in most cases, we did not track them, we applied the static classification tool to set apart dead NK from the PI intensity level. We used the same technique to define a clear-cut LAMP1 positive class when appropriate. If the NK tracks were available, we used the signal annotation tool to annotate manually NK that are forming synapses with the MCF-7 cells.

4.3.2 Detection of cell death

4.3.2.1 PI as a marker

Cell death events could successfully be identified from PI signals, as dying cells exhibited an irreversible increase in PI fluorescence level, measured in the nucleus. Figure 4.12a shows that in the absence of effector cells and of antibodies, very few cells exhibited a PI response, whereas more than the majority of cells exhibited a pronounced PI increase (over a magnitude) in the presence of 100 pM of CE4-28 antibody and effector cells during the observation window.

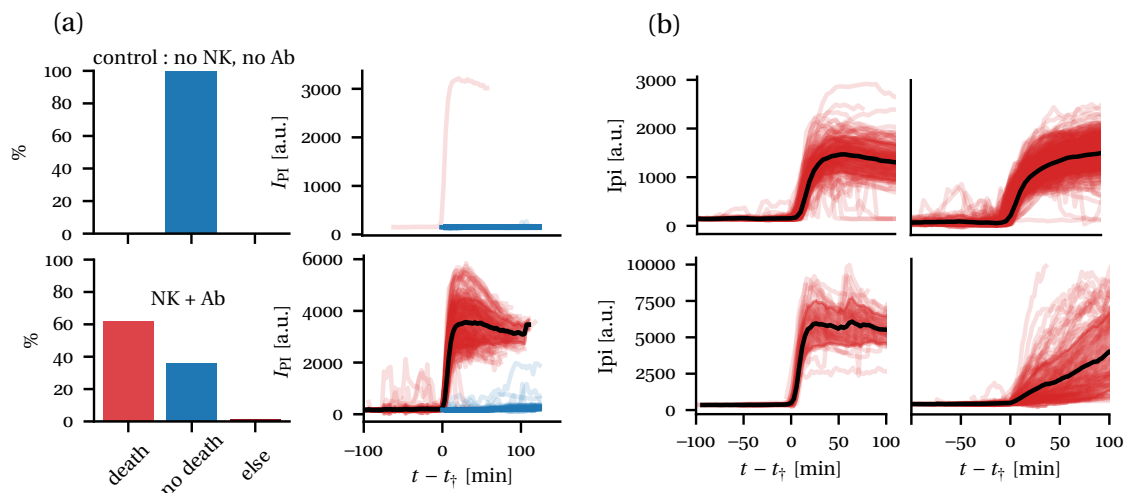


FIGURE 4.12 – PI as a marker of cell death. a) MCF-7 cell death event classification based on the PI signal for negative control position (no NK and no antibody) and a positive control position (NK and 100 pM of CE4-28 bsAb). The black line is the mean PI response over all cells, and the filled area is the associated standard deviation. b) a variety of PI responses have been observed across experiments. One positive control position is selected to represent each experiment.

Repeated experiments from Beatriz Díaz-Bello, Lorna Ammer, and Florian Dupuy showed a variety of PI response patterns (figure 4.12b), with a configuration that shows a slow and linear PI increase instead of a strong almost sigmoidal response. This configuration happened more than once and manifested up to two phases of PI response. First, a low signal enters the cytoplasm of the cells, growing linearly in intensity. This increase can be detected by representing the PI signal in log scale or monitoring directly the PI channel images. We checked all other channels to rule out a fluorescence leak. Second, an intake in the nucleus could follow, systematically accompanied by a strong fluorescence increase (of a magnitude order). A visual inspection of strong PI intake configurations showed that the initial cytoplasm intake was extremely transient if at all. The PI increase was observed to be irreversible, any signal decrease being due to the nucleus going up the plane, out of focus, or the trajectory being lost. Unless mentioned otherwise, we took the time of death t_{\dagger} as being the first frame with a PI signal, whether it was in the cytoplasm or directly in

the nucleus.

4.3.2.2 Apparent nucleus area as a marker

The nucleus area transitions around the death time of the MCF-7 cell. We observe an apparent reduction that correlates well with strong PI intake events as illustrated in figure 4.13. The correlation plot seems to indicate that the apparent nucleus shrinking tends to occur slightly before the strong PI intake, but since the difference is of the order of a few frames at most, we cannot conclude on an actual chronology of the event. We observe from the confusion matrix that over 99 % of the apparent nucleus shrinking events are associated with a strong PI response. On the other hand, 8 % of the PI intakes are not associated with a nucleus shrinking event.

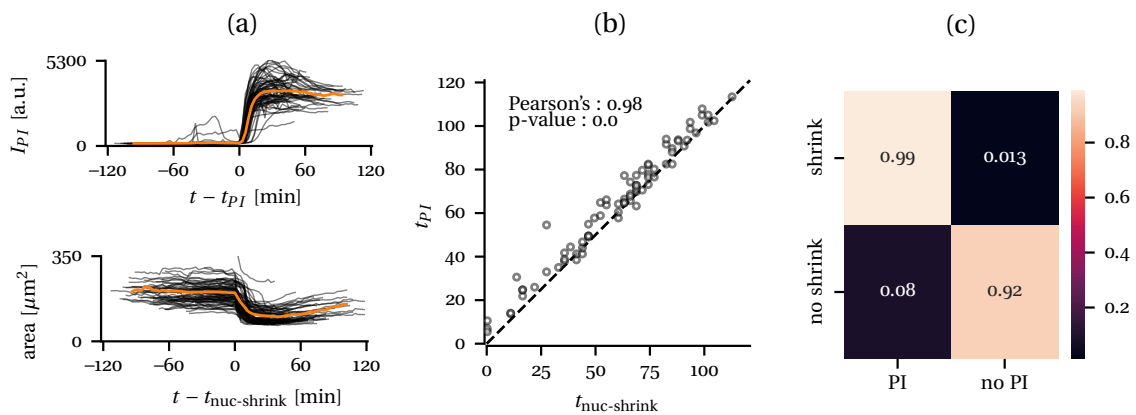


FIGURE 4.13 – A strong PI intake correlates well with apparent nucleus shrinking. a) strong PI intake events, characterized by a time t_{PI} and apparent nucleus shrinking ($t_{nuc-shrink}$) are annotated independently from respectively the PI and nucleus area signals. b) both t_{PI} and $t_{nuc-shrink}$ are linearly correlated with a Pearson's coefficient of 0.98 and a p-value close to zero. c) a confusion matrix shows co-occurrence probabilities between nucleus states and PI states.

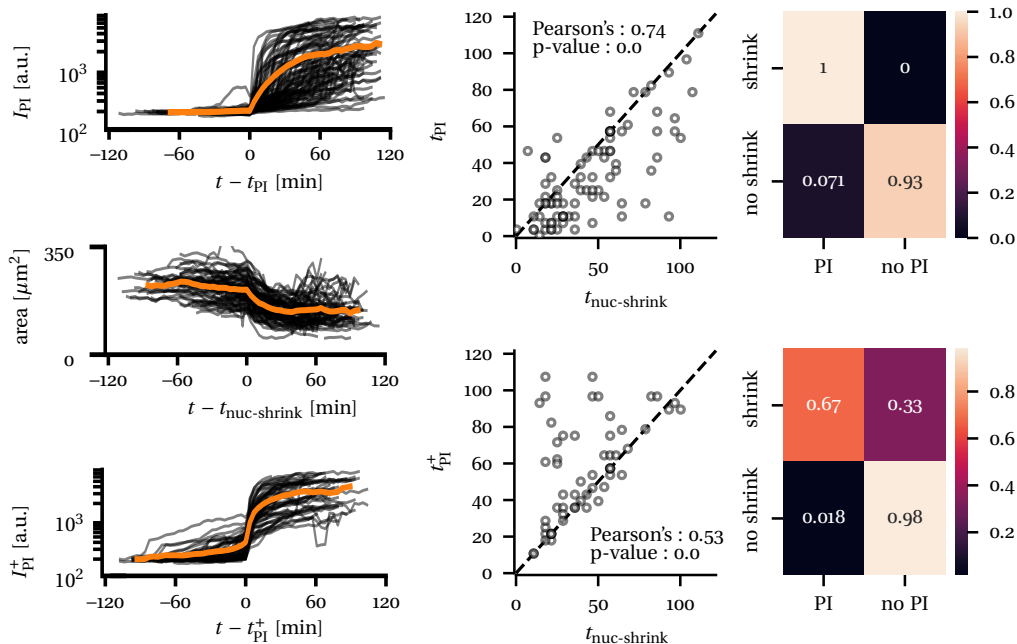
To push this study further, we exploited data from an experiment performed by Florian Dupuy that exhibited the biphasic PI response described in the previous section. As detailed in figure 4.14, a double annotation was performed to differentiate low PI intake (t_{PI}) from the strong PI arrival in the nucleus (t_{PI}^+). We define the low PI intake event as the first time a MCF-7 cell is visible on the PI channel, even if it is a faint signal. The strong PI intake event is defined as the arrival of PI in the nucleus, exhibiting a bright PI increase in the nucleus. This translates into an inflection of the log of the PI signal at the time of the event. Both times were compared independently to the annotated nucleus shrinking time yielding two very different correlation plots. Low PI intake events seemed to occur for the vast majority of cases before any apparent nucleus shrinking event. The confusion matrix highlights that 100 % of the shrinking events are associated with a low PI intake, whereas around 7 % of the low PI intakes could not be associated with a nucleus shrinking event. The strong PI intake tells a slightly different story, with the majority of events occurring after

the nucleus shrinking events. The confusion matrix shows that a large fraction of shrinking events (33 %) could not be associated with a strong PI intake event. On the other hand, the absence of a shrinking event was associated less than 2 % of the times with a strong PI intake.

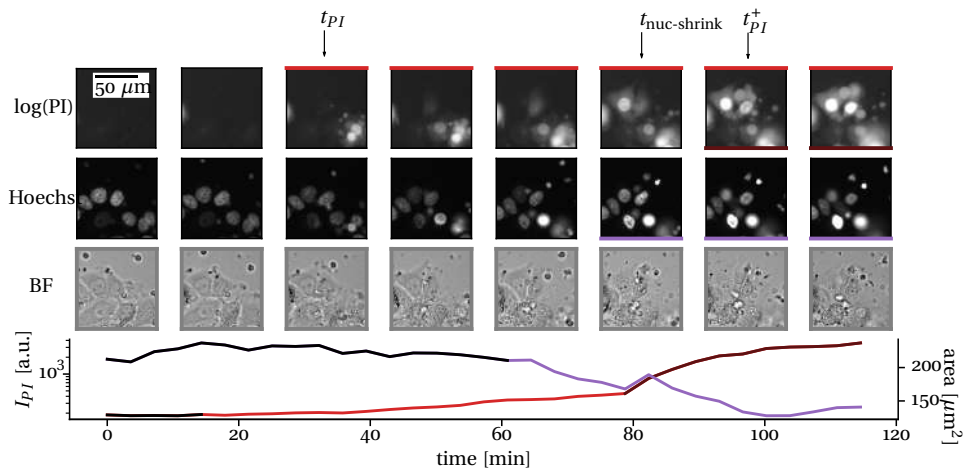
We interpret these events as being chronologically related, but not always detectable as such. First, the low PI intake starts, then it is accompanied by an apparent nucleus shrinking, and finally PI reaches the nucleus and a strong fluorescence increase is observed in the nucleus. Figure 4.14b shows such a chronology for a sampled single cell that exhibited the three events consecutively.

4.3.2.3 Dye interaction

Although we do not understand why a PI response is as it is for a given experiment, despite testing various PI compounds, we identified at least one confounding factor, which is the other nuclear stain Hoechst, co-responding in various ways with PI, as illustrated in figure 4.15. Hoechst also transitions at t_{\dagger} but the observed patterns are even more varied than the ones observed for PI. Step function decrease, local intensity peak (black arrows), or even slight and irreversible intensity increase have been observed across experiments. We suspect the nucleus area also plays a role, making it a tripartite response that could be de-correlated in the future.



(a) correlating complex PI response to apparent nucleus shrinking



(b) cell death chronology

FIGURE 4.14 – Chronology of PI intake and apparent nucleus shrinking. a) the time of first PI intake t_{PI} , of strong PI intake t_{PI}^+ and of nucleus apparent shrinking $t_{nuc-shrink}$ are annotated independently from respectively the PI signal and the nucleus area signal on the same dataset. All cells presented here exhibited at least a low PI intake event, sometimes followed by a nuclear area decrease and a strong PI intake event. The $(t_{nuc-shrink}, t_{PI})$ and $(t_{nuc-shrink}, t_{PI}^+)$ correlation plots are shown as well as their respective confusion matrices. b) The chronology of cell death is shown for a single cell over two hours. Three channels are shown at 15-minute intervals. The red color codes for the low PI intake event taking place, the purple color for the apparent shrinking event, and the brown color for a strong PI intake.

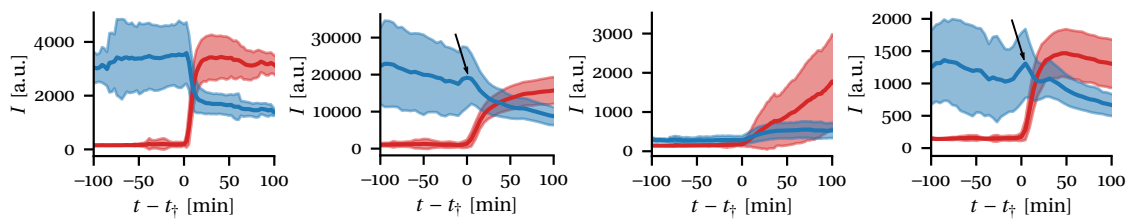


FIGURE 4.15 – PI-Hoechst co-response. The Hoechst signal has been observed to transition around the lysis time t_{\ddagger} with a pattern that varied wildly across experiments. The black arrow indicates an apparent increase in intensity that occurs right before death in some conditions. Each graph represents a position sampled from different experiments with mean and SD from around 150–400 cells.

4.3.3 Cell morphologies : MCF-7

In the next three sections, we will exploit a manual annotation of the MCF-7 cell shape to look for the best estimator of cell shape and neighborhood, to describe as accurately as practically possible cell-cell interactions in the survival study.

4.3.3.1 Manual annotation and observations

Detection is challenging. In theory, the shape of the MCF-7 cells can be identified from brightfield images [51]. In practice, numerous cell junctions are blurry, and poor contrast can make it very difficult to separate the cell membrane from the surface of the sample, making the segmentation process difficult. The authors of the LiveCell dataset mentioned for the MCF-7 cells that “locat[ing] cell boundaries [was challenging]”. Unlike other cell types in the dataset, the MCF-7 were annotated directly from the phase contrast images without access to other modalities. Visual inspection of some of the images as in figure 4.16 shows that although some cells can indeed be identified, with a favorable contrast and exploiting nucleus texture, others are a blur (black arrow). It turns out that the authors of LiveCell did not annotate the cells in such conditions, preferring to leave the annotation incomplete. Models were trained on the partial annotations [51, 131], which is not a conventional practice in supervised learning, as the loss function should be modified to account for the incompleteness of the annotations. At the very least, this means that whatever the model outputs in these dense MCF-7 regions should not be taken for granted as it was never taught what to do in such regions in the first place.

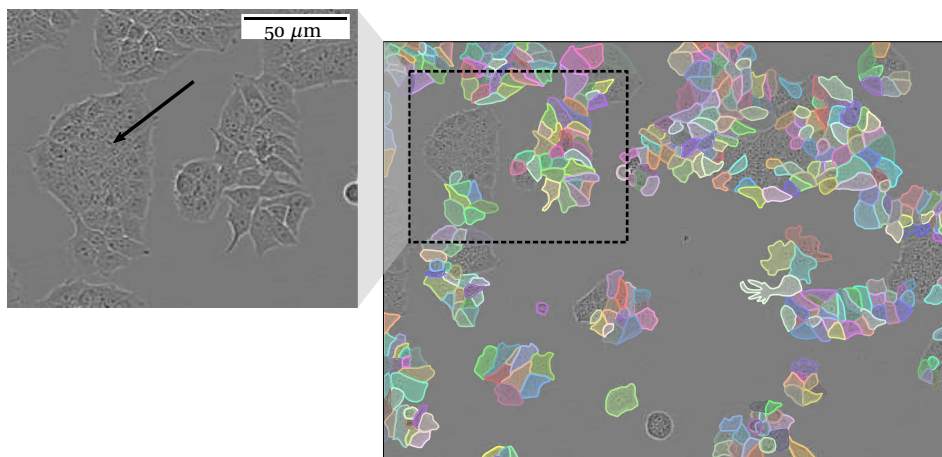


FIGURE 4.16 – MCF-7 cells in the LiveCell dataset [51]. An image sample of training data from the Live-Cell dataset showing MCF-7 cells observed at 10X magnification in phase contrast using an Incucyte S3 Live-Cell Analysis system. In the crop of the image, we emphasize with a black arrow a region of tightly packed MCF-7 where accurate segmentation cannot be achieved from phase contrast alone and was not performed in the LiveCell dataset.

Partial annotations. To study the morphology of the MCF-7 cells in the ADCC assay without having to make arbitrary choices we decided to perform a partial

annotation from the brightfield images, using the Hoechst channel when needed. To avoid adding complexity to this task, we focused on images that were taken before NK cell introduction. We selected some positions from an ADCC experiment performed by Beatriz Dìaz-Bello. Highly contrasted MCF-7 cells, for which cell-cell contacts are visible or cells constrained by their neighbors were annotated manually in napari through Celldetective. From the total count of MCF-7 nuclei, we could only annotate about 50 – 60% of the cells unambiguously in our images.

Observations. The MCF-7 cells exhibit a large range of morphologies in the ADCC assay, as shown in figure 4.17. The area distribution is spread, the cells are only moderately circular and can be oriented in any direction. We observed a mean area of $500 \pm 217 \mu\text{m}^2$ and a mean eccentricity of 0.81 ± 0.14 which compares well with a previous area estimate of $478 \mu\text{m}^2$ but is more eccentric than the accompanying estimate of 0.58 [114]. The major axis of the cells, used as a proxy for the size, averaged at $37 \pm 11 \mu\text{m}$, with a maximum value of $76 \mu\text{m}$, showing how elongated a single cell can be. The minor axis averages $19 \pm 5 \mu\text{m}$, highlighting once again the eccentricity of the cells. The PCA projection in figure 4.17b-c shows the variety of observed MCF-7 phenotypes, ranging from the perfectly circular (left) to the most eccentric (bottom right), from large (top) to tightly packed (bottom left), with no obvious cluster emerging, implying a continuity of variations.

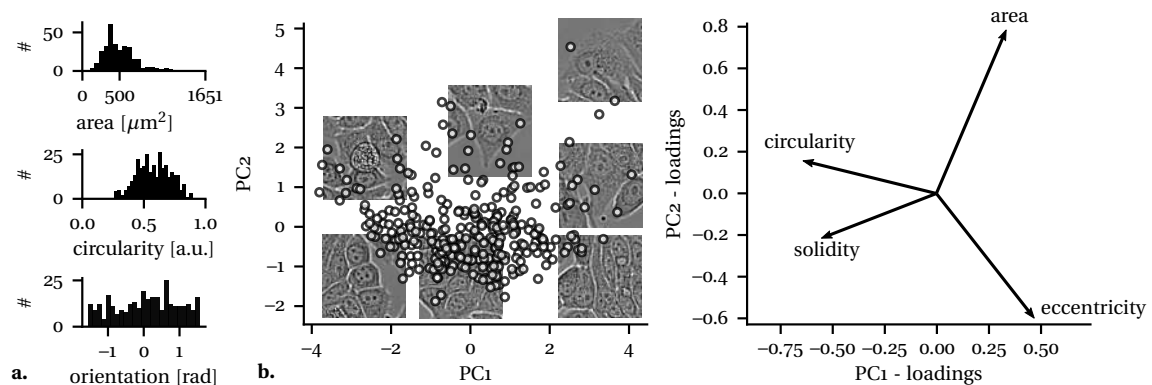


FIGURE 4.17 – MCF-7 cells showcase a variety of morphologies. a) Histograms of the MCF-7 area, circularity, and orientation estimated from a partial and manual annotation. b) PCA construct (two components) of morphological features of the MCF-7. Each feature was independently standardized. c) Loading plot showing the weights of each morphological feature selected in the PCA.

4.3.3.2 Deep learning approach

Optimization on partial annotations. We assessed the performance of two generalist Cellpose models to segment the MCF-7 cells. We devised an optimization scheme exploiting our partial annotations to *optimize* Cellpose predictions. The principle could be decomposed as follows : first, we took at random combinations of a

Cellpose pre-trained model (between *cyto2* and *livecell*) and parameters (`cellprob_threshold`, `flow_threshold` & `diameter`). Then for each annotated cell, we located at the center of mass the mask predicted by Cellpose. We computed the IoU between the annotated and predicted cell mask for each cell. If Cellpose predicted the background, we set this IoU to 0. From the collection of IoU we defined several average metrics such as the mean, median, and fraction of cells with an IoU higher than a threshold, the fraction of IoU equal to zero (a false negative prediction). This process was done across several images paired with partial annotations to make the optimized model robust to different images. For the *cyto2* model we passed the brightfield channel in the first channel slot and the Hoechst channel in the second. For the *livecell* model we only passed the brightfield channel in the first slot. Both the `cellprob_threshold` and the `flow_threshold` range from -6 to 6. We let the cell diameter range from 50 px to 100 px (15 μm to 30 μm).

Optimized model. The median IoU for all tested models is shown in figure 4.18a. Yellow lines indicate that the combination of parameters yielded a high median IoU. If we introduce a filter to focus on the combination of parameters that yielded the highest score, specific solutions emerge. First, the *livecell* model is over-represented compared to the *cyto2* model, which is expected since the former was trained specifically on phase contrast images, very similar to brightfield images, that included MCF-7 cells. Second, the optimal diameter ranges between 60-90 pixels (19-28 μm), which matches with the estimates for the minor and major axes of the MCF-7 obtained in the previous section. The `cellprob_threshold` is contained between -0.5 and 0, whereas the `flow_threshold` can take multiple values. The very best model has a mean IoU of 0.76 and a median IoU of 0.81. 28 % of the cells exhibited an IoU > 0.85, whereas 3 % of the cells were missed by the optimized model. Figure 4.19 highlights how the morphological descriptors computed on the masks produced by the model correlate well with the morphological descriptors associated with the partially annotated cells. The best match is the area, with a Pearson's coefficient of 0.91, followed by the eccentricity with a Pearson's of 0.81. The orientation score is lower but this can be attributed to the indetermination of this estimate for the most circular cells. As a reminder, these results reflect exclusively the segmentation performance on the annotated cells, leaving a blind spot on the remaining cells.

Evaluating the blind spot. Since we can segment the MCF-7 nuclei much more robustly than the membranes, we can exploit nuclei location to comment on the segmentation quality on the cells that were not annotated. First, we use Celldetective to apply StarDist's *versatile fluorescence* model on the Hoechst channel to efficiently segment the MCF-7 nuclei and perform a quality check. Then we can match the partially annotated cell masks to their nuclear masks by performing a 1-to-1 closest neighbor mapping. In other words, we associate the closest nucleus to each annotated cell mask, using the center of mass. The pairing of the annotated cell masks to their nuclear masks provides a reference point when quantifying the segmentation quality on the other cells. For each nucleus, we set two conditions to accept the Cellpose mask. First, the nucleus must be mostly contained in the Cellpose mask

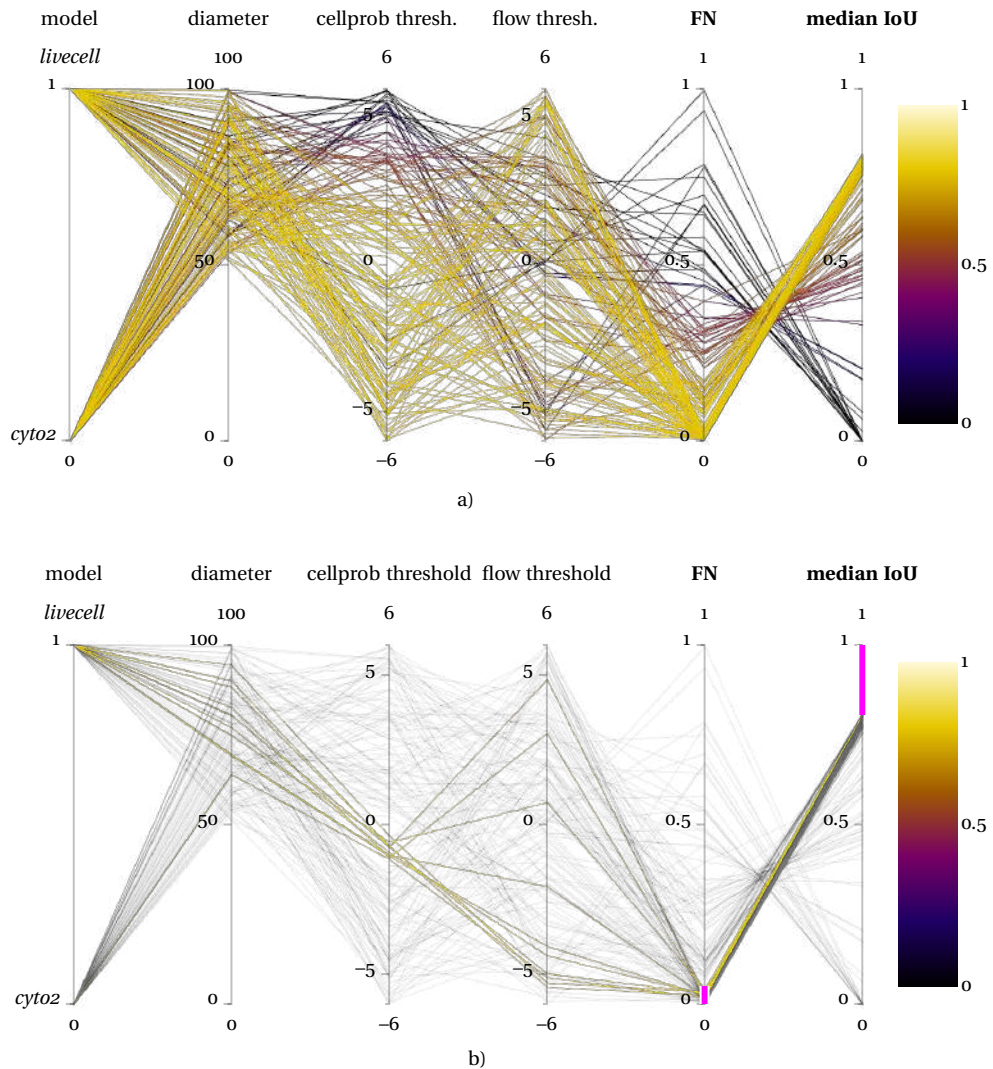


FIGURE 4.18 – Optimization scheme for Cellpose. a) Parallel coordinates plot showing, for each combination of Cellpose inference parameters (pre-trained model chosen, diameter, cellprob threshold, flow threshold) the fraction of false negative predictions and the median IoU per cell (the line color represents this quantity). b) The parallel coordinates plot is filtered (purple gates) to highlight the parameters that yielded simultaneously the highest median IoU values (> 0.805) and lowest false negative fraction (< 0.05).

coinciding with the center of mass of the nucleus. We set a threshold at 95 % below which we reject a nucleus as being too much “outside” the cell mask, which tells

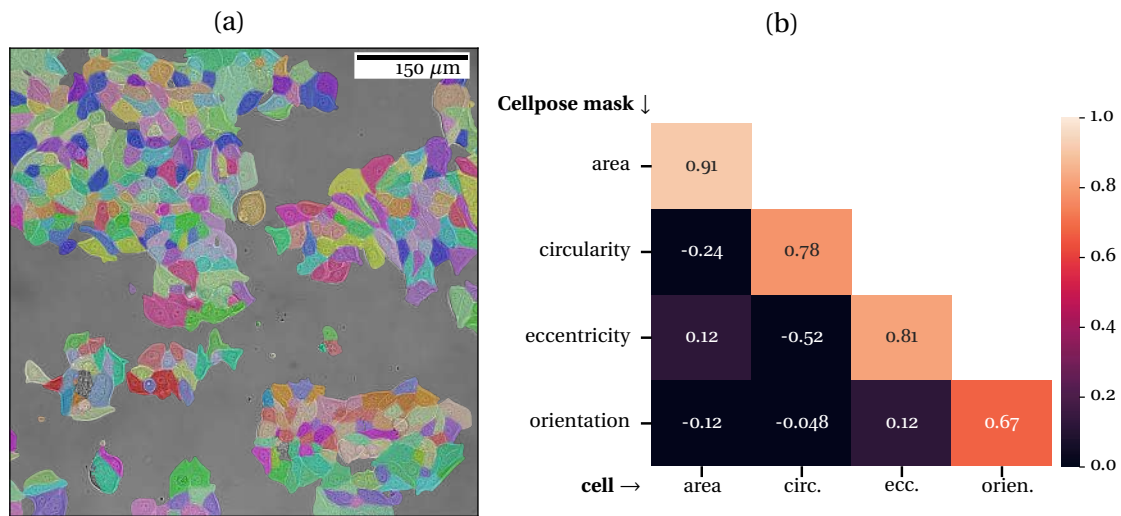


FIGURE 4.19 – The optimized Cellpose segmentation is a good estimator of MCF-7 cell morphology. a) The combination of parameters that maximized the median IoU with our partial annotation was applied to one of the partially annotated images. We applied the *livecell* model on a brightfield image, with a diameter estimate of 77 pixels ($\sim 24 \mu\text{m}$), a flow threshold of -4.37 , and a cellprob threshold of -0.93 . **b)** The morphological descriptors of the predicted cell masks are correlated to the descriptors of the paired cell (Pearson's correlation coefficient). All morphological features are strongly correlated between the two sets.

us that the mask is inaccurate. The second condition is that there should not be more than one nucleus in the cell mask that we are assessing. For this condition, we introduce another threshold of 10 %, in such a way that if two nuclei or more have over 10 % of their area in the cell mask, the cell mask is considered inaccurate. Otherwise, *i.e.* if there is one nucleus only that is inside the cell mask, the mask is accepted. Overall, we find that 30 % of the nuclei are not associated with an accurately predicted cell mask. Furthermore, the score is imbalanced between the annotated cells and the remaining cells, as the rejected fraction for nuclei that were matched with the annotated cells is much lower (14 %) than that of the remaining cells (54 %). These results imply that Cellpose can perform very well on cells that are visible by eye from brightfield but performs much worse on the remaining cells. Since we are not able, in general, to produce a complete and accurate MCF-7 cell segmentation, even with the nuclear information, we cannot train a model.

Population mixture. Annotation of the cell shape becomes even more complicated in the presence of the NK cells, as they tend to accumulate at MCF-7 monolayer edges, and cell-cell contacts, hiding the contours of the MCF-7 cells. We applied the optimized model to a brightfield image of the MCF-7 cells in the presence of NK cells. The segmentation performance degraded, Cellpose picking up many NK despite the morphological difference. Therefore, we cannot use Cellpose to identify MCF-7 cells from brightfield (and nuclei markers) reliably. The last resort would be to introduce a membrane marker for the MCF-7 cells, hoping that there is no fluorescence crossing to the NK and that all cell contacts are identifiable from this

hypothetical fluorescence channel.

4.3.3.3 Estimators

MCF-7 nuclei are poor estimators of the cell shape We can exploit the cell-nucleus mask pairing that we have performed for the partially annotated cells to test whether or not the nucleus could be used as an estimator of cell shape. As a quality control to the pairing, we can represent the distribution of d_{shift} , the distance between the center of mass of the nucleus and that of the paired cell, in figure 4.20a. We can express this quantity as relative to the semi-major axis of the cell to ensure that it does not exceed 1, which would imply a nucleus outside of its cell. Figure 4.20b shows such pairing errors do happen, though very rarely, in which case we simply filter out the pair from the subsequent analysis. On average, the nuclei are 26 ± 17 % off-center compared to the cell mask, making them good estimators of MCF-7 position. The second quality control we can perform is to test the fraction of rejected masks using the method described in the previous section. We find that 11 % of the masks do not satisfy at least one of the conditions, which is only 3 % less than the Cellpose prediction. This highlights how even our manual annotation is not perfect, despite focusing on the least ambiguous cells.

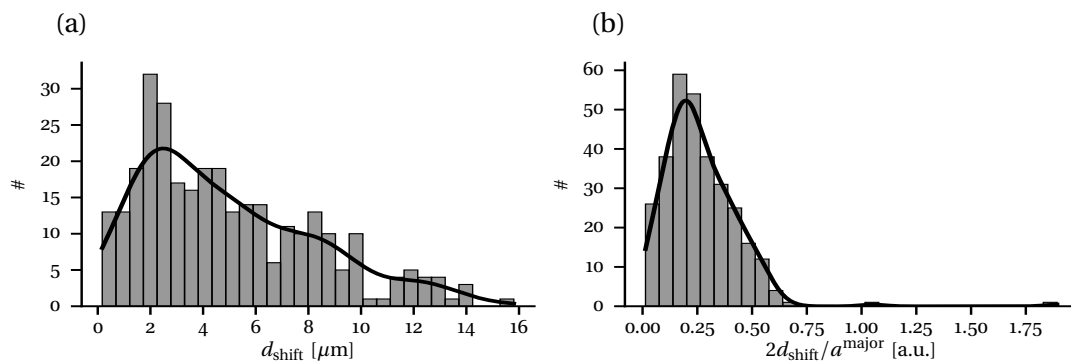


FIGURE 4.20 – MCF-7 nuclei are often off-center. a) The distribution of the relative distance d_{shift} between the center of mass of the nucleus and that of the paired cell. b) d_{shift} is expressed relative to the semi-major axis of the paired cell $\frac{1}{2}a^{\text{major}}$.

Figure 4.21 summarizes correlation results between the morphological features of the nuclei and that of the paired cells. For the most part, the nuclei are poor estimators of the MCF-7 cell morphology. The nucleus area is fairly correlated to the total area of the MCF-7 cells, with a Pearson's of 0.52. Similarly, the orientation of the nucleus is fairly correlated with that of the cell (0.38). Filtering cells based on the eccentricity of their nucleus shows that highly eccentric nuclei are more likely to be oriented like their respective cell (figure 4.21b). Such a selection drastically reduces the number of cells for which we have orientation information. c) Pushing this further, we can bin the cells simultaneously by their eccentricity and that of

their nuclei and observe an increase in orientation correlation, as shown in figure 4.21c.

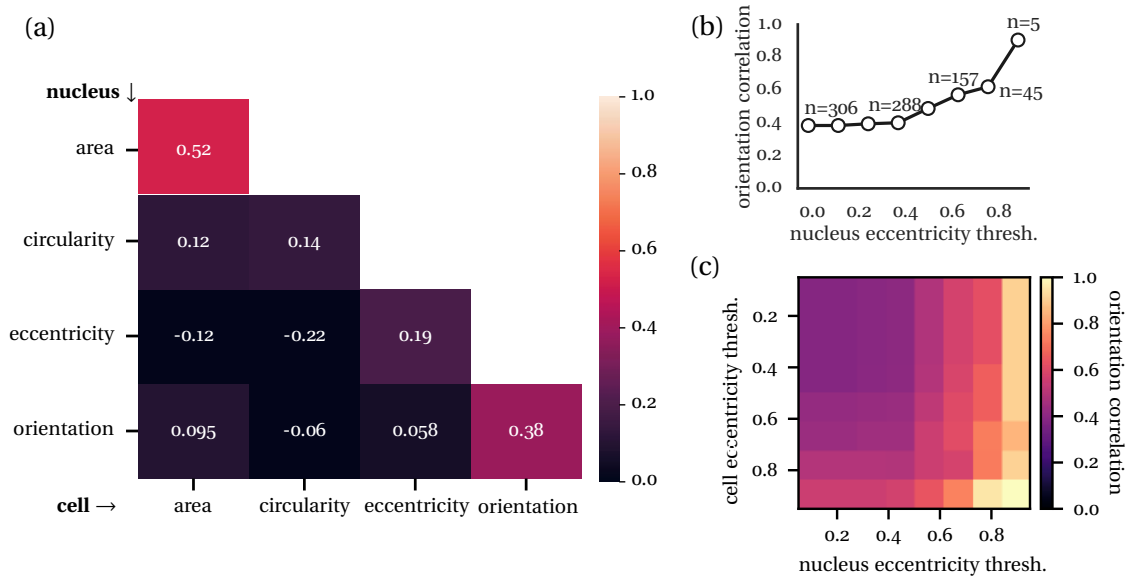


FIGURE 4.21 – Nuclei are moderate estimators of MCF-7 cell morphology. a) Nucleus morphological descriptors are correlated with the descriptors of the paired cell. The correlation score used is Pearson’s. The area of the nucleus is moderately correlated to that of the cell (0.52), and the orientation is poorly correlated to that of the cell (0.38). b) Segregating cells with more and more eccentric nuclei show a sharp increase in orientation correlation, albeit with a loss of statistics. c) Co-varying the threshold on nucleus eccentricity and cell eccentricity show similar results although eccentric cells can have non-eccentric nuclei that do not correlate well in orientation. d) Eccentricity correlation remains poor whatever the cell or nucleus’ eccentricity. Highly eccentric nuclei are usually uncorrelated with the eccentricity of the cell.

MCF-7 cells cannot be approximated by their Voronoi construct A traditional technique to infer cell shape from the nuclei coordinates is to compute a Voronoi diagram [83, 84]. We use the centroid of the previously segmented cell nuclei as input to a Delaunay tessellation. Then we reconstruct the Voronoi partitions from the Delaunay triangles. Since the MCF-7 do not always reach a density high enough to form a perfect monolayer, there are holes in the surface. Cells at the edges of the monolayers are associated with unrealistically large Voronoi partitions. We can eliminate these with an area filter at $1000 \mu\text{m}^2$. Figure 4.22a-b shows the Voronoi diagram respectively before and after the filter. The correlations between the morphological descriptors of the cells and that of the associated Voronoi partition are shown in 4.22c. The highest correlation is obtained for the area, with a Pearson’s of 0.53, similar to what was obtained with the nucleus as an estimator. The orientation correlation, on the other hand, is much poorer than before (0.16, where it was 0.38 for the nucleus estimator). As shown in figure 4.22d, no binning in eccentricity can improve this result, showing that it is not a problem of sensitivity in the orientation estimate. As

a conclusion, the MCF-7 cell shape in the ADCC assay is poorly approximated by the Voronoi partitions.

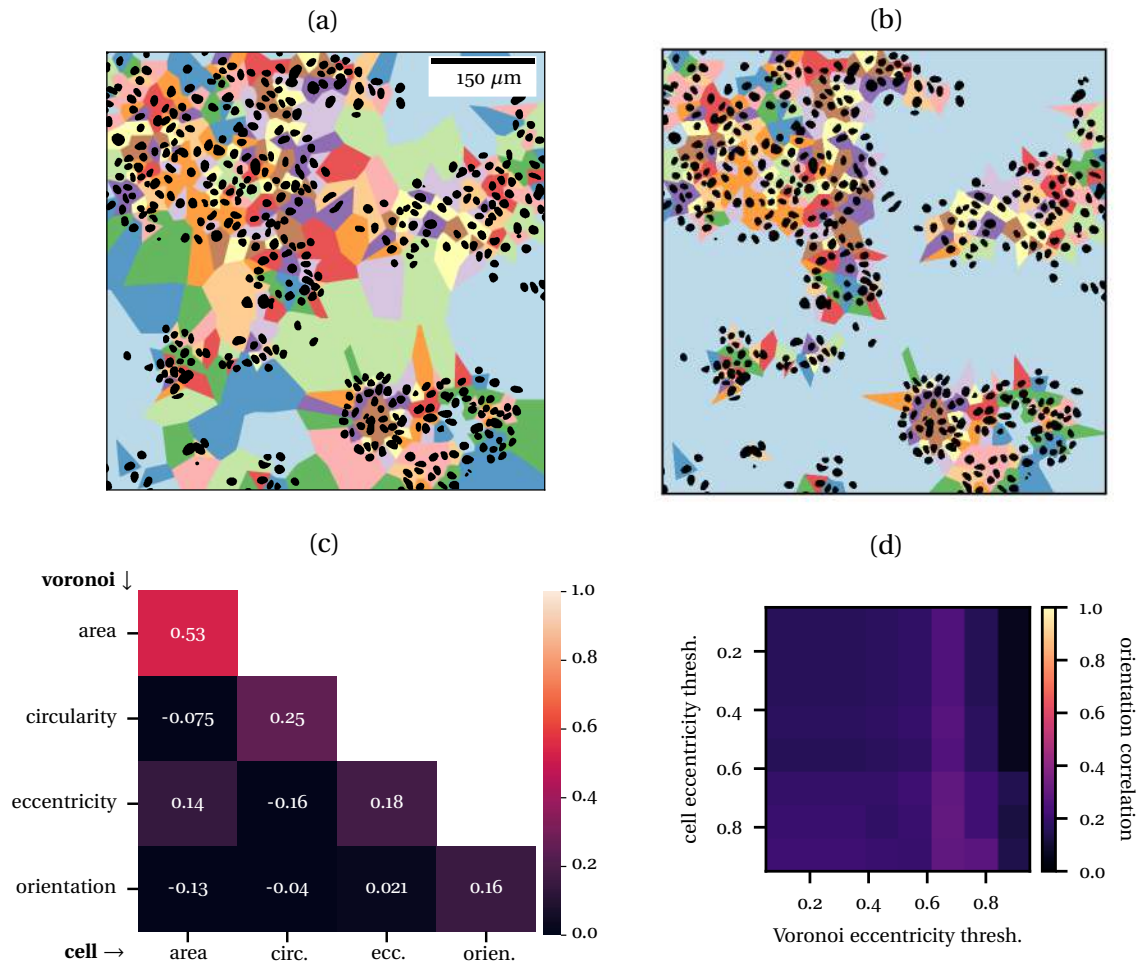


FIGURE 4.22 – Voronoi partitions are poor estimators of MCF-7 cell morphology. a) The Voronoi partitions are built from the centroids of all the cell nuclei. The nuclei masks in black are shown with their Voronoi partitions (alternating colors). b) The largest Voronoi partitions are filtered (area > 1000 μm²). c) The morphological descriptors of filtered Voronoi partitions are correlated (Pearson's) with the descriptors of the paired cell masks. d) Co-varying the threshold on Voronoi partition eccentricity and cell eccentricity does not increase the orientation correlation.

4.3.3.4 Lack of a robust estimator of MCF-7 cell shape

We lack a robust estimator of MCF-7 cell shape. Figure 4.23 shows that only the optimized Cellpose model achieves a consistently strong correlation between the predicted cell morphology and that associated with the manual annotations. This is quite unfortunate as only the nucleus and Voronoi estimators can easily be estimated for all cells at all time points, even in the presence of NK cells. We have shown that

the Cellpose model performs poorly on non-annotated cells, whereas we can expect consistent results with the other two methods. No obvious estimator for MCF-7 cell shape emerges here.

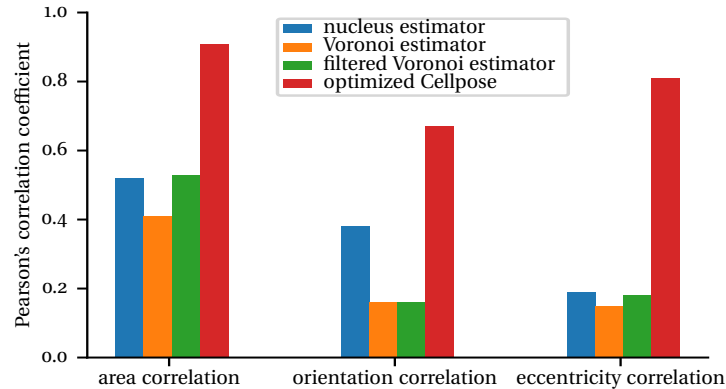


FIGURE 4.23 – Comparison of MCF-7 cell shape estimators. The correlation coefficients on morphological descriptors, between annotated cell masks and estimator predictions, are summarized side by side for four estimators.

4.3.4 Cell morphologies : primary NK

4.3.4.1 Manual annotations and observations

Method. Since we have annotated NK cells to train segmentation models, we can exploit these annotations to measure NK cell morphology as we did for the MCF-7 cells.

Observations. The NK cells exhibit a quite reproducible morphology. A visual inspection of the PCA decomposition in figure 4.24 does not yield obvious morphological differences. Some cells can be larger and more polarized than others but overall these variations are much smaller than the size of the MCF-7 cells. A mean area ratio between the NK and MCF-7 cells shows that NK cover on average less than 10 % of the area occupied by MCF-7 cells. The standard deviation of NK area represents only a 20 % fluctuation around the mean, unlike that of MCF-7 cells that reach over 40 %. We observed a mean NK cell area of $45 \pm 11 \mu\text{m}^2$. As can be seen in the histogram for the circularity in figure 4.24, two populations emerge between the perfectly circular NK and the others. We can interpret the less-circular population as being polarized or engaged in cell-cell contact. Eccentricity averages at 0.48 ± 0.17 . The cell size can be described by the major and minor axes that average respectively to $8.4 \pm 1.7 \mu\text{m}$ and $6.95 \pm 0.89 \mu\text{m}$, compatible with the 6 – 7 μm diameter from [44].

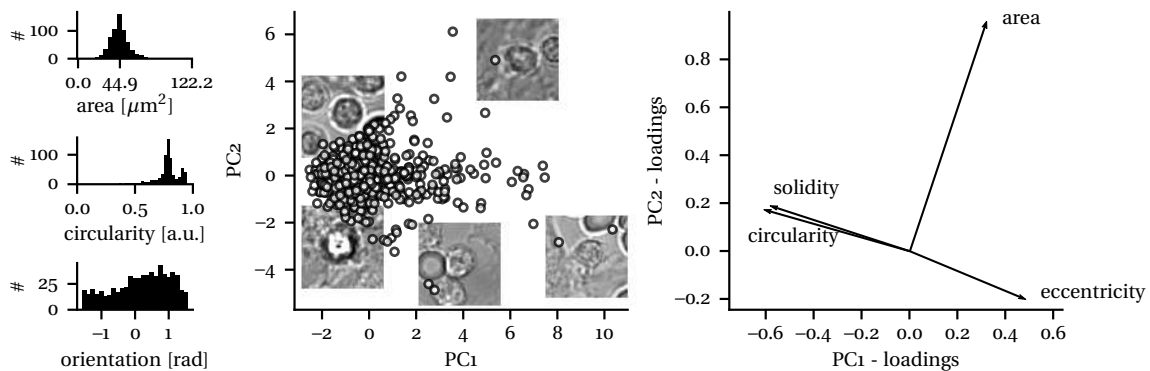


FIGURE 4.24 – NK cell morphology. a) Histograms of the NK cell area, circularity, and orientation estimated from manual annotation on CFSE and brightfield. b) PCA construct (two components) of morphological features of the NK cells. Each feature was independently standardized. c) Loading plot showing the weights of each morphological feature selected in the PCA.

4.3.5 neighborhood

Now that we have established the shape of MCF-7 and primary NK cells independently, we can investigate the spatial co-distribution of these cells to develop the best neighborhood estimate for this system.

4.3.5.1 Exact neighborhood

Method To characterize the exact NK neighborhood of MCF-7 cells, at least once to have a ground truth to refer to, we propagated our NK-less partial annotation of the MCF-7 cells to the first image captured after the NK introduction. Performing a quality control on the MCF-7 segmentation, we noticed that the cells moved slightly during that time interval. Once again, we took the time to correct in napari through Celldetective all obvious segmentation errors, to have the most accurate MCF-7 segmentation in the presence of NK. To quantify the exact neighborhood of the MCF-7 cells, we projected a segmentation of all the NK cells using one of our custom and specific StarDist models (brightfield + Hoechst). Then we could count the number of NK cells overlapping with each available MCF-7 cell mask.

NKs like to be at the MCF-7 edges We observed that NK had a tendency to stand at MCF-7 edges. To quantify this observation, we decided to dilate the masks of the MCF-7 by a circular (25×25) pixel kernel ($7.8 \times 7.8 \mu\text{m}$). This operation added an edge region to the MCF-7 mask with a thickness of about $3.7 \mu\text{m}$, which is around half the size of a NK cell. By projecting the center of mass of the segmented NK, we could count 1) the number of NK hovering above each MCF-7 cell n_{above} and 2) the number of NK at the edge n_{edge} . Some sampled neighborhoods are shown in figure 4.25. We observed that, on average, 68 % of the NK neighbors to a MCF-7 cell stand at the edge, which is a spatial over-representation considering that the edge area is much smaller than that of the inside of the cell. If we estimate the area

ratio between the edge region and the inside for each cell, we can set a counting weight to overweight NK at the edge proportionally. We normalize the weights to one. This process yields a mean weight for the cells at the edge of 0.69 and 0.31 for the cells inside. We multiply the number of neighbor cells in both cases by their associated weight per cell and sum up across all cells. We find that once we correct for area imbalance the NK cell has an 81 % chance to go to the edge. Therefore, our neighborhood estimate cannot be too conservative as we might miss most of the NK neighbors if we do not account for the edge region.

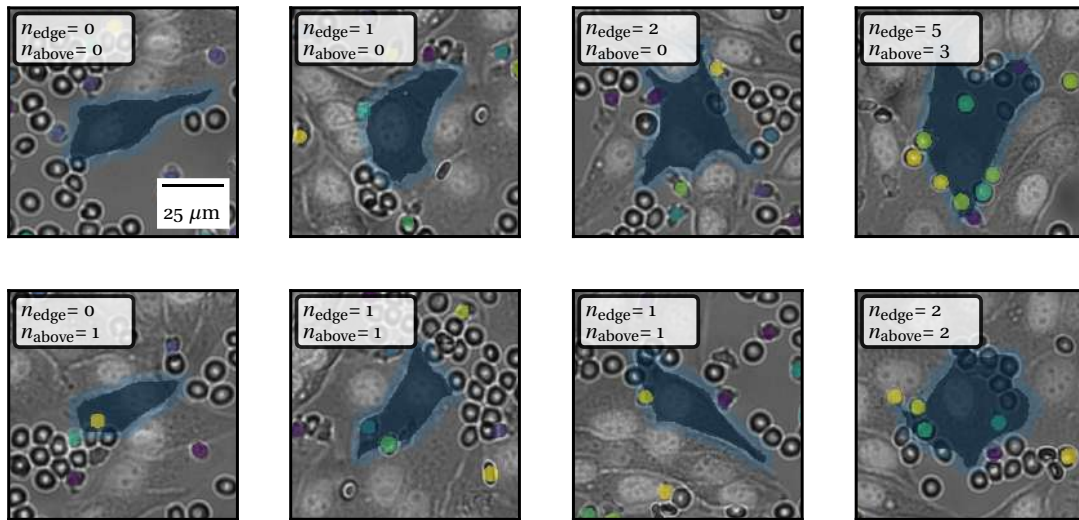


FIGURE 4.25 – Neighborhood from manual annotations for MCF-7 cells. Semi-transparent masks of sampled MCF-7 cells and NK in close vicinity, on brightfield images. The MCF-7 cell mask (prussian blue region) is dilated (light blue region) to measure NK cell presence at the edges. For each target, the number of NK at the edges and directly on top of each MCF-7 cell is reported.

Effects of cellular density The partial annotation does not allow us to estimate directly cell density and relate it to the cell area. We can use the available nucleus segmentation to estimate cellular density for all of the annotated cells. We compute the neighborhood of the nuclei with themselves, in a radius of 31 μm . We count the number of nuclei in each neighborhood defined as such. We do not count a nucleus as being neighbor to itself, therefore the counts start at zero. The idea behind this approach is that since we can quite easily and accurately estimate cell density from the nuclei, this information could be used to guess the MCF-7 area. Figure 4.26a shows that there is indeed a slight decrease in MCF-7 area at higher densities but it is negligible compared to the area dispersion. The mean area of the MCF-7 was estimated at $500 \pm 217 \mu\text{m}^2$ in the previous sections. Here, the variation in the mean area is of the order of $250 \mu\text{m}^2$ from the lowest to the highest density which is slightly more than the overall standard deviation in areas (on the figure, only the median values are shown). Similarly, we can exploit the “exact” neighborhood to

relate the number of observed NK cells to the target density. We observe a slight anti-correlation between the number of NK neighbors and the target density, which may depend on the E : T ratio (here 2.5). The amount of target cells for which we could estimate the neighborhood using this technique is only 250 cells, from a single position. A more thorough study is needed to assess the effects of antibodies, E : T ratio, and other biological conditions on cell spatial co-distributions. Still, we conclude from these observations that MCF-7 cell density, as determined from nuclei location, is not a strong determinant of MCF-7 cell area and cannot be used as an estimator.

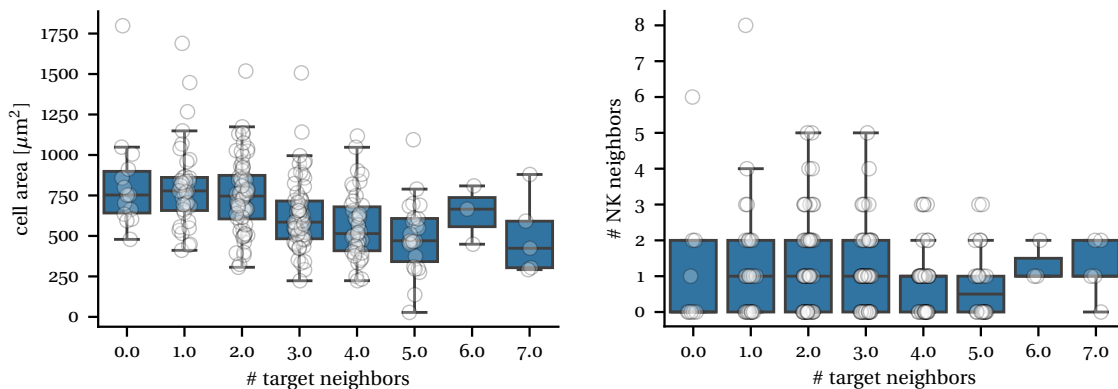


FIGURE 4.26 – MCF-7 density and neighborhood. The area of annotated MCF-7 cells is related to the MCF-7 cell density (using the number of MCF-7 nuclei in a $31 \mu\text{m}$ neighborhood as a proxy). The number of NK overlapping with the MCF-7 cell masks (with the edge region) is related to the same density estimator.

4.3.5.2 Isotropic neighborhood

The most robust estimate we can make for the neighborhood of the MCF-7 cells is to build a circular, isotropic, region around the center of mass of the nucleus at each time point. The only degree of freedom is the radius of that circle that has to be tuned. We can perform an optimization scheme to find the radius that yields the best match with our “ground-truth” neighborhood described in the previous section. There are two scales over which we can tune this radius :

- at the single-cell scale we can find the radius that minimizes the difference in neighbor count for each MCF-7 cell. Similarly, we can find the radius that minimizes the difference in NK neighbor attribution : NK i has to be in the neighborhood of target j , with no compensation between targets.
- at the cell population scale, we can find the radius that minimizes the difference in the total number of NK neighbors around the target population considered, with compensation between target cells. Symmetrically, we can impose an attribution condition at the population scale to ensure that the same NK are found in the ground truth and predicted neighborhood.

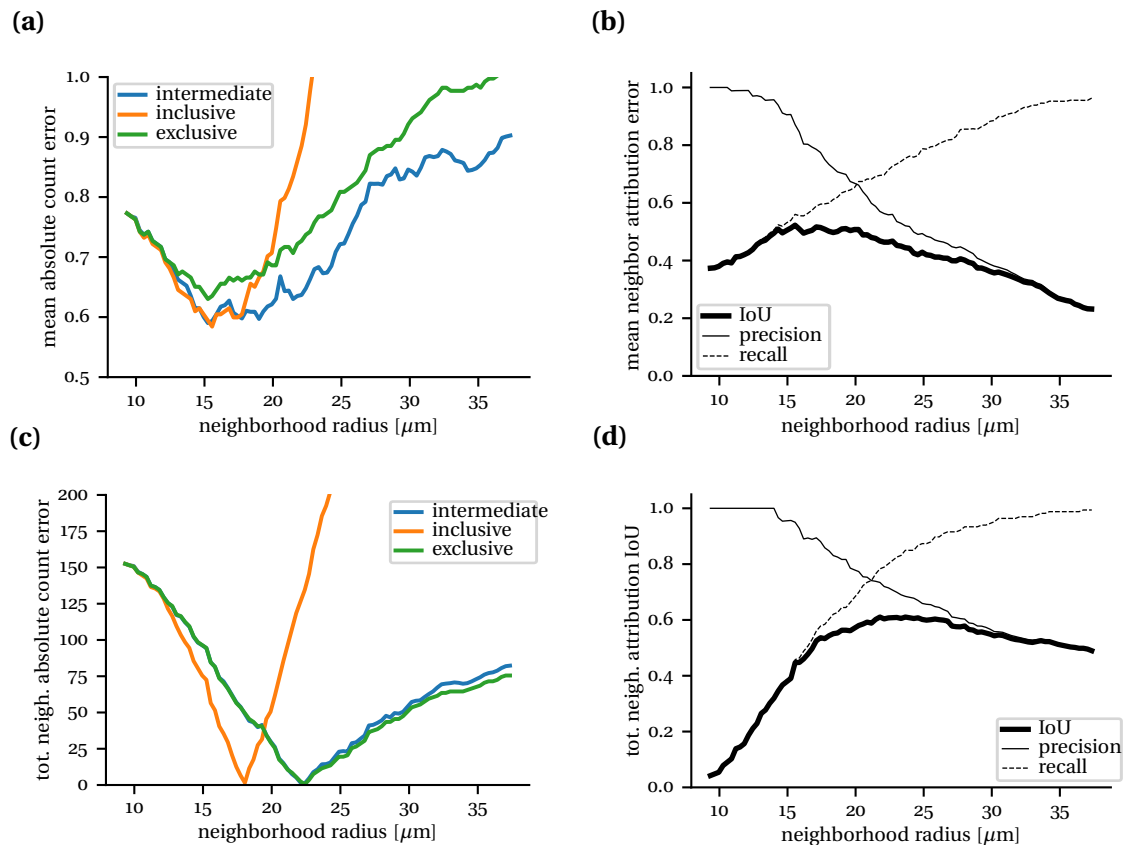


FIGURE 4.27 – Isotropic neighborhood optimization. a) the mean across all annotated MCF-7 cells of the difference in neighbor counts between the isotropic neighborhood prediction and the “exact” neighborhood, using three different counting methods for the isotropic neighborhood. b) the mean across all annotated MCF-7 cells of the neighbor attribution IoU. c) the absolute value of the difference in neighbor count for the whole population of MCF-7 cells using the three counting methods. d) the overall neighbor attribution IoU for the population of MCF-7 cells.

The optimal result must balance all of these considerations. To perform these measurements, we start from the location of the MCF-7 cell nuclei on one hand and of the NK cells on the other hand. We set a neighborhood radius and look at the NK neighbors for the subset of MCF-7 nuclei that were paired to a cell mask in the previous section (and for which we estimated an “exact” neighborhood).

For the single-cell scale tuning, we compare the number of NK neighbors using either the intermediate, inclusive, or exclusive counting method (described in chapter 3.3.8) to the “exact” number of NK neighbors, n_{true} . In the “exact” count, we arbitrarily set a weight of 0.5 to all NK standing at the edges, to introduce a notion of attention weight even though it cannot be computed from the partial annotation. For each MCF-7 cell, we compute the absolute difference in counts between the three methods and n_{true} . Then we average this counting error across all cells and repeat the process for the next neighborhood radius. The resulting profiles are shown

in figure 4.27a. This result suggests, as expected, that the exclusive method is the one that makes the largest counting error per neighborhood. Both the intermediate and inclusive counting method reach the same average error of 0.6 with slightly different neighborhood radius ranges. The error explodes using the inclusive counting method at around $17\ \mu\text{m}$ whereas the intermediate method remains quite stable, increasing only slightly until $22\ \mu\text{m}$. For the attribution problem, the scheme is similar, but instead, we compare directly the identities of the NK neighbors in the “exact” neighborhood and the one defined by the circle. To compute an attribution error per cell we use an IoU formulation, defining true positives as matching NK cells in the two neighborhood sets, false positives as cells in the isotropic neighborhood but not in the exact one and false negatives as missing cells in the isotropic prediction. To disentangle the IoU, we also compute the precision and recall scores. In the special configuration where there should be no neighbor and none are predicted, the IoU is set to one. Thus, we obtain a set of scores per cell, that we can average across all cells and redo the process for each neighborhood radius, yielding the plot of figure 4.27b. The average attribution IoU reaches a maximum of around 0.5, for a neighborhood radius between 14 and $20\ \mu\text{m}$. To capture all “exact” neighbors in the isotropic neighborhood, the radius must be larger than $32\ \mu\text{m}$ (recall > 0.95), but this is at the cost of many false positives and therefore a degraded precision and IoU.

For the population scale tuning, we can reiterate the same processes with the subtlety that instead of averaging counting and attribution errors across single cells, we compute one score for the whole population of annotated MCF-7 cells at each radius. Figure 4.27c shows that the inclusive counting method starts over counting neighbors at around $18\ \mu\text{m}$, whereas this happens at around $22\ \mu\text{m}$ for both the intermediate and exclusive methods. The attribution IoU is also maximal at this radius, reaching 0.61 and remaining stable until around $25\ \mu\text{m}$ in neighborhood size. To balance all of these scores and have a single value for the ADCC assay, the neighborhood radius is set to $20\ \mu\text{m}$ in the following sections, which almost coincides with the average minor axis of the MCF-7 cells. Unless mentioned otherwise, we will use the intermediate counting method to count the NK neighbors, as it is as accurate as the inclusive method per cell, does not overcount the number of neighbors in a population, and is overall more stable (*i.e.* the error increases more slowly) than the inclusive method.

4.3.6 Target-centric survival analysis

4.3.6.1 Survival function and lysis rate

Once the death events for the target cells have been characterized using the time of first PI entry as the criterion, t_{\dagger} (defined in section 4.3.2.1), we can set $T = 0$ min as the reference time and build survival functions for the MCF-7 cells. The few cells already dead at the beginning of the movie are ignored, and cells “born” after the initial frame through mitosis have already been filtered out at the tracking post-processing step.

In practice, we can group the target cells spatially by well or position, yielding respectively a survival function “pooled” over the well or a sub-sampled per-position survival. Later, we will explore more sophisticated cell binning. For now, we can define an over-simplistic model for the survival function as :

$$\frac{dT}{dt} = -kT \quad (4.9)$$

where $T(t')$ is the fraction of target cells still alive at time $t \leq t'$ and k a lysis rate term, assumed constant, that is a function of control parameters such as the E : T ratio of the experiment, the antibody concentration, the donor, and other parameters. If not mentioned otherwise, the E : T ratio is set to 2.5. Integrating on both sides yields the following solution :

$$T(t) = e^{-kt} \quad (4.10)$$

where we enforced that $T(0) = 1$. Figure 4.28 shows some experimental survival functions, represented in semi-log to quickly assess how well the exponential model applies. In this instance, real survival functions deviate in several ways from the model, the fit of which only captures the average initial slope of the survival. Two of the most recurring discrepancies with the model were 1) a delay for the beginning of the lysis response and 2) a slowdown if not complete halt of the response after some time that varied from experiment to experiment. A hypothesis for the apparent killing slowdown was that NK cells died over time. We checked extensively that this was not the case, from the PI level of the NK cells, ruling out this hypothesis. We will revisit this point in section 4.3.7.4.

In this section, we focus only on capturing the average initial lysis response, modeled approximately by equation 4.10, to have a first estimate of the effect of antibody conditions on ADCC.

4.3.6.2 First biological observations

Determining the optimal antibody quantity We have used the ADCC assays to investigate the optimal amount of a bsAb needed to trigger a strong ADCC response. This effect was measured for different donors independently so that donor variability could not interfere with the results. Experimentally, bsAbs were introduced at

increasing concentration across the wells. We have thus characterized two bsAbs (CE4-21 and CE4-28). The results presented throughout this section are extracted from a series of experiments performed by Beatriz Díaz-Bello. Figure 4.28 shows the survival response as a function of CE4-28 bsAb concentration for a single donor. We observe a small response in the absence of an antibody, highlighting the spontaneous lytic activity of the NK cells from this donor on MCF-7 cells. The lysis rate takes off between 1 pM and 100 pM of CE4-28 bsAb. Here, the maximum tested concentration was not high enough to show a saturation of the lysis.

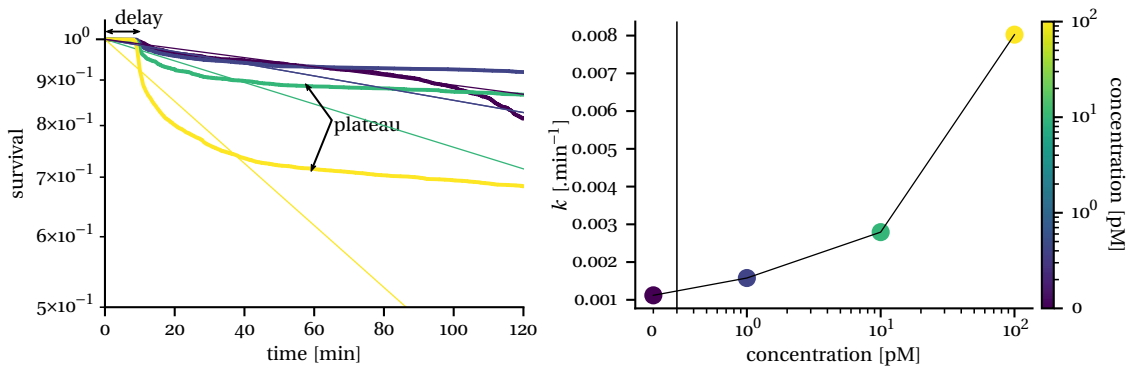


FIGURE 4.28 – CE4-28 antibody-concentration dependence assessment within a single ADCC assay. a) pooled survival functions associated with four conditions in which the concentration of CE4-28 bsAb is increased in magnitude from 0 to 100 pM. The cell populations are MCF-7 wild type & primary NK cells. The straight lines show the fit of the survival values over the first hour with the model 4.10. b) Lysis rate k as a function of CE4-28 antibody concentration.

Effect of over-expressing HER2 Simultaneously to the antibody-concentration effect, we tested the effect of HER2 overexpression on the surface of MCF-7 cells on ADCC. Figure 4.28 is revisited in figure 4.29 to show the distinct response for the MCF-7 WT on the one hand and the MCF-7 HER2+ cells on the other hand. In most instances, we observed a stronger lytic response on HER2+ cells for antibody concentrations higher than 1 pM.

High donor variability Figure 4.30 summarizes lysis rate estimates across several donors, highlighting a high donor variability. An average increase in the lysis rate with CE4-28 bsAb concentration was observed in most cases. The magnitude of the response was very donor-dependent. The baseline activity of the NK, in the absence of antibodies, was extremely heterogeneous across donors.

As illustrated in figure 4.31, the lysis response was usually observed to be stronger on HER2+ MCF-7 cells than WT, but donor variability and most notably baseline NK activity blurs the effect. Depending on how the baseline NK activity is taken into account, results have more or less statistical significance.

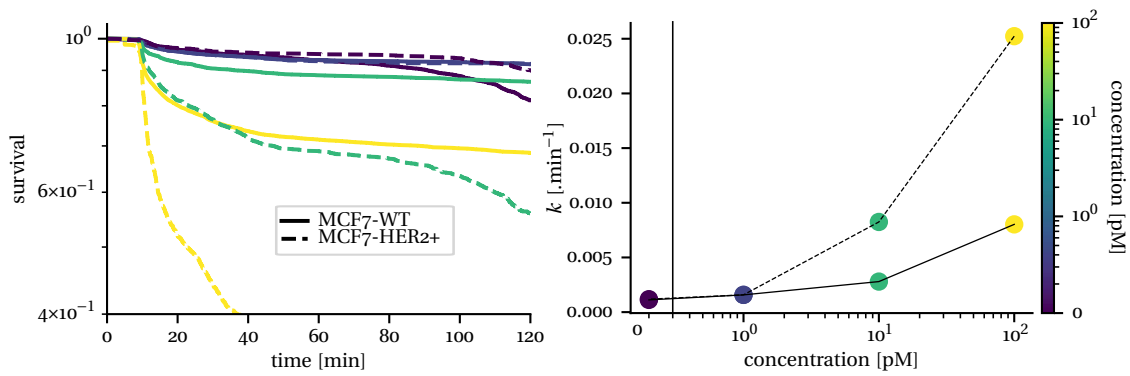


FIGURE 4.29 – CE4-28 antibody-concentration dependence for two MCF-7 cell populations. a) pooled survival functions associated to the four CE4-28 antibody-concentration conditions for MCF-7-WT (full line) and MCF-7-HER2+ (dotted line). b) Lysis rate k as a function of CE4-28 antibody concentration for both target cell populations.

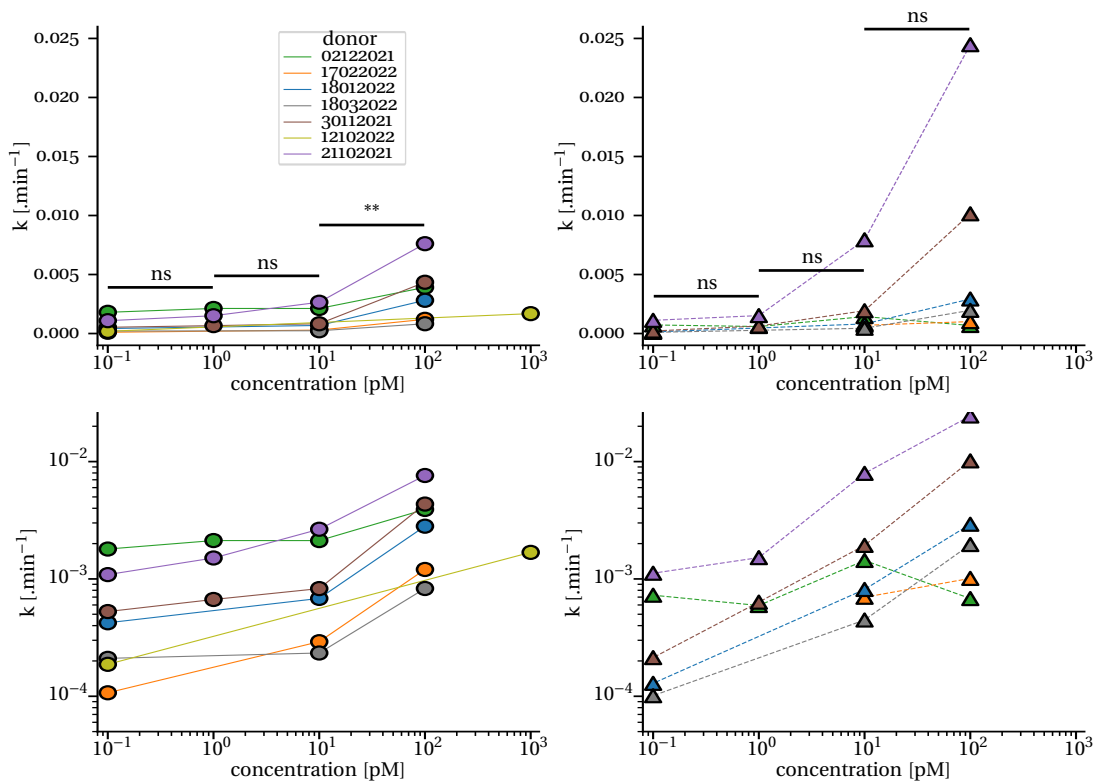


FIGURE 4.30 – CE4-28 antibody-concentration assessments show high variability across donors. Lysis rates k at increasing CE4-28 antibody concentrations for different donors following equation 4.10. The response for MCF-7-WT (left) and MCF-7-HER2+ (right) is shown in linear (top) and log scale (bottom) as a function of the antibody concentration (log-scale). Statistical test for the difference of the mean of the lysis rates across donors at consecutive concentrations was assessed using a relative t-test.

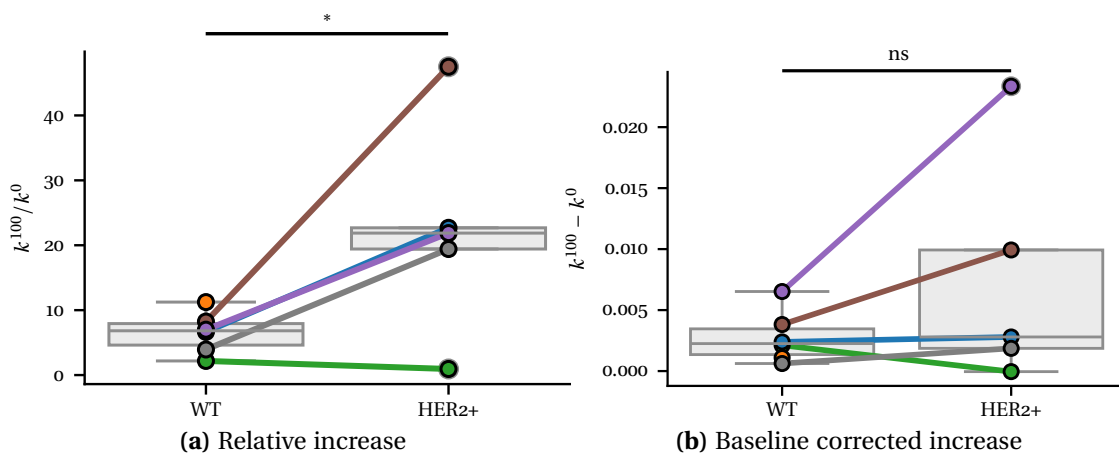


FIGURE 4.31 – Lysis is measured stronger on HER2+ cells. Categorical plot comparing the corrected lysis rate associated with MCF-7 HER2+ cells and WT cells with 100 pM of CE4-28 bsAb. The lysis rate is either expressed relative to the baseline rate, in the absence of bsAb (k^0), or corrected by subtraction with k^0 . Statistical test for the difference of the mean of the normalized lysis rates across donors was assessed using a relative t-test.

4.3.6.3 Comparison with RTCA

Microscopy and RTCA ADCC experiments have been performed in parallel using the same donor cells to compare the antibody response measured by both techniques. The RTCA measurement surface exceeds that of the microscopy technique, which is why RTCA can be expected to be less sensitive to sampling bias than microscopy. On the other hand, variation of impedance is arguably a response less specific to ADCC than a direct count of the number of killed cells, as achieved in microscopy. Figure 4.32 shows side-by-side responses from both techniques on cells from the same donor. For RTCA, we represent the NCI relative to the proliferation signal $NCI^{\bar{P}}(t)$, whereas for microscopy we represent the survival function $S(t)$, that excludes cells born after the beginning of the observation. First, the RTCA response can be quite different between WT and HER2+ MCF-7 cells, particularly for intermediate antibody concentrations. The same observation can be made in microscopy. Second, there is a perfect ranking agreement between the two techniques : more CE4-28 antibody leads to a stronger response. On the other hand, the strongest RTCA response (17022022 donor, MCF-7-WT) turns out to be associated with one of the lowest killings, as assessed in microscopy, which either suggests a strong difference in killing between the two approaches or, more likely, a problem of interpretation and normalization of RTCA measurements. The plateau effect often observed in microscopy survival functions was never observed over the same timescale in the RTCA measurements.

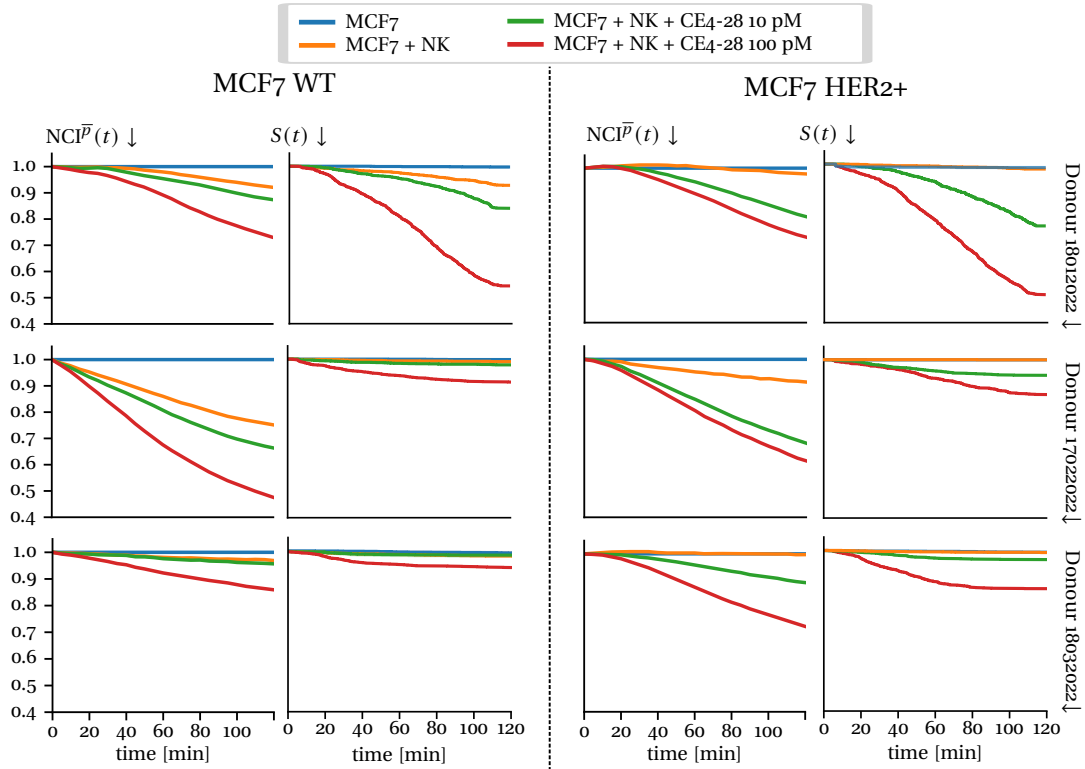


FIGURE 4.32 – RTCA measurements correlate well with MCF-7 survival from microscopy images. RTCA and microscopy measurements were performed by Beatriz Díaz-Bello in parallel using cells from the same donor. The NCI^p signal is shifted to the normalization time and shown for two hours. The survival signal extracted from the microscopy data is represented in the same time window on the right side of the RTCA curves. The comparisons are grouped by cell type (the two columns : MCF-7-WT and MCF-7-HER2+) and donor (rows). The condition ranking is perfectly conserved using both techniques, although the amplitude of the response can vary considerably from RTCA to survival.

4.3.6.4 Inter-position variability

Pooling the cells from many positions to estimate the survival function for an ADCC condition usually guarantees a large number of points (> 1000 cells). We end up with an average reading of the survival for the condition that masks any inter-position dispersion. One could argue that if we build a survival function for a position, then its 95 % confidence interval should at least contain the pooled survival function which, we assume, converges to the global survival response of the well. In other words, we are sampling from a global response and would like the confidence interval to reflect that. Figure 4.33 shows that as soon as we start building per-position survival functions, there is often at least one survival function for which the confidence interval never intersects with that of the pooled survival function. We hypothesized that this could be due to actual heterogeneity on the sample in its “control parameters” such as the E : T ratio or, less likely, the amount of antibody, and that therefore, we were not pooling strictly comparable data.

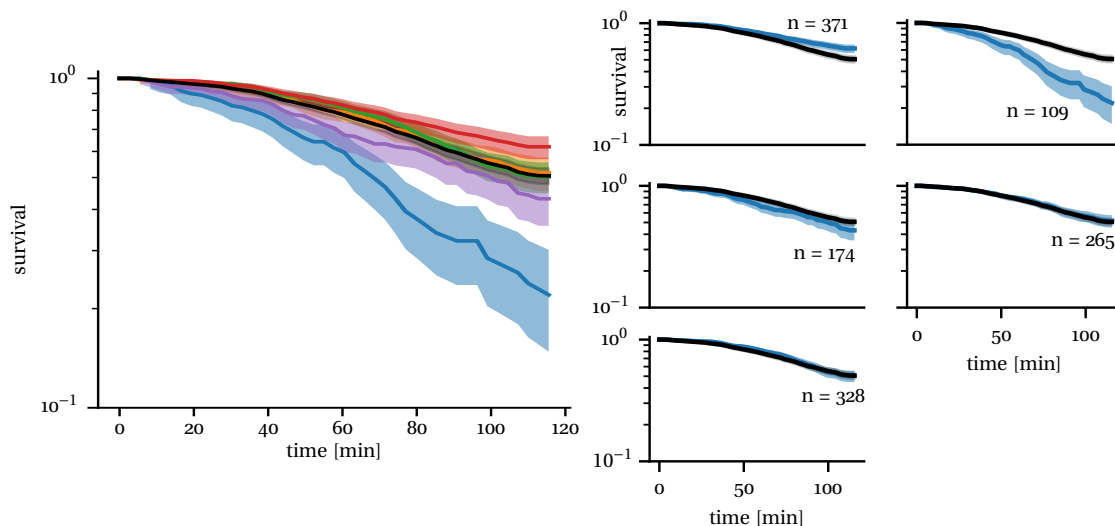


FIGURE 4.33 – Spatial sub-sampling of the survival response shows high heterogeneities that cannot be explained by statistics alone. Survival function estimated for each observed position of a single well with MCF-7-HER2+ cells, primary NK cells, and 100 pM of CE4-28 antibody. The survival function for the pool of all positions is shown in black. The survival function of each position matches more or less with that of the pool of all positions, except one position that never overlaps with the 95 % interval confidence of the pool survival.

Therefore, we would like to investigate how cells are organized locally, in their cell-cell contacts, and how this may affect survival chances at population scale.

4.3.7 Target-effector interactions

4.3.7.1 Survival depends on local NK concentration

Performing ADCC under the microscope allows us to know quite precisely how the NK cells are spatially distributed at each time point. Using CellDetective's neighborhood scheme, with a radius of $20\ \mu\text{m}$ (following the results of section 4.3.5.2), we could estimate the number of NK that actually visited each target. We used the intermediate counting method, and unless mentioned otherwise, the number of NK neighbors per target cell refers to the average number of NK neighbors experienced by a MCF-7 cell per frame until death (or until the end of the movie if it survives). Similarly, we computed a larger neighborhood of $31\ \mu\text{m}$ between MCF-7 nuclei to estimate the local target density (inclusive counting method, average until death).

To test the effect of the number of NK cells on MCF-7 survival, Lorna Ammer performed an experiment in which the E : T ratio was varied systematically across wells. The survival response was compared with and without CE4-21 bsAb at $1\ \text{nM}$. Figure 4.34 shows that the killing was much stronger in the antibody condition, with a pronounced divergence from the control occurring between E : T = 1 and E : T = 5. The lysis rate increased as a function of E : T and seemed to saturate in the antibody condition.

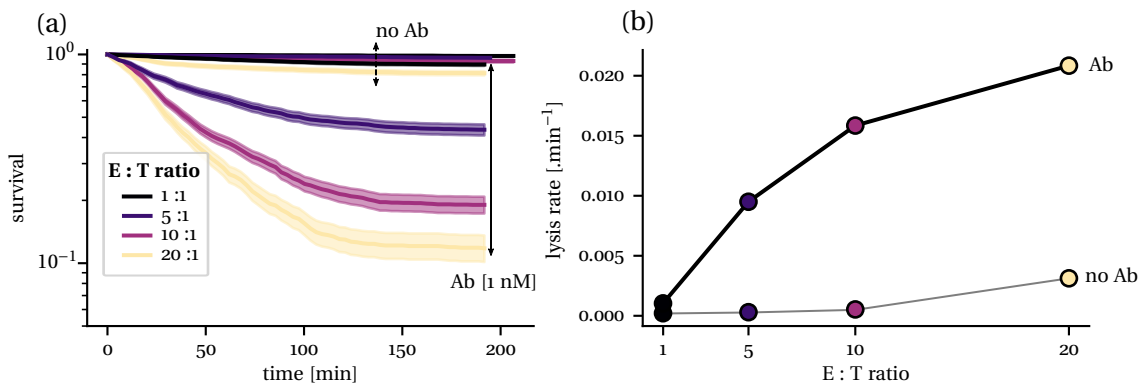


FIGURE 4.34 – Survival vs E:T. a) The survival response in the presence or absence of CE4-21 antibody ($1\ \text{nM}$) is plotted for different E:T ratios. The survival function is fit over the first 45 min to avoid the plateau effect following equation 4.10 to estimate the lysis rate k , plotted in b).

We decided to relate the E : T to the number of NK neighbors around each MCF-7 cell. We observed that the E : T is not linearly related to the observed number of NK neighbors around each target cell, as highlighted in figure 4.35. The distribution of NK neighbor counts spreads towards higher values as the E : T increases, in a skewed manner, with a mode remaining stable at a low NK count value. To explain this divergence between the E : T and the number of NK neighbors we went back to the images and noticed that a lot of NK cells tended to accumulate in regions void of MCF-7 cells. A lot of NK cells struggled to hop onto the MCF-7 monolayers, leaving them out of neighborhood counts. Therefore, using the E : T as a proxy for

the local number of NK cells around each target is likely to overestimate the local number of NK. The only exception would occur if the MCF-7 cells form a perfect monolayer on the whole surface, which did not occur in our experiments.

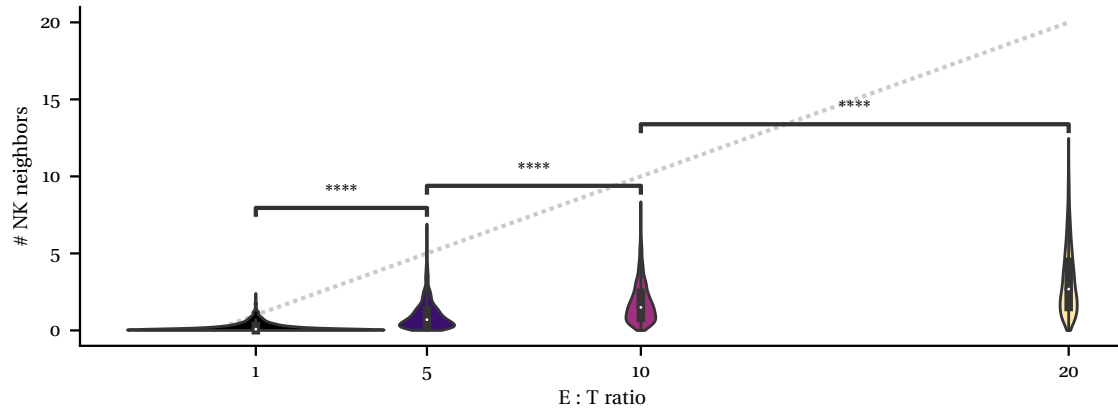


FIGURE 4.35 – E : T ratio decorrelates with NK neighbors. The distribution of observed NK neighbor counts is plotted at each E : T ratio. Each violin has the same area. The gray dotted line represents the identity function. Statistical difference between consecutive distributions of NK neighbors was assessed using the two-sample KS test.

We decided to segregate the MCF-7 cells based on the estimated number of NK neighbors. We grouped cells that shared a similar average number of NK neighbors, in bins of size 0.5, from all wells at different ratios, conserving the antibody condition. In each bin, we could determine a survival function. Figure 4.36 shows that MCF-7 survival decreases sharply with the number of NK neighbors. The effect is much stronger in the presence of antibodies. The associated lysis rates seem to increase almost linearly with the number of NK neighbors. Pearson's correlation coefficient reaches 0.97 if we limit the fit to numbers of NK neighbors up to 4 in the antibody condition. We could not reach saturation while conserving good statistics.

This almost linear relationship between the number of NK neighbors and the lysis rate was measured many times in our ADCC experiment, usually at a lower E : T = 2.5. We could never explore average NK neighbor counts much higher than 2 due to the lower E : T. We hypothesize that this apparent linearity could be due to the existence of a low fraction of NK that can actually kill, in which case having more NK neighbors increases the probability of having at least one such “active” cell.

4.3.7.2 Survival depends on target density

We observed that there was usually more and faster cell death at low MCF-7 cell density. As a result, we tested the effect of cellular density on survival. First, we reiterated the same binning process as with the NK neighbors, this time defining bins of 1 in number of target neighbors. Figure 4.37a shows how, for the most part, target cell survival tends to increase at higher cell densities. This dependence seems weaker than the one obtained for the number of NK neighbors, suggesting that

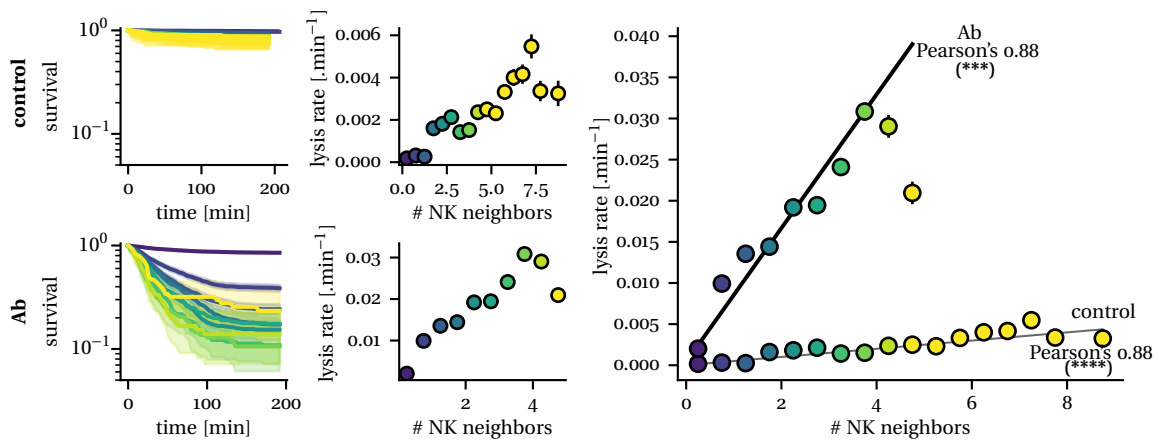


FIGURE 4.36 – Survival decreases with the number of NK neighbors. MCF-7 cells are binned by their number of NK neighbors. For each bin, if there are more than 30 MCF-7 cells, a survival function is evaluated and fitted over the first 45 minutes to avoid the plateau effect with equation 4.10. The resulting lysis rate k is compared directly with and without antibodies (CE4-21 bsAb at 1 nM). The Pearson's correlation coefficient is computed and evaluates to 0.88 for both conditions with a significant p-value.

the number of NK neighbors may not be much correlated to the target density. Avoiding all the binning approaches, we could fit a Cox model on the survival data, showing that increasing the number of target neighbors by one unit seems to have a protective effect comparable to the risk increase due to adding one NK in the neighborhood.

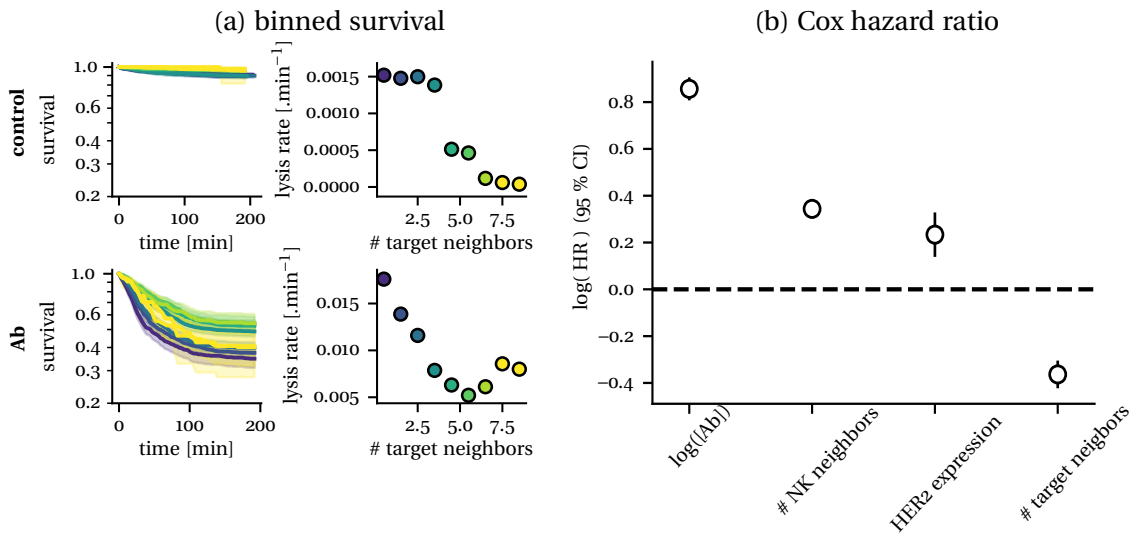


FIGURE 4.37 – Survival increases with target density. a) MCF-7 cells are binned by their number of target neighbors. For each bin, if there are more than 30 MCF-7 cells, a survival function is evaluated and fitted over the first 45 minutes to avoid the plateau effect with equation 4.10. The lysis rate, fitted with equation 4.10 is shown for each antibody condition as a function of the number of target neighbors. b) The Cox model is fitted on a set of covariates following equation 4.5, to extract the hazard ratios, measuring the risk induced by increasing a covariate by one unit. The log of the antibody concentration is used instead of the actual concentration to show the effect of increasing the concentration by a magnitude. The HER2 expression is binarized (0 for WT and 1 for HER2+ MCF-7 cells).

If the number of NK neighbors and the number of target neighbors are correlated, even in a non-linear way, then we are not separating properly each variable's contribution to the survival. Cox analysis does it to some extent, using a simplistic model for the effect of each covariate. Therefore, we represented the relationship between the number of NK neighbors and the target cell density in figure 4.38. As expected, there is a non-linear relationship, as well as a large dispersion. The number of NK neighbors does not vary, on average, when the target nuclei count exceeds 6 in the neighborhood. Below 6, and as target density decreases, the average number of NK neighbors increases.

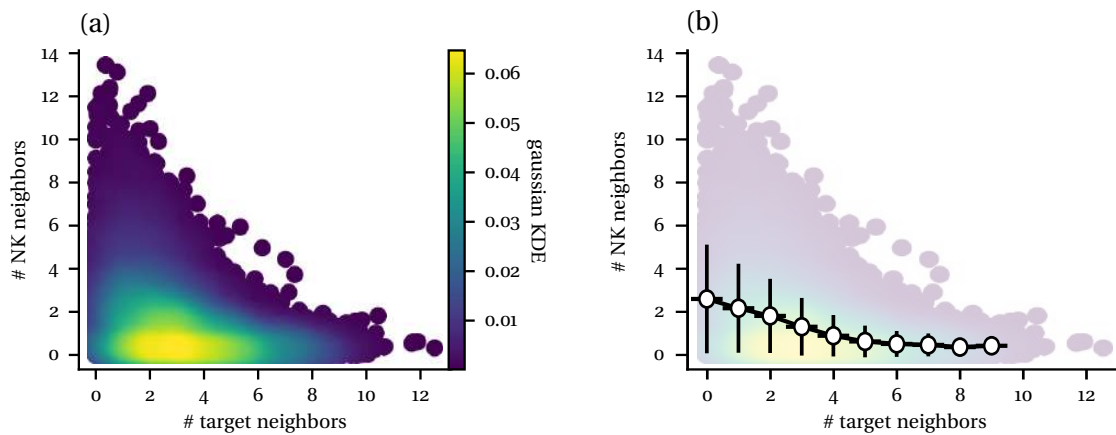


FIGURE 4.38 – Joint distribution of neighbors. a) The density of the scatter plot is estimated using a Gaussian kernel. b) Binning in target density shows that the number of NK neighbors is related non-linearly to the target density, at a very high dispersion level.

4.3.7.3 Survival : co-dependence of NK neighbors and target density

To decorrelate the effect of NK presence and the effect of the target density on MCF-7 survival, we performed a double binning on both of these quantities to establish a lysis map for each condition. Figure 4.39 shows the obtained maps for both conditions, as established on the NK ratio experiment. This kind of result could be produced for various experiments, exploiting the naturally occurring joint distribution of neighbors to explore the phase space, with lower statistics in general. The trend shows an effect of both variables on lysis, as expected, with a large region of the phase space that is not explored (*e.g.* there are never many NK neighbors at high target densities). Increasing the number of NK neighbors seems to increase the lysis rate on average, whereas increasing the number of target neighbors decreases the lysis rate on average. This protective effect was also measured by the Cox model. The effect is visible at high concentrations of antibodies but not so much in the absence of bsAb.

We wanted to know if the variation in lysis rate induced by introducing one more NK neighbor is stronger or not, on average, than increasing the target density by one unit. To do this assessment, we proposed to fix the number of target neighbors, *i.e.* select a column, and perform a linear fit to extract the slope. The slope can be defined as the variation of lysis rate over the variation of NK neighbor counts in the column : $\Delta k / \Delta \#NK$ at a fixed target density. Repeating the process for each column, we can collect many lysis rate variations per NK neighbor, always at a fixed number of target cell neighbors. Then we reiterate a similar process but this time row by row : we fix the number of NK neighbors and explore the variation of lysis rate per one unit increase in target cell neighbors. Here we take the opposite value of the slope, to account for the fact that lysis rate decreases with more target neighbors. Figure 4.40 shows the extracted lysis rate variations as the number of neighbors is increased by one unit both for NK and target neighbors. In the absence of bsAb, no

obvious trend emerges, both variables seem to have a similar, low effect on varying the lysis rate. In the presence of antibodies, on the other hand, the effect of adding one NK in the neighborhood seems quite stronger on the lysis than the protective effect brought by adding one target cell.

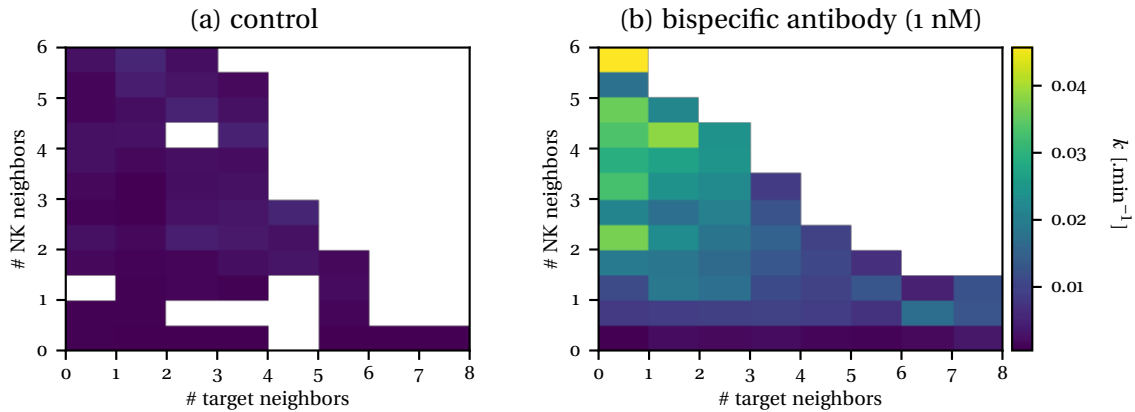


FIGURE 4.39 – Lysis rate decomposition. A double binning is performed on the local number of target neighbors (columns) and the mean number of NK neighbors until death (rows). In each bin, if there are more than 15 cells, the survival function is computed and fit with equation 4.10 over the first 45 minutes to extract the lysis rate k and an estimate of the fit error. This process is done in the absence (a) and presence (b) of CE4-21 bsAb at a 1 nM concentration.

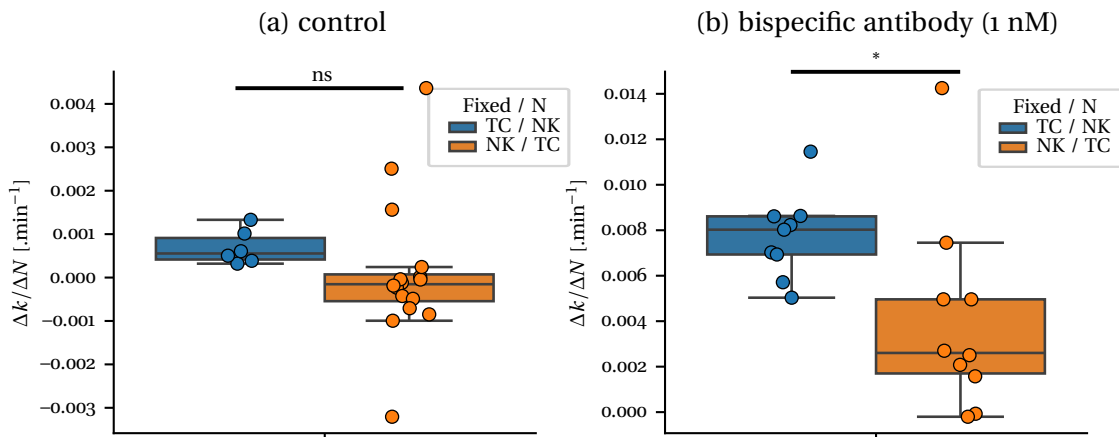


FIGURE 4.40 – Lysis rate variation for each variable. The lysis matrix is explored row-by-row to fix the number of NK neighbors and fit the lysis rate increase per target neighbor. Then the same process is reiterated column-by-column for which the number of target neighbors is fixed and the lysis rate increase by NK is fitted. The distribution of the magnitude of this rate-increase-per-cell is shown a) in the absence and b) presence of CE4-21 bsAb at 1 nM. Statistical test for the difference of the mean was assessed using an independent t-test.

Such a lysis map is a representation of the response at a fixed antibody-concentration condition. To measure the effect of an antibody at perfectly comparable conditions (same number of NK neighbors, same target density) one can pick the value in a

single bin, with good statistics, and project it across all lysis maps at a fixed condition. Figure 4.41 shows the different steps in the process for a different experiment in which the antibody concentration was increased for WT and HER2+ MCF-7 cells.

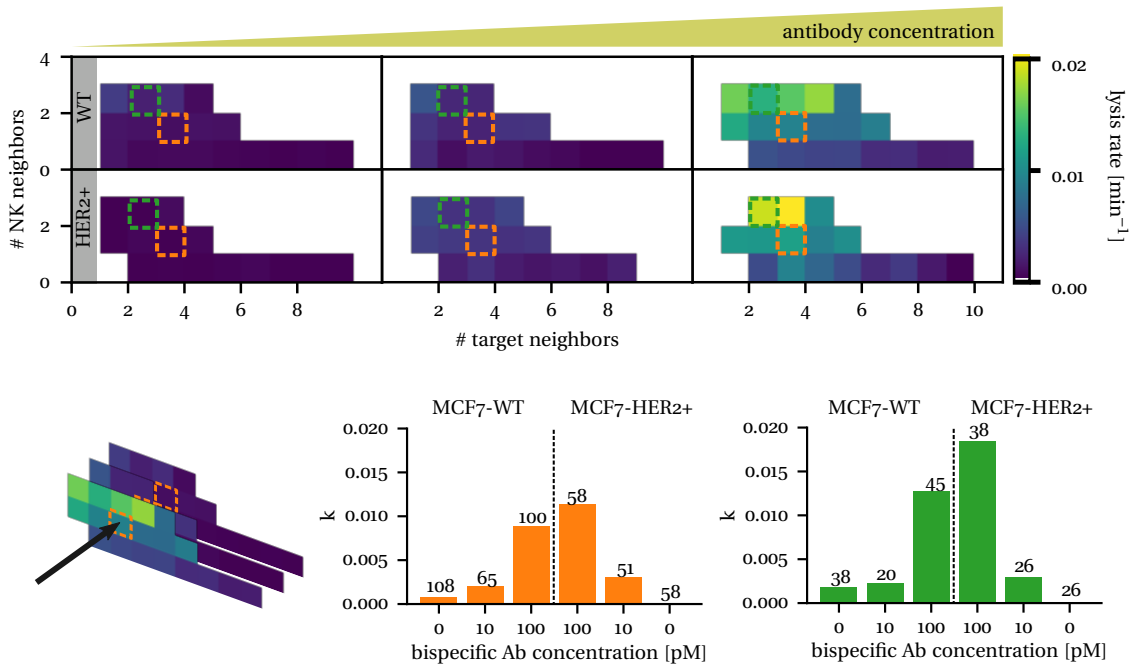


FIGURE 4.41 – Antibody efficiency assessment at fixed neighbors. The lysis rate as a function of the number of NK neighbors and the target density can be established in each well for a given experiment (by Beatriz Díaz-Bello in this example). Here, the concentration of CE4-28 bsAb was increased from 0 to 100 pM for MCF-7-WT on the one hand and MCF-7-HER2+ on the other hand, with a E : T ratio of 2.5. Selecting a specific bin and projecting the lysis values in all the wells yields an estimate of the lysis rate at fixed neighbor counts, for each condition. The color of the barplot matches the dotted contour of the selected bin. The number of cells in each bin is shown on top of the bar plot.

4.3.7.4 Per-NK lysis constant extraction

In the previous section, we observed that the target density has a lesser effect on lysis than the number of NK neighbors. In addition, we measured a linear relationship between the number of NK neighbors and the apparent lysis rate for up to 4 NK in the neighborhood, on average. In the following, we focus on the cells with an average target density (bin of 3-4 target neighbors), which we know implies an average number of NK neighbors of about 1-2, and not consider the quantity again. We checked from the lysis maps that the linearity of the lysis rate with the number of NK neighbors still holds in this target density bin.

We propose to revisit model 4.10 by introducing the mean alive NK neighbor counts for a population ($N(t)$). We have shown that $k(t) \propto N(t)$. Therefore we can write :

$$\frac{dT}{dt} = -k_{\text{per-NK}}NT \quad (4.11)$$

where $k_{\text{per-NK}}$ is a “per-NK neighbor” estimate of the lysis rate. We know from the existence of plateaus in cell survival even though NK are still alive, that this lysis rate should be a function of time to be accurate. Let $L(t)$ be the lysis function, per-NK, of the system. We hypothesize that $L(t)$ can be written as $L(t) = k_{\text{per-NK}}\alpha(t)$, where $k_{\text{per-NK}}$ is now a constant lysis rate per NK and the $\alpha(t)$ function contains the time dependence. To check the validity of this model, we propose to measure numerically :

$$L(t) = k_{\text{per-NK}}\alpha(t) = -\frac{1}{T} \frac{1}{N} \frac{dT}{dt} \quad (4.12)$$

Figure 4.42 shows the live target profile $T(t)$ (or survival function) in all wells of an experiment comparing WT and HER2+ cells with increasing concentration of CE4-28 bsAb (at 0, 10 and 100 pM). Similarly, the mean NK neighbor profile $N(t)$ is shown for the same wells in figure 4.43 as well as the derivative of the target profile in figure 4.44.

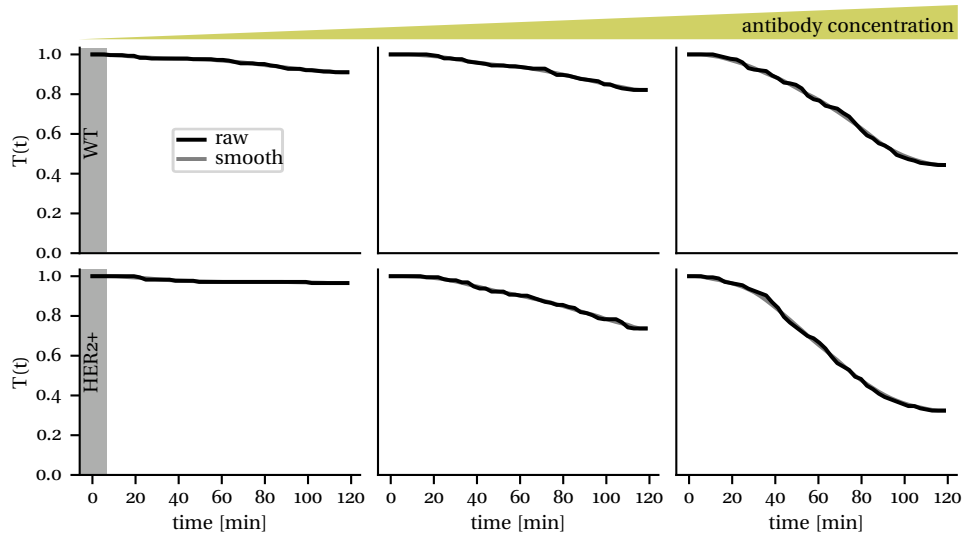


FIGURE 4.42 – Normalization : target survival in each condition. The fraction of targets alive at time t , $T(t)$ is decomposed for each condition, for the subset of target cells that have an average number of target neighbors between 3 and 4. In this experiment, the concentration of CE4-28 antibody is varied between 0, 10 and 100 pM (left to right), with MCF-7-WT (top) and MCF-7-HER2+ cells (bottom). A smooth (mean filtering sliding window of 8 frames / 22 min) is performed on the survival profiles (gray).

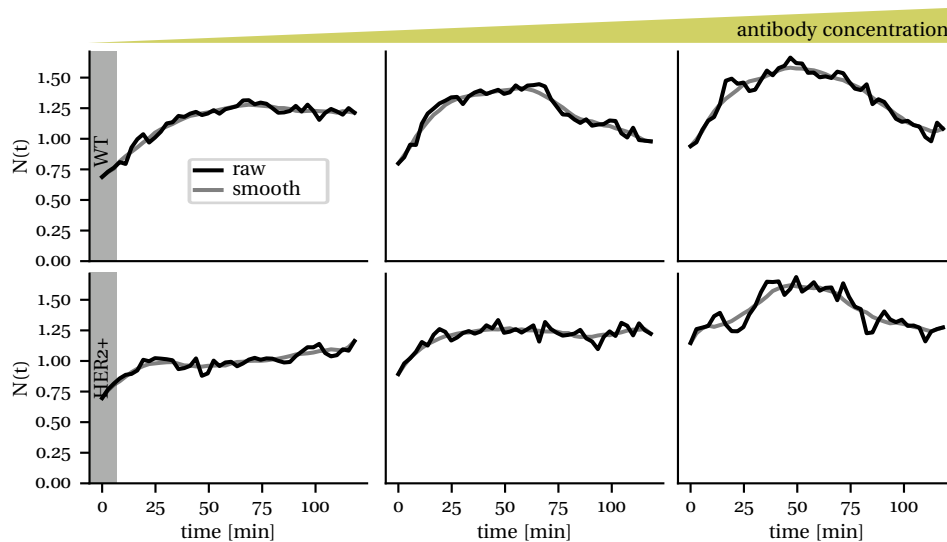


FIGURE 4.43 – Normalization : dynamic mean number of NK neighbor per cell. The alive NK neighbor count profile per cell is averaged over the whole population, as $N(t)$. A smooth (mean filtering sliding window of 8 frames / 22 min) of the signal is shown in gray.

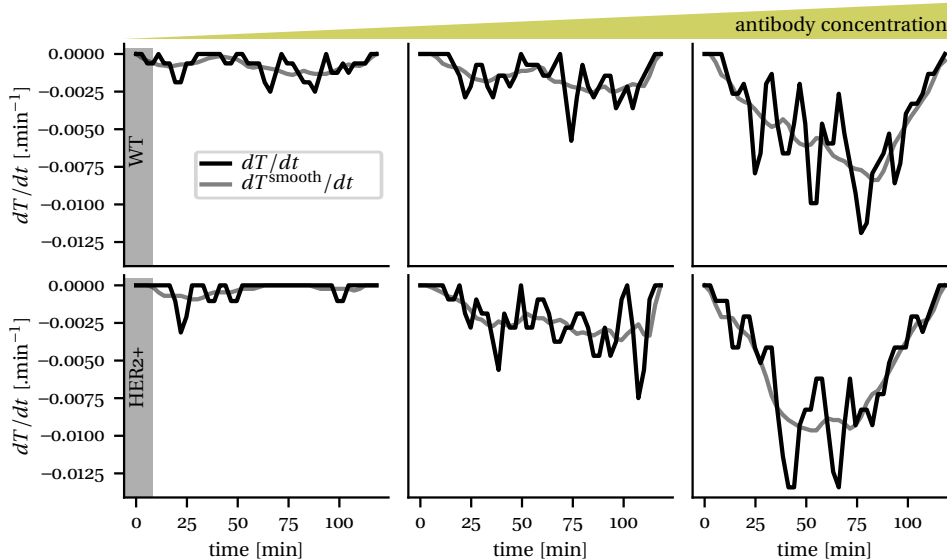


FIGURE 4.44 – Normalization : derivative of the survival. The survival functions are differentiated with respect to time numerically, using a 3-frame window (8.25 min). The black line shows the result when the raw survival function is differentiated, whereas the gray line shows the result when the smoothed survival function is differentiated.

All components are assembled into the lysis function $L(t)$ in figure 4.45. At this stage, we noticed some regularities in several experiments, namely a pattern due to delay and plateaus of the survival often quite reproducible in the wells associated with a target cell type. We decided to perform a signal collapse by amplifying the lysis function at lower antibody concentrations to match the pattern found at the

highest concentration. A median pattern was computed and arbitrarily normalized to the peak of the lysis function observed at the highest bsAb concentration. As a result, we could introduce a normalized time-dependent signal shared across several wells, $\bar{\alpha}(t)$.

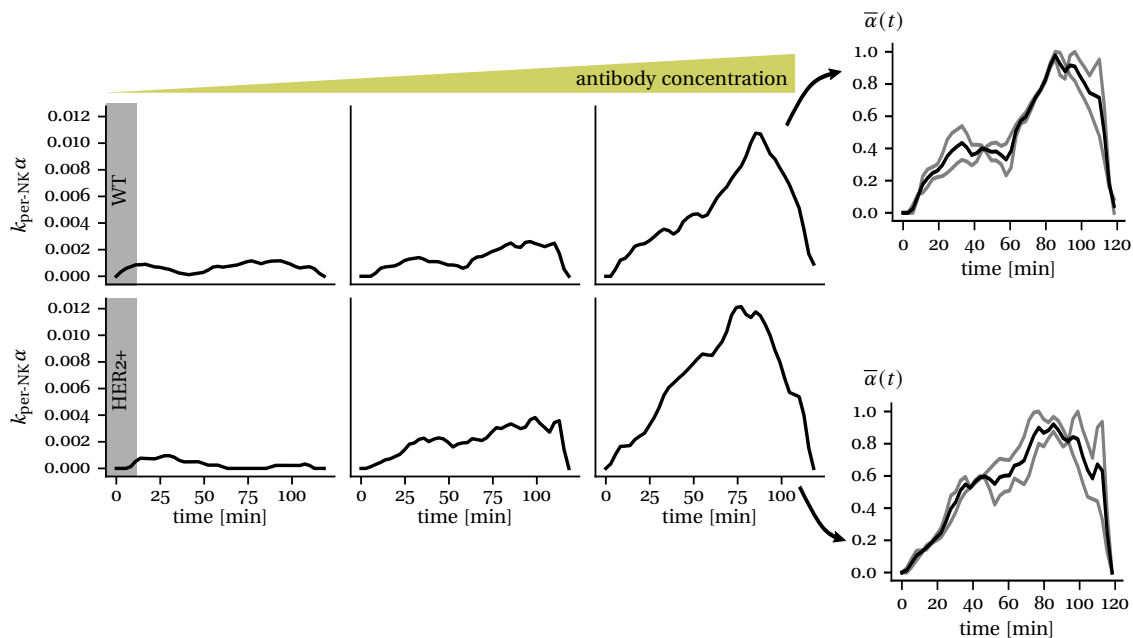


FIGURE 4.45 – Normalization : total lysis function. The survival functions $T(t)$, mean NK live neighbor profiles $N(t)$ and survival derivative profiles $\frac{dT}{dt}$ are assembled into the lysis function $L(t)$. Exploiting regularities in the shape of the lysis functions, we fit an average time-dependent profile $\bar{\alpha}(t)$ shared in the different conditions associated to a cell type.

Dividing $L(t)$ by this signal yielded an estimate for a single $k_{\text{per-NK}}$ coefficient, as illustrated in figure 4.46. In many cases, we could isolate an almost constant per-NK lysis rate, therefore decomposing the lysis response into a constant, per-NK rate and a time-dependent signal.

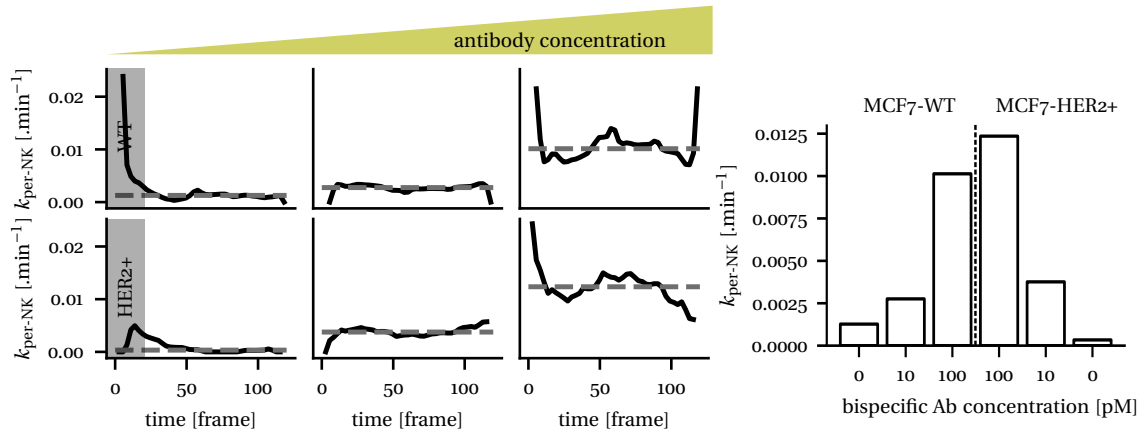


FIGURE 4.46 – Extraction of a constant lysis rate per NK neighbor. The mean $\bar{\alpha}(t)$ functions fitted for each cell type are divided to the lysis function $L(t)$ in such a way as to make apparent the supposedly constant $k_{\text{per-NK}}$. The median of $L(t)/\bar{\alpha}(t)$ (dashed line in gray) is taken as the estimate for the constant per-NK rate. The coefficients are collected and compared for each biological condition.

We proceeded at scale with this technique to estimate the per-NK lysis rate constant and α functions for several donors, tested against CE4-28 bsAb as shown in figure 4.47. In addition, we report several α function profiles, that usually share an increasing and decreasing phase, that we associate respectively to the delays and plateaus observed in the survival. Often, the area under the curve of the α profile increases with the MCF-7 HER2+ cells and the time of maximum can be shifted to a higher value. We hypothesize that the plateau effect might be due to toxic conditions under the microscope over large time scales and/or an immobilization of NK over time, not able to detach from target cells fast enough to commit serial killing.

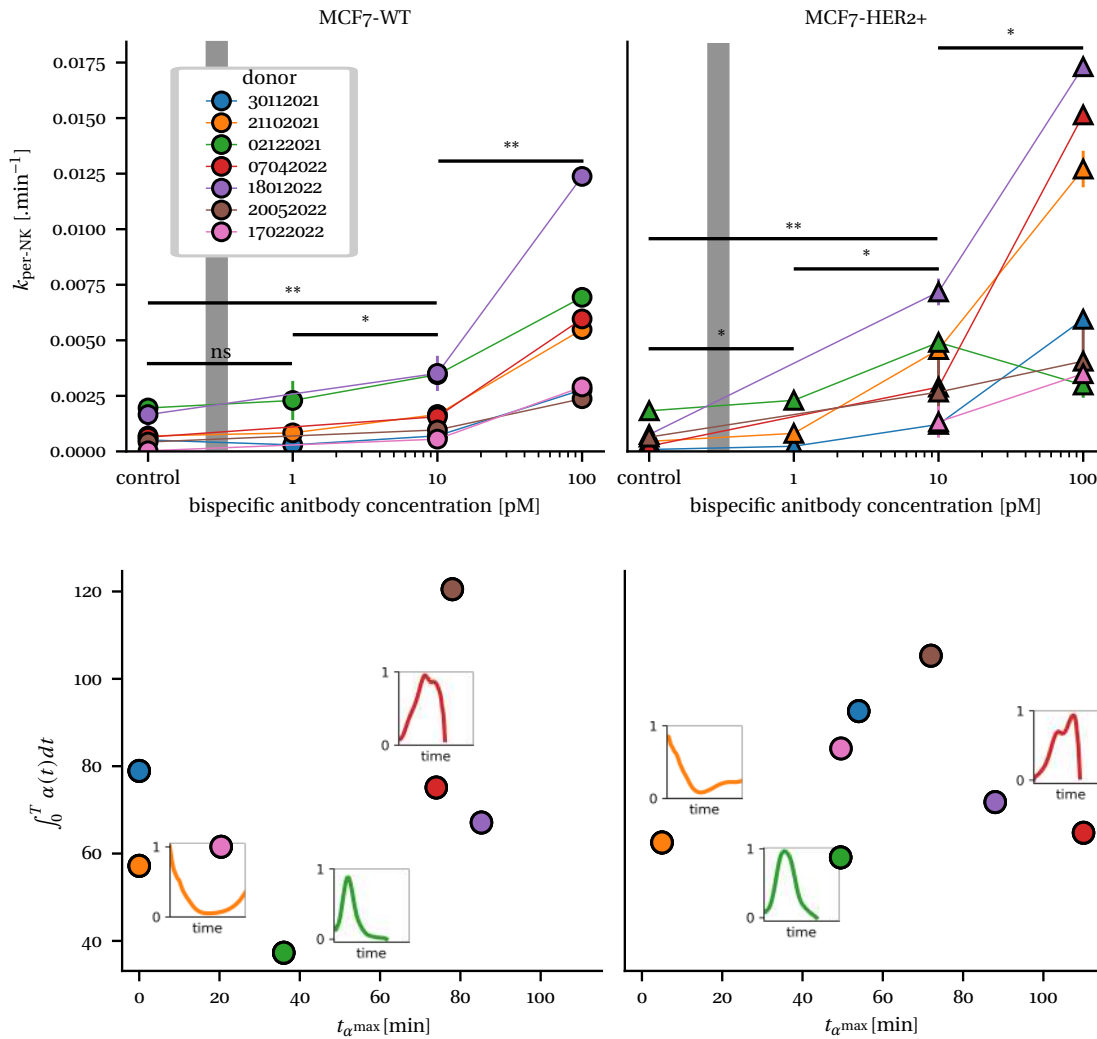


FIGURE 4.47 – Assessment of per-NK lysis rates and α functions for several donors. Per-NK lysis rates $k_{\text{per-NK}}$ coefficients are extracted using the method described above for several donors tested against increasing concentrations of CE4-28 bsAb. The integral under the curve and time of maximal α function is reported for all of these donors, with select functions shown directly. Statistical test for the difference of the mean of the lysis rates across donors at consecutive concentrations was assessed using a relative t-test.

4.3.7.5 NK dynamics changes in contact with MCF-7

An important aspect of cell-cell interactions is relative motion. Here, we exploit an ADCC experiment imaged by Lorna Ammer at a higher time and spatial resolution, at the cost of reduced throughput, to measure the dynamics of the NK cells before and after contact with the target cells. In all of the following results, the negative control (no bsAb) with MCF-7 HER2+ cells is missing due to lack of time to perform the analysis. We observed qualitatively that NK cells could be subject to strong

convection flows when not interacting with the target cells. As a result, we propose to use a Brownian-drift model to characterize NK cell diffusion, while measuring a convection/active velocity component, that we call *drift velocity* for simplicity.

First, we define target/effector contact using a neighborhood scheme with the standard radius. Any effector with more than one target neighbor at time t is instantaneously classified as being “in contact”. Using such a classification, three families of NK trajectories emerge : 1) NK that are in contact with target cells from beginning to the end of the observation, 2) NK that are never in contact and 3) NK that transition from one state to the other, as illustrated in figure 4.48a. For the “in” and “off” contact groups, diffusion coefficients can be estimated over the whole trajectories. A comparison of the diffusion coefficient and the drift velocity between cells of the two contact groups across all wells is shown in figure 4.48b. A significant reduction in diffusion coefficients is systematically observed between the cells of the two contact groups. The effect seems stronger in when the target cells overexpress HER2. The difference in drift velocity is much less obvious and depends mostly on how much convection is observed in a given position.

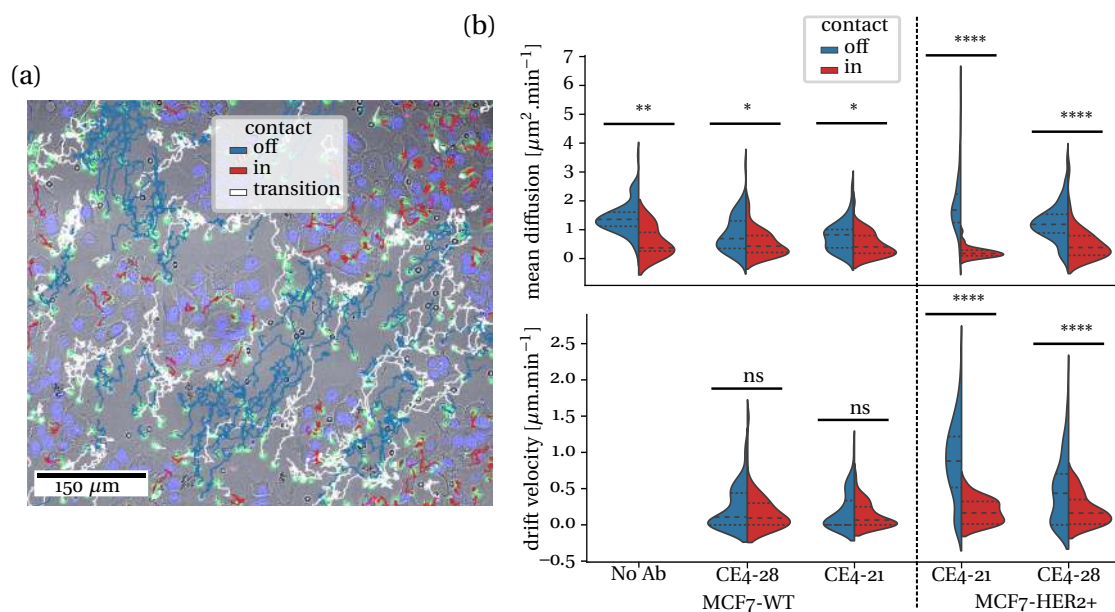


FIGURE 4.48 – NK cells move differently in and off-contact to the target cells. a) NK trajectories are classified as being in contact with target cells throughout the whole observation window (red), never being in contact (blue), or switching contact status (white). The full trajectories are shown. b) Violin plot showing a kernel density estimate of the distribution in trajectory-wise diffusion coefficient and drift velocity, comparing cells in and off-contact for each well. The violin plot shows the data quartiles. Statistical difference between off/in contact distributions was assessed using a two-sample KS test.

We propose to explore a subset of the transitioning trajectory, namely the NK cells that are observed to make irreversible contact with the target cells. To detect these cells automatically, we fit the binary and instantaneous on/off contact attribute with

a step function. If the fit quality is high enough (as assessed with $R^2 > 0.75$) and the final state is 1 then we collect the time of contact t_{contact} and select the cell. Figure 4.49a illustrates this fit approach on a noisy irreversible cell-cell contact. Since we aim to describe a transition in dynamics, we need local estimators for cell dynamics. We propose to measure the instantaneous velocity in a window of 3 frames (5.2 min) at each time point, as well as an instantaneous estimator for the diffusion, and drift velocity, adapting the sliding MSD approach from [127] and fitting with the Brownian drift model. The sliding window is set to 13 frames (22 min) and the MSDs are fit over the first three points. Figure 4.49b shows the three signals centered about t_{contact} for one well (CE4-21, HER2+ target cells). For the three instances, there seems to be a faint transition (a decrease) around t_{contact} but these signal representations are noisy. Since individual dynamic cell signals are quite transient, averaging the collapsed signals over several cells does not yield a clear result. Therefore, we propose to measure for each cell the average of each quantity respectively before and after t_{contact} . Then we take the ratio of the mean of the quantity post-contact over the mean pre-contact. These ratios are shown for each well next to the signal plot of the variable of interest. The instantaneous velocity and instantaneous diffusion strongly reduce post contact with HER2+ target cells. The effect is less clear on WT target cells. The drift velocity is observed to decrease on three conditions post contact (HER2+, and CE4-21 with WT).

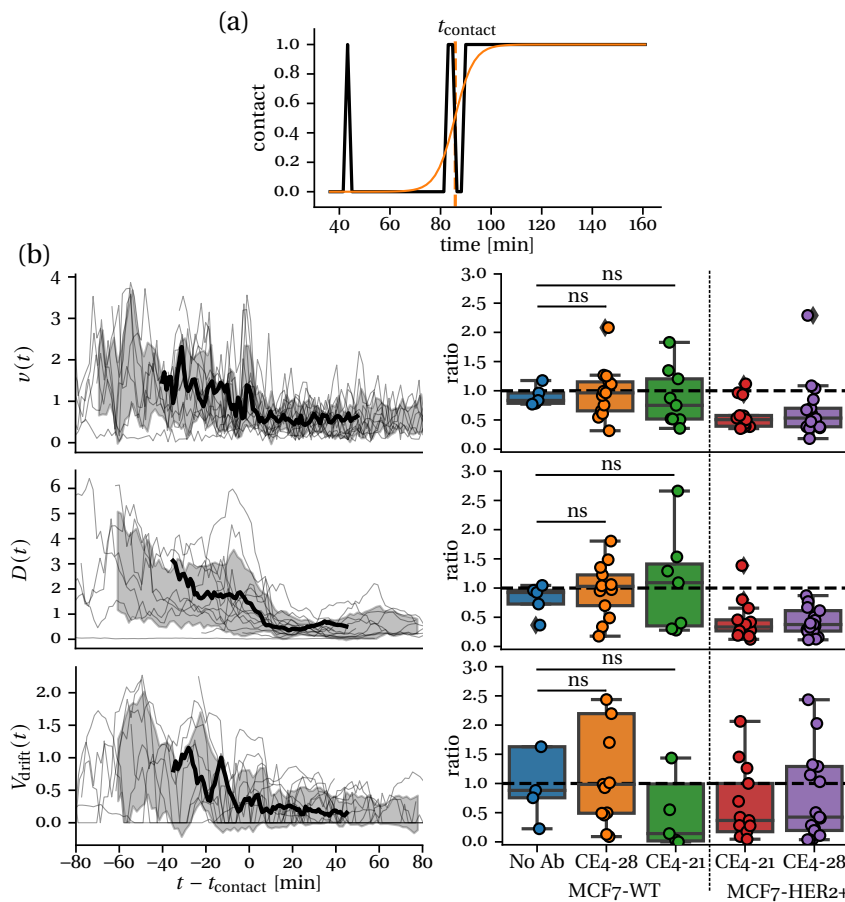


FIGURE 4.49 – NK seem to slow down upon contact with targets. a) The contact time t_{contact} is extracted from the binary cell-cell contact signal using a step function. b) Instantaneous velocity, diffusion and drift velocity signals are collapsed with respect to t_{contact} . The mean \pm STD signal across all cells is shown in thick black. The ratio of the mean value per track of each quantity after and before the contact is plotted for each condition on the right side of the associated signal plot. Statistical difference in the mean of the ratios was assessed using an independent t-test.

Overall, these measurements show that there is a slow down of NK cell dynamics upon contact with the MCF-7 cells that is noisy. The effect seems consistently stronger on HER2+ target cells than wild-type cells.

4.3.7.6 NK synapses increase with the antibody concentration

We characterized synapse formation in the ADCC system visually using CellDetective's signal annotator. We annotated as synapse a NK cell with a weak to null motion relative to one or more surrounding target cells for an extended period. Qualitatively, this looked like a synchronized and jiggly motion between the NK and its surroundings. Synapse annotation was performed on the brightfield channel, mostly blind to MCF-7 cell death to avoid bias, as illustrated in figure 4.50. The synapse formation time was hard to estimate precisely. It was set conservatively before the

actual time, as close to the correct time as possible.

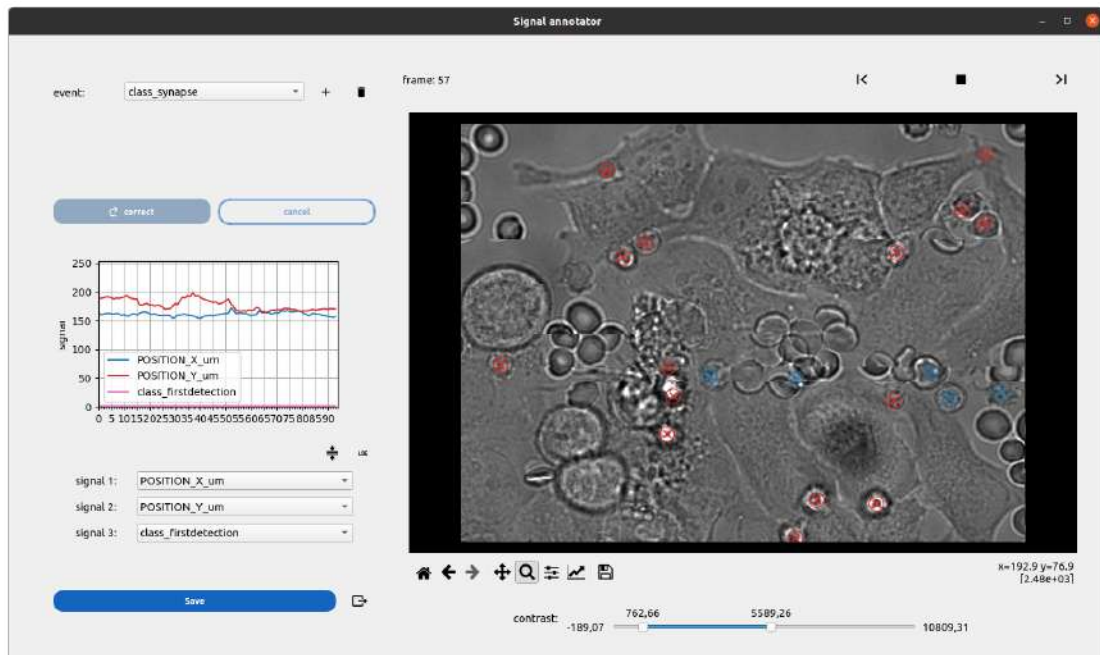


FIGURE 4.50 – Synapse annotation with Celldetective. The NK tracks and brightfield channel are loaded into Celldetective’s signal annotation tool. We define manually a synapse class and look for NK cells with constrained motion. Since the switch between free motion and a synapse state can be very subtle, we attribute a conservative time to the synapse event, *i.e.* we set it lower than what it might truly be. We do not worry at that stage about which target the NK is docked to.

We revisited the contact groups of the NK cells to differentiate between a NK cell in contact but not forming a synapse and a NK cell in contact through a synapse. As a result, NK cells could belong to one of three groups at each time point. In each group, the mean of the instantaneous diffusion was estimated per track. Figure 4.51a shows this quantity decomposed per group and per well. The diffusion for the synapse group is systematically much lower than that of the other two groups. With WT target cells, the difference between off-contact NK cells and NK in contact without a synapse becomes systematically nonsignificant. This result explains why our previous slow-down measurements were so noisy as only a fraction of NK cells are technically immobilized upon contact. In the HER2+ condition, a difference between these two groups is still observed.

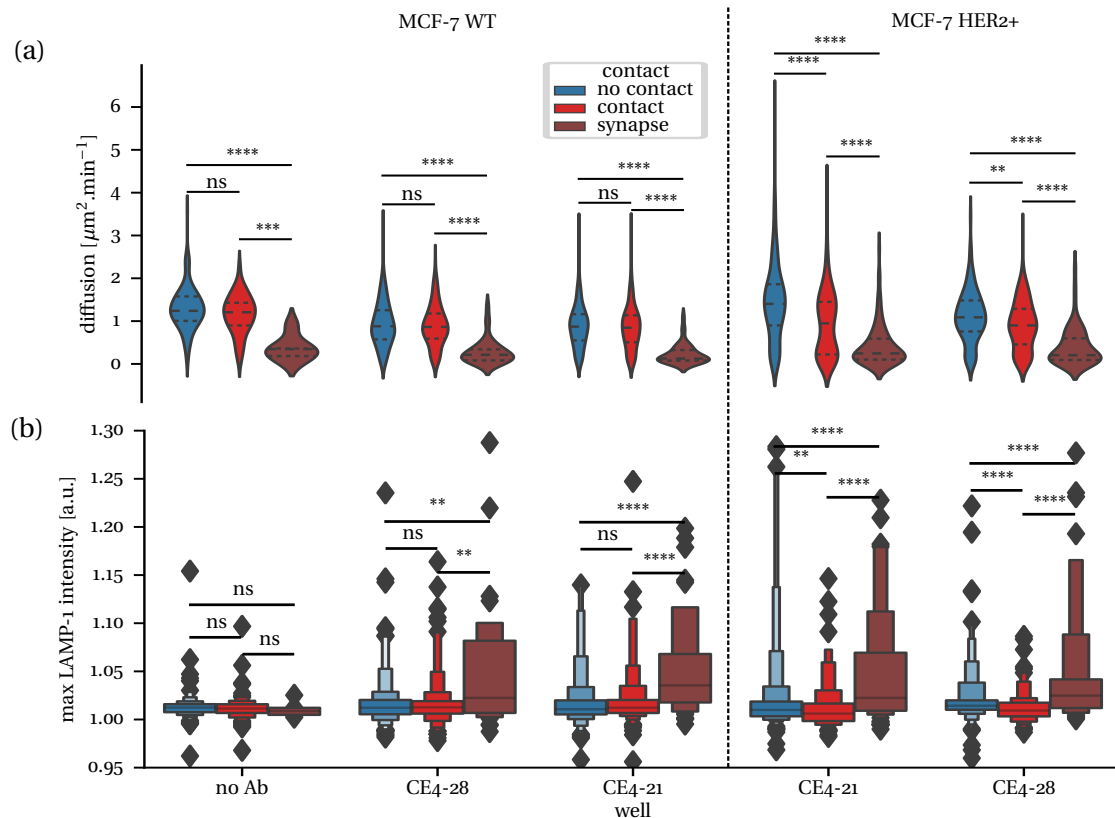


FIGURE 4.51 – NK in synapse exhibit different features. a) Violinplot showing a kernel density estimate of the distribution in mean instantaneous diffusion coefficient per contact group for each well. The violinplot shows the data quartiles. b) Boxenplot showing several quantiles of the distribution in maximum LAMP1 intensity per track in each contact group and each well. Two-sample KS test for difference is performed between each contact group.

In addition, we could exploit LAMP1 intensity measurements to show that NK in synapse express more LAMP1 than the other cells. For each contact group, instead of taking the mean of the LAMP1 signal per track, we took the maximum value, as we noticed that LAMP1 could be quite transient. Figure 4.51b shows that LAMP1 expression was much higher overall in the presence of antibodies than in the control and that the fraction of LAMP1 positive NK cells was much higher in the synapse group than either the off or in contact groups, with systematic statistical difference (except in the control where LAMP1 is almost absent).

Finally, we relate the number of synapses observed in each well to the number of targets killed per condition. Figure 4.52a shows that the raw counts of both synapses and target killed increase considerably in the presence of bsAbs. CE4-21 seems to favor more synapse formation and more target kills than CE4-28 both with WT and HER2+ cells. The number of observed synapses is much larger than the number of killed targets, which implies that many of these synapses might be inefficient or of shared action. The presence of synapses but the absence of kill in the control condition seems to suggest that some synapses are inefficient. Figure 4.52b shows

the time evolution of the ratio of the number of synapses to the number of killed targets at each time point. HER2 overexpression tends to favor inefficient synapses (ratio of 3 and 3.5) compared to about 2 in the WT-MCF-7 condition but does lead to higher kill counts.

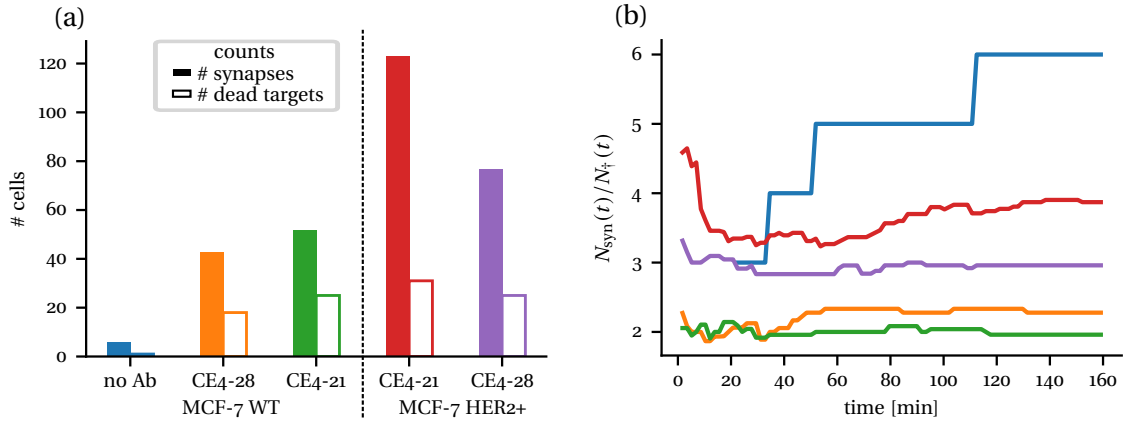


FIGURE 4.52 – More synapses than targets killed. a) Barplot of the total number of synapses and dead targets observed in each condition. b) Dynamic ratio of the number of synapses formed before time t , $N_{\text{synapse}}(t)$ and the cumulated number of dead target cells at time t , $N_{\dagger}(t)$.

4.3.7.7 Who's the killer?

Introduction A complete and independent tracking of both the MCF-7 cells and the NK cells does not solve the difficult problem of pairing killing NK cells and their target victims due to reasons evoked throughout the chapter, such as the difficulty of establishing a true neighborhood for the target cells. In particular, we find the task visually challenging as NK cells may form a synapse at the interface between several target cells. Still, after careful observations, discussions with the experimentalists, and literature scouting we came up with a set of clues that we believe can give away a killer in a neighborhood. The objective of this section is to validate whether or not our clues are relevant to the victim/killer pair detection.

Set up of the problem In this study, we focused on the subset of target cells that exhibited a lysis event during the experiment. For each of those cells, first, we performed a broad isotropic neighborhood matching ($R = 32 \mu\text{m}$). Then for each target/effector pair, we computed a series of descriptors d_i summarized in table 4.4. Some of those descriptors involved a time-average of a dynamic signal (d_{rel} , v_{rel} , I_{LAMP1}). We introduced a parameter θ_t that controls the time window around t_{\dagger} over which to average them. Moreover, these quantities were normalized using custom activation functions described in figure 4.53. The remaining quantities are by design already constrained between 0 and 1. We built the final probability for a target/effector to be a victim/killer pair as a linear combination of the different descriptors :

Table 4.4 – Features of target/effector pairs. The table summarizes the different features considered to build the probability of finding the NK killer for the target considered. Non-normalized features are normalized using custom activation functions described in figure 4.53.

Descriptor	Activation	Time-average window	Relative	Weight	Comments
d_{rel}	step function 4.53a	$[t_{\dagger} - \theta_t, t_{\dagger}]$	True	w_d	$d_{\text{rel}} = \sqrt{\bar{x}^2 + \bar{y}^2}$
v_{rel}	skewed function 4.53b	$[t_{\dagger} - \theta_t, t_{\dagger}]$	True	w_v	$v_{\text{rel}} = \frac{d}{dt} d_{\text{rel}}$ $\frac{d}{dt}$: 3-frame window bidirectional
$t_{\text{res}}^{\%}$	None	$[0, t_{\dagger}]$	True	w_t	$t_{\text{res}}^{\%} = \frac{t_{\in N}}{t_{\dagger}}$
I_{LAMP1}	step function 4.53c	$[t_{\dagger} - \theta_t, t_{\dagger} + \theta_t]$	False	w_I	Effector LAMP1 expression
class synapse	None	ANY in $[t_{\dagger} - \theta_t, t_{\dagger}]$	False	w_s	Effector classification Manual annot. *

$$\mathcal{P}(\text{victim / killer}) = \sum_{d_i \in \text{desc.}} w_i d_i \quad (4.13)$$

with the following constraint on the weights w_i in such a way that this probability can never exceed 1 :

$$\sum_{d_i \in \text{desc.}} w_i = 1 \quad (4.14)$$

Setting $\theta_t = 10$ frames (~ 17 min), and assuming first an equal weight for each clue, we generated a matrix per position where each row is a target that exhibited a lysis event and each column a different effector that belongs to the neighborhood of at least one of these targets. Figure 4.54 translates one such matrix into what it means on the image, by showing the target/effector system at t_{\dagger} and projecting the probabilities on the NK masks. A visual inspection of the results showed that in most instances, the NK that we believe is the killer is one of the top contenders in this probability scheme but not always the first.

Optimization of the descriptor weights Assuming equal weights for each of the hypotheses is a strong choice, as we may have redundant descriptors or some that are too noisy to be helpful in the system. Furthermore, the time window on which to average the quantity is also a strong choice, that should not be imposed. Finally, using the synapse class is problematic as it was curated manually, making it a quantity

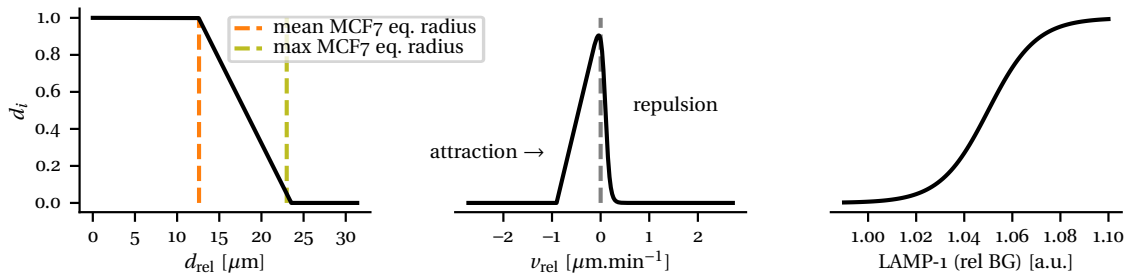


FIGURE 4.53 – Empirical activation functions for determining NK killers. a) The mean relative distance between the nucleus of a MCF-7 cell and a NK neighbor, in a time window θ_t before the lysis event is mapped to a step-like activation function. For distances smaller than the average MCF-7 size, the activation is maximal. Beyond this value, it decreases linearly until the distance reaches the maximum observed MCF-7 size $*$. b) The mean relative velocity in the same time window θ_t is mapped to a skewed activation function, favoring low velocities. The instantaneous velocity v_t is computed bidirectionally using a three-frame sliding window. The activation function is skewed toward negative values to not penalize NK getting closer to the target at the time of the lysis event. c) the mean normalized LAMP1 signal around the time of the lysis event (in a window $\pm\theta_t$) is activated by the sigmoidal function, with a critical LAMP1 value of 5 % above background.

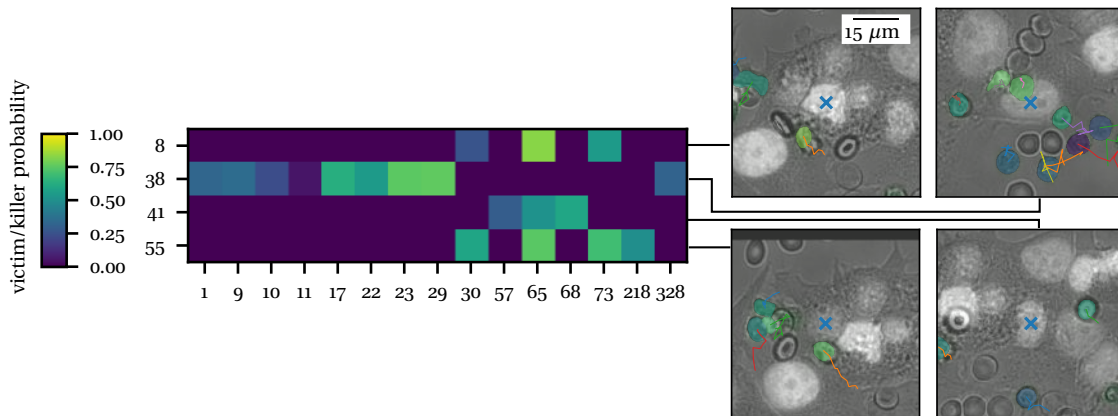


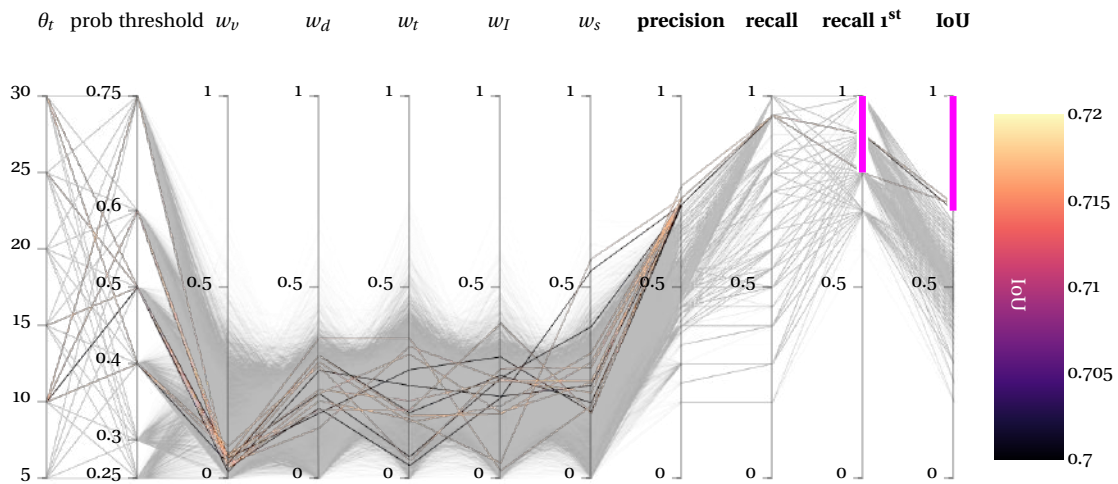
FIGURE 4.54 – Probability of a victim/killer pair. a) the matrix shows the probability of having a victim/killer for each target/effector pair in this position. Only victim targets are considered here. b) snapshot of the target at t_{\dagger} (brightfield and Hoechst in gray, CFSE channel in green). The NK in its neighborhood are recolored to match their probability of being the killer.

subject to bias and painstaking to obtain. In addition, since synapse identification relies on relative motion, the synapse class makes relative distance and relative velocity descriptors quite redundant. It is for all of those reasons that we decided to perform an optimization scheme to find the best combination of parameters to detect the real killer with a high enough probability.

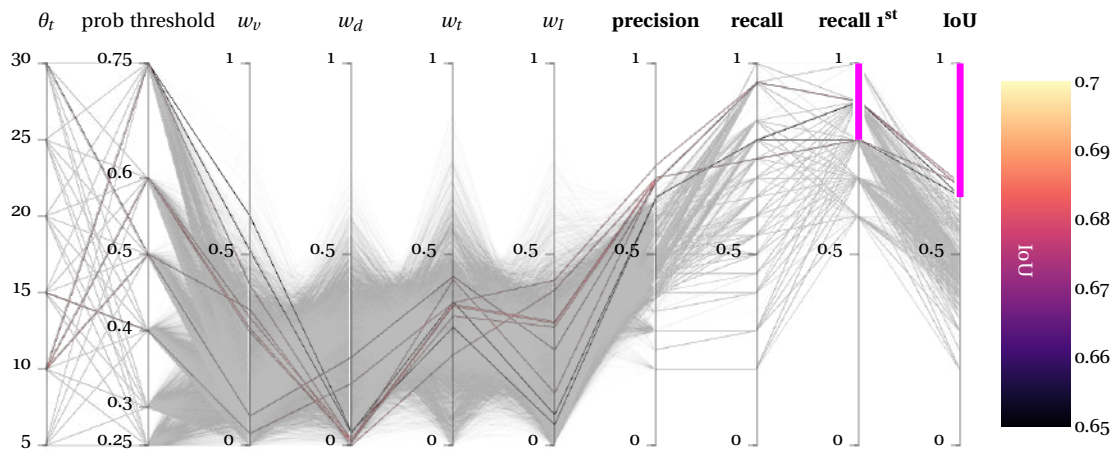
We manually curated a little set of ground truth victim/target pairs (14 potential NK cell killers among 10 target victims). We used Celldetective to identify the most likely killer candidates from brightfield images. When we could not decide between two NK, which can happen due to all the difficulties mentioned at the beginning of

this section, we decided that a good detection should find both candidates at a high enough probability level. In practice, at a given θ_t and probability threshold, we took at random $n = 3000$ combination of weights and for each target neighborhood computed the probability of being the killer for each effector. If the target was part of the ground-truth dataset, we checked whether or not the annotated killer coincided with a NK with a probability higher than the probability threshold, making it a true positive. If unrelated NK had probabilities higher than the threshold they were counted as false positives. Finally, if an annotated killer was not predicted with a high enough probability, we marked it as a false negative. For each neighborhood, we thus computed an IoU, precision, and recall score. For each combination of detection parameters, we recorded the mean across all dead target cells of these scores. We also assess whether or not one of the annotated killers ends up being the NK associated with the highest probability in the neighborhood. We call this score the recall 1st.

Results We performed two separate optimization schemes, with and without the class synapse descriptor. The results are presented in figure 4.55. The optimal weights are quite different depending on whether or not this descriptor is included. The class synapse descriptor is systematically attributed a lot of weight (~ 0.25) to yield the highest scores (IoU, recall 1st). In this configuration, the weight of the relative velocity is close to zero. In the absence of the class synapse descriptor, the relative velocity descriptor takes most of the weight (~ 0.4), whereas the relative position weight decreases considerably.



(a) Optimization with the synapse annotation.



(b) Optimization without the synapse annotation.

FIGURE 4.55 – Optimization of victim/killer detection parameters. Parallel coordinates plot reporting the combination of detection parameters that maximizes the mean IoU and recall 1st score when (a) the synapse annotation is one of the descriptors and (b) this descriptor is removed. The last four vertical axes are metrics computed for the subset of cells that are part of the ground truth set. A filter (purple gate) is set on two of those metrics (mean IoU and recall 1st) to highlight the combination of parameters that maximize those scores. The line colors are contrasted to high values of the mean IoU, according to the color bar on the right side, to show differences among the best solutions.

Table 4.5 summarizes the combinations of descriptor weights yielding the best performance, in the absence of the class synapse descriptor. The combinations are ranked by best mean IoU. The best solution, yielding a better precision and recall than the others is obtained for a relatively low weight on the relative velocity and a higher weight on the relative distance. For all of the subsequent solutions, it is

the relative velocity descriptor that takes most of the weight. The time of residence and LAMP1 descriptors are systematically associated with a high weight, showing how important they are to the detection of killers. We interpret the switch between the relative velocity, position, and class synapse descriptors as being because these descriptors are correlated and therefore redundant, to some extent. As a result, we highlighted at least three clear descriptors to identify victim/killer pairs. The best solution achieves a precision of 0.73 and a recall of 0.95 on our ground-truth dataset. 90 % of the time, the first predicted cell turns out to be one of the cells we believed to be the killer. This solution proposes a weight of 0.03 for the relative velocity and 0.16 for the relative distance (*i.e.* a total of 0.19 on the motion descriptors), as well as 0.37 for the residence time and 0.43 for LAMP1, showing the importance of the latter two descriptors. We recompute the probability of the victim/killer pair using the optimized weights as illustrated in figure 4.56.

Table 4.5 – Optimization results on victim/killer detection parameters without the synapse class. The table shows the 10 best combinations of parameters to successfully find the annotated victim/killer pairs from the ground truth set using all but the synapse class as clues. The first few lines correspond to the colored lines in figure 4.55b.

θ_t	threshold	w_v	w_d	w_t	w_l	IoU	Precision	Recall	Recall 1 st
15	0.400	0.032	0.162	0.374	0.432	0.683	0.733	0.950	0.900
10	0.500	0.356	0.000	0.237	0.407	0.683	0.700	0.750	0.800
10	0.600	0.335	0.018	0.338	0.310	0.683	0.700	0.750	0.800
10	0.600	0.306	0.009	0.365	0.320	0.683	0.700	0.750	0.800
10	0.600	0.297	0.011	0.369	0.323	0.683	0.700	0.750	0.800
10	0.750	0.420	0.010	0.434	0.137	0.683	0.700	0.750	0.800
10	0.500	0.387	0.000	0.215	0.398	0.683	0.700	0.750	0.700
10	0.600	0.436	0.018	0.262	0.284	0.683	0.700	0.750	0.700
10	0.600	0.493	0.007	0.233	0.267	0.683	0.700	0.750	0.700
10	0.500	0.413	0.000	0.199	0.388	0.683	0.700	0.750	0.600
10	0.500	0.250	0.250	0.250	0.250	0.450	0.500	0.650	0.800

The optimization was performed on a train set without any consideration for validation or test set due to the very low number of identified killers in the ground-truth dataset. We had not guaranteed from the beginning that the descriptors we introduced were sensitive enough to identify NK killers. As it turns out, even on the train set, 1 NK killer is not predicted first, implying that some visual information, used to annotate the ground-truth, is lost by the descriptors. On the other hand, we observed systematically that all descriptors were relevant to get a good detection of the killers. The only subtlety is that there is some redundancy between the relative velocity, position, and synapse class descriptors but at least one of them is always needed. A larger dataset would be required to investigate the predictive power of such descriptors, which is not easy to achieve due to the challenge of balancing

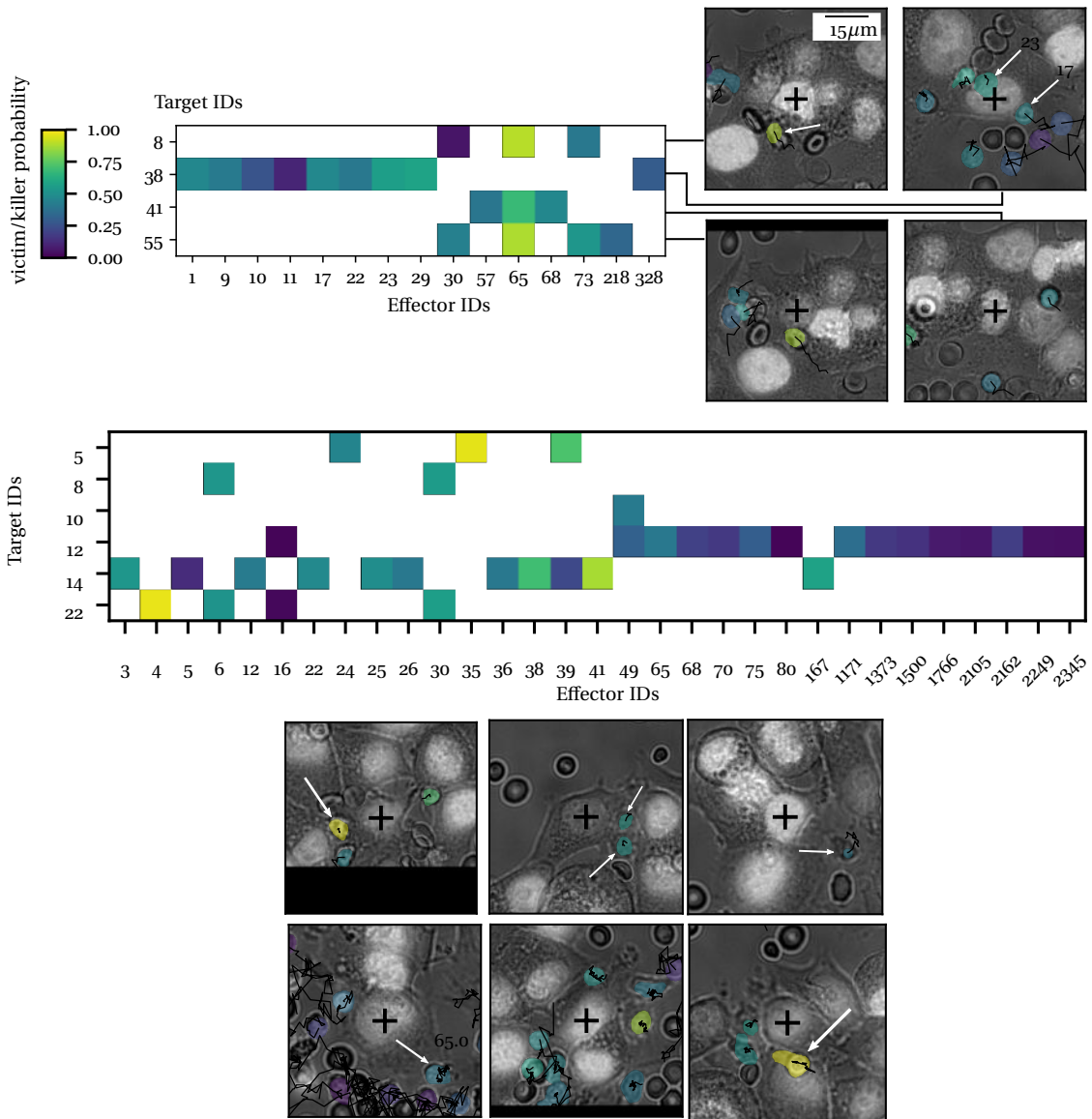


FIGURE 4.56 – Optimized probability of a victim/killer pair. a) The matrix shows the optimized probability of being a victim/killer pair for each target/effector pair in this position. The probabilities shown here use the weights of the first line of table 4.5. White arrows indicate NK cells that were annotated as potential killers in the ground-truth dataset.

spatio-temporal resolution with throughput.

5 Cell-surface interaction assay

5.1 Introduction

In this chapter, we propose to replace the target cells with a substrate covered with antibodies or bsAbs. As discussed in section 2.2, the interface between immune cells and functionalized surfaces can be imaged in great detail using optical microscopy techniques. The reflection interference contrast microscopy (RICM) technique, being label-free, was the method of choice here. Here we exploit Celldetective to study a spreading assay of primary NK cells on surfaces covered with bsAb, imaged in RICM. The second part of the chapter is exploratory and proposes image analysis methods to classify cell phenotypes in this biological system. Eventually, we study the problem of topography reconstruction of parts of single cells from RICM images.

5.1.1 RICM historical development

In 1964, Curtis used principles described by Vasicek [180] and Van den Tempel [177] on thin-layer optics to measure the gap between a glass substrate and the bottom of an adhering living cell, imaged with an optical microscope [36]. The technique named interference reflection microscopy (IRM) exploits interference of light to estimate cell-surface distance. Light is reflected at each interface with a change of refractive index and interferes with previous reflections, hence the name of the technique. Despite the numerous improvements that followed, the distance measurements remained qualitative, an indicator of adhesion, as perfect knowledge of the refractive indices at each interface was needed to interpret the interferences. Unfortunately, living cells are optically heterogeneous.

Ploem introduced the antiflex technique in 1975 to considerably improve the contrast and signal-to-noise ratio of IRM images, re-baptizing the technique “reflection contrast microscopy” (RCM) in the process [56]. The antiflex technique removes all extraneous reflections by using polarized light coupled to an analyzer inserted before the camera as well as inserting a lambda-quarter plate in the light path and the entry/exit of the objective. Shortly after, the RCM was renamed “reflection interference contrast microscopy (RICM)”. Sackmann and Rädler applied the microscopy technique to model systems easier to interpret than cells such as colloidal beads and synthetic membranes (supported lipid bilayers, giant unilamellar vesicles) [139, 198].

5.1.2 Cellular foot-print

The simplest application of RICM (or IRM) is to detect cell adhesion and quantify spreading area in response to a substrate [45, 46, 62, 160]. Joint RICM and fluorescence acquisitions have established that focal adhesions translate into dark patches in RICM [102, 142, 152]. Contrary to expectations, it has been shown that these adhesion patches can grow under a detaching force [142]. Some cells that do not adhere through focal adhesion while still exhibiting dark patches in RICM have been associated with tight adhesion and do not detach under flow [136]. Zones of close contact within the cellular footprint have been identified in RICM [160].

RICM has been extensively used to quantify the dynamics of cell spreading. Wahl et al. [183] reported the average increase of the spreading area of T cells over time, originating at the introduction of the cells in the experimental chamber. The velocity of the leading edge of the adhesion footprint of single T cells was reported in reference [46]. Several stages of spreading have been reported, both for nonmotile and highly motile cells [38, 47, 160, 183].

5.1.3 Cell to surface distance

The determination of the distance between two surfaces can be achieved using an interference technique. As such, RICM is well adapted. Going beyond the binary description of adhered versus non-adhered cells, one can exploit an optical model to extract surface-separating distances from the intensities. A simple case study is for an interference emerging from the reflection between two successive interfaces (*e.g.* an object hovering above a glass surface with a separation h). The resulting intensity can be expressed as a function of the distance separating the two surfaces with the famous periodic relation :

$$I = I_1 + I_2 + 2\sqrt{I_1 I_2} \cos \left[\frac{4\pi n_1}{\lambda} h + \phi \right] \quad (5.1)$$

where I_0 is a monochromatic incident ray (with wavelength λ), I_1 is the first reflected beam at the glass/medium interface (refractive index of the medium is n_1), I_2 the beam reflected at the medium/object interface. h is the distance separating the object from the surface. The reflected beams I_1 , I_2 depend on the refractive index of each layer. As can be seen in this equation, the solution is degenerated due to the phase factor in the cosine, which means that several separation distances d are associated with the same reflected intensity and vice-versa. When more than one interface are stacked on each other, the successive reflections and refractions can be calculated in terms of Fresnel coefficients and propagated using the Jones matrix formalism, as described in review [104].

In the case of the synthetic membrane of giant vesicles, where the refractive indices of all the layers are known and the only unknown is the membrane-to-surface distance, the simple thin-film model was successfully applied to cases where

the membrane is close enough that one is always on the 0th order fringe. In case the membrane was further, this problem was solved by illuminating with two wavelengths [104].

In the context of cells, there are many more unknowns. The refractive index of the cell can vary locally and considerably depending on local variations of membrane composition, the presence of internal structures such as stress fibers close to the membrane [13], the presence of the nucleus itself and other internal membrane-bound structures. In addition, the cell being mostly transparent, light can be reflected from the upper membrane of the cell as well as from every internal structure, making the interference more complex [13, 40, 182]. In red blood cell (RBC) adhesion, strong fringes can be seen due to reflection from the upper membrane despite the lower membrane being tightly bound to the surface [69].

While measuring absolute height needs special precaution and rigor, the relative height, determined by application of the simple sinusoidal formula and only a single wavelength measurement was reported [16, 135, 197]. The most efficient way to lift the ambiguity in the phase factor of the intensity-to-height relationship (or any such expression derived from a more complex model) is to vary the control parameters, namely the wavelength λ and the illumination numerical aperture (INA), which is related to the angle of the cone of illumination. It has been shown that visibility decreases and fringe spacing gets stretched with increasing INA [59]. The additional periodicity and boundary conditions introduced by adding these extra illumination conditions can lift the degeneracy and enable absolute height measurements. One can also reconstruct fringe by fringe if the interface is monotonous [104].

A recent effort inverted an optical model to reconstruct the topography (distances and refractive indices) of the lamellipod region of a single spreading cell [40]. At each pixel location on the image, the refractive index of the cytoplasm, the surface-to-membrane distance h , and the lower to upper membrane distance d were assumed to be unknown. An optical model accounting for reflection from the upper membrane was used to simulate the illumination sequence expected for as many combinations of these unknown topography parameters as possible. The illumination sequence consisted of three λ combined with five INA to lift as many degeneracies as possible. The illumination sequence measured at each pixel location was regressed on all of the simulated sequences to extract the topography parameters most likely to explain the observed illumination sequence. This “brute-force” method for reconstruction is long, which prevents the reconstruction of more complex cell regions such as the nucleus.

5.1.4 Rationale

Spreading assays are well adapted to the scope of Celldetective, with spreading events acting as obvious single-cell events. Yet, systematic and synchronized single-cell characterization is quite uncommon for such assays, with population averages being usually preferred. Here, we describe an extensive application of Celldetective

to an assay of primary NK cells spreading on a substrate functionalized with a bsAb. In addition, we explore texture measurements and a DL approach to classify cell phenotypes.

For sub-cellular reconstruction, a bottleneck of current approaches is simulation and reconstruction time. We ask to what extent a Deep-learning model can be adapted to approximate the inverse optical transform, finding a direct path to reconstruct a topography from an illumination sequence instead of using a “brute force” approach.

5.2 Materials and methods

5.2.1 Substrate preparation

Uncoated eight-well chambered polymer coverslip-bottom from Ibidi (80821, Ibidi®) are initially rinsed with PBS, then incubated in a solution of Biotin-labeled bovine albumin (A8549-10MG, Merck®) diluted in PBS at $100\mu\text{g}/\text{mL}$ for 30 min at room temperature (RT) with agitation. To remove non-adsorbed BSA-biotin, the wells are rinsed four times with PBS. Afterward, the wells are incubated in a $10\mu\text{g}/\text{mL}$ Neutravidin solution (31000, Thermo Scientific™) diluted in PBS for 30 min at RT with agitation. After a four-time PBS wash, the wells receive a HER2/ERBB2 Protein solution (10004-H27H-B, Sinobiological®) diluted in 0.2% BSA at $10\text{ nM}/\text{mL}$ for 30 minutes at RT with agitation, followed by another four-time PBS wash.

5.2.2 Cells

Primary human NK cells. see 4.2.1.

NK-92. An immortalized immune cell line, isolated in 1992 from a patient who had a rare NK cell non-Hodgkin-lymphoma. NK-92 cells have characteristics similar to that of NK cells.

5.2.3 Microscopy techniques

5.2.3.1 Reflection interference contrast microscopy (RICM)

Figure 5.1a illustrates the different components of our RICM optical setup. Quasi-monochromatic light (at wavelength λ) exits the LED light source (CoolLED pE-300^{ultra} or a filtered Halogen light source) and travels in an optical fiber to reach the base of the microscope (Axio Observer, Zeiss). The light passes through two adjustable diaphragms, respectively the motorized aperture diaphragm and the field diaphragm, before reaching a reflector cube composed of a polarizer, a semi-reflecting mirror (SRM), and an analyzer. The light incoming from the source is sent to the objective (63X 1.25 NA Neofluar Antiflex) equipped with a $\lambda/4$ -waveplate.

The light linearly polarized by the polarizer gets circularly polarized by the $\lambda/4$ -waveplate. The light reflected from the sample crosses again the $\lambda/4$ -waveplate and passes through the analyzer, in such a way that only the light reflected by the object participates in the formation of the image on a EM-CCD camera (Andor iXon) [182]. The opening of the aperture diaphragm controls the INA, *i.e.* the numerical aperture of the exit pupil of the objective [104]. Keeping the INA as small as possible makes light incidence as perpendicular (point-like) as possible, increasing the depth of focus. On the other hand, a larger INA increases lateral resolution and decreases the depth of focus, limiting the risk of reflection from upper surfaces.

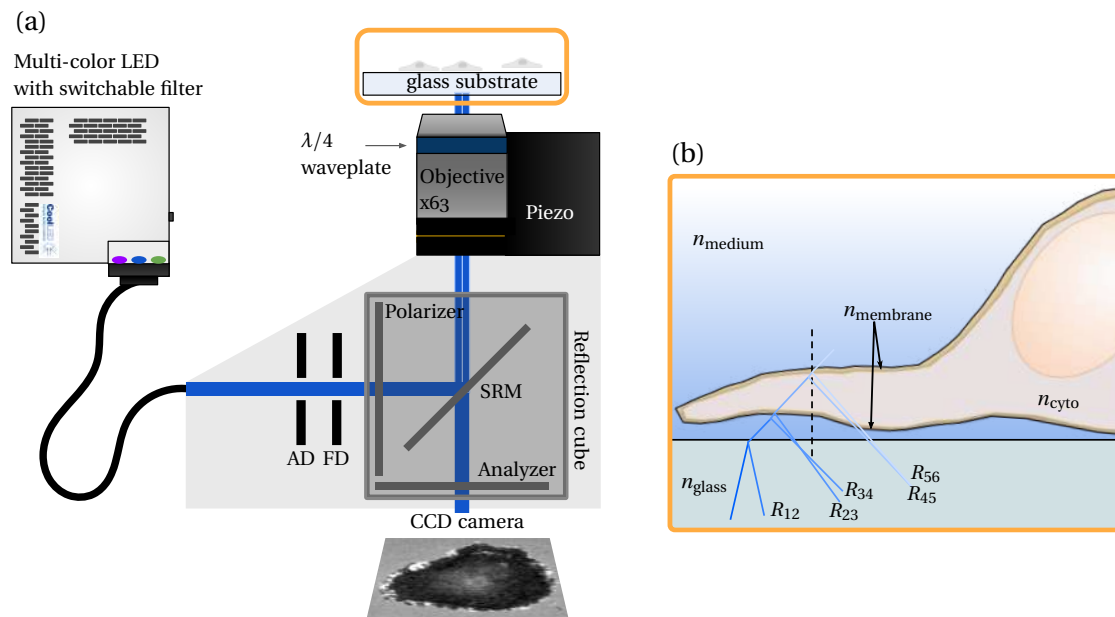


FIGURE 5.1 – The RICM microscopy technique. a) Optical path of the light from the LED light source to image formation. b) Zoom at the cell-surface interface, showing light reflection across each interface, characterized by a change in refractive index.

Figure 5.1b emphasizes what happens at the interface between the glass and the sample. Light is reflected and refracted every time there is a change in refractive index. The reflected beams interfere together, forming the RICM image [104].

5.2.3.2 Spreading assay protocol

Primary NK assay. Freshly isolated primary human NK cells were added at a concentration of 200 000 cells/mL in an uncoated eight-well chambered polymer coverslip-bottom from Ibidi (80821, Ibidi®). Surface preparation follows the protocol described in section 5.2.1. The Ibidi chamber was then placed on a microscope at 37°C. Before the experiment, the PBS was replaced with C7b-21 bispecific antibody at various concentrations and left for 30 minutes before adding NK cells. For the positive control, the antiCD16 antibody was introduced at a concentration of 26 nM. Cell spreading dynamics was observed in RICM. An antireflex Zeiss objective

(NA = 1.25) was used with a green LED light source ($\lambda = 546$ nm) and a 14-bit CCD detector (Andor iXonEM, Oxford instruments). This configuration allows live cell observations at 37°C. Images were acquired after cell deposition in the device. To evaluate the spreading kinetics of NK cells, multiple fields of view were selected (sixteen per condition) and subjected to cyclic imaging over a 10-minute interval, facilitated by a motorized stage from Physik Instrumente, Germany. The temporal interval between successive images of a given field typically ranged from 15 to 20 seconds.

5.2.3.3 Protocol for reconstruction acquisition

Reconstruction of the topography of a cell or model system requires a variation of the control parameters of the RICM microscopy technique, such as the wavelength of the incoming light λ and the INA controlled by the aperture diaphragm. Therefore, a system intended for reconstruction has to be imaged using as many λ and INA combinations as practically achievable. In practice, we imaged the systems with up to three colors provided by the CoolLED pE-300^{ultra} (UV, blue, and green) combined with up to five INA regularly spaced between 0.38 and 1.15 (yielding 15 images). In addition, to limit the amount of noise the process is reiterated many times on fixed samples. We use a piezo to compensate for a slight focus shift as the color changes, due to a significant chromatic aberration of the antilex objective.

5.3 Results

5.3.1 Anatomy of a RICM image

The field diaphragm is conjugated to the focal plane which is adjusted at the surface of the sample, making it a convenient reference to find the correct focus. Figure 5.2 showcases what the diaphragm looks like on the RICM image if it is not fully opened during acquisition. Spread cells make a footprint with well-defined contours, usually darker than the background. Hovering cells, usually interacting with the surface at a larger distance, can be seen as bright blobs, sometimes containing interference fringes. Leftover RBCs that have not been filtered properly from the blood bag can also be observed in RICM as bright blobs with characteristic interference fringes quite easy to distinguish from hovering NK cells.

Overall, the background can be quite nonuniform and depends on the INA, λ but also the surface layers and thickness of the medium.

5.3.2 An improved RICM normalization technique

A critical step in the analysis of RICM images, whether for segmentation or reconstruction, is the normalization. Normalization, in this framework, involves reconstructing the background image. The acquisition of a “white” image before cell

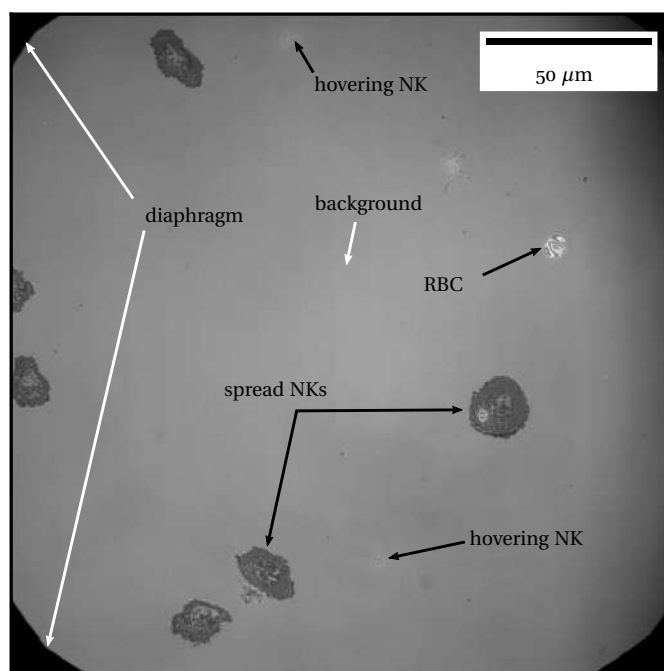


FIGURE 5.2 – Anatomy of a RICM image. Hovering cells are bright spots. Spread cells are usually darker than the background, on average. Interference fringes at cell edges can betray a topographical slope, such as the upper membrane thinning out at the tip of a lamellipodium. RBCs can remain from the blood filtering, but they never spread on our functionalized surfaces. The field diaphragm is visible at the edges.

introduction can be painstaking as several positions have to be imaged, usually for each well, properly labeled to be assembled into a background image post-acquisition. The introduction of the cell medium can create reflections that are not captured by the “white” image and shift the intensity values slightly. As a result, we propose refinements on the median-background technique which turned out to be the easiest and least biased background estimation technique in the context of spreading assays. We describe the upgraded pipeline in figure 5.3. We assume that there is a regularity in the background for each well and generate a single background image per well. In some instances (such as close to a well edge) we observed that this assumption does not hold, in which case the best background estimate can only be generated from the very first frames of the movies (before cell spreading) or using a model estimate.

The first refinement over previous methods is to mask roughly anything that is on the early frames of the movies, in such a way that the masked pixels are ignored in the pixel-by-pixel median projection. This step introduces two tuning parameters; the size of the standard-deviation filter k and a threshold value on the filtered image SD_{thresh} , that may have to be tuned every time*. This refinement allowed us to

*. This normalization procedure can also apply to brightfield images, in which case we know that the parameters change considerably.

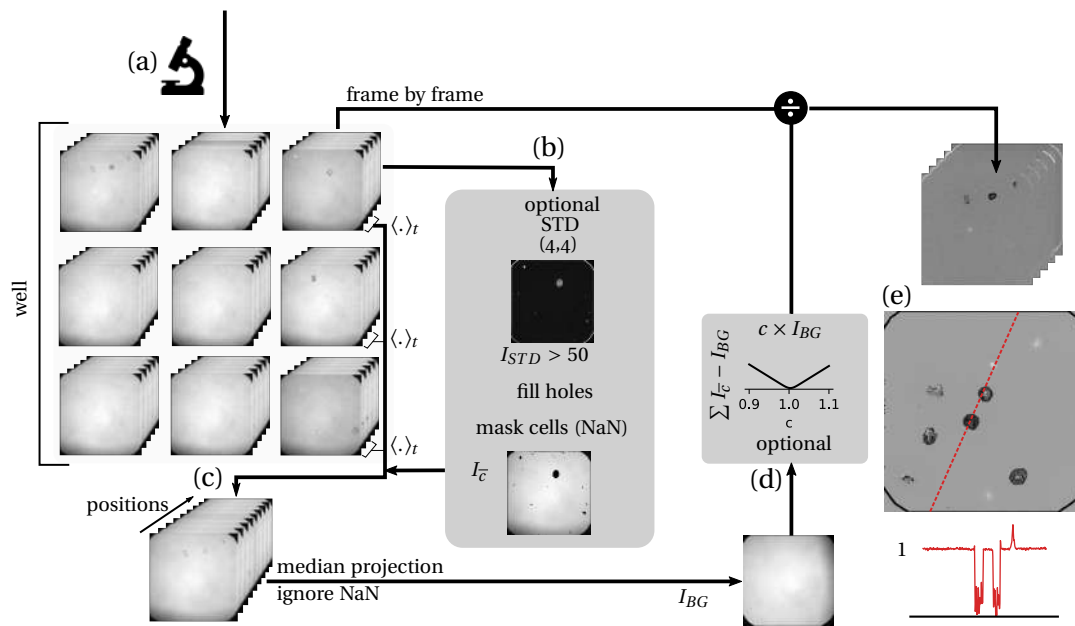


FIGURE 5.3 – Improved pipeline for RICM normalization. a) A single background is reconstructed for each well by exploiting each position. The initial frames of each position are first averaged. b) If cells are already visible in these early frames, a rough segmentation with a standard deviation filter and a fill holes operation is performed to mark the cells as not-a-number (NaN). c) The background is reconstructed by performing a median projection of the average initial frame across all positions, ignoring NaN values. Each frame of each position is divided by the background image to be normalized. d) Optionally, the values of the estimated background can be amplified to match better with the values of the background of the image. e) A RICM intensity profile on a normalized image shows how spread cells appear darker than the background and hovering cells appear brighter. The normalized image now has a uniform background.

reconstruct an accurate background on 1) fixed samples, 2) spreading assays where the sedimentation time was particularly fast, *i.e.* where a lot of cells are already spread at the start of recording. An example of the effect of the normalization on the distribution of intensities is shown in figure 5.4.

The assumption that one background image is enough to fit all positions and time points within a well may be overly optimistic. Therefore, we propose a second refinement, which consists of modulating the background image to match that of each image as well as possible. The instantaneous and incomplete background for each image is estimated using the standard deviation filter technique. The difference between the modulated well-background and the image's background is assessed on the non-masked values using MSE. The optimal modulating factor c is then retained for the well-background and we perform the normalization through division.

We implemented this pipeline in a Jupyter Notebook that can be directly applied to a CellDetective experiment well.

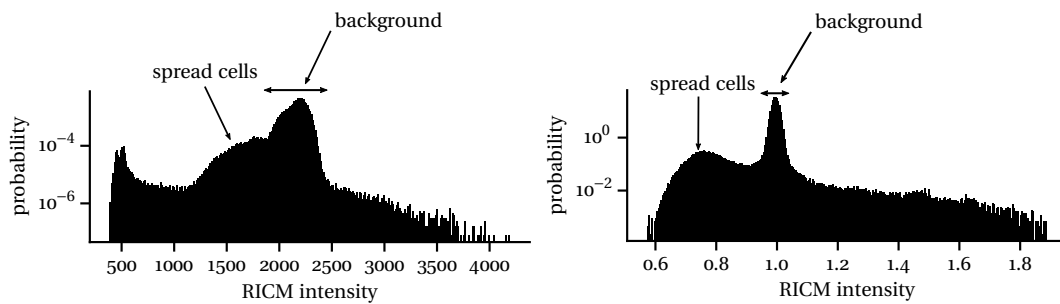


FIGURE 5.4 – RICM normalization : histograms. Histogram of the intensities of a single RICM image of spreading NK cells before and after normalization by the background, using the method described above.

5.3.3 Alignment on surface defects

The registration of RICM images is difficult because of the scarcity of anchor objects. Before cell spreading, the only clue that the image is not properly registered is the jiggly motion of surface defects. We adapted a technique, that I developed for traction force microscopy images (article 1), to the registration of RICM images. The method illustrated in figure 5.5 consists of tracking the surface defects using either TrackMate or Trackpy's Laplacian-of-Gaussian-like detectors. If needed, ROIs can be defined before tracking, limiting the number of false positive (FP) detections. Then we filter out the shortest tracks and estimate the mean displacement of all objects between each frame. This mean displacement signal estimate can be incomplete due to gaps in the trajectories. If so, we interpolate the gaps in the signal and then proceed with correcting for the displacement. Since a lot of these displacements are of the order of the pixel size, each image is Fourier-transformed and the opposite shift is applied in Fourier space. Then we inverse-Fourier transform the image. All images are thus properly aligned to the initial frame of the movie, which facilitates cell tracking and enables accurate cell dynamics quantification.

5.3.4 Single-cell analysis with Celldetective

The results presented in the following sections were obtained from a spreading assay experiment conducted by Dalia El-Arawi.

Segmentation Since we routinely normalize by the background RICM images as a first step towards being quantitative, we can quite easily apply traditional segmentation pipelines, as long as the cell density is not too high. For high-quality images, we can perform kernel-free segmentation, which preserves optimally the contour of the cells. This process is illustrated in figure 5.6. Since cells can be both brighter (hovering) and darker (spread) than the background, we subtract the mean background value of 1.0 from the image and then take the absolute value of all intensities before applying a threshold. If needed, we can apply a slight Gaussian blur after

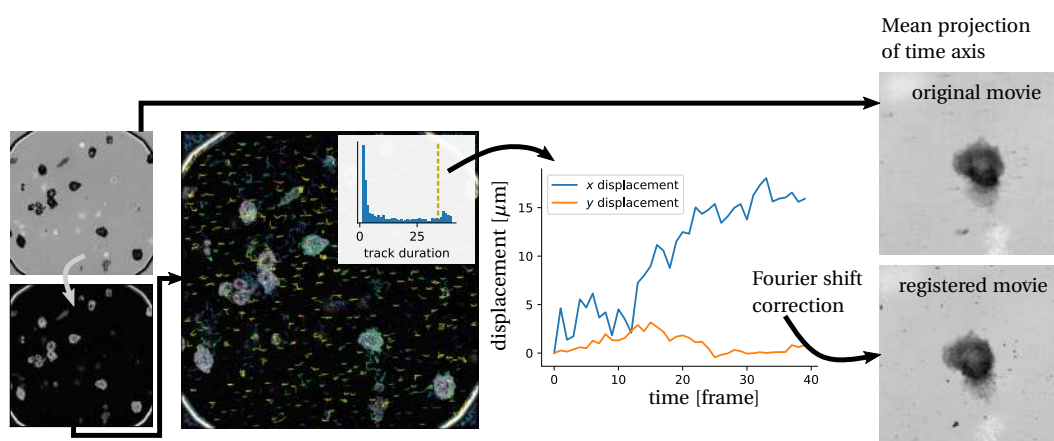


FIGURE 5.5 – Alignment on surface defects. A RISM stack is prefiltered to make the detection of surface defects easier. Since the image is normalized, the “prefilters” consist of removing 1 and taking the absolute value. TrackPy is applied with a diameter of 7 px and a search distance of 20 px to detect and track all objects on the image. The longest trajectories are selected and the mean $-x$ and $-y$ shift per frame is computed. The image is registered in Fourier space by applying the opposite shift to each frame resulting in a perfectly stable image where defects do not move, unlike cells as shown by mean projections of the time axis.

the absolute value operation to smooth contours and facilitate the segmentation of hovering cells. On lower quality images, *i.e.* where the background is not strictly 1.0 everywhere or where the focus is lost, we can apply a Gaussian blur and standard deviation filter (4×4 kernel) before applying a threshold on the standard-deviation image. We tune the marker separation to the average size of the cells and apply the watershed. Finally, we apply a filter on minute objects (less than 100 px^2) and a radial filter to eliminate FP detections near the image edge (where the field diaphragm usually triggers FP). The remaining FP detections come from surface defects and have to be handled manually as it can be hard to distinguish them from a cell that just started spreading, without integrating time information.

The kernel-free segmentation solution was a great starting point to pre-annotate the cells for segmentation using a Deep-learning model. We used it extensively to build a dataset of primary NK cells segmented in RISM. This dataset was used to train a new Cellpose model sensitive to both hovering and spread cells. This model could then be used as an alternative segmentation solution, able to ignore surface defects and segment cells at much higher densities. A variant Cellpose model was generated from combined brightfield and RISM images, for an even more robust segmentation of cells. For this configuration, we annotated the union of the cell shape in brightfield and RISM. For the hovering cell, the shape was observed to be slightly larger in brightfield although the hovering spot in RISM reflected well the shape of the cell, whereas for a spread cell, we usually observed a good match between the contours seen in brightfield and the contours of the footprint in RISM. On the other hand, the transition between hovering and spread cells using such annotations can be quite tricky, the cell becoming darker in RISM in only sub-

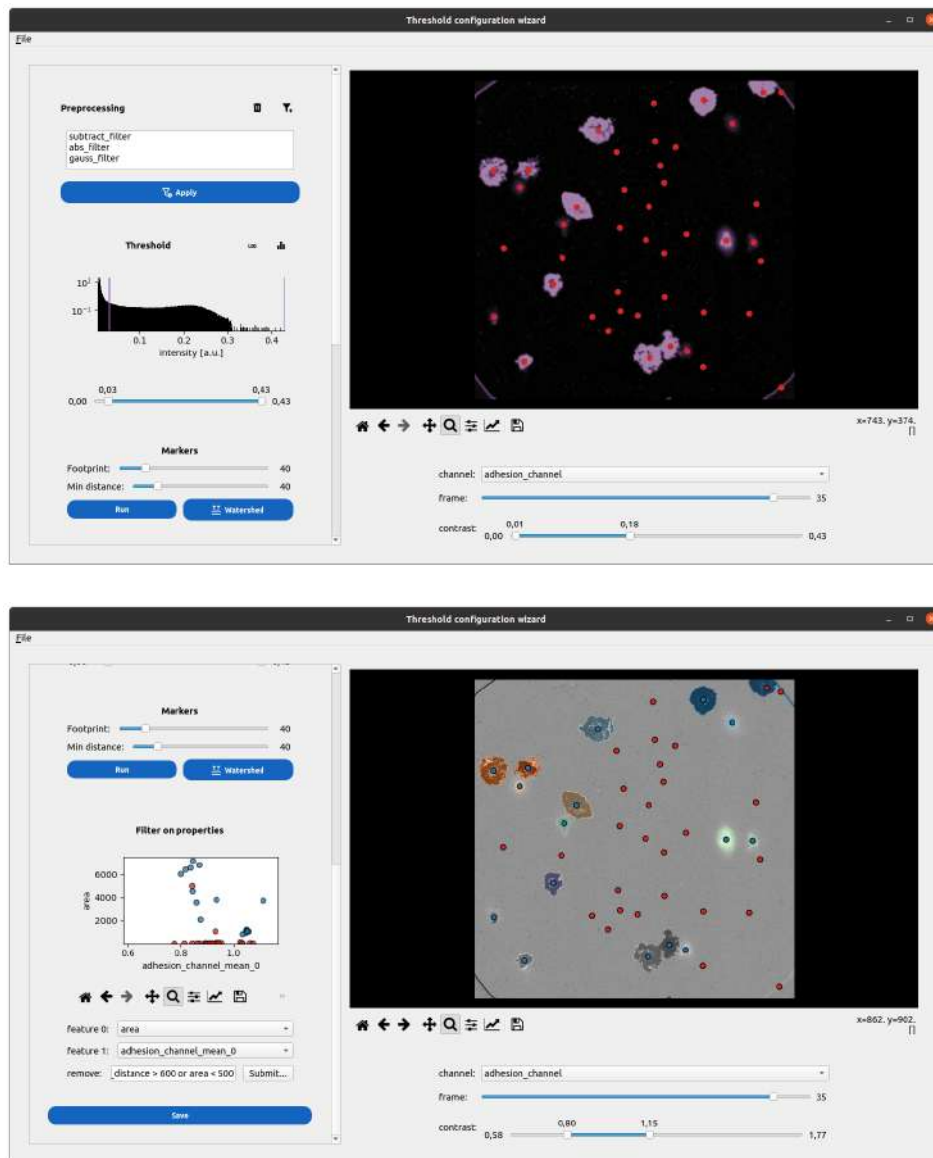


FIGURE 5.6 – Traditional segmentation pipeline for RICM. The TCW in Celldetective is applied to a RICM image to segment both spread and hovering cells. Top : the `subtract_filter` removes one to the image and the `abs_filter` takes the absolute value of the image. A Gaussian blur (kernel 4 px) is applied to smooth the edges of hovering cells. A threshold is applied to the transformed image and peak detection is performed in a footprint size of 40 px allowing a minimum distance of 40 px. Bottom : watershed is applied and a filter is applied on single object features to remove objects with an area smaller than 500 px² and objects beyond a radial distance of 600 px (at image edge such as diaphragm region).

regions of its segmented surface, leading to complications in intensity measurements. Since these models are quite recent, the results presented in the following sections are based on traditional segmentation pipelines using either RICM or brightfield as the input instead, avoiding these complications.

Tracking Since the morpho-tonal transition of spreading cells is quite abrupt, we do not use features in the tracking module. The “apoptosis”, and “branch” hypotheses are removed from bTrack. The first position in the trajectory is backpropagated (sustained) to the beginning of the movie to be able to measure the background to the hovering cell transition. Track gaps are interpolated.

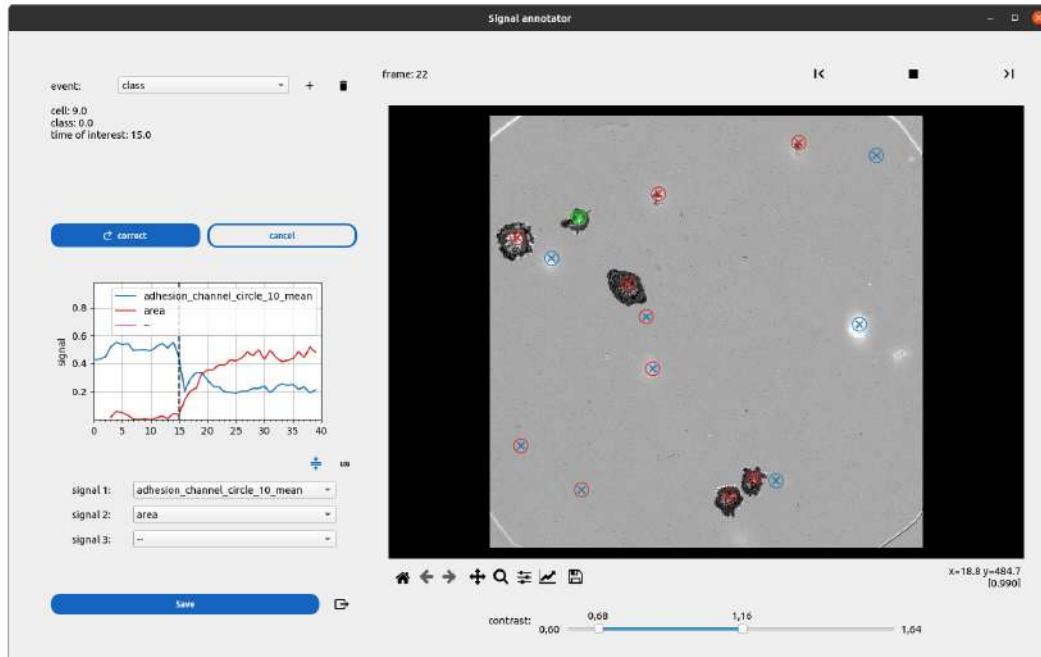


FIGURE 5.7 – Spreading event identification from signals. The continuous intensity signal coupled with the area signal are used to estimate t_{spread} . The signals of the selected cell (in green) are represented with an automatic per-feature normalization, on the left side of the window. The automatic estimate for t_{contact} is monitored and corrected, if needed, as a separate event class.

Measurements & signal analysis The RICM intensity is measured continuously in a circle of radius 10 pixels from the beginning of the movie to the end of a cell trajectory. In addition, we measure the average intensity over the cell masks and morphological features (area, eccentricity) from the masks. The time of first contact, t_{contact} is defined as the time of first detection of a cell, becoming visible for the first time on the RICM image, as a hovering cell. This time is collected automatically in Celldetective, before track interpolation. We use the signal annotator to annotate spreading events and define the spreading time t_{spread} as the time of first and irreversible[†] crossing of value 1.0 on the continuous intensity signal. The annotation process is illustrated in figure 5.7.

[†]. At the timescale of minutes

5.3.5 Hovering survival of cells

We characterized the hovering duration of primary NK cells on surfaces covered with C7b-21 bsAb at increasing concentration. Figure 5.8 showcases the different observed configurations.

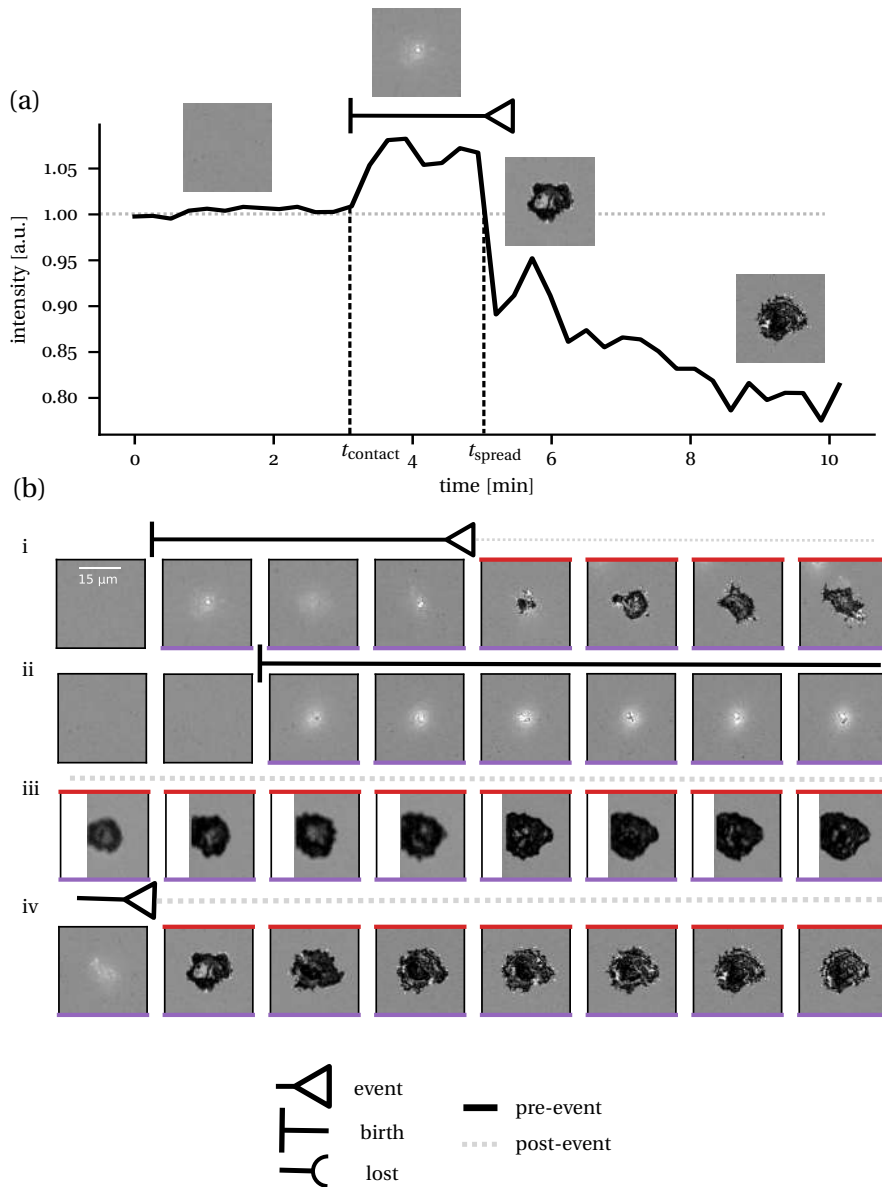


FIGURE 5.8 – Characterizing a hovering survival in RICM. a) A typical single-cell continuous intensity signal is illustrated with sample images corresponding to each phase, related to a contact and spreading event. i) Single-cell spreading events follow a sequence of appearing on the RICM image after a variable sedimentation time, hovering for a duration Δt_{hover} , before engaging in spreading. ii) Some cells are not observed to spread. iii) Other cells have spread earlier than the beginning of the acquisition, preventing us from recording the event sequence. iv) some cells are observed to spread but not to appear, which prevents an estimate of Δt_{hover} .

As NK cells sediment they start becoming visible as a bright blob when they get close enough to the functionalized surface and interact slightly. A complete timeline of a spreading event (figure 5.8a) involves first an appearance of the cell on the image (the “birth”, characterized by a time t_{contact} , then the cell hovers for a duration $\Delta t_{\text{hover}} = t_{\text{spread}} - t_{\text{contact}}$, before engaging in an irreversible spreading at t_{spread} . In some cases, the spreading event was not observed during the observation window, as in figure 5.8b. Therefore the duration Δt_{hover} is right censored, which can be handled in a survival framework. Similarly, some cells are already spread at the beginning of the observation and have to be excluded from survival analysis, although they can be counted when studying the dynamic (or static) fraction of adhered cells over time (figure 5.8c). Finally, some cells might have a left censored Δt_{hover} because they were already close to the surface at the beginning of the observation and t_{contact} could not be estimated.

The hovering duration Δt_{hover} or the decision time for the NK to spread after initial interaction with the surface ranged from a few dozen seconds to a few minutes with the human primary NK cells on bsAb covered surfaces (C7b-21, CE4-21). In a different system of mice T cells, the hovering duration was much shorter, in the order of a few seconds only, requiring a faster acquisition rate. In some conditions, the cells did not exhibit a clear hovering/spread binary state, making this kind of quantification quite ill-defined. For the data presented here, we ensured first that the vast majority of cells could fit in this hovering/spread description. Figure 5.9 shows the measured Δt_{hover} for increasing concentration of C7b-21 bsAb. We observe two things : 1) a qualitative decrease of the hovering duration with the increase of bsAb concentration and 2) a strong increase in the number of durations measured per condition, and therefore the number of spreading events.

As a result, it is quite natural to adopt instead a survival representation, that describes the chance for a hovering cell to spread over time. With the Kaplan-Meier formulation, each cell is synchronized at t_{contact} . Figure 5.10a shows the survival function associated with each antibody concentration. In a nutshell, increasing the concentration increases both the slope (*i.e.* the decision rate for the cells to spread) and the final adhered fraction. The final fraction saturates with the concentration whereas the decision rate keeps increasing. This survival quantity can be compared to what could be achieved before, namely the fraction of spread cells at any time point (in absolute observation time, without any synchronization). Figure 5.10b shows this quantity over time. The first striking difference is that the fraction seems to increase linearly over time for each concentration. This “linear response” depends on two quantities : the sedimentation time of a cell (which can be uncontrolled across conditions) and the hovering time of the cell. Unlike the survival function, it includes all cells, as cells already spread at the beginning of the observation add an offset at the origin. The endpoint values are similar to one minus the endpoint of the survival function.

Figure 5.11a compares directly these two quantities for each concentration, showing a similar response of a saturation of the fraction of adhered cells with bsAb

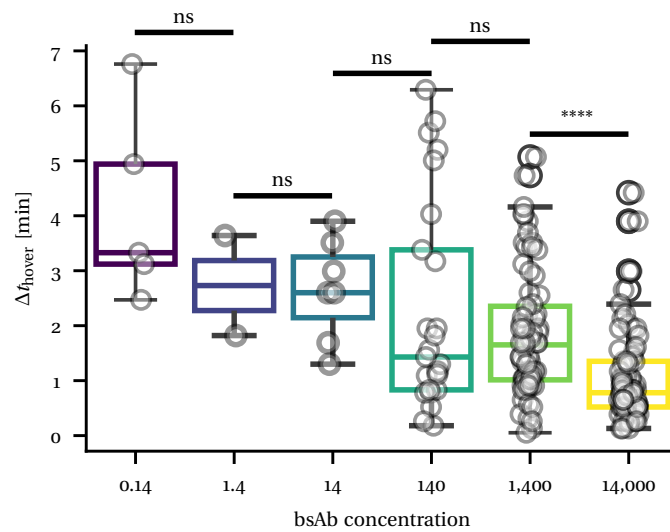


FIGURE 5.9 – Hovering duration distribution depends on bsAb concentration. Boxplot representing the Δt_{hover} measured for each cell that exhibited a spreading event for increasing concentrations of C7b-21 bsAb. A two-sample KS test for difference was applied between consecutive distributions.

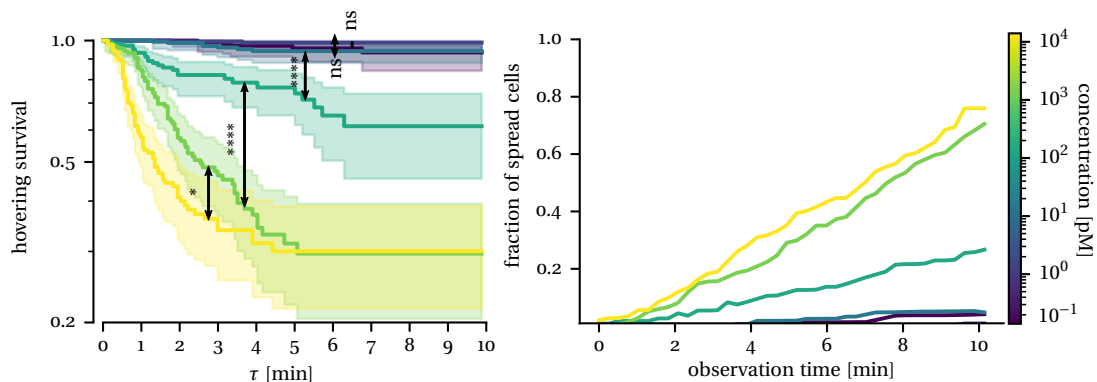


FIGURE 5.10 – Spreading survival. a) A Kaplan-Meier estimator is fit on the Δt_{hover} times and spreading events for each bsAb concentration condition, to show the probability of a cell to still be hovering after a hover duration τ . Statistical test for the difference between consecutive survival data is assessed using a pairwise log-rank test. b) The fraction of spread cells over the absolute observation time is decomposed for each bsAb concentration condition.

concentration. Figure 5.11b on the other hand highlights the absence of saturation in the decision rates measured using a pure exponential model (equation 4.10 from the previous chapter). We interpret these results as there being a fraction of NK cells that will never spread if it did not in the 0-5 min timescale after the first interaction with the surface at high bsAb concentration.

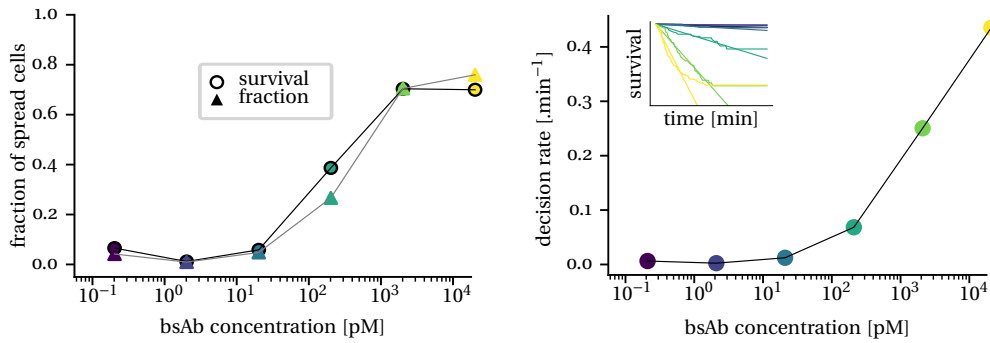


FIGURE 5.11 – Decision rates and spread fractions. a) One minus the endpoint survival, *i.e.* the probability to be spread after a duration $\tau = 10$ min, is represented for each bsAb concentration. Simultaneously, the endpoint fraction measured at the end of the observation is represented for each condition. b) the hovering survival functions are fit with a pure exponential model (equation 4.10) over the first 5 minutes after first appearance ($\tau \leq 5$ min) for each bsAb concentration.

5.3.6 Spreading dynamics

In the previous section, we only focused on the decision time and fraction of the NK cells that decide to spread without trying to characterize the spreading event itself. Visually, a spreading event in RICM is a transition from a bright blob-like object to a relatively dark cell (compared to the background), with well-defined contours and a larger size than the hovering blob. As a result, we looked closely at the RICM intensity and area signals around the spreading time t_{spread} . Figure 5.12 shows the area signal for each spreading cell collapsed at t_{spread} .

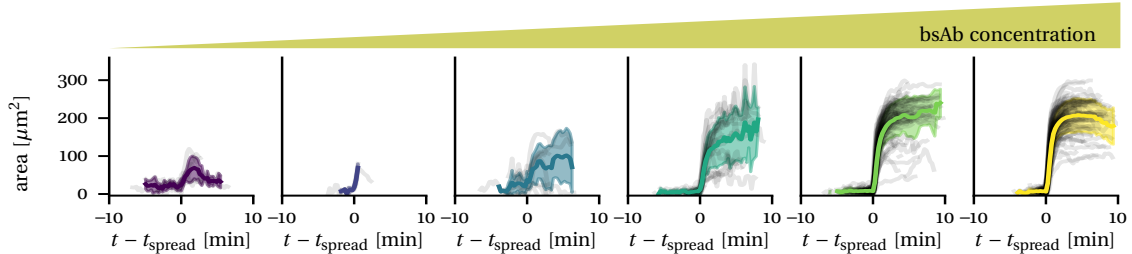


FIGURE 5.12 – Spreading area response. For each bsAb concentration, each single-cell area signal is represented collapsed at t_{spread} . The thick colored line is the mean response across all cells, with the standard deviation.

The first observation is that at low bsAb concentration, the few cells that spread never reach a large area. The second observation is that there is little difference in maximum area between 1 nM and 10 nM, the highest concentrations. Single-cell areas in the intermediate concentration of 100 pM seem to keep increasing after 10 minutes, on average, despite not reaching the maximum area observed at higher concentrations. Looking up close, we occasionally detected almost biphasic spreading for some of the cells, as shown in figure 5.13.

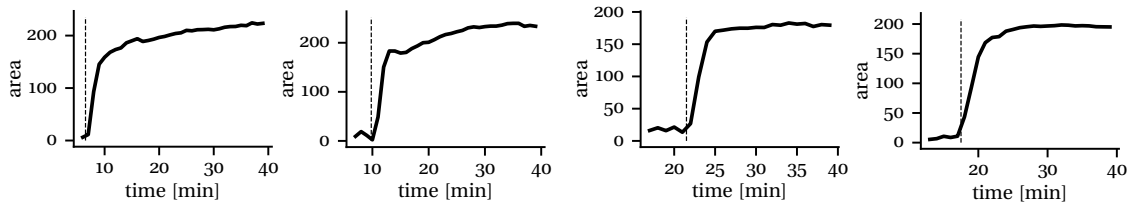


FIGURE 5.13 – Spreading area of single-cells. The vertical dashed line corresponds to t_{spread} . The area of the cell mask is in μm^2 . Some cells keep spreading at a steady but slower rate after the early spreading phase.

To dig deeper, while accounting for this observation, we decided to study the spreading rate for the cells in a non-parametric approach. We proposed another survival formulation for the spreading of the cells : the time of reference is t_{spread} (therefore all non-spreading cells are excluded) and the event time is the time at which the cell reaches its maximum spreading area $t_{\text{area-max}}$, defining Δt_{spread} . As a result, cells that did not attain their maximum spreading area during the observation are considered as “no event”. In practice, we realized that taking the time of the maximum area value as $t_{\text{area-max}}$ was quite noisy, due to occasional focus loss and segmentation errors. Instead, we took the time at which the area reached 90 % of the area max as our event completion time, which was much more stable and realistic. A pitfall of this approach is that if the maximum area event happens shortly after the end of the acquisition, then 90 % of the maximum area event was achieved before the end of observation and the cell is misclassified as exhibiting no event. Figure 5.14 shows the “spreading survival” for the three highest bsAb concentration conditions, where many cells do spread.

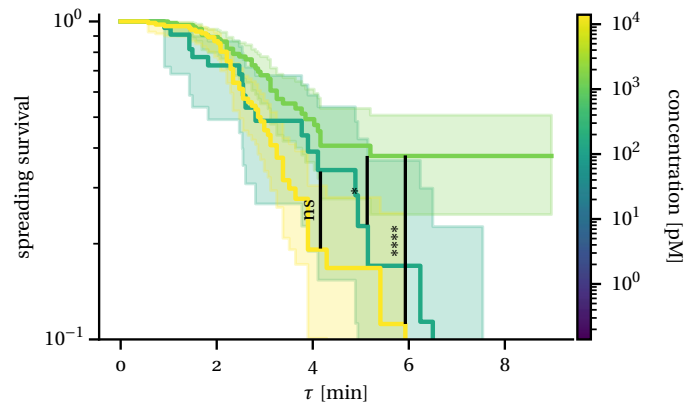


FIGURE 5.14 – Spreading survival. Fraction of the spreading cells that reached 90 % of their maximum spreading area within a duration $\tau = t_{\text{area-max}} - t_{\text{spread}}$. For clarity, only the 100 pM, 1 nM, and 10 nM bsAb concentrations are shown, for which there are many spreading events. Statistical difference between the survival functions was assessed using a pairwise log-rank test.

All survival functions share the same delay at the beginning, suggesting an incompressible time for spreading. Differences in rate and final spread fraction start to

emerge after 2 minutes, particularly between the 1 nM and 10 nM conditions. The 100 pM estimate is quite noisy due to the smaller number of spreading cells. At 1 nM, only around 60 % of the cells reached 90 % of their maximum observed area during the observation, whereas at 10 nM pretty much all cells reached it before the end of the observation. To decompose the problem further, and decorrelate survival results from the fraction of cells that exhibited the event, we can look at the distribution of maximum spreading areas, spreading times Δt_{spread} and velocities v_{spread} . Figure 5.15 shows the distribution of these three quantities for each bsAb concentration condition. Due to the survival formalism, any cell that does not reach a maximum area before the end of the observation is not included here. As mentioned before, very few cells spread in the 0.14, 1.4, and 14 pM conditions. The maximum spreading area seems to saturate after 1.4 nM. For the spreading duration, the transition point seems also to be the 140 pM condition where a few cells take a long time to reach their maximum area. The spreading duration seems to slightly go down at the highest bsAb concentration, without significance. Finally, the spreading rate shows a saturated increase, with an EC_{50} somewhere between 140 pM and 1.4 nM.

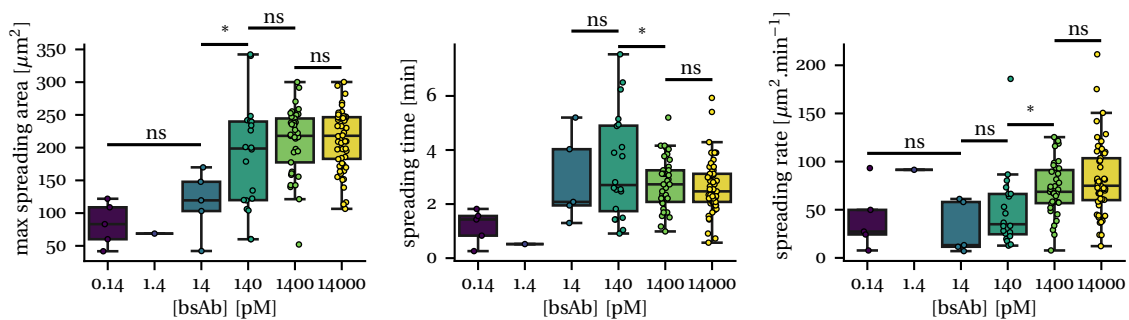


FIGURE 5.15 – Spreading quantification. Spreading cells that reached their maximum spreading area during the observation have their maximum area, spreading duration ($\Delta t_{\text{spread}} = t_{90\% \text{area-max}} - t_{\text{spread}}$) and spreading rate $\frac{d}{dt} \text{area} = (\text{max area} - \text{area}(t_{\text{spread}})) / \Delta t_{\text{spread}}$. Independent Student's t-tests are performed between consecutive concentrations to test the hypothesis that the left distribution is lower (max spread area, rate) or higher (spreading time).

We emphasize again that a pitfall of the survival formulation to quantify spreading is that all cells not reaching their maximum area are excluded, reducing the size of the distributions and blurring statistical differences. We devised another way to measure the spread rate which does not rely on any estimate of the maximum area. The idea is to perform an instantaneous derivative of the area signal and to pick up the value at t_{spread} , yielding an early estimator of spreading rate. Figure 5.16 shows the distribution of this estimator for each concentration. Since the quantity can be computed for any cell that spreads, we achieve more statistical significance between each condition. A notable pitfall of an instantaneous estimate for the rate is that it cannot capture biphasic spreading patterns, which is reflected in the apparent

increase of the spread rate at 140 pM compared to the one measured previously. Similarly, there are very few low rates for the highest concentrations, unlike before, completely hiding inhomogeneities in spreading.

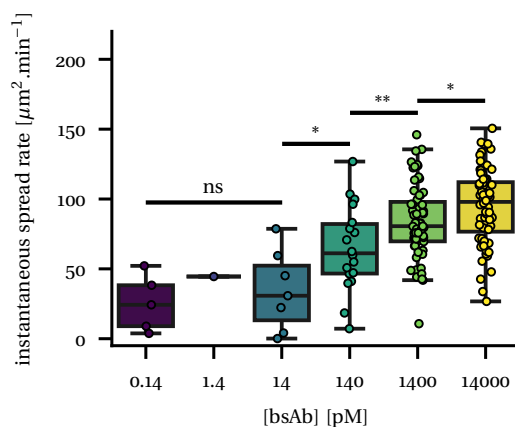


FIGURE 5.16 – Instantaneous spreading rate hides biphasic behavior. The area signal is differentiated with a sliding window of 5 frames (= 1 min 18 s) oriented forward (derivative at time t_k is estimated in the window $t_{k+5} - t_k$). The value of the derivative is picked up at t_{spread} . Independent Student's t-test is performed between consecutive concentrations to test the hypothesis that the left distribution is lower.

In addition to the area, the second signal to monitor during spreading events is the normalized RICM intensity signal, as the measured intensities relate to the topography of the cell (height, thickness) with the complication brought by the interferences. Any qualitative difference in RICM intensity between cells in similar surface conditions most certainly pertains to a different topography. Figure 5.17 shows single-cell intensity signals collapsed on the time of spreading t_{spread} .

The global pattern is that when a cell makes its first contact with the surface it is measured brighter than the background (~ 1.1). Then it decides to spread quasi-irreversibly at t_{spread} chosen as the moment the intensity crosses 1.0. Measuring the intensity in a circle and back-propagating the first position to the beginning of the movie allows us to capture the contrast between the background and the intensity of a hovering cell. At this transition, a single-cell signal exhibits a step function from 1 to about 1.1. Here, on the mean response, we observe a gradual increase in this region due to the asynchronicity of cell arrival on the surface. No obvious difference between the bsAb conditions emerges in this representation, except an apparent higher final intensity level in the low concentration conditions, with sometimes a slow return to 1.0 suggesting cells that do not spread tightly on the surface and that even engage in detaching. The last observation is that using the circle (isotropic) measurement instead of the cell mask shows a subtle rebound of the intensity right after t_{spread} , within the first minute at the highest concentrations (black arrows). A visual inspection showed that we are measuring the nuclear region of the cell that becomes transiently quite brighter than the cytoplasm in the early phase of spreading.

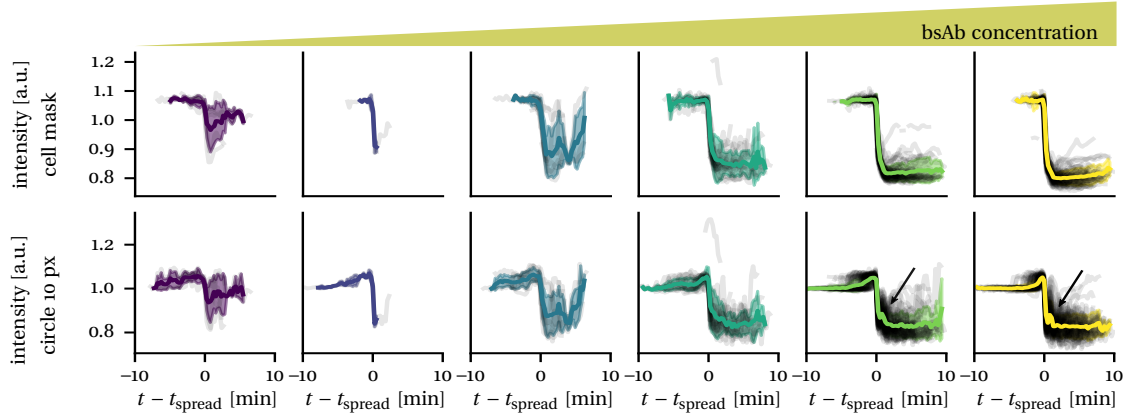


FIGURE 5.17 – RICM intensities during spreading. a) single-cell signals of the normalized RICM intensity averaged over the whole cell mask collapsed with respect to t_{spread} for each condition. The thick colored lines show the mean response across all cells, with standard deviation. b) The same representations except that it is the RICM intensity is averaged in a circle of 10 px ($\sim 2\mu\text{m}$) centered about the center of mass of the cell, making it a smaller region than the cell mask. A small rebound of the intensity after spreading is indicated by the black arrows.

To summarize, we can represent the mean response for each condition on the same plot for both the area signal and one of the intensity signals. This is represented in figure 5.18.

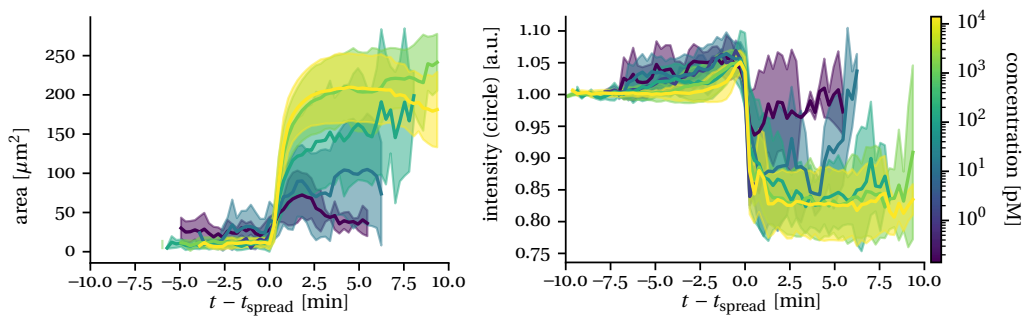


FIGURE 5.18 – Mean signal response during spreading. The mean of the single-cell area and RICM circle-measured intensity signals and the standard deviation is represented for all bsAb concentrations.

The mean area signal representation shows little difference between the two highest concentrations, which was captured by spreading rate estimates. For lower concentrations, both the rate and maximum area do not reach the same levels. The same thing can be said of the intensity signals, with the pM range intensity signals differing more and more from the nM range signals as the concentration decreases. To complete the story of spreading behavior, we can temporarily give less importance to time and study the phase portrait transitions in the (area,intensity) plane for spreading cells. Figure 5.19 shows these phase portraits for all conditions, using either the intensity local to the center of mass (a) or the intensity averaged over the whole cell mask (b). The rebound of the intensity at the center shortly after

spreading is even more visible using this kind of representation, on the nM bsAb concentrations.

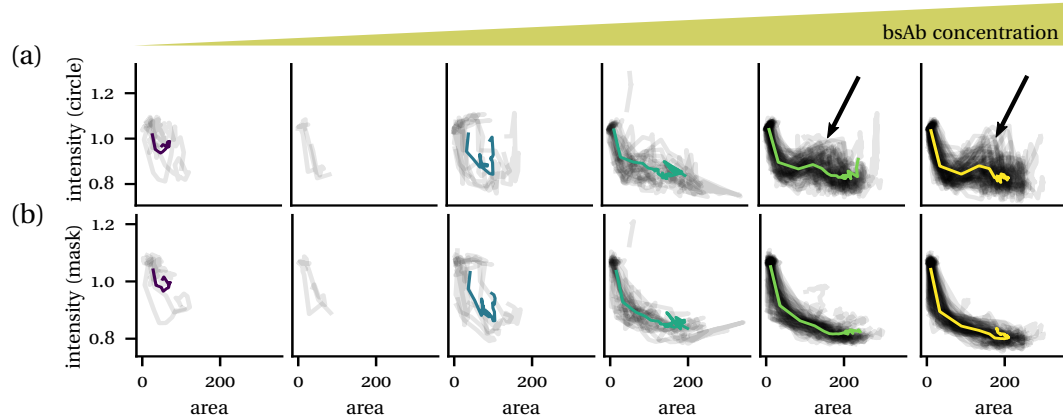


FIGURE 5.19 – Spreading phase portrait in the (area, intensity) plane. The transition from a small blob-like bright object (top left) to a darker and larger cell is shown for each spreading single cell in all conditions. a) the intensity measurement represented in $-y$ is the mean intensity in a 10 px ($2 \mu\text{m}$) circle centered about the center of mass of the cell (\sim nuclear region). Black arrows indicate a rebound in the intensity value as the cells approach their maximum area. b) the intensity is the mean area over the cell mask. Colored lines show the mean (area,intensity) response across all cells of the condition, all synchronized at t_{spread} .

In figure 5.20, we compare directly the mean phase-portrait traces for these two highest C7b-21 bsAb concentrations as well as with a positive control (anti-CD16 at a 26 nM concentration) that was omitted from the discussion of this section for clarity. This positive control exhibited strictly the same maximum spreading areas and similar spreading rates. The two bsAb traces are very similar, with a small lateral shift in the rebound region which could be explained by the slightly different spreading rates associated with these conditions. For the anti-CD16 condition, on the other hand, the rebound is stronger, reaching higher intensity values. The visual assessment confirms that it is due to the nuclear region, as illustrated in the sample images of a single cell spreading in this condition. We understand this difference as being due to a different structural reorganization of the cell upon adhesion, such as a shorter distance of the nucleus to the surface in the control.

In a different system of mice T cells (collaboration with Marie Dessard), we observed fast and strong detaching of the cells that we could also characterize using a survival formulation. For the human primary NK cells presented here, detaching was quite modest and was not worth investigating.

5.3.7 Texture for cell classification

We exploited texture measurements that can be performed in Celldetective to classify different cell phenotypes observed in spreading assay experiments. We found it

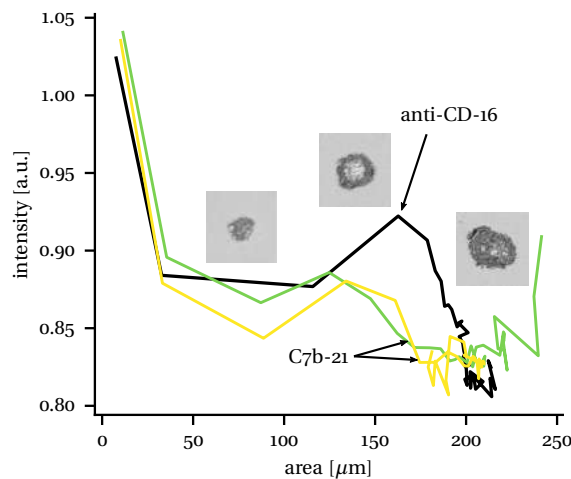


FIGURE 5.20 – Spreading phase portrait varies with the antibody. The mean (area,intensity[*circle*]) trace for the two highest C7b-21 concentrations is compared to that of a positive control on an anti-CD16 surface. The sample images illustrate a single cell spreading on an anti-CD16 surface.

challenging to interpret texture measurements in general. Here we exploit a bright-field image containing three cell phenotypes that exhibit strong texture differences to better understand the interplay between texture features and provide a viable classification method. To avoid background heterogeneities that could bias texture measurements, the image was normalized using the technique described in section 5.3.2. An initial segmentation of the cells was performed in Celldetective using a traditional pipeline with a standard deviation filter. Segmentation errors (particularly on spread cells) were corrected by hand for this study. Three “fake” background cells were added by hand, to collect background texture measurements. Texture measurements were carried out directly in Celldetective. The image was downscaled by 50 %, normalized using the 0.01 % and 99.9 % percentiles, and digitized to 256 values. The distance over which to evaluate co-gray-level probabilities was set to 1. The 13 Haralick texture features were measured over each cell ROI, yielding one set of values per cell. Cell classes, among “spread NK cell”, “hovering NK cell” and “RBC” were annotated by hand in the signal annotator. Figure 5.21a shows the full field of view with all of the annotated cells. A quick visual assessment shows that spread NK cells have a poor contrast, being sometimes hard to distinguish from the background. Hovering NK and RBCs both exhibit a strong contrast, with a dark ring at the edge. RBCs have a very characteristic distribution of intensities with a bright ring at the periphery and a darker center.

Intuitively, texture is also a property of the image itself. To better understand how texture measurements relate to cells and not just the background we show the raw texture measurements for the cells on one hand and the background on the other hand in figure 5.21b. The first observation is that the range of values can be quite different for the 13 texture features. Second, cell texture can be higher or smaller

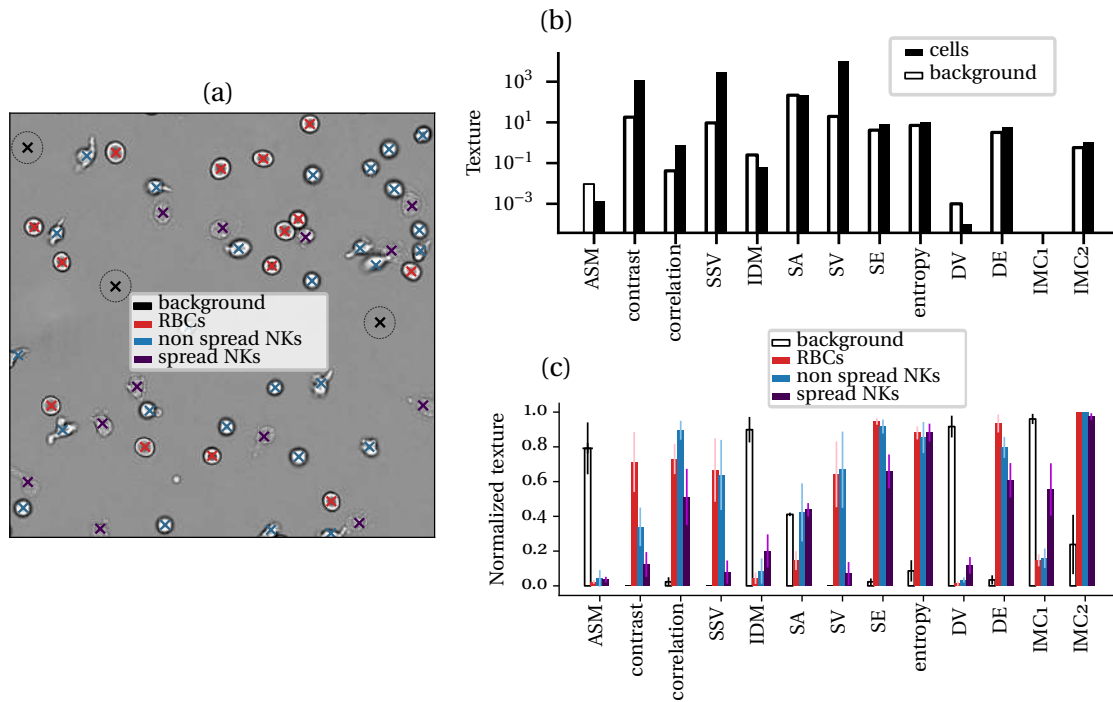


FIGURE 5.21 – Texture quantification in a spreading assay. a) spread (purple) and hovering (blue) NK cells, RBCs (red), and background “fake cells” had their texture features measured. b) The mean of each of the 13 Haralick texture features is compared between the cells and the background. ASM is short for angular second moment, SSV for sum of squares variance, IDM for inverse difference moment, SA for sum average, SV for sum variance, SE for sum entropy, DV for difference variance, DE for difference entropy, IMC1 and IMC2 for respectively information measure of correlation 1 & 2. c) Each texture feature is normalized independently using a min-max operation with bounds estimated from all measurements, including background. The bar plot shows, for each cell phenotype, the mean and the standard deviation. Outliers can compress the apparent range of the normalized values.

than background texture by up to two orders of magnitude. We perform a min-max normalization of each texture feature independently, including the background measurements. Results are shown in 5.21c decomposed by cell phenotype class. This representation shows quite clearly which texture features contain information to discriminate the cells. For example, the only feature we could describe qualitatively, the contrast, separates quite well the three phenotypes, with spread NK having the lowest contrast, followed by hovering NK and finally RBCs. The difference entropy measurement encapsulates similar information, whereas the correlation measurements put the hovering NK on top, above RBCs, and spread NK cells. The other features separate only one of the phenotypes from the others. For example, the sum average separates quite well hovering NK cells from RBCs.

Figure 5.23a shows the distributions associated with the three texture features that discriminate best the three cell phenotypes : contrast, correlation, and difference entropy. Statistical significance, measured by t-test is achieved for each distribution.

We wondered how stable these measurements were to image perturbation such

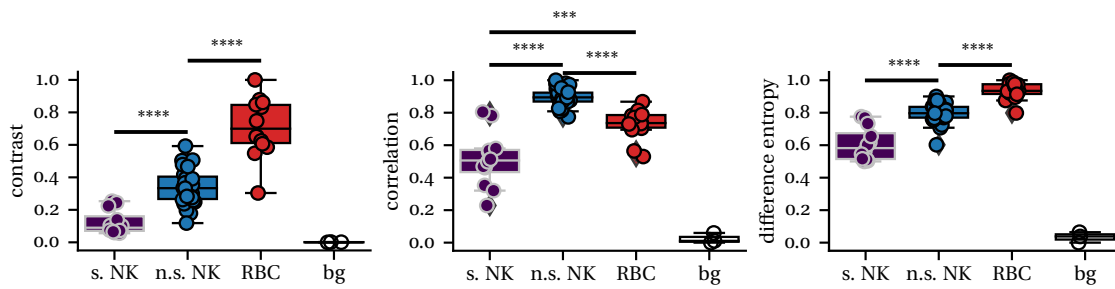


FIGURE 5.22 – Select texture features separate well the cell phenotypes. The distribution of contrast, correlation and difference entropy is shown decomposed by cell class. Statistical test for difference is assessed using independent t-tests.

as blur, that can often occur in a movie when focus is lost. The second open question was whether or not including background measurements can stabilize the normalization of the texture features, particularly when image conditions change slightly (blur, noise). In figure 5.23b, we show the amount of difference introduced by blurring the image with a Gaussian kernel of 2 px or 5 px. We assess the effect of including background measurements in the normalization. We observed on average over the 13 features less shift in the normalized values when the background was included in the normalization. The effect is quite strong for the correlation and difference entropy features. On the other hand, we observed that introducing noise in the image gave opposite results, including background measurements was increasing differences. Ideally, we would like to investigate stability over a movie to exploit texture features as signals just like any fluorescent or morphological features to characterize, for example, cell spreading.

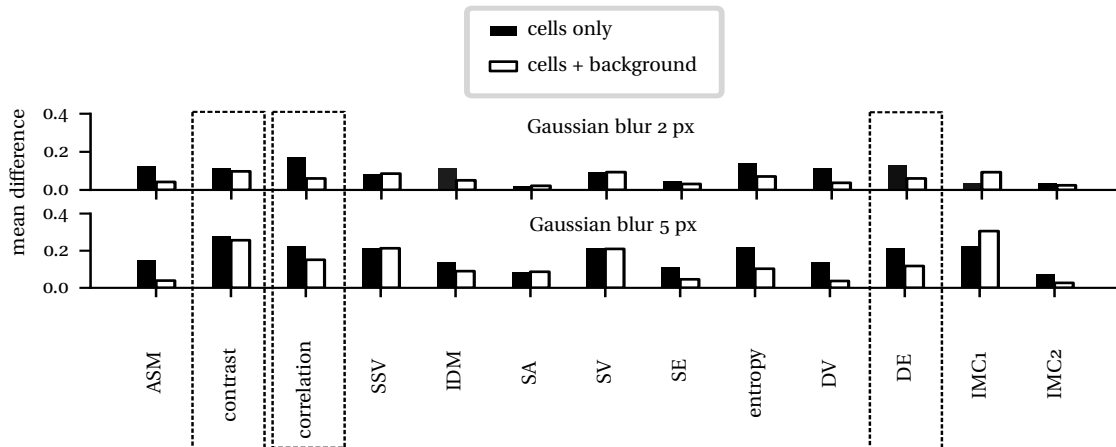


FIGURE 5.23 – Perturbation of image shifts texture values. The mean normalized texture absolute value shift is assessed when a Gaussian blur is applied (2 px kernel or 5 px kernel) either when no background measurement is included in the normalization (black) or when it is included (white). The features selected in figure 5.22 are highlighted. The average error over all features reaches 0.09 / 0.06 respectively without and with the background in the normalization at 2 px blur. At 5 pixels the error averages 0.17 / 0.13 for the same conditions.

To quantify the impression that the Haralick texture features contain all the information needed to classify the three phenotypes under study, we decided to build principal component analysis (PCA) representations. Figure 5.24 shows three different PCA representations : 1) without any background measurement, 2) with background measurements in the feature normalization and the PCA, 3) with background measurements only contributing to the normalization and omitted from the PCA. The three features we selected previously are shown in bold on the loading plot. Both approaches 1) and 2) give similar weights to most features, organizing them along different axes. Having the background in the PCA dwarfs the differences among the three cell phenotypes. The best separation is arguably achieved with method 3), where the select features also come out stronger than less relevant features concentrated at low weights.

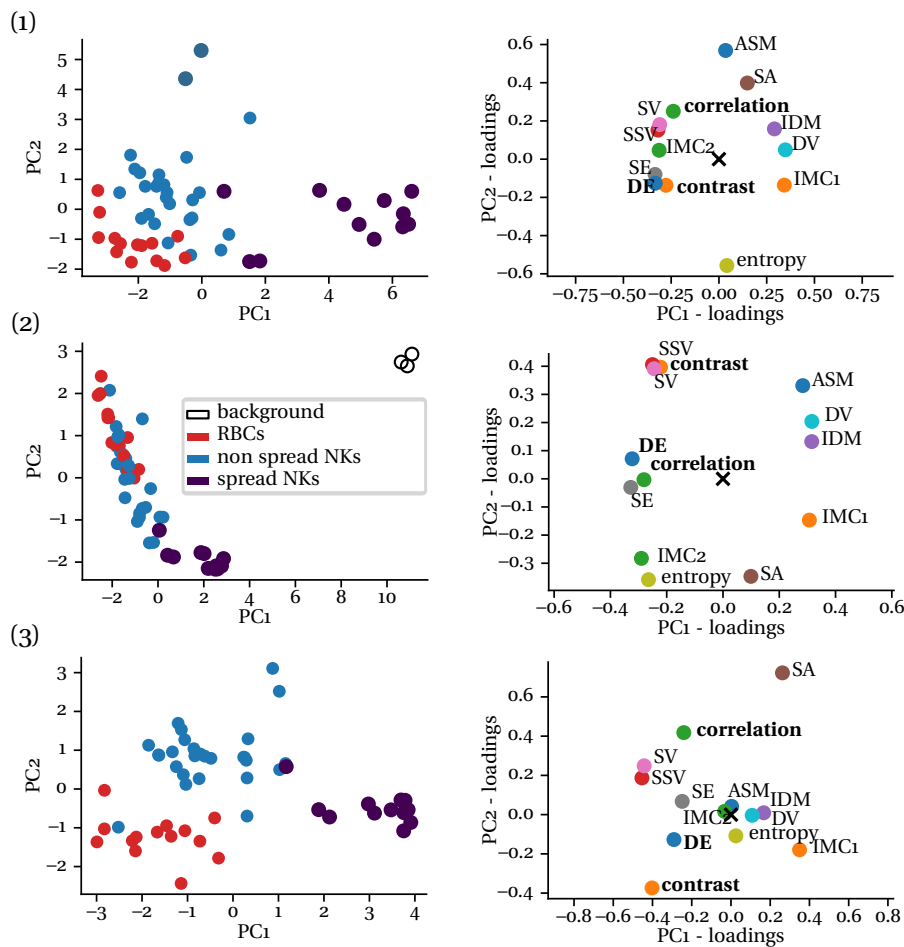


FIGURE 5.24 – PCA representations of texture features. A PCA with two principal components. The loading plot shows the weight attributed to each texture feature. 1) background measurements are excluded from standardization, 2) background textures are included in the standardization as well as in the PCA, and 3) background is included in the standardization but not in the PCA.

PCA does not provide classification per se. For that purpose we decided to turn

towards decision trees, a non-parametric supervised machine learning technique to classify data (and perform regression) from features. Decision trees are very simple to interpret as can be seen in figure 5.25. This instance first separates the data based on correlation, which we observed to be one of the most relevant features to separate the cell phenotypes. On the left branch, a cut on the sum average allows the safe classification of 12 RBCs out of 14. For the remaining data on the branch, a threshold on the inverse different moment separates one non-spread NK from 12 spread NK. Another way to read this is that if correlation ≤ 0.807 AND sum average ≤ 0.185 then most certainly we are looking at a RBC. The same kind of decomposition can be made on the right branch. A single decision tree will always find a solution to classify all of the data by overfitting. Instead, we can fit a random forest, with $n = 100$ such trees, on a fraction of the data. The idea is that even if a hundred trees overfit, their average prediction must be quite robust. We perform a five-fold cross-validation to estimate the average performance of a random forest trained on our data. We report an average balanced accuracy score of 0.91. Here the dataset was very small, containing around 50 cells. This implies that any decision tree of the random forest was trained with fewer points than this, which is not a lot in a 3-class problem.

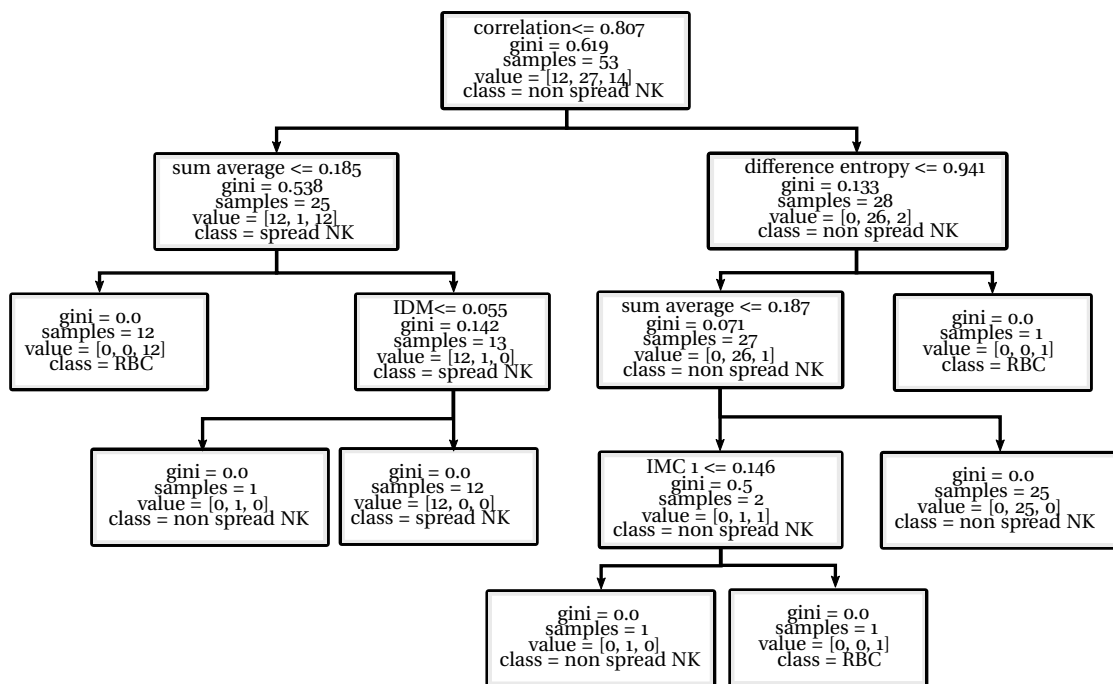


FIGURE 5.25 – Decision tree. A decision tree is fit on texture features to classify the three cell phenotypes. The Gini index measures how mixed or impure the dataset is at each branch level, with 0 being a perfectly pure dataset.

5.3.8 Deep-learning classification of cross-modality phenotypes

Measuring texture and other descriptors can be quite painstaking, requiring extreme care in the preprocessing steps. Not all cells can be identified by texture alone : sometimes it takes more than one modality to identify the cell clearly, and sometimes minute differences that can be seen by the eye are not well captured by tonal, textural, and morphological features. We have explored a completely different way to classify cells, that bypasses segmentation and measurement stages. We trained DL models to classify cells directly from multimodal images. While this process is quite standard in the community, there remains a gap of knowledge in biology labs where such techniques are rarely implemented (*e.g.* my host labs). We present the technique here as a potential future feature to Celldetective, that can provide the training data needed for such approaches.

Dataset. The dataset consists of (100 px × 100 px) crops ($\sim 20 \times 20 \mu\text{m}$) centered about the center of mass of NK and RBCs observed in both brightfield and RICM. The dataset was extracted from many spreading assay experiments for which cells were segmented and quantified using a Fiji filtering and thresholding pipeline[‡]. The classification of cells between “NK” and “RBC” was carried out by eye from both modalities. 1934 NK cells and 1247 RBCs were thus annotated. Each image was normalized independently using a percentile cut on each channel at 1 % and 99 %, with clipping. The data is partitioned into a 60 % train set, a 20 % validation set, and a 20 % test set.

Model. The model is a traditional convolutional encoder, consisting of three successive convolutions, batch normalization, and max pooling layers. The convolution is activated with ReLU to introduce nonlinearity. The last max pooling operation is replaced with a global average pooling layer to remove the X and Y dimensions and work on a vector representation, processed by the classification head. The head consists of a Dense layer for collection of the CNN output, a dropout layer at 50 % to fight overfitting, and a last layer of two neurons (for the two classes) activated with a sigmoid function.

Optimization. The optimizer is Adam, with a learning rate of 10^{-4} . Class weights are introduced to compensate for the slight class imbalance. The loss function is the binary cross-entropy. The batch size is set to 8. Since the classes are quite balanced, the model achieving the best accuracy on the validation set replaces the previous one at each epoch. The model is trained for a hundred epochs. The model’s accuracy is evaluated at over 99.4 % accuracy on the test set and avoids over-fitting thanks to the batch normalization layers and the dropout in the head.

To interpret what is learned by the model and how it simply works, we forced the model to output the tensor output at each layer of the convolutional core. We picked on one hand an image of a spread NK from the test set (figure 5.26) and on the other hand an image of a RBC surrounded by several RBCs (figure 5.27).

In each figure, the 2-channel input (respectively brightfield and RICM) is first

‡. This predates Celldetective, which accomplish the same thing.

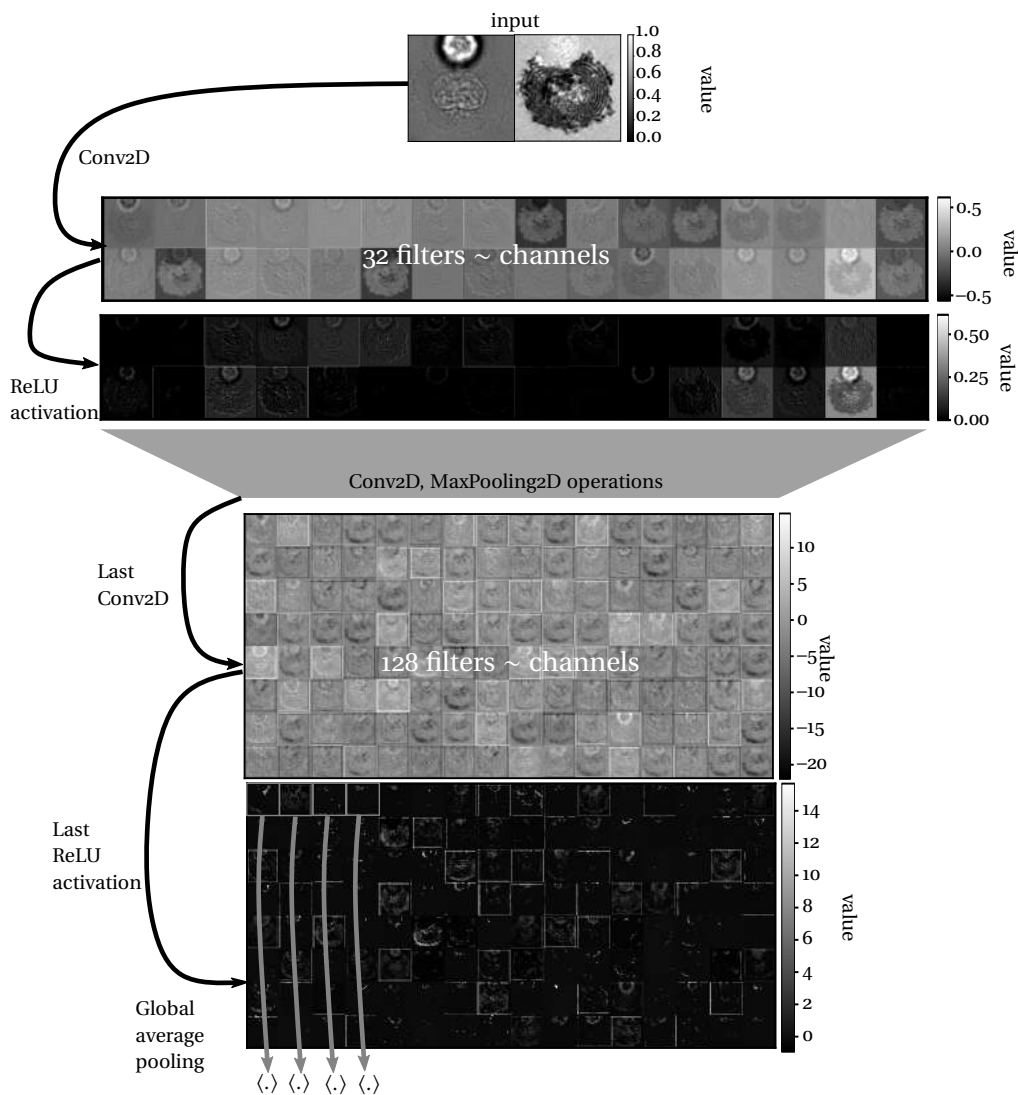


FIGURE 5.26 – CNN classifier activations : NK cell. A sampled multimodal image (brightfield & RICM) of a spread NK cell is processed by the convolution-based classifier. The output of the first convolution layer, the first ReLU activation, the last convolution layer, and the last ReLU activation are shown (not to scale). The global average pooling operation at the end compresses each filter image into its average value, turning the output tensor of dimension XYC into a vector of length C .

processed by 32 convolutions, associated with 32 kernels of shape $(3, 3, 2)$ whose coefficients have been determined by the model training process (plus 32 biases, but for simplicity we will ignore that). In other words, the 2-channel input is filtered with 32 different filters, yielding 32 representations mixing the multimodal input. Some values on these representations are positive and some are negative. This is where the ReLU activation function comes into play, by essentially clipping the negative values, and “switching off” irrelevant parts of the images. The X and Y dimensions of these images are divided by 2 using the max pooling operation (taking the maximum

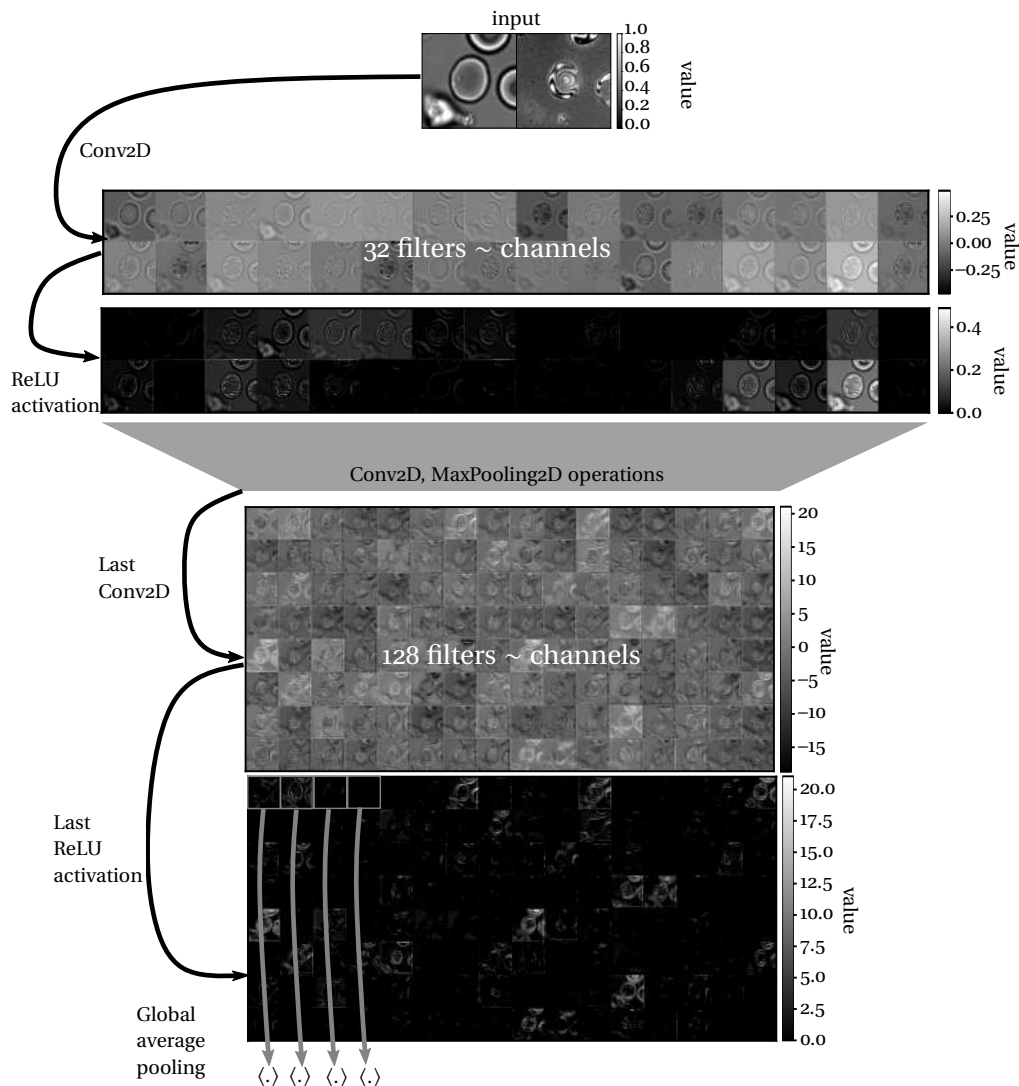


FIGURE 5.27 – CNN classifier activations : RBC. A sampled multimodal image (brightfield & RICM) of a RBC is processed by the same convolution-based classifier as the NK cell in figure 5.26. The output of the first convolution layer, the first ReLU activation, the last convolution layer, and the last ReLU activation are shown (not to scale). The filters showing strong activation can be different from the ones of the NK cell example. The global average pooling operation at the end compresses each filter image into its average value, turning the output tensor of dimension XYC into a vector of length C .

value to cast the values in a smaller matrix). This new representation becomes the input to the next layer and the process starts again. In both figures we show the output of the last convolution layer, generating 128 filters that are clipped with ReLU. This penultimate output of the convolutional core is critical. Depending on whether an NK or a RBC is on the image the same filters are activated. The global average pooling operation replaces each of the 128 filter images by its average value. The 128 filter images are effectively transformed into a 128-slot vector, not unlike the vectors

of 13 Haralick texture measurements we associated with similar cells before.

This classifier head forms different linear combinations of these 128 “measurements”, conceptually similar to PCA, except that the weights were “learned” during training. The ReLU activation switches off the negative neuron outputs. The dropout layer randomly switches off neurons to force the model to have backup neuron solutions. Finally, the last two neurons yield a probability for either “NK” or “RBC”, activated with a sigmoid to saturate the probability to 1 and 0 for negative values.

We worked on variations of this classifier model to classify spread NK cells from hovering cells, cell clusters from cells isolated, polarized NK cells or not, and NK cells hovering on cancer cells or not. The latter application is critical to defining precisely cell-cell contacts, which is relevant to the previous chapter. This application requires more work to be presented in this manuscript (more annotations and model optimization needed) but would be a precious feature to add to Celldetective. Indeed, the initial step of cell segmentation provides the center of mass required to make the image crops. Celldetective’s signal annotation functions make it possible and practical to annotate cell states. The states plus the locations can train a classifier model that can essentially automatize the cell state annotation.

5.3.9 Cell topography reconstruction

5.3.9.1 Model-driven reconstruction of NK cell lamellipodium

Here, we are to reconstruct the lamellipod region of a spread NK-92 cell following the technique introduced in reference [40]. We performed a multi-color/multi-aperture of several single NK-92 cells in a spread state on an anti-CD16 surface following the protocol from section 5.2.3.3. Figure 5.28a illustrates one such acquisition with two colors and four INA. The cell presented here is imaged live, with no fixation. As such, no time average can be performed without introducing motion blur. Each illumination condition (or channel) is carefully normalized following the refined protocol described in section 5.3.2. Picking any pixel of the image and projecting on all illumination conditions shows a characteristic profile with most often a rupture at the color switch that depends on the underlying topography.

On the simulation side, the first step is to build an optical model that can describe how light is modified as it passes through all of the optical components of the RICM setup described in figure 5.1. All of the unknowns are concentrated at the sample level. We assume that at the pixel scale ($0.125 \mu\text{m}$), the system is flat enough to be approximated by stacked flat surfaces characterized by different thicknesses and refractive indices. Figure 5.28b shows the stacked-surfaces description for the lamellipod region, with glass, the medium with refractive index $n_{\text{medium}} = 1.33$ and unknown thickness h , for height, the first lipid layer with a thickness of 4 nm and refractive index $n_{\text{lipid}} = 1.486$, the cytoplasm with unknown thickness d and unknown refractive index n_{cyto} and finally the lipid layer again followed by the medium layer, with quasi-infinite thickness. For as many realistic combinations of

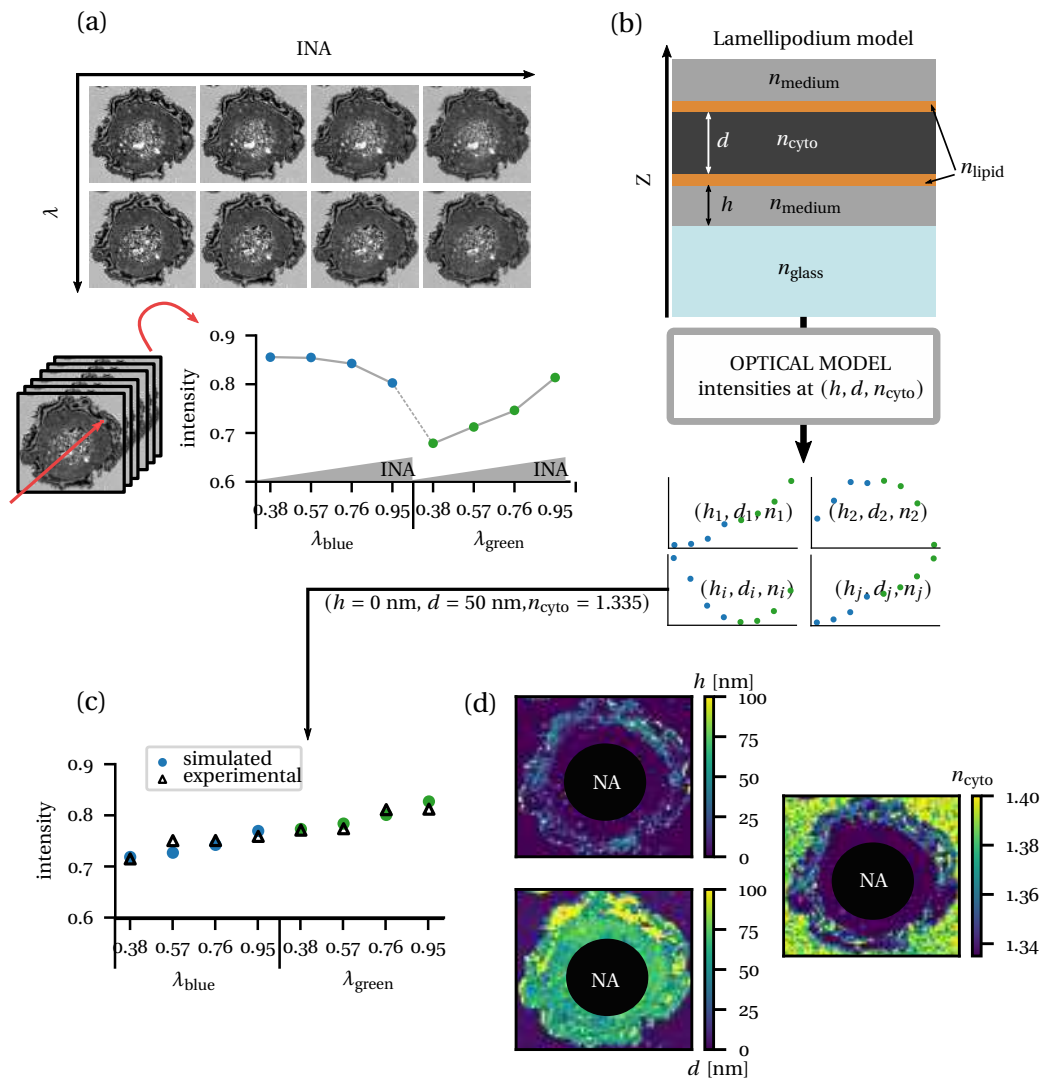


FIGURE 5.28 – Principle of topography reconstruction from RICM images. a) A cell is imaged using as many combinations of λ and INA as possible (here two λ and four INA). For each spatial location (i, j) , projecting across the whole acquisition yields an illumination sequence. b) A plausible model of stacked flat surfaces, for the lamellipod region, is embedded in a model of the optical transform of light in the RICM setup. For each combination of topography parameters in the lamellipod model, illumination sequences are generated at the same control parameters (λ +INA) as the experimental images. c) For each pixel in the experimental image, the simulated topography that gave rise to the best matching illumination sequence is selected, reconstructing pixel-by-pixel to topography landscape from the illumination sequence. d) Output topographies are shown for the example cell, with a not-applicable region in the center to mask the nuclear region where the lamellipod model most certainly does not apply.

(h, d, n_{cyto}) as possible, we simulate the RICM intensity, normalized by background, for all experimental control parameters.

The reconstruction is an optimization problem for each pixel of the experimen-

tal images. We want to find the combination of simulated topography parameters (h, d, n_{cyto}) that gave rise to the closest intensity sequence across all illumination conditions. This reconstruction process involves computing a loss function. The authors of [40] introduced a relative loss function defined as the sum of the squared deviations over the simulated intensity values. We also explored using a more conventional squared error loss, the sum of the squared deviations, routinely used in optimization problems. The optimization converged to similar solutions for both losses.

The representation in figure 5.28c is quite critical to assess the quality of the fit between the experimental illumination sequence and the simulated one. Here, we show a match that seems plausible, with low error. In practice, a lot of fits do not look as likely, suggesting that there might be a problem in the model when applied to the NK-92 cells. For example, some interference pattern residues can still be seen at the edge of the cell on the reconstructed height and thickness, implying an unsuccessful reconstruction in these regions. This could be due to a breaking of the flat-layer assumption in this region, due to a slope of the upper or lower membrane that is far from negligible and that explains the amount of interference in the first place. Another reason could be that the control parameters ($\lambda \times \text{INA}$) are not as controlled as believed. For example, the green or blue light used in this acquisition has a wavelength bandwidth larger than 10 nm, whereas the model simulates intensity for light with a pure, single λ .

5.3.9.2 Deep-learning approximation of the reconstruction process

We proposed to use supervised convolutional DL models, usually associated with computer vision tasks, to approximate the reconstruction process, learning to output topography parameters from simulated intensity inputs. The intended purpose was to be able to apply such a model to each pixel of an experimental acquisition to reconstruct the topography of the lamellipodium and other cell parts much faster. Indeed, the traditional reconstruction process involves comparing an experimental intensity sequence to all simulated sequences, which is tedious computationally and can take hours on a moderately sized image (e.g. 100×100 px).

We formulated the input as an intensity vector, with slots associated strictly with an illumination condition (λ, INA). Such intensity vectors are simulated using the optical model. We experimented with various input shapes such as a ($n_\lambda \times n_{\text{INA}}$) shape or passing a (1×1) tensor with $n_\lambda \times n_{\text{INA}}$ channels. To exploit convolutions we usually had to perform some reshaping in the first layer, using typically an upsampling operation. Overall, all of these approaches gave similar results.

The model backbone is either a traditional convolution encoder, as described in section 5.3.8, or a ResNet-like model as described extensively in section 3.2.2. The optimizer was Adam with a learning rate tested in the range $10^{-4} - 10^{-2}$. The task was to minimize the mean-square error (or mean-absolute error) on the topography parameters (h, d, n_{cyto}) from the illumination sequence.

As illustrated in figure 5.29a, we can never completely fit the inverse optical transform. We tried to remove validation and test sets to force the model to over-fit and it could not. It works very precisely for many topographies but occasionally jumps to another solution that was not, in fact, a real solution. Instead, at these instabilities, the model predicts an average between two or more topography parameters sharing quasi-identical intensity sequences. In other words, there were still many degeneracies, despite the effort in varying the illumination conditions, that were identified in figure 5.29b. To find them, all simulated illumination sequences have to be compared to each other. Any pair of sequences for which the intensity difference is smaller than a threshold (say 10^{-3}) for each slot is considered as a degeneracy. The choice of the threshold depends on how confident one can be about the measured normalized intensity. Even our best normalization rarely had an accuracy higher than 10^{-3} , meaning a background value of 0.999 or 1.001. Unlike the published method where a list of topography parameters among all simulated values, ranked by error, could be extracted, this DL approach was always going to yield a single solution, that may or may not be real [187].

Any easy way to picture this issue is to take a much simpler, degenerate function and try to invert it, such as a sine wave, $\sin(\theta)$, showcased in figure 5.29c. A DL model can be trained to take sine values as its input and output the most likely θ . Now, if the model is trained on θ values $\in [0, \frac{\pi}{2}]$, the model can achieve a very high performance in retrieving θ from $\sin(\theta)$. The same can be said if $\theta \in [\frac{3\pi}{2}, 2\pi]$ or if θ comes from both combined intervals. On the other hand, if the model is trained from $\theta \in [0, 2\pi]$, it will output only two solutions : $\frac{\pi}{2}$ or $\frac{2\pi}{2}$. This is because the system is degenerate at any other point, so minimizing error implies picking the solution that gives the least amount of error. This could go two ways : predict one solution only and ignore the other, or predict a mean of both solutions. It turns out that the former is quite unstable, and the models usually converge to the latter.

5.3.9.3 How to lift degeneracies ?

There could be a solution using a different and potentially more extensive combination of illumination conditions ($\lambda \times \text{INA}$). This should be assessed by simulating the RICM intensities for more colors and apertures that could be available experimentally, combining them as different illumination sequences and checking systematically for degeneracies. The process is long and tedious but can pay off. There is still a risk that the topography parameters that are not simulated, the ones falling within the simulation increment, give rise to degeneracies that are simply not simulated, and therefore not addressed, but that could be picked up by an AI when approximating the continuous model.

Reformulating the optimization scheme can constrain the Deep-learning models to only output real solutions. Indeed, instead of minimizing the error on the topography parameters, the loss could be computed on the illumination sequence using a slightly different approach. In the “tandem neural network” formulation

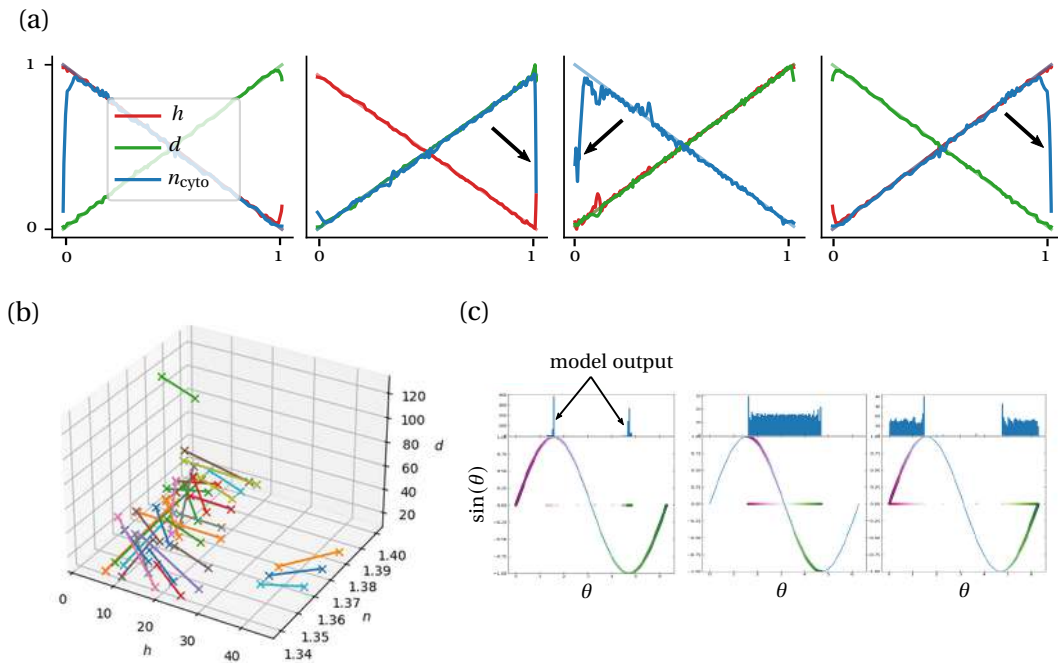


FIGURE 5.29 – Deep learning reconstruction of topography parameters. a) A ResNet model was trained to predict topography parameters from illumination sequences. Here, the model is asked to recover linear (h, d, n_{cyto}) profiles from the associated simulated intensities, computed using the optical model. The parameters are normalized independently from 0 to 1 for clarity. The semi-transparent diagonals are the real parameters, and the thick lines are the predicted ones. Perfect diagonals indicate a match between the predicted parameters and the real ones. Black arrows indicate wrong answers. b) 3D representation that links together normalized topography parameters that share the same illumination sequence, at a difference level of the order of 10^{-3} in all of the intensity values. c) A convolution model's predictions on inverting the sine function, depending on which data is passed to train the model. The sine of the data passed to train the model is colored. The output is shown on the $\sin(\theta) = 0$ horizontal line and in the histogram above.

[191], absorption spectra are first encoded into design parameters, mimicking the inverse optical transform. Then, the parameters are sent through a “forward” network, approximating the optical transform. The loss is computed as an MSE between the input absorption spectra and the absorption spectra reconstructed at the output of the model. Since a mixture of solutions necessarily yields the wrong spectrum when passing through the optical transform (as it is not one of the real solutions), the error is high when comparing the spectra. While this kind of approach solves the problem of mixtures of solutions, it selects a unique solution among all of the degenerated ones, preventing an easy estimate of how degenerate a solution is and therefore of the confidence associated with the estimate.

An alternative formulation that can predict multiple real solutions is the conditional generative adversarial network (GAN), where a generator model (similar to the convolution encoder) outputs topography parameters, from an illumination

sequence complemented with a “noise vector”, and a discriminator (or critic) model judges how realistic this output is. Once the generator can fool the discriminator, the training has converged : the generator yields a plausible output. The “noise vector” allows the generator to jump from one solution branch to another, meaning that repeated predictions with the cGAN can give a distribution of solutions and therefore an estimate of confidence. A variation of the cGAN introduces a “forward” network trained to perform the “forward” optical transform [105]. The parameters predicted by the generator, in addition to being criticized by the discriminator, are also sent to the forward model, providing another loss on the reconstructed illumination. GAN-derived models are known to be hard to train, requiring minute parameter adjustments. While alternative solutions have been suggested [187], they remain hard to train and design. Furthermore, all of these techniques are based on simulated data, meaning that they can never outperform in accuracy an iterative method, but are usually faster at performing the task. They approximate, with an average quality. Some approaches such as physics-informed neural networks (PINNs) try to bypass simulated data altogether, by trying to solve partial differential equations with a neural network approximator, using physical loss functions to drive the optimization [140]. These methods have been mostly applied to solve hydrodynamics equations. A paradigm shift happened with the introduction of stable-diffusion models, that improved considerably the quality of the “plausible outputs” [137]. These techniques are currently mostly applied to generate images from text prompts that condition the image, just like control parameters (λ , INA) condition the illumination sequence.

Conclusion and perspectives

Throughout this manuscript, we have introduced and applied single-cell analysis methods to study cell-cell and cell-surface interactions from microscopy images. Most of these methods were integrated into a user-friendly software, Celldetective, developed for biologists. A lot of effort was put into making Celldetective as broad in scope as possible while remaining adapted to study complex and dynamic cell-cell interactions in cell population mixtures. The software has been tested by several colleagues (Ph.D., post-docs, interns) on other single-cell data not mentioned in this manuscript. Nevertheless, the project is far from complete as there are critical needs that are not addressed yet by the software. First, we would like to address soon the limitation of not being currently able to perform sub-cellular measurements. Single-cell masks provide a formidable canvas to describe the distribution of intensities, count and quantify sub-cellular structures (nuclei, organelles, fluorescent clusters). This is particularly relevant to the cell-surface application imaged in RICM where we have shown through isotropic measurements around the center of the cell that nuclei can exhibit very contrasted reflections that evolve dynamically and that are poorly captured by average measurements over the whole cell masks. Similarly, LAMP1 expression at the surface of NK cells in the ADCC assays is rarely homogeneous and shows instead little clusters, that accumulate on one side of the cell, probably giving information as to how the NK synapse is oriented. Counting these clusters and characterizing their position or peripherality would be a feature of choice for Celldetective. As usual, the difficulty does not lie in *how* to compute these quantities but in how to make their implementation and the setup of their parameters user-friendly.

Another software feature that we would like to improve is the cell signal annotation tool, as it is one major innovation brought by the software. Currently, it allows monitoring one population at a time only, which means that when we established the victim/killer pairs in the ADCC chapter, we had to monitor separately the targets, write down their location and identities, and then look at the effectors and establish the pairs. Monitoring both sets of trajectories at the same time is a simple feature to implement from the current visualizer. In that configuration one may want to annotate independent events for each population, opening the door for a characterization of synapse formation on the effector side, leading to target death on the target side, yielding a $\Delta t = t_{\dagger} - t_{\text{synapse}}$ and therefore a description of target survival upon synapse formation.

A use that we would like to develop is based directly on the needs of my biologist colleagues. Most “single-cell” data available in their respective projects is not dyna-

mic. They can still use Celldetective to segment and quantify their cells using the trick described in the Celldetective chapter. But they lack a way to visualize “*in-situ*” the measurements they obtained for each cell, by clicking on the cell itself as can be done with the signal annotator (for tracked cells). We can replace the animation with a “one-frame-at-a-time” exploration of the movies, where each frame is a position, and replace single-cell signal traces with bar plots showing all measurements of interest scaled by the measurements over the whole population, similar to how we represented the Haralick texture measurements in the cell-surface interaction chapter. Annotation of cells into classes would be instantaneous, and complement a software feature already introduced to classify instantly single cells from their measurements.

On the ADCC assays, we have highlighted a linear relationship between the lysis rate and the number of alive NK neighbors in the neighborhood of the targets. We did not provide a clear explanation for this, as we could not extract an obvious answer from the single-cell data. To face this limitation, I co-supervised an intern, Corentin Barzic, to implement a simulation of the whole ADCC assay, taking the experimental initial positions of all cells and estimates for their dynamics as input and letting the populations evolve following a Brownian model (with drift to mimic convection flows). Effector cells can pass on the target monolayer with a probability to optimize and form synapses (characterized by arrest) with another probability to optimize. The output of the simulation is processed in Celldetective like a real ADCC assay. We make hypotheses as to what triggers a target death to estimate death times for the simulated assay. Among the hypotheses, we propose that one effector cell staying long enough with a characteristic time τ triggers the target death, that the cumulated effector cell presence builds up to τ to trigger the death, that only a fraction of the effector cells can kill, and other variations. The survival associated with these death times is compared to the experimental survival function on the ADCC assay sharing the same initial conditions. Since the simulation is completely set up, we hope to be able to answer these biophysical questions soon.

On the RICM images, we performed segmentation using a traditional segmentation pipeline, which was efficient at low cell densities although it required a lot of manual corrections to remove false positive detections. We have been actively collecting annotations exploiting these traditional segmentation pipelines to remove as much annotation bias as possible. Most of the annotation work consists of separating cell-cell contacts and removing the false positive objects. This dataset needs more work to successfully train a Deep-learning segmentation model but highlights our approach to annotations for segmentation. Our exploration of texture features from brightfield images to classify cell phenotypes suggests that we could completely bypass RICM imaging and still measure fractions of adhered cells from images, provided we can segment the cells accurately from brightfield.

We have barely scratched the surface of applications for Celldetective. While not revolutionary, we hope that this completely open-source software can simplify and democratize access to refined single-cell analysis for researchers who do not have

the time or will to learn all of the details of the integrated modules. Over time, we will keep upgrading the different modules to provide even more functionalities, guided by users' needs, and explore new applications, to converge towards a comprehensive solution for single-cell analysis.

Bibliography

- [1] Jannis AHLERS, Daniel ALTHVIZ MORÉ, Oren AMSALEM, Ashley ANDERSON, Grzegorz BOKOTA, Peter BOONE, Jordão BRAGANTINI, Genevieve BUCKLEY, Alister BURT, Matthias BUSSONNIER et al. *Napari : A Multi-Dimensional Image Viewer for Python*. Version vo.4.18. Zenodo, 5 juil. 2023. DOI : 10.5281/zenodo.8115575. URL : <https://zenodo.org/records/8115575> (visité le 06/01/2024).
- [2] Galit ALTER, Jessica M. MALENFANT et Marcus ALTFELD. « CD107a as a Functional Marker for the Identification of Natural Killer Cell Activity ». In : *Journal of Immunological Methods* 294.1-2 (nov. 2004), p. 15-22. ISSN : 0022-1759. DOI : 10.1016/j.jim.2004.08.008. pmid : 15604012.
- [3] *APC Anti-Human CD107a LAMP-1 Antibody Anti-CD107a - H4A3*. URL : <https://www.biolegend.com/en-gb/products/apc-anti-human-cd107a-lamp-1-antibody-5428?GroupID=BLG10252> (visité le 24/01/2024).
- [4] Martin ARJOVSKY, Soumith CHINTALA et Léon BOTTOU. *Wasserstein GAN*. 6 déc. 2017. DOI : 10.48550/arXiv.1701.07875. arXiv : 1701.07875 [cs, stat]. URL : <http://arxiv.org/abs/1701.07875> (visité le 02/02/2024). preprint.
- [5] A. M. ATTALLAH, T. J. YEATMAN, P. D. NOGUCHI et J. B. JOHNSON. « Antibody-Dependent Cell-Mediated Cytotoxicity : Detection by Automated Flow Cytometry with Ultramicro Techniques ». In : *Science (New York, N.Y.)* 209.4454 (18 juil. 1980), p. 404-406. ISSN : 0036-8075. DOI : 10.1126/science.7384812. pmid : 7384812.
- [6] Benjamin L. BANGASSER, Ghaidan A. SHAMSAN, Clarence E. CHAN, Kwaku N. OPOKU, Erkan TÜZEL, Benjamin W. SCHLICHTMANN, Jesse A. KASIM, Benjamin J. FULLER, Brannon R. McCULLOUGH, Steven S. ROSENFELD et David J. ODDE. « Shifting the Optimal Stiffness for Cell Migration ». In : *Nature Communications* 8 (22 mai 2017), p. 15313. ISSN : 2041-1723. DOI : 10.1038/ncomms15313. pmid : 28530245. URL : <https://www.ncbi.nlm.nih.gov/pmc/articles/PMC5458120/> (visité le 22/01/2024).
- [7] Peter BANKHEAD, Maurice B. LOUGHREY, José A. FERNÁNDEZ, Yvonne DOMBROWSKI, Darragh G. MCART, Philip D. DUNNE, Stephen MCQUAID, Ronan T. GRAY, Liam J. MURRAY, Helen G. COLEMAN et al. « QuPath : Open Source Software for Digital Pathology Image Analysis ». In : *Scientific Reports* 7.1 (14 déc. 2017), p. 16878. ISSN : 2045-2322. DOI : 10.1038/s41598-017-17204-5. URL : <https://www.nature.com/articles/s41598-017-17204-5> (visité le 14/01/2024).
- [8] Eli BARKAI, Yuval GARINI et Ralf METZLER. « Strange Kinetics of Single Molecules in Living Cells ». In : *Physics Today* 65.8 (1^{er} août 2012), p. 29. ISSN : 0031-9228. DOI : 10.1063/PT.3.1677. URL : <https://physicstoday.scitation.org/doi/abs/10.1063/PT.3.1677> (visité le 01/06/2020).
- [9] Ruth BARSHIR, Omer BASHA, Amir ELUK, Ilan Y. SMOLY, Alexander LAN et Esti YEGER-LOTEM. « The TissueNet Database of Human Tissue Protein-Protein Interactions ». In : *Nucleic Acids Research* 41 (Database issue jan. 2013), p. D841-844. ISSN : 1362-4962. DOI : 10.1093/nar/gks1198. pmid : 23193266.

- [10] Ghislaine BEHAR, Sophie SIBÉRI, Agnès GROULET, Patrick CHAMES, Martine PUGNIÈRE, Charlotte BOIX, Catherine SAUTÈS-FRIDMAN, Jean-Luc TEILLAUD et Daniel BATY. « Isolation and Characterization of Anti-Fcγ₃ (CD16) Llama Single-Domain Antibodies That Activate Natural Killer Cells ». In : *Protein engineering, design & selection : PEDS* 21.1 (jan. 2008), p. 1-10. ISSN : 1741-0126. DOI : [10.1093/protein/gzm064](https://doi.org/10.1093/protein/gzm064). pmid : 18073223.
- [11] Beatriz BELLO, Rémy TORRO, Adrien AIMARD, Florian DUPUY, Lorna AMMER, Francesco PIAZZA, Brigitte KERFELEC, Patrick CHAMES et Laurent LIMOZIN. *AI-enhanced Real-Time Immune Killing Imaging : From Single Cell to Ensemble Assay*. preprint.
- [12] F. BELLOC, P. DUMAIN, M. R. BOISSEAU, C. JALLOUSTRE, J. REIFFERS, P. BERNARD et F. LACOMBE. « A Flow Cytometric Method Using Hoechst 33342 and Propidium Iodide for Simultaneous Cell Cycle Analysis and Apoptosis Determination in Unfixed Cells ». In : *Cytometry* 17.1 (1^{er} sept. 1994), p. 59-65. ISSN : 0196-4763. DOI : [10.1002/cyto.990170108](https://doi.org/10.1002/cyto.990170108). pmid : 7528124.
- [13] J BEREITER-HAHN, C H FOX et B THORELL. « Quantitative Reflection Contrast Microscopy of Living Cells. » In : *Journal of Cell Biology* 82.3 (1^{er} sept. 1979), p. 767-779. ISSN : 0021-9525. DOI : [10.1083/jcb.82.3.767](https://doi.org/10.1083/jcb.82.3.767). URL : <https://doi.org/10.1083/jcb.82.3.767> (visité le 02/02/2024).
- [14] Stuart BERG, Dominik KUTRA, Thorben KROEGER, Christoph N. STRAEHLE, Bernhard X. KAUSLER, Carsten HAUBOLD, Martin SCHIEGG, Janez ALES, Thorsten BEIER, Markus RUDY et al. « Ilas-tik : Interactive Machine Learning for (Bio)Image Analysis ». In : *Nature Methods* 16.12 (12 déc. 2019), p. 1226-1232. ISSN : 1548-7105. DOI : [10.1038/s41592-019-0582-9](https://doi.org/10.1038/s41592-019-0582-9). URL : <https://www.nature.com/articles/s41592-019-0582-9> (visité le 22/06/2023).
- [15] Serge BEUCHER. « Use of Watersheds in Contour Detection ». In : *Proc. Int. Workshop on Image Processing, Sept. 1979*. 1979, p. 17-21.
- [16] Arikta BISWAS, Amal ALEX et Bidisha SINHA. « Mapping Cell Membrane Fluctuations Reveals Their Active Regulation and Transient Heterogeneities ». In : *Biophysical Journal* 113.8 (17 oct. 2017), p. 1768-1781. ISSN : 1542-0086. DOI : [10.1016/j.bpj.2017.08.041](https://doi.org/10.1016/j.bpj.2017.08.041). pmid : 29045871.
- [17] Ulrich BRINKMANN et Roland E. KONTERMANN. « The Making of Bispecific Antibodies ». In : *mAbs* 9.2 (10 jan. 2017), p. 182-212. ISSN : 1942-0862. DOI : [10.1080/19420862.2016.1268307](https://doi.org/10.1080/19420862.2016.1268307). pmid : 28071970. URL : <https://www.ncbi.nlm.nih.gov/pmc/articles/PMC5297537/> (visité le 15/01/2024).
- [18] Alexandre BRODOVITCH, Eugene SHENDEROV, Vincenzo CERUNDOLO, Pierre BONGRAND, Anne PIERRES et Philip Anton van der MERWE. « T Lymphocytes Need Less than 3 Min to Discriminate between Peptide MHCs with Similar TCR-binding Parameters ». In : *European Journal of Immunology* 45.6 (juin 2015), p. 1635-1642. ISSN : 1521-4141. DOI : [10.1002/eji.201445214](https://doi.org/10.1002/eji.201445214). pmid : 25782169.
- [19] Tom BROWN, Benjamin MANN, Nick RYDER, Melanie SUBBIAH, Jared D KAPLAN, Prafulla DHARIWAL, Arvind NEELAKANTAN, Pranav SHYAM, Girish SASTRY, Amanda ASKELL et al. « Language Models Are Few-Shot Learners ». In : *Advances in Neural Information Processing Systems*. T. 33. Curran Associates, Inc., 2020, p. 1877-1901. URL : <https://papers.nips.cc/paper/2020/hash/1457c0d6bfc4967418bfb8ac142f64a-Abstract.html> (visité le 08/01/2024).
- [20] K. T. BRUNNER, J. MAUEL, J. C. CEROTTINI et B. CHAPUIS. « Quantitative Assay of the Lytic Action of Immune Lymphoid Cells on 51-Cr-labelled Allogeneic Target Cells in Vitro ; Inhibition by Isoantibody and by Drugs ». In : *Immunology* 14.2 (fév. 1968), p. 181-196. ISSN : 0019-2805. pmid : 4966657.

- [21] David BUNK, Julian MORIASY, Felix THOMA, Christopher JAKUBKE, Christof OSMAN et David HÖRL. « YeastMate : Neural Network-Assisted Segmentation of Mating and Budding Events in *Saccharomyces Cerevisiae* ». In : *Bioinformatics* 38.9 (28 avr. 2022), p. 2667-2669. ISSN : 1367-4803. DOI : [10.1093/bioinformatics/btac107](https://doi.org/10.1093/bioinformatics/btac107). URL : <https://doi.org/10.1093/bioinformatics/btac107> (visité le 04/01/2024).
- [22] Juan C. CAICEDO, Jonathan ROTH, Allen GOODMAN, Tim BECKER, Kyle W. KARHOHS, Matthieu BROISIN, Csaba MOLNAR, Claire McQUIN, Shantanu SINGH, Fabian J. THEIS et Anne E. CARPENTER. « Evaluation of Deep Learning Strategies for Nucleus Segmentation in Fluorescence Images ». In : *Cytometry. Part A : The Journal of the International Society for Analytical Cytology* 95.9 (sept. 2019), p. 952-965. ISSN : 1552-4930. DOI : [10.1002/cyto.a.23863](https://doi.org/10.1002/cyto.a.23863). pmid : 31313519.
- [23] Grace CAMPAGNOLA, Kanti NEPAL, Bryce W. SCHRODER, Olve B. PEERSEN et Diego KRAPP. « Superdiffusive Motion of Membrane-Targeting C2 Domains ». In : *Scientific Reports* 5.1 (7 déc. 2015), p. 17721. ISSN : 2045-2322. DOI : [10.1038/srep17721](https://doi.org/10.1038/srep17721). URL : <https://www.nature.com/articles/srep17721> (visité le 01/06/2020).
- [24] *Carl Zeiss Microscopy, LLC - Filter Assistant - Overview of Filter Sets - Filter Set 25*. URL : <https://www.micro-shop.zeiss.com/en/us/shop/filterAssistant/filtersets/488025-0000-000> (visité le 31/01/2024).
- [25] *Carl Zeiss Microscopy, LLC - Filter Assistant - Overview of Filter Sets - Filter Set 38 HE*. URL : <https://www.micro-shop.zeiss.com/en/us/shop/filterAssistant/filtersets/489038-9901-000> (visité le 31/01/2024).
- [26] *Carl Zeiss Microscopy, LLC - Filter Assistant - Overview of Filter Sets - Filter Set 49*. URL : <https://www.micro-shop.zeiss.com/en/us/shop/filterAssistant/filtersets/488049-9901-000> (visité le 31/01/2024).
- [27] Anne E. CARPENTER, Thouis R. JONES, Michael R. LAMPRECHT, Colin CLARKE, In Han KANG, Ola FRIMAN, David A. GUERTIN, Joo Han CHANG, Robert A. LINDQUIST, Jason MOFFAT et al. « CellProfiler : Image Analysis Software for Identifying and Quantifying Cell Phenotypes ». In : *Genome Biology* 7.10 (31 oct. 2006), R100. ISSN : 1474-760X. DOI : [10.1186/gb-2006-7-10-r100](https://doi.org/10.1186/gb-2006-7-10-r100). URL : <https://doi.org/10.1186/gb-2006-7-10-r100> (visité le 15/10/2023).
- [28] *CellProfiler : Published Pipelines*. URL : <https://cellprofiler.org/published-pipelines> (visité le 17/10/2023).
- [29] Patrick CHAMES et Daniel BATY. « Bispecific Single Domain Antibodies ». In : *Bispecific Antibodies*. Springer, 2011, p. 101-114.
- [30] S. CHANDRASEKHAR. « Stochastic Problems in Physics and Astronomy ». In : *Reviews of Modern Physics* 15.1 (1^{er} jan. 1943), p. 1-89. DOI : [10.1103/RevModPhys.15.1](https://doi.org/10.1103/RevModPhys.15.1). URL : <https://link.aps.org/doi/10.1103/RevModPhys.15.1> (visité le 12/06/2020).
- [31] Kyunghyun CHO, Bart van MERRIENBOER, Caglar GULCEHRE, Dzmitry BAHDANAU, Fethi BOUGARES, Holger SCHWENK et Yoshua BENGIO. *Learning Phrase Representations Using RNN Encoder-Decoder for Statistical Machine Translation*. 2 sept. 2014. DOI : [10.48550/arXiv.1406.1078](https://doi.org/10.48550/arXiv.1406.1078). arXiv : 1406.1078 [cs, stat]. URL : <http://arxiv.org/abs/1406.1078> (visité le 29/01/2024). preprint.
- [32] François CHOLLET et al. *Keras*. 2015. URL : <https://keras.io>.
- [33] François CHOLLET. *Deep Learning with Python*. 1^{re} éd. USA : Manning Publications Co., nov. 2017. 384 p. ISBN : 978-1-61729-443-3.

- [34] Dan CIRESAN, Alessandro GIUSTI, Luca GAMBARDELLA et Jürgen SCHMIDHUBER. « Deep Neural Networks Segment Neuronal Membranes in Electron Microscopy Images ». In : *Advances in Neural Information Processing Systems*. T. 25. Curran Associates, Inc., 2012. URL : https://papers.nips.cc/paper_files/paper/2012/hash/459a4ddcb586f24efd9395aa7662bc7c-Abstract.html (visité le 14/01/2024).
- [35] Albert H. COONS, Hugh J. CREECH, R. Norman JONES et Ernst BERLINER. « The Demonstration of Pneumococcal Antigen in Tissues by the Use of Fluorescent Antibody¹ ». In : *The Journal of Immunology* 45.3 (1^{er} nov. 1942), p. 159-170. ISSN : 0022-1767. DOI : 10.4049/jimmunol.45.3.159. URL : <https://doi.org/10.4049/jimmunol.45.3.159> (visité le 02/02/2024).
- [36] A. S. CURTIS. « THE MECHANISM OF ADHESION OF CELLS TO GLASS. A STUDY BY INTERFERENCE REFLECTION MICROSCOPY ». In : *The Journal of Cell Biology* 20.2 (fév. 1964), p. 199-215. ISSN : 0021-9525. DOI : 10.1083/jcb.20.2.199. pmid : 14126869.
- [37] Kevin J. CUTLER, Carsen STRINGER, Teresa W. LO, Luca RAPPEZ, Nicholas STROUSTRUP, S. BROOK PETERSON, Paul A. WIGGINS et Joseph D. MOUGOUS. « Omnipose : A High-Precision Morphology-Independent Solution for Bacterial Cell Segmentation ». In : *Nature Methods* 19.11 (11 nov. 2022), p. 1438-1448. ISSN : 1548-7105. DOI : 10.1038/s41592-022-01639-4. URL : <https://www.nature.com/articles/s41592-022-01639-4> (visité le 04/01/2024).
- [38] Damien CUVELIER, Manuel THÉRY, Yeh-Shiu CHU, Sylvie DUFOUR, Jean-Paul THIÉRY, Michel BORNENS, Pierre NASSOY et L. MAHADEVAN. « The Universal Dynamics of Cell Spreading ». In : *Current biology : CB* 17.8 (17 avr. 2007), p. 694-699. ISSN : 0960-9822. DOI : 10.1016/j.cub.2007.02.058. pmid : 17379524.
- [39] Thomas DE MEYER, Serge MUYLDERMANS et Ann DEPICKER. « Nanobody-Based Products as Research and Diagnostic Tools ». In : *Trends in Biotechnology* 32.5 (mai 2014), p. 263-270. ISSN : 1879-3096. DOI : 10.1016/j.tibtech.2014.03.001. pmid : 24698358.
- [40] Marie-Julie DEJARDIN, Arnaud HEMMERLE, Anaïs SADOON, Yannick HAMON, Pierre-Henri PUECH, Kheya SENGUPTA et Laurent LIMOZIN. « Lamellipod Reconstruction by Three-Dimensional Reflection Interference Contrast Nanoscopy (3D-RICN) ». In : *Nano Letters* 18.10 (10 oct. 2018), p. 6544-6550. ISSN : 1530-6992. DOI : 10.1021/acs.nanolett.8b03134. pmid : 30179011.
- [41] Johanna F. DEKKERS, Maria ALIEVA, Astrid CLEVEN, Farid KERAMATI, Amber K. L. WEZENAAR, Esmée J. van VLIET, Jens PUSCHHOF, Peter BRAZDA, Inez JOHANNA, Angelo D. MERINGA et al. « Uncovering the Mode of Action of Engineered T Cells in Patient Cancer Organoids ». In : *Nature Biotechnology* 41.1 (1 jan. 2023), p. 60-69. ISSN : 1546-1696. DOI : 10.1038/s41587-022-01397-w. URL : <https://www.nature.com/articles/s41587-022-01397-w> (visité le 23/01/2024).
- [42] Salil Vasudeo DEO, Vaishali DEO et Varun SUNDARAM. « Survival Analysis—Part 2 : Cox Proportional Hazards Model ». In : *Indian Journal of Thoracic and Cardiovascular Surgery* 37.2 (mar. 2021), p. 229-233. ISSN : 0970-9134. DOI : 10.1007/s12055-020-01108-7. pmid : 33642726. URL : <https://www.ncbi.nlm.nih.gov/pmc/articles/PMC7876211/> (visité le 21/10/2023).
- [43] Jacob DEVLIN, Ming-Wei CHANG, Kenton LEE et Kristina TOUTANOVA. « BERT : Pre-training of Deep Bidirectional Transformers for Language Understanding ». In : *Proceedings of the 2019 Conference of the North*. Proceedings of the 2019 Conference of the North. Minneapolis, Minnesota : Association for Computational Linguistics, 2019, p. 4171-4186. DOI : 10.18653/v1/N19-1423. URL : <http://aclweb.org/anthology/N19-1423> (visité le 08/01/2024).
- [44] Alexandra J. DICKINSON, Megan MEYER, Erica A. PAWLAK, Shawn GOMEZ, Ilona JASPERS et Nancy L. ALLBRITTON. « Analysis of Sphingosine Kinase Activity in Single Natural Killer Cells from Peripheral Blood ». In : *Integrative biology : quantitative biosciences from nano to macro* 7.4 (avr. 2015), p. 392-401. ISSN : 1757-9694. DOI : 10.1039/c5ib00007f. pmid : 25786072. URL : <https://www.ncbi.nlm.nih.gov/pmc/articles/PMC4566154/> (visité le 18/01/2024).

- [45] Pierre DILLARD, Fuwei PI, Annemarie C. LELLOUCH, Laurent LIMOZIN et Kheya SENGUPTA. « Nano-Clustering of Ligands on Surrogate Antigen Presenting Cells Modulates T Cell Membrane Adhesion and Organization ». In : *Integrative Biology : Quantitative Biosciences from Nano to Macro* 8.3 (14 mar. 2016), p. 287-301. ISSN : 1757-9708. DOI : 10.1039/c5ib00293a. pmid : 26887857.
- [46] Pierre DILLARD, Rajat VARMA, Kheya SENGUPTA et Laurent LIMOZIN. « Ligand-Mediated Friction Determines Morphodynamics of Spreading T Cells ». In : *Biophysical Journal* 107.11 (2 déc. 2014), p. 2629-2638. ISSN : 0006-3495. DOI : 10.1016/j.bpj.2014.10.044. pmid : 25468342. URL : <https://www.ncbi.nlm.nih.gov/pmc/articles/PMC4255222/> (visité le 29/01/2024).
- [47] Hans-Günther DÖBEREINER, Benjamin DUBIN-THALER, Grégory GIANNONE, Harry S. XENIAS et Michael P. SHEETZ. « Dynamic Phase Transitions in Cell Spreading ». In : *Physical Review Letters* 93.10 (2 sept. 2004), p. 108105. DOI : 10.1103/PhysRevLett.93.108105. URL : <https://link.aps.org/doi/10.1103/PhysRevLett.93.108105> (visité le 02/02/2024).
- [48] Alexey DOSOVITSKIY, Lucas BEYER, Alexander KOLESNIKOV, Dirk WEISSENBORN, Xiaohua ZHAI, Thomas UNTERTHINER, Mostafa DEGHANI, Matthias MINDERER, Georg HEIGOLD, Sylvain GELLY et al. *An Image Is Worth 16x16 Words : Transformers for Image Recognition at Scale*. 3 juin 2021. DOI : 10.48550/arXiv.2010.11929. arXiv : 2010.11929 [cs]. URL : <http://arxiv.org/abs/2010.11929> (visité le 14/01/2024). preprint.
- [49] Oliver DÜRR et Beate SICK. « Single-Cell Phenotype Classification Using Deep Convolutional Neural Networks ». In : *Journal of Biomolecular Screening* 21.9 (oct. 2016), p. 998-1003. ISSN : 1552-454X. DOI : 10.1177/1087057116631284. pmid : 26950929.
- [50] Arthur D EDELSTEIN, Mark A. TSUCHIDA, Nenad AMODAJ, Henry PINKARD, Ronald D. VALE et Nico STUURMAN. « Advanced Methods of Microscope Control Using μ Manager Software ». In : *Journal of Biological Methods* 1.2 (7 nov. 2014), e10. ISSN : 2326-9901. DOI : 10.14440/jbm.2014.36. URL : <https://polscientific.com/jbm/index.php/jbm/article/view/36>.
- [51] Christoffer EDLUND, Timothy R. JACKSON, Nabeel KHALID, Nicola BEVAN, Timothy DALE, Andreas DENGEL, Sheraz AHMED, Johan TRYGG et Rickard SJÖGREN. « LIVECell—A Large-Scale Dataset for Label-Free Live Cell Segmentation ». In : *Nature Methods* 18.9 (9 sept. 2021), p. 1038-1045. ISSN : 1548-7105. DOI : 10.1038/s41592-021-01249-6. URL : <https://www.nature.com/articles/s41592-021-01249-6> (visité le 09/11/2022).
- [52] Philipp ELLINGER et August HIRT. « Mikroskopische Untersuchungen an lebenden Organen ». In : *Zeitschrift für Anatomie und Entwicklungsgeschichte* 90.5 (1^{er} nov. 1929), p. 791-802. ISSN : 1432-0568. DOI : 10.1007/BF02117979. URL : <https://doi.org/10.1007/BF02117979> (visité le 02/02/2024).
- [53] J. W. ELLWART et P. DÖRMER. « Vitality Measurement Using Spectrum Shift in Hoechst 33342 Stained Cells ». In : *Cytometry* 11.2 (1990), p. 239-243. ISSN : 0196-4763. DOI : 10.1002/cyto.990110204. pmid : 1690626.
- [54] Dmitry ERSHOV, Minh-Son PHAN, Joanna W. PYLVÄNÄINEN, Stéphane U. RIGAUD, Laure LE BLANC, Arthur CHARLES-ORSZAG, James R. W. CONWAY, Romain F. LAINE, Nathan H. ROY, Daria BONAZZI et al. « TrackMate 7 : Integrating State-of-the-Art Segmentation Algorithms into Tracking Pipelines ». In : *Nature Methods* 19.7 (7 juil. 2022), p. 829-832. ISSN : 1548-7105. DOI : 10.1038/s41592-022-01507-1. URL : <https://www.nature.com/articles/s41592-022-01507-1> (visité le 14/01/2024).
- [55] Kenneth N. FISH. « Total Internal Reflection Fluorescence (TIRF) Microscopy ». In : *Current protocols in cytometry / editorial board, J. Paul Robinson, managing editor ... [et al.]* 0 12 (oct. 2009), Unit12.18. ISSN : 1934-9297. DOI : 10.1002/0471142956.cy1218s50. pmid : 19816922. URL : <https://www.ncbi.nlm.nih.gov/pmc/articles/PMC4540339/> (visité le 02/02/2024).

- [56] Ralph van FURTH. *Mononuclear Phagocytes : In Immunity, Infection, and Pathology*. Oxford : Blackwell Scientific, 1975. 1062 p. ISBN : 978-0-632-00471-3.
- [57] Miguel A. GARCÍA-ÁLVAREZ, Elena CHAVES-POZO et Alberto CUESTA. « Cytotoxic Activity and Gene Expression during in Vitro Adaptive Cell-Mediated Cytotoxicity of Head-Kidney Cells from Betanodavirus-Infected European Sea Bass ». In : *Developmental & Comparative Immunology* 152 (1^{er} mar. 2024), p. 105124. ISSN : 0145-305X. DOI : 10.1016/j.dci.2023.105124. URL : <https://www.sciencedirect.com/science/article/pii/S0145305X23012776> (visité le 31/01/2024).
- [58] K. A. GEILER-SAMEROTTE, C. R. BAUER, S. LI, N. ZIV, D. GRESHAM et M. L. SIEGAL. « The Details in the Distributions : Why and How to Study Phenotypic Variability ». In : *Current Opinion in Biotechnology* 24.4 (août 2013), p. 752-759. ISSN : 1879-0429. DOI : 10.1016/j.copbio.2013.03.010. pmid : 23566377.
- [59] D. GINGELL et I. TODD. « Interference Reflection Microscopy. A Quantitative Theory for Image Interpretation and Its Application to Cell-Substratum Separation Measurement ». In : *Biophysical Journal* 26.3 (1^{er} juin 1979), p. 507-526. ISSN : 0006-3495. DOI : 10.1016/S0006-3495(79)85268-6. URL : <https://www.sciencedirect.com/science/article/pii/S0006349579852686> (visité le 02/02/2024).
- [60] Estibaliz GÓMEZ-DE-MARISCAL, Carlos GARCÍA-LÓPEZ-DE-HARO, Wei OUYANG, Laurène DONATI, Emma LUNDBERG, Michael UNSER, Arrate MUÑOZ-BARRUTIA et Daniel SAGE. « DeepImageJ : A User-Friendly Environment to Run Deep Learning Models in ImageJ ». In : *Nature Methods* 18.10 (10 oct. 2021), p. 1192-1195. ISSN : 1548-7105. DOI : 10.1038/s41592-021-01262-9. URL : <https://www.nature.com/articles/s41592-021-01262-9> (visité le 15/10/2023).
- [61] Anna S. GONCHAROVA, Alf HONIGMANN, Florian JUG et Alexander KRULL. *Improving Blind Spot Denoising for Microscopy*. 19 août 2020. DOI : 10.48550/arXiv.2008.08414. arXiv : 2008.08414 [cs, eess]. URL : <http://arxiv.org/abs/2008.08414> (visité le 02/02/2024). preprint.
- [62] Cristina GONZÁLEZ, Patrick CHAMES, Brigitte KERFELEC, Daniel BATY, Philippe ROBERT et Laurent LIMOZIN. « Nanobody-CD16 Catch Bond Reveals NK Cell Mechanosensitivity ». In : *Biophysical Journal* 116.8 (23 avr. 2019), p. 1516-1526. ISSN : 0006-3495. DOI : 10.1016/j.bpj.2019.03.012. URL : <https://www.sciencedirect.com/science/article/pii/S0006349519301985> (visité le 06/01/2024).
- [63] Allen GOODMAN, Anne CARPENTER, Elizabeth PARK, jlefman-NVIDIA, JOSETTE_BOOZALLEN, KYLE, MAGGIE, NILOFER, Peter SEDIVÉC et Will CUKIERSKI. *2018 Data Science Bowl*. Kaggle, 2018. URL : <https://kaggle.com/competitions/data-science-bowl-2018>.
- [64] Major GREENWOOD. *A Report on the Natural Duration of Cancer*. H.M. Stationery Office, 1926. 26 p. Google Books : EhVAGwAACAAJ.
- [65] Karolin GULDEVAL, Ludwig BRANDT, Elin FORSLUND, Karl OLOFSSON, Thomas W. FRISK, Per E. OLOFSSON, Karin GUSTAFSSON, Otto MANNEBERG, Bruno VANHERBERGHEN, Hjalmar BRISMAR et al. « Microchip Screening Platform for Single Cell Assessment of NK Cell Cytotoxicity ». In : *Frontiers in Immunology* 7 (2016), p. 119. ISSN : 1664-3224. DOI : 10.3389/fimmu.2016.00119. pmid : 27092139.
- [66] Carolina GUTIERREZ et Rachel SCHIFF. « HER2 : Biology, Detection, and Clinical Implications ». In : *Archives of Pathology & Laboratory Medicine* 135.1 (jan. 2011), p. 55-62. ISSN : 1543-2165. DOI : 10.5858/2010-0454-RAR.1. pmid : 21204711.
- [67] C. HAMERS-CASTERMAN, T. ATARHOUC, S. MUYLDERMANS, G. ROBINSON, C. HAMERS, E. B. SONGA, N. BENDAHMAN et R. HAMERS. « Naturally Occurring Antibodies Devoid of Light Chains ». In : *Nature* 363.6428 (3 juin 1993), p. 446-448. ISSN : 0028-0836. DOI : 10.1038/363446a0. pmid : 8502296.

- [68] Robert M. HARALICK, K. SHANMUGAM et Its'Hak DINSTEIN. « Textural Features for Image Classification ». In : *IEEE Transactions on Systems, Man, and Cybernetics* SMC-3.6 (nov. 1973), p. 610-621. ISSN : 2168-2909. DOI : 10.1109/TSMC.1973.4309314.
- [69] Alina HATEGAN, Kheya SENGUPTA, Samuel KAHN, Erich SACKMANN et Dennis E. DISCHER. « Topographical Pattern Dynamics in Passive Adhesion of Cell Membranes ». In : *Biophysical Journal* 87.5 (1^{er} nov. 2004), p. 3547-3560. ISSN : 0006-3495. DOI : 10.1529/biophysj.104.041475. URL : <https://www.sciencedirect.com/science/article/pii/S0006349504738199> (visité le 02/02/2024).
- [70] Kaiming HE, Xiangyu ZHANG, Shaoqing REN et Jian SUN. *Deep Residual Learning for Image Recognition*. 10 déc. 2015. DOI : 10.48550/arXiv.1512.03385. arXiv : 1512.03385 [cs]. URL : <http://arxiv.org/abs/1512.03385> (visité le 07/01/2024). preprint.
- [71] John Frederick William HERSCHEL. « IV. Ἀμόρφωτα, No. I.— on a Case of Superficial Colour Presented by a Homogeneous Liquid Internally Colourless ». In : *Philosophical Transactions of the Royal Society of London* 135 (jan. 1997), p. 143-145. DOI : 10.1098/rstl.1845.0004. URL : <https://royalsocietypublishing.org/doi/10.1098/rstl.1845.0004> (visité le 02/02/2024).
- [72] Geoffrey E. HINTON, Nitish SRIVASTAVA, Alex KRIZHEVSKY, Ilya SUTSKEVER et Ruslan R. SALAKHUTDINOV. *Improving Neural Networks by Preventing Co-Adaptation of Feature Detectors*. 3 juil. 2012. DOI : 10.48550/arXiv.1207.0580. arXiv : 1207.0580 [cs]. URL : <http://arxiv.org/abs/1207.0580> (visité le 10/01/2024). preprint.
- [73] Sepp HOCHREITER et Jürgen SCHMIDHUBER. « Long Short-Term Memory ». In : *Neural Computation* 9.8 (15 nov. 1997), p. 1735-1780. ISSN : 0899-7667. DOI : 10.1162/neco.1997.9.8.1735. URL : <https://doi.org/10.1162/neco.1997.9.8.1735> (visité le 08/01/2024).
- [74] Mingzhe HU, Shaoyan PAN, Yuheng LI et Xiaofeng YANG. « Advancing Medical Imaging with Language Models : A Journey from n-Grams to Chatgpt ». 2023.
- [75] J. D. HUNTER. « Matplotlib : A 2D Graphics Environment ». In : *Computing in Science & Engineering* 9.3 (2007), p. 90-95. DOI : 10.1109/MCSE.2007.55.
- [76] Alexandre IANNELLO et Ali AHMAD. « Role of Antibody-Dependent Cell-Mediated Cytotoxicity in the Efficacy of Therapeutic Anti-Cancer Monoclonal Antibodies ». In : *Cancer and Metastasis Reviews* 24.4 (1^{er} déc. 2005), p. 487-499. ISSN : 1573-7233. DOI : 10.1007/s10555-005-6192-2. URL : <https://doi.org/10.1007/s10555-005-6192-2> (visité le 06/01/2024).
- [77] Plotly Technologies INC. *Plotly*. 2015. URL : <https://plot.ly>.
- [78] Sergey IOFFE et Christian SZEGEDY. *Batch Normalization : Accelerating Deep Network Training by Reducing Internal Covariate Shift*. 2 mar. 2015. DOI : 10.48550/arXiv.1502.03167. arXiv : 1502.03167 [cs]. URL : <http://arxiv.org/abs/1502.03167> (visité le 10/01/2024). preprint.
- [79] Naylor Peter JACK, Walter THOMAS, Laé MARICK et Reyal FABIEN. *Segmentation of Nuclei in Histopathology Images by Deep Regression of the Distance Map*. Version 1.0. Zenodo, fév. 2018. DOI : 10.5281/zenodo.1175282. URL : <https://doi.org/10.5281/zenodo.1175282>.
- [80] Nick JAGIELLA, Benedikt MÜLLER, Margareta MÜLLER, Irene E. VIGNON-CLEMENTEL et Dirk DRASDO. « Inferring Growth Control Mechanisms in Growing Multi-cellular Spheroids of NSCLC Cells from Spatial-Temporal Image Data ». In : *PLOS Computational Biology* 12.2 (11 fév. 2016), e1004412. ISSN : 1553-7358. DOI : 10.1371/journal.pcbi.1004412. URL : <https://journals.plos.org/ploscompbiol/article?id=10.1371/journal.pcbi.1004412> (visité le 14/01/2024).

- [81] Matti JANHUNEN, Antti KAUSE, Harri VEHVILÄINEN et Otso JÄRVISALO. « Genetics of Microenvironmental Sensitivity of Body Weight in Rainbow Trout (*Oncorhynchus Mykiss*) Selected for Improved Growth ». In : *PLOS ONE* 7.6 (11 juin 2012), e38766. ISSN : 1932-6203. DOI : 10.1371/journal.pone.0038766. URL : <https://journals.plos.org/plosone/article?id=10.1371/journal.pone.0038766> (visité le 29/01/2024).
- [82] Khuloud JAQAMAN, Dinah LOERKE, Marcel METTLEN, Hirotaka KUWATA, Sergio GRINSTEIN, Sandra L. SCHMID et Gaudenz DANUSER. « Robust Single-Particle Tracking in Live-Cell Time-Lapse Sequences ». In : *Nature Methods* 5.8 (août 2008), p. 695-702. ISSN : 1548-7105. DOI : 10.1038/nmeth.1237. URL : <https://www.nature.com/articles/nmeth.1237> (visité le 01/06/2020).
- [83] Thouis R. JONES, Anne CARPENTER et Polina GOLLAND. « Voronoi-Based Segmentation of Cells on Image Manifolds ». In : *Computer Vision for Biomedical Image Applications*. Sous la dir. d'Yanxi LIU, Tianzi JIANG et Changshui ZHANG. Lecture Notes in Computer Science. Berlin, Heidelberg : Springer, 2005, p. 535-543. ISBN : 978-3-540-32125-5. DOI : 10.1007/11569541_54.
- [84] Quentin JUPPET, Fabio DE MARTINO, Elodie MARCANDALLI, Martin WEIGERT, Olivier BURRI, Michael UNSER, Cathrin BRISKEN et Daniel SAGE. « Deep Learning Enables Individual Xenograft Cell Classification in Histological Images by Analysis of Contextual Features ». In : *Journal of Mammary Gland Biology and Neoplasia* 26.2 (1^{er} juin 2021), p. 101-112. ISSN : 1573-7039. DOI : 10.1007/s10911-021-09485-4. URL : <https://doi.org/10.1007/s10911-021-09485-4> (visité le 22/06/2023).
- [85] John D. KALBFLEISCH et Ross L. PRENTICE. *The Statistical Analysis of Failure Time Data*. Wiley, 2 mai 1980. 344 p. ISBN : 978-0-471-05519-8. Google Books : zdpQAAAAMAAJ.
- [86] Lee KAMENSKY, Thouis R. JONES, Adam FRASER, Mark-Anthony BRAY, David J. LOGAN, Katherine L. MADDEN, Vebjorn LJOSA, Curtis RUEDEN, Kevin W. ELICEIRI et Anne E. CARPENTER. « Improved Structure, Function and Compatibility for CellProfiler : Modular High-Throughput Image Analysis Software ». In : *Bioinformatics (Oxford, England)* 27.8 (15 avr. 2011), p. 1179-1180. ISSN : 1367-4811. DOI : 10.1093/bioinformatics/btr095. pmid : 21349861.
- [87] Mobin A. KARIMI, Eric LEE, Michael H. BACHMANN, Ana Maria SALICIONI, Edward M. BEHRENS, Taku KAMBAYASHI et Cynthia L. BALDWIN. « Measuring Cytotoxicity by Bioluminescence Imaging Outperforms the Standard Chromium-51 Release Assay ». In : *PLoS ONE* 9.2 (19 fév. 2014), e89357. ISSN : 1932-6203. DOI : 10.1371/journal.pone.0089357. pmid : 24586714. URL : <https://www.ncbi.nlm.nih.gov/pmc/articles/PMC3929704/> (visité le 15/01/2024).
- [88] Dan KHO, Christa MACDONALD, Rebecca JOHNSON, Charles P. UNSWORTH, Simon J. O'CARROLL, Elyce Du MEZ, Catherine E. ANGEL et E. Scott GRAHAM. « Application of xCELLigence RTCA Biosensor Technology for Revealing the Profile and Window of Drug Responsiveness in Real Time ». In : *Biosensors* 5.2 (2 juin 2015), p. 199-222. ISSN : 2079-6374. DOI : 10.3390/bios5020199. URL : <https://www.mdpi.com/2079-6374/5/2/199> (visité le 31/12/2023).
- [89] Mohammad Ali KHORSHIDI, Bruno VANHERBERGHEM, Jacob M. KOWALEWSKI, Kym R. GARROD, Sara LINDSTRÖM, Helene ANDERSSON-SVAHN, Hjalmar BRISMAR, Michael D. CAHALAN et Björn ÖNFELT. « Analysis of Transient Migration Behavior of Natural Killer Cells Imaged in Situ and in Vitro ». In : *Integrative Biology : Quantitative Biosciences from Nano to Macro* 3.7 (juil. 2011), p. 770-778. ISSN : 1757-9708. DOI : 10.1039/c1ib00007a. pmid : 21687858.
- [90] Diederik P. KINGMA et Jimmy BA. *Adam : A Method for Stochastic Optimization*. 29 jan. 2017. DOI : 10.48550/arXiv.1412.6980. arXiv : 1412.6980 [cs]. URL : <http://arxiv.org/abs/1412.6980> (visité le 08/01/2024). preprint.
- [91] Alexander KIRILLOV, Eric MINTUN, Nikhila RAVI, Hanzi MAO, Chloe ROLLAND, Laura GUSTAFSON, Tete XIAO, Spencer WHITEHEAD, Alexander C. BERG, Wan-Yen LO et al. « Segment Anything ». 2023.

- [92] *Kit de Prolifération Cellulaire CellTrace™ CFSE Pour Cytométrie En Flux*. URL : <https://www.thermofisher.com/order/catalog/product/fr/fr/C34570> (visité le 24/01/2024).
- [93] C. KORZENIEWSKI et D. M. CALLEWAERT. « An Enzyme-Release Assay for Natural Cytotoxicity ». In : *Journal of Immunological Methods* 64.3 (25 nov. 1983), p. 313-320. ISSN : 0022-1759. DOI : 10.1016/0022-1759(83)90438-6. pmid : 6199426.
- [94] Lucas KREISS, Shaowei JIANG, Xiang LI, Shiqi XU, Kevin C. ZHOU, Kyung Chul LEE, Alexander MÜHLBERG, Kanghyun KIM, Amey CHAWARE, Michael ANDO et al. « Digital Staining in Optical Microscopy Using Deep Learning - a Review ». In : *Photonix* 4.1 (10 oct. 2023), p. 34. ISSN : 2662-1991. DOI : 10.1186/s43074-023-00113-4. URL : <https://doi.org/10.1186/s43074-023-00113-4> (visité le 02/02/2024).
- [95] Alex KRIZHEVSKY, Ilya SUTSKEVER et Geoffrey E HINTON. « ImageNet Classification with Deep Convolutional Neural Networks ». In : *Advances in Neural Information Processing Systems*. T. 25. Curran Associates, Inc., 2012. URL : https://proceedings.neurips.cc/paper_files/paper/2012/hash/c399862d3b9d6b76c8436e924a68c45b-Abstract.html (visité le 14/01/2024).
- [96] Florian KROMP, Eva BOZSAKY, Fikret RIFATBEGOVIC, Lukas FISCHER, Magdalena AMBROS, Maria BERNEDEK, Tamara WEISS, Daria LAZIC, Wolfgang DÖRR, Allan HANBURY et al. « An Annotated Fluorescence Image Dataset for Training Nuclear Segmentation Methods ». In : *Scientific Data* 7.1 (11 août 2020), p. 262. ISSN : 2052-4463. DOI : 10.1038/s41597-020-00608-w. URL : <https://www.nature.com/articles/s41597-020-00608-w> (visité le 16/10/2023).
- [97] Alexander KRULL, Tim-Oliver BUCHHOLZ et Florian JUG. *Noise2Void - Learning Denoising from Single Noisy Images*. 5 avr. 2019. DOI : 10.48550/arXiv.1811.10980. arXiv : 1811.10980 [cs]. URL : <http://arxiv.org/abs/1811.10980> (visité le 02/02/2024). preprint.
- [98] Neeraj KUMAR, Ruchika VERMA, Deepak ANAND, Yanning ZHOU, Omer Fahri ONDER, Efstratios TSOUGENIS, Hao CHEN, Pheng-Ann HENG, Jiahui LI, Zhiqiang HU et al. « A Multi-Organ Nucleus Segmentation Challenge ». In : *IEEE Transactions on Medical Imaging* 39.5 (mai 2020), p. 1380-1391. ISSN : 1558-254X. DOI : 10.1109/TMI.2019.2947628. URL : <https://ieeexplore.ieee.org/document/8880654> (visité le 29/12/2023).
- [99] Tian LAN, Kai CHENG, Tina REN, Stephen Hugo ARCE et Yiider TSENG. « Displacement Correlations between a Single Mesenchymal-like Cell and Its Nucleus Effectively Link Subcellular Activities and Motility in Cell Migration Analysis ». In : *Scientific Reports* 6.1 (1 27 sept. 2016), p. 34047. ISSN : 2045-2322. DOI : 10.1038/srep34047. URL : <https://www.nature.com/articles/srep34047> (visité le 22/01/2024).
- [100] L. D. LANDAU et E. M. LIFSHITZ. *Statistical Physics : Volume 5*. Elsevier, 22 oct. 2013. 563 p. ISBN : 978-0-08-057046-4.
- [101] Y. LECUN, B. BOSER, J. S. DENKER, D. HENDERSON, R. E. HOWARD, W. HUBBARD et L. D. JACKEL. « Backpropagation Applied to Handwritten Zip Code Recognition ». In : *Neural Computation* 1.4 (déc. 1989), p. 541-551. ISSN : 0899-7667. DOI : 10.1162/neco.1989.1.4.541. URL : <https://ieeexplore.ieee.org/document/6795724> (visité le 14/01/2024).
- [102] J. LEE et K. JACOBSON. « The Composition and Dynamics of Cell-Substratum Adhesions in Locomoting Fish Keratocytes ». In : *Journal of Cell Science* 110 (Pt 22) (nov. 1997), p. 2833-2844. ISSN : 0021-9533. DOI : 10.1242/jcs.110.22.2833. pmid : 9427291.
- [103] Jeongwoo LEE, Do Young HYEON et Daehee HWANG. « Single-Cell Multiomics : Technologies and Data Analysis Methods ». In : *Experimental & Molecular Medicine* 52.9 (9 sept. 2020), p. 1428-1442. ISSN : 2092-6413. DOI : 10.1038/s12276-020-0420-2. URL : <https://www.nature.com/articles/s12276-020-0420-2> (visité le 29/01/2024).

- [104] Laurent LIMOZIN et Kheya SENGUPTA. « Quantitative Reflection Interference Contrast Microscopy (RICM) in Soft Matter and Cell Adhesion ». In : *ChemPhysChem* 10.16 (2009), p. 2752-2768. ISSN : 1439-7641. DOI : 10.1002/cphc.200900601. URL : <https://onlinelibrary.wiley.com/doi/abs/10.1002/cphc.200900601> (visité le 15/10/2023).
- [105] Zhaocheng LIU, Dayu ZHU, Sean P. RODRIGUES, Kyu-Tae LEE et Wenshan CAI. « A Generative Model for Inverse Design of Metamaterials ». In : *Nano Letters* 18.10 (10 oct. 2018), p. 6570-6576. ISSN : 1530-6984, 1530-6992. DOI : 10.1021/acs.nanolett.8b03171. arXiv : 1805.10181 [physics]. URL : <http://arxiv.org/abs/1805.10181> (visité le 03/02/2024).
- [106] David G. LOWE. « Distinctive Image Features from Scale-Invariant Keypoints ». In : *International Journal of Computer Vision* 60.2 (1^{er} nov. 2004), p. 91-110. ISSN : 1573-1405. DOI : 10.1023/B:VISI.0000029664.99615.94. URL : <https://doi.org/10.1023/B:VISI.0000029664.99615.94> (visité le 15/10/2023).
- [107] Alex X. LU, Oren Z. KRAUS, Sam COOPER et Alan M. MOSES. « Learning Unsupervised Feature Representations for Single Cell Microscopy Images with Paired Cell Inpainting ». In : *PLOS Computational Biology* 15.9 (3 sept. 2019), e1007348. ISSN : 1553-7358. DOI : 10.1371/journal.pcbi.1007348. URL : <https://journals.plos.org/ploscompbiol/article?id=10.1371/journal.pcbi.1007348> (visité le 29/01/2024).
- [108] Jean-Baptiste LUGAGNE, Haonan LIN et Mary J. DUNLOP. « DeLTA : Automated Cell Segmentation, Tracking, and Lineage Reconstruction Using Deep Learning ». In : *PLOS Computational Biology* 16.4 (13 avr. 2020), e1007673. ISSN : 1553-7358. DOI : 10.1371/journal.pcbi.1007673. URL : <https://journals.plos.org/ploscompbiol/article?id=10.1371/journal.pcbi.1007673> (visité le 04/01/2024).
- [109] Narendra MAHESHRI et Erin K. O'SHEA. « Living with Noisy Genes : How Cells Function Reliably with Inherent Variability in Gene Expression ». In : *Annual Review of Biophysics and Biomolecular Structure* 36 (2007), p. 413-434. ISSN : 1056-8700. DOI : 10.1146/annurev.biophys.36.040306.132705. pmid : 17477840.
- [110] N. MALPICA, C. O. de SOLÓRZANO, J. J. VAQUERO, A. SANTOS, I. VALLCORBA, J. M. GARCÍA-SAGREDO et F. del POZO. « Applying Watershed Algorithms to the Segmentation of Clustered Nuclei ». In : *Cytometry* 28.4 (1^{er} août 1997), p. 289-297. ISSN : 0196-4763. DOI : 10.1002/(sici)1097-0320(19970801)28:4<289::aid-cyto3>3.0.co;2-7. pmid : 9266748.
- [111] Soham MANDAL et Virginie UHLMANN. « Splinedist : Automated Cell Segmentation With Spline Curves ». In : *2021 IEEE 18th International Symposium on Biomedical Imaging (ISBI)* (13 avr. 2021), p. 1082-1086. DOI : 10.1109/ISBI48211.2021.9433928. URL : <https://ieeexplore.ieee.org/document/9433928/> (visité le 14/01/2024).
- [112] Mojca MATTIAZZI USAJ, Clarence Hue Lok YEUNG, Helena FRIESEN, Charles BOONE et Brenda J. ANDREWS. « Single-Cell Image Analysis to Explore Cell-to-Cell Heterogeneity in Isogenic Populations ». In : *Cell Systems* 12.6 (16 juin 2021), p. 608-621. ISSN : 2405-4712. DOI : 10.1016/j.cels.2021.05.010. URL : <https://www.sciencedirect.com/science/article/pii/S2405471221001964> (visité le 29/01/2024).
- [113] Katie McDOLE, Léo GUIGNARD, Fernando AMAT, Andrew BERGER, Grégoire MALANDAIN, Loïc A. ROYER, Srinivas C. TURAGA, Kristin BRANSON et Philipp J. KELLER. « In Toto Imaging and Reconstruction of Post-Implantation Mouse Development at the Single-Cell Level ». In : *Cell* 175.3 (18 oct. 2018), 859-876.e33. ISSN : 0092-8674. DOI : 10.1016/j.cell.2018.09.031. URL : <https://www.sciencedirect.com/science/article/pii/S0092867418312431> (visité le 09/11/2022).

- [114] Aidan J. MCLAUGHLIN, Anthony J. KANISKI, Darena I. MATTI et Besa XHABIJA. « Comparative Morphological Analysis of MCF10A and MCF7 Cells Using Holographic Time-lapse Microscopy ». In : *Anticancer Research* 43.9 (1^{er} sept. 2023), p. 3891-3896. ISSN : 0250-7005, 1791-7530. DOI : 10.21873/anticancer.16576. pmid : 37648303. URL : <https://ar.iiajournals.org/content/43/9/3891> (visité le 17/01/2024).
- [115] Claire McQUIN, Allen GOODMAN, Vasilij CHERNYSHEV, Lee KAMENSKY, Beth A. CIMINI, Kyle W. KARHOHS, Minh DOAN, Liya DING, Susanne M. RAFELSKI, Derek THIRSTRUP et al. « CellProfiler 3.0 : Next-generation Image Processing for Biology ». In : *PLOS Biology* 16.7 (3 juil. 2018), e2005970. ISSN : 1545-7885. DOI : 10.1371/journal.pbio.2005970. URL : <https://journals.plos.org/plosbiology/article?id=10.1371/journal.pbio.2005970> (visité le 18/10/2023).
- [116] Amine MEROUANE, Nicolas REY-VILLAMIZAR, Yanbin LU, Ivan LIADI, Gabrielle ROMAIN, Jennifer LU, Harjeet SINGH, Laurence J. N. COOPER, Navin VARADARAJAN et Badrinath ROYSAM. « Automated Profiling of Individual Cell-Cell Interactions from High-Throughput Time-Lapse Imaging Microscopy in Nanowell Grids (TIMING) ». In : *Bioinformatics (Oxford, England)* 31.19 (1^{er} oct. 2015), p. 3189-3197. ISSN : 1367-4811. DOI : 10.1093/bioinformatics/btv355. pmid : 26059718.
- [117] F. MEYER et S. BEUCHER. « Morphological Segmentation ». In : *Journal of Visual Communication and Image Representation* 1.1 (1^{er} sept. 1990), p. 21-46. ISSN : 1047-3203. DOI : 10.1016/1047-3203(90)90014-M. URL : <https://www.sciencedirect.com/science/article/pii/104732039090014M> (visité le 17/10/2023).
- [118] Michelle L. MILLER et Olivera J. FINN. « Flow Cytometry-Based Assessment of Direct-Targeting Anti-Cancer Antibody Immune Effector Functions ». In : *Methods in Enzymology* 632 (2020), p. 431-456. ISSN : 1557-7988. DOI : 10.1016/bs.mie.2019.07.026. pmid : 32000909.
- [119] Kenneth MURPHY, Casey WEAVER et Charles JANEWAY. *Janeway's Immunobiology*. 9th edition. New York : Garland Science, 2017. 904 p. ISBN : 978-0-8153-4505-3.
- [120] Farah MUSTAPHA, Martine PELICOT-BIARNES, Remy TORRO, Kheya SENGUPTA et Pierre-henri PUECH. *Cellular Forces during Early Spreading of T Lymphocytes on Ultra-Soft Substrates*. 11 fév. 2022. DOI : 10.1101/2022.02.11.480084. URL : <https://www.biorxiv.org/content/10.1101/2022.02.11.480084v1> (visité le 10/11/2022). preprint.
- [121] D. L. NELSON, C. C. KURMAN et D. E. SERBOUSEK. « 51Cr Release Assay of Antibody-Dependent Cell-Mediated Cytotoxicity (ADCC) ». In : *Current Protocols in Immunology* Chapter 7 (mai 2001), Unit 7.27. ISSN : 1934-368X. DOI : 10.1002/0471142735.im0727s08. pmid : 18432838.
- [122] Marie NGUYEN, Adele DE NINNO, Arianna MENCATTINI, Fanny MERMET-MEILLON, Giulia FORNABAI, Sophia S. EVANS, Mélissande COSSUTTA, Yasmine KHIRA, Weijing HAN, Philémon SIRVEN et al. « Dissecting Effects of Anti-cancer Drugs and Cancer-Associated Fibroblasts by On-Chip Reconstitution of Immunocompetent Tumor Microenvironments ». In : *Cell Reports* 25.13 (26 déc. 2018), 3884-3893.e3. ISSN : 2211-1247. DOI : 10.1016/j.celrep.2018.12.015. pmid : 30590056.
- [123] Wayne NIBLACK. *An Introduction to Digital Image Processing*. DNK : Strandberg Publishing Company, sept. 1985. 215 p. ISBN : 978-87-87200-55-4.
- [124] Falk NIMMERJAHN, Sina GORDAN et Anja LUX. « FcγR Dependent Mechanisms of Cytotoxic, Agonistic, and Neutralizing Antibody Activities ». In : *Trends in Immunology* 36.6 (juin 2015), p. 325-336. ISSN : 1471-4981. DOI : 10.1016/j.it.2015.04.005. pmid : 25981969.
- [125] Kuo NIU et Chao TIAN. « Zernike Polynomials and Their Applications ». In : *Journal of Optics* 24.12 (nov. 2022), p. 123001. ISSN : 2040-8986. DOI : 10.1088/2040-8986/ac9e08. URL : <https://dx.doi.org/10.1088/2040-8986/ac9e08> (visité le 14/01/2024).

- [126] Maria Carmen OCHOA, Luna MINUTE, Inmaculada RODRIGUEZ, Saray GARASA, Elisabeth PEREZ-RUIZ, Susana INOGÉS, Ignacio MELERO et Pedro BERRAONDO. « Antibody-Dependent Cell Cytotoxicity : Immunotherapy Strategies Enhancing Effector NK Cells ». In : *Immunology & Cell Biology* 95.4 (2017), p. 347-355. ISSN : 1440-1711. DOI : 10.1038/icb.2017.6. URL : <https://onlinelibrary.wiley.com/doi/abs/10.1038/icb.2017.6> (visité le 06/01/2024).
- [127] Per E. OLOFSSON, Elin FORSLUND, Bruno VANHERBERGHEN, Ksenia CHECHET, Oscar MICKELIN, Alexander Rivera AHLIN, Tobias EVERHORN et Björn ÖNFELT. « Distinct Migration and Contact Dynamics of Resting and IL-2-Activated Human Natural Killer Cells ». In : *Frontiers in Immunology* 5 (7 mar. 2014), p. 80. ISSN : 1664-3224. DOI : 10.3389/fimmu.2014.00080. pmid : 24639676. URL : <https://www.ncbi.nlm.nih.gov/pmc/articles/PMC3945532/> (visité le 19/10/2023).
- [128] OPENAI, Josh ACHIAM, Steven ADLER, Sandhini AGARWAL, Lama AHMAD, Ilge AKKAYA, Florencia Leoni ALEMAN, Diogo ALMEIDA, Janko ALTENSCHMIDT, Sam ALTMAN et al. *GPT-4 Technical Report*. 18 déc. 2023. DOI : 10.48550/arXiv.2303.08774. arXiv : 2303.08774 [cs]. URL : <http://arxiv.org/abs/2303.08774> (visité le 14/01/2024). preprint.
- [129] C. ORTIZ DE SOLÓRZANO, E. GARCÍA RODRIGUEZ, A. JONES, D. PINKEL, J. W. GRAY, D. SUDAR et S. J. LOCKET. « Segmentation of Confocal Microscope Images of Cell Nuclei in Thick Tissue Sections ». In : *Journal of Microscopy* 193 (Pt 3 mar. 1999), p. 212-226. ISSN : 0022-2720. DOI : 10.1046/j.1365-2818.1999.00463.x. pmid : 10199001.
- [130] Nobuyuki OTSU. « A Threshold Selection Method from Gray-Level Histograms ». In : *IEEE Transactions on Systems, Man, and Cybernetics* 9.1 (jan. 1979), p. 62-66. ISSN : 2168-2909. DOI : 10.1109/TSMC.1979.4310076. URL : <https://ieeexplore.ieee.org/document/4310076> (visité le 15/10/2023).
- [131] Marius PACHITARIU et Carsen STRINGER. « Cellpose 2.0 : How to Train Your Own Model ». In : *Nature Methods* 19.12 (12 déc. 2022), p. 1634-1641. ISSN : 1548-7105. DOI : 10.1038/s41592-022-01663-4. URL : <https://www.nature.com/articles/s41592-022-01663-4> (visité le 15/10/2023).
- [132] Francesco PADOVANI, Benedikt MAIRHÖRMANN, Pascal FALTER-BRAUN, Jette LENGEFELD et Kurt M. SCHMOLLER. « Segmentation, Tracking and Cell Cycle Analysis of Live-Cell Imaging Data with Cell-ACDC ». In : *BMC Biology* 20.1 (5 août 2022), p. 174. ISSN : 1741-7007. DOI : 10.1186/s12915-022-01372-6. URL : <https://doi.org/10.1186/s12915-022-01372-6> (visité le 22/06/2023).
- [133] J. PARKIN et B. COHEN. « An Overview of the Immune System ». In : *Lancet (London, England)* 357.9270 (2 juin 2001), p. 1777-1789. ISSN : 0140-6736. DOI : 10.1016/S0140-6736(00)04904-7. pmid : 11403834.
- [134] PAUL WILMOTT. *The Mathematics of Financial Derivatives*. Avec la coll. d'INTERNET ARCHIVE. Cambridge University Press, 1995. 342 p. ISBN : 978-0-521-49789-3. URL : <http://archive.org/details/mathematicsoffin00wilm> (visité le 29/01/2024).
- [135] Anne PIERRES, Anne-Marie BENOLIEL, Dominique TOUCHARD et Pierre BONGRAND. « How Cells Tiptoe on Adhesive Surfaces before Sticking ». In : *Biophysical Journal* 94.10 (15 mai 2008), p. 4114-4122. ISSN : 0006-3495. DOI : 10.1529/biophysj.107.125278. pmid : 18234815. URL : [https://www.cell.com/biophysj/abstract/S0006-3495\(08\)70411-9](https://www.cell.com/biophysj/abstract/S0006-3495(08)70411-9) (visité le 06/01/2024).

- [136] Anne PIERRES, Philippe EYMERIC, Emmanuelle BALOCHE, Dominique TOUCHARD, Anne-Marie BENOLIEL et Pierre BONGRAND. « Cell Membrane Alignment along Adhesive Surfaces : Contribution of Active and Passive Cell Processes ». In : *Biophysical Journal* 84.3 (1^{er} mar. 2003), p. 2058-2070. ISSN : 0006-3495. DOI : 10.1016/S0006-3495(03)75013-9. pmid : 12609907. URL : [https://www.cell.com/biophysj/abstract/S0006-3495\(03\)75013-9](https://www.cell.com/biophysj/abstract/S0006-3495(03)75013-9) (visité le 06/01/2024).
- [137] Dustin PODELL, Zion ENGLISH, Kyle LACEY, Andreas BLATTMANN, Tim DOCKHORN, Jonas MÜLLER, Joe PENNA et Robin ROMBACH. *SDXL : Improving Latent Diffusion Models for High-Resolution Image Synthesis*. 4 juil. 2023. DOI : 10.48550/arXiv.2307.01952. arXiv : 2307.01952 [cs]. URL : <http://arxiv.org/abs/2307.01952> (visité le 03/02/2024). preprint.
- [138] Chang QIAO, Di LI, Yuting GUO, Chong LIU, Tao JIANG, Qionghai DAI et Dong LI. « Evaluation and Development of Deep Neural Networks for Image Super-Resolution in Optical Microscopy ». In : *Nature Methods* 18.2 (2 fév. 2021), p. 194-202. ISSN : 1548-7105. DOI : 10.1038/s41592-020-01048-5. URL : <https://www.nature.com/articles/s41592-020-01048-5> (visité le 02/02/2024).
- [139] Joachim RÄDLER et Erich SACKMANN. « Imaging Optical Thicknesses and Separation Distances of Phospholipid Vesicles at Solid Surfaces ». In : <http://dx.doi.org/10.1051/jp2:1993163> 3 (1^{er} mai 1993). DOI : 10.1051/jp2:1993163.
- [140] Maziar RAISSI, Paris PERDIKARIS et George Em KARNIADAKIS. *Physics Informed Deep Learning (Part I) : Data-driven Solutions of Nonlinear Partial Differential Equations*. 28 nov. 2017. DOI : 10.48550/arXiv.1711.10561. arXiv : 1711.10561 [cs, math, stat]. URL : <http://arxiv.org/abs/1711.10561> (visité le 05/02/2024). preprint.
- [141] Arjun RAJ et Alexander van OUDENAARDEN. « Nature, Nurture, or Chance : Stochastic Gene Expression and Its Consequences ». In : *Cell* 135.2 (17 oct. 2008), p. 216-226. ISSN : 1097-4172. DOI : 10.1016/j.cell.2008.09.050. pmid : 18957198.
- [142] D. RIVELINE, E. ZAMIR, N. Q. BALABAN, U. S. SCHWARZ, T. ISHIZAKI, S. NARUMIYA, Z. KAM, B. GEIGER et A. D. BERSHADSKY. « Focal Contacts as Mechanosensors : Externally Applied Local Mechanical Force Induces Growth of Focal Contacts by an mDia1-dependent and ROCK-independent Mechanism ». In : *The Journal of Cell Biology* 153.6 (11 juin 2001), p. 1175-1186. ISSN : 0021-9525. DOI : 10.1083/jcb.153.6.1175. pmid : 11402062.
- [143] Yair RIVENSON, Tairan LIU, Zhensong WEI, Yibo ZHANG, Kevin de HAAN et Aydogan OZCAN. « PhaseStain : The Digital Staining of Label-Free Quantitative Phase Microscopy Images Using Deep Learning ». In : *Light : Science & Applications* 8.1 (1 6 fév. 2019), p. 23. ISSN : 2047-7538. DOI : 10.1038/s41377-019-0129-y. URL : <https://www.nature.com/articles/s41377-019-0129-y> (visité le 02/02/2024).
- [144] Olaf RONNEBERGER, Philipp FISCHER et Thomas BROX. « U-Net : Convolutional Networks for Biomedical Image Segmentation ». In : *Medical Image Computing and Computer-Assisted Intervention – MICCAI 2015*. Sous la dir. de Nassir NAVAB, Joachim HORNEGGER, William M. WELLS et Alejandro F. FRANGI. Lecture Notes in Computer Science. Cham : Springer International Publishing, 2015, p. 234-241. ISBN : 978-3-319-24574-4. DOI : 10.1007/978-3-319-24574-4_28.
- [145] Valerie RUBIO, Tor B. STUGE, Naileshni SINGH, Michael R. BETTS, Jeffrey S. WEBER, Mario ROEDERER et Peter P. LEE. « Ex Vivo Identification, Isolation and Analysis of Tumor-Cytolytic T Cells ». In : *Nature Medicine* 9.11 (nov. 2003), p. 1377-1382. ISSN : 1078-8956. DOI : 10.1038/nm942. pmid : 14528297.

- [146] Curtis T. RUEDEN, Mark C. HINER, Edward L. EVANS, Michael A. PINKERT, Alice M. LUCAS, Anne E. CARPENTER, Beth A. CIMINI et Kevin W. ELICEIRI. « PyImageJ : A Library for Integrating ImageJ and Python ». In : *Nature Methods* 19.11 (11 nov. 2022), p. 1326-1327. ISSN : 1548-7105. DOI : 10.1038/s41592-022-01655-4. URL : <https://www.nature.com/articles/s41592-022-01655-4> (visité le 31/01/2024).
- [147] Curtis T. RUEDEN, Johannes SCHINDELIN, Mark C. HINER, Barry E. DEZONIA, Alison E. WALTER, Ellen T. ARENA et Kevin W. ELICEIRI. « ImageJ2 : ImageJ for the next Generation of Scientific Image Data ». In : *BMC Bioinformatics* 18.1 (29 nov. 2017), p. 529. ISSN : 1471-2105. DOI : 10.1186/s12859-017-1934-z. URL : <https://doi.org/10.1186/s12859-017-1934-z> (visité le 15/10/2023).
- [148] Dirk SAERENS, Gholamreza Hassanzadeh GHASSABEH et Serge MUYLDERMANS. « Single-Domain Antibodies as Building Blocks for Novel Therapeutics ». In : *Current Opinion in Pharmacology* 8.5 (oct. 2008), p. 600-608. ISSN : 1471-4892. DOI : 10.1016/j.coph.2008.07.006. pmid : 18691671.
- [149] Nohemí SALINAS-JAZMÍN, Emiliano HISAKI-ITAYA et Marco A. VELASCO-VELÁZQUEZ. « A Flow Cytometry-Based Assay for the Evaluation of Antibody-Dependent Cell-Mediated Cytotoxicity (ADCC) in Cancer Cells ». In : *Methods in Molecular Biology (Clifton, N.J.)* 1165 (2014), p. 241-252. ISSN : 1940-6029. DOI : 10.1007/978-1-4939-0856-1_16. pmid : 24839029.
- [150] Merlin SANICAS, Remy TORRO, Laurent LIMOZIN et Patrick CHAMES. *Antigen Density and Applied Force Control Enrichment of Nanobody-Expressing Yeast Cells in Microfluidics*. 3 jan. 2024. DOI : 10.1101/2024.01.03.574015. URL : <https://www.biorxiv.org/content/10.1101/2024.01.03.574015v1> (visité le 04/01/2024). preprint.
- [151] Saheli SARKAR, Wenjing KANG, Songyao JIANG, Kunpeng LI, Somak RAY, Ed LUTHER, Alexander R. IVANOV, Yun FU et Tania KONRY. « Machine Learning-Aided Quantification of Antibody-Based Cancer Immunotherapy by Natural Killer Cells in Microfluidic Droplets ». In : *Lab on a Chip* 20.13 (30 juin 2020), p. 2317-2327. ISSN : 1473-0189. DOI : 10.1039/D0LC00158A. URL : <https://pubs.rsc.org/en/content/articlelanding/2020/lc/d0lc00158a> (visité le 09/11/2022).
- [152] Ruth M. SAUNDERS, Mark R. HOLT, Lisa JENNINGS, Deborah H. SUTTON, Igor L. BARSUKOV, Andrey BOBKOV, Robert C. LIDDINGTON, Eileen A. ADAMSON, Graham A. DUNN et David R. CRITCHLEY. « Role of Vinculin in Regulating Focal Adhesion Turnover ». In : *European Journal of Cell Biology* 85.6 (juin 2006), p. 487-500. ISSN : 0171-9335. DOI : 10.1016/j.ejcb.2006.01.014. pmid : 16584805.
- [153] J. SAUVOLA et M. PIETIKÄINEN. « Adaptive Document Image Binarization ». In : *Pattern Recognition* 33.2 (1^{er} fév. 2000), p. 225-236. ISSN : 0031-3203. DOI : 10.1016/S0031-3203(99)00055-2. URL : <https://www.sciencedirect.com/science/article/pii/S0031320399000552> (visité le 13/01/2024).
- [154] Johannes SCHINDELIN, Ignacio ARGANDA-CARRERAS, Erwin FRISE, Verena KAYNIG, Mark LONGAIR, Tobias PIETZSCH, Stephan PREIBISCH, Curtis RUEDEN, Stephan SAALFELD, Benjamin SCHMID et al. « Fiji : An Open-Source Platform for Biological-Image Analysis ». In : *Nature Methods* 9.7 (7 juil. 2012), p. 676-682. ISSN : 1548-7105. DOI : 10.1038/nmeth.2019. URL : <https://www.nature.com/articles/nmeth.2019> (visité le 15/10/2023).
- [155] Uwe SCHMIDT, Martin WEIGERT, Coleman BROADDUS et Gene MYERS. « Cell Detection with Star-Convex Polygons ». In : *Medical Image Computing and Computer Assisted Intervention – MICCAI 2018*. Sous la dir. d'Alejandro F. FRANGI, Julia A. SCHNABEL, Christos DAVATZIKOS, Carlos ALBEROLA-LÓPEZ et Gabor FICHTINGER. Lecture Notes in Computer Science. Cham : Springer International Publishing, 2018, p. 265-273. ISBN : 978-3-030-00934-2. DOI : 10.1007/978-3-030-00934-2_30.

- [156] Caroline A. SCHNEIDER, Wayne S. RASBAND et Kevin W. ELICEIRI. « NIH Image to ImageJ : 25 Years of Image Analysis ». In : *Nature Methods* 9.7 (7 juil. 2012), p. 671-675. ISSN : 1548-7105. DOI : 10.1038/nmeth.2089. URL : <https://www.nature.com/articles/nmeth.2089> (visité le 15/10/2023).
- [157] Morgan Sarah SCHWARTZ, Erick MOEN, Geneva MILLER, Tom DOUGHERTY, Enrico BORBA, Rachel DING, William GRAF, Edward PAO et David Van VALEN. *Caliban : Accurate Cell Tracking and Lineage Construction in Live-Cell Imaging Experiments with Deep Learning*. 12 sept. 2023. DOI : 10.1101/803205. URL : <https://www.biorxiv.org/content/10.1101/803205v4> (visité le 14/01/2024). preprint.
- [158] Andrew M. SCOTT, Jedd D. WOLCHOK et Lloyd J. OLD. « Antibody Therapy of Cancer ». In : *Nature Reviews. Cancer* 12.4 (22 mar. 2012), p. 278-287. ISSN : 1474-1768. DOI : 10.1038/nrc3236. pmid : 22437872.
- [159] Arindrajit SEAL, Arunava DAS et Prasad SEN. « Watershed : An Image Segmentation Approach ». In : *International Journal of Computer Science and Information Technologies* 6.3 (2015), p. 2295-2297.
- [160] Kheya SENGUPTA, Helim ARANDA-ESPINOZA, Lee SMITH, Paul JANMEY et Daniel HAMMER. « Spreading of Neutrophils : From Activation to Migration ». In : *Biophysical Journal* 91.12 (15 déc. 2006), p. 4638-4648. ISSN : 0006-3495. DOI : 10.1529/biophysj.105.080382. pmid : 17012330. URL : <https://www.ncbi.nlm.nih.gov/pmc/articles/PMC1779913/> (visité le 02/02/2024).
- [161] Karen SIMONYAN et Andrew ZISSERMAN. « Very Deep Convolutional Networks for Large-Scale Image Recognition ». 2014.
- [162] Mark X. SLIWKOWSKI et Ira MELLMAN. « Antibody Therapeutics in Cancer ». In : *Science (New York, N.Y.)* 341.6151 (13 sept. 2013), p. 1192-1198. ISSN : 1095-9203. DOI : 10.1126/science.1241145. pmid : 24031011.
- [163] Mark J. SMYTH, Erika CRETNEY, Janice M. KELLY, Jennifer A. WESTWOOD, Shayna E. A. STREET, Hideo YAGITA, Kazuyoshi TAKEDA, Serani L. H. van DOMMELEN, Mariapia A. DEGLI-ESPOSTI et Yoshihiro HAYAKAWA. « Activation of NK Cell Cytotoxicity ». In : *Molecular Immunology* 42.4 (fév. 2005), p. 501-510. ISSN : 0161-5890. DOI : 10.1016/j.molimm.2004.07.034. pmid : 15607806.
- [164] Berend SNIJDER, Raphael SACHER, Pauli RÄMÖ, Eva-Maria DAMM, Prisca LIBERALI et Lucas PELKMANS. « Population Context Determines Cell-to-Cell Variability in Endocytosis and Virus Infection ». In : *Nature* 461.7263 (7263 sept. 2009), p. 520-523. ISSN : 1476-4687. DOI : 10.1038/nature08282. URL : <https://www.nature.com/articles/nature08282> (visité le 29/01/2024).
- [165] H. D. SOULE, J. VAZGUEZ, A. LONG, S. ALBERT et M. BRENNAN. « A Human Cell Line from a Pleural Effusion Derived from a Breast Carcinoma ». In : *Journal of the National Cancer Institute* 51.5 (nov. 1973), p. 1409-1416. ISSN : 0027-8874. DOI : 10.1093/jnci/51.5.1409. pmid : 4357757.
- [166] Sophie STEELAND, Roosmarijn E. VANDENBROUCKE et Claude LIBERT. « Nanobodies as Therapeutics : Big Opportunities for Small Antibodies ». In : *Drug Discovery Today* 21.7 (juil. 2016), p. 1076-1113. ISSN : 1878-5832. DOI : 10.1016/j.drudis.2016.04.003. pmid : 27080147.
- [167] David R. STIRLING, Madison J. SWAIN-BOWDEN, Alice M. LUCAS, Anne E. CARPENTER, Beth A. CIMINI et Allen GOODMAN. « CellProfiler 4 : Improvements in Speed, Utility and Usability ». In : *BMC Bioinformatics* 22.1 (10 sept. 2021), p. 433. ISSN : 1471-2105. DOI : 10.1186/s12859-021-04344-9. URL : <https://doi.org/10.1186/s12859-021-04344-9> (visité le 18/10/2023).

- [168] George Gabriel STOKES. « XXX. On the Change of Refrangibility of Light ». In : *Philosophical Transactions of the Royal Society of London* 142 (jan. 1997), p. 463-562. DOI : 10.1098/rstl.1852.0022. URL : <https://royalsocietypublishing.org/doi/10.1098/rstl.1852.0022> (visité le 02/02/2024).
- [169] Carsen STRINGER, Tim WANG, Michalis MICHAELOS et Marius PACHITARIU. « Cellpose : A Generalist Algorithm for Cellular Segmentation ». In : *Nature Methods* 18.1 (1 jan. 2021), p. 100-106. ISSN : 1548-7105. DOI : 10.1038/s41592-020-01018-x. URL : <https://www.nature.com/articles/s41592-020-01018-x> (visité le 22/06/2023).
- [170] Gemini TEAM, Rohan ANIL, Sebastian BORGEAUD, Yonghui WU, Jean-Baptiste ALAYRAC, Jiahui YU, Radu SORICUT, Johan SCHALKWYK, Andrew M. DAI, Anja HAUTH et al. *Gemini : A Family of Highly Capable Multimodal Models*. 18 déc. 2023. DOI : 10.48550/arXiv.2312.11805. arXiv : 2312.11805 [cs]. URL : <http://arxiv.org/abs/2312.11805> (visité le 14/01/2024). preprint.
- [171] Kurt THORN. « Genetically Encoded Fluorescent Tags ». In : *Molecular Biology of the Cell* 28.7 (avr. 2017), p. 848-857. ISSN : 1059-1524. DOI : 10.1091/mbc.e16-07-0504. URL : <https://www.molbiolcell.org/doi/10.1091/mbc.e16-07-0504> (visité le 02/02/2024).
- [172] Jean-Yves TINEVEZ, Nick PERRY, Johannes SCHINDELIN, Genevieve M. HOOPES, Gregory D. REYNOLDS, Emmanuel LAPLANTINE, Sebastian Y. BEDNAREK, Spencer L. SHORTE et Kevin W. ELICEIRI. « TrackMate : An Open and Extensible Platform for Single-Particle Tracking ». In : *Methods. Image Processing for Biologists* 115 (15 fév. 2017), p. 80-90. ISSN : 1046-2023. DOI : 10.1016/j.ymeth.2016.09.016. URL : <http://www.sciencedirect.com/science/article/pii/S1046202316303346> (visité le 01/06/2020).
- [173] Iva Marija TOLIĆ-NØRRELYKKE, Emilia-Laura MUNTEANU, Genevieve THON, Lene ODDERSHEDE et Kirstine BERG-SØRENSEN. « Anomalous Diffusion in Living Yeast Cells ». In : *Physical Review Letters* 93.7 (13 août 2004), p. 078102. ISSN : 0031-9007. DOI : 10.1103/PhysRevLett.93.078102. pmid : 15324280.
- [174] Rémy TORRO, Beatriz DÍAZ-BELLO, Dalia El ARAWI, Lorna AMMER, Patrick CHAMES, Kheya SENGUPTA et Laurent LIMOZIN. *Celldetective : An AI-enhanced Image Analysis Tool for Unraveling Dynamic Cell Interactions*. 17 mar. 2024. DOI : 10.1101/2024.03.15.585250. URL : <https://www.biorxiv.org/content/10.1101/2024.03.15.585250v1> (visité le 08/04/2024). preprint.
- [175] Marc TURINI, Patrick CHAMES, Pierre BRUHNS, Daniel BATY et Brigitte KERFELEC. « A FcγRIII-engaging Bispecific Antibody Expands the Range of HER2-expressing Breast Tumors Eligible to Antibody Therapy ». In : *Oncotarget* 5.14 (11 juin 2014), p. 5304-5319. ISSN : 1949-2553. pmid : 24979648. URL : <https://www.ncbi.nlm.nih.gov/pmc/articles/PMC4170649/> (visité le 15/01/2024).
- [176] Kristina ULICNA, Giulia VALLARDI, Guillaume CHARRAS et Alan R. LOWE. « Automated Deep Lineage Tree Analysis Using a Bayesian Single Cell Tracking Approach ». In : *Frontiers in Computer Science* 3 (2021). ISSN : 2624-9898. URL : <https://www.frontiersin.org/articles/10.3389/fcomp.2021.734559> (visité le 09/11/2022).
- [177] M VAN DEN TEMPEL. « Distance between Emulsified Oil Globules upon Coalescence ». In : *Journal of Colloid Science* 13.2 (1^{er} avr. 1958), p. 125-133. ISSN : 0095-8522. DOI : 10.1016/0095-8522(58)90015-1. URL : <https://www.sciencedirect.com/science/article/pii/0095852258900151> (visité le 02/02/2024).
- [178] Stefan VAN DER WALT, Johannes L SCHÖNBERGER, Juan NUNEZ-IGLESIAS, François BOULOGNE, Joshua D WARNER, Neil YAGER, Emmanuelle GOUILLART et Tony YU. « Scikit-Image : Image Processing in Python ». In : *PeerJ* 2 (2014), e453.

- [179] Irene van der HAAR ÀVILA, Patricia MARMOL, Jeannette CANY, Rolf KIESSLING et Yago PICO DE COAÑA. « Evaluating Antibody-Dependent Cell-Mediated Cytotoxicity by Flow Cytometry ». In : *Methods in Molecular Biology (Clifton, N.J.)* 1913 (2019), p. 181-194. ISSN : 1940-6029. DOI : 10.1007/978-1-4939-8979-9_13. pmid : 30666607.
- [180] Antonín. VAŠÍČEK. *Optics of Thin Films*. Trad. par H. WATNEY-KACZÉR. Reworked and supplemented ed.] Amsterdam, New York : North-Holland Pub. Co. ; Interscience Publishers, 1960. 403 p.
- [181] Ashish VASWANI, Noam SHAZEER, Niki PARMAR, Jakob USZKOREIT, Llion JONES, Aidan N. GOMEZ, Lukasz KAISER et Illia POLOSUKHIN. *Attention Is All You Need*. 1^{er} août 2023. DOI : 10.48550/arXiv.1706.03762. arXiv : 1706.03762 [cs]. URL : <http://arxiv.org/abs/1706.03762> (visité le 14/01/2024). preprint.
- [182] Hendrik VERSCHUEREN. « Interference Reflection Microscopy in Cell Biology : Methodology and Applications ». In : *Journal of Cell Science* 75.1 (1^{er} avr. 1985), p. 279-301. ISSN : 0021-9533. DOI : 10.1242/jcs.75.1.279. URL : <https://doi.org/10.1242/jcs.75.1.279> (visité le 24/01/2024).
- [183] Astrid WAHL, Céline DINET, Pierre DILLARD, Aya NASSEREDDINE, Pierre-Henri PUECH, Laurent LIMOZIN et Kheya SENGUPTA. « Biphasic Mechanosensitivity of T Cell Receptor-Mediated Spreading of Lymphocytes ». In : *Proceedings of the National Academy of Sciences* 116.13 (26 mar. 2019), p. 5908-5913. DOI : 10.1073/pnas.1811516116. URL : <https://www.pnas.org/doi/10.1073/pnas.1811516116> (visité le 06/01/2024).
- [184] C. WÄHLBY, I.-M. SINTORN, F. ERLANDSSON, G. BORGEFORS et E. BENGTTSSON. « Combining Intensity, Edge and Shape Information for 2D and 3D Segmentation of Cell Nuclei in Tissue Sections ». In : *Journal of Microscopy* 215.1 (2004), p. 67-76. ISSN : 1365-2818. DOI : 10.1111/j.0022-2720.2004.01338.x. URL : <https://onlinelibrary.wiley.com/doi/abs/10.1111/j.0022-2720.2004.01338.x> (visité le 17/10/2023).
- [185] Carolina WÄHLBY. « Algorithms for Applied Digital Image Cytometry ». In : (2003). URL : <https://urn.kb.se/resolve?urn=urn:nbn:se:uu:diva-3608> (visité le 17/10/2023).
- [186] Michael L. WASKOM. « Seaborn : Statistical Data Visualization ». In : *Journal of Open Source Software* 6.60 (2021), p. 3021. DOI : 10.21105/joss.03021. URL : <https://doi.org/10.21105/joss.03021>.
- [187] Peter R. WIECHA, Arnaud ARBOUET, Christian GIRARD et Otto L. MUSKENS. « Deep Learning in Nano-Photonics : Inverse Design and Beyond ». In : *Photonics Research* 9.5 (1^{er} mai 2021), B182-B200. ISSN : 2327-9125. DOI : 10.1364/PRJ.415960. URL : <https://opg.optica.org/prj/abstract.cfm?uri=prj-9-5-B182> (visité le 02/02/2024).
- [188] R. W. WILKINSON, A. E. LEE-MACARY, D. DAVIES, D. SNARY et E. L. ROSS. « Antibody-Dependent Cell-Mediated Cytotoxicity : A Flow Cytometry-Based Assay Using Fluorophores ». In : *Journal of Immunological Methods* 258.1-2 (1^{er} déc. 2001), p. 183-191. ISSN : 0022-1759. DOI : 10.1016/S0022-1759(01)00474-4. pmid : 11684135.
- [189] Martin WILSON. « Collecting Light : The Importance of Numerical Aperture in Microscopy ». In : (12 juil. 2017). URL : <https://www.leica-microsystems.com/science-lab/microscopy-basics/collecting-light-the-importance-of-numerical-aperture-in-microscopy/> (visité le 30/01/2024).
- [190] Makiko YAMASHITA, Shigehisa KITANO, Hiroaki AIKAWA, Aya KUCHIBA, Mitsuhiro HAYASHI, Noboru YAMAMOTO, Kenji TAMURA et Akinobu HAMADA. « A Novel Method for Evaluating Antibody-Dependent Cell-Mediated Cytotoxicity by Flowcytometry Using Cryopreserved Human Peripheral Blood Mononuclear Cells ». In : *Scientific Reports* 6.1 (1 27 jan. 2016), p. 19772. ISSN : 2045-2322. DOI : 10.1038/srep19772. URL : <https://www.nature.com/articles/srep19772> (visité le 15/10/2023).

- [191] Christopher YEUNG, Ju-Ming TSAI, Brian KING, Benjamin PHAM, David HO, Julia LIANG, Mark W. KNIGHT et Aaswath P. RAMAN. « Multiplexed Supercell Metasurface Design and Optimization with Tandem Residual Networks ». In : *Nanophotonics* 10.3 (3 jan. 2021), p. 1133-1143. ISSN : 2192-8614. DOI : 10.1515/nanoph-2020-0549. URL : <https://www.degruyter.com/document/doi/10.1515/nanoph-2020-0549/html?lang=en> (visité le 03/02/2024).
- [192] Abolfazl ZARGARI, Gerrald A. LODEWIJK, Najmeh MASHHADI, Nathan COOK, Celine W. NEUDORF, Kimiasadat ARAGHBIDIKASHANI, Robert HAYS, Sayaka KOZUKI, Stefany RUBIO, Eva HRABETA-ROBINSON et al. « DeepSea Is an Efficient Deep-Learning Model for Single-Cell Segmentation and Tracking in Time-Lapse Microscopy ». In : *Cell Reports Methods* 3.6 (26 juin 2023), p. 100500. ISSN : 2667-2375. DOI : 10.1016/j.crmeth.2023.100500. pmid : 37426758.
- [193] Hong ZHAO, Jadwiga OCZOS, Pawel JANOWSKI, Dominika TREMBECKA, Jurek DOBRUCKI, Zbigniew DARZYNKIEWICZ et Donald WLODKOWIC. « Rationale for the Real-Time and Dynamic Cell Death Assays Using Propidium Iodide ». In : *Cytometry. Part A : the journal of the International Society for Analytical Cytology* 77.4 (avr. 2010), p. 399-405. ISSN : 1552-4922. DOI : 10.1002/cyto.a.20867. pmid : 20131407. URL : <https://www.ncbi.nlm.nih.gov/pmc/articles/PMC3646415/> (visité le 18/10/2023).
- [194] Xiao ZHOU, Renping ZHAO, Karsten SCHWARZ, Matthieu MANGEAT, Eva C. SCHWARZ, Mohamed HAMED, Ivan BOGESKI, Volkhard HELMS, Heiko RIEGER et Bin QU. « Bystander Cells Enhance NK Cytotoxic Efficiency by Reducing Search Time ». In : *Scientific Reports* 7 (13 mar. 2017), p. 44357. ISSN : 2045-2322. DOI : 10.1038/srep44357. pmid : 28287155.
- [195] Xingwu ZHOU, Moyuan QU, Peyton TEBON, Xing JIANG, Canran WANG, Yumeng XUE, Jixiang ZHU, Shiming ZHANG, Rahmi OKLU, Shiladitya SENGUPTA et al. « Screening Cancer Immunotherapy : When Engineering Approaches Meet Artificial Intelligence ». In : *Advanced Science* 7.19 (2020), p. 2001447. ISSN : 2198-3844. DOI : 10.1002/advs.202001447. URL : <https://onlinelibrary.wiley.com/doi/abs/10.1002/advs.202001447> (visité le 15/01/2024).
- [196] Zongwei ZHOU, Md Mahfuzur RAHMAN SIDDIQUEE, Nima TAJBAKHSH et Jianming LIANG. « UNet++ : A Nested U-Net Architecture for Medical Image Segmentation ». In : *Deep Learning in Medical Image Analysis and Multimodal Learning for Clinical Decision Support*. Sous la dir. de Danail STOYANOV, Zeike TAYLOR, Gustavo CARNEIRO, Tanveer SYEDA-MAHMOOD, Anne MARTEL, Lena MAIER-HEIN, João Manuel R.S. TAVARES, Andrew BRADLEY, João Paulo PAPA, Vasileios BELAGIANNIS et al. Lecture Notes in Computer Science. Cham : Springer International Publishing, 2018, p. 3-11. ISBN : 978-3-030-00889-5. DOI : 10.1007/978-3-030-00889-5_1.
- [197] Alexandra ZIDOVSKA et Erich SACKMANN. « Brownian Motion of Nucleated Cell Envelopes Impedes Adhesion ». In : *Physical Review Letters* 96.4 (1^{er} fév. 2006), p. 048103. DOI : 10.1103/PhysRevLett.96.048103. URL : <https://link.aps.org/doi/10.1103/PhysRevLett.96.048103> (visité le 02/02/2024).
- [198] A. ZILKER, H ENGELHARDT et Erich SACKMANN. « Dynamic Reflection Interference Contrast (RIC-) Microscopy : A New Method to Study Surface Excitations of Cells and to Measure Membrane Bending Elastic Moduli ». In : <http://dx.doi.org/10.1051/jphys:019870048012021390048> (1^{er} déc. 1987). DOI : 10.1051/jphys:0198700480120213900.

Articles

Rémy TORRO, Beatriz DÌAZ-BELLO, Dalia El ARAWI, Lorna AMMER, Patrick CHAMES, Kheya SENGUPTA et Laurent LIMOZIN. *Celldetective : An AI-enhanced Image Analysis Tool for Unraveling Dynamic Cell Interactions*. 17 mar. 2024. DOI : 10.1101/2024.03.15.585250. URL : <https://www.biorxiv.org/content/10.1101/2024.03.15.585250v1> (visité le 08/04/2024). preprint

Celldetective: an AI-enhanced image analysis tool for unraveling dynamic cell interactions

Rémy Torro^{1,2*}, Beatriz Díaz-Bello¹, Dalia El Arawi¹,
Lorna Ammer^{1,3}, Patrick Chames³, Kheya Sengupta²,
Laurent Limozin^{1*}

^{1*}Aix-Marseille Univ, CNRS, INSERM, Turing Centre for Living
systems, LAI, Marseille, France.

²Aix-Marseille Univ, CNRS, Turing Centre for Living systems, CINAM,
Marseille, France.

³Aix-Marseille Univ, CNRS, INSERM, Institut Paoli-Calmettes, CRCM,
Marseille, France.

*Corresponding author(s). E-mail(s): remy.torro@inserm.fr;
laurent.limozin@inserm.fr;

Abstract

A current key challenge in bioimaging is the analysis of multimodal and multidimensional data reporting dynamic interactions between diverse cell populations. We developed Celldetective, a software that integrates AI-based segmentation and tracking algorithms and automated signal analysis into a user-friendly graphical interface, offering complete interactive visualization, annotation, and training capabilities. We demonstrate it by analyzing original experimental data of spreading immune effector cells as well as antibody-dependent cell cytotoxicity events using multimodal fluorescence microscopy.

Keywords: bioimage analysis, multimodal microscopy, artificial intelligence, immune cell interactions

Modern biomedical research relies on high throughput and high resolution experimental assays which require advanced and powerful analysis tools. High content, multi-channel spatio-temporal imaging of living cells is an important example. Deep learning (DL) has revolutionized this field [1, 2]. Yet, extracting scientific

insights from such complex data remains challenging, requiring coding skills [3] or proficiency in integrating/mastering disparate tools [4]. A primary step in image analysis is cell segmentation, for which DL tools are highly successful [5, 6], but rely on pretrained models for which the original dataset is not always accessible or too remote from user’s data [7], preventing transfer learning. For dynamic data, the tracking of cells is also crucial [8, 9]. Currently, there are almost no solutions that integrate the two tasks [10]. Furthermore, single-cell image sequences contain time-dependent signals giving access to functional information, traditionally collected or treated manually [11, 12]. Existing softwares, though sometimes capable of measuring features [13], are not conceived for dynamic signals, nor linked to DL based event-detection. Here, we introduce Celldetective, an open-source Python-based solution with a graphical user interface (GUI) for annotation and dynamic analysis of 2D multimodal time-lapse microscopy sequences from mixed cell populations. Celldetective incorporates advanced functionalities such as state-of-the-art segmentation, tracking, signal-analysis, event-detection, and cell-cell interaction analysis. The framework accommodates complete retraining within the GUI. We demonstrate the software capabilities through two applications: i) measuring immune cell decision time in a cell-surface assay using label-free microscopy and ii) measuring dynamic cell-cell interactions in a multiwell co-culture of immune and target cells, an established cytotoxic assay, using multi-color fluorescence microscopy.

Typically used for multi-dimensional images from biological samples in multi-well chambers (Fig. 1 Top and Supplementary Fig. 1), Celldetective generates quantitative output such as cell trajectories, time-dependent signals and event-detections. The analysis pipeline is shown in Fig. 1, featuring main functions of the software (left column) and data input/output (right column). For cell segmentation, generalist DL models StarDist [5] and Cellpose [6] are used and both are made available natively (Supplementary Tab. 1). However, these models exhibit limited performance when faced with a mixture of cell types with different sizes (Supplementary Fig. 2A-D) or modalities not encountered during training (Supplementary Fig. 2E-H). We therefore specifically trained models using dedicated datasets for the applications described below. The GUI emulates a napari visualization tool [4] to allow manual correction of segmentation masks (Supplementary Fig. 3). Corrected masks serve as ground truth to fine-tune the generalist DL model [4, 6] or train a specialized model from scratch (Supplementary Fig. 4). Cell tracking is performed by the Bayesian tracker btrack [8] which is fully parametrizable in the GUI, with options for adding a selection of cell features for improved performance, post-processing of tracks (Supplementary Fig. 5) and visualization via Napari. Single-cell measurements are based either on the segmentation masks, which include morphology, texture and tone, or on trajectories centered ROIs, providing continuous intensity signal measurements. Based on time-traces, single-cell event-detection can be performed by time-series analysis using a dedicated visualization and manual annotation menu (Supplementary Fig. 6). Automated classification and regression are available as a DL approach (Supplementary Fig. 7 and Tab. 4). Signal annotations can be used as training data to enhance or automatize the event-detection DL model. The tracking and measurement data can be exported as tables for each labeled cell population,

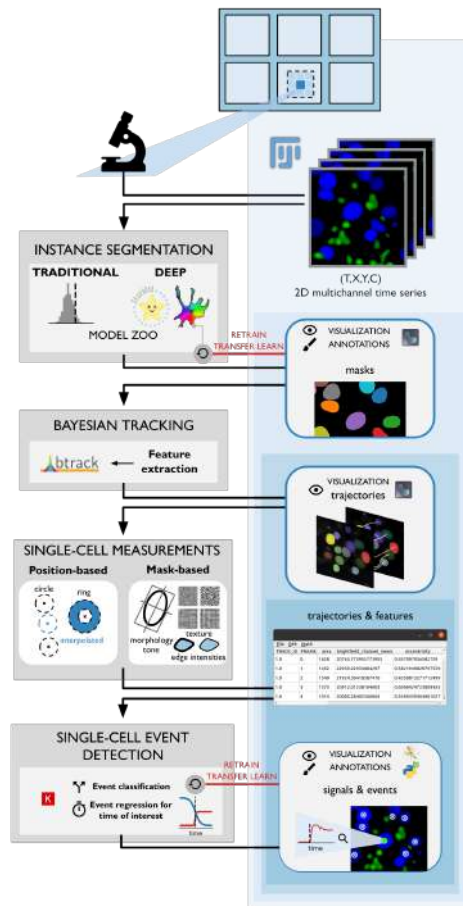


Fig. 1 Functional description of Celldetective. Multi-channel timeseries microscopy data is fed into Celldetective, in a file structure mimicking that of multi-well plates. The processing modules are shown on the left column, whereas the output and visualization modules are displayed on the right column. The pipeline features successively (from top to bottom): 1. Instance segmentation (either with traditional thresholding or Deep Learning, based on a model zoo, using StarDist [5] or Cellpose [6]). The output data are masks, which can be visualized and annotated using Napari [4], for optional retraining of the model. 2. Bayesian tracking associated with feature extraction (btrack [8]), the output data being trajectories, which can also be visualized with Napari. 3. Single cell measurements of intensity, morphology, texture (based on cell position or on mask), the output being tables of trajectories enriched with features. 4. Event-detection from single cell time signal based on DL analysis. The output are time-dependent states which can be visualized on a home-made interface, designed for further annotation. Newly annotated data can be used for model retraining and transfer learning, as indicated by red lines.

allowing further exploitation. The software is compatible with standard data formats, typically generated using acquisition plugins like micromanager [14]. Data are stored at each step of the analysis (optimized for memory usage, tested on 8 Gb movies, total experiment size up to 100 Gb). The diverse software functionalities are listed in Supplementary Tab. 5, and compared to existing software. Notably, Celldetective

stands out by offering training and transfer options in segmentation, as well as signal annotation and survival analysis. The software manual is available online. To demonstrate its capabilities, we present analysis of an original cell spreading assay and a cornerstone antibody-dependent cell cytotoxicity (ADCC) setup (Fig. 2).

In the first application, we study the dynamics of Natural Killer (NK) cells spreading on a cancer cell mimetic surface (Fig. 2A-E). A potentially therapeutic bispecific antibody (bsAb) bridges the NK cell CD16 receptors, essential for ADCC, and the surface-anchored antigen HER-2. Cell-surface contact and spreading are detected by reflection interference contrast microscopy (RICM) [4, 5]. The segmentation of the contact patch is achieved after a thresholding procedure (Supplementary Fig. 8) and manual correction (Supplementary Fig. 3). The pipeline is summarized in Supplementary Fig. 9. Tracked masks, represented by contours in Fig. 2A, enable the measurement and plotting of cell-area and their normalized intensity over time (Fig. 2B). The moment of contact (t_{contact}) and onset of spreading (t_{spread}) are determined from intensity values according to principles of RICM as the point at which intensity becomes respectively greater than and less than the background. Cell trajectories in the intensity *vs* area plane are represented as a scatter plot with the color code indicating the time counted from t_{spread} (Fig. 2C). The hovering duration, calculated for each cell as $t_{\text{spread}} - t_{\text{contact}}$ (Supplementary Fig. 10), is compiled for the whole cell population as a survival curve and reported for various bsAb concentrations (Fig. 2D). We observed significant variations in cell decision time within the 10-100 pM range of bsAb. The spreading velocity at the onset of spreading is also measured for each cell and illustrated in a scatter plot as a function of bsAb concentration (Fig. 2E). Overall, the decision time of individual cells to spread, measured at high-throughput, illustrates the capabilities of CellDetective in the context of cell-surface interactions.

In the second application, we study ADCC in a high-density co-culture of effector NK cells and target tumor cells, optionally in presence of bsFab (Fig. 2F-K). Live cell nuclei, NK cytoplasm, dying cells, and NK's cells degranulation (CD107a or LAMP-1) are labelled and imaged by fluorescence microscopy (Fig. 2F). First, in a target-centric approach, target nuclei are segmented using a customized StarDist model that detects selectively target nuclei among all nuclei (Supplementary Tab. 2) and are subsequently tracked. The pipeline is summarized in Supplementary Fig. 11. Nuclear radius and fluorescent intensity of the cell death marker are measured and plotted as a function of time (Figs. 2G and Supplementary Fig. 6). Non-dying cells show no increase in the fluorescent signal, and maintain a constant apparent nuclear area. Conversely, dying target cells display a simultaneous increase in the intensity signal and decrease in the apparent area of the nucleus. Onset of both events, determined using a trainable DL model, mark the time of cell death (Supplementary Fig. 7). The compilation of dying times for the entire cell population is then presented as a survival curve, for each different tested concentrations of bsAb (Fig. 2H). The mean death time is 63 min after putting cells in co-culture with 100 pM bsAb. Next, shifting the focus to effectors, individual NK cells are segmented using a customized Cellpose model (Supplementary Tab. 3) and tracked. Finally, the target neighborhood is configured (Supplementary Figs. 12, 13) and a significant reduction in velocity of proximal NK cells, as well as an increase in LAMP-1 signal, is observed in the presence of bsAb (Fig. 2J). To

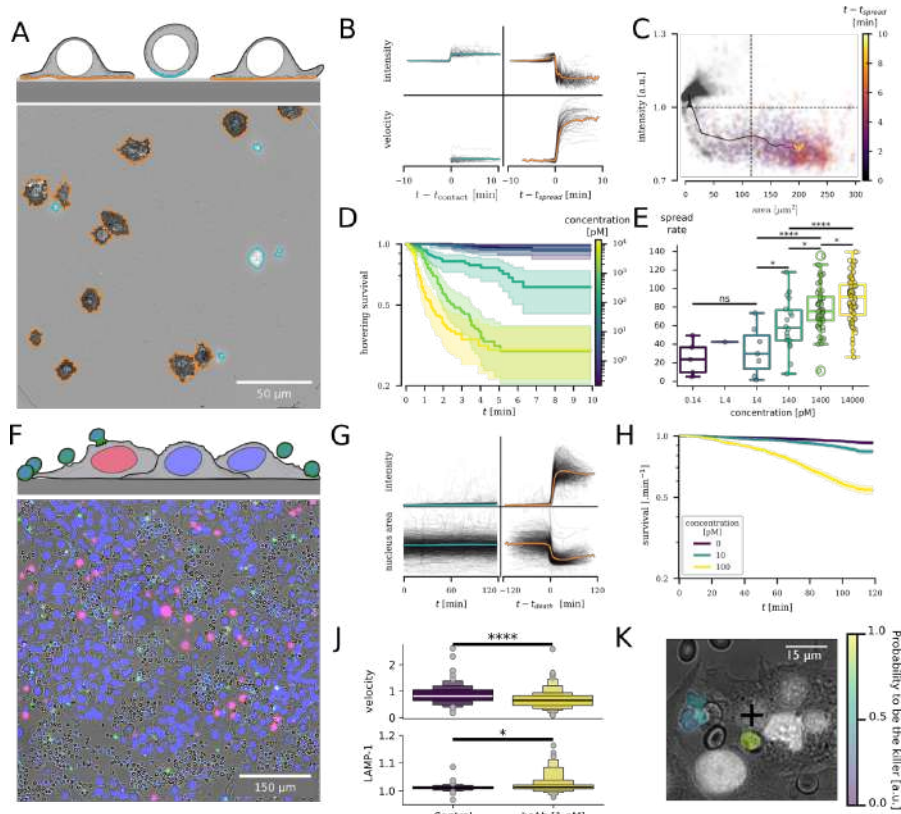


Fig. 2 Cell spreading and cytotoxicity analyzed with CellDetective. A. Top. Schematics of NK cell spreading on an antigen coated surface mediated by a bispecific antibody. Bottom. Representative normalized RICM image showing cells at different stages of spreading. Masks determined by segmentation are shown as colored contours (orange for spreading cells, blue for non-spreading cells). B. Intensity and area of contact as a function of time, for a set of non-spreading cells (left) and spreading cells (right). The reference time is the first detection t_{contact} for non-spreading cells and the onset of spreading t_{spread} for spreading cells. The colored curves represent the mean of all curves. C. Intensity vs area plot for all cells at all measured points with a time color code for spreading cells. The plain line represents the average trajectory. D. Hovering survival as a function of bispecific antibody concentration (see color code). The hovering duration is defined as $t_{\text{spread}} - t_{\text{contact}}$. E. The initial spread rate (in $\mu\text{m}^2/\text{min}$) is represented as a function of bispecific antibody concentration. F. Top. Schematics of target/NK cells co-culture assay for bispecific ADCC. Bottom. Representative multimodal composite image with target nuclei labelled in blue, dying cells in red and NK cells in green. G. Intensity and nucleus apparent area for a set of non-dying target cells (left) and of dying cells (right); the reference time is the death time for the dying cells. H. Survival curve for different antibody concentrations. J. Comparison of NK cells in the neighbourhood of targets cells in the absence (Control) or presence of bispecific Ab. Top: Velocity. Bottom: Normalized Lamp-1 signal. K. Target-centered snapshot (central cross) showing the potential killer NKs with a mask whose color indicates the probability to be the killer (see Supplementary Fig. 14 for details).

identify the NK cells responsible for the death of a given tumor cell, a pair-wise probability is expressed as a linear combination of four parameters (Supplementary Tab. 6 and Fig. 14A-C). The weight for each parameter is optimized based on a

manually annotated ground truth, in order to maximize the probability of identifying the true killer. An example of prediction is shown in Supplementary Fig. 14D-E, where we achieve a prediction of the true killer in 90% of cases. These results demonstrate that the software provides an automated method to determine killer/victim pairs in a dense population of each cell type, paving the way for a detailed and high-throughput analysis of individual cell behavior and interactions.

In conclusion, Celldetective is a user-friendly software designed for non-specialists, providing advanced cell-scale analysis for large cell populations. By combining high time-resolution with robust statistical capabilities, we have uncovered new fundamental parameters characterizing dynamic interactions between immune and tumor cells. We demonstrated the efficiency of Celldetective through two applications in the context of immunotherapy by isolating time-dependent cell-scale parameters and paired-interactions, in high cell-density environment. We believe that such approach holds great potential for enhancing the design and discovery of drugs in a more powerful and rational manner, while also finding broader applications in fundamental cell biology.

Supplementary information. Supplementary methods, tables, figures and movies are available online.

Author contributions. RT, BDB, LL conceived the project. PC, KS, LL supervised the project. RT designed and developed the software. RT, BDB tested the software. BDB, DEA, LA carried out experiments. PC contributed reagents. RT, BDB, DEA, LA, LL analyzed the data. RT, KS, LL wrote the manuscript. All authors critically revised the manuscript.

Acknowledgments. We thank Cristina Gonzalez and Maddy Messa N'Dong for preliminary experiments; Adrien Aimard, Dominique Touchard, Martine Biarnes and Florian Dupuy for excellent technical support; Pierre-Henri Puech and Thierry Galliano for fruitful discussions. We thank AMIDEX Emergence Innovation (project ForSelecAntibody), Plan Cancer PhysCancer program (project ComPhysAb). The project leading to this publication has received funding from France 2030, the French Government program managed by the French National Research Agency (ANR-16-CONV-0001) and from Excellence Initiative of Aix-Marseille University - A*MIDEX.

References

- [1] Moen, E. *et al.* Deep learning for cellular image analysis. *Nature Methods* **16**, 1233–1246 (2019).
- [2] Alieva, M., Wezenaar, A. K. L., Wehrens, E. J. & Rios, A. C. Bridging live-cell imaging and next-generation cancer treatment. *Nature Reviews Cancer* (2023).
- [3] Windhager, J. *et al.* An end-to-end workflow for multiplexed image processing and analysis. *Nature Protocols* (2023).
- [4] von Chamier, L. *et al.* Democratising deep learning for microscopy with ZeroCostDL4Mic. *Nature Communications* **12**, 2276 (2021).
- [5] Weigert, M., Schmidt, U., Haase, R., Sugawara, K. & Myers, G. *Star-convex Polyhedra for 3D Object Detection and Segmentation in Microscopy*, 3655–3662 (IEEE, Snowmass Village, CO, USA, 2020).
- [6] Pachitariu, M. & Stringer, C. Cellpose 2.0: How to train your own model. *Nature Methods* **19**, 1634–1641 (2022).
- [7] Edlund, C. *et al.* LIVECell—A large-scale dataset for label-free live cell segmentation. *Nature Methods* **18**, 1038–1045 (2021).
- [8] Ulicna, K., Vallardi, G., Charras, G. & Lowe, A. R. Automated deep lineage tree analysis using a Bayesian single cell tracking approach. *Frontiers in Computer Science* **3**, 734559 (2021).

- [9] Ershov, D. *et al.* TrackMate 7: Integrating state-of-the-art segmentation algorithms into tracking pipelines. *Nature Methods* (2022).
- [10] Padovani, F., Mairhörmann, B., Falter-Braun, P., Lengefeld, J. & Schmoller, K. M. Segmentation, tracking and cell cycle analysis of live-cell imaging data with Cell-ACDC. *BMC Biology* **20**, 174 (2022).
- [11] Salles, A. *et al.* Barcoding T Cell Calcium Response Diversity with Methods for Automated and Accurate Analysis of Cell Signals (MAAACS). *PLoS Computational Biology* **9**, e1003245 (2013).
- [12] Vanherberghen, B. *et al.* Classification of human natural killer cells based on migration behavior and cytotoxic response. *Blood* **121**, 1326–1334 (2013).
- [13] McQuin, C. *et al.* CellProfiler 3.0: Next-generation image processing for biology. *PLOS Biology* **16**, e2005970 (2018).
- [14] Edelstein, A. D. *et al.* Advanced methods of microscope control using μ Manager software. *Journal of Biological Methods* **1**, 10 (2014).
- [15] Limozin, L. & Sengupta, K. Quantitative Reflection Interference Contrast Microscopy (RICM) in Soft Matter and Cell Adhesion. *ChemPhysChem* **10**, 2752–2768 (2009).
- [16] Gonzalez, C. *et al.* Nanobody-CD16 Catch Bond Reveals NK Cell Mechanosensitivity. *Biophysical Journal* **116**, 1516–1526 (2019).

Supplementary Material

Celldetective

Remy Torro et al.

Methods

Antibodies design and production

The bispecific antibody (bsAb) C7b-21 (or CE4-28) is a fusion of two single domain antibodies (sdAb, also called nanobodies), sdAb CE4 (or C7b) targeting against Human epidermal growth factor receptor-2 (HER-2/neu or ErbB2) [1] and sdAb C21 (or C28) targeting human CD16 (Fc γ RIII), using the human CH1/Ck heterodimerization motif, corresponding to the bispecific Fab (bsFab) format [2]. bsFab CE4-28 was produced by co-transfection of two plasmids using the mammalian transient system Expi293 (Thermofisher) and purified as previously described [3].

Cell lines culture, effector extraction and phenotyping

Modified MCF7-HER2+ cells were stably transfected from MCF7 cell line to overexpress HER2 receptors. Determination of HER-2 levels on the cells was performed by flow cytometry with Herceptin antibody and a secondary fluorescent anti-human antibody. Fluorescence intensity was determined and correlated with HER-2 levels. Cells were maintained in RPMI 1640 media (Gibco, Life Technologies), supplemented with 10% of Fetal Bovine Serum, FBS (Gibco, Life Technologies), 50 mg/mL of hygromycin as an antibiotic resistance selection. Cells were amplified three times per week and keep in the incubator at 37°C under 5% CO₂ atmosphere.

Primary human NK cells. NK cells were isolated as described in [4]. Briefly, blood samples were obtained from the Etablissement Francais du Sang (Marseille, France), using the MACSxpress whole-blood human NK cell isolation kit (Miltenyi Biotec, Bergisch Gladbach, Germany) a negative selection was performed. The characterization of the sorted cells was determined by flow cytometry with anti-CD16, anti-CD3 and anti-CD56 antibodies. Cells were maintained in RPMI 1640 medium and 10% FBS at 37°C, 5% CO₂ and used in the following 24 hours.

Spreading Experiment

Freshly isolated primary human NK cells were used in this experiment. A concentration of 200 000 cells/mL was added to an uncoated eight-well chambered polymer coverslip-bottom from Ibidi (80821, Ibidi, Munich). For surface preparation, the Ibidi wells were initially rinsed with PBS, followed by incubation in a solution of Biotin-labeled bovine albumin (A8549-10MG, Sigma) diluted in PBS at 100 μ g/mL for 30 min at room temperature (RT) with agitation. To remove non-adsorbed BSA-biotin, the wells were rinsed four times with PBS. Afterwards, the wells were incubated in a 10 μ g/mL

Neutravidin solution (31000, Thermo Scientific) diluted in PBS for 30 min at RT with agitation. After a four-time PBS wash, the wells received an Her2/ERBB2 Protein solution (10004-H27H-B, Sinobiological) diluted in 0.2% BSA at 10 nM/mL for 30 minutes at RT with agitation, followed by another four-time PBS wash. The Ibidi chamber was then placed under a microscope at 37°C. Prior to the experiment, the NK were incubated with the desired concentration of bsFab (C7b-21) during 30 min at 37°C. They were then injected in the sample. Cell spreading dynamics were observed through reflection interference contrast microscopy (RICM), a technique sensitive to cell-surface distance. The RICM setup is described in [5]. An antireflex Zeiss objective (NA = 1.25) was used with a green LED light source ($\lambda = 546$ nm) and a 14-bit CCD detector (Andor iXonEM, Oxford instruments). This configuration allows live cell observations at 37°C. Images were acquired after cell deposition in the device. To evaluate the spreading kinetics of NK cells, multiple fields of view were selected (sixteen per condition) and subjected to cyclic imaging over a 10-minute interval, facilitated by a motorized stage from Physik Instrumente, Germany. The temporal interval between successive images of a given field typically ranged from 15 to 20 seconds. An image pre-treatment, described in Supplementary Fig. 15, is applied before use of CellDetective.

ADCC Experiment

MCF7-Mod cells were used as target cells. 80 000 cells/well were seeded in an 8-well chamber μ -Slide, polymer bottom, TC treated from Ibidi (Munich, Germany). Cells were cultured overnight in RPMI complemented media and allowed to reach exponential growth (at least 18 h) under 37°C and 5% of CO₂. Next day media was aspirated and cells were incubated with Hoechst 33342 in colorless RPMI media (5 μ g/mL), at 37°C during 10 min. After that, Hoechst solution were removed and the cells were rinsed 3 times with warm colorless RPMI media complemented with 10% of FBS (300 μ L/well). Cells were put back in the incubator. NK primary cells were stained with CFSE dye according to the manufacturer instructions (CFSE CellTrace). 2.5 M cells were centrifuged at 1500 rpm for 5 min; the supernatant was discarded and the cells were incubated with 2.5 mL of CFSE diluted in PBS for 20 min at 37°C. After that time 12.5 mL of colorless RPMI + 10% FBS were added to the cells and incubated for 5 minutes more. Then the cells were centrifuged at 1500 rpm for 5 min. Cells were resuspended in complemented media and put back in the incubator.

Dilutions of the bsAb CE4-28 were prepared to obtain a final concentration of 1, 10 and 100 pM. The proper bsAb solution was added to each well (2 μ g/mL) where the target cells were previously marked with Hoechst and incubated at 37°C during 20 min. After that time, Propidium Iodide (Sigma) was added in each well condition, then the cells were taken from the incubator and NK cells were added to each well to have a final E:T ratio of 2.5. The slide was then placed in the Zeiss AxioObserver epifluorescence microscope with temperature control at 37°C. The image acquisition consists of taking 5 to 9 fields per well, with a 20x / 0.4 objective (pixel size 0.31 μ m) each field was imaged using transmitted light (Bright field), Zeiss filter set 38 (CFSE), Zeiss filter set # 49 (Hoechst) and Zeiss filter set # 25 HE (Propidium iodide). Each position was imaged during 2-3 hours with approx. 3 min/frame

For NK tracking, the observation was realized with a 40x / 1.3 Oil Dic (UV) objective (pixel size 0.157 μm) and at 1.73 min per frame. Additionally, the NK to target ratio was set to 1:1. For monitoring degranulation, fluorescent anti-LAMP1 (Biolegend APC labelled Clone. H4A3 Cat. 328619) antibody were added at 5 μl for 1 M NK cells.

Hardware and software

Software development and analysis was carried on an Intel-core i9 CPU, NVIDIA RTX 3070 GPU, 16 Go of RAM, Ubuntu 20.04 desktop. The software was extensively tested on an Intel-core i9 CPU desktop running on Windows 11, an Intel-core i7-8565U laptop running on Windows 11, and an older Intel(R) Core(TM) i5 CPU 750 @ 2.67 GHz desktop running on Ubuntu 20.04.

The software is a python package augmented with a PyQt5 user-interface. The UI occasionally integrates Matplotlib canvases for image, animation and plot purposes. The GUI styling is based on Material Design. Each of the processing modules (segmentation, tracking, measurement, signal analysis) triggers a subprocess that applies to a single movie at a time. Upon completion of the subprocess, CPU and GPU memories are fully released, allowing to reiterate the process on the next movie or to unfreeze the GUI. Multi-threading was implemented where it is applicable and can be configured in the software.

At each module, an output (image, table) is written on the disk (in the experiment folder) and can be read as the input to the next module. This approach provides a regular and automatic saving of the data and the modularity allows flexibility in the input data that can be intuitively imported from external sources (ImageJ, Cellpose UI...). In more detail, the segmentation module outputs mask images (frame by frame). The tracking module outputs a trajectory table for the cell population of interest. The measurement and signal analysis modules build on the trajectory tables by adding columns. The neighborhood module adds columns to the trajectory tables and saves a pickle file with a nested-dictionary table with information about the neighbors at each time point.

Analysis

Signal analysis

The signals are normalized independently using user-defined choices (percentile min-max, absolute values, clipping or no clipping). Gaps in the signals are automatically interpolated. The data is split into a training, validation and test set. The signals from the training set are augmented using time shifts (translations along the time axis) to build artificially a uniform distribution of event times, eliminating bias, random signal amplification and noise.

The event detection models consist of two consecutive ResNet-like models sharing the same backbone but differing in the head and therefore the task, respectively classification and regression. The input signals are cast in a tensor of shape ($T \times n_{\text{channels}}$) where n_{channels} is the number of coupled signals (or channels) and T an arbitrary maximum signal length, usually taken at 128 (frames). The input is first

processed by a 1D convolution layer with a kernel of (1,) to cast the input into 64 filters. Then the tensor is sent to two consecutive 1D-resblocks with a kernel of (8,) and 64 filters, before a max pooling operation (size 2) accompanied by a doubling of the number of filters to 128. The tensor is processed by two additional 1D-resblocks before a global average pooling operation. A dense layer of 512 neurons is used to collect the convolution information. A dropout at 50 % is applied before the final layer that consists of three neurons for the classification with a softmax activation (“event”, “no event” and “already happened”) and 1 neuron with a linear activation for the regression (t_{event}). The models are trained for 300 and 600 epochs respectively, with the Adam optimizer and a user-controlled learning rate (typically 10^{-4}), to minimize the categorical cross-entropy for classification and mean squared error for regression. Class weights are introduced to fight class imbalance in the classification task. The batch size is also user controlled (typically set to 64 or 128 depending on the amount of signals available). Only cells belonging to the “event” class are sent to the regressor model (both in training and inference).

Area spreading rate

For each spread cell, the area is differentiated as a function of time using a sliding window of 5 frames (=1min 18s) looking 'forward'. The dA/dt at t_{spread} is reported, units= $[\mu\text{m}^2/\text{min}]$, decomposed for each bispecific antibody concentration. Statistical difference is assessed using T-test for the means of two independent samples of scores between each well combinations. For readability, only some of the p-values are shown.

NK contact mean velocity

A neighborhood scheme at 120 px (18.8 μm) is performed to link target and effector detections. At each timepoint, an effector with more than one target neighbour is instantaneously classified as being "in-contact" with the targets. The NK velocity is computed per track using a centered sliding window of 3 frames (5.19 min when no gap). All NK detections not "in-contact" are filtered out. Instantaneous velocities "in-contact" are averaged per-track, yielding one estimator per cell. The distribution of this estimator is compared in the absence and presence of bispecific antibody (CE4-28). Statistical difference is assessed using T-test for the means of two independent samples of scores, yielding a p-value of 8×10^{-6} / **** or Kolmogorov-Smirnov test yielding 1.7×10^{-5} / ****.

NK contact mean LAMP-1

For the LAMP-1 signal, we measure the mean LAMP-1 intensity, relative to the background, over the NK cell mask 16. As described above, cells that are not in-contact at time t are filtered out. Since LAMP-1 can be transient, instead of averaging this quantity per trajectory, we take the maximum value per track. As above, the distribution of this estimator is compared in the absence and presence of bi-specific antibody (CE4-28). Since the difference is contained in the tail of the distribution, more than around the mean, we perform a Kolmogorov-Smirnov test, yielding a p-value of 0.01 / *.

Supplementary Tables

Table 1 Generalist models. This table lists the different generalist models (Cellpose or StarDist) which can be called natively in Celldetective. The sample images are cropped to (200×200) px and rescaled homogeneously to fit in the table.

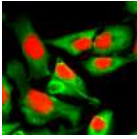
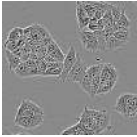
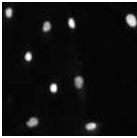
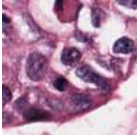
name	modalities	# channels	dataset	sample image
CP	cytoplasm nucleus	2	Cellpose [6]	
CP_cyto	cytoplasm nucleus	2	Cellpose [6]	/
CP_cyto2	cytoplasm nucleus	2	Cellpose [6] & user-submitted images	/
CP_livecell	cytoplasm (BF) blank	2	LiveCell [7]	
CP_tissuenet	cytoplasm nucleus	2	TissueNet[8]	/
CP_nuclei	nucleus blank	2	?	/
SD_paper_dsb2018	nucleus	1	subset of DSB 2018 [9]	
SD_versatile_fluo	nucleus	1	subset of DSB 2018 [9]	/
SD_versatile_he	H&E RGB	1	MonoNuSeg 2018 [10] TNBC 2018 [11]	

Table 2 MCF7 nuclei segmentation models in the presence of primary NK cells. Each model was trained on the same dataset of ADCC images, picking only the relevant channels.

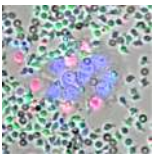
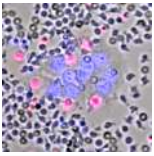
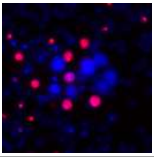
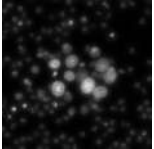
Name	Channels	Type	Pretrained	Spatial calib. (μm)	sample image
<i>MCF7_bf_pi_cfse_h</i>	brightfield PI CFSE Hoechst	StarDist	None	0.3112	
<i>MCF7_bf_h_pi</i>	brightfield Hoechst PI	StarDist	None	0.3112	
<i>MCF7_h_pi</i>	Hoechst PI	StarDist	None	0.3112	
<i>MCF7_h_versatile</i>	Hoechst	StarDist	<i>versatile_fluo</i>	0.3112	

Table 3 Primary NK segmentation models. The models have been trained on a dataset of annotated primary NKs in ADCC images (*primary_NKs_w_MCF7*).

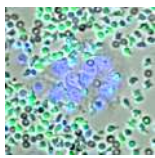
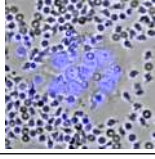
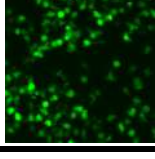
Name	Channels	Type	Pretrained	Spatial calib. (μm)	sample image
<code>primNK_multimodal</code>	brightfield CFSE Hoechst	Cellpose	None	0.2178	
<code>primNK_SD</code>	brightfield Hoechst	StarDist	None	0.3112	
<code>primNK_cfse</code>	CFSE None	Cellpose	CP-cyto2	0.2178	

Table 4 Event detection models. We trained the following 1D DL models to classify and regress events of interest. The mean event response, centered at the event time is shown for each channel in the pattern column.

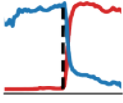
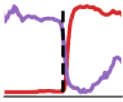
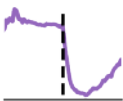
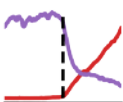
Name	Signals	Task	Pattern
<i>lysis_H_PI</i>	Hoechst PI	Strong PI intake	
<i>lysis_PI_area</i>	PI area	Strong PI intake	
<i>NucCond</i>	area	Nucleus shrinking	
<i>lysis_lowPI</i>	PI area	low PI intake	

Table 5 Comparative table of software functionalities with available solutions. By convention a ✓ can only be attributed if the task can be carried without coding requirement. The use of an integrated solution or plugin is indicated in parentheses.

Software feature	ImageJ/Fiji	CellProfiler	CellACDC	Celldetective
Traditional segmentation	✓	✓	✓	✓
DL segmentation	✓	✓	✓	✓
Corrections annotations	✓ (Labkit)	✓ (GIMP)	✓	✓ (napari)
Training	✗	✗	✗	✓
Transfer	✗	✗	✗	✓
Tracking	✓ (TrackMate)	✓ (TrackObjects)	✓	✓ (bTrack)
Visualization	✓ (TrackMate)	✗	✓	✓ (napari)
Position-based measurements	✓	✗	✗	✓
Measurement classification	✗	✓	✗	✓
Signal annotations	✗	✗	(✓) cell-cycle	✓
Interaction analysis	✗	✓	✗	✓
Experiment manager	✗	✗	✓	✓
Multi-condition data exploration	✗	✓ (CP Analyst)	✗	✓
Survival analysis	✗	✗	✗	✓

Table 6 Features of target/effector pairs. The table summarizes the different features considered to build the probability of finding the NK killer for the target considered. Non normalized features are activated using custom activation functions described in figure 14A-C.

Descriptor	Activation	Time-average window	Relative	Weight	Comments
d_{rel}	step function Fig. 14A	$[t_{\dagger} - \theta_t, t_{\dagger}]$	True	w_d	$d_{\text{rel}} = \sqrt{x^2 + y^2}$
v_{rel}	skewed function Fig. 14B	$[t_{\dagger} - \theta_t, t_{\dagger}]$	True	w_v	$v_{\text{rel}} = \frac{d}{dt} d_{\text{rel}}$ $\frac{d}{dt}$: 3-frame window bidirectional
$t_{\text{res}}^{\%}$	None	$[0, t_{\dagger}]$	True	w_t	$t_{\text{res}}^{\%} = \frac{t_{\in \mathcal{N}}}{t_{\dagger}}$
$I_{\text{LAMP-1}}$	step function Fig. 14C	$[t_{\dagger} - \theta_t, t_{\dagger} + \theta_t]$	False	w_I	Effector LAMP-1 expression

Supplementary Figures

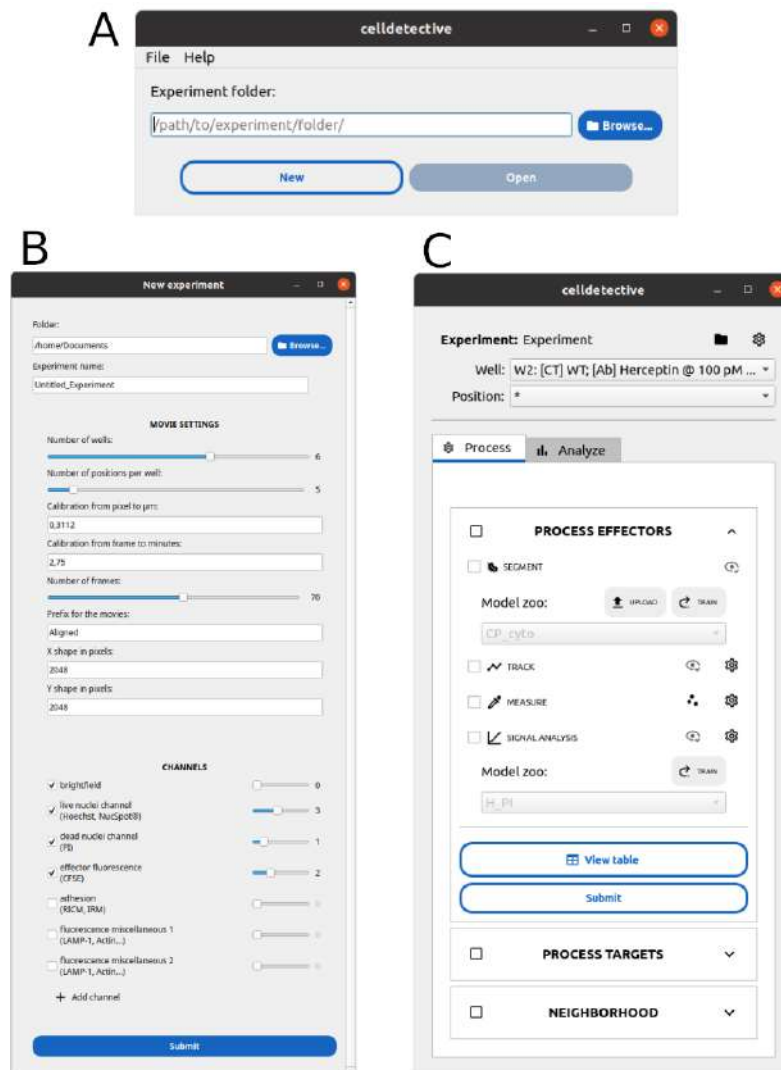


Fig. 1 CellDetective main GUI. A. Experiment selection window. B. Helper to organize a new experiment. The number of wells and number of positions per well sliders are needed to generate the folder tree. Upon clicking on the Submit button, a secondary window asks for the biological condition associated to each well. C. Main control panel allowing the analysis of selected wells and positions. The process tab is shown, featuring processing effectors, with the 4 main steps detailed in Fig. 1.

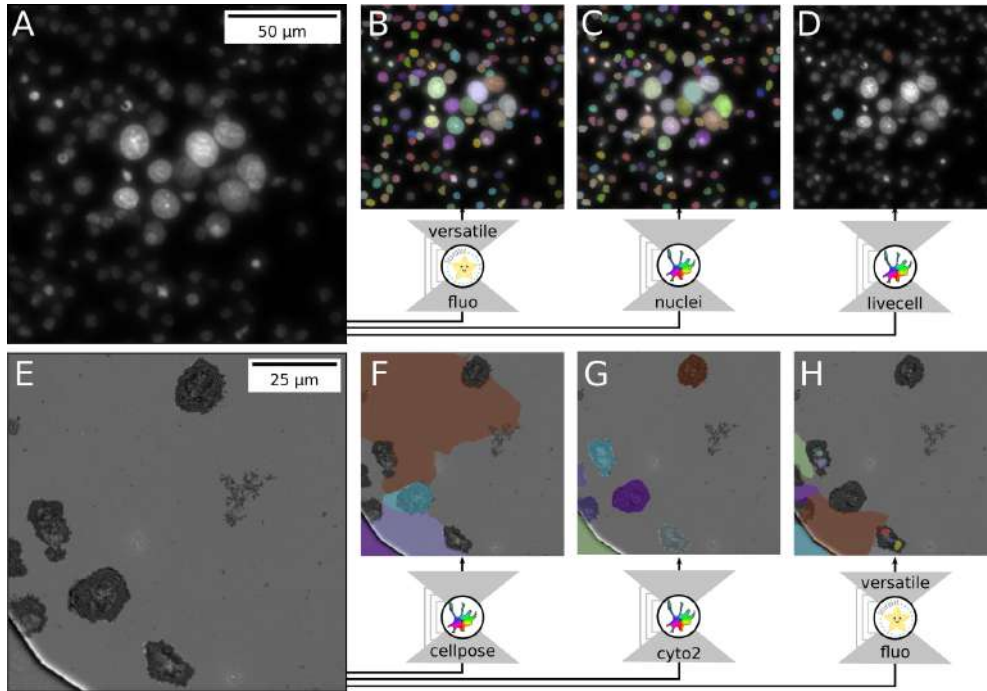


Fig. 2 Applicability of generalist models. Published generalist models (Tab. 1) can be applied to the user's microscopy data provided the images are not too different from the training set of those models. In general, these models will be non specific. A. Image of fluorescent nuclei of a mixed population of effector (human primary NK cells) and target cells (MCF7 breast cancer cells), segmented using different published models (B-D). B. StarDist *versatile fluo* model yields an excellent segmentation of both cell populations simultaneously but separating the cells in post can be a difficult process as a blurry NK nucleus is close in size to a small MCF7 nucleus. C. Cellpose *nuclei* model also achieves a high segmentation precision but the edges are pretty rough, as the images have to be considerably shrunk down before passing into the model (17 pixel nuclei). D. Cellpose *livecell* model, trained mostly on brightfield images, does not understand the nuclei data and misses most of the cells. E. RICM image of human primary NK cells spreading on a surface, segmented using different published models (F-H). F. Cellpose model misunderstands completely what a cell is in this kind of image. G. Cellpose *cyto2* model yields a very sharp segmentation of the spread cells but ignores non spread cells. It also mistakenly segments the diaphragm on at the bottom left corner of the image. H. the StarDist *versatile fluo* model is clearly a wrong model for this kind of data as the convex hypothesis is broken. Cellpose *cyto2* model is the best candidates for a transfer learning process.

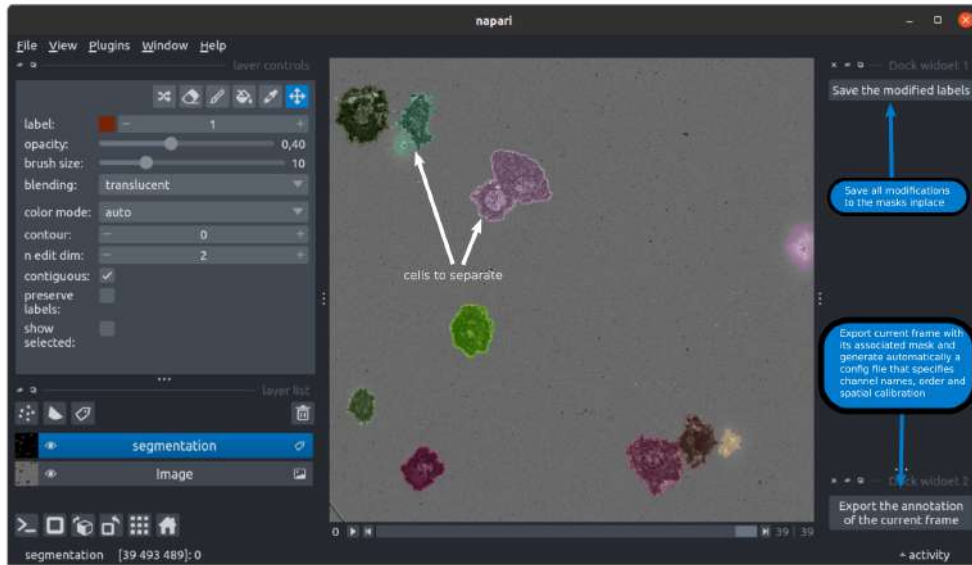


Fig. 3 Segmentation correction and annotation using Napari. Example of RICM modality with spreading NK cells. Colored masks are superimposed on the grey-scale RICM image. The user can correct the masks by painting directly on the image, for example to separate cells indicated by white arrows. New labels can be attributed and saved, the whole set of corrected masks can be exported for further tracking or retraining.

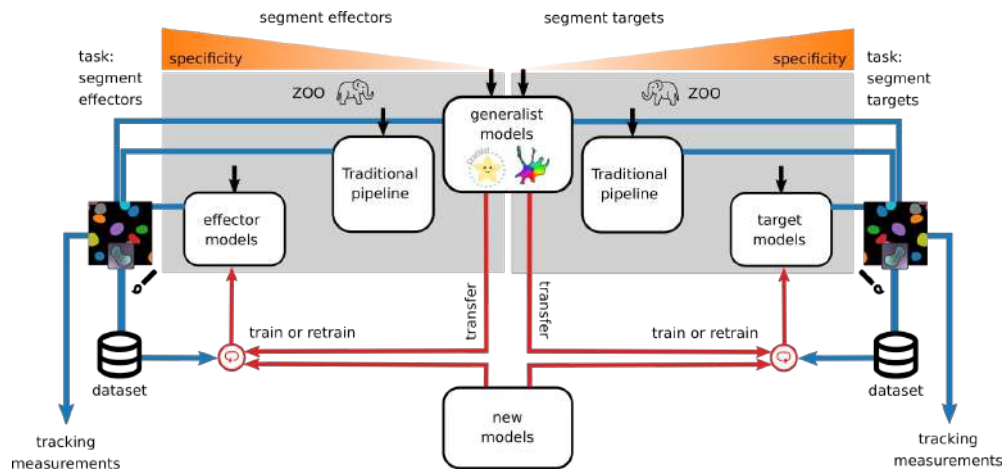


Fig. 4 Overview of segmentation options in Celldetective illustrated for a mixture of two cell populations, effector and targets. Celldetective provides several entry points (black arrows) to perform segmentation, with the intent of segmenting specifically a cell population (left: effectors, right: targets). The generalist models are listed in Tab. 1. Specific models are listed in Tab. 2 for targets and Tab. 3 for effectors. The traditional pipeline refers to a thresholding method accessible through the GUI (see Fig. 8). The masks output from each segmentation technique can be visualized and manually corrected in napari. Exporting those corrections into a dataset of paired image/masks can be used either to fit a generalist model (transfer learning) or train a new model from scratch.

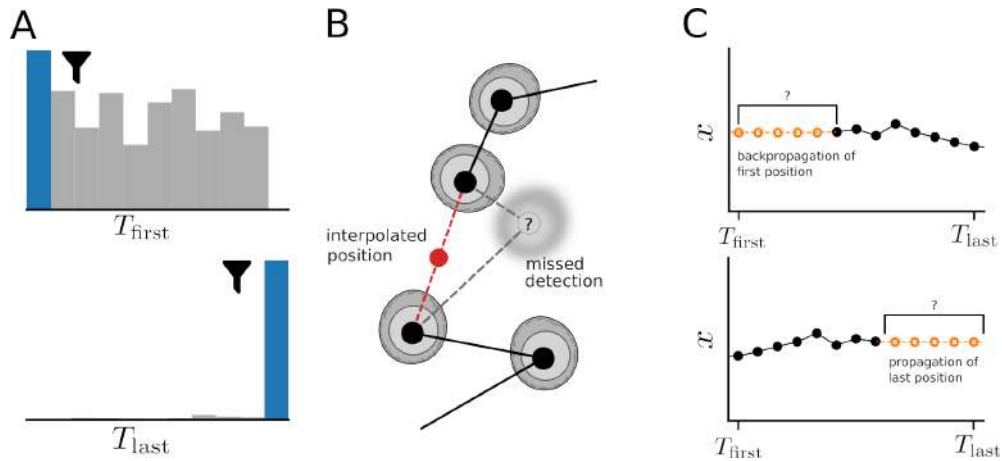


Fig. 5 Post-processing operations on trajectories. A. Endpoint filtering to remove tracks that do not start or end at the beginning and end of the movie. B. Interpolation of tracking gaps. C. Backward (resp. forward) propagation of first (resp. last) detected position to extend the time-range of the tracks.

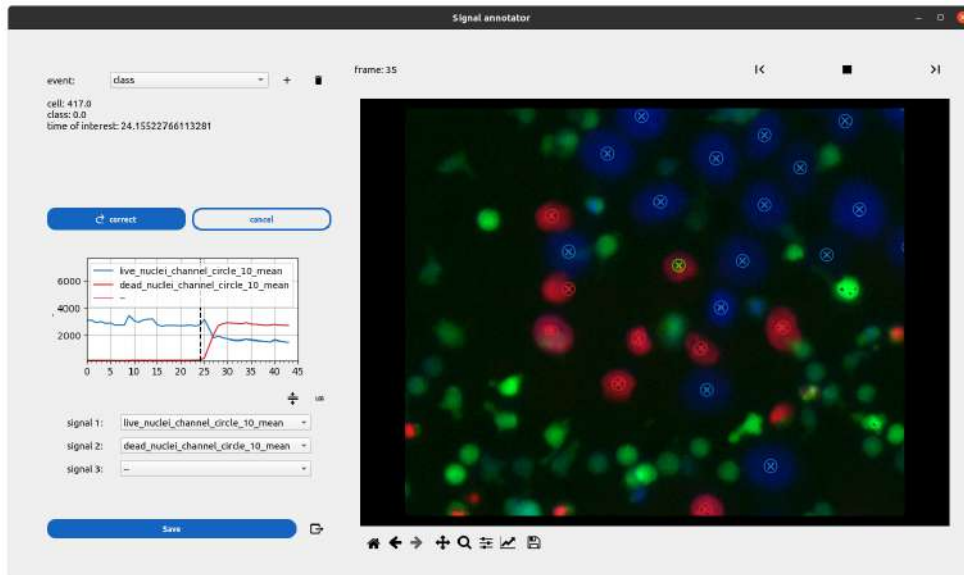


Fig. 6 Quality control on lysis detection with Celldetective, illustrated for cytotoxicity measurements. After applying the *lysis-H.PI* lysis detection model, a visual quality control is performed using Celldetective's signal annotation GUI. The image is part of a RGB composite sequence of 3 fluorescence channels (PI-red, CFSE-green and Hoechst-blue channels). The position-based intensity signal vs time is represented for the selected cell on the left graph for PI channel (red) and Hoechst channel (blue). The black vertical dotted line shows the death time t_{death} estimated by the DL model. This value can be manually corrected.

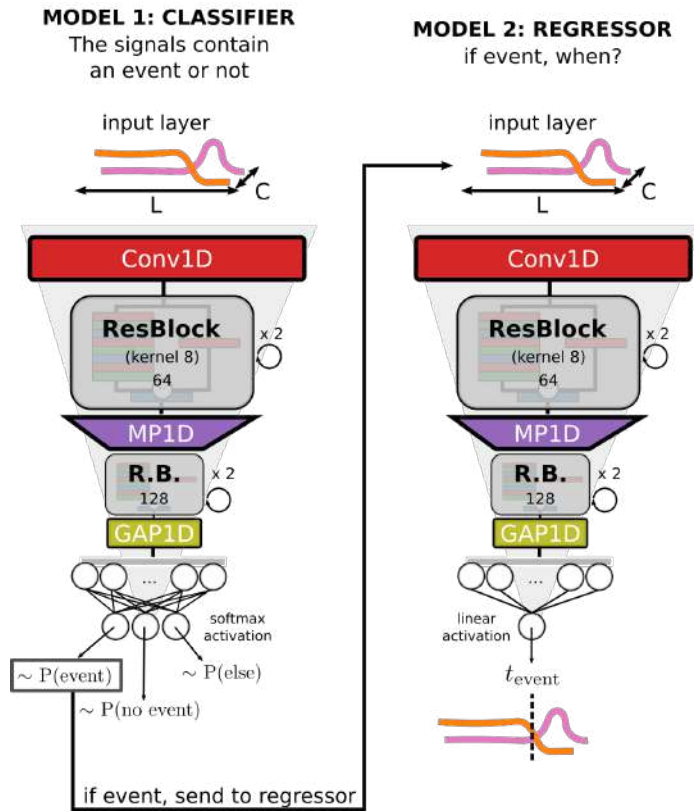


Fig. 7 Event detection by DL. The detection of a coordinated change in two fluorescence signals (Intensity vs time) is performed in parallel by a classifier and a regressor. In this example for cytotoxicity, the classifier indicates the probability of a death occurring during the observation of the signals, while the regressor indicates the date of death.

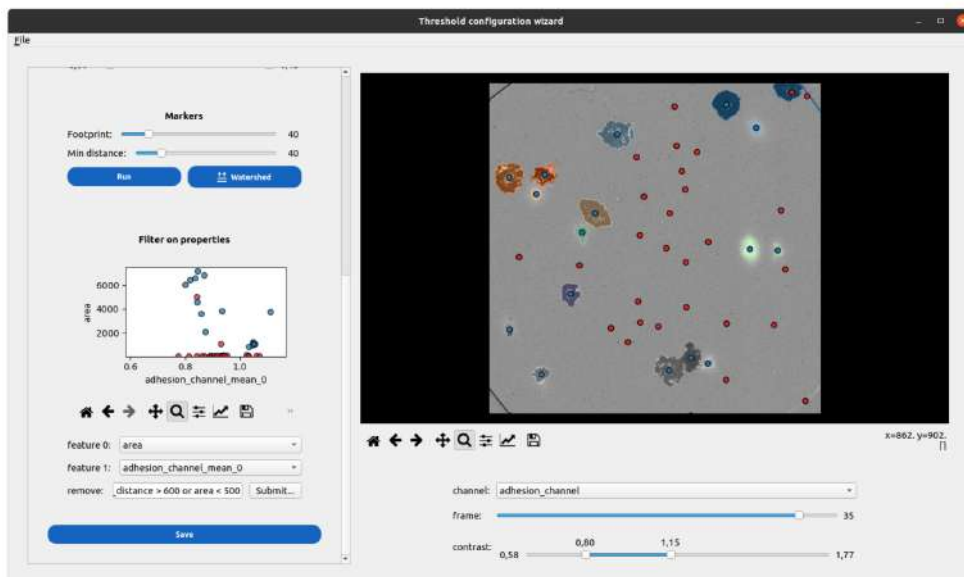
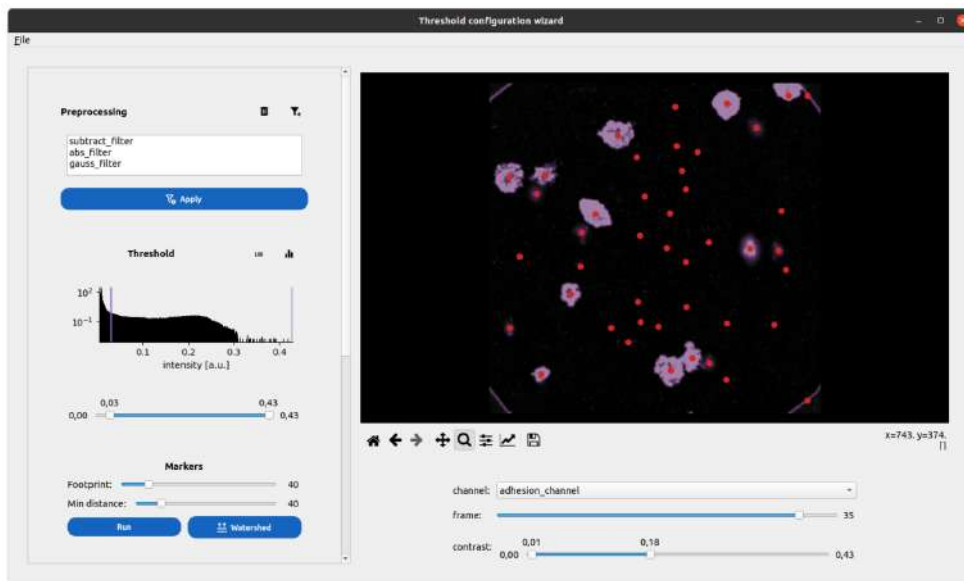


Fig. 8 Interface for segmentation by traditional thresholding with application to RICM images. Top: Selected preprocessing filters are applied followed by manual thresholding using interactive histogram. Bottom: instance segmentation after watershed algorithm and graphical sorting of masks according to selected features measured on the masks (left graph).

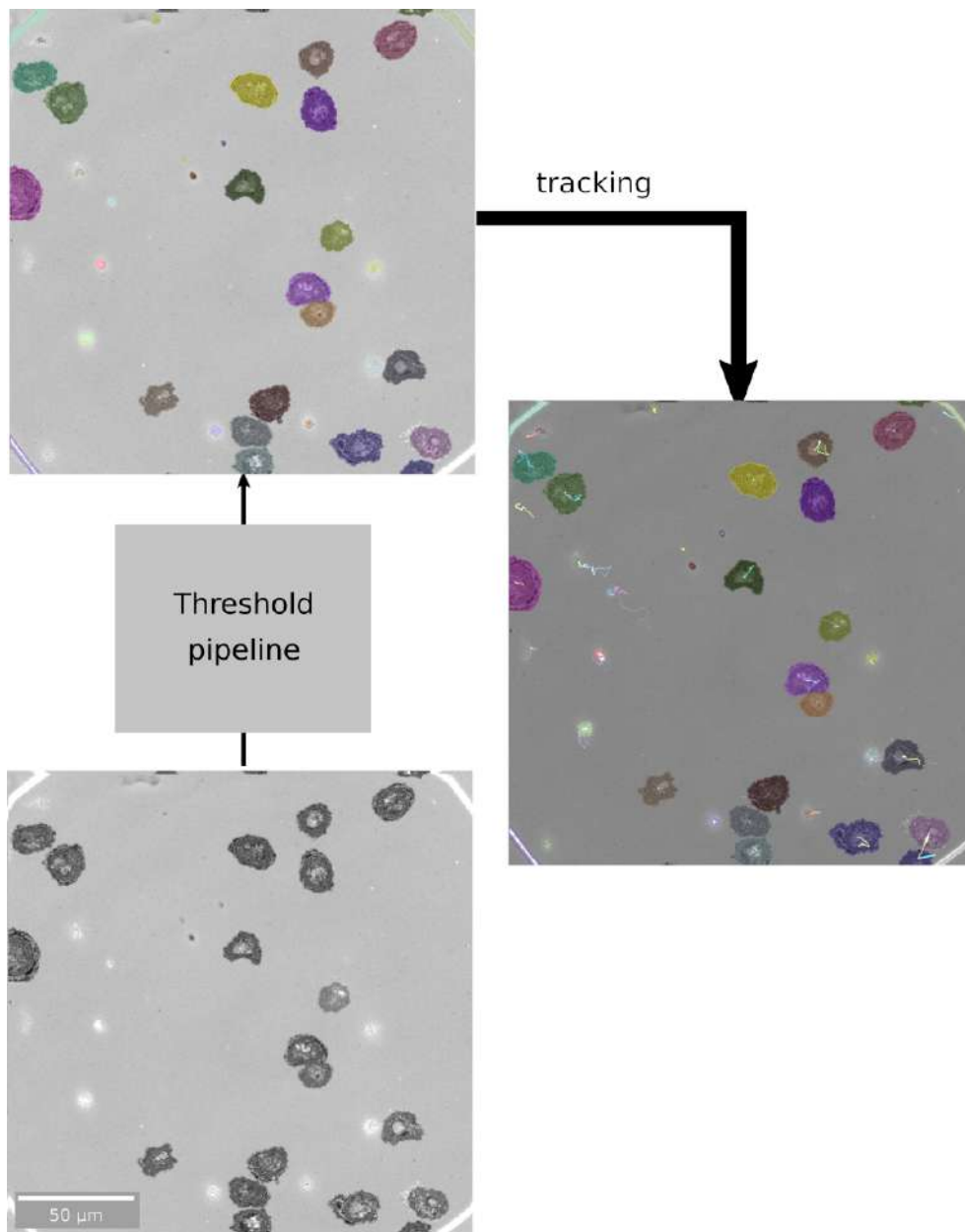


Fig. 9 Cell detection on a normalized RICM image is performed using a traditional segmentation pipeline consisting of a -1 subtraction and absolute value operation, followed by a threshold on the image to detect any cell or object that is different from background. A filter is automatically applied to remove small objects and some false positive detections. The masks are passed to btrack to track all objects before post-track filtering and measurements.

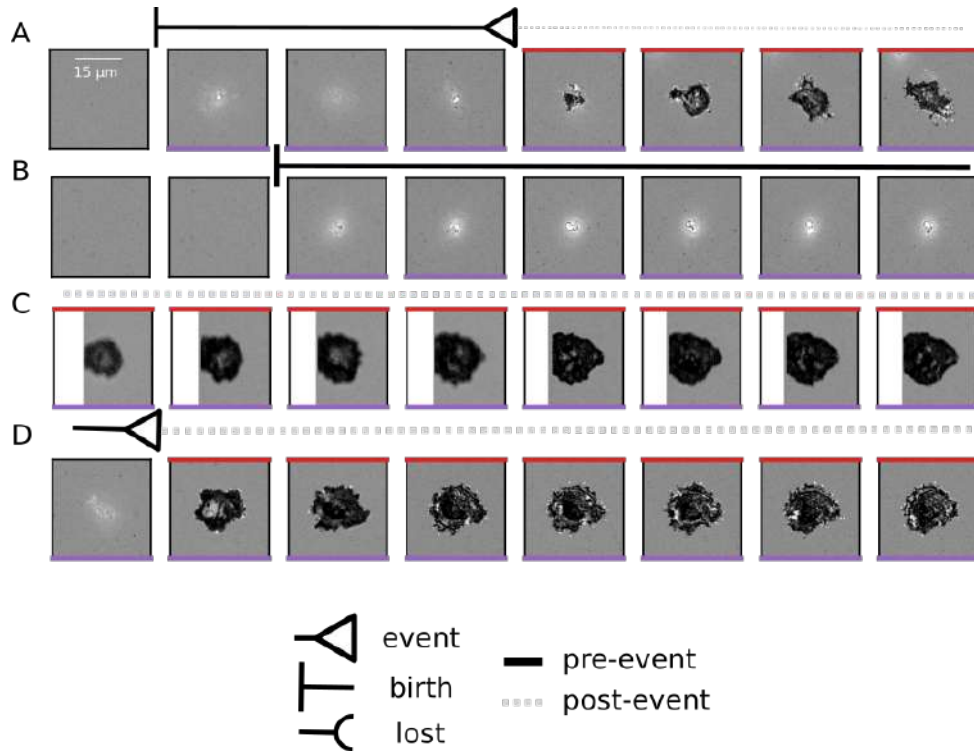


Fig. 10 Hovering duration measurement. A. Hovering duration counted from the first white blob appearance (cell-surface contact) until the first black patch appearance (onset of cell spreading on the surface). B. Hovering without spreading (right censoring). C. Spreading already started at the beginning of the sequence (rejection). D. Contact time not detected (rejection).

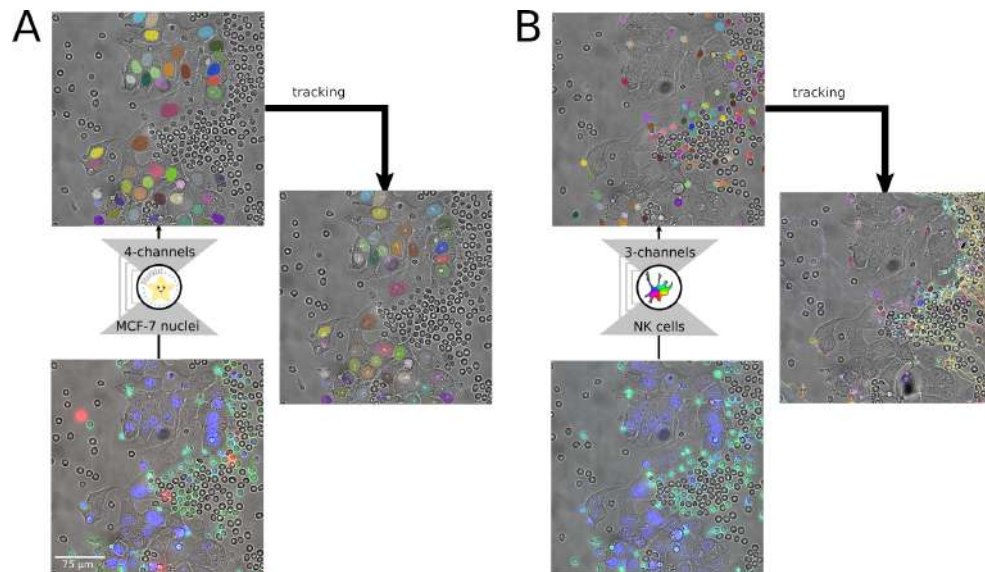


Fig. 11 Pipeline for ADCC analysis. A. A multimodal StarDist model is applied to a four channel ADCC image (brightfield, PI, Hoechst and CFSE) to detect the nuclei of MCF7 cells specifically. The masks are then passed to bTrack for tracking before single cell measurements and signal analysis. B. a multimodal Cellpose is applied to a 3-channel ADCC image (brightfield, CFSE and Hoechst) to segment specifically NK cells among MCF7 and RBCs. The masks are passed to bTrack for tracking, before the single cell measurement step.

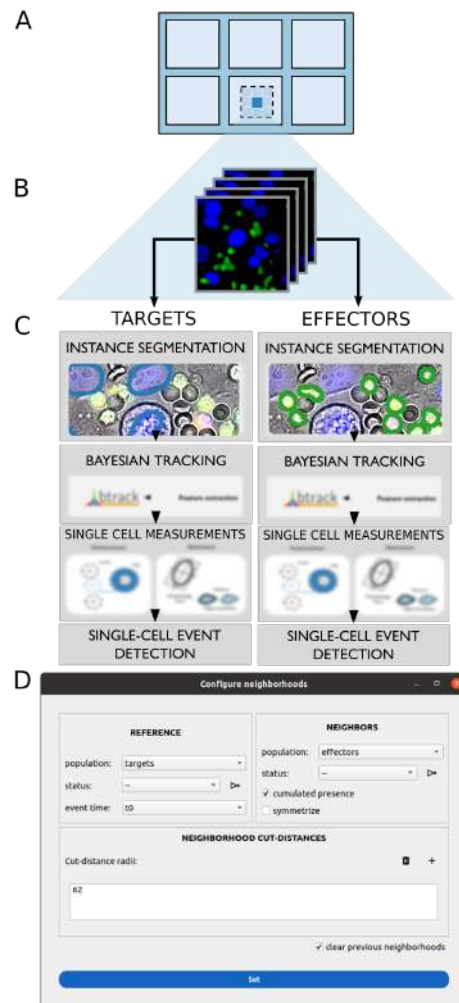


Fig. 12 Two populations analysis pipeline applied to ADCC. A. Multiwell sample. B. 2D multimodal time series. C. Selective segmentation of target cells (left) and effector cells (right), independent tracking of both species, event-detection or annotation, following the pipeline of Fig. 1. D. Software interface for neighbourhood analysis. Choice of reference cell population, status, event time and neighborhood radius list.

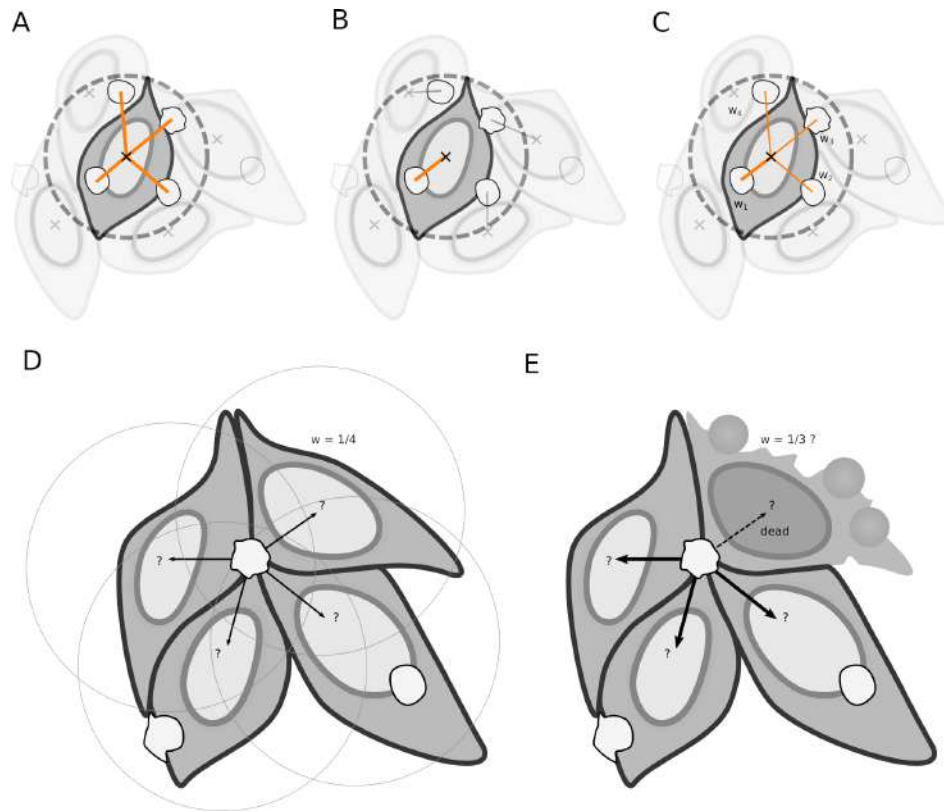


Fig. 13 Proposed neighborhood counting methods. A. Inclusive. B. Exclusive. C. Intermediate. D. the attention weights emerge in the frame of reference of the effector population. An effector may stand at the intersection of many target-centric neighborhoods. The attention weight tries to account both for uncertainty in neighbor attribution and for a potential dilution of the effector activity across the many targets. This weight is attached to the effector in each target neighborhood. Only the intermediate counting method is sensitive to the attention weights. E. In addition, a target that has known an event such as apoptosis may not mobilize an effector cell as much. Therefore, we propose to optionally exclude eventful cells from the attention mechanism.

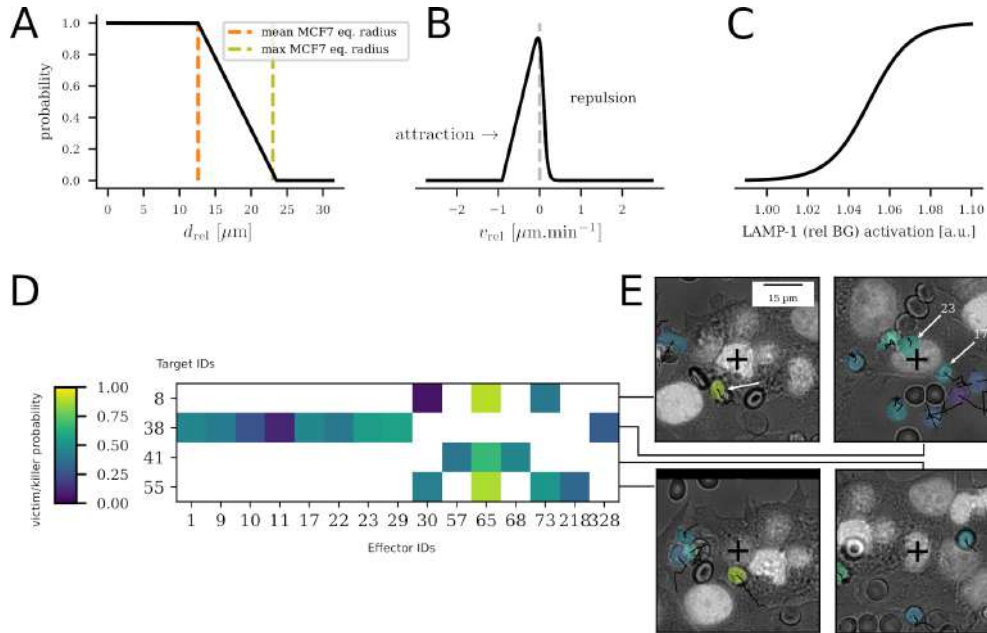


Fig. 14 Killer identification. A-C. Empirical activation functions for determining NK killers. A The mean relative distance between the nucleus of a MCF7 cell and a NK neighbour, in a time window θ_t before the lysis event is mapped to a step-like activation function. For distances smaller than the average MCF7 size, the activation is maximal. Beyond this value, it decreases linearly until the distance reaches the maximum observed MCF7 size. B. The mean relative velocity in the same time window θ_t is mapped to a skewed activation function, favouring low velocities. The instantaneous velocity v_t is computed bidirectionally using a three frames sliding window. The activation function is skewed toward negative values to not penalize NKs getting closer to the target at the time of the lysis event. C. the mean LAMP-1 signal around the time of the lysis event (in a window $\pm\theta_t$) is mapped to a sigmoidal activation function, with a critical LAMP-1 value of 5 % above background. D-E. Optimized probability of a victim/killer pair. D. the matrix shows the optimized probability of having a victim/killer for each target/effector pair in this position. E. Snapshot of the target indicated as a black cross at the center (brightfield and Hoechst in gray, slight CFSE channel in green). The NKs in its neighborhood are recolored to match their probability of being the killer. The probabilities shown here use the following settings and weights: $\theta_t = 15$, threshold=0.400 , $w_v = 0.032$, $w_d = 0.162$, $w_t = 0.374$, $w_I = 0.432$ resulting in $IoU = 0.683$. White arrows indicate the manually annotated most probable killers.

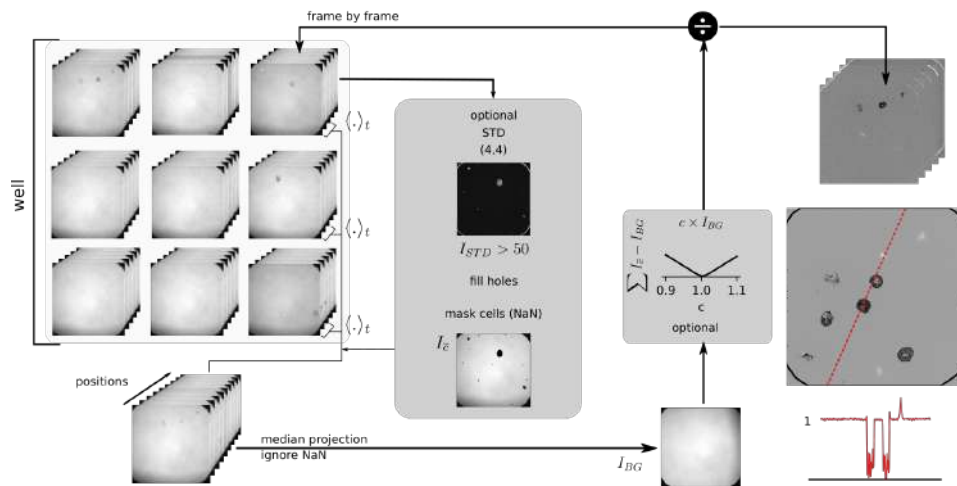


Fig. 15 Workflow for RICM normalization. A background is reconstructed for each experimental condition (well) by using information contained in every single position acquired. The early frames are averaged for each position stacked together. If cells are already visible in those frames, one may want to already mark the cells as “non background”. One quick way to achieve this is to perform a rough segmentation with a STD filter and a fill holes operation and mark the cell pixels as NaN. The background can then be reconstructed by performing a median projection of this multi-position stack. Each frame of each position is divided by this background image in order to normalize. Optionally, one can amplify the values of the background to better match with the values of the numerator image, as any loss of focus could change the intensity levels of the original image. A RICM intensity profile on a normalized image shows how spread cells appear darker than the background overall and hovering cells appear brighter.

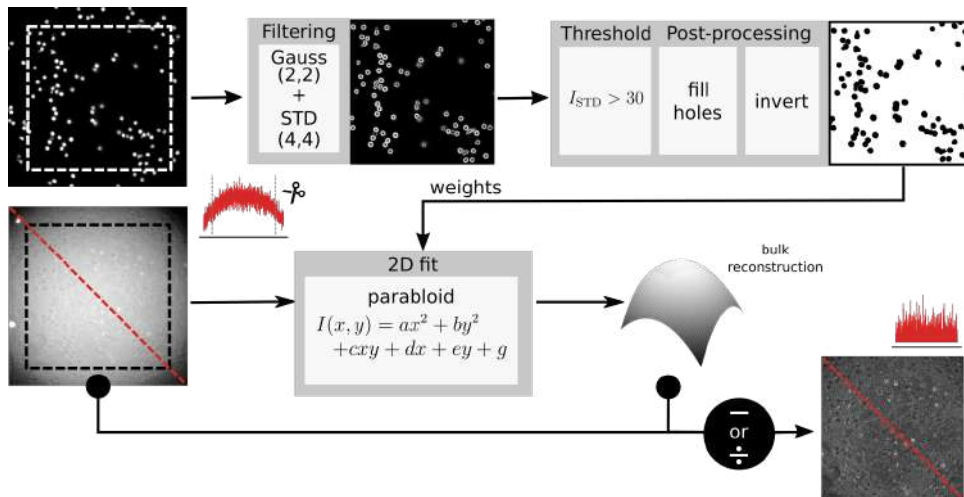


Fig. 16 Workflow for the correction of bulk fluorescence. The fluorescence image is cropped symmetrically along the $-x$ and $-y$ axes to avoid a diaphragm contribution to the intensity distribution. The cells are roughly segmented from the CFSE channel using successively a STD filter (kernel $(4, 4)$), a threshold on the STD transform to binarize the image, a fill holes operation to fill the inside of the detected cell edges and an inversion to set value 0 where the cells are, 1 otherwise. This binary image is used as a weight map to fit the background of the LAMP1 fluorescence image with a 6-parameter paraboloid model. The fitted background is then either subtracted or divided from the raw microscopy image. The process is then reiterated for the next frame.

References

- [1] Even-Desrumeaux, K. *et al.* Masked Selection: A Straightforward and Flexible Approach for the Selection of Binders Against Specific Epitopes and Differentially Expressed Proteins by Phage Display. *Molecular & Cellular Proteomics* **13**, 653–665 (2014).
- [2] Rozan, C. *et al.* Single-Domain Antibody-Based and Linker-Free Bispecific Antibodies Targeting Fc RIII Induce Potent Antitumor Activity without Recruiting Regulatory T Cells. *Molecular Cancer Therapeutics* **12**, 1481–1491 (2013).
- [3] Raynaud, A. *et al.* Anti-NKG2D single domain-based antibodies for the modulation of anti-tumor immune response. *OncoImmunology* **10**, 1854529 (2021).
- [4] Gonzalez, C. *et al.* Nanobody-CD16 Catch Bond Reveals NK Cell Mechanosensitivity. *Biophysical Journal* **116**, 1516–1526 (2019).
- [5] Limozin, L. & Sengupta, K. Quantitative Reflection Interference Contrast Microscopy (RICM) in Soft Matter and Cell Adhesion. *ChemPhysChem* **10**, 2752–2768 (2009).
- [6] Pachitariu, M. & Stringer, C. Cellpose 2.0: How to train your own model. *Nature Methods* **19**, 1634–1641 (2022).
- [7] Edlund, C. *et al.* LIVECell—A large-scale dataset for label-free live cell segmentation. *Nature Methods* **18**, 1038–1045 (2021).
- [8] Barshir, R. *et al.* The TissueNet database of human tissue protein–protein interactions. *Nucleic Acids Research* **41**, D841–D844 (2013).
- [9] Caicedo, J. C. *et al.* Nucleus segmentation across imaging experiments: The 2018 Data Science Bowl. *Nature Methods* **16**, 1247–1253 (2019).
- [10] Kumar, N. *et al.* A Multi-Organ Nucleus Segmentation Challenge. *IEEE Transactions on Medical Imaging* **39**, 1380–1391 (2020).
- [11] Naylor, P., Lae, M., Reyal, F. & Walter, T. Segmentation of Nuclei in Histopathology Images by Deep Regression of the Distance Map. *IEEE Transactions on Medical Imaging* **38**, 448–459 (2019).

Merlin SANICAS, Remy TORRO, Laurent LIMOZIN et Patrick CHAMES. *Antigen Density and Applied Force Control Enrichment of Nanobody-Expressing Yeast Cells in Microfluidics*. 3 jan. 2024. DOI : 10.1101/2024.01.03.574015. URL : <https://www.biorxiv.org/content/10.1101/2024.01.03.574015v1> (visité le 04/01/2024). preprint

Antigen density and applied force control enrichment of nanobody-expressing yeast cells in microfluidics

Merlin Sanicas^{1,2}, Rémy Torro², Laurent Limozin^{2#} and Patrick Chames^{1#}

¹ Aix-Marseille Université, CNRS, INSERM, Institute Paoli-Calmettes, CRCM, Marseille, France.

² Aix-Marseille Université, CNRS, INSERM, LAI, Marseille, France

#Equal Contribution. Correspondence : laurent.limozin@inserm.fr and patrick.chames@inserm.fr

Abstract

In vitro display technologies such as yeast display have been instrumental in developing the selection of new antibodies, antibody fragments or nanobodies that bind to a specific target, with affinity towards the target being the main factor that influences selection outcome. However, the roles of mechanical forces are being increasingly recognized as a crucial factor in the regulation and activation of effector cell function. It would thus be of interest to isolate binders behaving optimally under the influence of mechanical forces. We developed a microfluidic assay allowing the selection of yeast displaying nanobodies through antigen-specific immobilization on a surface under controlled hydrodynamic flow. This approach enabled enrichment of model yeast mixtures using tunable antigen density and applied force. This new force-based selection method opens the possibility of selecting binders by relying on both their affinity and force resistance, with implications for the design of more efficient immunotherapeutics.

Key words: Yeast Display, Laminar Flow Chamber, nanobodies, Cell Enrichment

Introduction

Immune cells apply and sense for mechanical forces that aid in cellular motility and in probing their proximal environment. Lymphocytes in particular have several modes of motility that makes use of mechanical forces depending on the environment that they are traversing: an integrin-dependent motility, an amoeboid-like adhesion-independent motility and the rolling, adhesion and transmigration used in long distance travel through blood vessels (1–3). Activating receptors of lymphocytes have also been shown to both apply and sense mechanical forces. T cell receptors (TCR) and their interaction with the peptide major histocompatibility complexes (pMHC) have been studied intensively for the past decades. In order to probe their environment, T cells generate piconewton (pN) forces to the pMHC (4,5) which may be involved in peptide discrimination (1). Indeed, the discrimination capabilities of the TCR is now admitted to be encoded in the life-time distribution of TCR-pMHC bonds, while equilibrium affinity is not sufficient to explain the exquisite capacity of the T cell to find rare agonists in a sea of non-agonists (6). The bond lifetime is modulated by the force applied to the bond, leading to catch bonds exhibiting longer lifetime under force or slip bonds exhibiting the opposite behaviour. Those behaviour

have been shown to play a central role in TCR-pMHC recognition (7–10). For Natural killer (NK) cells, the interaction of activating receptor NKG2D with one of its ligands, MICA, has been shown to be mechanosensitive (11) and is hypothesized to have catch-bond properties (12). Likewise, B cells physically pull on their target antigens to differentiate between a high affinity and a low affinity antigen (1,13,14), though the existence of a catch-bond BCR or antibody has yet to be clearly established (15). To our knowledge, only nanobodies (Nbs), corresponding to the variable fragment of the Heavy-chain only antibodies (VHH) from the Camelidae serum (16) have been shown to have catch bond properties, as shown for a Nb binding to FcγRIII (CD16) (17). This result suggests that Nbs could be selected to deliver biophysical cues leading to optimal immune cell activation and function.

Biophysical methodologies can be used to measure the force dependence of these ligand-receptor interactions at the cellular or molecular level. Single interaction techniques include Biomembrane Force Probe (BFP) (1), Optical Tweezers (1) and Atomic Force Microscopy (AFM) (18). Options with higher throughput include magnetic tweezers (19), acoustic force spectroscopy (AFS) (20,21) or the laminar flow chamber (LFC) (28). LFC uses microbeads coated with a specific receptor driven along the surface of a small channel derivatized with a very diluted cognate ligand. The interaction is viewed through a microscope focusing on the bond formation and rupture resulting in transient bead arrests under flow (17,22–24). In conditions of single bond observation, a direct measure of bond lifetime under force can be obtained. Similar microfluidic devices were used to immobilize target cells by coating the microfluidic surface with a capture antibody and flowing cells that present the cognate antigen on their surface (25–27).

In vitro display technologies have been versatile and powerful tools for the discovery of proteins that bind specifically to a target. This started with phage display (28) which paved the way to other display methods such as yeast display (29). In this case, the protein of interest is expressed on the yeast surface fused genetically to an anchor protein. Whole antibodies or antibody fragments such as single chain variable fragments (scFv) or Nbs can be expressed on the yeast surface. For instance, yeast display has been used in the discovery of scFvs that bind to West Nile virus envelope protein (30), antibodies against Botulinum neurotoxins (31), and Nbs that target human GPCRs (32) or SARS-CoV-2 receptor binding domain (RBD) (33). Advantages of yeast display include compatibility with flow cytometry, ease of manipulation and handling of yeast cells, eukaryotic post translational modifications and proper folding of the expressed proteins (34). A direct comparison between yeast and phage display using the same cDNA library of scFv showed that yeast display isolated more unique binders compared to its phage display (35). However, when used for antibody or antibody fragment selection, yeast display, similar to other in vitro display technologies, relies on antigen-antibody interaction in solution and is dictated by affinity alone, with no consideration to force sensitivity of the interaction.

In the past few years, several studies combined microfluidics and mycology, such as the so called ‘Fungi-on-a-chip’ platforms (36), one of which was used for adhesion-based cell separation (37). Here, we present a novel assay that combines Nb yeast display and LFC to capture yeast cells under flow in an antigen-specific manner. Two microfluidic devices were used, one to measure the antigen specific and non-specific adhesion of Nb-expressing yeasts, and another for enrichment of model mixtures of Nb-expressing yeasts analyzed by imaging and cytometry. The assay directly quantifies the adhesive properties of two different Nb-expressing yeast strains by monitoring the number of cells captured before and after flow. Force applied on cells was controlled through the shear rate to induce

detachment of non-specifically adhering cells from the surface while maintaining antigen-specific adhesion. Furthermore, we demonstrate how this device can be used for the enrichment of yeast displaying a antigen specific Nb under controlled antigen density and applied force, which has implications for the selection of Nbs with high affinity and resistance to force.

Methodology

Design of nanobody-expressing Yeast

The plasmid pYDS containing the pGAL1 for Nb expression, α -mating factor leader sequence, HA tag and 649 stalk sequence (32) was modified to contain either the Nef19 Nb (38) or CD16.21 Nb (17,39) gene using HiFi DNA Assembly Cloning kit (E5520S, New England BioLabs Inc.). The plasmids were transformed via LiAc/SS-carrier DNA/PEG method (40) into *Saccharomyces cerevisiae* (BJ5465).

Cytometry of yeast

For cytometry, 2×10^6 induced yeast cells were pipetted into wells of a V-bottom 96 well cytometry plate. The plate was centrifuged at $3500 \times g$, 4°C for 1 min and the pellets resuspend with $100 \mu\text{l}$ PBS 1x with 0.2 % BSA; this was repeated 3 times. The pellets were resuspended in $100 \mu\text{l}$ mixture of Nef-ATTO 647N or CD16a-ATTO 647N (10 nM) with anti-Hemagglutinin-PE (aHA-PE, $0.375 \mu\text{g}/\text{mL}$, Clone GG8-1F3.3.1, 130-120-717, Miltenyi Biotec) in PBS 1x with 0.2 % BSA and incubated at 4°C on a platform shaker for 1 h. After, the plate was washed 3x and fixed using PBS 1x containing 0.2 % BSA and 1 % Paraformaldehyde (PFA) diluted from 16 % PFA (043368.9M, Thermo Scientific). This was incubated at 4°C for 15 min on a platform shaker. After 3 washes using PBS 1x. MACS Quant (Miltenyi Biotec) cytometer was used to perform flow cytometry experiments. Cytometry channel settings used were as follows: Forward Scatter (FSC): 300 V, Side Scatter (SSC): 420 V, B1 (CFSE): 260 V, B2 (PE): 290V, V1 (Alexa Fluor 405): 240 V all on hlog. R1 (ATTO 647N) settings were measured at two different values, 440 and 580 V, to adjust to signal differences on the monoclonal yeasts. Compensation settings were as follows: V1 at VioBlue 1, B1 at FITC 1, B2 at VioBlue 0.01, B2 at PE 1, R1 at APC 1. Trigger setting was at FSC: 1 and Events: 30,000. Analysis of flow cytometry data was done using FlowLogic 8.6 (Inivai Technologies Pty Ltd) and apparent affinity was estimated using Prism v5.03 using the non-linear regression function $\log(\text{agonist})$ vs response – variable slope (four parameters).

Growth and preparation of yeast

The transformed yeast cells were grown as described in previous literature (32). Tryptophan drop-out media (-Trp) was used for cell culturing. Solid -Trp plates (3.8g Tryptophan drop-out media supplement, 6.7 g Yeast Nitrogen Base, 20 mL Penicillin-Streptomycin, 2 % v/v glucose, pH 6) were prepared with 1 L to 12 grams agar ratio. Liquid -Trp with glucose medium had the same compositions as solid -Trp medium except agar. Liquid -Trp with galactose medium also had the same composition as the previous liquid medium except for switching 2 % v/v glucose to 2 % v/v galactose.

For cell culturing, yeast cells were first grown on solid -Trp plates. To prepare cell suspension, a single colony of yeast growing on a designated -Trp plate was scraped up with a sterile inoculating loop and suspended in 10 mL liquid -Trp with glucose medium. Suspended yeast cells were incubated in an Erlenmeyer flask at 30°C with shaking at 220 rpm for 24 h. The suspension was centrifuged at $3500 \times g$ for 1 min at room temperature. The pellet was resuspended in 10 mL -Trp with galactose medium and

incubated in a new Erlenmeyer flask at 25 °C with shaking at 220 rpm for another 24 h to induce Nb expression on yeast surface. Cells were then prepared at an $OD_{600nm} = 1$ ($1.5 - 3.0 \times 10^7$ cells/mL) in -Trp with glucose medium.

Fabrication of Microfluidic Device

The 1 entry – 1 exit design was based on the design of the commercial μ -Slide VI 0.4 (80601, Ibidi) while the 2 entries – 2 exits design was a modified version from another publication (37) both shown in Fig 2A & Fig 3A, respectively. Both devices were prepared as a three-layer sandwich. The thick top layer of Polydimethylsiloxane (PDMS) was prepared using SYLGARDTM 184 Silicone Elastomer kit at a 10:1 ratio (10 Liquid PDMS to 1 curing agent) and mixed thoroughly. Bubbles were removed by centrifugation at 1500 rpm for 2 min. After, the liquid was poured on a large 150 x 15 mm circular petri dish to reach a height of 6 mm and de-gassed during 30 min to remove bubbles. The petri dish was transferred to a 65 °C oven to be cured for at least 3 h. The middle part was prepared by cutting a commercial 250 μ m thin PDMS sheet (Sterne Silicone Performance) using a Graphtec Craft Robo Pro. The channel design and dimensions were transferred into the software of Graphtec, and the cutting was performed automatically after aligning the cutter. The lowermost portion, a standard 75 x 25 mm microscope glass slide (1.2 – 1.5 mm, Fisher 1239-3118), was washed with MilliQ water followed by 5 % Decon 90, MilliQ, 96 % Ethanol, MilliQ and Isopropanol and dried using nitrogen, followed by surface treatment using oxygen plasma (Harrick Plasma) at high setting for 10 min. The sides to be fused were placed in the chamber facing up. Simultaneous to the 10-min plasma treatment, the previously cut 250 μ m thin PDMS was cleaned using MilliQ, Ethanol 96 %, MilliQ and 5 % Decon 90 and dried using nitrogen. Once dried and the microscope slide plasma treatment was finished, the clean 250 μ m PDMS was also placed in the chamber alongside the microscope slide to be treated with oxygen plasma for only 2 min at low settings. Once finished, the thin PDMS layer and the glass slide were removed. The treated surfaces of each layer were apposed firmly afterwards and were placed on a hot plate at 95 °C for 10 min glass side bottom. The thick 6 mm PDMS layer was cut to a 75 x 25 mm dimension using a scalpel and the previously designed channel entry points were punched appropriately using a 4 mm diameter puncher. This thick PDMS was also cleaned and dried like that of the thin PDMS layer except for the portion of the 5 % Decon 90 where the punched PDMS was placed in a beaker and sonicated for 10 min. The thick PDMS and the glass-thin PDMS were once again treated with plasma oxygen at low settings for 2 min with the PDMS layers facing up. The treated surfaces were apposed firmly and again placed on the 95 °C hot plate for 10 min. The channels were placed in the 65°C oven for at least 3 h prior to use.

Antigen Functionalization on Chamber Surface

Biotinylated BSA in PBS 1x (100 μ g/mL, aliquoted from 10 mg stock, A8549-10MG, Sigma-Aldrich) was adsorbed directly on the channel surface and incubated for 1 h at room temperature on a tilting shaker. After 3 washes with PBS 1x, streptavidin in PBS 1x (10 μ g/mL, 434302, Invitrogen) was incubated on the biotinylated BSA for 1 h. After 3 washes with PBS 1x, the chamber was incubated with Nef-biotin or CD16a-biotin in PBS 1x with 0.2 % BSA for 1 h. For the optimization experiment, a serial dilution was done with concentrations from 135 nM to 0.56 nM with 1/3 dilution factor per condition. For enrichment experiments, a constant concentration of 45 nM was used. The antigen incubation step was followed by 3 washes of PBS 1x followed by a passivation step with PBS 1x containing 2 % BSA to block

the uncoated channel surface and incubated for 1 h. After 3 washes with PBS 1x, the channel was ready to be used in the LFC experiment.

Microscope Settings

Microscopy was done using an inverted microscope (Axio Observer D1, Zeiss), controlled with Micro Manager 1.4.23 software and equipped with a 10x NA objective (Olympus A10PL 10x 0.25) with a 1.6x additional magnification. For fluorescence images, the light source used was PE-300 ultra (CoolLED) applying 100 % blue light (460 nm). For transmission images, halogen lamp at voltage 6 V was used. Fluorescence was recovered using Zeiss Filter set 16 (488016-9901-000, BP 485/20, FT 510, LP 515). Images were taken using Andor iXonEM + camera. Exposure times used were 10 or 500 ms for transmission microscopy images or fluorescence images, respectively). Electronic gain for fluorescence was set at 100. Pixel sizes of images corresponded to 0.787 μm per pixel. 8 images per condition (denoted after Preflow or Postflow) were taken at a 1000 μm distance lengthwise from the previous field of view. For experiments that included fluorescence images, the set of light microscopy images were taken first followed by going back to the initial field of view and manually switching to fluorescence imaging to take the same exact field of views.

Assay for Capture Optimization

For capture optimization experiments, pure populations of Nef19⁺ or CD16.21⁺ yeast cells were used in the 1 entry-1 exit coated PDMS channels (Fig 2A). The device was connected using custom piping (Polytetrafluoroethylene (PTFE) Tube, 0.8 mm inner diameter x 1.2 outer diameter, PTFE Tube Shop), with a 3-way valve (Masterflex®, MFLX30600-25) to allow manual control between a 10 mL glass syringe (549-0539, VWR) mounted on a syringe pump (Pump 11 Pico Plus Elite, Harvard Apparatus) or an entry point for the yeast suspension. The exit pipe was directly placed over a beaker. Prior to beginning any experiments, the channels were purged with –Trp media with 2 % v/v glucose and Penicillin-Streptomycin to ensure that no bubbles were within the circuit. Induced yeast cells were prepared at a density of 7.5×10^6 cells/mL and passed through a 27G 7/8-inch needle 10 times to dissociate yeast clumps (41). The yeasts sample was transferred to a sterile 1 mL plastic syringe and inserted on the appropriate 3-way valve entry port of the 1 entry- 1 exit channel. The valves were adjusted to ensure that the direction of the yeast suspension was towards the channel. Once infused, a 5 min incubation period was given to allow majority of the yeasts to sediment to the surface and allow for Nb-antigen interaction. 1 min prior to the end of the incubation period, 8 bright field (BF) images were taken across the length of the channel (1 mm distance between each picture taken) and represents ‘PreFlow’ images. We calculated the shear rate (G) in 1/s applying the formula (42): $G = 6Q/lh^2$, using the channel width l , height h and flow Q . Shear rates applied were varied between 168 and 926 1/s to apply a total volume of 6 mL per condition; the antigen incubation concentrations tested were 0.56, 1.67, 15, 45 and 135 nM. After the wash flow, another 8 pictures were taken again across the length of the channel and represents ‘PostFlow’ images.

Assay for Enrichment

The 2 entries – 2 exits channels (Fig 3A) were used and a mixture containing 1:1, 1:10 and 1:100 binders to non-binders ratios of Nb-expressing yeasts were used. Each of the entry and exit was fitted with custom piping connected to a 3-way valve to allow the proper control of shear rate and flow direction

during the entire enrichment process. This set-up required two different 10 mL glass syringe connected to the extreme ports (1st and 4th) and changed manually according to the needed direction of the flow. A schematic in Fig 3B illustrates the sequence of flowing and washing steps performed. First, both ports at the extreme ends (1st and 4th) were closed and the inner ports were opened (2nd and 3rd). The yeast cells were infused on the 2nd port, exiting to the 3rd port and allowed to sediment for 5 min. Pictures were taken as previously described in the optimization set-up, in bright field and in fluorescence (in the case of labelled negative yeasts). The 3-way valves were re-adjusted in such a way that the 1st port was closed, the 2nd port opened, the 3rd port closed and the 4th port opened. The 1st wash step was done with the direction of flow from the 4th port towards the 2nd port for 5 min at a shear rate of 337 1/s. The valves were again re-adjusted to have the 1st port opened, the 2nd port closed, the 3rd port opened and the 4th port closed. The 2nd wash step was done with the direction of flow from the 1st port towards the 3rd port, maintaining the shear rate and duration as wash 1. After the 2nd wash, pictures were taken representing 'PostFlow' images, in bright field and in fluorescence if relevant. The final adjustments of the ports were opening the extremes (1st and 4th) and closing the inner ports (2nd and 3rd). The elution phase, applying a significantly higher shear rate at 4800 1/s was used with the direction from 1st port to 4th port to detach the captured yeasts on the channel and recover them directly into a sterile 5 mL syringe attached to the 3-way valve in the 4th port and transferred into a 15 mL falcon tube. A 100 μ l aliquot was recovered for cell counting. The recovered yeasts were concentrated into a 700 μ l volume of -Trp with 2 % v/v glucose and Penicillin Streptomycin and incubated at 30 °C shaking at 220 rpm for at least 2 days in a 96-deep well plate. The media was changed into -Trp with 2 % v/v galactose and Penicillin Streptomycin and expanded to a volume of 5 mL in an Erlenmeyer flask and incubated for 1 day to induce expression. The induced yeast underwent cytometry to assess for enrichment.

Yeast Cell Detection and Image Analysis

To process the captured images, FIJI (ImageJ 1.53t) was used with a specific script that employed the plugin MorphoLibJ to perform Gray Scale Attribute Filtering (Operation = Top Hat, Area minimum=100, connectivity=4), thresholding (1400), and particle detection using 'Analyze Particles' (size=4 – infinity pixels, circularity=0.1-1.00), an example of this is shown in Suppl. Mat. Fig 1. Applying the conversion factor of 0.787 μ m per pixel, detection threshold was set at a minimum of 3.15 μ m. The cell counts and other parameters were such as the centroid of every detected cell and the XY coordinates within the image were saved as csv files. The detected yeast cells were saved as regions of interest (ROIs). This macro was compared to a manual annotation as ground truth. We applied a machine learning program, TrackPy (43), for the Fluorescence imaging and matching using locate yeast function. Spot diameter was set to 11 pixels and adjusted at the minimum integrated brightness of the spot (minmass) to minimize detection of false positives as established on a sample of unstained yeast cells. For matching, we performed a linking of the cells detected on the bright field (MorphoLibJ generated csv files) and attributed them to the nearest fluorescent cell at a maximal distance of 50 pixels. The matched cells were temporarily removed and the process was reiterated to match some of the left-over cells that are still within the 50-pixel distance threshold. All the detections were reassembled and evaluated for the fraction of yeast cells that have found a fluorescent match.

Results and Discussion

Yeasts express functional nanobodies on their surface

Yeasts transformed with a vector bearing the GAL1-10 promoter and encoding surface expression of HA-tagged Nbs directed against HIV-1 Nef (Nb Nef19) or against human CD16 (Nb CD16.21) were expanded and induced using the presence of galactose in the –Trp medium. These yeasts were incubated with aHA-PE (0.375 $\mu\text{g}/\text{mL}$) to assess for the expression levels of the Nef19⁺ and CD16.21⁺ yeasts by flow cytometry. The average expression levels were 34 to 41 % (Fig 1A and 1B). For comparison, other publications that used the same plasmid reported expression levels of ~25 % (32) and up to 70 % (44). We next studied the functionality of the expressed Nbs based on the binding schemes shown in Fig 1E.

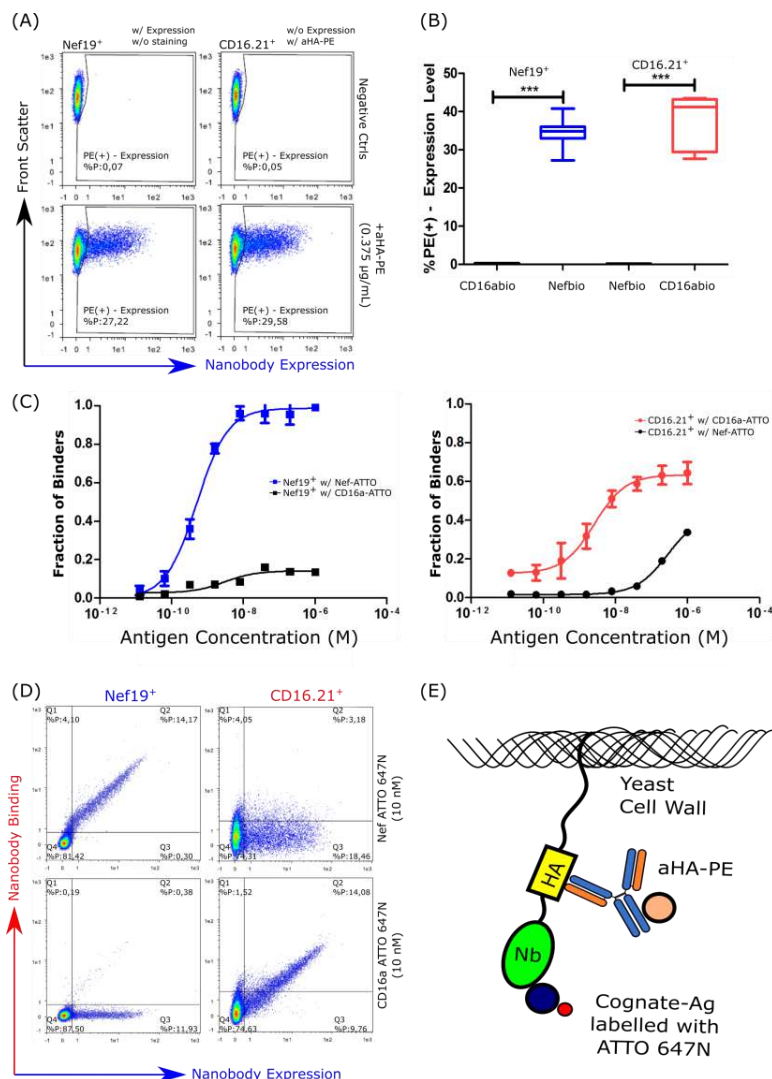


Figure 1. Nanobodies on the Yeast Surface (A) Cytometry scatter plot of Nef19⁺ & CD16.21⁺ yeasts. (B) A vertical box & whisker plot corresponding to 3 independent cytometry measurements of the percentage of expressing yeasts using a-HA PE. Error bars are the standard error of means (SEM) (s = 3) (***) indicates a Student's test with p ≤ 0.001). (C). An XY plot (fraction of binders as function of antigen concentration in M). The values on the x-axis were taken from a cytometry histogram elaborated in the Suppl. Mat Fig 2. This experiment was done 3 independent times. (D) 4 Quadrant gated scatter plots of the Nb-expressing yeast.

The Nb-expressing yeasts were incubated with 10 nM of either antigen. (E) A schematic of the yeast cell wall when incubated with aHA-PE and their cognate antigen (Ag) with ATTO 647N.

To measure the apparent affinity of the Nef19⁺ and CD16.21⁺ on yeast surface, we performed a serial dilution experiment with their cognate or irrelevant antigen labelled with ATTO 647N, while fixing the concentration of a-HA PE. The measured apparent affinities were 5.4×10^{-10} M for Nef19⁺ and 2.6×10^{-9} M for CD16.21⁺ (Fig 1C). These findings were comparable to the previous publication result of 2×10^{-9} M for Nef19 (38) and 1.0×10^{-8} to 1×10^{-9} M for CD16.21 (17,39). An example of 4 quadrant gating of these yeasts in either their cognate or irrelevant antigen is shown in Fig 1D.

Fluid-driven Yeasts specifically adhere to channel surface antigen

The Nb-expressing yeasts were driven along the surface of the 1 entry – 1 exit microfluidic channel derivatized with either their cognate or irrelevant antigen. The design of the microfluidic device and the application of flow and sequence of steps are shown in Fig 2A. The binding of the Nb-expressing yeast to their cognate antigens in flow is schematized in Suppl. Mat. Fig 3. The applied shear rates and antigen concentration on the channel surface were adjusted to maximize the ratio between specific and non-specific yeast capture using pure populations of Nef19⁺ or CD16.21⁺ yeasts separately. The surface of the channels were functionalized with various concentrations of target or irrelevant antigens, as performed for single bond measurements in LFC (17,22). We directly measured the effects of these changes by microscopy by counting the starting number of cells prior to flow and the remaining cells after the flow, as shown on bright field images of Fig 2B & 2C. The capture percentage (% Arrested Cells) was calculated by dividing the PostFlow count by PreFlow count and multiplied by a 100.

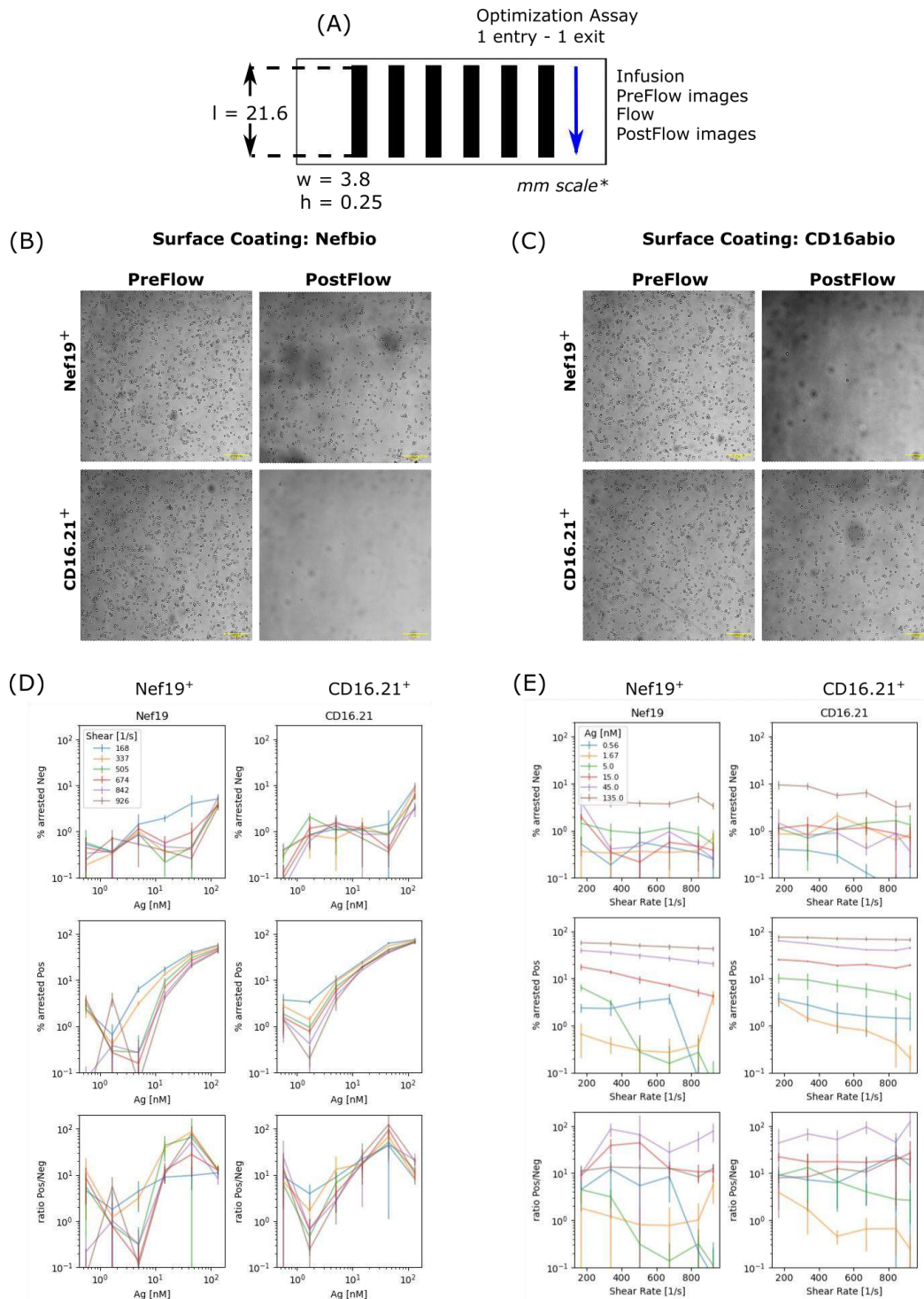


Figure 2. Optimization Assay microfluidic chamber, visualizing and optimizing specific adhesion by varying antigen concentration and Shear Rate. (A) 1 entry – 1 exit channel used for optimization based after the Ibidi μ -Slide VI 0.4. The direction of flow and indicated by the blue arrow and the sequence of steps are infusion of yeast cells, image acquisition prior to flow, application of flow and image acquisition after flow. The images of yeast cells driven along the surface of a channel incubated with either (B) Nefbio or (C) CD16abio. The top row corresponds to the Nef19⁺ yeast while the bottom row is for CD16.21⁺ yeast. The first and second column show a representative image PreFlow and PostFlow, respectively. (D) The columns correspond to the monoclonal yeast driven along the surface of a channel at varying concentrations of antigen. The 1st row

shows % Arrested on irrelevant antigen, the 2nd row % Arrested on their cognate antigen and the last row shows the ratio between the positive to negative (1st row to 2nd row). (E) Data showing monoclonal yeast at varying shear rates in a similar format as D.

We tested the Nef19⁺ and CD16.21⁺ yeasts on 6 different concentrations (0.56-135 nM) of their cognate or irrelevant antigen. Conversion of antigen incubation concentration to surface density of antigen on the chamber floor is further discussed in the Suppl. Mat. The general observed tendencies were a higher specific capture fraction at higher antigen concentrations for both antigens (Fig. 2D). However, the nonspecific capture also increased with increasing antigen concentration. The shear rates were varied between 168 and 926 1/s. The lowest tested shear rate of 168 1/s generally led to a high nonspecific capture that dropped to values around 1 % as soon as a shear rate of 337 1/s was used (Fig. 2E). The non-specific capture was generally independent of shear rate, whereas the specific capture decreased markedly with increasing shear rate.

To evaluate the optimal conditions leading the highest specific capture, we calculated the ratios of the capture fraction on the cognate antigen to the capture fraction on the irrelevant antigen. For CD16.21⁺ yeast, the condition with the highest ratio of positive to negative capture fractions was at 45 nM concentrations at a shear rate of 926 1/s, yielding a ratio of 124. For the Nef19⁺ yeast, the condition with the highest ratio was also at 45 nM but at a shear rate of 337 1/s with a ratio of 86. The antigen concentration of 45 nM, equivalent to 180 molecules/ μm^2 , thus consistently provided the highest ratio. Overall, the ratios were roughly independent of the shear rate above 168 1/s, being mostly set by the non-specific capture. We decided to move forward with the lower shear rate of 337 1/s, minimizing the shear rate applied while leading to less than 1 % nonspecific capture for both antigens.

We can estimate the number of bonds formed between the Nbs on the yeast and the antigen on the chamber surface. First, considering the length of the stalk between the Nb and the yeast surface ($L=100$ nm) and the typical yeast radius ($a = 5 \mu\text{m}$), the surface of contact between the cell and surface where the ligand and receptor can form a bond is $s = \pi.L.(2a-L) = 3 \mu\text{m}^2$. The antigen density on the channel surface based on our previous work (17) showed an incubation concentration of 7 nM corresponded to a density 30 molecules/ μm^2 . Here, an incubation concentration of 45 nM leads to an estimated antigen density $d_{Ag} = 180$ molecules/ μm^2 . The maximal number of antigens on the substrate which can form a bond with a Nb on the surface of the yeast in contact with the substrate can then be estimated as: $N_{AgContact} = d_{Ag} \cdot s, \sim 500$ molecules. A specific yeast display expression vector using Aga2p is known to express around $N_{NbTotal} = 10^4 - 10^5$ molecules per yeast but can vary between individual cells (45). If we assume similar expression levels, we could therefore estimate the number of Nbs in the contact surface $N_{NbContact} = s.N_{NbTotal} / 4\pi.a^2$, yielding a maximum of 100 Nbs for $N_{Nbtotal} = 10^4$ and a maximum of 1000 Nbs for $N_{Nbtotal} = 10^5$. Thus, the maximal number of bonds N_{max} , being the minimum of $N_{AgContact}$ and $N_{NbContact}$, should be limited by the number of antigens (500) for yeast with high nanobody display, or by the number of displayed nanobodies (100) for yeast with low nanobody display—We note that this high number of bonds will favour avidity as the control parameter of selection. To prevent an avidity effect during yeast arrest, the density of antigens on the surface can be highly diluted, so that statistically only one antigen molecule is available at a time for each binding yeast. This is the limit commonly achieved for single bond measurements with the laminar flow chamber (10,17,46). In this limit, the probability of

capture is only related to the apparent affinity K_d under flow which can be tuned by the velocity. The total force applied to a yeast can be estimated at $F = 2$ nN using the following formula (22):

$$F = 13.95\pi\mu a^2 G \sqrt{a/2L}$$

where $\mu = 0.001$ Pa.s is the medium viscosity. For $G = 337$ 1/s and if the force is equally shared between all the N_{max} bonds, the force per bond should vary between 4 pN (for highly covered yeast) and 20 pN (for sparsely covered yeast).

Enrichment using model mixtures of Nb-expressing yeast

Model selections were next performed using the optimized conditions in a new set up equipped with 2 entries - 2 exits for better control of the elution step as shown in Fig 3A & 3B, respectively.

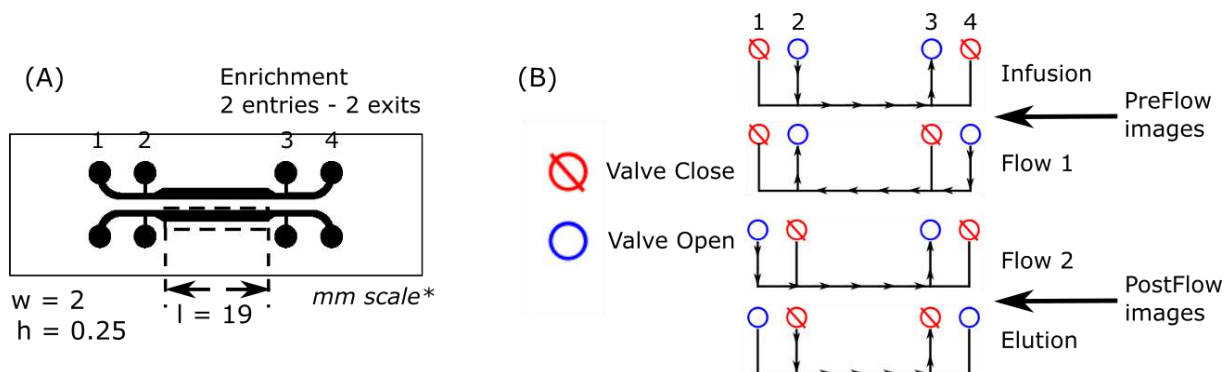


Figure 3. Enrichment Assay microfluidic chamber dimensions & sequence of steps. (A) 2 entries – 2 exits channel used for enrichment based from the design from Rienmets et al. 2019 (37). (B) The 4-step wash sequence used with corresponding closed and opened valves and the direction of flow applied.

To maintain the same shear rate G as the previous device, we applied a shear rate of 337 1/s. We used 3 different model mix with ratio of binders to non-binders of 1:1, 1:10 and 1:100. The antigen concentration on the channel surface was maintained at 45 nM for both CD16a-biotin and Nef-biotin. These mixes were subjected to one round of LFC-based enrichment performed at a shear rate of 337 1/s and elution was performed using a high shear rate of 4800 1/s. PreFlow and PostFlow cell counts were recorded and pure population samples were used as reference. As assessed by microscopy (Fig 4A), the percentages of arrested cells for the 1:1 mix (Fig 4B) driven along the Nef-biotin and CD16a-biotin derivatized channel surfaces were at 5 % and 4 % respectively, compared with 2 % and 2.4 % for the 1:10 mixes (Fig 4C), and 1 % for the 1:100 CD16.21⁺: Nef19⁺ mix on the CD16a-biotin channel (Fig 4D). To monitor the enrichment in real time and *in situ*, we stained the non-binding yeast with CFSE to visualize their presence before and after flow for ratios 1:10 and 1:100. A representative image in bright field and corresponding fluorescence is shown in Fig 4A, showing almost no fluorescent cells after flow. Specific and non-specific adhesion values were measured by calculating the ratios of fluorescent cells to non-fluorescent ones before and after flow to obtain the fraction of fluorescent non-binders (% Fluorescent

cells). By subtracting this fraction from 1, we get the estimated fraction of non-fluorescent binders (Fig 4E-G).

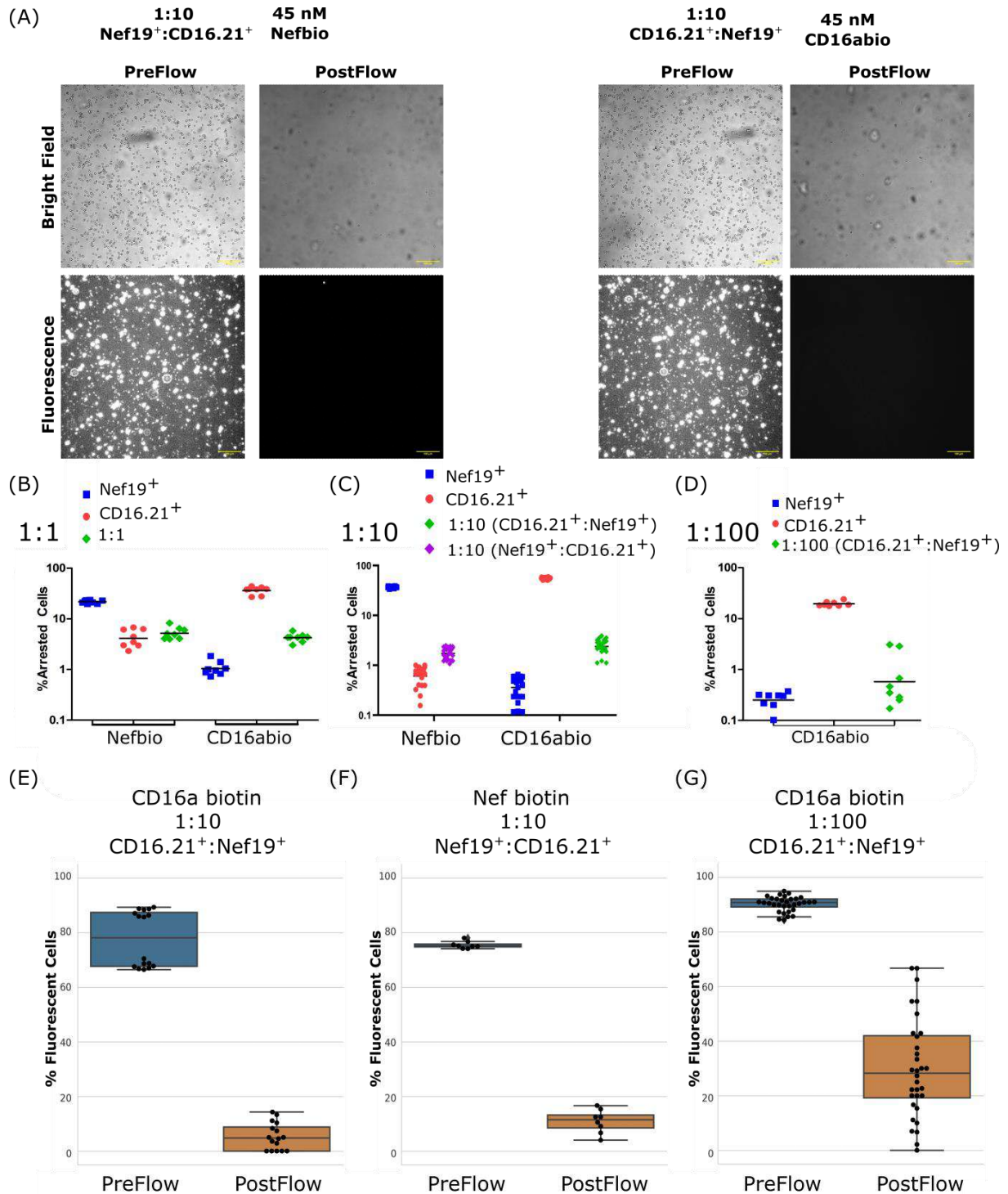


Figure 4. Monitoring of enrichment by microscopy. (A) An example image of the 1:10 mixes used for enrichment. The top row corresponds to the bright field PreFlow & PostFlow images and the lower images are the corresponding fluorescence images. The fluorescent cells are the non-binder cells. The scale bars correspond to 100 μ m. (B-D) % Arrested cells of the different ratios

(1:1, 1:10 & 1:100) and pure populations (blue and red) measured using bright field, PreFlow and PostFlow. (E-G) % Fluorescent cells of different model mixes before and after flow.

To confirm that enrichment did occur using a different approach, we used again flow cytometry. After the procedure, the eluted cells were amplified and nanobody expression was restored using a 3 days culture, before flow cytometry analysis. Using the quadrant definition shown in Fig1D, we estimated the fraction of positive cells before and after flow using the formula $Q2/(Q2+Q3)$ (see the Suppl. Mat. for the discussion of the limits of this choice) (Fig 5). For the 1:1 ratio, the ratio of binders to expressors increased from 0.49 to 0.66 and 0.86 when driven along the channel surface derivatized with CD16a-biotin and Nef-biotin respectively, i.e., yielding enrichment of 1.3 and 1.8.

For the 1:10 CD16.21⁺: Nef19⁺ mix over CD16a-biotin, the ratio of binders to expressors increased from 0.11 to 0.64, an enrichment factor of 5.8. For the 1:10 mix of Nef19⁺:CD16.21⁺ driven along a Nef-biotin functionalized channel surface, this ratio increased from 0.07 to 0.31, i.e., an enrichment factor of 4.4. The 1:100 ratio was only tested on CD16.21⁺: Nef19⁺ mix. Using this ratio, below 1 % of positive cells expected before enrichment falls below the background signal by flow cytometry and thus cannot be measured efficiently. Hence, instead of relying on the direct cytometry data, we used a theoretical value of 0.01 corresponding to the expected 1:100 mixture. The ratio of binders to expressors increased to 0.15, yielding an enrichment factor of 15.

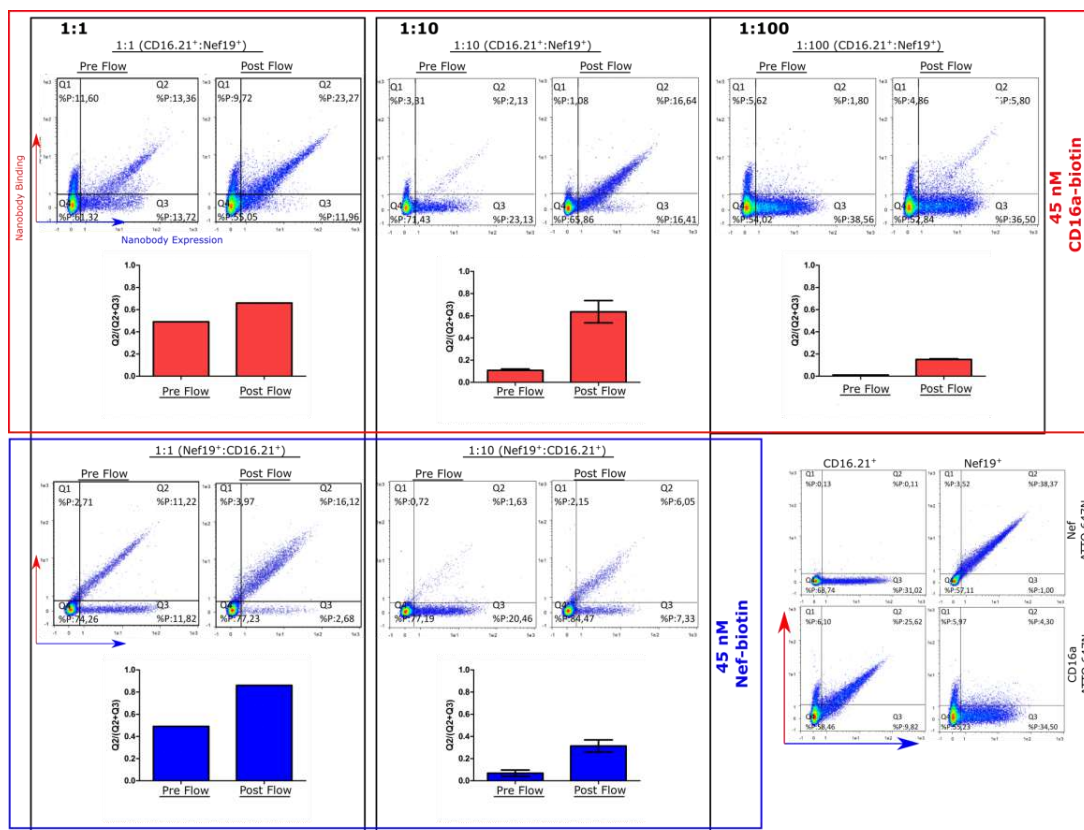


Figure 5. Monitor of Enrichment by Cytometry. The eluted cells were grown and characterized by flow cytometry. The top row shows the cytometry results and the estimated enrichment factor of all CD16.21⁺: Nef19⁺ mixes driven along a CD16a-biotin surface. The bottom row corresponds to the results of all different mixtures of Nef19⁺:CD16.21⁺ driven over a Nef-biotin

surface. The right bottom corner displays results obtained with pure populations of CD16.21⁺ or Nef19⁺ yeast with their corresponding cognate or irrelevant antigen as reference.

Thus, using this flow-based assay, we were able to reach up to a 15-fold enrichment of positive cells after a single round.

Predicting the Enrichment from adhesion

To further evaluate these results, we sought to predict the enrichments, as measured using cytometry and based on the adhesion measured in flow chamber by microscopy. We used the following nomenclatures: f^+ as the fraction of expressing positive cells, f^- as the fraction of expressing negative cells, a^+ as the captured fraction of positive cells after flow, a^- as the captured fraction of negative cells after flow. Assuming that non-expressing positive cells adhere similarly to negative ones (a^-), a theoretical enrichment (ϵ) may be calculated as follows (see the derivation in Suppl. Mat. Eq. (S1)):

$$\epsilon = \frac{1+y}{1+xy} \quad (\text{Eq. 1})$$

We can define a capture efficiency factor y as the product of f^+ and a term characterizing the selectivity of the channel dictated by the functionalized antigen on its surface

$$y = f^+ \left(\frac{a^+}{a^-} - 1 \right) \quad (\text{Eq. 2})$$

Figure 6A shows the theoretical enrichment ϵ of a model mixture as a function of the initial mix ratio x and calculated for various values of capture efficiency y . This shows how the enrichment is maximal for low mix ratio x but limited by the capture efficiency $y+1$. y can be measured using negative and positive adhesion tests or using the fluorescently labelled negative cells (see Suppl. Mat). Using Eq. 1 on our assays lead to a predicted enrichment ϵ similar for the 2 methods (See Suppl. Mat. Fig 4A, 4B, 4D & 4E). The capture efficiency y shows that the order of calculated y for the 1:10 ratios using Bright Field and Fluorescence were reversed between the 2 antigens but are both still within the same scale (Suppl. Mat Fig 4C & 4F). Thus, both *in situ* monitoring methods (Bright Field and Fluorescence) could be used to predict enrichment factors (Fig 6B & 6C) that are in good agreement with the enrichments experimentally measured using flow cytometry (Fig 6D) after expansion of the enriched cell populations.

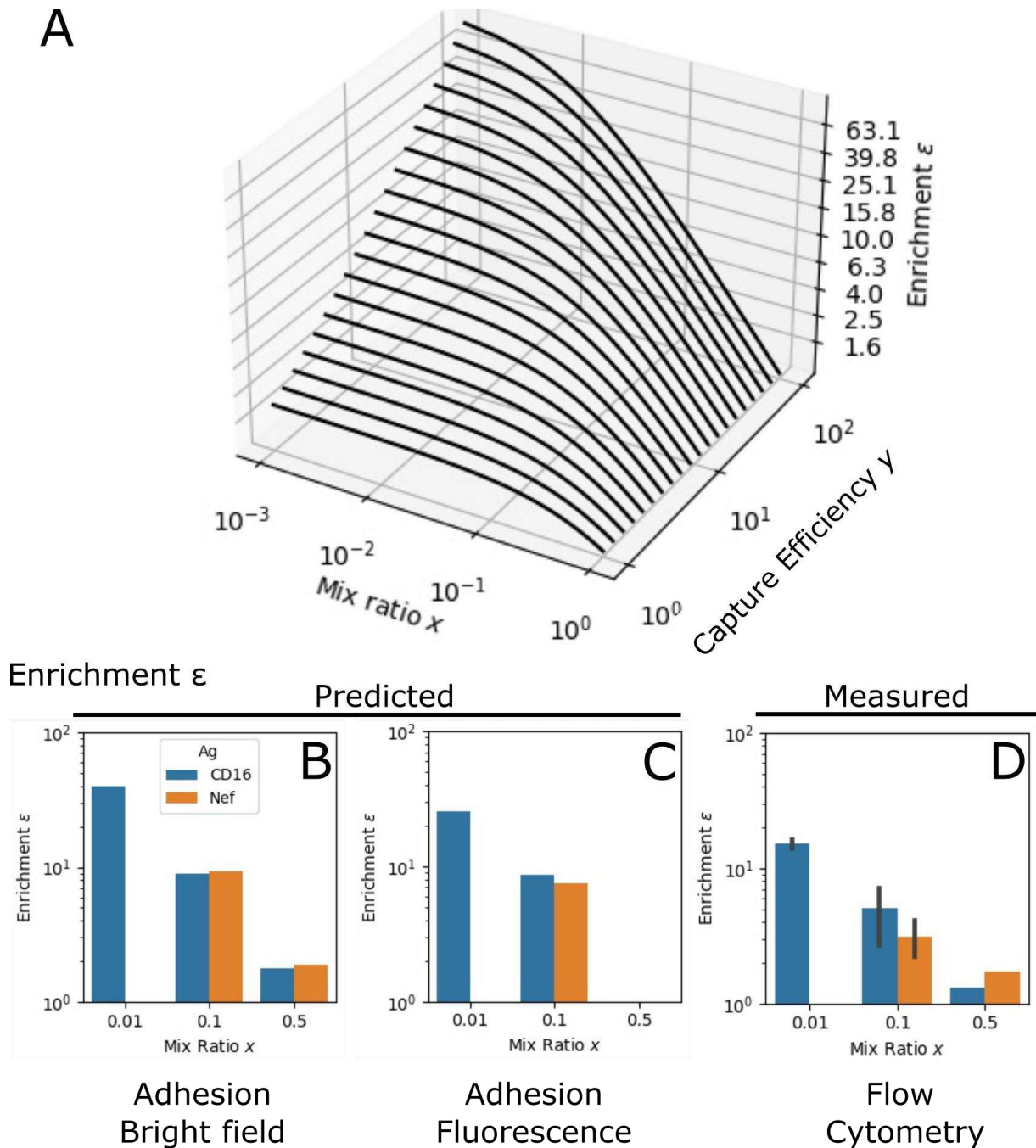


Figure 6. Measured and predicted enrichment of model mixes. (A) Theoretical enrichment ϵ as a function of the mix ratio x and Capture Efficiency y , using Eq. 1 & Eq 2. (B) The predicted enrichment ϵ based on the % of Arrested cells in bright field microscopy. (C) The predicted enrichment ϵ based on the % Fluorescent Cells in Fluorescence microscopy. (D) Enrichment measured by cytometry PreFlow and PostFlow. The bar graph colors correspond to the immobilized antigen (blue for CD16, orange for Nef).

Applying Eq. 1, one gets a theoretical enrichment ε measured through two different microscopy modalities that is consistent with the measured enrichment via cytometry. As a theoretical exercise mimicking a more realistic situation with rare binders within a library, such as a mix ratio x of $1:10^6$ and assuming capture efficiency y of 50, the fraction of positive yeasts will be 5.0×10^{-5} after round 1, 2.6×10^{-3} after round 2 and 1.3×10^{-1} after round 3, reaching a proportion of binders compatible with random picking of clones for deeper characterization, i.e. a frequency above 10% of positive clones. Of note, reducing the antigen density to avoid avidity effect is expected to yield a lower adhesive ratio. It may thus be applied after a first round of selection at high density, allowing a reduction of diversity and an increase in the copy number of each clone. Alternatively, a preliminary round using magnetic enrichment can also be used to reduce diversity prior to the use of the flow chamber.

Conclusion

This work validated the efficacy of a microfluidic assay to quantify both the antigen-specific and non-specific capture fraction of yeasts expressing a specific Nb on their surface and translating it into a method for enrichment of a model mix. This result was achieved through the precise control of shear rates and antigen surface densities, and the use of precise washing and elution steps. Our assay enabled the detection of antigen-specific capture and enrichment for yeasts that express antigen-specific Nbs. Importantly, our method provides a way to control the force applied to the interaction by modulating the shear rate, as well as the valency of the interaction, by modulating the antigen surface density. These are major parameters to ultimately tune the selection of binders with pre-determined force response and single/multivalent bond behaviour. Current yeast display strategies mainly use magnetic activated cell sorting or fluorescence activated cell sorting, two methods relying on affinity that do not take into consideration the forces surrounding the receptor-ligand interaction. Conversely, our force-based selection strategy has the potential to favor the selection of binders able to withstand a certain amount of external force. By allowing the force-based enrichment of yeasts displaying libraries of antibody fragments such as nanobodies, scFv, Fab, but also full-length antibodies, this strategy may represent an important step toward the engineering of more efficient immunotherapeutics.

Author Contributions

M. S. performed the experiments and analysed the data. M.S. was responsible for all cell manipulations, microfluidic channel fabrications and imaging. R.T. developed the image analysis software. L.L. derived the theoretical prediction model for enrichment. All authors conceived and designed the experiments and wrote and edited the manuscript.

Acknowledgements

We thank Yong Jian Wang, Dalia El Arawi, Luc David-Bruglio and Pierre Bohec for technical help with the microfluidics as well as Philippe Robert and Olivier Theodoly for fruitful discussions. We also thank Elise Termine, Remi Bonjean and Adrian Aimard for technical help with protein production and labelling and Timothee Chanier for technical help with flow cytometry. This work has been carried out thanks to the support of the A*MIDEX project (ANR-11-IDEX-0001-02) funded by the Investissements d'Avenir

program from the French government, managed by the French National Research Agency (ANR); and of the Physcancer program from Institut National du Cancer-Plan Cancer.

Conflict of Interest

There are no conflicts to declare.

References

1. Huse M. Mechanical Forces in the Immune System. *Nat Rev Immunol*. 2017 Nov;17(11):679–90.
2. Kopf A, Kiermaier E. Dynamic Microtubule Arrays in Leukocytes and Their Role in Cell Migration and Immune Synapse Formation. *Front Cell Dev Biol* [Internet]. 2021 [cited 2023 Feb 2];9. Available from: <https://www.frontiersin.org/articles/10.3389/fcell.2021.635511>
3. Dustin ML, Chakraborty AK, Shaw AS. Understanding the Structure and Function of the Immunological Synapse. *Cold Spring Harb Perspect Biol*. 2010 Oct 1;2(10):a002311.
4. Bashour KT, Gondarenko A, Chen H, Shen K, Liu X, Huse M, et al. CD28 and CD3 have complementary roles in T-cell traction forces. *Proc Natl Acad Sci*. 2014 Feb 11;111(6):2241–6.
5. Göhring J, Kellner F, Schrangl L, Platzer R, Klotzsch E, Stockinger H, et al. Temporal analysis of T-cell receptor-imposed forces via quantitative single molecule FRET measurements. *Nat Commun*. 2021 May 4;12(1):2502.
6. Ganti RS, Lo WL, McAfee DB, Groves JT, Weiss A, Chakraborty AK. How the T cell signaling network processes information to discriminate between self and agonist ligands. *Proc Natl Acad Sci*. 2020 Oct 20;117(42):26020–30.
7. Hong J, Persaud SP, Horvath S, Allen PM, Evavold BD, Zhu C. Force-Regulated In Situ TCR–Peptide-Bound MHC Class II Kinetics Determine Functions of CD4+ T Cells. *J Immunol*. 2015 Oct 15;195(8):3557–64.
8. Wang J huai. T cell receptors, mechanosensors, catch bonds and immunotherapy. *Prog Biophys Mol Biol*. 2020 Jul 1;153:23–7.
9. Sibener LV, Fernandes RA, Kolawole EM, Carbone CB, Liu F, McAfee D, et al. Isolation of a Structural Mechanism for Uncoupling T Cell Receptor Signaling from Peptide-MHC Binding. *Cell*. 2018 Jul;174(3):672-687.e27.
10. Limozin L, Bridge M, Bongrand P, Dushek O, van der Merwe PA, Robert P. TCR–pMHC kinetics under force in a cell-free system show no intrinsic catch bond, but a minimal encounter duration before binding. *Proc Natl Acad Sci*. 2019 Aug 20;116(34):16943–8.
11. Le Saux G, Bar-Hanin N, Edri A, Hadad U, Porgador A, Schwartzman M. Nanoscale Mechanosensing of Natural Killer Cells is Revealed by Antigen-Functionalized Nanowires. *Adv Mater*. 2019;31(4):1805954.

12. Fan J, Shi J, Zhang Y, Liu J, An C, Zhu H, et al. NKG2D discriminates diverse ligands through selectively mechano-regulated ligand conformational changes. *EMBO J.* 2022 Jan 17;41(2):e107739.
13. Natkanski E, Lee WY, Mistry B, Casal A, Molloy JE, Tolar P. B Cells Use Mechanical Energy to Discriminate Antigen Affinities. *Science.* 2013 Jun 28;340(6140):1587–90.
14. Jiang H, Wang S. Immune cells use active tugging forces to distinguish affinity and accelerate evolution. *Proc Natl Acad Sci.* 2023 Mar 14;120(11):e2213067120.
15. Faro J, Castro M. Affinity Selection in Germinal Centers: Cautionary Tales and New Opportunities. *Cells.* 2021 May;10(5):1040.
16. Hamers-Casterman C, Atarhouch T, Muyldermans S, Robinson G, Hammers C, Songa EB, et al. Naturally occurring antibodies devoid of light chains. *Nature.* 1993 Jun;363(6428):446–8.
17. González C, Chames P, Kerfelec B, Baty D, Robert P, Limozin L. Nanobody-CD16 Catch Bond Reveals NK Cell Mechanosensitivity. *Biophys J.* 2019 Apr 23;116(8):1516–26.
18. Heath GR, Kots E, Robertson JL, Lansky S, Khelashvili G, Weinstein H, et al. Localization atomic force microscopy. *Nature.* 2021 Jun;594(7863):385–90.
19. Kostrz D, Wayment-Steele HK, Wang J, Follenfant M, Pande VS, Strick TR, et al. A modular DNA scaffold to study protein protein interactions at single-molecule resolution. *Nat Nanotechnol.* 2019;14(10):988.
20. Sitters G, Kamsma D, Thalhammer G, Ritsch-Marte M, Peterman EJG, Wuite GJL. Acoustic force spectroscopy. *Nat Methods.* 2015 Jan;12(1):47–50.
21. Wang YJ, Valotteau C, Aimard A, Villanueva L, Kostrz D, Follenfant M, et al. Combining DNA scaffolds and acoustic force spectroscopy to characterize individual protein bonds. *bioRxiv.* Accepted to *Biophysical Journal.*; 2022. p. 2022.08.14.503897.
22. Pierres A, Benoliel AM, Bongrand P. Measuring the Lifetime of Bonds Made between Surface-linked Molecules (*). *J Biol Chem.* 1995 Nov 3;270(44):26586–92.
23. Pierres A, Feracci H, Delmas V, Benoliel AM, Thiery JP, Bongrand P. Experimental study of the interaction range and association rate of surface-attached cadherin 11. *Proc Natl Acad Sci.* 1998 Aug 4;95(16):9256–61.
24. Limozin L, Bongrand P, Robert P. A Rough Energy Landscape to Describe Surface-Linked Antibody and Antigen Bond Formation. *Sci Rep.* 2016 Oct 12;6(1):35193.
25. Li P, Gao Y, Pappas D. Multiparameter Cell Affinity Chromatography: Separation and Analysis in a Single Microfluidic Channel. *Anal Chem.* 2012 Oct 2;84(19):8140–8.
26. Cheng X, Irimia D, Dixon M, Sekine K, Demirci U, Zamir L, et al. A microfluidic device for practical label-free CD4+ T cell counting of HIV-infected subjects. *Lab Chip.* 2007;7(2):170–8.

27. Pullagurla SR, Witek MA, Jackson JM, Lindell MAM, Hupert ML, Nesterova IV, et al. Parallel Affinity-Based Isolation of Leukocyte Subsets Using Microfluidics: Application for Stroke Diagnosis. *Anal Chem*. 2014 Apr 15;86(8):4058–65.
28. Smith GP. Filamentous Fusion Phage: Novel Expression Vectors That Display Cloned Antigens on the Virion Surface. *Science*. 1985 Jun 14;228(4705):1315–7.
29. Boder ET, Wittrup KD. Yeast surface display for screening combinatorial polypeptide libraries. *Nat Biotechnol*. 1997 Jun;15(6):553–7.
30. Oliphant T, Engle M, Nybakken GE, Doane C, Johnson S, Huang L, et al. Development of a humanized monoclonal antibody with therapeutic potential against West Nile virus. *Nat Med*. 2005 May;11(5):522–30.
31. Kalb SR, Lou J, Garcia-Rodriguez C, Geren IN, Smith TJ, Moura H, et al. Extraction and Inhibition of Enzymatic Activity of Botulinum Neurotoxins/A1, /A2, and /A3 by a Panel of Monoclonal Anti-BoNT/A Antibodies. *PLoS ONE*. 2009 Apr 28;4(4):e5355.
32. McMahon C, Baier AS, Pascolutti R, Wegrecki M, Zheng S, Ong JX, et al. Yeast surface display platform for rapid discovery of conformationally selective nanobodies. *Nat Struct Mol Biol*. 2018 Mar;25(3):289–96.
33. Pymm P, Redmond SJ, Dolezal O, Mordant F, Lopez E, Cooney JP, et al. Biparatopic nanobodies targeting the receptor binding domain efficiently neutralize SARS-CoV-2. *iScience*. 2022 Nov 18;25(11):105259.
34. Teymennet-Ramírez KV, Martínez-Morales F, Trejo-Hernández MR. Yeast Surface Display System: Strategies for Improvement and Biotechnological Applications. *Front Bioeng Biotechnol*. 2022 Jan 10;9:794742.
35. Bowley DR, Labrijn AF, Zwick MB, Burton DR. Antigen selection from an HIV-1 immune antibody library displayed on yeast yields many novel antibodies compared to selection from the same library displayed on phage. *Protein Eng Des Sel*. 2007 Jan 1;20(2):81–90.
36. Richter F, Bindschedler S, Calonne-Salmon M, Declerck S, Junier P, Stanley CE. Fungi-on-a-Chip: microfluidic platforms for single-cell studies on fungi. *FEMS Microbiol Rev*. 2022 Nov 1;46(6):fuac039.
37. Reinmets K, Dehkharghani A, Guasto JS, Fuchs SM. Microfluidic quantification and separation of yeast based on surface adhesion. *Lab Chip*. 2019 Oct 9;19(20):3481–9.
38. Bouchet J, Basmaciogullari SE, Chrobak P, Stolp B, Bouchard N, Fackler OT, et al. Inhibition of the Nef regulatory protein of HIV-1 by a single-domain antibody. *Blood*. 2011 Mar 31;117(13):3559–68.
39. Behar G, Sibénil S, Groulet A, Chames P, Pugnière M, Boix C, et al. Isolation and characterization of anti-FcγRIII (CD16) llama single-domain antibodies that activate natural killer cells. *Protein Eng Des Sel*. 2008 Jan 1;21(1):1–10.

40. Gietz RD, Woods RA. Transformation of yeast by lithium acetate/single-stranded carrier DNA/polyethylene glycol method - ScienceDirect [Internet]. 2002 [cited 2022 Nov 9]. Available from: <https://www.sciencedirect-com.lama.univ-amu.fr/science/article/abs/pii/S0076687902509575?via%3Dihub>
41. Dagher Z, Xu S, Negoro PE, Khan NS, Feldman MB, Reedy JL, et al. Fluorescent Tracking of Yeast Division Clarifies the Essential Role of Spleen Tyrosine Kinase in the Intracellular Control of *Candida glabrata* in Macrophages. *Front Immunol*. 2018 May 16;9:1058.
42. Batchelor GK. *An Introduction to Fluid Dynamics*. Cambridge University Press; 2000. 615 p.
43. Crocker JC, Grier DG. Methods of Digital Video Microscopy for Colloidal Studies. *J Colloid Interface Sci*. 1996 Apr 15;179(1):298–310.
44. Kajiwara K, Aoki W, Ueda M. Evaluation of the yeast surface display system for screening of functional nanobodies. *AMB Express*. 2020 Mar 16;10(1):51.
45. Linciano S, Pluda S, Bacchin A, Angelini A. Molecular evolution of peptides by yeast surface display technology. *MedChemComm*. 2019 Sep 18;10(9):1569–80.
46. Robert P, Nicolas A, Aranda-Espinoza S, Bongrand P, Limozin L. Minimal Encounter Time and Separation Determine Ligand-Receptor Binding in Cell Adhesion. *Biophys J*. 2011 Jun 8;100(11):2642–51.

Supplementary Materials

Antigen Production and Conjugation

Nef-biotin was produced using BL21DE3 *E. coli* co-transformed with Nef-AviTag-6His and BirA-cm via heat shock. Transformed cells were grown in a 5 mL 2YT medium (16 g Tryptone, 10 g Yeast Extract, 5 g NaCl with 1 L MilliQ water) supplemented with 2 % v/v glucose, 100 µg/mL ampicillin and 50 µg/mL chloramphenicol and incubated at 37 °C shaking at 220 rpm for 5 hours. An appropriate volume from this starter was transferred into 100 mL of a similar media but without the 2 % v/v glucose to have a starting OD_{600nm} = 0.1. The culture was grown until an OD_{600nm} = 0.5-0.8 was reached and induced by adding 100 µM Isopropyl β-D-1-thiogalactopyranoside (IPTG) and 10 µM biotin and incubated overnight at 30 °C. Afterwards the cells were lysed using a mixture of BugBuster with Benzonase and Lysozine purified using cobalt resin (TALON superflow, GE Healthcare).

Nef-cmyc was produced using BL21DE3 *E. coli* transformed with Nef-cmyc-6His via heat shock. Transformed cells were grown in a 5 mL 2YT medium supplemented with 2 % v/v glucose and 100 µg/mL ampicillin and incubated at 37 °C shaking at 220 rpm for 5 hours. An appropriate volume from this starter was transferred into 100 mL of a similar media but without the 2 % v/v glucose to have a starting OD_{600nm} = 0.1. The culture was grown until an OD_{600nm} = 0.5-0.8 was reached and induced by adding 100 µM Isopropyl β-D-1-thiogalactopyranoside (IPTG) and incubated overnight at 30 °C. Afterwards the cells were lysed and purified as previously described.

CD16a-cmyc was produced using Expi293F cells (A14635, Gibco™) transformed with CD16a-cmyc-6His using Expifectamine DNA lipid complex as described in the product notes. After 1 week of growth, the supernatant was recovered and underwent overnight dialysis using Spectra/Por® 4 RC Dialysis Membrane Tubing at 2 mL/cm with a MWCO of 12,000-14,000 kD in PBS 1x. Purification was also done using cobalt resin.

Nef-cmyc and a portion of CD16a-cmyc underwent labelling with ATTO 647N using the bacterial transglutaminase (L107, TGase Q Protein Labeling Kit, Zedira) as described in the product notes. A portion of the CD16a-cmyc underwent conjugation with biotin using bacterial transglutaminase (L101) as described in the product notes.

CFSE Staining of Negative Yeast

CFSE (CellTrace, C34554A) staining of yeast was adapted from the supplier provided notes and from this staining protocol (41). Stock CFSE was reconstituted with 18 µL DMSO to create a starting concentration of 5 mM. The staining was done on induced yeasts washed and prepared to have an OD_{600nm} = 1 in 1x PBS by adding CFSE stock at a ratio of 1:1000 to reach a working concentration of 5 µM. This was incubated at room temperature on a Stuart tube rotator at 40 rpm for 30 min. Afterwards the yeast was washed twice; this was done by centrifuging the sample at 3500 x g for 1 min at room temperature and resuspending in PBS 1x with 2 % BSA. Staining was checked using cytometry and microscopy. The staining was generally performed on model enrichment trials with non-binding yeasts stained with CFSE, excluding the 1:1 model mixture.

Estimation of Antigen Concentration on the channel surface

In a previous publication (17), it was shown in a microfluidic chamber with glass bottom and PDMS channel, a 7 nM incubation concentration yielded a surface concentration of 30 molecules/ μm^2 , a conversion factor of 4. Applying this to the concentration used for enrichment, the 45 nM incubation concentration will have 180 molecules/ μm^2 . For the serial dilution in the optimization of the incubation concentration to be used in the microfluidic channel, the 135, 45, 15, 5, 1.67 and 0.56 nM converts to 540, 180, 60, 20, 7 and 2 molecules/ μm^2 , respectively.

Derivation of Eq. (1) and (2) from the main text

E^+ = fraction of Expressor Positive (Binding) Cells

E^- = fraction of Expressor Negative (Non-binding) Cells

NE^+ = fraction of Non-Expressor Positive Cells (contains the plasmid but not expressing the Nb)

NE^- = fraction of Non-Expressor Negative Cells

$f^+ = E^+ / (E^+ + NE^+) =$ fraction of Expressing Positive Cells

$f^- = E^- / (E^- + NE^-) =$ fraction of Expressing Negative Cells

α^+ = captured fraction of Positive Cells after flow

α^- = captured fraction of Negative Cells after flow

The sum of E^+ , NE^+ , E^- & NE^- equals 1. We assume x as the ratio of positive cells (bearing the positive plasmid) before flow where $x = E^+_{pre} + NE^+_{pre}$. Therefore, the fractions can be expressed as in Table 1.

Table 1. Fractions PreFlow and PostFlow

PreFlow	$E^+_{pre} = xf^+$	$E^-_{pre} = (1-x)f^-$
	$NE^+_{pre} = x(1-f^+)$	$NE^-_{pre} = (1-x)(1-f^-)$
PostFlow	$E^+_{post} = \alpha^+ xf^+ / S$	$E^-_{post} = \alpha^- (1-x)f^- / S$
	$NE^+_{post} = \alpha^- x(1-f^+) / S$	$NE^-_{post} = \alpha^- (1-x)(1-f^-) / S$

A sum S was applied to normalize the data and ensure a 1 for the sum of all fractions PostFlow. Additionally, we assume that non-expressing positive cells (NE^+) adhere like negative ones (α^-).

$$S = E^+_{post} + E^-_{post} + NE^+_{post} + NE^-_{post}$$

$$S = \alpha^+ xf^+ + \alpha^- (1-x)f^- + \alpha^- x(1-f^+) + \alpha^- (1-x)(1-f^-) \quad (\text{Eq. S1})$$

$$S = \alpha^- + (\alpha^+ - \alpha^-)xf^+$$

A theoretical enrichment (ϵ) in positive cells is defined as:

$$\epsilon = \frac{E^+_{post} + NE^+_{post}}{E^+_{pre} + NE^+_{pre}}$$

||

Adding the mix ratio x and the equations from Table 1, we get the following:

$$\varepsilon = \frac{[a^+ x f^+ + a^- x(1-f^+)]}{Sx} = \frac{a^+ x f^+ + a^- x(1-f^+)}{[a^- + (a^+ - a^-) x f^+] x}$$

leading to Eq. 1 and 2 in the main text.

Measurement of y using pure yeast population

The fraction of cells adhered after flow for a pure yeast population with the irrelevant Nb is: $(N_{post}/N_{pre})^- = S(x=0) = a^-$

$$S = a^- = \left(\frac{N_{post}}{N_{pre}}\right)^-$$

On the other hand, the fraction of cells adhered for a pure yeast population with the cognate Nb is:

$$\left(\frac{N_{post}}{N_{pre}}\right)^+ = S(x=1) = a^+ f^+ + a^- (1 - f^+)$$

When we replace these quantities from the previous equation of y we get:

$$y = f^+ \left(\frac{a^+}{a^-} - 1\right) = \frac{(N_{post}/N_{pre})^+}{(N_{post}/N_{pre})^-} - 1 \quad (\text{Eq. S2})$$

Interestingly, this equation shows that the measured capture efficiencies using the monoclonal control populations driven along a surface with an antigen of interest may be used to predict the theoretical enrichment ε .

Measurement of y using fluorescent negative yeasts in the mixture

Alternatively, the data from the *in-situ* fluorescence microscopy can be used to measure the adhesion. The number of positive cells corresponds to the total number of cells observed in bright field (BF) minus the number of fluorescent ones (Fluo). One defines therefore the negative and positive capture efficiencies respectively as:

$$\left(\frac{N_{post}}{N_{pre}}\right)^- = \left(\frac{N_{post}^{Fluo}}{N_{pre}^{Fluo}}\right)$$

$$\left(\frac{N_{post}}{N_{pre}}\right)^+ = \left(\frac{N_{post}^{BF} - N_{post}^{Fluo}}{N_{pre}^{BF} - N_{pre}^{Fluo}}\right)$$

which are used in Eq. S2 to determine y .

Cytometry Correction for Enrichment Prediction

In an ideal situation, Q1 would not contain any signal. So, if we assume $f^+ = f$, and $Q1 = 0$, we can calculate $E^+ = Q2$, $E^- = Q3$, $NE^+ = Q2Q4/(Q2+Q3)$ and $NE^- = Q3Q4/(Q2+Q3)$. In this case, we can calculate the mix ratio x as well as the enrichment ε as a function of Q2, Q3 and Q4. However, cytometry data show signals for both Q1 and Q2 even on a negative control. Using control yeasts in cytometry, we computed for autofluorescence (f_{AF}) and obtained a corrected f^+ as shown in the table below.

Table 2. Autofluorescence f_{AF} and expression fraction f^+ established using Controls

Control	parameter	Definition	Nef19	CD16.21
Negative	f_{AF}	$Q1^-/(Q1^-+Q4^-)$	0.003 ± 0.003	0.086 ± 0.022
Positive	f^+	$Q2-f_{AF}Q3$	0.26 ± 0.14	0.28 ± 0.09

The estimate for enrichment in the in-text Fig 5 was through $Q2/(Q2+Q3)$ for PreFlow and PostFlow which represents the fraction of binders over expressors and considering the ratio PostFlow/PreFlow. We can calculate those quantities using fractions, $Q2 = E^+$ and $Q3 = E^-$ and assume that $f^+ = f = f$.

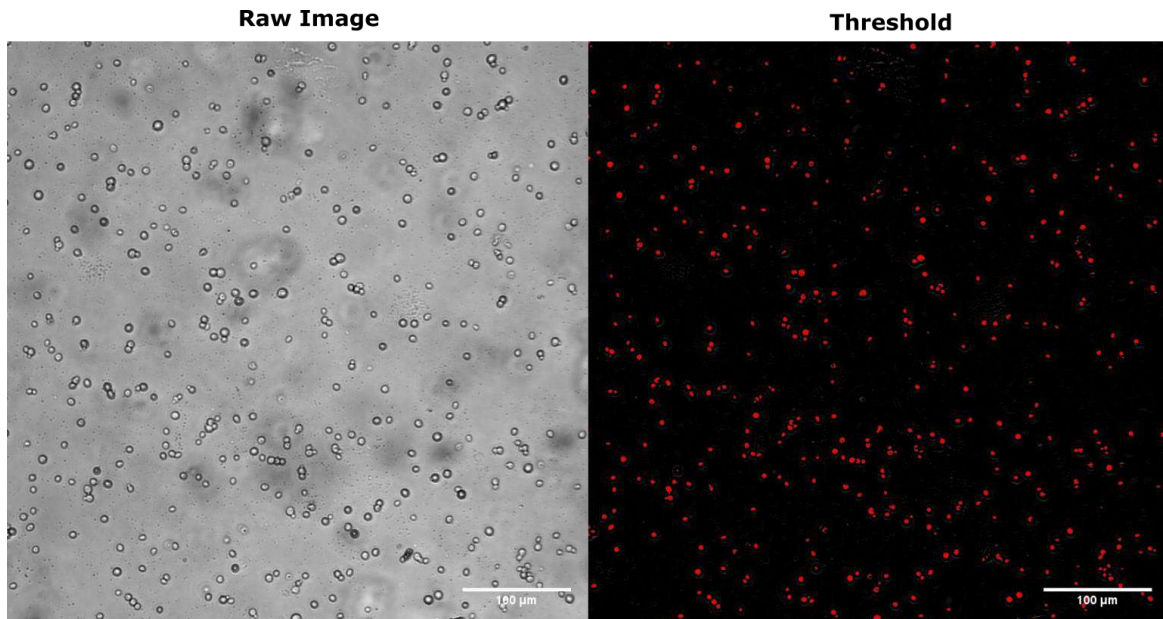
$$\left[\frac{Q2}{Q2 + Q2} \right]^{pre} = \frac{E_{pre}^+}{f} = \frac{xf}{f} = x$$

$$\left[\frac{Q2}{Q2+Q2} \right]^{post} = \frac{a^+xf}{a^+xf + a^-(1-x)f} \quad (\text{Eq. S3})$$

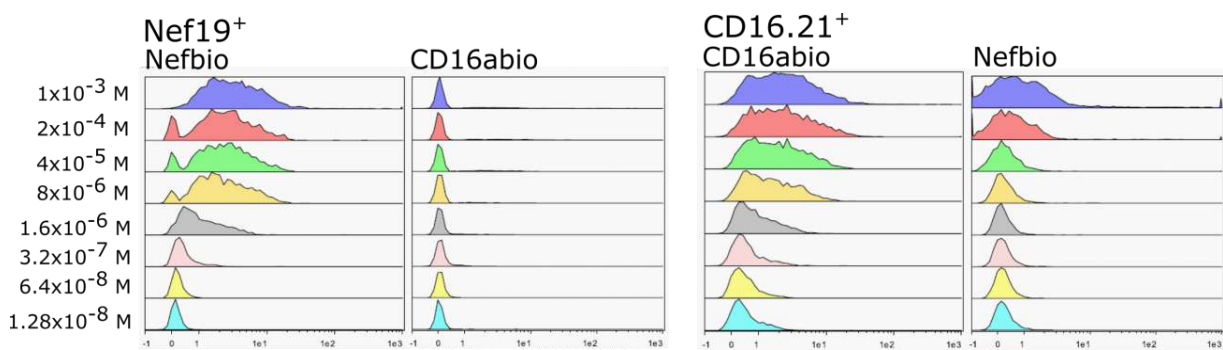
$$\frac{\left[\frac{Q2}{Q2+Q3} \right]^{post}}{\left[\frac{Q2}{Q2+Q3} \right]^{pre}} = \frac{a}{(a-1)x+1} = \varepsilon(f=1)$$

This is only applicable in a condition where $f = 1$, a condition that is not fulfilled as seen in Table 2. Thus, the ratio $Q2/(Q2+Q3)$ roughly underestimated the real enrichment factor if cytometry would be performed immediately after the selection. In practice, the cytometry measurements PostFlow is performed after 48-72h of cell culture to allow for cell expansion and induction of expression, a time sufficient to recover the initial fraction of expressors f^+ . We thus considered the enrichment estimated from $Q2/(Q2+Q3)$ to be valid. The predicted enrichment $\varepsilon(f=1)$ can also be calculated as the following: The factor $y(f^+)$ which corresponds to the real expression fraction f^+ is obtained using the adhesion measurements. We deduced the value of y corresponding to $f = 1$: $y(f=1) = y(f^+)/f^+$ therefore:

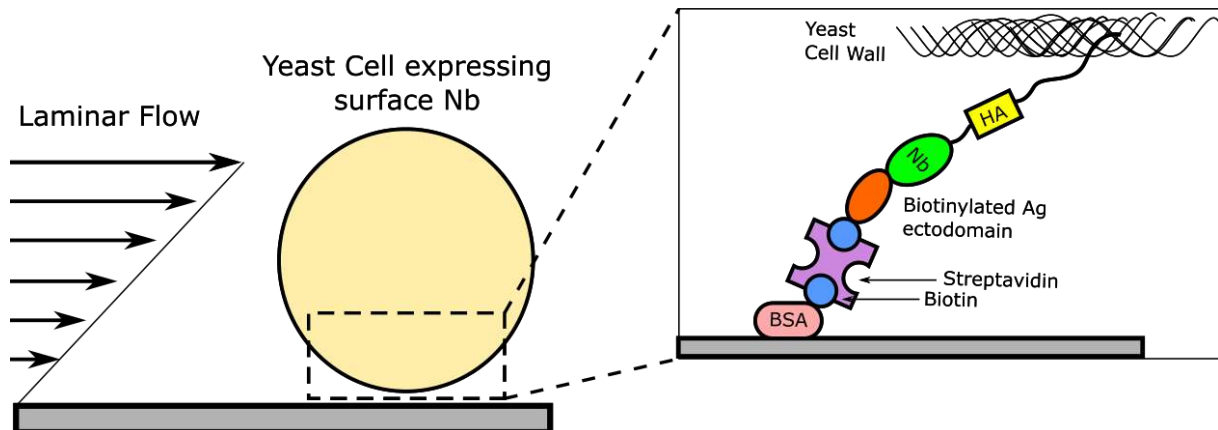
$$\varepsilon(f=1) = \frac{1 + y(f=1)}{1 + xy(f=1)} = \frac{f^+ + y(f^+)}{f^+ + xy(f^+)}$$



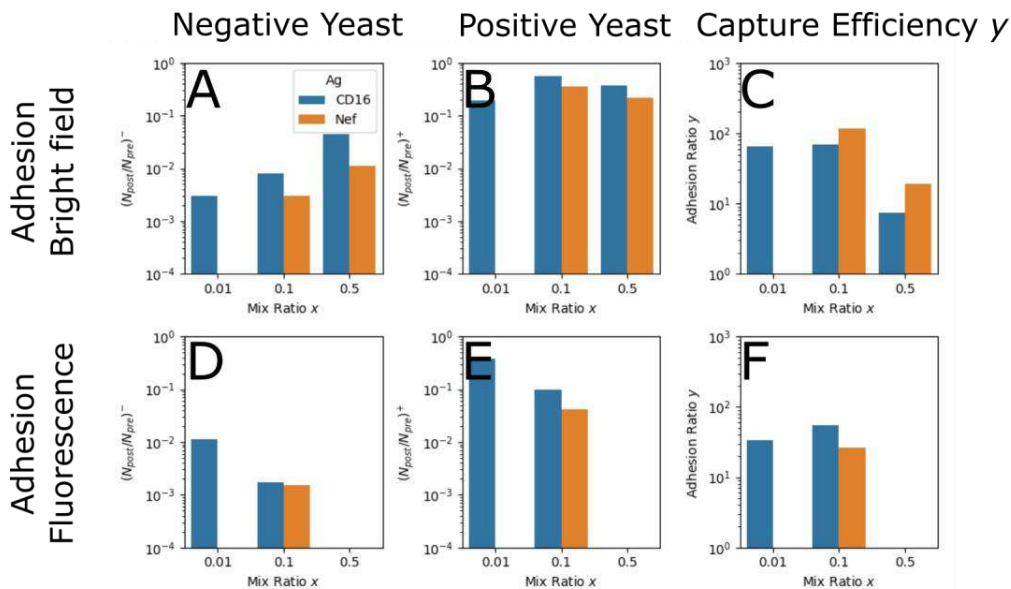
Supplementary Material Figure 1. Detection of Yeast Cells. Detection and counting of yeast cells was done using the MorphoLibJ plugin function Gray Scale Attribute Filtering with Top Hat in FIJI v1.53t. Here we show an example of an image in BF microscopy and the corresponding image after thresholding. The red dots on black background show the yeast cells detected and counted. White Scale bar is at 100 μm .



Supplementary Material Figure 2. Cytometry Histograms to estimate apparent affinity. The apparent affinity of the Nb on the yeast surface was estimated. Nef19⁺ & CD16.21⁺ were incubated with either their cognate or irrelevant antigen and differing concentrations. Each concentrations used are indicated on the corresponding row. Values used in main text Fig 1C were taken here gated using the lowest concentration on the irrelevant antigen.



Supplementary Material Figure 3. Yeast driven along the channel surface. A schematic showing the expected interaction between the flowing yeast cell on the channel surface and the antigen functionalized on the channel surface (image not to scale).



Supplementary Material Figure 4. Bright Field (BF), Fluorescence (Fluo) and Capture Efficiency y . (A) The fraction of cell count PostFlow to PreFlow of the pure non-binding yeast (negative) used as control during enrichment experiments imaged through BF Microscopy. (B) The fraction of cell count PostFlow to PreFlow of the pure binding yeast (positive) used as control during enrichment experiments imaged through BF Microscopy. (C) The calculated capture efficiency y using the BF data using Eq 2 of the main text. (D) The fraction of cell count PostFlow to PreFlow of the pure non-binding & fluorescent yeasts (negative) in the mixture during enrichment experiments imaged through Fluo Microscopy. (E) The fraction of cell count PostFlow to PreFlow of the pure non-binding & non-fluorescent yeast (positive) in the mixture during enrichment experiments imaged through Fluo Microscopy. (F) The calculated capture efficiency y using the Fluo data using Eq 2 of the main text.

Farah MUSTAPHA, Martine PELICOT-BIARNES, Remy TORRO, Kheya SENGUPTA et Pierre-henri PUECH. *Cellular Forces during Early Spreading of T Lymphocytes on Ultra-Soft Substrates*. 11 fév. 2022. DOI : 10.1101/2022.02.11.480084. URL : <https://www.biorxiv.org/content/10.1101/2022.02.11.480084v1> (visité le 10/11/2022).
preprint

Cellular forces during early spreading of T lymphocytes on ultra-soft substrates

Farah Mustapha^{1,2,3,4,5}, Martine Pelicot-Biarnes^{1,2,3,4}, Remy Torro^{1,2,3,4,5}, Kheya Sengupta^{4,5,*},
Pierre-henri Puech^{1,2,3,4,*}

Affiliations:

Laboratoire Adhésion et Inflammation (LAI)

¹ Aix Marseille University, LAI UM 61, Marseille, F-13288, France.

² Inserm, UMR_S 1067, Marseille, F-13288, France.

³ CNRS, UMR 7333, Marseille, F-13288, France.

CENTURI

⁴ Turing Centre for Living systems, Marseille, France

Centre Interdisciplinaire de Nanoscience de Marseille (CINAM)

⁵ CNRS - AMU UMR 7325, Marseille, F-13288, France

*To whom correspondence should be addressed :

sengupta@cinam.univ-mrs.fr, pierre-henri.puech@inserm.fr

Abstract

T cells use forces to read out and act on the mechanical parameters of their microenvironment, which includes antigen presenting cells (APCs). Here we explore the early interaction of T cells with an APC-mimicking ultra-soft polymer gel exhibiting physiologically relevant stiffness in the range of 350-450 Pa. We quantify the dependence of cell spreading and stiffness on gel elasticity, and measure early time traction forces. We find that coating the surface with an antibody against the CD3 region of the TCR-complex elicits small but measurable gel deformation in the early recognition phase, which we quantify in terms of stress or energy. We show that the time evolution of the energy follows one of three distinct patterns: active fluctuation, intermittent, or sigmoidal signal. Addition of either anti-CD28 or anti-LFA1 has little impact on the total integrated energy or the maximum stress. However, the relative distribution of the energy patterns does depend on the additional ligands. Remarkably, the forces are centrifugal at very early times, and only later turn into classical in-ward pointing centripetal traction.

1 Introduction

T cells are activated when with the membrane bound T cell receptors (TCRs) recognize foreign antigenic peptides presented by the major histocompatibility complexes (pMHCs) of antigen presenting cells (APCs), within a small cell-cell contact area termed the immune synapse (IS) (Reichardt, Dornbach, and Gunzer 2010; Grakoui et al. 1999; Monks et al. 1998). This interaction bridges the innate and adaptive immune responses, as the activated T cells multiply and further differentiate, depending on their sub-type, into Cytotoxic T cells that directly kill virally infected cells and cancer cells, and Helper and Regulatory T cells that activate and tune the effector functions of other cells in the immune system. In either case, a given T cell has the formidable task of identifying a particular cognate pMHC against a very noisy environmental background of endogenous self-pMHCs, and to do so quite rapidly as to avoid any potential damage to healthy tissue. Today, an extensive body of research exists describing the biochemical signaling pathways triggered upon the pMHC-TCR interaction, however, further work is needed to unravel the precise mechanism(s) of T-cell activation (He and Bongrand 2012; Malissen and Bongrand 2015; Puech and Bongrand 2021). The formation of the IS is preceded by very dynamic processes whereby the T cell deforms and spreads over the surface of the APC, by extensively reorganizing its cytoskeleton. Such elegant observations were the first indication that physical forces may potentially play a critical role in T cell activation (B.-C. Chen et al. 2014).

Indeed, early work on tissular cells, such as fibroblasts, has demonstrated that individual cells do have the capacity to generate forces (Pelham and Wang 1997). Similar cells were shown to generate relatively large forces, transmitted through well-defined adhesion structures such as focal adhesions or focal complexes (B. Geiger and Bershadsky 2001; Solon et al. 2007; Engler et al. 2006; Elosegui-Artola et al. 2016). This body of work brought to light the relative roles of actin and myosin in force generation and transduction, as well as the existence of cross-talk with adhesion molecules, other mechanosensitive proteins and different signaling pathways, making cell mechanobiology a complex corner-stone in understanding not only adhesion and migration but virtually all aspects of cellular physiopathology (Benjamin Geiger, Spatz, and Bershadsky 2009; Schwarz and Safran 2013; Janmey et al. 2009; Vogel and Sheetz 2006; Martino et al. 2018).

Immune cells on the other hand, including T cells, do not form focal-adhesion-like structures per se but do exert or feel forces during their physiological action. The forces exerted by these cells are expected to be comparatively feeble and less localized. Nevertheless, the ability of immune cells to generate and respond to forces is at the heart of their function in a variety of situations,

ranging from phagocytosis (Herant 2006; Vorselen et al. 2020; 2021; Jaumouillé and Waterman 2020) and stop/go signal for migration (Jannat, Dembo, and Hammer 2011; S. H. J. Kim and Hammer 2021; Huse 2017), to antigen extraction and maturation by B cells (Spillane and Tolar 2018; Kumari et al. 2019) and early activation of T cells (Hu and Butte 2016; Thauland et al. 2017; Klotzsch and Schütz 2013; Y. Liu et al. 2016).

Indeed, recent studies have shown that T cells are not only sensitive, but also responsive, to forces acting at both the molecular and cellular scale (Huse 2017; Limozin and Puech 2019; Puech and Bongrand 2021).

At the molecular scale, the modification of the kinetics of the pMHC-TCR bond under force is thought to be implicated in its ability to distinguish different peptidic antigens (Limozin and Puech 2019; Y. Chen et al. 2017). Measuring single pMHC-TCR rupture forces using Atomic Force Microscopy did not reveal any strong differences upon peptide variation (Puech et al. 2011), however, Biomembrane Force Probe experiments did identify the bond lifetime as a potential key parameter in determining the outcome of the interaction (Ju et al. 2017). It has also been proposed that pMHC-TCR bond may function as a catch bond (B. Liu et al. 2014), whereby the lifetime of the bond is prolonged upon the application of physical force; nevertheless, this point, and in particular the origin of such a complex behavior, is still a matter of debate (Limozin et al. 2019; B. Liu, Kolawole, and Evavold 2021). Even more, the geometry of the applied force has also been investigated using Optical Tweezers and Micropipettes (S. T. Kim et al. 2012; 2009), and led to the proposal that its evaluation by the cell is another important modulator of recognition.

The importance of mechanics at the cell-scale has also been demonstrated (Judokusumo et al. 2012; O'Connor et al. 2012; Wahl et al. 2019; Hivroz and Saitakis 2016; Saitakis et al. 2017), and recently emphasized by showing that immune cells, in particular APCs, possess particular mechanical features that can be modulated as a function of the inflammatory conditions (Bufi et al. 2015), and that T cells are capable of probing and reacting to this modulation (Judokusumo et al. 2012; O'Connor et al. 2012; Wahl et al. 2019). Interestingly, T cells have also been shown to sense resistance to forces parallel to their membrane plane, thus being able to respond to ligand mobility (Dillard et al. 2014; Jankowska et al. 2018; Comrie, Babich, and Burkhardt 2015), as well as readily modulate their viscoelastic properties in response to specific signals at very short scales compared to the ones recorded for calcium fluxes, a hallmark of internal signal transduction (Zak et al. 2021).

Despite the highly detailed knowledge we have gathered thus far, it seems that the full description of cell-scale mechanosensitivity, as well as its link to molecular scales, is still far

from being achieved.

Clearly, an important aspect of understanding cell-scale mechanosensitivity is obtaining a reliable and early measurement of forces exerted by T cells when contacting a cognate surface. As mentioned above, T cells do not exhibit focal adhesion like structures, and moreover at short contact times, the traction forces applied by leukocytes in general, and T cells in particular, are expected to be comparatively low in magnitude and deployed on small, less defined, contact zones as compared to that of large fibroblasts or epithelial cells. From a physiological point of view, T cells are very reactive cells and may also exist in different initial states, ranging from naive to anergized (i.e. non-reactive state). This potentially leads to force amplitude and patterns that differ even within a given cell population. This in itself portrays a challenge for quantification, analysis, and interpretation, even in hybrid *in vitro* systems such as cells interacting with deformable gels.

Here we use well-characterized and reproducible ultra-soft polyacrylamide gels (PAGs) of variable elasticity (0.4-200kPa) to quantify the stresses exerted by T cells during their early spreading (first 15-30 minutes). We employ Traction force microscopy (TFM, (Style et al. 2014; Lekka et al. 2021)) to follow the dynamics, magnitude, and directionality of the stresses generated during the first minutes of T cell engagement with PAGs of stiffness similar to that of non-activated DCs and B cells, that is to say, about 400 Pa (Bufi et al. 2015). The cells are specifically engaged via the CD3 domain of the TCR complex, and/or the co-receptor CD28, and/or the T cell integrin LFA. To our knowledge, TFM at such a low elasticity and early interaction time is novel for T cells. We compare these results to those generated on stiffer, yet still biologically relevant, gels (\approx 2kPa, similar to activated DCs and macrophages (Bufi et al. 2015)). Our dynamic force measurements reveal new patterns of force application over time, that are modulated as a function of substrate mechanics and functionalization, and that are also impacted by the genetic manipulation of cells to introduce fluorescent reporters at the membrane or in the cytoskeleton.

2 Results and discussion

Characterization of soft PAA gels with and without nano-beads

Our goal was to reach ultra-soft substrate rigidities compatible with the ones of physiological APCs (Bufi et al. 2015), laterally homogeneous on length scales similar to the T cell size, and in glass bottom petri dish compatible with our AFM setup and sample heating systems. We optimized the protocols readily available in literature, mainly focusing on that from (Tse and Engler 2010), to obtain thin, but thick enough, films of well-defined and reproducible rigidity (Mustapha, Sengupta, and Puech 2022). We systematically quantified the relative intra- and inter-gel variation of elasticities using AFM microindentation with soft AFM cantilevers, each decorated with a bead of a radius compatible to typical T cells size ($\sim 5\text{-}10\mu\text{m}$ in diameter, Fig. 1A,B).

On Fig.1, we present our measurement strategy. The typical measured thickness of the gels was $\sim 80\mu\text{m}$. Fig. 1C presents a typical force curve obtained while pushing (light red) then pulling (dark red) with the Hertz model fit superimposed (in green). Note that all data presented in Fig. 1C-E was obtained on bead-free gels. The pulling part of the curve shows that very little adhesion is present, allowing us to use a Hertz-like model on the pushing part for quantifying the Young modulus of the gel (the larger the Young modulus, the stiffer the gel). By laterally displacing the indenter, one can map the Young modulus to record the lateral homogeneity. Here we used beads of the same size as the T cells ($5\text{ to }10\mu\text{m}$ diameter) and a similar lateral spacing for the indentation zones (typically $8\mu\text{m}$). Such a map is shown on Fig1D for a 400Pa nominal rigidity gel. The maps revealed rather homogeneous elasticities, with a dispersion within a given gel being of the same order as the one in between samples (Fig.1E, insert is a zoom on 0.4kPa repeats). As such, using our refined protocol, we were able to produce gels with a very large range of well defined and reproducible rigidities (nominal $0.4\text{kPa} - 200\text{kPa}$), encompassing the reported range for macrophages and dendritic cells at different moments of the inflammatory process ($0.4\text{kPa}-4\text{kPa}$, Fig. 1E). While cell spreading and cell elasticity measurements were done on the entire gel-elasticity range, we selected the softer gels corresponding to reported APC elasticities for TFM experiments. This also maximizes the displacement of reporter-nanobeads for feeble applied forces as expected for the early interaction of the cells with the gels (Kumari et al. 2019). We verified that these gels are elastic within our experimental margins (Suppl. Fig. 1).

Next we then characterized the very soft PAA gels when doped with fluorescent nanobeads. As reported before (Mustapha, Sengupta, and Puech 2022), a layer of nanobeads is formed close to each of the two interfaces of the gel (Fig. 1F). The typical position of the top layer, facing the cells, was found to be $\sim 2\mu\text{m}$ from the gel surface, allowing us to observe, at $40\times$, the nanobeads

and the cells simultaneously. The density of nanobeads in the upper layer was observed to be fairly homogeneous (Fig 1G), and rather high, which is an advantage for performing TFM based on PIV analysis (see Material and Methods). Typically, we had four beads in an area of $2.5 \times 2.5 \mu\text{m}^2$ ($16 \times 16 \text{ px}^2$).

We observed an increase of the Young modulus of the doped gels by a factor ~ 2 , due to the presence of the nanobeads (Fig. 1I). Since the nanobeads were washed before inclusion in the gels, this could not be attributed to modification of gel chemistry by an agent in the bead solution. We therefore concluded that at the moderate indentation forces used here, we were probing a zone close to the one dense in beads, in the vertical 'z' direction. Since we expect similar forces and therefore similar probing of depth from the cells, this apparent value of Young modulus (400Pa) was used in the TFM calculations, instead of the nominal value for bead-less gels. In addition, we note that using unwashed nanobeads makes the gels less reproducible, and also usually produces softer gels (not shown). We attributed this to the presence of chemicals (in particular sodium azide for preventing bacterial growth) which most likely perturb the polymerisation of PA. Interestingly, for the 2kPa gel, elasticity was only very weakly perturbed by the presence of the nanobeads (not shown).

Covalent binding of fluorescent antibodies to the gels ensured a homogeneous lateral (x,y) coating (Fig. 1H and J). The measured fluorescent signal was confined to the surface, indicating that the gels have negligible porosity. We subsequently quantified the amount of grafted antibodies using fluorescence microscopy following (Hornung et al. 2020) to be ~ 640 molecules/ μm^2 for a 2 hrs of incubation with a $30 \mu\text{l/ml}$ solution of antibody (Suppl.Fig 1).

As a conclusion, we revealed that, for these very soft gels, the local elasticity in the vicinity of the surface is influenced by the presence of beads over the depths that are of the order of the ones probed by the stress generated by the cells. This again underlines that the impact of any reporter molecule or other object included in a mechanosensory study needs to be carefully investigated and reported, as we have previously shown for fluorescent calcium reporters (Cazaux et al. 2016; Sadoun et al. 2021).

Cell adhesion, spreading, and mechanics are modulated by PAA gels elasticity

To quantify the effect of substrate rigidity on cell spreading and mechanics, we seeded Lifeact-GFP transfected cells on nanobead-free gels of various rigidities, which were surface grafted with aCD3. The apparent spreading area of the cells was quantified, at a given time point, using fluorescence microscopy. In separate experiments, their young modulus was measured by

indenting them with a moderate force by AFM, leading to depths of indentation $< 1 \mu\text{m}$, which represents $\sim < 10\%$ of cell diameter.

Fig.2A shows a sketch of the spreading experiments. The blue band depicts the depth at which we set the focus by detecting small defects or dust-particles on the gel surface by transmission microscopy. A typical cell fluorescence image is shown on Fig. 2B, after 20 min of sedimentation and contact. We made sure that the cells we evaluated were mostly adherent by gently tapping on the microscope base and observing their immobility. After image acquisition, we delineated using Fiji freehand selection tool, the contour of the cell to extract the apparent cell (contact) area (Fig. 2C). The measured area of the cells was widely distributed, and the median values were weakly, but significantly, dependent on substrate elasticity. We observed that the cells have a tendency to spread, on average, more on the softer, more physiological substrate. This observation is in good agreement with (Wahl et al. 2019). However, one should note that here we report the apparent area whereas it would be more rigorous to measure the contact area using a surface technique like reflection interference or total reflection microscopy (Wahl et al. 2019). However, PAA gels are not amenable to either technique, since their index is close to that of the medium, and they have a non-negligible thickness.

In separate experiments, the elasticity of the cells was measured after they interacted with a surface for 20 min. For the measurements, the AFM head has to be lowered towards the surface through the medium using stepper motors so that the cantilever can be close to the surface (Fig. 2D, E). The resultant mechanical perturbations lead to the lifting of almost all cells from the substrate for the softest gels. In this case, reproducible indentations were impossible to perform: cells appeared to slide away from the AFM cantilever bead tip and the indentation force curves looked distorted. We therefore cannot report a reliable value for this case (Fig. 2F). In all the other cases, cells were not visibly perturbed by the approach of the AFM head, and the measured Young modulus is typical for Jurkat cell line and other lymphocytes (Cazaux et al. 2016; Sadoun et al. 2021; Zak et al. 2021). The value of the Young modulus does not show strong variation with substrate elasticity, except for the harder gels (Fig. 2F), which could indicate that the deformation of the gel under the cells can be neglected (Rheinlaender et al. 2020). The order of magnitude of the cell Young modulus, when spread on our aCD3 gels, should then be taken as the average of the ones measured over the two “softer” gels (namely 2 and 20 kPa here), leading to a value $\sim 100 \text{ Pa}$. On the stiffer gels that do not mimic per se any relevant APC (Bubi et al. 2015), the situation of the spreading could be very different, similar to what we reported for the effect of relaxing any shape constraint (Sadoun et al. 2021). Nevertheless, one has to note that the order of magnitude of the Young modulus stays very close to the one usually reported as it is

here ($\sim 100\text{Pa}$), far more than what has been reported to be measured using dynamic AFM modes ($> 10\text{kPa}$, (Jung et al. 2021)) which strengthen our conclusion above.

In the first part of this work, we produced well controlled PAA gels and laterally characterized their mechanical properties using indentation maps in AFM with moderate forces, on scales that are compatible with immune cell dimensions. These properties are homogeneous, tunable over a large range of elasticities, and down to physiological antigen presenting cell ones (Bufi et al. 2015). Such approaches are consistent with the work of others, on B lymphocytes and neutrophils in particular, in terms of gel or substrate elasticity (Kumari et al. 2019; 2020; Henry et al. 2015). Nevertheless, we used antibody-only substrate decorations, and softer substrates as compared to previous reports on Jurkat cells, where polylysine was used as an underlying layer, which likely increased the spreading of the cells via non-specific, charge-based interactions (Hui et al. 2015). By doing so, we were looking to compare situations where only specific signals, with a non specific interaction background as low and controlled as possible, were made available to the cells as in (Dillard et al. 2014; Wahl et al. 2019). As such, potential smaller spreading areas were expected, together with reduced stresses as when superimposed with non specific eg. electrostatic interactions, since the PAA gels are intrinsically non-fouling substrates, ie. essentially not adherent for cells in general, which applies to T cells (not shown here, but see below for IgG2a coated gels).

Early spreading on very soft gels reveals three distinct force application behavior

On Fig. 3A, we summarize our strategy for performing traction force microscopy with open-source tools (Mustapha, Sengupta, and Puech 2022). To capture the first moments of recognition, image acquisition is started before seeding cells, which allows us to use the first frame of our movies as a reliable reference for the unperturbed state of the nanobeads in the gel. Taking simultaneous images of the cells (fluorescence or transmission) and the nanobeads (fluorescence) (Fig 3B), we tracked the changes in the position of the nanobeads under a given cell. This was done by calculating the displacement of the beads at each time point using PIV (Fig. 3C, normalized). The first frame was used as a reference, and sample drift was quantified and compensated for. By applying FTTC, we were able to obtain maps of stress vectors, from which we plotted maps of stress-norms for given time points, in order to observe lateral distribution and magnitude of the stress (Fig. 3D). We summarized these series of snap-shots of stress maps into graphs that track, as a function of time, either the sum of the stress-norms over the whole image, (Fig. 3E top, 'stress-sum' in Pa), or the scalar product of the displacements and forces at each reconstituted pixel (Fig. 3E bottom, 'Energy' in J). The latter was offset to zero from a baseline, whose value appeared to be robust between experiments (not shown here), and

was defined using the first few time points recorded before the arrival of a cell. In the following discussion, we shall focus on the time dependent evolution of the Energy (time-energy curves), and the peak value of the stress-sum (Max Stress Sum). The regularization factor, always required for TFM quantification, was optimized for our experiments (Suppl. Fig. 2) and set to the empirically obtained value of $9E-10$ (Mustapha, Sengupta, and Puech 2022), which is coherent with previous reports using the same data processing procedure (Tseng et al. 2012).

Experimentally, we first verified that no significant nanobead motion was detected on IgG2a (isotype control) coated gels. In contrast, all cells, with some rare exceptions, caused small but visible nanobead displacements when the substrate was coated with the activating antibody aCD3, which was used either alone, or with aCD28 against the coreceptor CD28 or with aCD11a that targets the integrin LFA1. This demonstrates that the cell-gel interaction is highly specific, and that no non-specific interaction occurs with the PAA, decorated or not with a non relevant antibody.

Next we focused on gels that were functionalized with aCD3. Interestingly, the time evolution of the energy shows three distinct and typical patterns (Fig. 4A). In the first case, which we call sigmoidal signal, the energy remains low for a while and then jumps to a value whose magnitude is large compared to the small fluctuations visible before the arrival of the cell, and stays at this value during the remaining entire time (15 minutes) of experiment. In the second case, the energy slowly climbs to a high magnitude (comparable to sigmoidal signal) but then decreases again. We call this the intermittent signal. Finally, the third case is where the signal fluctuates around a low value which is nevertheless higher than the noise detected before arrival of cells (see below). We call this the active fluctuation case. To our knowledge, the time evolution of traction forces was never followed during early spreading events, especially for leukocytes, and such temporal patterns were never reported before.

The three types of time-energy profiles were seen also in cases where either aCD28 or aCD11a was present in addition to aCD3. However, in case of IgG2a, a small noisy fluctuating signal was obtained, which was indistinguishable from the noise before seeding of the cells.

To ascertain the 'active fluctuation' case was indeed not noise, we analyzed the standard-deviation of the fluctuating energy curves obtained from under cells seeded on IgG2a and the aCD3 combinations and compared them to cell-free zones of aCD3 coated gels, since the last can be considered to be a robust readout of the noise level of the measurements. Interestingly, we observed that in the control case, as for IgG2a, the standard deviation did not

vary between before cell seeding or after 20 sec of cell introduction, while it was significantly increased for the aCD3 combinations (Fig. 4B). The 20 sec time cut-off corresponds to the typical time needed for the cells to sediment on the gel. We can therefore distinguish the signal on IgG2a that we qualify as “passive noise” and the aCD3 combinations that we call “active fluctuations”, as stated above. The observation of only passive, noise-like fluctuations under cells on IgG2a confirms our previous conclusion that, as expected, no interaction occurs between the cell and the surface on the isotype control.

We note that the fluctuations we observed are reminiscent of the tiptoeing of cells above substrates before the cells make any decision to spread or not (Pierres et al. 2008; Brodovitch, Bongrand, and Pierres 2013). Unfortunately, due to the loss of lateral resolution imposed by the PIV/FTTC methodology, we could not resolve the real lateral size of the zones where these oscillations were present. Most likely, the active fluctuations could arise due to active dynamics of microvilli, the tip of which is meant to be a mechanosensitive probe of substrates (Brodovitch, Bongrand, and Pierres 2013) which can even penetrate the target cell to probe its mechanics while increasing the effective contact area of the functional structures (H.-R. Kim et al. 2018; Sage et al. 2012).

Quantifying the occurrence of the three types of time-energy curves, we observed that the relative frequency of each type depends on the molecular coating of the gel (Fig. 4C). Intermittent and sigmoid signals, with large magnitude, dominate on aCD3 and aCD3/aCD28 coatings, whereas active fluctuations, of relatively smaller magnitude, are significantly present for the aCD3/aCD11a coating. As already mentioned, cells on IgG2a coating only presented very small magnitude, passive and noisy fluctuations.

Ignoring for the moment the various time-energy curve types, we pooled the entire population of cells for each antibody case. The Max Stress Sum (Fig. 4D) and the integrated energy (Fig. 4E) were, as expected, significantly higher for the aCD3 combinations than for the IgG2a control. Note that for the integrated energy, slightly negative values were sometimes obtained for the fluctuations (both passive and active) due to the baseline correction which did not take the slow decreases of the average signal observed on certain curves into account. Of note, we did not observe on the pooled populations (Fig. 4D,E) a strong dependence of either Max Stress Sum or integrated energy on the molecular details of the substrate for the activating substrates. Moreover, we observed that the time when the maximal force peak occurs was delayed for the aCD3 combinations compared to IgG2a (not shown), coherent with the typical times needed for the cells to be activated (Sadoun et al. 2021).

Intermittent signals were for each substrate, as expected, of lower integrated energy than for sigmoid ones, aCD3/aCD11a being the lowest, while aCD3 and aCD3/aCD28 were of a similar and higher magnitude. Nevertheless, for these latter, the medians showed the same tendency for the two substrate types, aCD3 being slightly higher than aCD3/aCD28. This not so strong role of aCD28 together with aCD3 is reminiscent of our recent observation that aCD28 did not strongly influence the spread area of the same cell line on soft substrates (Wahl et al. 2019), while it could be different for primary cells (Judokusumo et al. 2012).

As a consequence, we can hypothesize that the modulations we observed on the integrated energies when pooling the data for all curves is a combination of the magnitude of the TFM characteristic signals we detected and of the relative occurrence of the fluctuating vs. intermittent vs. sigmoid behaviors. We can therefore propose that the substrate type dictates not only the morphology but also the magnitude of the displacements and resulting stresses generated for the early recognition of a given substrate.

Our data, per se, do not push us to link the observed difference in both the relative fractions and integrated energies of the three energy morphologies with the cells being in different pre-activation states, since we used the Jurkat cell line as model T lymphocytes. It much more reveals the relative effects of substrate decoration on their early recognition by these cells. Aside, such variability of behavior has rarely, if ever, been reported in literature, but could be present in any TFM-like experiment when the processes are occurring early in the interaction with the substrates, followed over time and not at a single, later time point, which may complexify the description and understanding of the data.

We then compared in coupled experiments the behaviors of the same Lifeact cells on CD3 coated substrates with a Young modulus of $\sim 400\text{Pa}$ vs $\sim 2\text{kPa}$. Interestingly, we observed that the fraction of intermittent morphology was dominating the more rigid gel (Fig. 1G). Consequently, the pooled maximal stress sum and integrated energy were lower in this later case (Fig. 4H and I). The separation of the integrated energies per morphology is shown on Fig. 4J for completeness. These observations underline the necessity of using very soft gels, and show why using typical “soft” gels in the range of 2-5kPa as for adherent cells is surely not optimal: the intermittent population may be missed depending on the moment where the exploration of the samples are performed, leading to the false impression that very little cells are indeed pulling / pushing on the gels, if any.

Stress vectors are initially pointing outwards while the cell spreads, then reverse their direction at longer times

When extending the observation duration from 15 to 30 min, we observed that the cells may change their behavior over time. Below 15min, they mainly spread, and as consequence the beads below them displace outward (Suppl. Fig. 4A), the resulting stresses pointing also outwards (Suppl. Fig. 4B). The number of PIV calculated pixels exhibiting a displacement above the noise level detected outside the zone below the cells increased with the accumulated energy (Suppl. Fig. 4C). For longer times, cells start to pull, potentially retract, and bead displacements will point inward, with the resulting stress vectors pointing inwards. Eventually, as exemplified in Suppl. Fig. 4, the cell may stop interacting, or at least, to generate detectable beads motions. This is coherent with the observations made with soft micropillar experiments with different cellular systems (Bashour et al. 2014; Henry et al. 2015; Jin et al. 2019) and with micro-mechanical manipulations (Husson et al. 2011; Sawicka et al. 2017; Hu and Butte 2016; Thauland et al. 2017). Such a contraction at later times during a contact is reminiscent of typical observation for activating T cells: they stop migrating first, and then change shape by rounding while becoming polarized; when micro-manipulated against an activating bead or an AFM cantilever, they start to push, then pull on the object.

Fluorescent reporters may modulate TFM energy patterns

In the bulk of this study, Jurkat cells transfected with a cytoskeletal fluorescent reporter (Lifeact-GFP) were used. The use of fluorescent cells in TFM eases their detection and allows the use of multiband filter sets and diodes for changing the illumination without introducing any mechanical action on the microscope which may perturb the lateral/vertical position of the sample compared to the control image. However, though often these labelings are used as simple reporters, without verifying their impact on the biophysical or even biochemical properties of interest, they may in fact impact the final readout.

To assess the possible impact of using genetically modified cells, we compared the behavior of Jurkat WT (non-fluorescent, carrier cell line), Jurkat transfected with a membrane fluorescent construct (Lck-GFP) or with a cytoskeletal fluorescent construct (Lifeact-GFP, which had been used for the rest of our study). The cells were allowed to interact with aCD3 coated 400Pa PAA gels. The first observation was that the WT cells and the two modified cell lines exhibited the same type of shapes in energy vs. time curves. Nevertheless, their relative proportions varied depending on the cell type, from having the three populations in Jurkat Lck-GFP to only two in the Jurkat Lifeact-GFP and WT cases (Fig. 5A). Thus, in the Lck-GFP case, the intermittent

behavior dominates, while for WT it is the sigmoid one. The behavior of Lifeact-GFP cells is close to that of the WT.

Even if no significant difference is detected in either the pooled maximum stress (Fig. 5B) or integrated energy (Fig. 5C), trends do appear. The Lifeact-GFP variant does have a lower median value of maximal stress than that of the WT, coherent with the impact of intercalating a dye in the actin cytoskeleton, which may impair its capacity to exert local forces. Nevertheless, when considering the integrated energy, the signals which are present are more of a long lasting morphology for the Lifeact-GFP, leading to larger values. Interestingly, the Lck-GFP variant, which is often used as a simple membrane reporter, appears to behave more like the WT case for the max stress sum, since its cytoskeleton is not affected by the labeling, but shows strong modulations of the energy signal morphologies, towards short lived or only fluctuating ones, and very few sustained, sigmoid signals : this results in a large dispersion of the energies, with very low values and very high ones.

The two variants then show a visible difference compared to WT cells. When separating the integrated energy along the different signal types, the spreading of the data leads us to conclude that for this parameter, the median data was not strongly influenced by the cell type, on aCD3 (Fig. 5D). As such, we may propose that the introduction of the fluorescent reporters may indeed have a subtle impact on the local capacities of cells to exert forces, but the major effect is on the capability to add up these forces to build up consequent stress signals over an early time frame. The absence of fluctuating signals for Lifeact-GFP tagged cells in this set of data may indicate that they potentially cannot exert small forces, while for Lck-GFP cells, the membrane modification creates something defavorable to large and long lasting signals (see Fig. 5D where intermittent low integrated energy cells are present, pointing towards the existence of short-lived transitory events).

As a matter of fact, the large dispersion we observe also underlines the possibility for the expression level of the two constructs to play a role on the stress levels and resulting morphologies of energy curves. Further experiments, eg. using scanning confocal microscopy to quantify the entire cell fluorescence level as a reporter of expression of a given reporter, together with obtaining sub populations with clearly separated fluorescence levels by cell sorting, will be needed to clarify that very precise point.

The fact that stresses and energies morphologies were modified for Lifeact-GFP cells as a comparison to WT cells, in our experiments, is well in line with the observations that Lifeact is

not a simple reporter and that its expression can deeply affect the cell mechanics and biophysical responses as reported recently (Flores et al. 2019; Sliogeryte et al. 2016).

As a summary, we observed here the existence of differences in behavior due to labeling different compartments of the cells that have a strong implication either in cell contact to the substrate and its organization (the membrane), or the forces that can be exerted via ligand/receptor interactions (the actin cytoskeleton), pointing to the necessity of being careful when using labeled cells as surrogates of WT ones, in particular when performing single cell based biophysical assays. Again, as already discussed above, the introduction of a modification such as here the expression of a marker, which in many studies is thought to be benign and the modified cells considered to be faithful reporters of the WT cell line, may have profound effects in the case of mechano-transduction studies with very sensitive cells such as lymphocytes (Cazaux et al. 2016; Sadoun et al. 2021). As such, these modifications that are often used to observe cell position or shape may modify their initial state and initial response upon activation, as exemplified here with micromechanical measurements over time. Since we observe such effects on a cell line that is considered by many as a robust model for T cells, we raise the pitfall that such effects could be more important on primary cells, which may have a different, more subtle, activation history.

3 Conclusion

We presented traction force microscopy experiments with well-characterized, ultra-soft, poly acrylamide gels. Using open source software solutions, we quantified the early stresses that model T lymphocytes of the Jurkat cell line applied when interacting with aCD3, or aCD3 in combination with an antibody against a coreceptor (aCD28) or an adhesion molecule (aCD11a). We observed that the patterns of time-evolution of stress and energy can be classified into three distinct categories, the frequency of each depends on the specific antibody or antibodies used to coat the gel. One of these morphologies consists of enhanced fluctuations as compared to controls, reminiscent of cells tiptoeing on substrates before taking a decision to spread or not, as reported by others. The two other categories were an intermittent signal, which grows then disappears in the 15 min observation frame, and a sigmoid signal which, once started, lasts until the end of the experiment, the cell reaching a kind of steady state in stress application.

The distribution of the categories as well as the magnitude of stress or energy are affected concomitantly by the molecular details of the coating of the gel surface. Also, we demonstrated that the ultra-soft gels were needed to detect cellular action; slightly stiffer gels resulted in mainly transient signals which are very prone to be missed by the experimentalist, depending on the time frame of the observation or the sensibility of the method in use.

When extending the observation windows to longer times, we observed that the stress vectors point outwardly when the cell spreads but often reverse direction at longer times, with the cells starting to pull on the substrate. This was coherent with reports on neutrophils by others.

Importantly, we observed modulations of the behavior, in terms of time-energy morphologies as well as magnitudes, when using variants of the Jurkat cell line, expressing a membrane or cytoskeletal reporter. We highlighted the fact that such modifications may have a profound and crucial impact on cell mechanotransduction, in particular in the early moments of the cell's interaction with a target surface, potentially even more if it is a real APC, even if such cellular modifications are often thought to be benign and used to facilitate imaging of certain cellular compartments or organizations.

Overall, here we reveal that at early times, and on ultra-soft gels of physiological stiffness, spreading T cells exert forces in centripetal, rather than centrifugal, direction, and that such forces are applied in three distinct time patterns. Our results provide a new insight into early stages of mechanotransduction of lymphocytes.

4 Material and methods

Cell line, culture and modifications Human Jurkat T cells (clone E6-1, ATCC TIB-152), as a model for lymphocytes, were obtained from ATCC. Cells were counted and cultured three times a week, and their viability assessed by the use of Trypan Blue labeling. The cell culture medium (RPMI 1640) and complements (10% FBS, 1% Hepes 1M, 1% Glutamax, 1% Pen/Strep) were obtained from Gibco (Life technologies). Cells were monthly tested for the presence of mycoplasma.

Cell transfection & cytometry *LifeActGFP* transfected Jurkat was obtained in the following manner: Lentivirus expressing LifeAct-GFP were produced in HEK 293T cells by cotransfecting the lentiviral plasmids pLenti.PGK.LifeAct-GFP.W (a gift from Rusty Lansford, Addgene plasmid #51010; Watertown, MA) with psPAX2 and pMD2. G (a gift from Didier Trono, Addgene plasmid #12260 and #12259). Jurkat cells were transduced by spinoculation of virus using polybrene. The expression of LifeAct-GFP was controlled by flow cytometry using LSRFortessa X20 (BD Biosciences, Franklin Lakes, NJ). Cells expressing high levels of Life-Act GFP were sorted with BD FACSMelody cell sorter (BD Biosciences, Franklin Lakes, NJ).

Lck-GFP transfected Jurkat was obtained thus: Jurkat cells were electroporated with 1 μ g of DNA plasmid pcDNA3.1_mLck_GFP (produced in the lab, AM Lellouch) with Nucleofector 2b device (Lonza), and selected by antibiotic G418. The expression of Lck-GFP was controlled by flow cytometry using LSRFortessa X20 (BD Biosciences, Franklin Lakes, NJ). Cells expressing high levels of mLck-GFP were sorted with BD FACSMelody cell sorter (BD Biosciences, Franklin Lakes, NJ).

Fabrication and Functionalization of Polyacrylamide gels PAGs were casted between APTES/Glutaraldehyde treated glass-bottom petri dishes (FD35-100, World Precision Instruments) and cholo-silanized glass coverslips (12mm glass coverslips, Fischer Scientific). The detailed procedure can be found in a companion protocol (Mustapha, Sengupta, and Puech 2022). Hereafter, we give the main reactants and directions .

Solutions of acrylamide (40% wt/vol, A4058, Sigma) and N, N-methylene-bis-acrylamide (BIS, 2% wt/vol, M1533, Sigma) were mixed with PBS to obtain: (i) 3% acrylamide and 0.06% BIS (for a stiffness of 0.4 kPa), (ii) 3% acrylamide and 0.1% BIS (for a stiffness of 1 kPa), (iii) 4% acrylamide and 0.1% BIS (for a stiffness of 2 kPa), (iv) 10% acrylamide and 0.225% BIS (for a stiffness of 20 kPa), and (v) 10% acrylamide and 10% BIS (for a stiffness of 200 kPa). To these formulations, 0.7% of orange fluorescent beads (0.2 μ m, carboxylate modified, F8809, Thermo Fisher) was incorporated.

Crosslinking was initiated through the addition of 1% ammonium persulfate (A3678, Sigma) and 0.1% Tetramethylethylenediamine (T7024, Sigma). The entire assembly was then turned upside down (to allow the beads to move closer to the surface) and left to polymerize at 4°C. After 1hr, the petri dishes were immersed in PBS for 20 min and the top coverslips were carefully peeled off using a needle-tip.

The obtained gels were then stored overnight in PBS at 4°C and used the day after fabrication to ensure reproducible polymerization. The thickness of the obtained gels was measured to be typically $\approx 80 \mu\text{m}$, using a motorized inverted microscope.

Prior to experimentation, antibodies of choice were covalently attached to the surface of the gels using the photoactivatable heterobifunctional reagent sulfo-SANPAH (sulfosuccinimidyl 6 (4-azido-2-nitrophenyl-amino) hexanoate, 803332, Sigma). Briefly, the PBS was drained off the surface of the PAGs and 200 μl of sulfo-SANPAH (1 mM in 50 mM HEPES, pH 8.5) was applied. The surface of each gel was then exposed to a 365 nm UV radiation for 2min at 100% power in a UV-KUB 2 oven. The darkened sulfo-SANPAH solution was rinsed off using PBS and the photoactivation procedure was repeated a second time. Once the photoactivation was done, the gels were immediately incubated with anti-CD3 (OKT3, 14-0037-82, Thermo Fisher), anti-CD28 (14-0289-82, Thermo Fisher), anti-LFA-1 (14-0119-82, Thermo Fisher), anti-IgG2a (14-4724-85, Thermo Fisher) or a 1:1 combination of anti-CD3 and CD-28 or anti-CD3 and anti-LFA1-1, always to a final concentration of 30 $\mu\text{g}\cdot\text{ml}^{-1}$ each and for 2hrs at room temperature. After 2hrs, the gels were rinsed 3 times with PBS and the petri dishes were transferred to the microscope holder, pre-heated to 37°C, for imaging.

Fluorescence quantification of antibody density Alexa Fluor 488 conjugated anti-human CD3 OKT3 (eBioscience by Thermo Fisher Scientific) antibody was used for the quantification of polyacrylamide gel coatings. A bulk calibration data was initially set up by measuring the fluorescence intensity of 41- μm -thick channels passivated with 1% Pluronic F127 (Sigma-Aldrich) and filled with antibody solutions at concentrations of 3.75, 7.5, 15, and 30 $\mu\text{g}\cdot\text{mL}^{-1}$. In parallel, polyacrylamide gels were coated with 30 $\mu\text{g}\cdot\text{mL}^{-1}$ of the anti-human CD3 OKT3 Alexa Fluor 488 antibody for 2 hrs at room temperature, and then imaged using the same microscope configuration as for the channels. Images were then analyzed by Fiji software and the average fluorescence intensity at three different positions was converted into surface density using the bulk calibration following (Hornung et al. 2020).

AFM set-up The set-up has been described in previous reports (Puech et al. 2011; Cazaux et al. 2016; Sadoun et al. 2021). It consists of an AFM head (Nanowizard I, JPK Instruments, Berlin)

mounted on an inverted microscope (Zeiss Axiovert 200). The AFM head uses a 15 μm z-range linearised piezoelectric scanner for motion and an infrared laser for detection. The set-up sits on an active damping table (Halcyonics). AFM measurements were performed in closed loop, constant height feedback mode. Bruker MLCT-UC cantilevers, which are not gold coated, hence less sensitive to thermal drift (Cazaux et al. 2016) were used ; glass beads (5 μm or 10 μm in diameter, silica beads from Kisker Biotech GmbH, larger than cantilever tip) were glued at their extremity using micropipette micromanipulation and UV optical glue (OP-29, Dymax) cured in a UV oven (10 min at maximal power , BioForce Nanosciences). To reduce adhesion to the gels, decorated cantilevers were passivated with 2% Pluronic F127 (in Milli-Q water) for 30 min at 4°C. Alternatively to MLCT-UC, SAA-HPI cantilevers (6 μm in diameter) were used without passivation since they proved experimentally to have a very small adhesion to gels or cells (not shown). The sensitivity of the optical lever system was calibrated on a glass substrate, in PBS at 37°C temp, together with the cantilever spring constant (by using the thermal noise method (Butt and Jaschke 1995), using JPK SPM software routines (JPK Instrument)) at the start of each experiment. The calibration procedure for each cantilever was repeated three times to rule out possible errors and spring constants were found to be consistently close to the manufacturer's nominal values.

The inverted microscope was equipped with 10x (used for laser alignment) and 40xNA0.9 (used for tip positioning and TFM measurements) objectives and a CoolSnap HQ2 camera (Photometrics). Bright field images were used to select the zone of interest on the gels. Images were obtained through either Zen software (Zeiss) or μ Manager (A. Edelstein et al. 2010; A. D. Edelstein et al. 2014). A Petri Dish Heater module (JPK Instruments) allows setting the temperature at the desired value, with a stability of a fraction of a degree over hours.

Gels and T cell mechanics using AFM First, the AFM cotelever bearing the bead was positioned above a selected region of the gel or on the center of an adhered cell. The maximal force to be applied was set at 2000pN for gels and 500 pN for cells (leading to indentation depths of the order of one μm for cells) using a contact duration of 0 sec. If not stated explicitly, the speed of pressing and pulling was $2\mu\text{m}\cdot\text{s}^{-1}$, with an imposed maximal displacement of 7 μm . Then, either (i) a single force curve or a laterally resolved map (of $48\times 48\mu\text{m}^2 = 6\times 6$ zones, each corresponding roughly to the size of a single T cell) was obtained and repeated on several zones of the gels (up to 5 maps at 5 locations for a given gel) or (ii) a single or up to 5 force curves were recorded for each adhered T cell tested. Data was typically recorded at 2048 Hz.

For determination of the Young modulus for T cells, each experimental force curve was examined by eye (to reject evident “bad” curves) and processed with the “Hertz model

procedure” for a spherical tip included in JPK DP software (JPK Instruments), with the hypothesis that the cell behaves as an incompressible material ($\nu \sim 0.5$). Here, only a subset of the entire force span (from the baseline to the maximal contact force) was fitted : for cells we chose to fit over $0.5 \mu\text{m}$ of indentation to minimize contributions from the nucleus (Sadoun et al. 2021). Young modulus were found to be coherent with published ones for T cells specifically and immune cells in general (Cazaux et al. 2016; Zak et al. 2021; Sadoun et al. 2021; Bufi et al. 2015).

For the gels, the JPK-DP software was used to convert the (compressed) force curves to text files and remove bad curves as detected by the experimentalist eye if needed. They were then batch processed using an in-house Python script similar to JPK-DP fitting procedures. Young modulus maps are then rebuilt together with histograms. We verified that the values obtained by this method are in good agreement with the ones of the manual processing using JPK-DP (the difference was observed to be less than 2% in absolute value (not shown)).

For evaluating the visco-elasticity of the gels, experiments were performed with varying the speed of the indentation between 0.1 and $10 \mu\text{m}\cdot\text{s}^{-1}$. It is expected that if the Young modulus is largely not dependent on speed, then the material can be considered as mainly elastic for the range of speeds/frequencies tested.

A median value per gel or cell was then calculated and tabulated in each condition. We validated this way of pooling the data experimentally since no obvious correlation between the Young modulus and the force curve number (corresponding to the « mechanical history » of the cell or gel) was observed (not shown).

All experiments were performed at 37°C .

T cell spreading experiments After the gels were fabricated and functionalized as described above, they were then transferred to the pre-heated epi-fluorescence microscope (described below) and left to equilibrate at 37°C for approximately 20 min before the Jurkat Lifeact-GFP cells were added. The cells were left to interact with the gels for 20 min before image acquisition started. The system was focused just above the gel surface (Fig. 2A). The images were captured through Zen software (Zeiss), and the imaging parameters were set to 25% excitation power, 100 ms exposure time for the GFP-labeled cells (488 nm). The obtained images were processed using Fiji/ImageJ (Schindelin et al. 2012), as shown on Fig. 2B, by delineating the contour of the cells to quantify the apparent cell area.

TFM set-up and experiments The optical microscope set-up described above (for the AFM) was used, with a $40\times\text{NA}0.9$ air objective and a CoolSnap HQ2 camera (Photometrics). The

microscope was also equipped with a LED illumination system (Colibri 2, Zeiss) and suitable filter sets (Cazaux et al. 2016) for fluorescence imaging, as well as the Petri Dish Heater module (JPK Instruments) for experimentation at 37°C. To measure the traction forces generated by Jurkat T cells, movies of live cells and fluorescent beads were acquired typically every 5 sec during T cell spreading for 15min in phase contrast for the WT Jurkat T cells, in the 488 nm channel for the GFP-labeled Jurkat T cells, and in the 555nm channel for the orange/red beads. For some movies, the duration was extended to 30min and/or the time between frames set to 2.5 sec.

The polyacrylamide gels were mounted on the microscope and left to equilibrate at 37°C for approximately 20min before the cells were added. Beads were brought into focus. Note that since the layer of microspheres is only a couple of microns beneath the gel surface (due to the flipping of the gel during the polymerization step above), the cells can still be easily seen and tracked while the focus is set on the bead layer. Image acquisition started a few seconds before cell addition, allowing us to obtain the relaxed state of the gel without the need for cell detachment using trypsin.

The movies were captured through Zen software (Zeiss), and the imaging parameters were set to: 20 ms exposure time for the non-labeled cells (phase contrast), 25% excitation power 100 ms exposure time for the GFP-labeled cells (488 nm), and 50% excitation power 200 ms exposure time for the orange beads (555 nm) (Cazaux et al. 2016).

Traction Force Microscopy Image sequences of the fluorescent beads were first aligned to correct experimental drift by first extracting the trajectories of the beads on the full field images using the ImageJ “TrackMate” plugin, and then utilizing the obtained trajectories to align the images with the help of the following in-house Python 3.8 Jupyter Notebook <https://github.com/remyeltorro/SPTAlign>. 128x128 px² (equivalent to 20x20µm²) regions of interest were then selected and cropped out using ImageJ’s ROI 1-click tool and the MultiCrop macro (<https://github.com/phpuech/TFM>) respectively. The displacement fields in the selected regions were subsequently calculated using the ImageJ “PIV” plugin (<https://sites.google.com/site/qingzongtseng/piv> ; give the ref of the PNAS paper from QT), specifically the Advanced Iterative PIV option. The following parameters were set for the iterations: IW1= 64 SW1= 128 VS1= 32, IW2= 32 SW2= 64 VS2= 16, IW3= 16 SW3= 32 VS3= 8 (where IW: Interrogation window, SW: Search window, VS: Vector spacing) and a correlation threshold of 0.6. The resulting final grid size for the displacement field was ~ 2.5x2.5 µm², with an average of four beads per interrogation window. Then the traction stress fields were reconstructed using the Fiji “FTTC” plugin (<https://sites.google.com/site/qingzongtseng/tfm>).

The regularization parameter was set at 9×10^{-10} for all traction stress reconstructions. Since the ImageJ “PIV” and “FTTC” Plugins only process two images at a time and our experimental data consists of movies (made up of ≈ 200 frames), we wrote a function to consecutively run the two plugins over the full length image sequences of all the selected regions, always taking the first frame in each segment as the reference frame (<https://github.com/phpuech/TFM>). From this data, the sum of stress moduli, the stored energy as defined in (Butler et al. 2002) and the integrated energy over time (after a baseline correction for the beginning of the curve) were calculated and plotted using Python macros (<https://github.com/phpuech/TFM>). We described the entire detailed procedure in a recently published protocol (Mustapha, Sengupta, and Puech 2022).

Data processing, visualization and statistics AFM data was processed partly using JPK-DP (JPK Instruments, Berlin) and partly using an in-house Python 3.8 set of functions to quantify and represent the Young modulus maps and distributions.

TFM movies were processed using a combination of Fiji/ImageJ (Schindelin et al. 2012) and in-house Python 3.8 functions. Alignment of images was performed using Trackmate (Tinevez et al. 2017) together with an in-house Python code, while PIV and FTTC calculations were performed using modified versions of Q. Tseng set of functions for Fiji/ImageJ (<https://sites.google.com/site/qingzongtseng/>; (Tseng et al. 2012)), with further plotting and calculations made using Python 3.8 homemade functions (<https://github.com/phpuech/TFM>). We used the Anaconda Python distribution (<https://www.anaconda.com/>), with the packages Seaborn, Matplotlib, Scipy, Numpy, Scikit as main dependencies. All data analysis was performed on Linux 64 bits machines.

Data plotting and significance testing were performed on Linux or Windows 64 bits machines using Python, R and/or Graphpad Prism (6 or 7). We used non parametric tests by default since our data was observed to be often largely distributed and not gaussian. If not stated otherwise, one data point corresponds to one measurement, that is, either one median value for a gel or a cell (AFM), or the one value calculated for a cell (spreading, TFM).

Acknowledgments

The authors thank the INSERM Cell Culture Facility (PCC).

Part of this work was supported by institutional grants from INSERM, CNRS and Aix-Marseille University to the LAI and CINAM.

FM was supported by a PhD grant from the European Union's Horizon 2020 research and innovation programme under the Marie Skłodowska-Curie grant agreement 713750, with the financial support of the Regional Council of Provence- Alpes-Côte d'Azur and with of the A*MIDEX (ANR-11-IDEX-0001-02), funded by the Investissements d'Avenir project funded by the French Government, managed by the French National Research Agency (ANR)

RT was supported by a PhD grant from CENTURI (Turing Center for Living systems, Marseille, France), funded from the « Investissements d'Avenir » French Government program managed by the French National Research Agency (ANR-16-CONV-0001) and from Excellence Initiative of Aix-Marseille University - A*MIDEX.

We also thank CENTURI for the help we got from Q. Tseng for using his set of macros, under the form of a shared project in the frame of the engineer platform (<https://centuri-livingsystems.org/multi-engineering-platform/>). The authors want to personally thank him for his dedication and help over the very troubled pandemic times we are through.

Contributions

FM did the experimental work, analyzed the data and wrote the article. MPB did all cell constructs and helped for cell maintenance and FACS analysis. RT implemented the refined alignment procedure used in the analysis. KS and PHP designed the study, performed some experiments, implemented novel analysis and wrote the article. All co-authors edited the manuscript.

The authors declare no competing interests.

References

- Bashour, Keenan T, Jones Tsai, Keyue Shen, Joung-Hyun Lee, Eileen Sun, Michael C Milone, Michael L Dustin, and Lance C Kam. 2014. 'Cross Talk between CD3 and CD28 Is Spatially Modulated by Protein Lateral Mobility'. *Molecular and Cellular Biology* 34 (6): 955–64. <https://doi.org/10.1128/MCB.00842-13>.
- Brodovitch, Alexandre, Pierre Bongrand, and Anne Pierres. 2013. 'T Lymphocytes Sense Antigens within Seconds and Make a Decision within One Minute'. *Journal of Immunology (Baltimore, Md.: 1950)* 191 (5): 2064–71. <https://doi.org/10.4049/jimmunol.1300523>.
- Bufi, Nathalie, Michael Saitakis, Stéphanie Dogniaux, Oscar Buschinger, Armelle Bohineust, Alain Richert, Mathieu Maurin, Claire Hivroz, and Atef Asnacios. 2015. 'Human Primary Immune Cells Exhibit Distinct Mechanical Properties That Are Modified by Inflammation'. *Biophysical Journal* 108 (9): 2181–90. <https://doi.org/10.1016/j.bpj.2015.03.047>.
- Butler, James P, Iva Marija Tolić-Nørrelykke, Ben Fabry, and Jeffrey J. Fredberg. 2002. 'Traction Fields, Moments, and Strain Energy That Cells Exert on Their Surroundings'. *American Journal of Physiology-Cell Physiology* 282 (3): C595–605. <https://doi.org/10.1152/ajpcell.00270.2001>.
- Butt, H.-J., and M. Jaschke. 1995. 'Calculation of Thermal Noise in Atomic Force Microscopy'. *Nanotechnology* 6 (1): 1. <https://doi.org/10.1088/0957-4484/6/1/001>.
- Cazaux, Séverine, Anaïs Sadoun, Martine Biarnes-Pelicot, Manuel Martinez, Sameh Obeid, Pierre Bongrand, Laurent Limozin, and Pierre-Henri Puech. 2016. 'Synchronizing Atomic Force Microscopy Force Mode and Fluorescence Microscopy in Real Time for Immune Cell Stimulation and Activation Studies'. *Ultramicroscopy* 160 (January): 168–81. <https://doi.org/10.1016/j.ultramic.2015.10.014>.
- Chen, Bi-Chang, Wesley R. Legant, Kai Wang, Lin Shao, Daniel E. Milkie, Michael W. Davidson, Chris Janetopoulos, et al. 2014. 'Lattice Light-Sheet Microscopy: Imaging Molecules to Embryos at High Spatiotemporal Resolution'. *Science* 346 (6208): 1257998. <https://doi.org/10.1126/science.1257998>.
- Chen, Yunfeng, Lining Ju, Muaz Rushdi, Chenghao Ge, and Cheng Zhu. 2017. 'Receptor-Mediated Cell Mechanosensing'. *Molecular Biology of the Cell* 28 (23): 3134–55. <https://doi.org/10.1091/mbc.E17-04-0228>.
- Comrie, William A., Alexander Babich, and Janis K. Burkhardt. 2015. 'F-Actin Flow Drives Affinity Maturation and Spatial Organization of LFA-1 at the Immunological Synapse'. *The Journal of Cell Biology* 208 (4): 475–91. <https://doi.org/10.1083/jcb.201406121>.
- Dillard, Pierre, Rajat Varma, Kheya Sengupta, and Laurent Limozin. 2014. 'Ligand-Mediated Friction Determines Morphodynamics of Spreading T Cells'. *Biophysical Journal* 107 (11): 2629–38. <https://doi.org/10.1016/j.bpj.2014.10.044>.
- Edelstein, Arthur, Nenad Amodaj, Karl Hoover, Ron Vale, and Nico Stuurman. 2010. 'Computer Control of Microscopes Using MManager'. *Current Protocols in Molecular Biology / Edited by Frederick M. Ausubel ... [et Al.]* Chapter 14 (October): Unit14.20. <https://doi.org/10.1002/0471142727.mb1420s92>.
- Edelstein, Arthur D., Mark A. Tsuchida, Nenad Amodaj, Henry Pinkard, Ronald D. Vale, and Nico Stuurman. 2014. 'Advanced Methods of Microscope Control Using MManager Software'. *Journal of Biological Methods* 1 (2): e10. <https://doi.org/10.14440/jbm.2014.36>.
- Elosegui-Artola, Alberto, Roger Oria, Yunfeng Chen, Anita Kosmalka, Carlos Pérez-González, Natalia Castro, Cheng Zhu, Xavier Trepast, and Pere Roca-Cusachs. 2016. 'Mechanical Regulation of a Molecular Clutch Defines Force Transmission and Transduction in Response to Matrix Rigidity'. *Nature Cell Biology* 18 (5): 540–48. <https://doi.org/10.1038/ncb3336>.
- Engler, Adam J., Shamik Sen, H. Lee Sweeney, and Dennis E. Discher. 2006. 'Matrix Elasticity Directs Stem Cell Lineage Specification'. *Cell* 126 (4): 677–89. <https://doi.org/10.1016/j.cell.2006.06.044>.

- Flores, Luis R., Michael C. Keeling, Xiaoli Zhang, Kristina Sliogeryte, and N ria Gavara. 2019. 'Lifeact-TagGFP2 Alters F-Actin Organization, Cellular Morphology and Biophysical Behaviour'. *Scientific Reports* 9 (1). <https://doi.org/10.1038/s41598-019-40092-w>.
- Geiger, B., and A. Bershadsky. 2001. 'Assembly and Mechanosensory Function of Focal Contacts'. *Curr Opin Cell Biol* 13 (5): 584–92.
- Geiger, Benjamin, Joachim P. Spatz, and Alexander D. Bershadsky. 2009. 'Environmental Sensing through Focal Adhesions'. *Nature Reviews Molecular Cell Biology* 10 (1): 21–33. <https://doi.org/10.1038/nrm2593>.
- Grakoui, A., S. K. Bromley, C. Sumen, M. M. Davis, A. S. Shaw, P. M. Allen, and M. L. Dustin. 1999. 'The Immunological Synapse: A Molecular Machine Controlling T Cell Activation'. *Science* 285 (5425): 221–27.
- He, Hai-Tao, and Pierre Bongrand. 2012. 'Membrane Dynamics Shape TCR-Generated Signaling'. *Frontiers in Immunology* 3: 90. <https://doi.org/10.3389/fimmu.2012.00090>.
- Henry, Steven J., Christopher S. Chen, John C. Crocker, and Daniel A. Hammer. 2015. 'Protrusive and Contractile Forces of Spreading Human Neutrophils'. *Biophysical Journal* 109 (4): 699–709. <https://doi.org/10.1016/j.bpj.2015.05.041>.
- Herant, M. 2006. 'Mechanics of Neutrophil Phagocytosis: Experiments and Quantitative Models'. *Journal of Cell Science* 119 (9): 1903–13. <https://doi.org/10.1242/jcs.02876>.
- Hivroz, Claire, and Michael Saitakis. 2016. 'Biophysical Aspects of T Lymphocyte Activation at the Immune Synapse'. *Frontiers in Immunology* 7 (February). <https://doi.org/10.3389/fimmu.2016.00046>.
- Hornung, Alexander, Thomas Sbarrato, Nicolas Garcia-Seyda, Laurene Aoun, Xuan Luo, Martine Biarnes-Pelicot, Olivier Theodoly, and Marie-Pierre Valignat. 2020. 'A Bistable Mechanism Mediated by Integrins Controls Mechanotaxis of Leukocytes'. *Biophysical Journal* 118 (3): 565–77. <https://doi.org/10.1016/j.bpj.2019.12.013>.
- Hu, Kenneth H., and Manish J. Butte. 2016. 'T Cell Activation Requires Force Generation'. *The Journal of Cell Biology* 213 (5): 535–42. <https://doi.org/10.1083/jcb.201511053>.
- Hui, King Lam, Lakshmi Balagopalan, Lawrence E. Samelson, and Arpita Upadhyaya. 2015. 'Cytoskeletal Forces during Signaling Activation in Jurkat T-Cells'. *Molecular Biology of the Cell* 26 (4): 685–95. <https://doi.org/10.1091/mbc.E14-03-0830>.
- Huse, Morgan. 2017. 'Mechanical Forces in the Immune System'. *Nature Reviews Immunology* 17 (11): 679–90. <https://doi.org/10.1038/nri.2017.74>.
- Husson, Julien, Karine Chemin, Armelle Bohineust, Claire Hivroz, and Nelly Henry. 2011. 'Force Generation upon T Cell Receptor Engagement'. Edited by Javed N. Agrewala. *PLoS ONE* 6 (5): e19680. <https://doi.org/10.1371/journal.pone.0019680>.
- Jankowska, Katarzyna I., Edward K. Williamson, Nathan H. Roy, Daniel Blumenthal, Vidhi Chandra, Tobias Baumgart, and Janis K. Burkhardt. 2018. 'Integrins Modulate T Cell Receptor Signaling by Constraining Actin Flow at the Immunological Synapse'. *Frontiers in Immunology* 9 (January). <https://doi.org/10.3389/fimmu.2018.00025>.
- Janmey, Paul A., Jessamine P. Winer, Maria E. Murray, and Qi Wen. 2009. 'The Hard Life of Soft Cells'. *Cell Motility and the Cytoskeleton* 66 (8): 597–605. <https://doi.org/10.1002/cm.20382>.
- Jannat, Risat A., Micah Dembo, and Daniel A. Hammer. 2011. 'Traction Forces of Neutrophils Migrating on Compliant Substrates'. *Biophysical Journal* 101 (3): 575–84. <https://doi.org/10.1016/j.bpj.2011.05.040>.
- Jaumouill , Valentin, and Clare M. Waterman. 2020. 'Physical Constraints and Forces Involved in Phagocytosis'. *Frontiers in Immunology* 11. <https://doi.org/10.3389/fimmu.2020.01097>.
- Jin, Weiyang, Fella Tamzalit, Parthiv Kant Chaudhuri, Charles T. Black, Morgan Huse, and Lance C. Kam. 2019. 'T Cell Activation and Immune Synapse Organization Respond to the Microscale Mechanics of Structured Surfaces'. *Proceedings of the National Academy of Sciences* 116 (40): 19835–40. <https://doi.org/10.1073/pnas.1906986116>.
- Ju, Lining, Yunfeng Chen, Kaitao Li, Zhou Yuan, Baoyu Liu, Shaun P. Jackson, and Cheng Zhu. 2017. 'Dual Biomembrane Force Probe Enables Single-Cell Mechanical Analysis of Signal Crosstalk between Multiple Molecular Species'. *Scientific Reports* 7 (1).

- <https://doi.org/10.1038/s41598-017-13793-3>.
- Judokusumo, Edward, Erdem Tabdanov, Sudha Kumari, Michael L. Dustin, and Lance C. Kam. 2012. 'Mechanosensing in T Lymphocyte Activation'. *Biophysical Journal* 102 (2): L5-7. <https://doi.org/10.1016/j.bpj.2011.12.011>.
- Jung, Philipp, Xiangda Zhou, Sandra Iden, Markus Bischoff, and Bin Qu. 2021. 'T Cell Stiffness Is Enhanced upon Formation of Immunological Synapse'. *ELife* 10 (July): e66643. <https://doi.org/10.7554/eLife.66643>.
- Kim, Hye-Ran, YeVin Mun, Kyung-Sik Lee, Yoo-Jin Park, Jeong-Su Park, Jin-Hwa Park, Bu-Nam Jeon, et al. 2018. 'T Cell Microvilli Constitute Immunological Synaptosomes That Carry Messages to Antigen-Presenting Cells'. *Nature Communications* 9 (1). <https://doi.org/10.1038/s41467-018-06090-8>.
- Kim, Sarah Hyun Ji, and Daniel A. Hammer. 2021. 'Integrin Cross-Talk Modulates Stiffness-Independent Motility of CD4+ T Lymphocytes'. *Molecular Biology of the Cell* 32 (18): 1749–57. <https://doi.org/10.1091/mbc.E21-03-0131>.
- Kim, Sun Taek, Yongdae Shin, Kristine Brazin, Robert J. Mallis, Zhen-Yu J. Sun, Gerhard Wagner, Matthew J. Lang, and Ellis L. Reinherz. 2012. 'TCR Mechanobiology: Torques and Tunable Structures Linked to Early T Cell Signaling'. *Frontiers in Immunology* 3: 76. <https://doi.org/10.3389/fimmu.2012.00076>.
- Kim, Sun Taek, Koh Takeuchi, Zhen-Yu J Sun, Maki Touma, Carlos E Castro, Amr Fahmy, Matthew J Lang, Gerhard Wagner, and Ellis L Reinherz. 2009. 'The Alphabeta T Cell Receptor Is an Anisotropic Mechanosensor'. *J Biol Chem* 284 (45): 31028–37. <https://doi.org/10.1074/jbc.M109.052712>.
- Klotzsch, Enrico, and Gerhard J Schütz. 2013. 'Improved Ligand Discrimination by Force-Induced Unbinding of the T Cell Receptor from Peptide-MHC'. *Biophysical Journal* 104 (8): 1670–75. <https://doi.org/10.1016/j.bpj.2013.03.023>.
- Kumari, Anita, Judith Pineau, Ana-Maria Lennon-Duménil, Martial Balland, and Paolo Pierobon. 2020. 'Traction Force Microscopy to Study B Lymphocyte Activation'. *JoVE (Journal of Visualized Experiments)*, no. 161 (July): e60947. <https://doi.org/10.3791/60947>.
- Kumari, Anita, Judith Pineau, Pablo J. Sáez, Mathieu Maurin, Danielle Lankar, Mabel San Roman, Katharina Hennig, et al. 2019. 'Actomyosin-Driven Force Patterning Controls Endocytosis at the Immune Synapse'. *Nature Communications* 10 (1): 2870. <https://doi.org/10.1038/s41467-019-10751-7>.
- Lekka, Małgorzata, Kajangi Gnanachandran, Andrzej Kubiak, Tomasz Zieliński, and Joanna Zemła. 2021. 'Traction Force Microscopy – Measuring the Forces Exerted by Cells'. *Micron* 150 (November): 103138. <https://doi.org/10.1016/j.micron.2021.103138>.
- Limozin, Laurent, Marcus Bridge, Pierre Bongrand, Omer Dushek, Philip Anton van der Merwe, and Philippe Robert. 2019. 'TCR-PMHC Kinetics under Force in a Cell-Free System Show No Intrinsic Catch Bond, but a Minimal Encounter Duration before Binding'. *Proceedings of the National Academy of Sciences of the United States of America* 116 (34): 16943–48. <https://doi.org/10.1073/pnas.1902141116>.
- Limozin, Laurent, and Pierre-Henri Puech. 2019. 'Membrane Organization and Physical Regulation of Lymphocyte Antigen Receptors: A Biophysicist's Perspective'. *The Journal of Membrane Biology* 252 (4–5): 397–412. <https://doi.org/10.1007/s00232-019-00085-2>.
- Liu, Baoyu, Wei Chen, Brian D. Evavold, and Cheng Zhu. 2014. 'Accumulation of Dynamic Catch Bonds between TCR and Agonist Peptide-MHC Triggers T Cell Signaling'. *Cell* 157 (2): 357–68. <https://doi.org/10.1016/j.cell.2014.02.053>.
- Liu, Baoyu, Elizabeth M. Kolawole, and Brian D. Evavold. 2021. 'Mechanobiology of T Cell Activation: To Catch a Bond'. *Annual Review of Cell and Developmental Biology* 37 (1): 65–87. <https://doi.org/10.1146/annurev-cellbio-120219-055100>.
- Liu, Yang, Lori Blanchfield, Victor Pui-Yan Ma, Rakieb Andargachew, Kornelia Galior, Zheng Liu, Brian Evavold, and Khalid Salaita. 2016. 'DNA-Based Nanoparticle Tension Sensors Reveal That T-Cell Receptors Transmit Defined PN Forces to Their Antigens for Enhanced Fidelity'. *Proceedings of the National Academy of Sciences* 113 (20): 5610–15.

- <https://doi.org/10.1073/pnas.1600163113>.
- Malissen, Bernard, and Pierre Bongrand. 2015. 'Early T Cell Activation: Integrating Biochemical, Structural, and Biophysical Cues'. *Annual Review of Immunology* 33 (1): 539–61. <https://doi.org/10.1146/annurev-immunol-032414-112158>.
- Martiel, Jean-Louis, Aldo Leal, Laetitia Kurzawa, Martial Balland, Irene Wang, Timothée Vignaud, Qingzong Tseng, and Manuel Théry. 2015. 'Measurement of Cell Traction Forces with ImageJ'. In *Methods in Cell Biology*, 125:269–87. Elsevier. <https://doi.org/10.1016/bs.mcb.2014.10.008>.
- Martino, Fabiana, Ana R. Perestrello, Vladimír Vinarský, Stefania Pagliari, and Giancarlo Forte. 2018. 'Cellular Mechanotransduction: From Tension to Function'. *Frontiers in Physiology* 9. <https://www.frontiersin.org/article/10.3389/fphys.2018.00824>.
- Monks, Colin R. F., Benjamin A. Freiberg, Hannah Kupfer, Noah Sciaky, and Abraham Kupfer. 1998. 'Three-Dimensional Segregation of Supramolecular Activation Clusters in T Cells'. *Nature* 395 (6697): 82–86. <https://doi.org/10.1038/25764>.
- Mustapha, Farah, Kheya Sengupta, and Pierre-Henri Puech. 2022. 'Protocol for Measuring Weak Cellular Traction Forces Using Well-Controlled Ultra-Soft Polyacrylamide Gels'. *STAR Protocols* 3 (1): 101133. <https://doi.org/10.1016/j.xpro.2022.101133>.
- O'Connor, Roddy S, Xueli Hao, Keyue Shen, Keenan Bashour, Tatiana Akimova, Wayne W Hancock, Lance C Kam, and Michael C Milone. 2012. 'Substrate Rigidity Regulates Human T Cell Activation and Proliferation.' *Journal of Immunology (Baltimore, Md. : 1950)* 189 (3): 1330–39. <https://doi.org/10.4049/jimmunol.1102757>.
- Pelham, Robert J., and Yu-li Wang. 1997. 'Cell Locomotion and Focal Adhesions Are Regulated by Substrate Flexibility'. *Proceedings of the National Academy of Sciences* 94 (25): 13661–65. <https://doi.org/10.1073/pnas.94.25.13661>.
- Pierres, Anne, Anne-Marie Benoliel, Dominique Touchard, and Pierre Bongrand. 2008. 'How Cells Tiptoe on Adhesive Surfaces before Sticking.' *Biophysical Journal* 94 (10): 4114–22. <https://doi.org/10.1529/biophysj.107.125278>.
- Puech, Pierre-Henri, and Pierre Bongrand. 2021. 'Mechanotransduction as a Major Driver of Cell Behaviour: Mechanisms, and Relevance to Cell Organization and Future Research'. *Open Biology* 11 (11): 210256. <https://doi.org/10.1098/rsob.210256>.
- Puech, Pierre-Henri, Damien Nevoltris, Philippe Robert, Laurent Limozin, Claude Boyer, and Pierre Bongrand. 2011. 'Force Measurements of TCR/PMHC Recognition at T Cell Surface'. Edited by Daniel J. Muller. *PLoS ONE* 6 (7): e22344. <https://doi.org/10.1371/journal.pone.0022344>.
- Reichardt, Peter, Bastian Dornbach, and Matthias Gunzer. 2010. 'APC, T Cells, and the Immune Synapse'. *Current Topics in Microbiology and Immunology* 340: 229–49. https://doi.org/10.1007/978-3-642-03858-7_12.
- Rheinlaender, Johannes, Andrea Dimitracopoulos, Bernhard Wallmeyer, Nils M. Kronenberg, Kevin J. Chalut, Malte C. Gather, Timo Betz, Guillaume Charras, and Kristian Franze. 2020. 'Cortical Cell Stiffness Is Independent of Substrate Mechanics'. *Nature Materials* 19 (9): 1019–25. <https://doi.org/10.1038/s41563-020-0684-x>.
- Sadoun, Anaïs, Martine Biarnes-Pelicot, Laura Ghesquiere-Dierickx, Ambroise Wu, Olivier Théodoly, Laurent Limozin, Yannick Hamon, and Pierre-Henri Puech. 2021. 'Controlling T Cells Spreading, Mechanics and Activation by Micropatterning'. *Scientific Reports* 11 (1): 6783. <https://doi.org/10.1038/s41598-021-86133-1>.
- Sage, Peter T, Laya M. Varghese, Roberta Martinelli, Tracey E. Sciuto, Masataka Kamei, Ann M. Dvorak, Timothy A. Springer, Arlene H. Sharpe, and Christopher V. Carman. 2012. 'Antigen Recognition Is Facilitated by Invadosome-like Protrusions Formed by Memory/Effector T Cells'. *The Journal of Immunology* 188 (8): 3686–99. <https://doi.org/10.4049/jimmunol.1102594>.
- Saitakis, Michael, Stéphanie Dogniaux, Christel Goudot, Nathalie Bui, Sophie Asnacios, Mathieu Maurin, Clotilde Randriamampita, Atef Asnacios, and Claire Hivroz. 2017. 'Different TCR-Induced T Lymphocyte Responses Are Potentiated by Stiffness with Variable Sensitivity'. *eLife* 6 (June). <https://doi.org/10.7554/eLife.23190>.

- Sawicka, Anna, Avin Babataheri, Stéphanie Dogniaux, Abdul I. Barakat, David Gonzalez-Rodriguez, Claire Hivroz, and Julien Husson. 2017. 'Micropipette Force Probe to Quantify Single-Cell Force Generation: Application to T-Cell Activation'. *Molecular Biology of the Cell* 28 (23): 3229–39. <https://doi.org/10.1091/mbc.E17-06-0385>.
- Schindelin, Johannes, Ignacio Arganda-Carreras, Erwin Frise, Verena Kaynig, Mark Longair, Tobias Pietzsch, Stephan Preibisch, et al. 2012. 'Fiji: An Open-Source Platform for Biological-Image Analysis'. *Nature Methods* 9 (7): 676–82. <https://doi.org/10.1038/nmeth.2019>.
- Schwarz, Ulrich S., and Samuel A. Safran. 2013. 'Physics of Adherent Cells'. *Reviews of Modern Physics* 85 (3): 1327–81. <https://doi.org/10.1103/RevModPhys.85.1327>.
- Sliogeryte, Kristina, Stephen D. Thorpe, Zhao Wang, Clare L. Thompson, Nuria Gavara, and Martin M. Knight. 2016. 'Differential Effects of LifeAct-GFP and Actin-GFP on Cell Mechanics Assessed Using Micropipette Aspiration'. *Journal of Biomechanics* 49 (2): 310–17. <https://doi.org/10.1016/j.jbiomech.2015.12.034>.
- Solon, Jérôme, Ilya Levental, Kheya Sengupta, Penelope C. Georges, and Paul A. Janmey. 2007. 'Fibroblast Adaptation and Stiffness Matching to Soft Elastic Substrates'. *Biophysical Journal* 93 (12): 4453–61. <https://doi.org/10.1529/biophysj.106.101386>.
- Spillane, Katelyn M., and Pavel Tolar. 2018. 'Mechanics of Antigen Extraction in the B Cell Synapse'. *Molecular Immunology* 101 (September): 319–28. <https://doi.org/10.1016/j.molimm.2018.07.018>.
- Style, Robert W., Rostislav Boltianskiy, Guy K. German, Callen Hyland, Christopher W. MacMinn, Aaron F. Mertz, Larry A. Wilen, Ye Xu, and Eric R. Dufresne. 2014. 'Traction Force Microscopy in Physics and Biology'. *Soft Matter* 10 (23): 4047–55. <https://doi.org/10.1039/C4SM00264D>.
- Thauland, Timothy J., Kenneth H. Hu, Marc A. Bruce, and Manish J. Butte. 2017. 'Cytoskeletal Adaptivity Regulates T Cell Receptor Signaling'. *Science Signaling* 10 (469): eaah3737. <https://doi.org/10.1126/scisignal.aah3737>.
- Tinevez, Jean-Yves, Nick Perry, Johannes Schindelin, Genevieve M. Hoopes, Gregory D. Reynolds, Emmanuel Laplantine, Sebastian Y. Bednarek, Spencer L. Shorte, and Kevin W. Eliceiri. 2017. 'TrackMate: An Open and Extensible Platform for Single-Particle Tracking'. *Methods (San Diego, Calif.)* 115 (February): 80–90. <https://doi.org/10.1016/j.jymeth.2016.09.016>.
- Tse, Justin R., and Adam J. Engler. 2010. 'Preparation of Hydrogel Substrates with Tunable Mechanical Properties'. *Current Protocols in Cell Biology* 47 (1): 10.16.1-10.16.16. <https://doi.org/10.1002/0471143030.cb1016s47>.
- Tseng, Qingzong, Eve Duchemin-Pelletier, Alexandre Deshiere, Martial Balland, Hervé Guillou, Odile Filhol, and Manuel Théry. 2012. 'Spatial Organization of the Extracellular Matrix Regulates Cell-Cell Junction Positioning'. *Proceedings of the National Academy of Sciences of the United States of America* 109 (5): 1506–11. <https://doi.org/10.1073/pnas.1106377109>.
- Vogel, Viola, and Michael Sheetz. 2006. 'Local Force and Geometry Sensing Regulate Cell Functions'. *Nature Reviews Molecular Cell Biology* 7 (4): 265–75. <https://doi.org/10.1038/nrm1890>.
- Vorselen, Daan, Sarah R Barger, Yifan Wang, Wei Cai, Julie A Theriot, Nils C Gauthier, and Mira Krendel. 2021. 'Phagocytic “Teeth” and Myosin-II “Jaw” Power Target Constriction during Phagocytosis'. Edited by Pekka Lappalainen, Suzanne R Pfeffer, Pekka Lappalainen, and Renaud Poincloux. *ELife* 10 (October): e68627. <https://doi.org/10.7554/eLife.68627>.
- Vorselen, Daan, Yifan Wang, Miguel M. de Jesus, Pavak K. Shah, Matthew J. Footer, Morgan Huse, Wei Cai, and Julie A. Theriot. 2020. 'Microparticle Traction Force Microscopy Reveals Subcellular Force Exertion Patterns in Immune Cell-Target Interactions'. *Nature Communications* 11 (1). <https://doi.org/10.1038/s41467-019-13804-z>.
- Wahl, Astrid, Céline Dinet, Pierre Dillard, Aya Nassereddine, Pierre-Henri Puech, Laurent Limozin, and Kheya Sengupta. 2019. 'Biphasic Mechanosensitivity of T Cell Receptor-Mediated Spreading of Lymphocytes'. *Proceedings of the National Academy of*

Sciences 116 (13): 5908–13. <https://doi.org/10.1073/pnas.1811516116>.
Zak, Alexandra, Sara Violeta Merino-Cortés, Anaïs Sadoun, Farah Mustapha, Avin Babataheri, Stéphanie Dogniaux, Sophie Dupré-Crochet, et al. 2021. 'Rapid Viscoelastic Changes Are a Hallmark of Early Leukocyte Activation'. *Biophysical Journal* 120 (9): 1692–1704. <https://doi.org/10.1016/j.bpj.2021.02.042>.

Figures captions

Fig. 1: Gel characterization using atomic force microscopy. A: Schematics of gel indentation using a bead modified AFM cantilever. B: Transmission micrograph showing the cantilever on the gel. C: Representative force vs. indentation curve (light red) with a Hertz-like adjustment (green). The retract curve (dark red) shows very little adhesive hysteresis. D: Representative map of the Young modulus, each pixel being of a size comparable to a T cell. E: Measured Young modulus vs. expected modulus from the gel composition (see Material and Methods) with the region of interest corresponding to APCs (Bufi et al. 2015) indicated together with the traditional range used in TFM; insert represents the dispersion between three gels obtained three different days. F: Schematic of the antibody decorated gels, doped with fluorescent nanobeads. Two layers are seen close to the two interfaces. G: Fluorescence image at the focus on the upper nanobeads layer (bar = 50 μm). H: Image taken from the upper substrate interface when coated with a fluorescent antibody (bar = 50 μm). I: Effect of the presence of the nanobeads on the apparent Young modulus of the softest gels. J: Intensity profiles of the image in H, color coded as the lines in H, showing the homogeneity of the fluorescence intensity in the image.

Fig. 2: T cell spreading on gels and mechanical properties A: Schematics of the spreading experiments on antiCD3 coated gels of variable rigidity, the colored zone indicates the zone on which the focus is made to measure the cell's apparent area. B: Micrographs of a Lyf-GFP cell showing the presence of cellular extensions. C: Quantification of the apparent area of cells on the different substrates. Please note that this area is *not* the contact area per se. Typically ~ 200 cells were used in total per case. D: Schematics of the AFM indentation experiments on cells adhered on similar substrates as for spreading experiments. E: Micrograph showing the bead (white round spot) glued on the cantilever (dark gray triangle) in close proximity to a cell. F: Young modulus measurements as a function of substrate rigidity. The Young modulus has not been measured faithfully on cells adhered on the softest substrate (see text) and led us to report a NA here. Typically ~ 20 cells were used per condition.

Fig. 3 : Traction Force Microscopy. A: TFM experiment schematics, with the reference image taken before cell landing. B: Merged image of nanobeads (before displacement in cyan, after in blue) and of the cell sitting on the gel. C: Normalized map of PIV obtained from the nanobeads displacement. D: Stress norm map as calculated by FTTC with a regularization factor of $9\text{e-}10$. E: Typical curve of sum of stresses (bottom) and total stored energy (top) on the entire map vs. time during the early recognition of the substrate by the cell. Typically, the two curves have the same overall morphologies.

Fig. 4: Traction Force Microscopy of Lyf-GFP cells on different substrates. A: Three types of energy vs. time curves are typically observed, of very different morphologies (here with their baseline offset to zero after calculation before a 20 sec cut-off, red dashed line). B: Quantification of the SD of the fluctuating curves obtained for different coatings, at the very beginning of the experiments, where the cells are not exerting forces, and later, when they may do. This shows that fluctuating curves observed for bare or IgG2a coated substrates and aCD3 based ones are different, the latter exhibiting larger fluctuations of energy more likely due to cell interactions. C: Relative occurrence of the types of curves obtained in the different situations with antibody decorated substrates. D: Pooled maximum of the sum of stresses as a function of substrate coating. E: Pooled integrated energy over the time of the experiment (15 min). F: Integrated energy as a function of curve type and substrate (same data as in E). G: Relative occurrence of energy curve morphology for the same cell preparations seeded on gels of two gels of different rigidities, coated with aCD3. Note the small variability of the relative proportions of events introduced by cell culture aleas, compared with C. H: Pooled max stress sum and I: Pooled integrated energy for cells sitting on these gels. J: Same data as in I, separated by energy curve morphology and gel elasticity.

Fig. 5: Effect of transfection on the levels of stresses exerted by the cells on aCD3 coated gels. A: Quantification of the types of morphologies of energy curves. B: Pooled maximum of the sum of stresses and C: Pooled integrated energy as a function of the cell type. D: same data as in C, separated by energy curve morphology and cell type. Note that due to the coupling of experiments per cell culture lots, the data presented here for Lifeact-GFP cells is the same as in Fig. 4G to J.

Graphical abstract

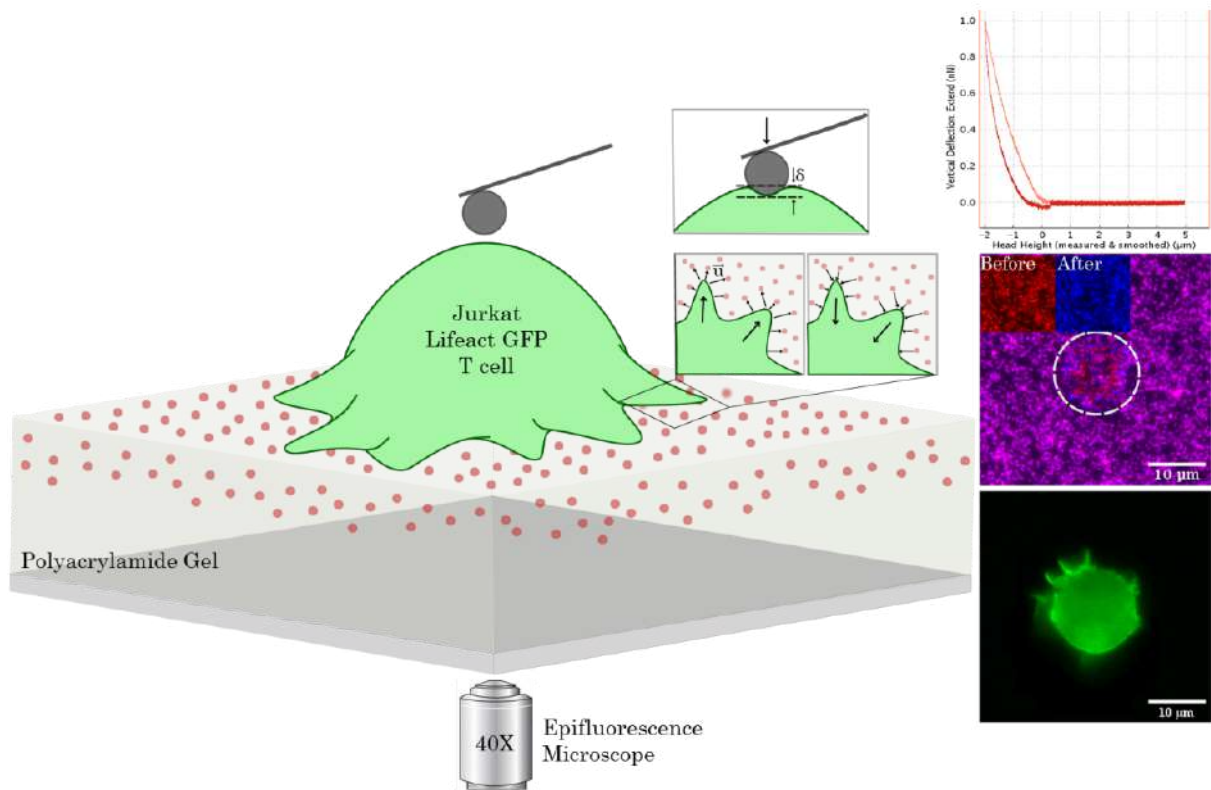


Figure 1

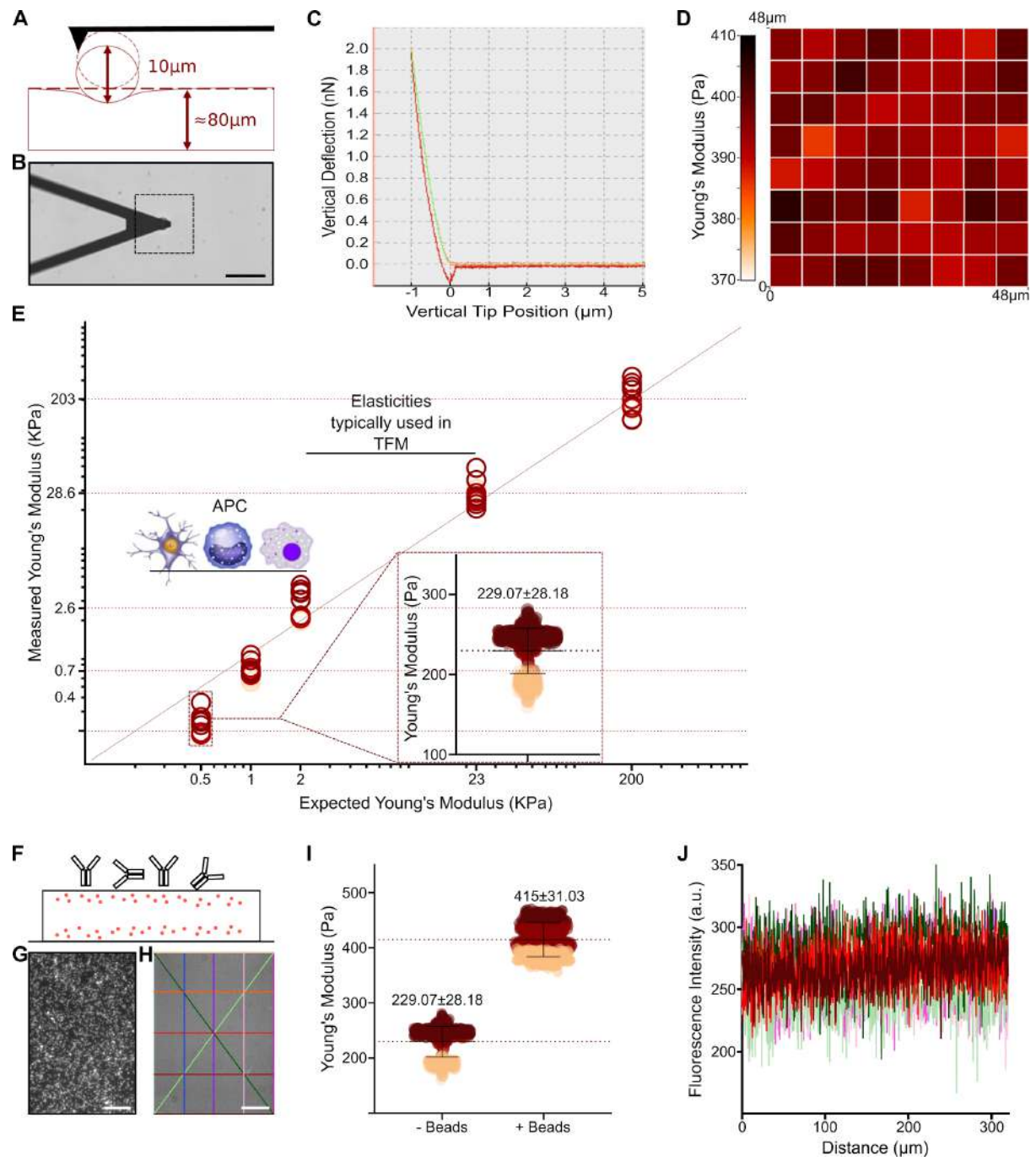


Figure 2

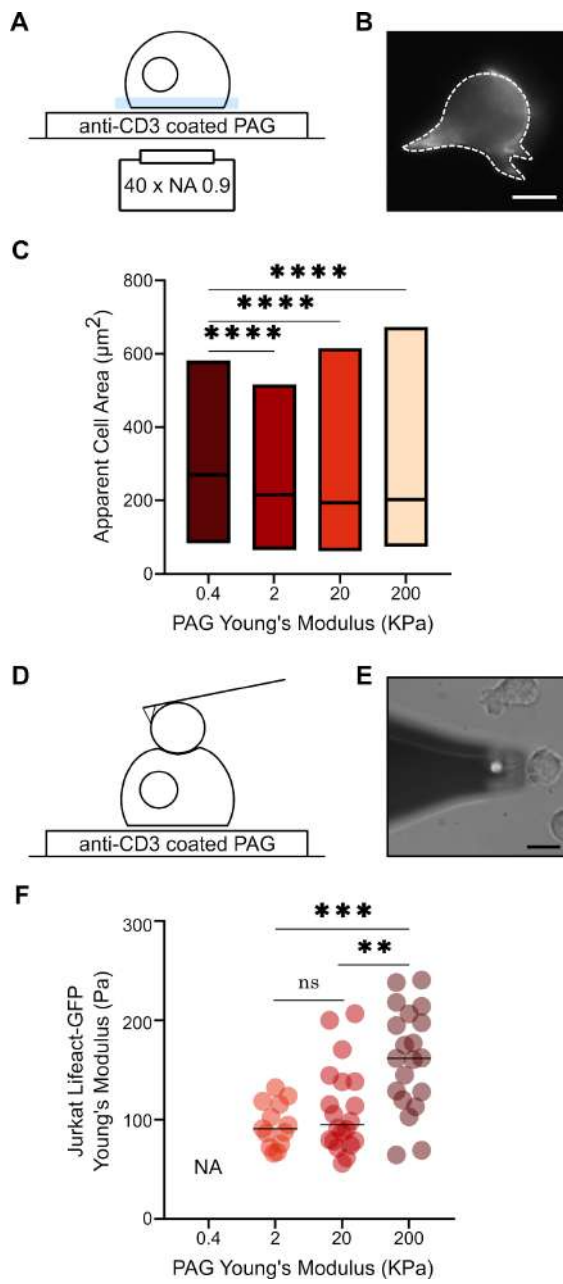


Figure 3

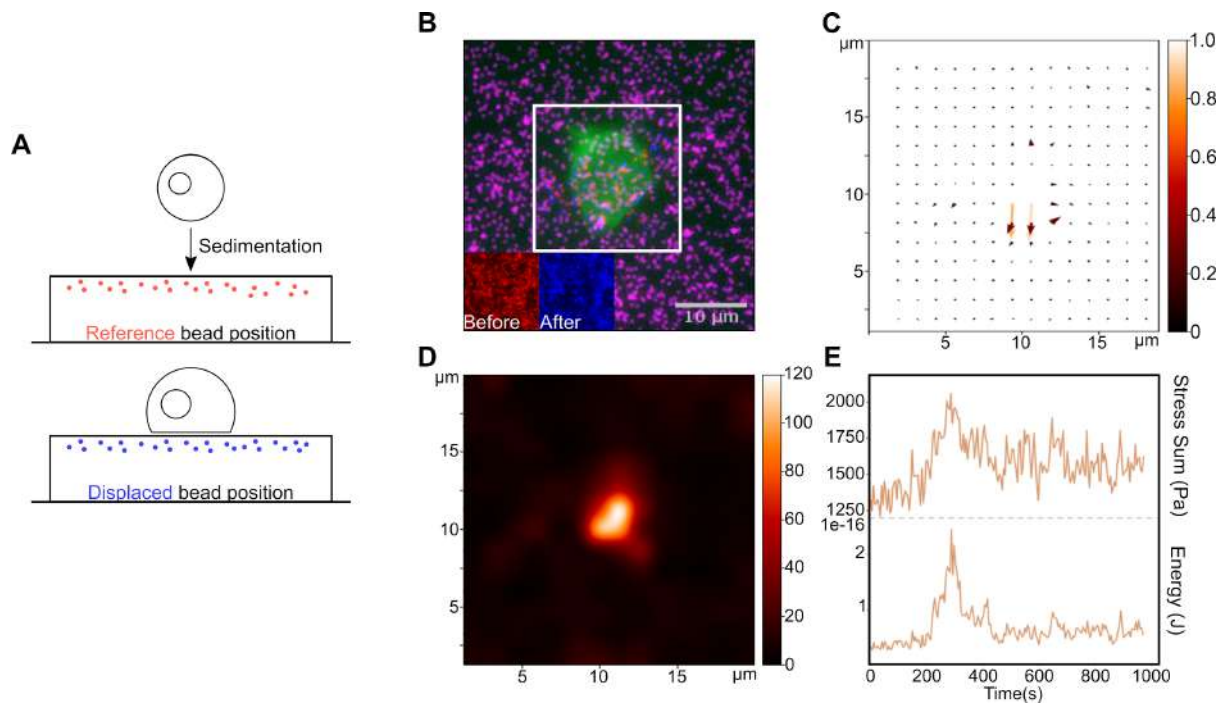


Figure 4

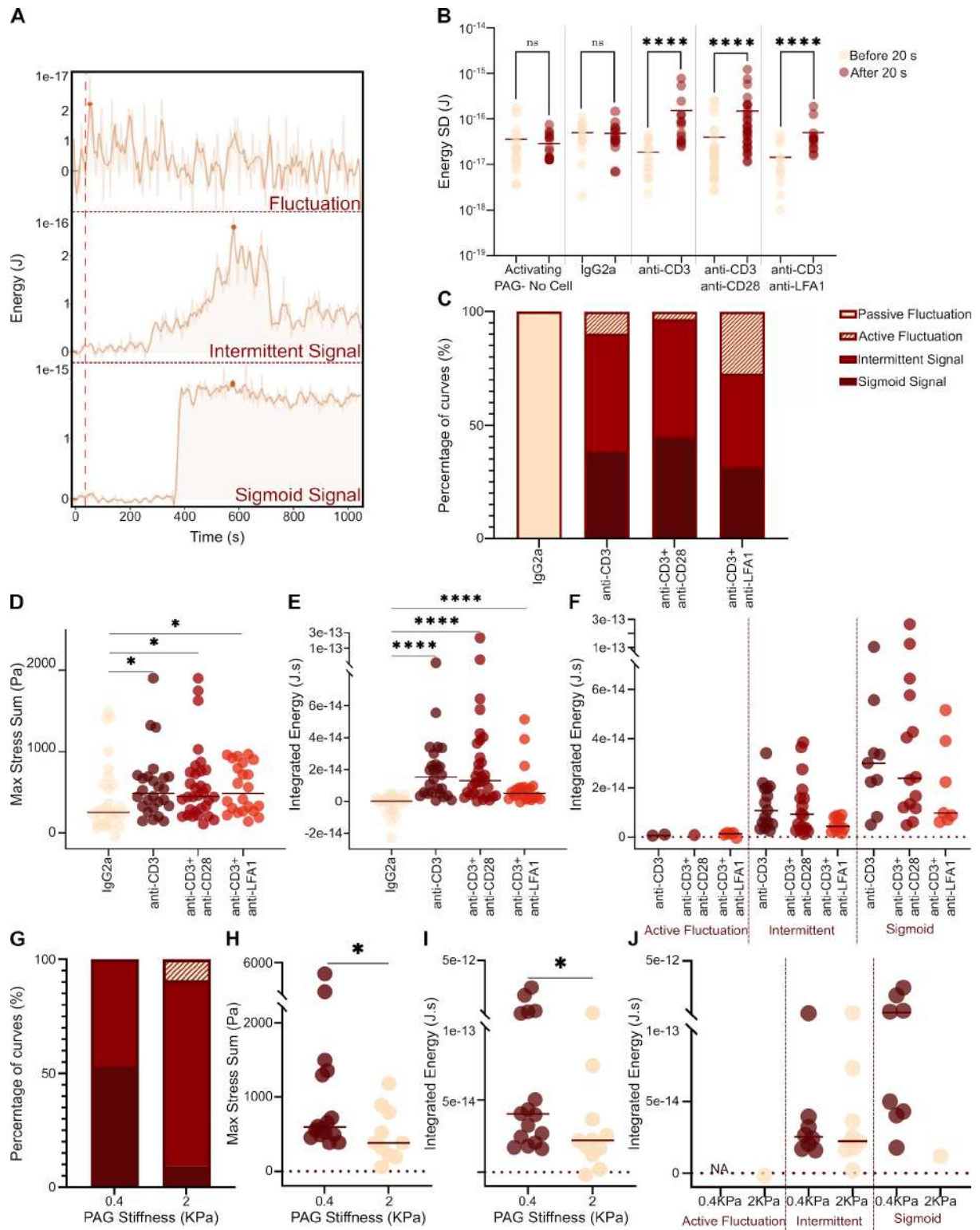
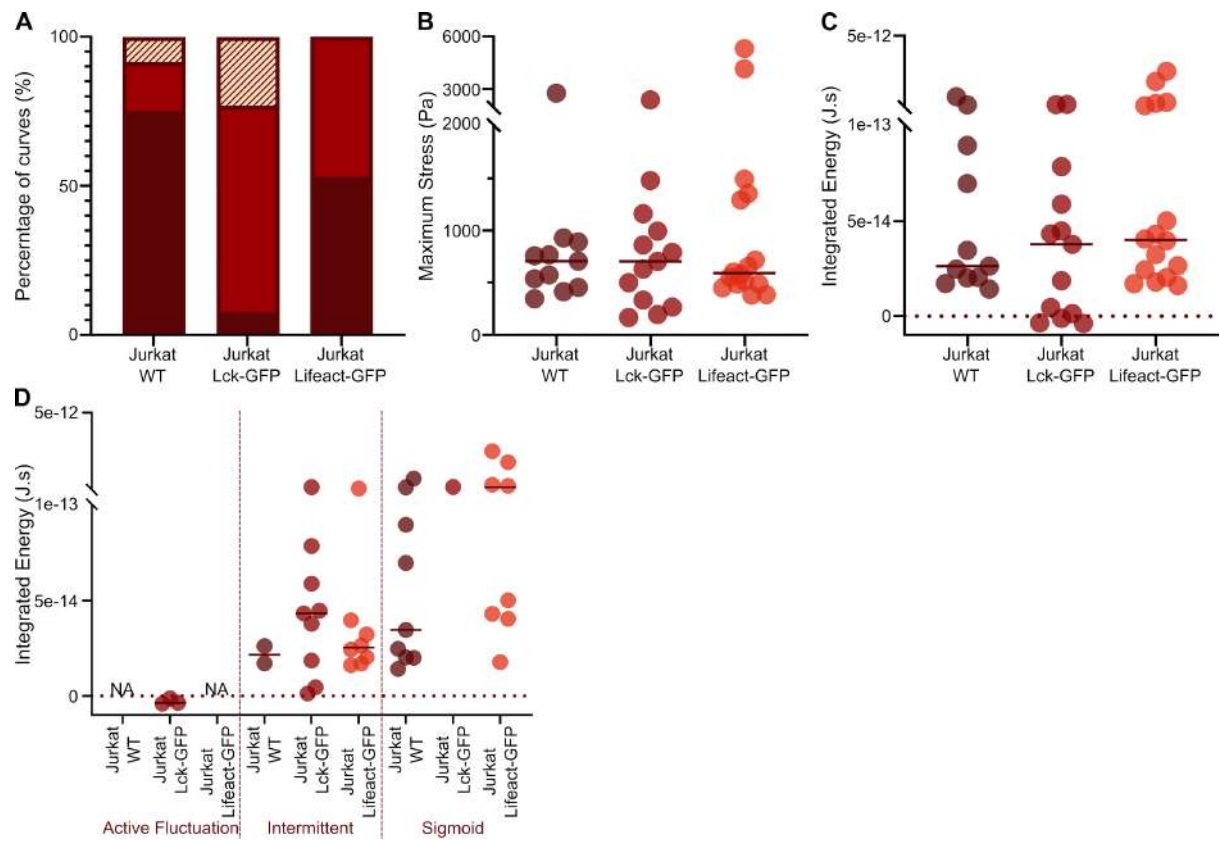


Figure 5



Supplementary figures captions

FigS1: Cytometry. Spectra for Jurkat WT, Lck-GFP (membrane labeling) and LifeAct-GFP (actin labeling) transfected Jurkat after cell sorting for high levels of expression post transfection..

FigS2: Gels mechanics and coating. A: Young moduli of the softest gels as a function of the indentation speed in the range accessible by classical AFM indentation on our set-up, with the same typical contact force (2 nN). No large variation is observed, pointing toward a rather elastic behavior. B: Calibration curve (see text and (Hornung et al. 2020)) that allows us to determine the average density of grafted antibodies from the intensities as measured in I. The red point corresponds to the average fluorescence intensity of the surface of the gel (> 3 samples), which allows us to estimate the coating density reported in the main text.

FigS3 : Optimisation of the regularization parameter for FTTC. A: Type of data (Force vs. time) that was used to optimize the parameter, with the regions where baseline (noise) and signal were analyzed. B: Variation of the signal, noise and signal/noise as a function of the regularization factor. An evident change in intensity for both signals (decrease of the noise faster than the signal ; increasing S/N) was observed around 10^{-9} . C: Beads images (overlay) and calculated PIV for a given time frame of a movie used for A, in the 'signal' zone. D: Reconstructed normalized force vector fields using FTTC and different regularization factors showing zones of interests. Left to right, as the regularization factor increases : decrease of the noise levels out of the higher signal zone, decrease of badly oriented force vectors, disappearance of bad vectors, loss of all signals. E: Energy values calculated vs. time for different regularization factors, showing the same patterns, but absolute levels decreasing as the regularization factor is increased. As a consequence, we choose to use the higher factor before the transitions observed in A, namely 9×10^{-9} (Mustapha, Sengupta, and Puech 2022), which is consistent with values reported in the literature for similar cellular systems (B cells, (Kumari et al. 2020)) and by the published works of the developer of the FTTC Fiji plugin we used (Martiel et al. 2015; Tseng et al. 2012).

Fig. S4 : From spreading to contracting. A: Normalized PIVs and B: Corresponding normalized stress maps for different times points, one for each colored zone in C (number of pixels having a displacement norm larger than the noise in the initial image, vs. time) and D (corresponding calculated energy vs time). The cell spreads first (outward arrows in the second columns of vector maps) then pulls on the gel (inward arrows on the third column). The number of apparent pixels on which noticeable stresses are occurring increase (light yellow, orange, red) then decreases (red, light yellow) as the cell detaches, the energy coming back to its initial level,

and even less (the noise here almost canceled in the end, and the cell had move away from the zone, the system then behaving as a cell free system, see Fig. 4).

Fig. S1

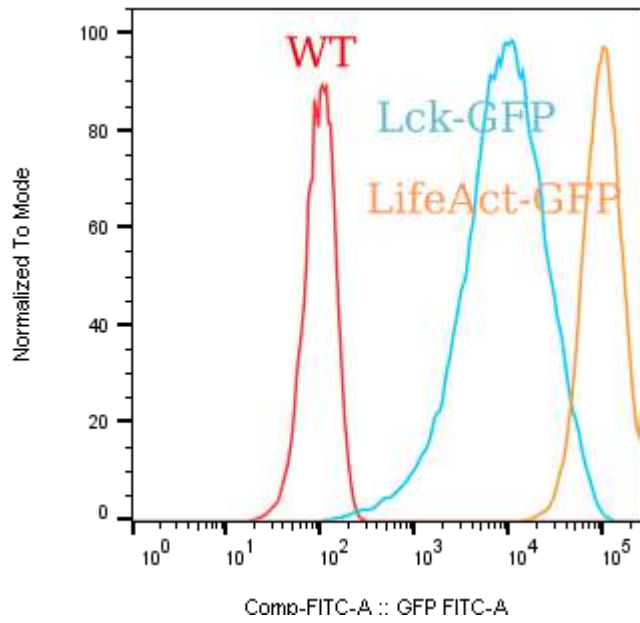


Fig. S2

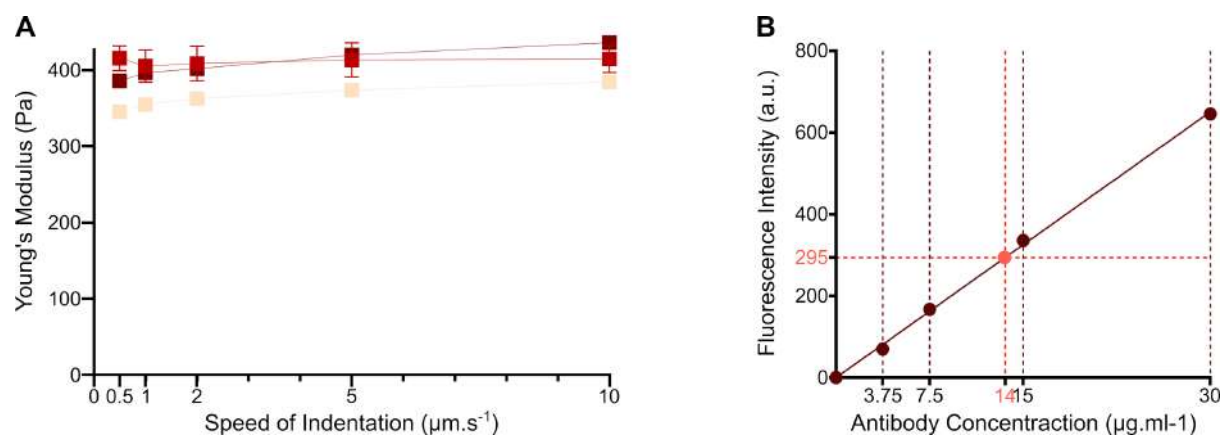


Fig. S3

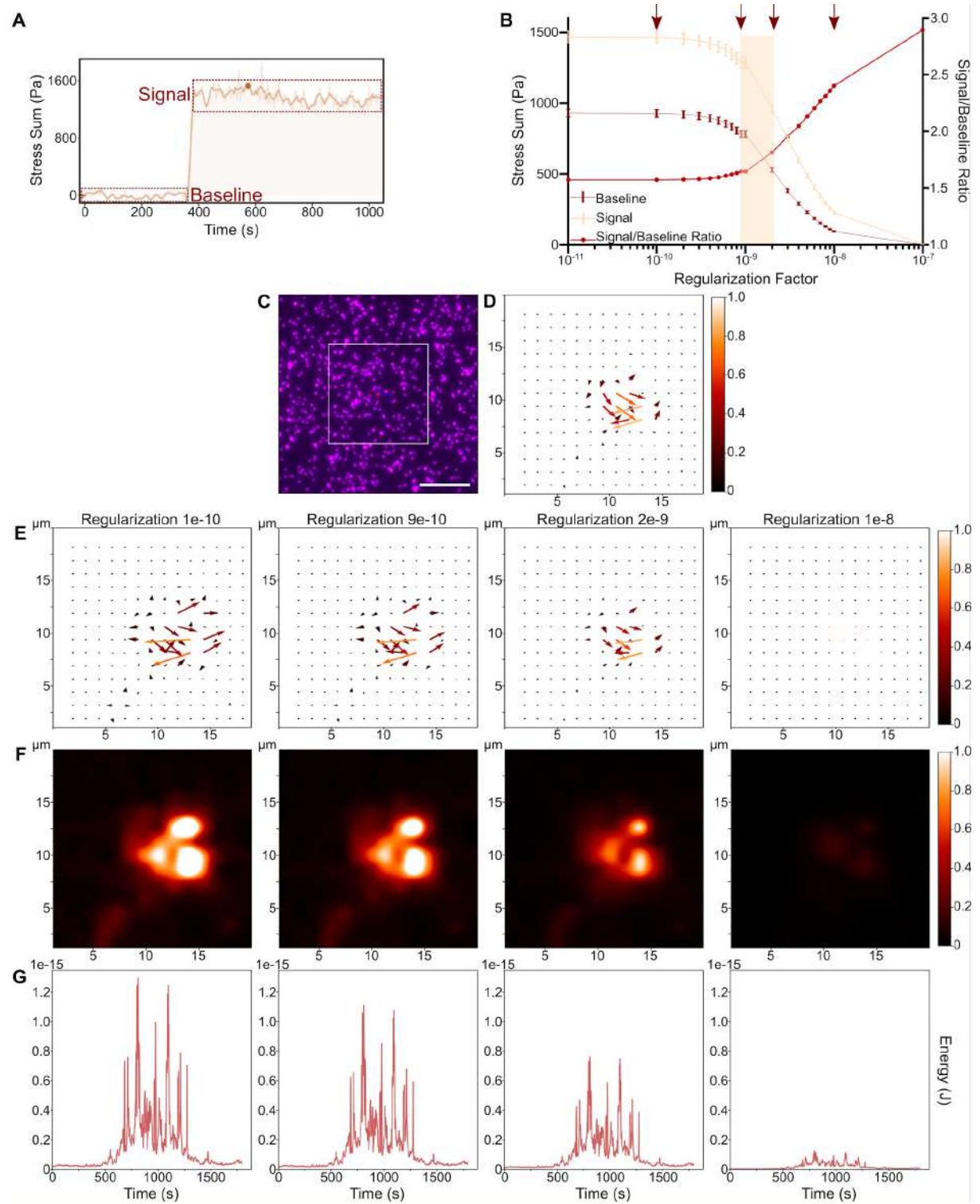


Fig. S4

